Nanotechnology in Catalysis

Volume 3

Nanostructure Science and Technology

Series Editor: David J. Lockwood, FRSC
National Research Council of Canada
Ottawa, Ontario, Canada

Current volumes in this series:

Alternative Lithography: Unleashing the Potentials of Nanotechnology
Edited by Clivia M. Sotomayor Torres

Interfacial Nanochemistry: Molecular Science and Engineering at Liquid–Liquid Interfaces
Edited by Hiroshi Watarai, Norio Teramae, and Tsuguo Sawada

Nanoparticles: Building Blocks for Nanotechnology
Edited by Vincent Rotello

Nanoscale Assembly: Chemical Techniques
Edited by Wilhelm T.S. Huck

Nanostructured Catalysts
Edited by Susannah L. Scott, Cathleen M. Crudden, and Christopher W. Jones

Nanotechnology for Electronic Materials and Devices
Edited by Anatoli Korkin, Jan Labanowski, Evgeni Gusev, and Serge Luryi

Nanotechnology in Catalysis, Volumes 1 and 2
Edited by Bing Zhou, Sophie Hermans, and Gabor A. Somorjai

Nanotechnology in Catalysis, Volume 3
Edited by Bing Zhou, Scott Han, Robert Raja, and Gabor A. Somorjai

Ordered Porous Nanostructures and Applications
Edited by Ralf Wehrspohn

Polyoxometalate Chemistry for Nano-Composite Design
Edited by Toshihiro Yamase and Michael T. Pope

Self-Assembled Nanostructures
Jin Z. Zhang, Zhong-lin Wang, Jun Liu, Shaowei Chen, and Gang-yu Liu

Self-Organized Nanoscale Materials
Edited by Motonari Adachi and David J. Lockwood

Semiconductor Nanocrystals: From Basic Principles to Applications
Edited by Alexander L. Efros, David J. Lockwood, and Leonid Tsybeskov

Surface Effects in Magnetic Nanoparticles
Edited by Dino Fiorani

A Continuation Order Plan is available for this series. A continuation order will bring delivery of each new volume immediately upon publication. Volumes are billed only upon actual shipment. For further information please contact the publisher.

Nanotechnology in Catalysis

Volume 3

Edited by

Bing Zhou

Headwaters Nano Kinetix, Inc.
Lawrenceville, New Jersey

Scott Han

Rohm & Haas Co.
Spring House, Pennsylvania

Robert Raja

University of Southampton
Southampton, United Kingdom

and

Gabor A. Somorjai

University of California
Berkeley, California

Springer

Bing Zhou
Headwaters Nano Kinetix, Inc.
1501 New York Avenue
Lawrenceville, NJ 08648
USA
bzhou@headwaters.com

Scott Han
Research Laboratories
Rohm & Haas Company
727 Norristown Road
Spring House, PA 19477
USA
shan@rohmhass.com

Robert Raja
Structural and Materials Chemistry
School of Chemistry
University of Southampton
Highfield
Southampton SO17 1BJ
UK
R.Raja@soton.ac.uk

Gabor A. Somorjai
Department of Chemistry
University of California at Berkeley
Berkeley, CA 94720
USA
somorjai@socrates.berkeley.edu

Series Editor:
David J. Lockwood
National Research Council of Canada
Ottawa, Ontario
Canada

Library of Congress Control Number: 2006926825

ISBN-10: 0-387-34687-2 e-ISBN-10: 0-387-34688-0
ISBN-13: 978-0387-34687-8 e-ISBN-13: 978-0387-34688-5

Printed on acid-free paper.

© 2007 Springer Science+Business Media, LLC
All rights reserved. This work may not be translated or copied in whole or in part without the written permission of the publisher (Springer Science+Business Media, LLC, 233 Spring Street, New York, NY 10013, USA), except for brief excerpts in connection with reviews or scholarly analysis. Use in connection with any form of information storage and retrieval, electronic adaptation, computer software, or by similar or dissimilar methodology now known or hereafter developed is forbidden.
The use in this publication of trade names, trademarks, service marks, and similar terms, even if they are not identified as such, is not to be taken as an expression of opinion as to whether or not they are subject to proprietary rights.

9 8 7 6 5 4 3 2 1

springer.com

Contributors

Xiaohui Cai, Alan G. MacDiarmid Institute, State Key Lab of Inorganic Synthesis & Preparative Chemistry, Jilin University, Changchun 130012, China

W. Geoffrey Chan, Philip Morris USA Research Center, 4201 Commerce Road, Richmond, VA 23234

Bert D. Chandler, Department of Chemistry, Trinity University, San Antonio, TX 78212

Valentino R. Cooper, The Makineni Theoretical Laboratories, Department of Chemistry, University of Pennsylvania, Philadelphia, PA 19104-6323

Sheng Dai, Chemical Sciences Division, Oak Ridge National Laboratory, Oak Ridge, TN 37831-6201

Blaise Didillon, RHODIA, PPD, P.O. Box 9837 Oldbury, West Midlands, B69 4WD, UK

Na Guo, Alan G. MacDiarmid Institute, Jilin University, Changchun, 130012, China

Ting Guo, Chemistry Department, University of California, One Shields Ave., Davis, CA 95616

Mohammad R. Hajaligol, Philip Morris USA Research Center, 4201 Commerce Road, Richmond, VA 23234

Graham J. Hutchings, School of Chemistry, Cardiff University, Cardiff CF10 3TB, UK

Luhua Jiang, Direct Alcohol Fuel Cell Laboratory, Dalian Institute of Chemical Physics, P.O. Box 110, Dalian 116023, China

Nancy Kariuki, Department of Chemistry, State University of New York at Binghamton, Binghamton, NY 13902

Timothy R. Kline, Department of Chemistry, The Pennsylvania State University, University Park, PA 16802

Alexie M. Kolpak, The Makineni Theoretical Laboratories, Department of Chemistry, University of Pennsylvania, Philadelphia, PA 19104-6323

Harold H. Kung, Department of Chemical and Biological Engineering, Northwestern University, Evanston, IL 60108-3120

Mayfair C. Kung, Department of Chemical and Biological Engineering, Northwestern University, Evanston, IL 60108-3120

Stephanie I-Im Lim, Department of Chemistry, State University of New York at Binghamton, Binghamton, NY 13902

Yan Lin, Department of Chemistry, State University of New York at Binghamton, Binghamton, NY 13902

Huifang Long, Department of Chemistry, Trinity University, San Antonio, TX 78212

Jin Luo, Department of Chemistry, State University of New York at Binghamton, Binghamton, NY 13902

Thomas E. Mallouk, Department of Chemistry, The Pennsylvania State University, University Park, PA 16802

Mathew M. Maye, Department of Chemistry, State University of New York at Binghamton, Binghamton, NY 13902

Donald E. Miser, Philip Morris USA Research Center, 4201 Commerce Road, Richmond, VA 23234

Derrick Mott, Department of Chemistry, State University of New York at Binghamton, Binghamton, NY 13902

Peter Njoki, Department of Chemistry, State University of New York at Binghamton, Binghamton, NY 13902

Steven H. Overbury, Chemical Sciences Division, Oak Ridge National Laboratory, Oak Ridge, TN 37831-6201

Thierry Pagès, IFP Solaize BP no. 3, 69390 Vernaison, France

Walter F. Paxton, Department of Chemistry, The Pennsylvania State University University Park, PA 16802

Andrew M. Rappe, The Makineni Theoretical Laboratories, Department of Chemistry, University of Pennsylvania, Philadelphia, PA 19104-6323

Paul Ratnasamy, National Chemical Laboratory, Pune 411008, India

Wolfgang M.H. Sachtler, Department of Chemistry and Institute for Environmental Catalysis, Northwestern University, Evanston, IL

Mark Schadt, Department of Chemistry, State University of New York at Binghamton, Binghamton, NY 13902

Ayusman Sen, Department of Chemistry, The Pennsylvania State University University Park, PA 16802

Eun-Jae Shin, Colorado School of Mines, Department of Chemical Engineering, Golden, CO 80401

Darbha Srinivas, National Chemical Laboratory, Pune 411008, India

Gongquan Sun, Direct Alcohol Fuel Cell Laboratory, Dalian Institute of Chemical Physics, P.O. Box 110, Dalian 116023, China

Denis Uzio, IFP Solaize BP no. 3, 69390 Vernaison, France

Stephan Verdier, RHODIA, CRA 52, rue de la Haie Coq 93308 Aubervilliers Cedex, France

Ce Wang, Alan G. MacDiarmid Institute, Jilin University, Changchun 130012, China

Lingyan Wang, Department of Chemistry, State University of New York at Binghamton, Binghamton, NY 13902

Suli Wang, Direct Alcohol Fuel Cell Laboratory, Dalian Institute of Chemical Physics, P.O. Box 110, Dalian 116023, China

Erik H. Williamson, Princeton University, Princeton Institute for the Science and Technology of Materials, 70 Prospect Avenue, Princeton, NJ 08540

Qin Xin, State Key Laboratory of Catalysis, Dalian Institute of Chemical Physics, P.O. Box 110, Dalian 116023, China

Wenfu Yan, Chemical Sciences Division, Oak Ridge National Laboratory, Oak Ridge, TN 37831-6201

Nan Yao, Princeton University, Princeton Institute for the Science and Technology of Materials, 70 Prospect Avenue, Princeton, NJ 08540

Yashar Yourdshahyan, The Makineni Theoretical Laboratories, Department of Chemistry, University of Pennsylvania, Philadelphia, PA 19104-6323

Chuan-Jian Zhong, Department of Chemistry, State University of New York at Binghamton, Binghamton, NY 13902

Bing Zhou, Headwaters NanoKinetix Inc., 1501 New York Avenue, Lawrenceville, NJ 08648

Zhenhua Zhou, Headwaters NanoKinetix Inc., 1501 New York Avenue, Lawrenceville, NJ 08648

Guangshan Zhu, Alan G. MacDiarmid Institute, State Key Lab of Inorganic Synthesis & Preparative Chemistry, Jilin University, Changchun 130012, China

Preface

Catalysts, heterogeneous, homogeneous, and enzyme, are usually nanoparticles. These are of vital for the functioning of the human body, for photosynthesis, and for producing fuels and chemicals in the petroleum and chemical industries. Interest in nanoscience and in nanotechnology in recent years has focused attention on the opportunity to develop catalysts that exhibit 100% selectivity for a desired product, thus removing byproducts and eliminating waste. This type of selective process is often called green chemistry or green technology.

This book is the third Volume of Nanotechnology in Catalysis. It is mainly based on the symposium on Nanotechnology in Catalysis III which was held in fall 2004 at the ACS 228th National Meeting in Philadelphia, PA. Several chapters were also from the authors who did not attend the symposium. We invited a few experts in the field to write on a topic which we see is needed to make the book comprehensive.

It has been about 2 years since Volumes 1 and 2 were published. Many new contributions and breakthroughs have been made by researchers worldwide, showing the dynamics in the area of nanotechnology in catalysis.

Nanotechnology has become a hot area globally since a few years ago. Governments and industry have steadily increased the investment in nanotechnology. The European Commission estimated that public funding for nanotechnology R&D has grown from 200 million euros in 1997 to 1 billion euros in 2005 (Electronic Chemicals News, June 30, 2005). In 2004, the US invested $1 billion, and China and Japan each invested almost $900 million in nanotechnology research and development. Globally in 2004 $8.6 billion was invested, $4.6 billion by governments and $4 billion by companies and venture capitalists (Business Voice, Vol. 6, No. 6, May 13, 2005).

Fundamentally, nanotechnology is about manipulating and making materials at the atomic and molecular level. While many people consider this a new field yielding cutting-edge applications to consumer products, catalysis researchers and the chemical industry have been working in this area for decades. What we call nanoparticle catalysis today actually began in the 1950s. This was a time when research labs, in an attempt to reduce the cost for large commercial applications, developed supported precious metal catalysts with particle sizes of less than 10 nm—"nanotechnology" is defined as the understanding and control of matter with dimensions less than 10 nm (National Nanotech Initiative, *What is Nanotechnology?*, *at* http://www.nano.gov/html/facts/whatIsNano.html).

In the following decades, researchers in catalysis turned their efforts to controlling molecular *structure* as well as size. The catalyst zeolite paved the way. In the late 1960s, researchers at Mobil Oil Co. were able to synthesize zeolite by deliberately designing and preparing the structure of catalysts at the atomic and molecular levels. The resulting nanostructured crystalline material (ZSM-5)—with a 10-atom ring and pore size of 0.45–0.6 nm—enabled the control of selectivity in petrochemical processes at the

molecular level. Such nanoparticle catalysts have revolutionized the petrochemical industry. Today, zeolite catalysts are used in processing over seven billion barrels of petroleum and chemicals annually.

Chemical catalysis research and development have been conducted at the nanoscale ever since. The recent development of advanced tools for characterizing materials at the nano- or sub-nanoscale provides scientists with new insights for understanding and improving existing catalysts and clues for ways to design new nanostructured materials for making better catalysts. The chemical industrial applications for these advances in nanocatalysis are significant and growing, and the market potential is only just beginning to be realized.

It is obviously a difficult task to cover all the aspects of a dynamic research area such as nanotechnology in catalysis. This book, together with Volumes 1 and 2 of Nanotechnology in Catalysis, has tried to include as much as possible the recent advances and breakthroughs in the area made by research groups all over the world. Through the editorial work, and by reading all the contributions, a guideline emerged. Although there is no clear cut guidelines to assign each contribution to well-defined sections, the topics can be grouped into the following four sections.

Section I reviews the new concepts and applications of nanotechnology for catalysis. Chapter 1 provides an overview on how nanotechnology impacts catalyst preparation with more control of active sites, phases, and environment of actives sites. The values of catalysis in advancing development of nanotechnology where catalysts are used to facilitate the production of carbon nanotubes, and catalytic reactions to provide the driving force for motions in nano-machines are also reviewed. Chapter 2 investigates the role of oxide support materials in modifying the electronic structure at the surface of a metal, and discusses how metal surface structure and properties influence the reactivity at molecular level. Chapter 3 describes a nanomotor driven by catalysis of chemical reactions.

Section II is about the new structure and understanding of nanocatalysts. Chapters 4 and 5 provide insight for understanding the structure and reactivity of gold catalyst. Chapters 6 and 7 disclose new methods for making nanoparticle catalysts in a control way by using the sol–gel technique and dendrimer template, respectively. Chapter 8 reviews the synthesis, structure, and applications of tungsten oxide nanorods.

Section III focuses on metal or metal oxide nanoparticle catalysts. By controlling the nanoparticle size and the environment where the nanoparticle is formed, several examples are described to show how the metal or metal oxide nanopartcle catalysts can be formed and how their unique structure and properties affect the chemical reaction they catalyze. These examples provide clues for understanding the nanoparticle catalysts, which may guide the future generation catalysts development.

Section IV emphasizes on nanoparticle catalysts for fuel cell applications. Fuel cell is a clean and desired future energy source. It is interesting to see that nanoparticle electrocatalysts play an important role in fuel cell development. Chapters 14 and 15 explore how nanoparticle catalysts can efficiently catalyze the reactions at anode and cathode of the fuel cells.

We want to acknowledge the American Chemical Society (ACS) Secretariat of Surface Science and Catalysis (CATL), the principal sponsor of the symposium on Nanotechnology in Catalysis. Thanks also extend to ACS Divisions of Colloid, Petroleum, and Industrial&Engineering Chemistry for cosponsoring the symposium. Financial

support from ACS Petroleum Research Fund, ACS Division of the Colloid Chemistry, Engelhard, Headwaters NanoKinetix, Inc. and Rohm&Haas is highly appreciated.

Last but not the least, we want to express our deep gratitude to Springer for the opportunity to publish this book. We believe that its vision in promoting science and technology will certainly improve the living standard of our society in the future.

Gabor A. Somorjai
Bing Zhou

Review Committee

Jingguang G. Chen
University of Delaware
Newark, DE

Martin Fransson
Headwaters NanoKinetix, Inc.
Lawrenceville, NJ

Ray Gorte
University of Pennsylvania
Philadelphia, PA

Ting Guo
University of California
Davis, CA

Scott Han
Rohm & Haas Company
Spring House, PA

Christopher Martin
Headwaters NanoKinetix, Inc.
Lawrenceville, NJ

Robert Raja
University of Southampton
Southampton, UK

Kelly Repoley
Headwaters NanoKinetix, Inc.
Lawrenceville, NJ

Michael Rueter
Headwaters NanoKinetix, Inc.
Lawrenceville, NJ

Brett Silverman
Headwaters NanoKinetix, Inc.
Lawrenceville, NJ

Gabor A. Somorjai
University of California
Berkeley, CA

Horacio Trevino
Headwaters NanoKinetix, Inc.
Lawrenceville, NJ

Nan Yao
Princeton University
Princeton, NJ

Cheng Zhang
Headwaters NanoKinetix, Inc.
Lawrenceville, NJ

Chuan-Jian Zhong
State University of New York at Binghamton
Binghamton, NY

Bing Zhou
Headwaters NanoKinetix, Inc.
Lawrenceville, NJ

Contents

Volume 3

Section I
New Concept and Applications of Nanotechnology for Catalysis

Preface .... **ix**

CHAPTER 1. Nanotechnology and Heterogeneous Catalysis **1**

Harold H. Kung and Mayfair C. Kung

1.1. Introduction 1
1.2. Nanotechnology for Catalysis 2
1.2.1. Synthesis of Metal Active Sites and Oxide Active Phases 2
1.2.2. Environment Around an Active Site 5
1.2.3. Nanoreactors 6
1.3. Catalysis for Nanotechnology 8
1.4. Conclusion 9

CHAPTER 2. Oxide-Supported Metal Thin-Film Catalysts: The How and Why **13**

Valentino R. Cooper, Alexie M. Kolpak, Yashar Yourdshahyan and Andrew M. Rappe

2.1. Introduction 13
2.1.1. The Theory of Molecular Adsorption on Metal Surfaces 14
2.2. Methodology 15
2.3. Co Chemisorption to Alumina-Supported Pt Thin Films 16
2.3.1. CO Binding to Transition Metal Surfaces 16
2.3.2. Metallic Deposition on an Electronegative Support: Pt/O_T 17
2.3.3. Correlating Chemisorption Trends with Shifts in DOS 18
2.4. Summary/Conclusion 19

CHAPTER 3. Developing Catalytic Nanomotors **23**

Timothy R. Kline, Walter F. Paxton, Thomas E. Mallouk, Ayusman Sen

3.1. Background 23
3.1.1. Externally Driven Methods for Movement 23
3.1.2. Self Driven Methods for Movement 24
3.2. Synthetic Catalytic Motors 25
3.2.1. Background 25
3.2.2. Fabrication of the Motor 25
3.2.3. Analyzing the Motor Movement 26
3.2.4. Mechanism for Movement 28
3.3. Evolution of Catalytic Motors 31
3.3.1. Microfabricated Motors 31
3.3.2. Remotely Steered Motors 31
3.4. Possible Applications 35
3.4.1. Biomedical 35
3.4.2. Roving Sensors 35
3.5. Conclusion 35

Section II
New Methods, Structure and Understanding of Nanocatalysts

CHAPTER 4. Catalysis by Gold: Recent Advances in Oxidation Reactions **39**

Graham J. Hutchings

4.1. Introduction 39
4.2. Background: Early Work on Gold Catalyst 40
4.2.1. Ethyne Hydrochlorination 40
4.2.2. Carbon Monoxide Oxidation 43
4.3. Low Temperature Co Oxidation: Nature of the Active Site 45
4.4. Competitive Oxidation of Carbon Monoxide in the Presence of Hydrogen 47
4.5. Oxidation of Alcohols 48
4.6. Selective Oxidation of Hydrogen to Hydrogen Peroxide 50
4.7. Concluding Comments 51

CHAPTER 5. Gold Catalysts Supported on Nanostructured Materials: Support Effects **55**

Wenfu Yan, Steven H. Overbury, and Sheng Dai

5.1. Introduction 55
5.2. Experimental Section 56
5.2.1. Preparation of Gold Nanocatalysts Supported on Anatase and Brookite 56
5.2.2. Preparation of Gold Nanocatalysts Supported on Mesoporous Silica Modified with Oxide Monolayer 57

5.2.3. Preparation of Gold Nanocatalysts Supported on Silica Modified with Oxide Double Layers 57
5.2.4. Measurements of Catalytic Performance for CO Oxidation 58
5.2.5. Characterization Methods 58
5.3. Results and Discussion 59
5.3.1. Support Effects from Structural Differences of the TiO_2 Allotropes (Anatase and Brookite) 59
5.3.2. Support Effects from Surface-Modified Mesostructured Substrates 62
5.3.3. Support Effects from the Different Combinations of Oxide Monolayers Sequentially Coated on the Surface of Amorphous Silica 65
5.4. Conclusions 68

CHAPTER 6. Highly Effective Nanocatalysts Prepared Through Sol–Gel Technique 73

Guangshan Zhu, Ce Wang, Na Guo and Xiaohui Cai

6.1. Highly Effective Sulfated Zirconia Nanocatalysts Grown out of Colloidal Silica At High Temperature 73
6.1.1. Introduction 73
6.1.2. Experimental Section 74
6.1.3. Results and Discussion 75
6.2. Ag/SiO_2 Composite Nanocatalysts 81
6.2.1. Introduction 81
6.2.2. Experimental Section 82
6.2.3. Results and Discussion 84

CHAPTER 7. Dendrimer Templates for Supported Nanoparticle Catalysts 91

Huifang Lang and Bert D. Chandler

7.1. Introduction 91
7.1.1. Traditional Routes to Supported Metal Nanoparticle Catalysts 92
7.1.2. Molecular Clusters as Precursors to Supported Metal Catalysts 92
7.1.3. Applying Nanotechnology to the Catalytic Sciences 93
7.2. Dendrimers and Dendrimer Encapsulated Nanoparticles (DENs) 94
7.3. Homogeneous Catalysis by DENs 97
7.4. Immobilization & Deposition of DENs 98
7.4.1. Deposition onto Preformed Supports 98
7.4.2. Sol–Gel Immobilization 99
7.5. Activation and Dendrimer Removal 99
7.5.1. Immobilized In-tact DENs 99
7.5.2. Activation Conditions 100

7.6. Dendrimer Templated Heterogeneous Catalysts 103
7.6.1. Catalysis by Platinum 103
7.6.2. Bimetallic Catalysts 105
7.6.3. Evaluating Support Effects 108
7.7. Summary and Conclusions 110

CHAPTER 8. Tungsten Oxide Nanorods: Synthesis, Characterization, and Application 115

Erik H. Williamson and Nan Yao

8.1. Introduction 115
8.2. Tungsten–Oxygen Chemistry 116
8.2.1. Oxidation and Reduction of Tungsten and Tungsten Oxides 116
8.2.2. Thermodynamic and Kinetic Properties of WO_x Reactions 118
8.3. Synthetic Methods to $WO_{2.72}$ Nanorods 120
8.4. Crystal Structure and Growth 124
8.5. Applications of $WO_{2.72}$ and Other Tungsten Oxides 126
8.5.1. Electro-Optical Properties and Quantum Confinement 126
8.5.2. Use as Gas Sensors 129
8.5.3. Tungsten Oxide Nanorods as Field Emitters 131
8.5.4. Tungsten Oxide as a Catalyst 131
8.5.5. Tungsten Oxide and Titanium Oxide as a Heterocatalyst 133
8.5.6. Tungsten Oxide and Titanium Oxide as Colloids 134
8.6. Conclusion 135

Section III
Nanoparticles Catalysts

CHAPTER 9. Catalysis by Metal and Oxide Nanoparticles, Single Metal Atoms and Di-Nuclear Oxo-Ions in Zeolites 139

Wolfgang M. H. Sachtler

9.1. Introduction 139
9.2. Supported Metal Clusters 140
9.3. Chemical Anchoring and De-Anchoring 143
9.4. Monoatomic Platinum in Zeolites 145
9.5. Transition Metal Oxides and Oxo-Ions 147
9.6. Conclusions 149

CHAPTER 10. A Dual Catalytic Role of Co Nanoparticles in Bulk Synthesis of Si-Based Nanowires 153

Ting Guo

10.1. Background 153
10.1.1. Overview 153

10.1.2. Silicon-Based Nanowires 154
10.1.3. Outline of This Chapter 158
10.2. Experimental Details 158
10.2.1. Nanoparticle Synthesis 159
10.2.2. Analytical Methods 160
10.3. Results 161
10.3.1. Nanoparticle Deposition on Si and Al_2O_3 Wafers 161
10.3.2. Nanowires Formation 162
10.3.3. Composition of Nanowires 167
10.3.4. Growth of Nanowires 170
10.4. Discussion 174
10.4.1. Composition and Morphology of the Silicon Nanowires 174
10.4.2. Growth Mechanisms 174
10.5. Future Work 178

CHAPTER 11. Influence of Particle Size and Interaction with the Support on Redox and Catalytic Properties of Metals, Metal Oxides, and Metal Complexes 183

Darbha Srinivas and Paul Ratnasamy

11.1. Introduction 183
11.2. Supported Metals 184
11.2.1. Ni–CeO_2–ZrO_2 for Steam Reforming 185
11.2.2. Au and Au–Pt Bimetallic Nanoparticles in MCM-41 for Preferential Oxidation of CO in the Presence of H_2 195
11.2.3. Pt- and Pd-TS-1 for Selective Oxidation 196
11.3. Supported Metal Oxides 200
11.3.1. CuO–CeO_2–ZrO_2 for Preferential Oxidation of CO 200
11.4. Metal Complexes Encapsulated in Molecular Sieves 208
11.4.1. Dimeric Copper Acetate Complexes 208
11.4.2. Transition Metal Salen Complexes 211
11.5. Summary and Conclusions 214

CHAPTER 12. Thermo-Catalytic Oxidation of Dihydroxybenzenes in the Presence of Nanoparticle Iron Oxide 221

Eun-Jae Shin, Mohammad R. Hajaligol, Donald E. Miser, and W. Geoffrey Chan

12.1. Introduction 221
12.2. Experimental 222
12.2.1. Material and Characterization Procedure 222
12.2.2. Reactor Setup and Procedure for Oxidative Cracking 223
12.3. Results and Discussion 225
12.3.1. Characterization of the Iron Oxide Before and After Use 225
12.3.2. Decomposition of the Reactants 234
12.3.3. Product Distributions 236

12.3.4. Effects of Oxygen 241
12.3.5. Factor Analysis 243
12.4. Conclusion 252

CHAPTER 13. Synthesis of Palladium-Based Supported Catalysts by Colloidal Oxide Chemistry 255

Blaise Didillon, Thierry Pagès, Stephan Verdier, and Denis Uzio

13.1. Introduction 255
13.2. Synthesis of Monometallic Catalysts 258
13.2.1. Synthesis of Palladium Oxide Hydrosols 258
13.2.2. Synthesis of Tin Oxide Hydrosols 267
13.2.3. Alumina-Supported Palladium Catalyst 271
13.3. Bimetallic Catalysts Prepared by Colloidal Synthesis 274
13.3.1. Palladium–Tin Catalysts 274
13.3.2. Palladium–Silver Catalysts 278
13.4. Application to Catalysis: Selective Hydrogenation Reactions 280
13.4.1. Hydrogenation of Phenylacetylene on Pd Monometallic Catalysts 280
13.4.2. Hydrogenation of Butadiene on Bimetallic Palladium–Tin Catalysts 281
13.4.3. Hydrogenation of Acetylene on Bimetallic Palladium–Silver Catalysts 284
13.5. Conclusion 284

Section IV
Nanoparticle Catalysts for Fuel Cell Applications

CHAPTER 14. Gold-Based Nanoparticle Catalysts for Fuel Cell Reactions 289

Chuan-Jian Zhong, Jin Luo, Mathew M. Maye, Nancy Kariuki, Lingyan Wang, Derrick Mott, Peter Njoki, Mark Schadt, Stephanie I-Im. Lim, and Yan Lin

14.1. Introduction 289
14.2. Experimental 292
14.3. Characterizations of Nanostructured Catalysts 292
14.3.1. Size and Composition 292
14.3.2. XRD Characterization 294
14.3.3. FTIR Characterization of CO Adsorption 296
14.4. Electrocatalytic Activity of Nanostructured Catalysts 298
14.4.1. Electrocatalytic Reduction of Oxygen 298
14.4.2. Electrocatalytic Oxidation of Methanol 300
14.5. Conclusion 302

CHAPTER 15. Carbon-Supported Core-Shell PtSn Nanoparticles: Synthesis, Characterization and Performance as Anode Catalysts for Direct Ethanol Fuel Cell **309**

Luhua Jiang, Gongquan Sun, Suli Wang, Qin Xin, Zhenhua Zhou, and Bing Zhou

15.1. Introduction 309
15.2. Experimental Details 310
15.2.1. Chemicals 310
15.2.2. Preparation of Catalyst 311
15.2.3. Physical Chemical Characterizations 311
15.2.4. Electrochemical Characterization 312
15.2.5. Single-Cell Performance Tests 312
15.3. Results and Discussion 313
15.4. Conclusions 322

Index **325**

1

Nanotechnology and Heterogeneous Catalysis

Harold H. Kung* and Mayfair C. Kung

1.1. INTRODUCTION

Worldwide in the past decade, nanoscience and nanotechnology has become a popular field for research and development. As an example to explain its potential significance, heterogeneous catalysis was cited as a successful application that has great benefits for society. Thus, it is reasonable to expect that the explosion in new developments in nanoscience and nanotechnology would have a significant impact on the understanding, practice, and applications of catalysis. In this paper, a brief account is presented using selected examples to illustrate ways that these recent developments have advanced heterogeneous catalysis, both in terms of better control of heterogeneous catalytic processes, and of applying catalysis to developments in nanotechnology.

According to the U.S. National Nanotechnology Institute,[1] nanotechnology encompasses research and development to synthesize, control, and manipulate structures, devices, and systems of novel properties and functions because of their size at the atomic, molecular, or macromolecular levels in the length scale ranging from approximately 1 to 100 nanometers. Indeed, this length scale is of particular relevance to heterogeneous catalysis, where the active sites are small crystallites or domains of the active phase. The reaction typically involves atom-molecule interactions, and the active sites are placed in or on an extended solid where the access paths to the active sites are tens to hundreds of nanometers. The issue of access path is a familiar territory in

Department of Chemical and Biological Engineering, Northwestern University, Evanston, IL 60108-3120

* To whom correspondence should be addressed. E-mail: hkung@northwestern.edu

heterogeneous catalysis: zeolites are a type of widely applied catalysts, which derive much of their unique catalytic function by shape-selectivity. This is done by distinguishing molecules by their different diffusivities in and out of a zeolite particle due to their shapes and sizes relative to the channels, pores and cages of the zeolite. The shape constraint occurs far away from the active site and influences the reaction by controlling access to the active site. In recent years, new examples emerge that demonstrate other ways the environment affects a catalytic reaction.

In this brief overview, we will use selected examples to illustrate how nanotechnology impacts catalyst preparation and ways that catalytic reactions can be conducted. We will also discuss the impact of catalysis on nanotechnology using examples where catalysts are used to facilitate preparation of nanostructures and nanomaterials, and to produce motion in nanomachines.

1.2. NANOTECHNOLOGY FOR CATALYSIS

The long history of successful commercialization of catalysis is accompanied by the development of many different methods to prepare catalysts in an attempt to optimize their properties. However, in spite of the effort, the ability to custom design *active sites* and *site environments for perfect selectivity and desirable activity* continues to be a goal yet to be reached. The ultimate "control" of a catalytic process remains a great challenge. New techniques made available by nanotechnology have resulted in some progress toward achieving this goal. This can be illustrated by examples in the following three areas:

- Synthesis of metal active sites and oxide active phases.
- Effecting control of the environment around active sites.
- Constructing nanoreactors.

1.2.1. Synthesis of Metal Active Sites and Oxide Active Phases

It is well established that commercially important supported noble metal catalysts contain small metal crystallites that are typically smaller than a few nanometers. The surface of these crystallites is populated by different types of metal atoms depending on their locations on the surface, such as corners, edges, or terraces. In "structure sensitive" reactions, different types of surface metal atoms possess quite different properties. For example, in the synthesis of ammonia from nitrogen and hydrogen, different surface crystallographic planes of Fe metal exhibit very different activities.[2] Thus, one of the most challenging aspects in metal catalysis is to prepare samples containing metal particles of uniform shape and size. If the active phase is multicomponent, then it is also desirable to prepare particles of uniform composition.

A recently developed method to prepare particles of a narrow size distribution is the dendrimer-assisted method.[3] In this method (Fig. 1.1), metal ions in a solution are complexed to a dendrimer, mostly with the amine groups in the outer shell of an OH-terminated poly(amidoamine), for example.[4] The complexed metal ions are subsequently reduced to metal atoms which agglomerate into a metal particle. Because dendrimers can be prepared with high purity, and there is a strong binding of metal ions

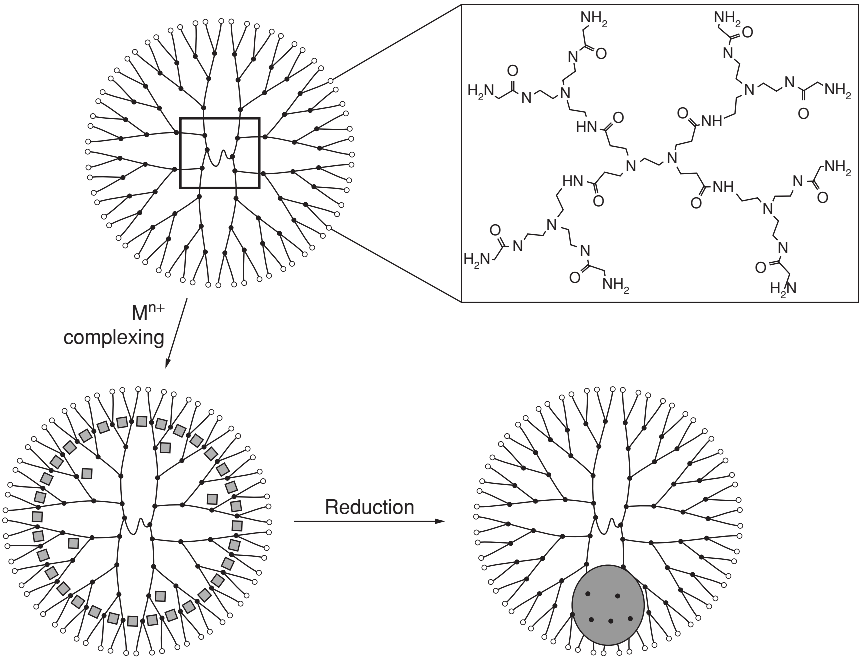

FIGURE 1.1. Schematic drawing of the dendrimer-assisted preparation of uniform-sized metal particles. Metal ions (Mn^+) are first complexed to a 4th generation OH-terminated poly(amidoamine) dendrimer. Then the metal ions are reduced to a metal particle, isolated from other metal particles.

to the amine groups such that there is only a small variation in the metal/amine ratio, the metal particle formed within each dendrimer is quite uniform in size. For example, the Pt particles prepared by this method show a much narrower size distribution than those prepared by conventional methods.[5] Because dendrimers can be prepared with different numbers of metal binding sites (e.g. different generations of dendrimer), this method offers the possibility of preparing uniform-sized metal particles over a wide range of sizes. This is an advantage compared with preparation using well-defined organometallic complexes, which is limited by the availability of metal complexes.

The dendrimer-assisted method can be extended to bimetallic clusters. The second metal ion can be introduced by partial displacement of the first metal, or sequentially after the first, or together with the first by cocomplexation.[3] Although these methods succeed in making bimetallic particles, it is not obvious that they can generate uniform composition particles. Thus, new methods or variations of the existing method have to be developed.

Making uniform nano-sized metal oxide particles is also of interest. Such particles could have a higher specific surface area and a higher density of surface defects than those made by conventional preparation methods. This could be beneficial to their catalytic properties. If the oxide particle is multi-component, then such nano-sized particles, each containing the various components would provide more intimate contact or

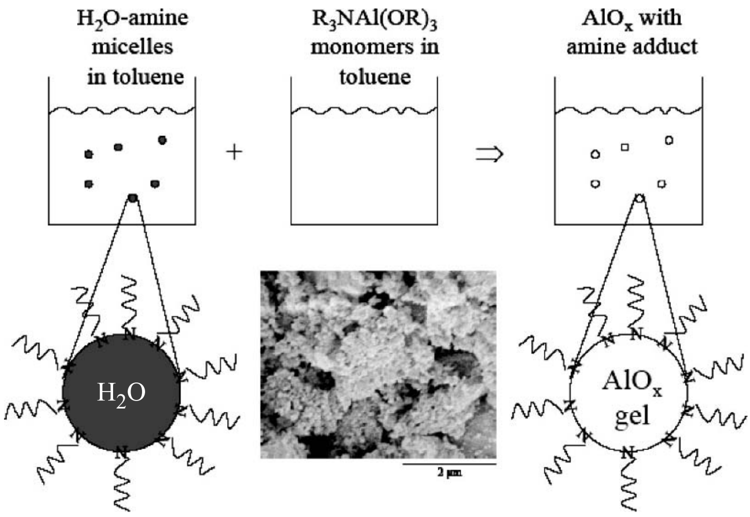

FIGURE 1.2. Formation of nanoparticles of metal oxide by reverse micelle method. A solution of inverse micelles is first formed by adding a long-chain alkylamine to a toluene solution. A small amount of water is trapped in the reverse micelle core. Mixing the reverse micelle solution with an aluminum alkoxy amine adduct results in hydrolysis of the aluminum alkoxide adduct and formation of nano-sized particles of aluminum oxyhydroxide after drying. These particles are shown in the SEM picture above.

better mixing of the components, such that the final product could be compositionally more uniform with less severe processing conditions (e.g. lower calcination temperature). One method to prepare metal oxide nanoparticles involves using reverse micelles. When a surfactant molecule that possesses a polar head group and a hydrophobic tail is placed in a nonpolar solvent, the surfactant molecules would aggregate into nano-sized, spherical structures of a core of polar headgroups and a shell of hydrophobic tails. Such a structure is a reverse micelle. If a small amount of polar solvent is present in the mixture, it would be enclosed in the core of the reverse micelles. If this polar solvent is an alcohol and it contains an oxide precursor such as a metal alkoxide, controlled hydrolysis of the precursor achieved by mixing in a small amount of water would generate a small particle of oxyhydroxymetal gel in the reverse micelle. After drying and calcination, small particles of metal oxide are obtained (Fig. 1.2). The SEM micrograph insert in Fig. 1.2 shows nanoparticles of aluminum oxide obtained by this method. Other examples, such as small particles of barium hexaaluminate, have been reported, and they demonstrate higher activity for methane combustion than those prepared by conventional methods.[6]

A variation of this method was used to control the surface properties of aluminum oxide particles, particularly the surface density of Lewis acid sites. Instead of using a long-chain amine surfactant, the solution of aluminum alkoxide precursor was mixed with a small amine to convert the alkoxide dimer (or oligomer in general) into monomeric alkoxide-amine adduct. Controlled hydrolysis of this adduct produces an aluminum oxyhydroxide in which the surface Al ions are coordinated to amine

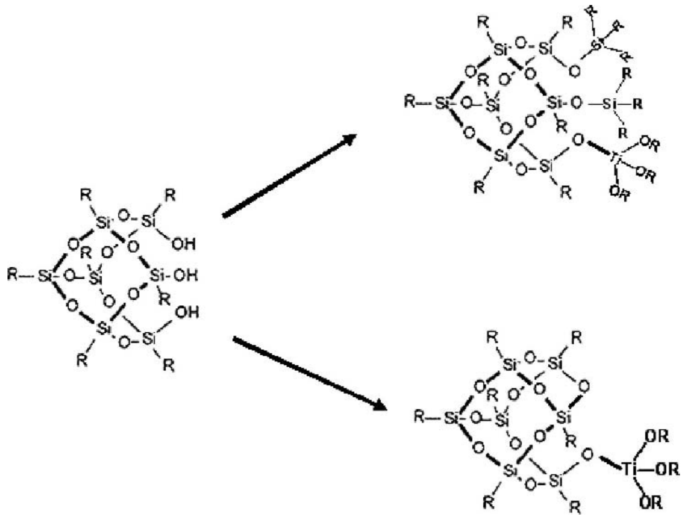

FIGURE 1.3. Effect of environment on the catalytic active site. The active center of a Ti alkoxide is bonded to one of the three hydroxyl groups of an incompletely condensed silsesquioxane. If the other two hydroxyl groups condense with each other (bottom scheme), the steric hindrance to the active site is much less than if they are converted to alklylsilane groups (top scheme). The latter is significantly less active than the less hindered active site.

molecules. That is, the Lewis acid sites of surface Al ions are coordinated to the amine.[7] This alumina, although prepared and used without being heated to higher than 70°C, is five times more active for aminolysis of epoxide than a conventional sol–gel preparation of alumina activated by heating to 500°C.[8]

1.2.2. Environment Around an Active Site

In homogeneous catalysis, the effect of steric hindrance by the ligands on the catalytic properties of the metal center is well established. Likewise, the effect of binding groups provided by amino acids far from the active site of an enzyme is also well known. In recent years, there have been an increasing number of examples in heterogeneous catalysis where the environment exerts an effect on an active site in a conceptually similar manner. One example is from modified silsesquioxane. Figure 1.3 shows an incompletely condensed silsesquioxane. The three hydroxyl groups are close to each other and can be converted to other groups by reaction with, for example a metal alkoxide. In the example shown in Fig. 1.3, one of the hydroxyl groups is converted to a titanium alkoxy group, and the other two are either converted to trimethylsiloxane or condensed with each other. The trimethylsiloxane groups are much bulkier, and they sterically hinder the approach of reactant molecules to the Ti alkoxide. Consequently, the former catalyst is much less active in the epoxidation of cyclohexene.[9] Thus, catalysis by the Ti active center can be affected by groups not directly bonded to the center.

Another example, also making use of the consequence of steric effects, is the hydrogenation of an unsaturated acid over a Rh or Pd complex. When a Rh complex, such as one with bidentate amine and norbonadiene ligands, is placed in a channel of about 3 nm diameter found in a MCM-41 material, access to the Rh center is restricted by the concave wall of the channel.[10] Thus, in the hydrogenation of E-α-phenylcinnamic acid, a higher enantioselectivity is obtained than in the homogeneous solution because the bulky phenyl groups of the cinnamic acid prefer to point away from the concave surface when approaching the Rh center. If the Rh complex is placed on a convex surface, such that the effect of the presence of the wall would be absent, then a similar enantioselectivity as in the homogeneous solution was obtained. Since it is possible to tune the diameter of a MCM-41 material,[11] these results suggest that it is possible to control the reaction selectivity using the environment provided by the channel walls.

In addition to steric effects, which make use of repulsive interactions between a reactant molecule and the environment of the active site, it is also possible to make use of attractive interactions. An example of this is the selective terminal activation of hexane by Co-AlPO. The high selectivity in the oxidation of hexane to 1,6-hexanediacid over a Co-AlPO (Co/Al = 0.1) catalyst was attributed to the attractive interaction of the hexane molecule with the cage wall of AlPO, orienting the molecule in such a way that the two terminal carbons are in close proximity to the two Co atoms.[12]

In these examples, the effect of the environment on the active sites is provided by the channel of the mesoporous MCM-41 material or the cavity of the molecular sieve. Because there are a limited number of such materials, there is also a limited variety of environments available for use or manipulation. Thus, it is desirable to be able to construct cages in ways that could offer the needed flexibility to modify the cage size, access window size, and the cage walls so that functional groups can be attached at specific positions. Such flexibility would enable the positioning of different active sites and reactant binding sites at specific locations with respect to each other, such that specific points of a reactant molecule can be activated. A possible approach in order to achieve this is to build the cage one siloxane unit at a time. To do so, new synthetic routes need to be developed, and recent progress in this direction has been encouraging. It is now possible to construct bicyclic siloxane compounds in which one can custom design the length of each siloxane bridge.[13] Figure 1.4 shows an example of such a cage, a bicyclo[7.5.3]octasiloxane, in which the three bridges emerging from the bridge heads contain one, two, and three siloxane units. An exciting aspect of this approach is that it is possible, in principle, to attach functional groups at any of the Si atoms on the bridges.[14]

1.2.3. Nanoreactors

As one increases the size of the cages, the cavity becomes sufficiently large to be used as a nanoreactor. In fact, nanometer size capsules or spheres made of lipid bilayers have been investigated for other applications including drug delivery.[15] However, without modification, such vesicles are probably not suitable as reactors since the lipid bilayer is rather fluid, and the lipid molecules exchange with free lipids in solution. In order to use such vesicles as reactors, it is necessary to convert them into a robust

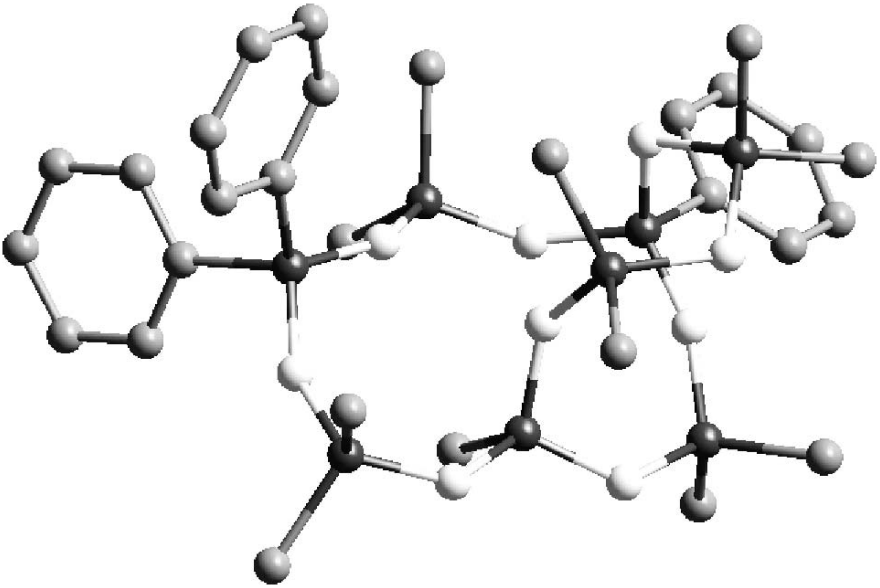

FIGURE 1.4. Structure (hydrogen atoms omitted) of a bicycle siloxane,1,5,5-triphenyl-3,3,7,7,9,11,11, 13,13, 16,16-undecamethylbicyclo[7.5.3]octasiloxane, synthesized using a stepwise method. White: oxygen; black: Si; grey: carbon.

structure. One approach is to use lipid molecules that contain conjugated carbon double bonds that can be photopolymerized, such as 10,12-pentacosadiynol.[16] Photopolymerization cross-links the lipid molecules and converts the vesicle into a robust structure. Other work indicates that it is possible to enclose smaller vesicles in a larger one,[17] opening up the possibility of conducting different reactions in separate compartments in a predetermined order.

In addition to mesoporous MCM-41 type of materials, there are now other ways to make nano-sized channels and tubes. One is by anodization of alumina under controlled conditions. Micrometer length, nanometer diameter, and regularly patterned channels can be grown as a thin layer on an aluminum substrate, which can be removed by dissolution to generate a thin, porous membrane.[18] The channel surface of the alumina is covered with hydroxyl groups, which can be used to react with metal complexes to deposit an atomic layer of metal oxide. By repeating this procedure, fine control of the channel diameter is achieved.[19] Since a variety of metal complexes can be used, this method can also be used to form channels coated with different oxide layers, significantly broadening the library of oxide channels.

Carbon nanotubes have nano-sized channels that have received significant attention in recent years, and there are rapid advances in techniques to produce them. However, currently researchers are still learning how to isolate, manipulate, and reduce the variations in the properties of these carbon nanotubes. Nonetheless, their potential in catalytic applications is evident. For example, it is possible to trap catalytic active sites inside a carbon nanotube.[20] In other developments, methods have been discovered

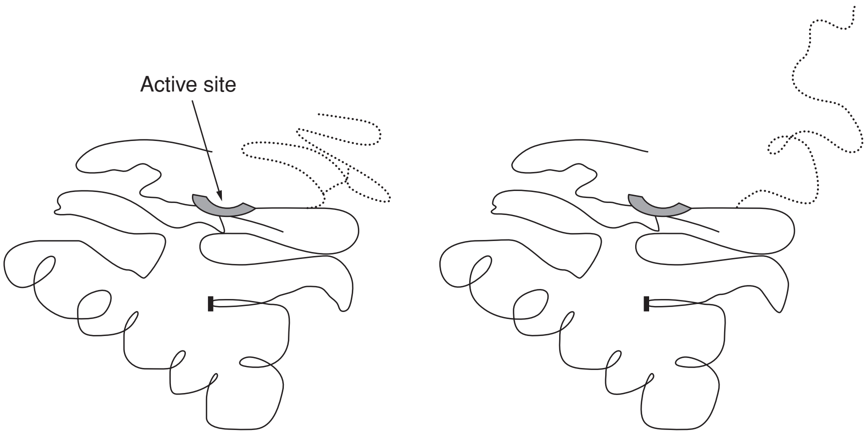

FIGURE 1.5. Schematic drawing showing the use of a temperature sensitive polymer to control access to the active sites of an enzyme. Access is denied when the polymer (dotted line) is in the crystalline state (left), and allowed when the polymer is in the flexible state (right).

to control access to nanotube channels. For example, the inlet of the tube can be functionalized with biotin that can coordinate streptavidan and block transport in and out of the channel.[21] The concept of turning on and off a catalytic site by controlling its access path has been demonstrated in enzyme catalysis. When a temperature-responsive polymer was strategically attached to the endoclucanase, it was shown that the enzymatic activity can be greatly reduced by warming the mixture past the transition temperature where the flexible polymer becomes crystalline, since the crystalline form of the polymer blocks the active site from the reactant (Fig. 1.5).[22] Lowering the temperature reconverts the polymer into the flexible form and recovers the enzymatic activity.

1.3. CATALYSIS FOR NANOTECHNOLOGY

One area where catalysis has made a significant impact is in the production of carbon nanotubes. Although carbon nanotubes possess many unusual properties including high mechanical strength and tunable electrical conductivity, attempts to incorporate them into devices have been limited by the fact that there is not a good method of production to form carbon nanotubes with uniform properties. The properties of a carbon nanotube depend on the diameter and chirality of the tube, as well as whether it is single-walled or multi-walled. Fortunately, many advances have been reported recently. In the earlier preparations, the carbon nanotubes were formed by plasma assisted pyrolysis or hydrogenolysis of hydrocarbons or carbon-containing species. Later, catalytic hydrogenolysis of hydrocarbons was found to be superior. Since the diameter of the nanotube is closely related to the particle size of the metal catalyst, the ability to generate uniform-size metal particles has enabled production of uniform diameter nanotubes.[23] By changing the composition of the catalyst particle, it is also possible to produce either single-walled or multi-walled nanotubes.[24,25]

Another application of catalysis is to use catalytic reactions to provide the driving force for motions in nanostructures. This concept has been demonstrated in a recent publication which reports using the hydrogen peroxide decomposition reaction as a source of motion. In this example, tiny Au rods were coated on one end with Pt,[26] and when the tiny rods were submerged in a solution containing hydrogen peroxide, the platinum catalyzed the decomposition of the peroxide. This led to a change of the surface tension at one end of the rod and propelled the rod in the solution. One can imagine that catalytic reactions can be used to generate motion in parts or components of nanomachines.

1.4. CONCLUSION

The recent advances in nanotechnology, particularly when coupled with fundamental understanding of the techniques and phenomena, have opened new avenues for catalytic technology. The few examples mentioned in this chapter serve to illustrate that control of catalytic systems, at the molecular and atomic level, has been achieved in some systems and is within reach in others. Clearly, there are many more opportunities for improvement, especially in controlling the details of the active sites, such as their compositions and atomic arrangements, but advances in nanotechnology have demonstrated that it is now also possible to control a catalytic reaction by controlling the environment around the active site. In other words, researchers are beginning to control heterogeneous catalytic reactions in similar ways to what have been commonly practiced in homogeneous catalysis using organometallic complexes and in enzymatic catalysis, yet in ways that are more versatile because of the flexibility that many inorganic and organic-inorganic hybrid materials offer. It should be feasible to begin thinking about turning on and off catalytic active sites at will, and tuning selectivity of a reaction by design.

Equally exciting are examples of contributions of heterogeneous catalysis to advances in the field of nanotechnology. While this area is very much in its infancy, as nanotechnology achieves a wider range of applications, there will be more and more possibilities of impact. Nanomachinery is an application well suited for heterogeneous catalysis, since catalytic reactions can provide the energy to power such machines. It would not be surprising if this area will attract a great deal of interest in the near future.

ACKNOWLEDGMENT

Support of this work is provided by the U.S. Department of Energy, Department of Science, Chemical Sciences.

REFERENCES

1. http://www.nano.gov/html/facts/whatIsNano.html, December 30, 2004.
2. F. Zaera, A. J. Gellman, and G. A. Somorjai, Surface science studies of catalysis: classification of reactions, *Acc. Chem. Res.* **19,** 24 (1986).

3. R. M. Crooks, M. Zhao, L. Sun, V. Chechik, and L. K. Yeung, Dendrimer-encapsulated metal nanoparticles: Synthesis, characterization, and applications to catalysis, *Acc. Chem. Res.* **34,** 181 (2001).
4. M. Zhao, L. Sun, and R. M. Crooks, Preparation of Cu nanoclusters within dendrimer templates, *J. Am. Chem. Soc.* **120,** 4877 (1998).
5. H. Lang, R. A. May, B. L. Iverson, and B. D. Chandler, Dendrimer-encapsulated nanoparticle precursors to supported platinum catalysts, *J. Am. Chem. Soc.* **125,** 14832 (2003).
6. A. J. Zarur, and J. Y. Ying, *Nature* **403,** 65 (2000).
7. A. I. Kozlov, M. C. Kung, W. M. Xue, and H. H. Kung, A "soft-chemical" method to synthesize Lewis acid surfaces of aluminum oxide, *Angew. Chem. Int. Ed.* **42,** 2415 (2003).
8. W. M. Xue, M. C. Kung, A. I. Kozlov, K. E. Popp, and H. H. Kung, Catalytic aminolysis of epoxide by alumina prepared from amine-protected Al precursor, *Catal. Today* **85**(24), 219 (2003).
9. M. C. Klunduk, T. Maschmeyer, J. M. Thomas, and B. F. G. Johnson, The influence of steric congestion on the catalytic performance of Ti^{IV} active centers in the epoxidation of alkenes, *Chem. Eur. J.* **5,** 1481 (1999).
10. M. D. Jones, R. Raja, J. M. Thomas, B. F. G. Johnson, D. W. Lewis, J. R. Kenneth, and D. M. Harris, Enhancing the enantioselectivity of novel homogeneous organometallic hydrogenation catalysts, *Angew. Chem. Int. Ed.* **42,** 4326 (2003).
11. J. S. Beck, J. C. Vartuli, W. J. Roth, M. E. Leonowicz, C. T. Kresge, K. D. Schmitt, C. T. W. Chu, D. H. Olson, E. W. Sheppard, S. B. McCullen, J. B. Higgins, and J. L. Schlenker, A new family of mesoporous molecular sieves prepared with liquid crystal templates, *J. Am. Chem. Soc.* **114,** 10834 (1992).
12. J. M. Thomas, R. Raja, G. Sankar, and R. G. Bell, Molecular-sieve catalysts for the selective oxidation of linear alkanes by molecular oxygen, *Nature* **398,** 227 (1999); J. M. Thomas, Designing a molecular sieve catalyst for the aerial oxidation of n-hexane to adipic acid, *Angew. Chem. Int. Ed.* **39,** 2313 (2000).
13. W. M. Xue, M. C. Kung, and H. H. Kung, Rational synthesis of asymmetric bicyclic siloxane, *Chem. Commun.* 2164 (2005). ([AQ] Author: Please provide volume number in references [13], [14].)
14. Z. Chang, M. C. Kung, and H. H. Kung, Stepwise synthesis of siloxane chains, *Chem. Commun.* 206 (2004).
15. G. Huysmans, A. Ranquin, L. Wyns, J. Steyaert, and P. Van Gelder, Encapsulation of therapeutic nucleoside hydrolase in functionalised nanocapsules, *J. Control. Rel.* **102,** 171 (2005).
16. S. Okada, S. Peng, W. Spevak, and D. Charych, Color and chromism of polydiacetylene vesicles, *Acc. Chem. Res.* **31,** 229 (1998).
17. E. T. Kisak, B. Coldren, and J. A. Zasadzinski, Nanocompartments enclosing vesicles, colloids, and macromolecules via interdigitated lipid bilayers, *Langmuir* **18,** 284 (2002).
18. F. Li, L. Zhang, and R. M. Metzger, On the growth of highly ordered pores in anodized aluminum oxide, *Chem. Mater.* **10,** 2470 (1998).
19. J. W. Elam, D. Routkevitch, P. P. Mardilovich, and S. M. George, Conformal coating on ultrahigh-aspect-ratio nanopores of anodic alumina by atomic layer deposition, *Chem. Mater.* **15,** 3507 (2003).
20. M. K. Singh, E. Titus, P. K. Tyagi, U. Palnitkar, D. S. Misra, M. Roy, A. K. Dua, C. S. Cojocaru, and F. Le Normand, Ni and Ni/Pt filling inside multiwalled carbon nanotubes, *J. Nanosci. Nanotechnol.* **3,** 165 (2003).
21. B. J. Hinds, N. Chopra, T. Rantell, R. Andrews, V. Gavalas, and L. G. Bachas, Aligned multiwalled carbon nanotube membranes, *Science* **303,** 62 (2004).
22. T. Shimoboji, E. Larenas, T. Fowler, A. S. Hoffman, and P. S. Stayton, Temperature-induced switching of enzyme activity with smart polymer-enzyme conjugates, *Bioconjugate Chem.* **14** (3), 517 (2003).
23. H. Dai, Carbon nanotubes: Synthesis, integration, and properties, *Acc. Chem. Res.* **35,** 1035 (2002).
24. S. M. Bachilo, L. Balzano, J. E. Herrera, F. Pompeo, D. E. Resasco, and R. B. Weisman, Narrow (n,m)-distribution of single-walled carbon nanotubes grown using a solid supported catalyst, *J. Am. Chem. Soc.* **125,** 11186 (2003).

25. B. Chen, G. Parker II, J. Han, M. Meyyappan, and A. M. Cassell, Heterogeneous single-walled carbon nanotube catalyst discovery and optimization, *Chem. Mater*. **14,** 1891 (2002).
26. W. F. Paxton, K. C. Kistler, C. C. Olmeda, A. Sen, S. K. St. Angelo, Y. Cao, T. E. Mallouk, P. Lammert, and V. H. Crespi, Catalytic nanomotors: autonomous movement of striped nanorods, *J. Am. Chem. Soc.* **126,** 13424 (2004).

2

Oxide-Supported Metal Thin-Film Catalysts: The How and Why

Valentino R. Cooper, Alexie M. Kolpak, Yashar Yourdshahyan and Andrew M. Rappe*

2.1. INTRODUCTION

Oxide-supported metals play an important role in a wide variety of industrial chemical processes such as the catalytic treatment of automotive exhaust. The ability to exercise greater control over the interactions of molecules on metal surfaces will create new possibilities for pollution control and the provision of novel power sources. Furthermore, a deeper understanding of molecule surface interactions will present numerous opportunities for the design of nanocatalysts.

In recent years, metal nanoparticles and thin films supported on oxides have become fundamental components of many devices as their small dimensions present structures with new chemical and physical properties, often enhancing the reactivity of these surfaces relative to their bulk counterparts. Numerous theoretical and experimental studies show that the metal particle size and shape as well as direct adsorbate interactions with the oxide support can each play a key role in enhancing the reactivity of these surfaces.[1–7] Further investigations imply that the support material may

The Makineni Theoretical Laboratories, Department of Chemistry, University of Pennsylvania, Philadelphia, PA 19104-6323

* To whom correspondence should be addressed. E-mail: rappe@sas.upenn.edu

also influence the metal's intrinsic reactivity at these surfaces.[2,5,8–13] However, these studies were not able to isolate this effect from those of particle size, shape, and direct adsorbate-support interactions.

It was not until recently that Chen and Goodman probed the influence of the oxide support material on the intrinsic properties at the metal surface.[14] By covering a titania support with one or two flat atomic layers of gold they eliminated, direct adsorbate–support interactions as well as particle size and shape effects. Their results definitively showed that the electronic properties at the metal surface changed due to charge transfer between the support and the metal. Furthermore, their comparison of one- and two-layer films highlighted the dependence of these effects on the thickness of the metal slab.

These studies indicate that the charge transfer at the metal–oxide interface alters the electronic structure of the metal thin film, which in turn affects the adsorption of molecules to these surfaces. Understanding the effect that an oxide support has on molecular adsorption can give insight into how local environmental factors control the reactivity at the metal surface, presenting new avenues for tuning the properties of metal thin films and nanoparticles. Coupled with the knowledge of how particle size and shape modify the metal's electronic properties, these results can be used to predict how local structure and environment influence the reactivity at the metal surface.

2.1.1. The Theory of Molecular Adsorption on Metal Surfaces

While there is no complete theory of surface reactivity, an understanding of how reactant, intermediate, and product adsorbates interact with a surface often gives insight into the catalytic properties of a metal. Quantum mechanical theories show that as long as the perturbation due to the interacting systems is small, the interaction of two isolated systems can be estimated using second order perturbation theory:

$$\Delta E = \frac{|V_{ij}|^2}{\varepsilon_i - \varepsilon_j},$$

where ε_i and ε_j are the eigenvalues of the unperturbed isolated systems, and V_{ij} represents the coupling matrix for these interactions. When a molecule interacts with a metal surface, the interaction involves both a transfer of electrons from the molecule's highest occupied molecular orbital (HOMO) to the metal surface (direct bonding) and a shift of electrons from the metal surface to the molecule's lowest unoccupied molecular orbital (LUMO)(back bonding). For transition metal surfaces, the exchange of electrons is achieved through interactions with the metal d orbitals.

Using perturbation theory, Hammer and Nørskov developed a model for predicting molecular adsorption trends on the surfaces of transition metals (HN model). They used density functional theory (DFT) to show that molecular chemisorption energies could be predicted solely by considering interactions of a molecule's HOMO and LUMO with the center of the total d-band density of states (DOS) of the metal.[15,16] In particular,

their work showed that the chemisorption energy of a molecule to a metal surface is closely related to the center of the total d-band DOS of the metal:

$$E_{chem} = -4\left[f\frac{V_{LUMO}^2}{\varepsilon_{LUMO}-\varepsilon_d} + fS_{LUMO}V_{LUMO}\right] -2\left[(1-f)\frac{V_{HOMO}^2}{\varepsilon_d-\varepsilon_{HOMO}} + (1+f)S_{HOMO}V_{HOMO}\right],$$

where f is the filling of the metal d orbital and S is the overlap integral between the molecular orbital and the metal d orbitals. In this model, upward shifts in the d-band center will result in larger chemisorption energies, while downward shifts give weaker binding. This model has been successfully applied to the adsorption of CO and H_2 on a number of unsupported metal surfaces. However, nanoparticles may result in complicated rearrangements in the population and energy levels of the surface d orbitals due to the size and shape of the nanoparticle. Furthermore, supported particles and thin films can have changes in their electronic structure due to covalent or ionic bonding present at the metal–support interface. Such modifications of the metal surface d orbitals can have considerable consequences for molecular adsorption, by altering the interactions of the molecules' HOMO and LUMO orbitals with modified metal states.

In this chapter, we shall use DFT to investigate the extent to which the oxide support alters the electronic structure of the deposited metal as a result of charge transfer at the metal–oxide interface. We will use CO chemisorption as a function of Pt film thickness to demonstrate how changes in the metal electronic structure can lead to chemisorption trends that deviate from expectations based on the current theory of molecular adsorption.

2.2. METHODOLOGY

We examined the deposition of Pt thin films onto the strongly polar O-terminated (O_T) α-alumina surface. Studies have shown that this surface is stabilized by the adsorption of hydrogen or a supported metal.[17] We used a slab geometry with an in-plane $\sqrt{\mathbf{3}} \times \sqrt{\mathbf{3}}\mathbf{R30}^{\circ}$ unit cell and periodic boundary conditions to model the alumina surface.[18] The layer stacking can be represented by the formula $(Al\text{-}O_3\text{-}Al)_4\text{-}Al\text{-}O_3\text{-}(Pt_3)_n$, where n is the number of Pt layers. The interfacial Pt atoms are in the energetically preferred registry, directly above the surface O atoms, forming a Pt (111) film. All calculations were performed using density functional theory (DFT)[19,20] with the generalized gradient approximation[21] for the exchange-correlation functional, as implemented in the dacapo code,[22] with a plane-wave cutoff of 30 Ry, ultrasoft pseudopotentials[23] and a $2 \times 2 \times 1$ Monkhorst–Pack[24] k-point mesh. All slab calculations were performed with at least 12 Å of vacuum between periodic images in the [0001] direction. Total energies were tested to ensure that there were no surface interactions through the slab or the vacuum. The theoretical α-Al_2O_3 in-plane lattice constant of 4.798 Å was used (experimental = 4.759 Å[25]). In order to eliminate strain effects, all adsorption energies were compared to unsupported Pt (111) calculations at the same in-plane geometry as the supported metal. (This corresponds to the experimental Pt (111)

TABLE 2.1. CO top site binding energies relative to Pt (111), center of the total d-band DOS and the center of the partial DOS composed of unoccupied d_{z^2} states and occupied d_{xz} and d_{yz} states for the nPt/Al_2O_3 system. All energies are in eV.[29,30]

Pt Film Layers	Top Site ΔE_{chem}	Total d-Band Center	$d_{z^2} + d_{xz} + d_{yz}$ Band Center
1	0.68	−2.28	−1.20
2	−0.19	−1.72	−1.68
3	0.07	−1.68	−1.49
4	0.03	−1.69	−1.54
5	0.06	−1.70	−1.54
Pt (111)	0.00	−1.69	−1.53

in-plane lattice constant of 2.77 Å). For our simulations, we fixed the ions in the bottom two alumina layers to their theoretical positions, relaxed the third layer perpendicular to the surface, and fully relaxed the remaining alumina layers, Pt layers and adsorbates until the force on each atom was less than 0.01 eV/Å. We corrected for known DFT CO chemisorption errors[26,27] using the extrapolation method of Mason and coworkers[28] and estimated the error bar for computed chemisorption energies to be 0.01 eV.

2.3. CO CHEMISORPTION TO ALUMINA-SUPPORTED PT THIN FILMS

Table 2.1 shows the top site chemisorption energy for the adsorption of CO onto the Pt/O_T α-alumina system as a function of metal layers, relative to Pt (111). For the monolayer of metal on the surface there is an enhancement of the CO top site binding energy relative to Pt (111). On the other hand, the second layer of Pt/O_T shows a dramatic decrease in the top site chemisorption energy. For three layers of Pt on this surface, the chemisorption energy oscillates above the Pt (111) energy, eventually returning to the Pt (111) value for $n > 4$.

According to the HN model, an increase in chemisorption energy should correlate to an upward shift in the total d-band center of the metal. Contrary to this theory, the monolayer of Pt/O_T system shows stronger chemisorption but a large decrease (0.59 eV) in the d-band center (−2.28 eV) relative to bulk Pt (111) (−1.69 eV). Furthermore, the downward shift in the d-band center of the bilayer Pt/O_T system (0.03 eV) is too small to account for the reduction in chemisorption energy. To explain these deviations, it is necessary to understand how CO binds to a metal surface and how the oxide support alters the electronic properties of the metal surface to allow for changes in molecular adsorption.

2.3.1. CO Binding to Transition Metal Surfaces

Due to its importance in many industrial processes, the prototypical reaction of CO binding to metal surfaces has received much attention. Using Hückel molecular orbital theory, Blyholder showed that CO bonding at top sites consists of the donation of electrons from the filled CO 5σ HOMO to the metal d_{z^2} orbitals with a back-donation of electrons from the metal d_{xz} and d_{yz} orbitals to the CO $2\pi^*$ LUMO.[31] Consequently,

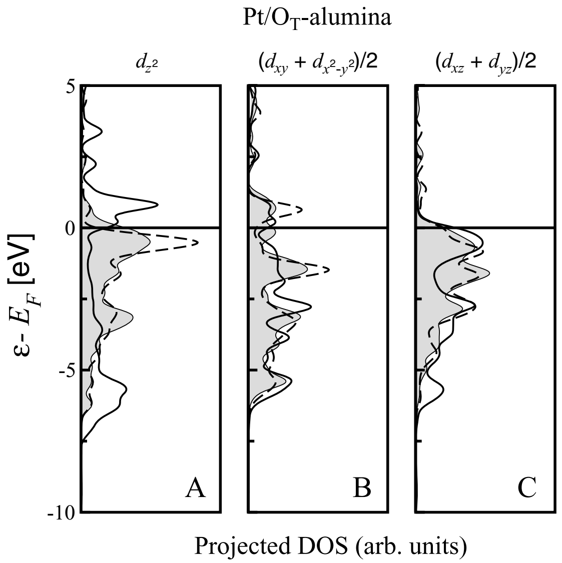

FIGURE 2.1. Orbital-projected DOS plots for the surface Pt atoms of the Pt/O$_T$-alumina system. The shaded regions represent the DOS of the Pt (111) surface, the solid (—) lines are for the Pt monolayer, and the dashed (- -) lines are for the bilayer.

it follows that to understand bonding at the top site it is necessary to consider changes in the free d_{z^2} DOS (for direct bonding) and the filled d_{xz} and d_{yz} DOS (for back-bonding). As such, the remainder of this chapter will focus on how charge transfer from the Al_2O_3 support material to the Pt thin film will alter the electronic structure of the individual Pt *d* orbitals, and the implications of these changes on the direct and back bonding of molecules to these surfaces.

2.3.2. *Metallic Deposition on an Electronegative Support:* Pt/O$_T$

The absence of Al atoms on the O$_T$ α-alumina surface leaves the surface oxygen ions electron deficient. As a result, the deposition of a metal onto this support will result in the formation of hybrid orbitals between the metal *d* orbitals and the oxygen *p* orbitals. Figure 2.1 shows the projected DOS of the surface Pt atoms for one and two layers of Pt deposited onto an O$_T$-alumina surface. Since the Pt atoms are deposited directly on top of oxygen ions, hybrid orbitals are formed with metal *d* orbitals with components perpendicular to the oxide surface (d_{z^2}, d_{xz} and d_{yz}). Each of these *d* states participates in a higher energy anti-bonding state and a lower energy bonding state. For the d_{z^2} orbital, the higher energy state is unoccupied ($\sim$1 eV above the Fermi level). Forming this hybrid orbital increases the number of free *d* states available for direct bonding with incoming adsorbate molecules. However, the newly formed d_{z^2} bonding orbital is quite low in energy ($\sim$6 eV below the Fermi level). This hybrid orbital reduces the number of occupied states near the Fermi level and results in a downward shift in the center of the metal *d*-band. The newly formed d_{xz} and d_{yz} bonding hybrid orbitals also decrease the number of filled states with energies just below the Fermi level and

increase the number of states with energies below −5.0 eV, with little or no change in the number of free states in these orbitals. Therefore, the formation of bonding hybrid orbitals will weaken the back bonding of molecules to these states and shift the center of the metal d-band downward. For a monolayer of Pt on Al_2O_3, the large enhancement in CO chemisorption energy is due to the formation of strong direct bonds between the filled CO 5σ and the unoccupied d_{z^2} antibonding hybrid states.

The second layer of Pt on O_T Al_2O_3 shows a smaller deviation from the HN model than the monolayer. In this system, Pt atoms on the surface occupy hollow sites of the interfacial Pt atoms, as in a fcc (111) surface. This allows the d orbitals of the interfacial Pt atoms to directly interact with the d_{xz} and d_{yz} orbitals of the second-layer atoms, forming metallic bands. Due to the influence of bonding at the metal–oxide interface, the d_{xz} and d_{yz} orbitals exhibit a slight downward shift in the center of the metal bands relative to Pt (111), implying that these orbitals will have only a slight change in their back bonding relative to Pt (111). On the other hand, the d_{z^2} states gain a fraction of an electron in response to the decreased electron–electron repulsions in the Pt atom due to the loss of electrons from the other d-orbitals. This gain in charge results in a dramatic reduction in free d_{z^2} states and shifts the d_{z^2} DOS upward due to strong electron–electron repulsions within this orbital. These changes suggest that the d_{z^2} orbitals will form much weaker direct bonds with adsorbed molecules as they will have fewer states to accept electrons. Therefore, the large decrease in bonding at the metal surface is due to the reduction in the number of unoccupied d_{z^2}. For three or more layers of Pt, metal charge screening effects prevail and the DOS of the surface atoms shift's back to Pt (111) values, thereby defining the length scale of the metal-support interactions.

2.3.3. Correlating Chemisorption Trends with Shifts in DOS

Models of CO adsorption show that top site binding is governed by the CO HOMO (5σ orbital) donating electrons into the metal unoccupied d_{z^2} states, with simultaneous back-donation of electrons from the metal's occupied d_{xz} and d_{yz} states into the CO LUMO ($2\pi^*$ orbital). Therefore, it follows that the standard chemisorption model, which considers shifts in the total d-band center, can be inaccurate for systems in which individual molecular orbitals, involved in bonding with the adsorbate, shift differently due to external interactions. In particular, we have shown that the formation of hybrid orbitals with the support material can lead both to downward shifts in the metal d-band center, which do not affect the adsorption of molecules to the metal surface, and to upward shifts that are vitally important.

An understanding of molecule–metal interactions suggests that in these systems it is necessary to only consider changes in states that are involved in bonding (i.e. d_{z^2} free states and d_{xz} and d_{yz} occupied states). Figure 2.2 shows a comparison of a partial d-band DOS center (constructed from only the d_{z^2} states and the d_{xz} and d_{yz} states) to the top site chemisorption energies for CO binding to the Pt/O_T system. Here we see that the chemisorption energy is directly related to the shifts in this partial DOS, confirming that the CO binding energy is dependent only on these states. Furthermore, these results suggest that chemisorption energies to transition metal surfaces can be predicted solely by using modified DOS d-band centers.

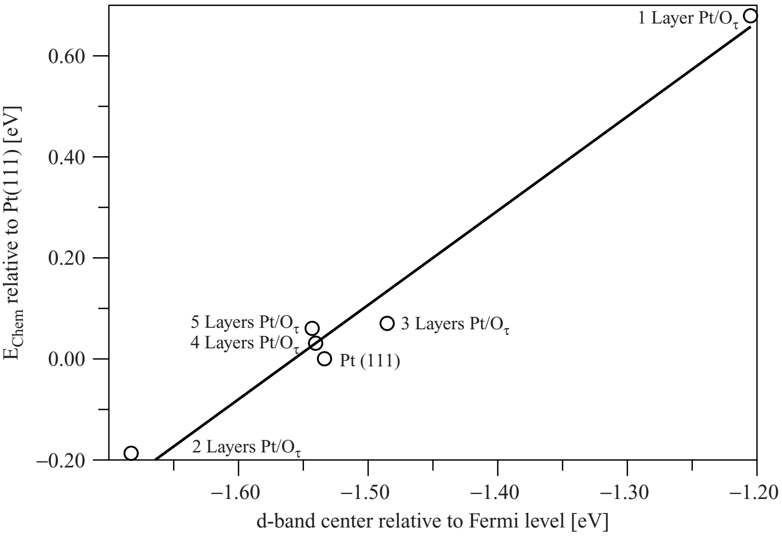

FIGURE 2.2. Comparison of DFT chemisorption energies (relative to Pt (111)) and the partial d-band center of the d_{z^2} free states and d_{xz} and d_{yz} occupied states as a function of Pt layer thickness for Pt/O_T α-alumina system.

2.4. SUMMARY/CONCLUSION

In this chapter, we have illustrated how chemisorption trends for oxide-supported metal systems can be correlated to shifts in the d-band center of a modified DOS constructed from the occupied and unoccupied states that are involved in bonding with the adsorbate molecule. While we presented specific results for Pt supported on an O_T alumina surface, similar investigations on Pd and Rh supported on the Al_T and O_T surfaces indicate that these results may be generalized for transition metals deposited on electronegative and electropositive supports. Furthermore, we use DFT and the adsorption of CO to the Pt surface to demonstrate how the orbital-specific electronic structure of a metal surface can be used to predict the strength of the metal's interaction with molecular adsorbates. We show that orbital-specific considerations are necessary to predict bonding, as metal–oxide interfacial charge transfer can have significant effects on the electronic structure of molecular orbitals which may result in shifts in the total d-band center which are not related to the binding of a molecule to the metal surface. The fact that these effects are greatly diminished at four or five layers indicates that the metal–support interactions have a small characteristic length scale on the order of the metal interlayer spacing. While it is known that low-coordinated sites greatly enhance the reactivity of metal particles, these results demonstrate the importance of metal-support charge transfer in defining the properties at the metal surface, offering further support for the recent work of Chen and Goodman. In addition, our findings suggest that increased reactivity at the perimeter of metal particles with diameters <5 nm may be partially attributed to the strong metal–oxide coupling accessible at

these boundaries. These concepts may be useful for applications as diverse as chemical sensors, fuel cells, and photochemical reactions.

ACKNOWLEDGMENTS

We thank Sara E. Mason and Ilya Grinberg for discussions on CO adsorption energy corrections. This work was supported by the Air Force Office of Scientific Research, Air Force Materiel Command, USAF, under Grant No. FA9550-04-1-0077 and by the NSF MRSEC Program, Grant DMR05-20020. Computational support was provided by the Defense University Research Instrumentation Program, and by the NSF CRIF Program, Grant CHE-0131132. V.R.C. thanks IBM and ACS for support through the IBM Graduate Student Award in Computational Chemistry. A.M.K. was supported by a GAANN fellowship.

REFERENCES

1. G. Mills, M. S. Gordon, and H. Metiu, The adsorption of molecular oxygen on neutral and negative Au_n clusters (n=2−5), *Chem. Phys. Lett.* **359,** 493–499 (2002).
2. Z. L. Wang, T. S. Ahmad, and M. A. El-Sayed, Steps, ledges and kinks on the surfaces of platinum nanoparticles of different shapes, *Surf. Sci.* **380,** 302–310 (1997).
3. J. W. Yoo, D. J. Hatcock, and M. A. El-Sayed, Propene hydrogenation over truncated octahedral Pt nanoparticles supported on alumina, *J. Catal.* **214,** 1–7 (2003).
4. B. Yoon, H. Hakkinen, and U. Landman, Interaction of O_2 with gold clusters: molecular and dissociative adsorption, *J. Phys. Chem.* A **107,** 4066–4071 (2003).
5. M. Haruta, Size- and support-dependency in the catalysis of gold, *Catal. Today* **36,** 153–166 (1997).
6. M. Valden, X. Lai, and D. W. Goodman, Onset of catalytic activity of gold clusters on titania with the appearance of nonmetallic properties, *Science* **281,** 1647–1650 (1998).
7. A. Sanchez, S. Abbet, U. Heiz, W. D. Schneider, H. Hakkinen, R. N. Barnett, and U. Landman, When gold is not noble: nanoscale gold catalysts, *J. Phys. Chem.* A **103,** 9573–9578 (1999).
8. C. Bozo, N. Guilhaume, and J.-M. Herrmann, The role of the ceria-zirconia support in the reactivity of platinum and palladium catalysts for methane total oxidation under lean conditions, *J. Catal.* **393,** 393–406 (2001).
9. E. J. Walter, S. P. Lewis, and A. M. Rappe, First-principles study of carbon monoxide adsorption on zirconia-supported copper, *Surf. Sci.* **495,** 44–50 (2001).
10. L. M. Molina, and B. Hammer, Active role of oxide support during CO oxidation at Au/MgO, *Phys. Rev. Lett.* **90,** 206102–206101 (2003).
11. R. Lindsay, E. Michelangeli, B. G. Daniels, M. Polick, A. Verdini, L. Floreano, A. Morgante, J. Muscat, N. M. Harrison, and G. Thornton, Surface to bulk charge transfer at an alkali metal/metal oxide interface, *Surf. Sci.* **547,** 859 (2003).
12. S. Roberts, and R. J. Gorte, A comparison of Pt overlayers on α-Al_2O_3(0001), ZnO(0001)Zn, and ZnO(000$\bar{1}$)O, *J. Chem. Phys.* **93,** 5337–5344 (1990).
13. W. T. Petrie, and J. M. Vohs, Interaction of platinum films with the (000$\bar{1}$) and (0001) surfaces of ZnO, *J. Chem. Phys.* **101,** 8098–8107 (1994).
14. M. S. Chen, and D. W. Goodman, The structure of catalytically active gold on titania, *Science* **306,** 252–255 (2004).
15. B. Hammer, and J. K. Nørskov, Electronic factors determining the reactivity of metal surfaces, *Surf. Sci.* **343,** 211–220 (1995).
16. B. Hammer, Y. Morikawa, and J. K. Nørskov, CO chemisorption at metal surfaces and overlayers, *Phys. Rev. Lett.* **76,** 2141–2144 (1996).

17. P. J. Eng, T. P. Trainor, G. E. Brown Jr., G. A. Waychunas, M. Newville, S. R. Sutton, and M. L. Rivers, Structure of the hydrated α-Al_2O_3 (0001) surface, *Science* **288,** 1029–1033 (2000).
18. L. Pauling, and S. B. Hendricks, The crystal structure of hematite and corundum, *J. Am. Chem. Soc.* **47,** 781 (1925).
19. P. Hohenberg, and W. Kohn, Inhomogeneous electron gas, *Phys. Rev.* **136,** 864 (1964).
20. W. Kohn, and L. J. Sham, Self-consistent equations including exchange and correlation effects, *Phys. Rev.* **140,** 1133 (1965).
21. J. P. Perdew, J. A. Chevary, S. H. Vosko, K. A. Jackson, M. R. Pederson, D. J. Singh, and C. Fiolhais, Atoms, molecules, solids and surfaces: Applications of the generalized gradient approximation for exchange and correlations, *Phys. Rev.* B **46,** 6671–6687 (1992).
22. B. Hammer, L. B. Hansen, and J. K. Nørskov, Improved adsorption energetics within density-functional theory using Perdew-Burke-Ernzerhof functionals, *Phys. Rev.* B **59,** 7413–7421 (1999).
23. D. Vanderbilt, Soft self-consistent pseudopotentials in a generalized eigenvalue formalism, *Phys. Rev. B Rapid Commun.* **41,** 7892–7895 (1990).
24. H. J. Monkhorst, and J. D. Pack, Special points for Brillouin-zone integrations, *Phys. Rev.* B **13,** 5188–5192 (1976).
25. W. E. Lee and K. P. D. Lagerlof, Structural and electron diffraction data for sapphire(α-Al_2O_3), *J. Electron Microsc. Techn.* **2,** 247 (1985).
26. P. J. Feibelman, B. Hammer, J. K. Nørskov, F. Wagner, M. Scheffler, R. Stumpf, R. Watwe, and J. Dumesic, The CO/Pt(111) puzzle, *J. Phys. Chem.* B **105,** 4018–4025 (2001).
27. I. Grinberg, Y. Yourdshahyan, and A. M. Rappe, CO on Pt(111) puzzle: A possible solution, *J. Chem. Phys.* **117,** 2264–2270 (2002).
28. S. E. Mason, I. Grinberg, and A. M. Rappe, First-principles extrapolation method for accurate CO adsorption energies on metal surfaces, *Phys. Rev. B Rapid Commun.* **69,** 161401–161404 (2004).
29. Y. Yourdshahyan, V. R. Cooper, A. M. Kolpak, and A. M. Rappe, Catalytic behaviour at the nanoscale: CO adsorption on Al_2O_3-supported Pt cluster, in *Proc. SPIE Int. Soc. Opt. Eng.*, edited by T. Lian and H.-L. Dai (2003), pp. 223–232.
30. V. R. Cooper, A. M. Kolpak, Y. Yourdshahyan, and A. M. Rappe, Support-mediated activation and deactivation of Pt thin-films. *Phys. Rev. B. Rapid. Comm.* **72,** 081409(R) (1-4) (2005)
31. G. Blyholder, Molecular orbital view of chemisorbed carbon monoxide, *J. Phys. Chem.* **68,** 2772–2778 (1964).

3

Developing Catalytic Nanomotors

Timothy R. Kline, Walter F. Paxton, Thomas E. Mallouk, Ayusman Sen*

3.1. BACKGROUND

3.1.1. Externally Driven Methods for Movement

One of the greatest challenges in the advancement of nanotechnology is the design of engines for nanoscale devices. Previous work focused on using external electric and magnetic fields to move nanoscale objects. For example, electric fields are commonly used to move colloidal silica particles[1] and other mesoscale objects.[2] Dielectrophoresis was responsible for the movement and alignment of the colloidal spheres in the former. An external electric stimuli to individually addressable microfabricated electrodes on silicon surfaces was also responsible for moving small objects akin to the dielectrophoretic force where the generated electric field moved the colloidal spheres.

Electric fields are not the only method to move nanoscale objects; magnetic fields are also used as an external method to drive nanoscale–microscale objects. For example, Whitesides used magnetite embedded in soft-lithographically defined microscale gears to assemble and spin them externally.[3] On a smaller scale, Crone used magnetism to spin nanowires with capped nickel ends.[4] The former discussed external methods, electric and magnetic to drive nanoscale objects, yet nature has been using localized energy sources to move cells and other biological objects of similiar size *in vivo*.

Department of Chemistry, The Pennsylvania State University,University Park, PA 16802
* E-mail: asen@chem.psu.edu

3.1.2. Self Driven Methods for Movement

3.1.2.1. Surface Energy Driven Phenomena. Camphor boats at the water–air interface were one of the first well-studied systems that move autonomously.[5] The motion of a camphor boat is accredited to the dissolution of camphor which lowers the interfacial tension of the surrounding water and moves the object until it is completely dissolved. Interfacial tension gradients are not exclusive to camphor boats in water. Another system where interfacial tension gradients are responsible for the non-Brownian motion of objects is in the motion of a mercury drop when placed in a solution of nitric acid and potassium dichromate.[6] Here, a new species, mercurous chromate is produced, thereby resulting a temporary asymmetry in the droplet of mercury and a nonuniformity in the interfacial tension as the new species diffuses into solution. The nonuniformity in interfacial tension results in the non-Brownian motion of the mercury drop, observable for long periods of time (100 to 300 s depending on the size of mercury drop) until the drop disappears and interfacial tension nonuniformities vanish.

A similar observation to that of the moving mercury drop and camphor systems but occurring as a result of a different mechanism is responsible for the "dancing" like movement of nanoscale Tin (Sn), approximately 0.60 μm in size on copper (111) surfaces.[7] In the Sn/Cu system, Sn is deposited onto a copper (111) surface. The Sn object moves around the surface in a non-Brownian fashion as an alloy of bronze is formed at the interface of the two surfaces. Brownian motion is described as movement arising from random thermal fluctuations lacking a defined direction of movement. The interaction of the residual Sn with the bronze surface is energetically unfavorable; therefore, the Sn moves to Cu regions to avoid interaction with the bronze thereby minimizing surface free energy.

3.1.2.2. Biological Motors. The work done on surface energy driven movement discussed thus far converts chemical to mechanical energy but motion ceased once the object of movement was consumed. In nature, biological motors utilize enzymes that use a "fuel" source for energy that may be converted to mechanical energy. Thus, the moving object is not consumed but itself consumes some type of "fuel." A well-known example is motility through the spatially controlled polymerization of actin.

Two examples where actin polymerization is observed in eukaryotes are in the bacterial pathogens *Listeria monocytogenes* and *Shigella flexneri*. The motion that the eukaryote pathogens exhibit is the actin based motility in the cytoplasm of their host. Actin polymerization is known to occur via an insertion polymerization mechanism. The movement is a result of site-directed tread-milling of the actin filaments. This type of movement is classified as a propulsive type motion. The driving force for actin polymerization as well as the next motor is the conversion of adenosine triphosphate (ATP) to adenosine diphosphate (ADP).[8]

3.1.2.3. F_1-ATPase Driven Nanomotors. Another type of biological driven engine is that of F_1-adenosine triphosphate synthease (F_1-ATPase) which hydrolyzes the ATP in the surrounding medium. Kinosita Jr. *et al.* observed the rotation of an actin filament attached to the F_1-ATPase motor.[9] Later, Montemagno followed with the incorporation of a nickel nanorod with the F_1-ATPase motor.[10] The outcome was the rotation of the

nickel rod at 8.3 rps driven locally by the hydrolysis of ATP. Engineering of the device required recombinant F_1-ATPase to permit binding to a biologically foreign device and nanofabrication to make the inorganic object.

3.2. SYNTHETIC CATALYTIC MOTORS

3.2.1. Background

The conversion of chemical energy to mechanical energy on the micro/nanoscale occurs readily in biological systems but synthetic analogs are virtually nonexistent. One of the first reported involved the movement of poly(dimethyl siloxane) boats that were about 9 mm in diameter with platinum rudders. In aqueous solutions of hydrogen peroxide (H_2O_2), the platinum catalyzed the decomposition of hydrogen peroxide to convert chemical energy into mechanical energy.[11] The decomposition of hydrogen peroxide results in water and oxygen according to the reaction (Eq. (1)).

$$2H_2O_2 \rightarrow 2H_2O + H_2O \tag{1}$$

The mechanism of movement is attributed to the rupture of oxygen bubbles creating a propulsive force driving the PDMS boat forward at the air/water interface.[11]

We were interested in scaling such a concept down to the nano/micron scale because at the nanoscale different physical forces dominate thereby making it difficult to readily control and move nanoscale objects.[12] We chose the fabricated nanorods as our first approach in making a nansocale motor because it is easy to impart catalytic asymmetry to the rod. Confining the reaction to one end of a rod sets up a gradient along the length of the rod and generates a force at one end.

3.2.2. Fabrication of the Motor

We chose to use a "sacrificial template" method to make our nanorods.[13] This method uses a membrane with nano/microscopic sized channels as a mold for the design of a nanowire, fiber, or rod, depending upon the intended use for the object and the materials comprising it.[13,14]

Polymers consisting of but not limited to polythiophene, polypyrrole and polyaniline have been extensively used to make polymer nanofibers.[15] In general, any metal that can be electroplated has most likely appeared in a nanowire. Semiconductors, polymers, and insulators have also been used in the design of nanowires.[16] Furthermore, different metals can be plated in succession to give striped nanowires.[17]

Our approach utilized the metals gold, platinum, then later gold, platinum, and nickel electroplated in succession because the catalytic decomposition of hydrogen peroxide reaction we tested was most efficiently catalyzed with platinum.[12,18,19] After fabrication of the nanowires they were freed by removing the conductive silver backing with nitric acid and the "sacrificial template" with a strong base, sodium hydroxide. Then nanorods were washed with deionized water and ultracentrifuged to achieve a neutral pH.

3.2.3. Analyzing the Motor Movement

3.2.3.1. Imaging Methods. Dilute solutions of the rods were primarily analyzed with dark-field microscopy because this method capitalizes on the reflectivity of objects. Another consideration in the motion of colloidal objects is hydrodynamic flows. Some of the sources of hydrodynamic flows are vibrations on the microscope stage, the tendancy for a water droplet to spread on a glass surface and evaporation of the water. Flows occurring around the nanorods would complicate the individual particle analysis; therefore we used imaging chambers available from Molecular Probes to reduce hydrodyamic flow and a coverslip to cap the solutions. The imaging chamber eliminates the spreading of water and the coverslip helps to reduce evaporation and elimates the natural convex shape of the water droplet making it easier to image the aqueous sample.

Other than hydrodynamic flows one must also take into account Brownian motion.[20,21] Brownian motion is observed as the random displacement of colloids caused by thermal energy. Batchelor deemed this force as a microhydrodynamic force because only small objects with a low Reynolds number exhibit Brownian motion.[22] Low Reynolds numbers are present in microhydrodynamic systems because inertia forces are small with respect to viscous forces.

In our system, Brownian forces are dominant when hydrogen peroxide, the "fuel" for the platinum catalyst, is absent. In the presence of dilute solutions of hydrogen peroxide a new force is observed. This force causes the nanorods to move in a non-Brownian fashion, platinum end forward, as the platinum end is decomposing hydrogen peroxide. Particle tracking was done to investigate the movement of the rods and obtain some physical parameters such as speed. Transmission electron microscopy allowed for the characterization of the rod surface morphology. Asymmetry in the system is also necessary because a gold–platinum–gold nanorod does not move.

3.2.3.2. Particle Tracking. Particle tracking was done using a program called PhysVis.[23] The tracking program allowed us to determine speeds, diffusion coefficients and two other parameters that were defined by Paxton.[12] These other parameters aided in distinugishing Brownian motion from that of non-Brownian motion. The first parameter, directionality, was defined as the cosine of the rod orientation and the direction of movement in between the frames. Frame intervals were 0.1 s for these studies. A particle with a directionality of 1, cos(0), has not changed direction between the frame intervals of interest. Directionalities of 0 or -1 represent a rod moving orthogonally or in the opposite direction with respect to its orientation. The second parameter measured was, the axial velocity (v_z), defined as the product of directionality and the center-to-center displacement per second. This parameter is a more accurate representation than the scaler speed alone because it corrects for speeds attributed to Brownian flucuations. A table of speeds, directionalities, and axial velocities (Table 3.1) demonstrates the dependence of nanorod speed on the concentration of hydrogen peroxide.

Particle tracking also produced trajectory paths of the Pt/Au nanorods based on displacement data collected for the head and tail of each nanorod. The head is defined as the direction in which the nanorod moves. The trajectory paths clearly distinguish the motion of a Pt/Au nanorod from that of a Brownian colloidal cylinder moving under the influence of thermal energy (Fig. 3.1). In addition, the trajectory path helps visualize some of the defined physical parameters.

TABLE 3.1. Effect of aquesou H_2O_2 concentration on the movement of 2 μm platinum/gold rods.[a]

H_2O_2 (wt.%)	Speed (μm/s)[b]	Directionality	v_z (μm/s)[b]
4.9	7.7 ± 0.9	0.78	6.6 ± 1.0
3.3	7.9 ± 0.7	0.75	6.6 ± 0.7
1.6	5.6 ± 0.6	0.65	4.0 ± 0.8
0.33	4.9 ± 0.3	0.60	3.4 ± 0.4
0.031	3.9 ± 0.5	0.19	0.9 ± 0.4
Pure water	3.7 ± 0.3	0.07	0.4 ± 0.1

[a] Rod diameter, 400 nm; Pt and Au segments 1 μm each; concentration of rods: 3.3×10^7 rods/mL.
[b] Error limits represent 90% confidence intervals. *(Reproduced with permission from J. Am. Chem. Soc.* ***2004****, 126, 13424–31. Copyright 2004 American Chemical Society.)*

3.2.3.3. Oxygen Evolution Studies. Kinetic studies for the evolution of oxygen were done to relate the catalyst efficiency to the nanorod speed observed. Gas chromatography was used to measure the rate of oxygen evolved from the platinum segment of the platinum/gold nanorod as a means of obtaining a turnover rate (Fig. 3.2). To minimize inflated oxygen evolution values in our data from atmospheric oxygen contributions we measured oxygen evolution in an argon saturated environment and calibrated our data against the natural abundance of nitrogen/oxygen in the atmosphere. Figure 3.2 shows the evolution of oxygen as a function of time for 2E6 platinum/gold nanorods in 10 ml of 3.74% w/w aqueous solution of hydrogen peroxide. The turnover rate of hydrogen peroxide to oxygen is 1E-15 mol/s rod. Oxygen diffuses through water at a rate of 2E-9 m^2/s at ambient temperature and pressure. One may compare the diffusion limited rate of oxygen (2E-9 m^2/s) to that of a rod 1E-12m^2 in surface area to obtain a surface normalized rate of 8.84E-4 mol/m^2 s which is about 1/2000 of the diffusion limited rate. Hence, the observed catalytic movement is limited by the

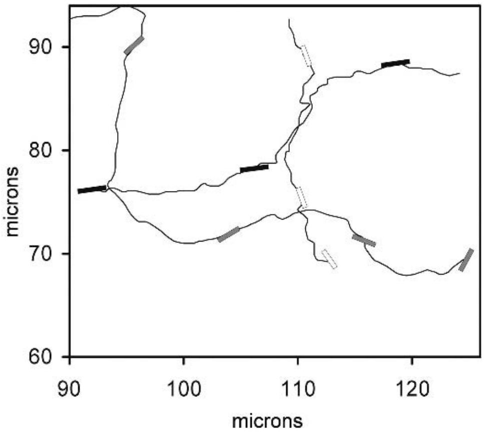

FIGURE 3.1. Trajectory paths of Pt/Au nanorods in 2.5% solution of hydrogen peroxide. (*Reproduced with permission from J. Am. Chem. Soc. 2004, 126, 13424–31. Copyright 2004 American Chemical Society.*)

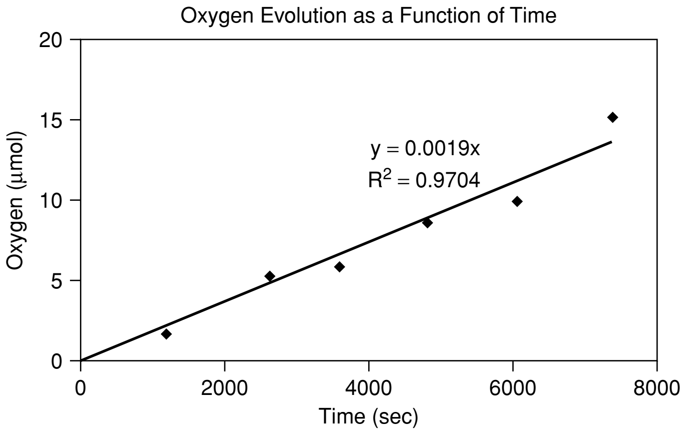

FIGURE 3.2. Oxygen evolution for 2E6 platinum/gold nanorods in 10 ml of a 3.74% w/w aqueous solution of hydrogen peroxide. The autocatalytic decomposition of hydrogen peroxide was less than 11E-9 mol/min and is therefore insignificant.

turnover rate of the catalyst and not diffusion of the hydrogen peroxide to the platinum surface.

3.2.4. Mechanism for Movement

3.2.4.1. Movement via Interfacial Tension Gradient. At this point we have discussed ways of analyzing the motion of the rods and proving that their movement is non-Brownian but we have not elaborated on why they move and why they move with platinum end forward, contrary to earlier literature involving the propulsive movement of PDMS discs driven by Pt rudders.[11] After eliminating other obvious propulsive mechanisms for movement, a gradient driven mechanism was investigated. Specifically, we investigated an interfacial tension gradient created by a change in temperature or concentration.

The platinum catalyzed decomposition of hydrogen peroxide is exothermic and would result in an oxygen and temperature gradient for the Pt/Au nanorod because the gold is inactive toward the decomposition of hydrogen peroxide. Therefore, a gradient of oxygen and temperature is created along the length of the rod. Now focusing on the oxygen gradient, the highest concentration of oxygen is at the source, platinum, and the lowest at the inactive gold end. The oxygen gradient would be maintained as long as hydrogen peroxide is in solution.

We can estimate the interfacial tension gradient created by the solute gradient by solving the convective-diffusion equation (Eq. (2)) for a moving rod where oxygen is the solute because water and hydrogen peroxide have similiar interfacial tensions. Oxygen is a nonpolar molecule that cannot act as a hydrogen bond donor, and it thus disrupts the hydrogen bonding network of liquid water. To simplify the problem, the liquid–solid interfacial tension is assumed to be drectly proportional to the mole fraction of oxygen in the solution. We then calculate the interfacial force a 2 μm long rod with

a 370 nm diameter by solving the convection diffusion equation under steady-state conditions to obtain the oxygen concentration gradient.

$$\frac{\partial C}{\partial t} = \upsilon \bullet \nabla C + D\nabla^2 C, \tag{2}$$

The uniform flux of oxygen, S, into the fluid along the Pt surface and zero flux along the Au surface provide boundary conditions for the convection–diffusion equation.

We now make two simplifications. One is that the rate of O_2 production is uniform over the curved part of the Pt surface, and we ignore the contribution from the end of the rod because it is small in surface area when compared to the rest of the rod. Second, the rod is permeable to O_2, with the same diffusion coefficient as in water because the rod is small with respect to the diffusion length in the volume of the solution for the time scale of motion. With these approximations, the problem can be solved by integrating the contributions of a continuum of point sources spread on the cylindrical Pt surface (Eq. (3))

$$C(r) \approx \frac{S}{4\pi D} \int_{Pt} \frac{d^2 r'}{|r - r'|}. \tag{3}$$

Only the difference in oxygen concentration between the Pt/Au junction and the extreme end of the Au part of the rod is needed to compute force resulting from an interfacial tension gradient.

To calculate the force created by this concentration gradient we must relate a difference in concentration to the interfacial tension (γ) difference at each end on the Au segment. First, we note that the interfacial tension of a solution may be taken as the mol fraction-weighted average of the component interface tensions (Eq. (4))

$$\gamma_{(solution))/X} = \sum_i \chi_i \gamma_{i/X}, \tag{4}$$

where X represents the contacting phase (solid or vapor) with the solution summed over all of the components in the solution. The interfacial tension of water and hydrogen peroxide are nearly identical, therefore reducing the number of components in solution by one. When considering the oxygen component the interfacial tension is approximately zero; therefore, the solution /Au interfacial tension may be determined using Young's equation (Eq. (5)),

$$\gamma_{vapor/Au} - \gamma_{solution/Au} = \cos(\theta)\gamma_{solution\,/\,vapor} \tag{5}$$

where $\cos(\theta) = 1$ rrespresents a hydrophilic gold segment (because a contact angle of 0 for water on a surface is defined as hydrophilic) and now we can differentiate Eq. (9) with respect to the water component (χ_{H2O}) and combine it with the concentration difference across the rod to obtain the force on the rod (Eq. (6))

$$F = \frac{S}{D}\pi R^2 \frac{\gamma_{H_2O/vapor}}{[H_2O]} \ln\left(\frac{L}{2R}\right) \tag{6}$$

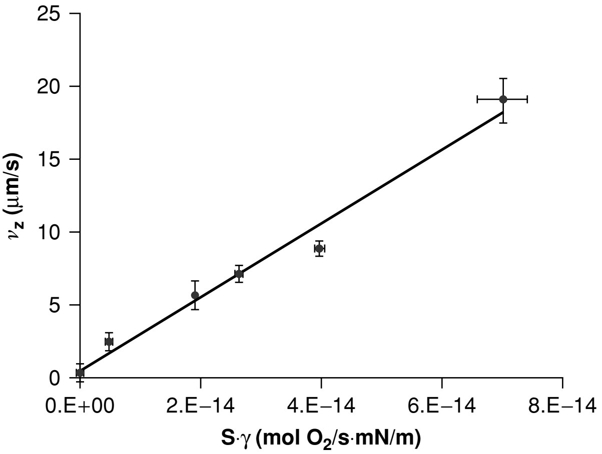

FIGURE 3.3. Effect of ethanol on the axial velocity of Pt/Au nanords in a dilute solution of hydrogen peroxide. *(Reproduced with permission from J. Am. Chem. Soc. 2004, 126, 13424–31. Copyright 2004 American Chemical Society.)*

The force in Eq. (6) is the interfacial tension force, where L represents the length of the rod and R the radius. Now the interfacial tension force may be equated with the drag force[12] to produce a steady-state velocity of a cylinder. Assuming that the logarithmic terms of the equation vary slowly with L and R, the scaling of velocity is related to the oxygen evolution rate, radius, interfacial tension, diffusion of oxygen, length, and viscosity according to the following relationship (Eq. (7)).

$$\upsilon \propto \frac{SR^2\gamma}{\mu DL} \tag{7}$$

The symbol, μ, represents the viscosity of the fluid. The predicted velocity is 17 μm/s for 2 μm long Pt/Au rods in 3.7% aqueous hydrogen peroxide where the interfacial tension is 72.0 mN/m, [H_2O] is 55M and the experimentally determined rate of oxygen evolution is 8.4E-8 mol/cm^2 s.

3.2.4.2. Evidence for an Interfacial Tension Mechanism. The mechanism was later tested with longer Pt/Au rods, various diameters and finally solutions of ethanol/water made up in varying ethanol concentrations. Ethanol was chosen because literature values exist for the interfacial tension of various ethanol/water compositions. Figure 3.3 shows the variation of the product of tension and the oxygen flux with particle speed as evidence in support of a interfacial tension mechanism.

To explain why platinum–gold nanorods move platinum end forward we investigated the surface effects of oxygen on the nanorod. We know that oxygen disrupts the hydrogen bonding network in water and therefore reduces the liquid/vapor interfacial tension. Therefore, the interfacial tension is lower at the platinum end of the rod where oxygen is being produced at a constant rate. Hence, the gold surface is the area of interest because it is the noncatalytic region where the gradient is established. A polar

gold surface would have a higher interfacial tension; therefore, the rod would move gold end forward if the gold were hydrophilic. On the other hand, a nanorod with a nonpolar or hydrophobic gold surface has a lower interfacial tension and would move platinum end forward. The gold would become hydrophobic if covered with oxygen vapor or bubbles. The latter was confirmed with liquid cell tapping mode atomic force microscopy. Tapping mode atomic force microscopy revealed bubbles pinned to the surface of the nanorod in an oxygen saturated water environment.

The concept of nanobubbles on surfaces[24] in oxygen saturated water produced the evidence to suggest that a Pt/Au nanorod forms nanobubbles on the gold surface. Therefore, the gold surface can be made hydrophobic *in situ*. The surface of the platinum is irrelevant because the gradient is not established over the platinum segment. This final piece of evidence was used to explain the direction of movement observed.

Other gradient forces as in local heating generated by the exothermic hydrogen peroxide reaction were determined to be negligible because their contribution to velocity was less than a micron/second. Therefore, the interfacial force due to a concentration gradient appears to be the most reasonable dominant driving force for the Pt/Au nanorods.

3.3. EVOLUTION OF CATALYTIC MOTORS

3.3.1. Microfabricated Motors

One of the potential applications of catalytically driven motors is in microelectromechanical devices (MEMS). Catchmark capitalized on the concept of the platinum–gold nanorods by designing gold gears (150 μm in size) with platinum spots on the teeth (Fig. 3.4) to produce the first rotating devices driven by the catalytic decomposition of hydrogen peroxide.

Rotation occurs because the platinum catalysts are located on the teeth of the gear and hang over the edge (inset of Fig. 3.4). According to the interfacial tension mechanism the gear should rotate platinum forward as observed in Fig. 3.5. The approximate rotational speed of the gear is one rotation per second but the translational speed of the gear ($\sim$390 μm/s) is approximately 400 times faster than the Pt/Au nanord which is in agreement with the scaling of the device from the nanoscale to the microscale.

The mechanism of movement was also confirmed to be similiar. Catchmark was able to control hydrophobicity of the gold through different wet chemistries, thereby demonstrating that a hydropbobic gold surface is necessary for movement to occur. This is in agreement with the interfacial tension gradient concept in that a hydrophobic gold surface is necessary to observe platinum end forward movement.

3.3.2. Remotely Steered Motors

3.3.2.1. Incorporating Magnetic Segments into Catalytic Motors. One of the short-falls with the Pt/Au nanorods was the poor directional control of the motor. Non-Brownian motion does not necessitate control over the direction of movement. A facile method to control the motion of autonomously moving Pt/Au nanorods is by

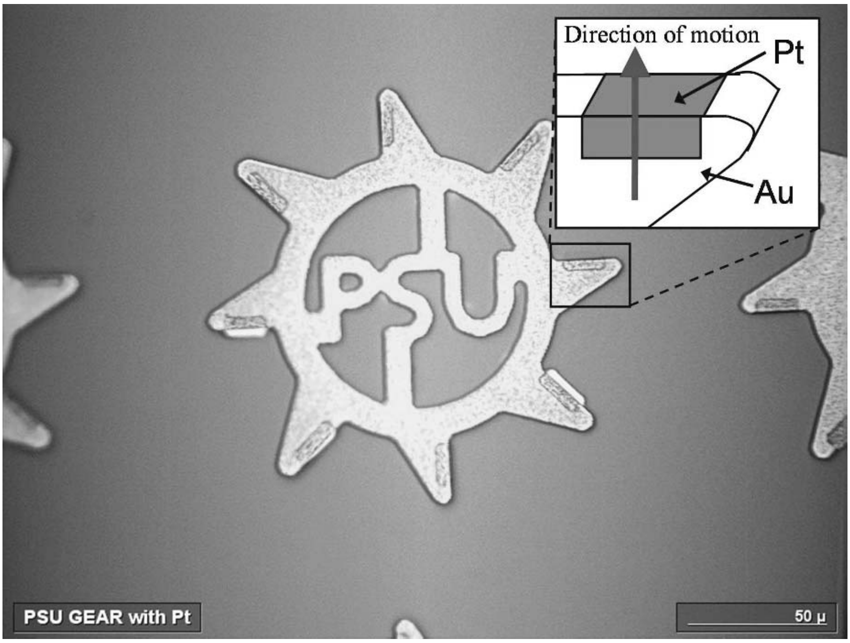

FIGURE 3.4. Image of gold gear with platinum teeth before freeing from the silicon oxide surface. *(Reproduced with permission from Small 2005, 1, 202–6. Copyright 2005 Wiley Inter Science.)*

incorporating magnetic segments into the wire. Nickel can be easily electroplated to form nanomotors with magnetic segments.

The use of magnetism to align nanoscale–mesoscale objects has been previously reported by Meyer and Whitesides.[25,26] Meyer used magnetism to self-assemble

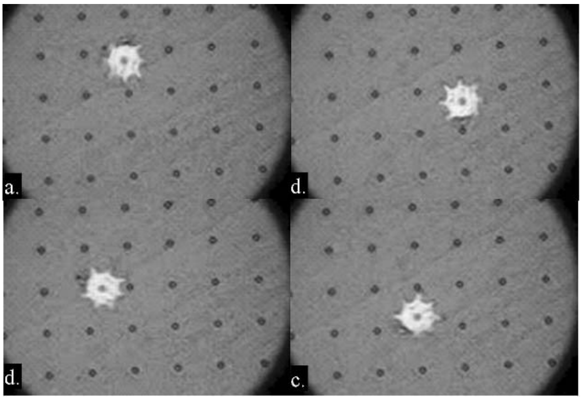

FIGURE 3.5. Rotation of a gear in a dilute solution of hydrogen peroxide on a silicon surface with posts on it. The gear rotates at a speed of about one micron per second, and is shown at (a) 0°, (b) 90°, (c) 180°, (d) 270°. *(Reproduced with permission from Small 2005, 1, 202-6. Copyright 2005 Wiley Inter Science.)*

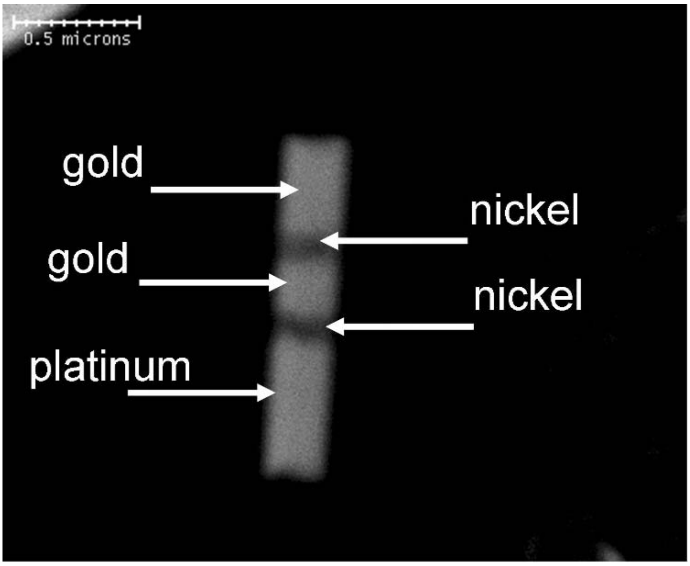

FIGURE 3.6. Scanning electron microscopy in back-scatter mode of a 400 nm by 1.5 μm striped Au/Ni/Au/Ni/Pt nanorod at 35,000x. *(Reproduced with permission from Angew. Chem. Int. Ed 2005, 44, 744–6. Copyright 2005 Wiley Inter Science.)*

flourescent and nonflourescent nanowires functionalized with porphyrins.[25] Whitesides also incorporated magnetic nickel segments into nanowires for self-assembly purposes.[26] Unlike Meyer, Whitsides made the diameter of the nickel segment to be larger than the length of the nickel segment in the nanowire. This dimensional change switches the easy axis of magnetization from longitudinal to transverse because the preferred axis for magnetic dipole alignment in magnetic materials is the longests axis. We combined the concept of a nanomotor with Whitesides approach and fabricated Pt/Ni/Au/Ni/Au striped nanorods (Fig. 3.6). We used the back-scatter mode in scanning electron microscopy to confrim the presence of our metals and their respective lengths. Back-scattering mode in scanning electron microscopy allows atomic number contrast. The dark colored segments in Fig. 3.6 are the two nickel segments that are approximately 100 nm in length and two of the white colored segments are gold 300 to 400 nm in length and the other segment is platinum about 500 nm in length.

3.3.2.2. Characterization. Optical microscopy techniques showed how a 550 Gauss strength magnetic field influenced the orientation of the rod. The magnetic field allowed the micron-scale control over the direction of motion (Fig. 3.7). Figure 3.7 shows the trajectory plot of one striped nanorod tracing out the letters “PSU” accompolished by steering the nanorod remotely with a strong magnet as it moves autonomously by the catalytic decomposition of hydrogen peroxide. The trajectory plot in Fig. 3.7 demonstrates our ability to control these nanorods with micron-scale precision using magnets.

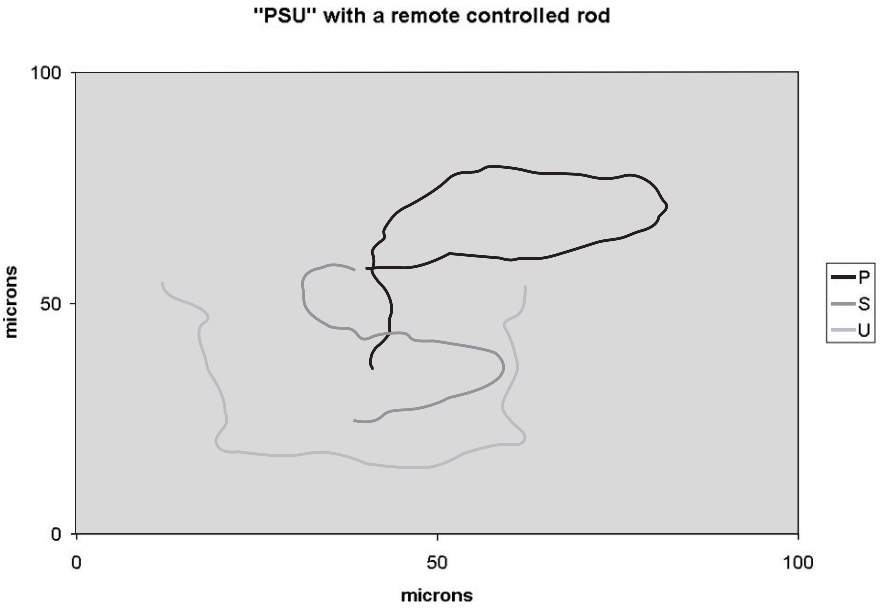

FIGURE 3.7. A Pt/Ni/Au/Ni/Au striped nanorod moving in 5% hydrogen peroxide to trace the trajectory of the letters "PSU." *(Reproduced with permission from Angew. Chem. Int. Ed 2005, 44, 744–6. Copyright 2005 Wiley Inter Science.)*

3.3.2.3. Particle Tracking. Particle tracking with PhysVis[23] was used to obtain Fig. 3.7 but it was also used to obtain quantitative data for various physical parameters. Specifically, we computed directionality values for the moving rods in and outside a magnetic field to demonstrate that the field is indeed aligning the moving nanorods. Secondly, we obtained axial velocity, product of directionality over 0.1 s time intervals and speed, to show that the magnetic field was not majorly influencing the speed of the rod. Finally, we obtained rotational diffusion coefficients to explicitly show the ability of the magnetic field to quench the 2-dimensional rotational motion of the nanorod (Table 3.2).

We chose longer directionalities, time intervals of 2 s in addition to those reported over 0.1 s time intervals, because the translational component to Brownian motion becomes less important as the time interval increases. Again, Brownian motion is the chaotic motion that arises from thermal energy and is readily apparent at short time intervals, 0.1 s. The higher directionalities over longer time intervals (2 s) show that the magnetic field is indeed influencing the direction of motion (0.85) versus those rods outside a field (0.6). Even rods without hydrogen peroxide in a magnetic field are observed to directionally aligned versus nonmagnetized rods without an applied field. The directionality results are the first piece of evidence that show the distinguishing effects of a magnetic field on the rod.

The second piece of evidence in distinguishing rods in a magnetic field to those out of the magnetic field was the rotational diffusion coefficient of the rod. It was the rotational diffusion coefficient that revealed the effect that an applied magnetic field had on a nanorod moving non-Brownian outside a field (2000 $^{\circ 2}$/s) and in it (70 $^{\circ 2}$/s).

TABLE 3.2. Data for striped nanorods in pure water and hydrogen peroxide with and without an applied magnetic field.[a]

H_2O_2 (wt.%)	Magnetic Field	Axial Velocity (μm/s)	Directionality (0.1 s)	Directionality (2 s)	Rotational Diffusion Coefficient ($^{\circ 2}$/s)
5%	Off	3.1(8)	0.5(1)	0.6(2)	2000
5%	On	2.4(7)	0.4(1)	0.85(6)	70
0%	On	0.2(2)	0.05(4)	0.3(2)	60
0%	Not magnetized	0.1(2)	0.01(6)	0.1(2)	700

[a] The sizes of the data sets from top to bottom are 22, 19, 21, 20 rods, respectively. *(Reproduced with permission from Angew. Chem. Int. Ed.* ***2005****, 744–6. Copyright 2004 Wiley-tech.)*

This demonstrates that the magnetic field strength of 500 Gauss is enough to quench the thermal motion in "*xy*" plane. We also calculated the magnetic torque of the nanorod from the bulk magnetization of nickel to be approximately 1E-15 A m^2 which produces a magnetic force of about 1E-17 N. The force due to thermal energy is approximately 1E-21 N. Comparing the two forces from the magnet and that of thermal energy shows that the magnetic force dominates by four orders of magnitude.

3.4. POSSIBLE APPLICATIONS

3.4.1. Biomedical

It was the latest evolution in nanorod motors that led us to imagine some of the possible biomedical applications of these devices. Specifically, when it was discovered that we were able to synthetically mimic magnetotactic bacteria because the magnetic moment of magnetotactic bacteria is on the order of the magnetic moment of a Pt/Ni/Au/Ni/Au striped nanorod.[27] In understanding how nature designs machines we may be able to better understand the complex mechanisms behind biological processes.

3.4.2. Roving Sensors

The idea of a roving sensor within the scope of this project is not far from reality either. In one aspect we have already created devices which are sensitive toward hydrogen peroxide. The next step is the design of devices that are powered by hydrogen peroxide but have built in sensors for a molecule of interest. A library already exists for tethering sensing molecules to inorganic devices so the concept is most definitely within grasp.

3.5. CONCLUSION

We have presented a method to move nano/microscale rods and gear-like structures using the platinum catalyzed decomposition of hydrogen peroxide. Then we proposed an interfacial tension mechanism as the cause for the autonomous movement. Experimental evidence to support the mechanism is discussed. Furthermore, we show how

it is possible to use external forces to steer the nanomotors and finally we suggest two possible applications of nanomotors.

ACKNOWLEDGMENT

We want to thank the Penn State Center for Nanoscale Science (NSF-MRSEC) for financial support.

REFERENCES

1. M. Abe, A. Yamamoto, M. Orita, T. Ohkubo, H. Sakai, and Z. Momozawa, Control of particle alignment in water by an alternating electric field, *Langmuir* **20,** 7021–7026 (2004).
2. A. O'Riordan, P. Delaney, and G. Redmond, Field configured assembly: Programmed manipulation and self-assembly at the mesoscale, *Nano Lett.* **4**(2), 761–765 (2004).
3. J. M. K. Ng, M. J. Fuerstman, B. Grzybowski, H. A. Stone, and G. M. Whitesides, Self-assembly of gears at a fluid/air interface, *J. Am. Chem. Soc.* **125,** 7948–7958 (2003).
4. A. K. Bentley, J. S. Trethewey, A. B. Ellis, and W. C. Crone, Magnetic manipulation of copper-tin nanowires capped with nickel ends, *Nano Lett.* **4**(3), 487–490 (2004).
5. S. Nakata, Y. Iguchi, S. Ose, M. Kuboyama, T. Ishii, and K. Yoshikawa, Self-rotation of a camphor scraping on water: new insight into the old problem, *Langmuir* **13,** 2254–2258 (1997).
6. N. Watanabe, K. Kutsumi, and O. Sano, Surface tension driven random motion of a mercury drop in HNO_3 and $K_2Cr_2O_7$ solution, *J. Phys. Soc. Jpn.* **63**(8), 2955–2963 (1994).
7. A. K. Schmid, N. C. Bartelt, and R. Q. Hwang, Alloying at surfaces by the migration of reactive two-dimensional islands, *Science* **290,** 1561–1564 (2000).
8. D. Pantaloni, C. Le Clainche, and M. Carlier, Mechanism of actin-based motility, *Science* **292,** 1502–1506 (2001).
9. H. Noji, R. Yasuda, M. Yoshia, and K. Kinosita Jr., Direct observation of the rotation of F_1-ATPase, *Nature* **386,** 299–302 (1997).
10. R. K. Soong, G. D. Bachand, H. P. Neves, A. G. Olkhovets, H. B. Craighead, and C. D. Montemagno, Powering an inorganic nanodevice with a biomolecular motor, *Science* **290,** 1555–1558 (2000).
11. R. F. Ismagilov, A. Schwartz, N. Bowden, and G. M. Whitesides, Autonomous movement and self-assembly, *Angew. Chem. Int. Ed.* **41**(4), 652–654 (2002).
12. W. F. Paxton, K. C. Kistler, C. C. Olmeda, A. Sen, S. K. St. Angelo, Y. Cao, T. E. Mallouk, P. E. Lammert, and V. H. Crespi, Catalytic nanomotors: Autonomous movement of striped nanorods, *J. Am. Chem. Soc.* **126,** 13424–13431 (2004).
13. C. R. Martin, Nanomaterials: A membrane-based synthetic approach, *Science*, **266,** 1961–1966 (1994).
14. B. R. Martin, D. J. Dermody, B. D. Reiss, M. Fang, L. Andrew Lyon, M. J. Natan, and T. E. Mallouk, Orthogonal self-assembly on colloidal gold-platinum nanorods, *Adv. Mater.* **11**(12), 1021–1025 (1999).
15. R. Hernandez, L. Richter, S. Semancik, S. Stranick, and T. E. Mallouk, Template fabrication of protein-functionalized gold-poly(pyrrole)-gold segmented nanowires, *Chem. Mater.* **16,** 3431–3438 (2004).
16. D. J. Pena, J. K. N. Mbindyo, A. J. Carado, T. E. Mallouk, C. D. Keating, B. Razavi, and T. S. Mayer, Template growth of photoconductive metal-CdSe-metal nanowires, *J. Phys. Chem.* B **106**(30), 7458–7462 (2002).
17. S. R. Nicewarner-Pena, R. G. Freeman, B. D. Reiss, L. He, D. J. Pena, I. D. Walton, R. Cromer, C. D. Keating, and M. J. Natan, Submicronmeter metallic barcodes, *Science* **294,** 137–141 (2001).
18. J. M. Catchmark, S. Subramanian, and A. Sen, Directed rotational motion of microscale objects using interfacial tension gradients continually generated via catalytic reactions, *Small* **1,** 1–5 (2005).

19. T. R. Kline, W. F. Paxton, T. E. Mallouk, and A. Sen, Catalytic nanomotors: Remote-controlled autonomous movement of striped metallic nanorods, *Angew. Chem. Int. Ed. Eng.* **ASAP** (2005).
20. H. W. Woodstra, Brownian movement and the coagulation of colloidal solutions, *Chemisch Weekblad* **15,** 679–680 (1918).
21. F. W. Tiebackx, The Brownian movements of colloids, *Pharmaceutisch Weekblad* **48,** 108–110 (1911).
22. G. K. Batchelor, Developments in microhydrodynamics, In *Theory and Applied Mechanics*, edited by W. T. Koiter, (North-Holland, Amsterdam) pp. 33–35.
23. PhysVis is a particle tracking program written by the Physics department at Kenyon college.
24. J. Yang, J. Duan, D. Fornasiero, and J. Ralston, Very small bubble formation at the solid-water interface, *J. Phys. Chem.* B **107,** 6139–6147 (2003).
25. M. Tanase, L. A. Bauer, A. Hultgren, D. M. Silevitch, L. Sun, D. H. Reich, P. C. Searson, and G. J. Meyer, Magnetic alignment of fluorescent nanowires, *Nano Lett.* **1**(3), 155–158 (2001).
26. J. C. Love, A. R. Urbach, M. G. Prentiss, and G. M. Whitesides, Three-dimensional self-assembly of metallic rods with submicron diameters using magnetic interactions, *J. Am. Chem. Soc.* **125,** 12696–12697 (2003).
27. H. Lee, A. M. Purdon, V. Chu, and R. M. Westervelt, Controlled assembly of magnetic nanoparticles from magnetotactic bacteria using microelectromagnets arrays, *Nano Lett.* **4**(5), 995–998 (2004).

4

Catalysis by Gold: Recent Advances in Oxidation Reactions

Graham J. Hutchings

4.1. INTRODUCTION

The discovery in the 1980s that finely supported divided nanoparticles of gold could act as catalysts for reactions at low temperatures has to be one of the most fascinating recent observations in chemistry, since most consider gold to be an unreactive metal. Gold for a long time had been considered to be a relatively inert material and particularly unpromising as a catalyst. In particular, due to its stability under most conditions it is really surprising that it can be a highly effective oxidation catalyst. Consequently, a large number of experimental and theoretical studies are being undertaken to try to elucidate the nature of this interesting catalytic activity. This recent research has been reviewed by Haruta,[1–5] Bond and Thompson,[6,7] Bond,[8] Thompson,[9] Freund and coworkers,[10] Cortie,[11] Hashmi,[12] Hutchings[13–15] and Hutchings and Scurrell.[16] It should be noted that copper and silver (both in the same triad of the periodic table as gold) are used in many large scale catalytic processes, and it has been known for many years that the preparation of active catalysts with copper and silver requires the metal to be well dispersed on a support. Hence, there should not be so much surprise when the same is observed for gold, but because gold was considered to be inert few experimental studies explored this area until the seminal studies of Haruta[17] who discovered the high activity of gold for CO oxidation at sub-ambient temperature. This new discovery brings with it the opportunity that gold, in an appropriate form, is perhaps the most interesting metal in the Periodic Table with respect to *table its potential* to act as a catalyst.

School of Chemistry, Cardiff University, Cardiff CF10 3TB, UK

Bond and coworkers[18] in early studies demonstrated that very small gold particles supported on silica could give interesting catalytic performance for hydrogenation, but until very recently the use of gold as a selective hydrogenation catalyst has received little attention.[19] In the 1980s there were two significant observations that completely changed this perception and highlighted the special attributes of gold as a heterogeneous catalyst:

- the discovery that supported Au catalysts are very active for low temperature CO oxidation.[17]
- the prediction that Au would be best catalyst for ethyne hydrochlorination.[20]

Since the 1980s publications involving gold as a catalyst have increased exponentially and even when normalized as a proportion of all scientific publications the number of papers concerning catalysis by gold has seen a 400% increase during this period.[12] In this chapter, these early studies will be considered, and against this background some recent research concerning the use of gold as a selective oxidation catalyst will be described and discussed as a way of providing a brief introduction into this fascinating new field to those interested in catalysis by nanoparticles.

4.2. BACKGROUND: EARLY WORK ON GOLD CATALYST

4.2.1. Ethyne Hydrochlorination

In the early 1980s one of the routes to the synthesis of vinyl chloride was based on ethyne hydrochlorination using mercuric chloride supported on carbon as a catalyst. This catalyst suffers from deactivation due to sublimation of the active component and so a replacement catalyst that was more stable was an important research goal. Based on a detailed study by Shinoda[21] it was observed that a range of metal chlorides supported on carbon could give a spectrum of activities for this reaction (Fig. 4.1). The data show a wide spectrum of activities and Shinoda attempted to correlate these data with the electron affinity. However, it is apparent that the $ZnCl_2$/carbon and the $HgCl_2$/carbon catalysts gave low and high activities respectively, yet Zn^{2+} and Hg^{2+} have virtually the same electron affinity. It was considered unlikely that the process of hydrochlorination involved a one-electron transfer in the rate limiting step and therefore it was considered equally unlikely that the catalytic activity could be correlated with a one-electron process represented by the electron affinity. In addition, there was no correlation with cations capable of forming metastable acetylides (represented by the filled symbols in Fig. 4.1). Furthermore, the data set out in Fig. 4.1 could not be used predictively, and consequently further experiments would be required to find an improved catalyst. It was considered more appropriate that the ethyne hydrochlorination reaction involved at least two electrons and most of the catalysts examined by Shinoda were based on divalent cations. Subsequently, the key observation was that the catalyst activity for ethyne hydrochlorination was correlated with the standard electrode potential (Fig. 4.2). The plot of conversion against the standard electrode potential gives a smooth curve and this predicts that gold, and more importantly Au^{3+}, will be the best catalyst for this reaction. This prediction[20] was subsequently confirmed experimentally.[22–24]

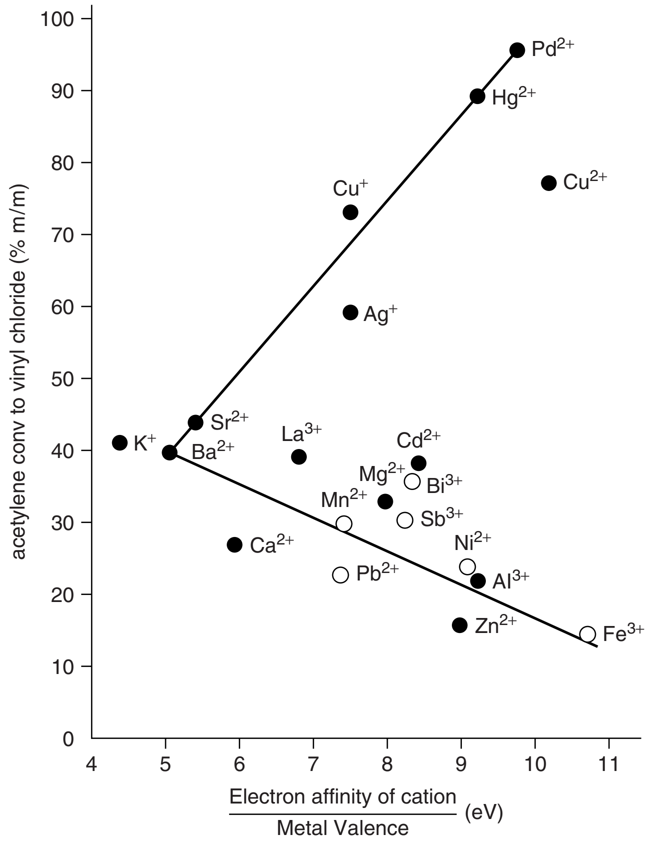

FIGURE 4.1. Correlation of activity for ethyne hydrochlorination with the electron affinity of the cation divided by the metal valence.[21]

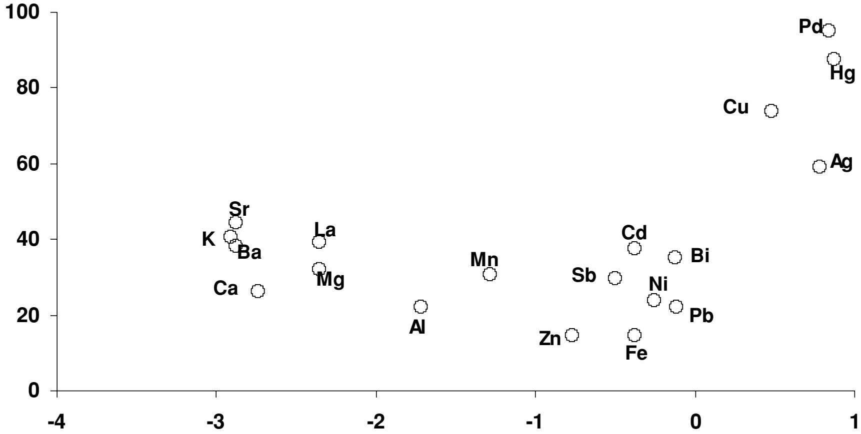

FIGURE 4.2. Correlation of activity for ethyne hydrochlorination with the standard electrode potential.[20]

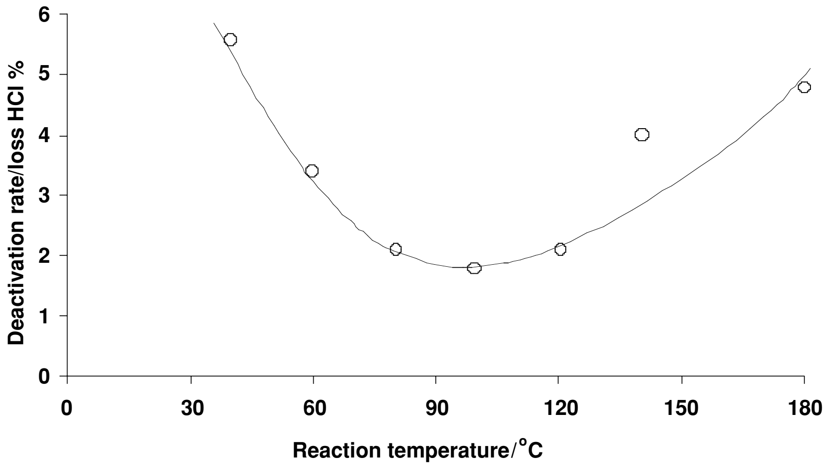

FIGURE 4.3. Deactivation rate of Au/carbon catalysts for ethyne hydrochlorination as a function of temperature (0.0005 mol Au/100 g catalyst, C_2H_2:HCl = 1:1.2).[23]

Although the gold catalysts were much more stable than the supported mercuric chloride catalysts, they still deactivated slowly with time and the rate of deactivation is dependent on temperature (Fig. 4.3). The deactivation rate was at a minimum at 100°C, but at this temperature the catalyst was not sufficiently active and temperatures of *ca.* 180°C are preferred. At temperatures below 100°C the deactivation was caused by deposition of polymeric carbonaceous materials and at higher temperatures the deactivation was caused by reduction of Au^{3+} to Au° as shown by detailed ^{197}Au Mössbauer spectroscopy (Fig. 4.4). This was a key observation and meant that the deactivation could be arrested by *in situ* reactivation by cofeeding dilute NO in with the reactor feedstock. This had no effect on catalyst selectivity but did stop deactivation (Fig. 4.5). This was the first demonstration of *in situ* reactivation of gold catalysts and also the first clear demonstration that *cationic* gold can be an effective heterogeneous catalyst. In this early study it was predicted, and subsequently verified, that gold was the catalyst of choice for this reaction. It was also recognized that Au^{3+} was the active form of gold. One interesting observation is that the catalysts could be easily prepared by a simple impregnation onto activated carbon of a gold solution in aqua regia; subsequently, it was observed that boiling deactivated catalysts in aqua regia restored the activity of the catalyst totally. This clearly demonstrates aspects of the unique robustness of supported gold catalysts. In this early study no emphasis was placed on the manner in which the supported gold catalysts were prepared. Effective catalysts could readily be prepared by impregnation and this led to the formation of relatively large gold nanoparticles. However, the spectroscopy studies detailed above clearly show that the enhanced activity is associated with cationic gold, although there is a sustained activity, albeit at a lower level, when the catalyst was deactivated following reaction for some time (Fig. 4.5). This may imply that metallic gold may play a role or that a low steady-state concentration of cationic gold was sustained during the catalytic cycle and this gives rise to the sustained catalytic performance. Since these early studies no further work

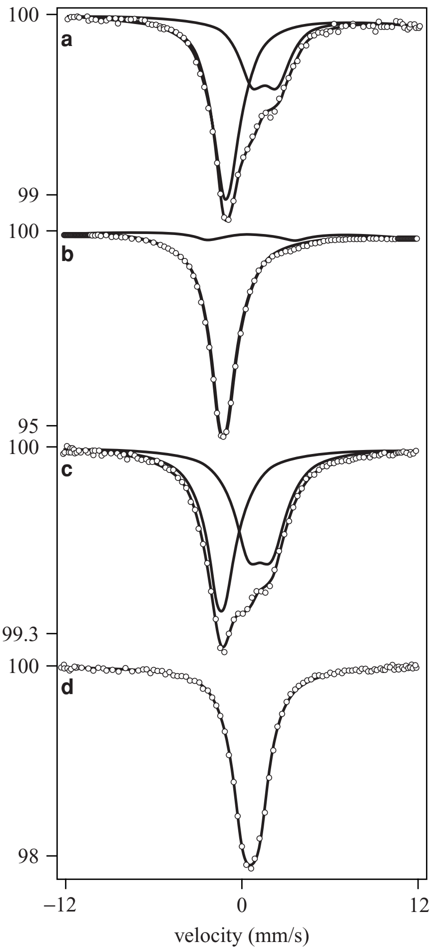

FIGURE 4.4. ^{197}Au Mössbauer spectra of: (a) 2% $HAuCl_4$/C adsorbed on activated carbon from an aqua regia solution, (b) the same catalyst after deactivation at 180°C for 6 h (GHSV = 1140 h^{-1}, C_2H_2:HCl = 1:1.1), (c) a sample of the same type after reactivation by boiling in aqua regia, and (d) crystalline $HAuCl_4 \cdot xH_2O$.[24]

has been published on ethyne hydrochlorination using gold catalysts, but the catalysts would prove interesting for *in situ* spectroscopic investigation to determine the relative roles played by Au^0 and Au^{3+}.

4.2.2. Carbon Monoxide Oxidation

Also in 1980s Haruta[16,25] recognized that supported gold nanocrystals can be highly effective catalysts for the oxidation of CO at very low temperatures (Fig. 4.6) and in particular at temperatures below 0°C. This is a surprisingly high activity and is not replicated by other metals. Haruta recognized that the method of preparation

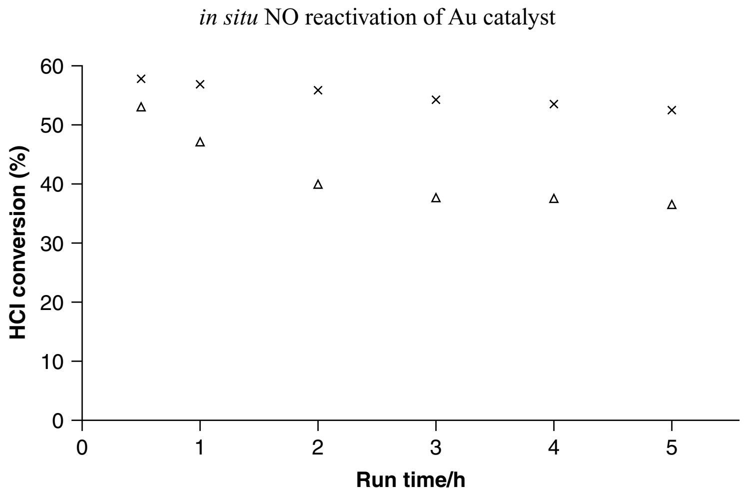

FIGURE 4.5. Effect of *in situ* reactivation of 2 wt.% Au/C catalyst at 180°C. Key: △ C_2H_2/HCl/N_2, × 0.42 vol.% NO cofed with reactants.[24]

was crucial to observe this high catalyst activity. For example, finely divided gold in a non-supported form only becomes active at *ca.* 280°C, whereas preparing α-Fe_2O_3-supported gold nanocrystals by impregnation produced a catalyst that was active at *ca.* 60°C. However, preparing the α-Fe_2O_3-supported gold nanocrystals by coprecipitation followed by calcination at 400°C produced a catalyst that was active at temperatures as low as −76°C. Haruta recognized that the very active catalysts comprised small gold nanoparticles *ca.* 2 to 4 nm in diameter. This amazing activity has now been replicated by many researchers, but it should be noted that each group appears to have their own techniques associated with preparing high activity catalysts. These early studies

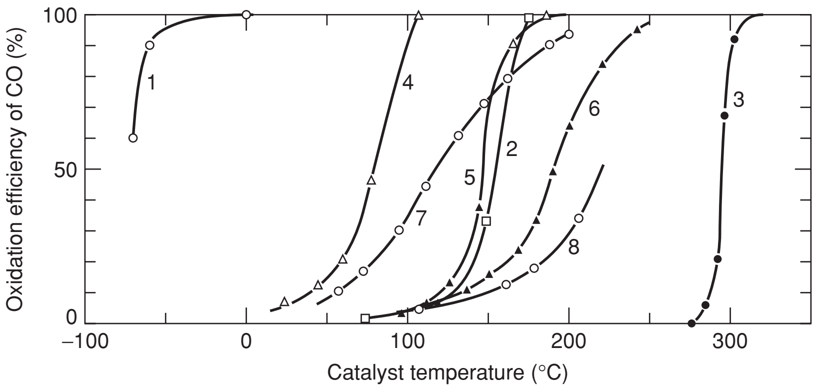

FIGURE 4.6. CO conversion over various catalysts as a function of temperature. 1, Au/α-Fe_2O_3 (Au/Fe = 1/19, coprecipitation, 400°C); 2, 0.5 wt.% Pd/γ-Al_2O_3 (impregnation, 300°C); 3, Au fine powder; 4, Co_3O_4 (carbonate, 400°C); 5, NiO (hydrate, 200°C); 6, α-Fe_2O_3 (hydrate, 400°C); 7, 5 wt.% Au/α-Fe_2O_3 (impregnation, 200°C); 8, 5 wt.% Au/ γ-Al_2O_3 (impregnation, 200°C).[25]

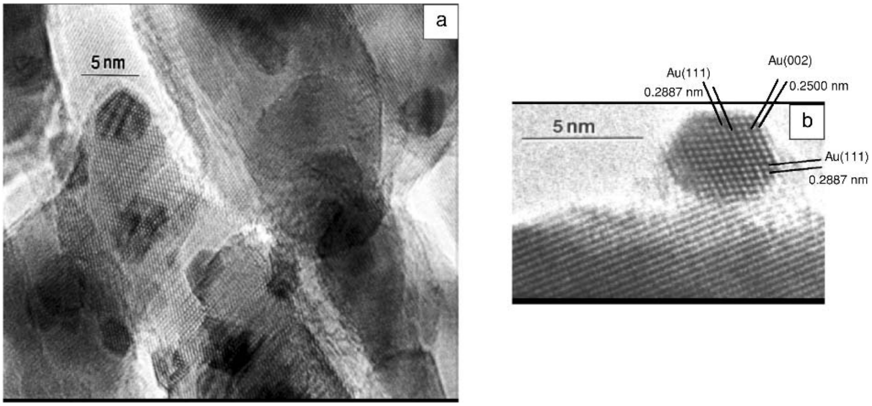

FIGURE 4.7. TEM micrographs for Au/ZnO catalyst calcined at 400°C showing the presence of 2 to 5 nm cuboctahedral gold particles.

also showed that the nature of the support was important and inferior catalysts are produced using γ-Al_2O_3 as support. However, it is the observation by Haruta that low temperature activity is feasible with supported gold nanocrystals that has spurred a great deal of the current research interest in gold today.[1–15] More recent studies have shown that low concentrations of water vapor are important for the observed catalysis and that TiO_2 is also an effective support.[26]

4.3. LOW TEMPERATURE CO OXIDATION: NATURE OF THE ACTIVE SITE

The early research indicated that catalysts must be prepared in a particular way using precipitation. Many of the active catalysts are typically found to comprise small crystallites, 2 to 4 nm in diameter, of gold supported on an oxide. There has been much debate concerning the nature of the active site for these catalysts and, recently, Bond and Thompson[7] have proposed a model where Au atoms at the interface between the Au particle and the oxide are the active oxidation centers. For example, Fig. 4.7 shows cuboctahedral gold nanoparticles supported on ZnO that is a very active CO oxidation catalyst. The periphery of the particle in association with the support is clearly visible and it is these peripheral atoms that have been the focus of much of the mechanistic debate. However, it remains unclear whether Au^{3+} or Au° is the active form of gold, and Bond and Thompson[7] have suggested that these peripheral atoms could be cationic gold and it is these atoms that are responsible for the activation of dioxygen in the catalytic process. Later Kung and coworkers[27] have also used this as the basis for their mechanistic discussion. However, it should be noted that this is an intense area of study at present, but although there has been much research using model systems a definitive study has not been published concerning the relative roles of Au^0 and Au^{n+} in the catalytic oxidation of CO. For example, Goodman and coworkers[28] using a combination of STM and spectroscopy considered that the unusual reactivity could be due to quantum size effects of the very small gold particles.

Indeed, the catalyst activity correlated with the transition of the electronic state of gold. As noted by Haruta,[5] this observation is questionable as far as CO oxidation is concerned, since the transition of the electronic state of gold was determined for one specific gold cluster of a defined diameter using STM under very controlled conditions, whereas the catalysis was determined using an entire Au/TiO_2 sample with a range of gold cluster diameters for which the mean diameter correlated with the observed STM electronic transition. Subsequently, Boyen *et al.*[29] concluded that Au particles containing 55 atoms, which are 1.4 nm in diameter, are extraordinarily stable and these Au_{55} particles could be active site for CO oxidation. Nørskov and coworkers[30] showed using DFT calculations that the activation of CO was energetically favored reaction path on Au particles with 10 atoms. However, others have focused on the role of Au^{3+}. In particular, Baker[31] noted that trying to explain the enhanced reactivity of small gold nanocrystals on the basis of size alone neglects the importance of the underlying support. Consequently, it is the interface between the small gold particles and the support that is important and this re-emphasizes the key part of the Bond Thompson mechanistic proposal.

However, it must be stressed that the model of the active site proposed by Bond and Thompson[7] or Kung and coworkers[26] has yet to be experimentally verified. A recent model study by Goodman and coworkers[32] has tried to address the role played by these peripheral atoms by designing well-ordered monolayers and bilayers of gold atoms that completely cover the TiO_2 support that clearly does not comprise any of these peripheral sites. They found that the bilayers were more active than the monolayers indicating that the catalysis can proceed on the extended gold surface so created. However, in this study no technique was used that could distinguish between cationic or metallic gold and consequently the effect on the electronic state of gold by the TiO_2 support cannot be ruled out.

Other researchers have used spectroscopic techniques in which cationic forms of gold can be observed, namely X-ray photoelectron spectroscopy and Mössbauer spectroscopy. Hutchings and coworkers[33] showed that Au^{3+} in Au / Fe_2O_3 was an important component of very active catalysts for the oxidation of CO. In 2003, Flytzani-Stephanopoulos and coworkers[34] demonstrated that the cationic form of gold was an important factor in obtaining high activity water gas shift catalyst based on Au added by deposition precipitation onto nanocrystalline 10% La-doped CeO_2 ($\sim$5 nm). The catalysts were subsequently leached with 2% NaCN removing 90% of the gold and, importantly, no Au particles remained after NaCN leaching. However the catalytic activity was not only retained but also significantly enhanced. CO oxidation can be viewed as an elementary reaction in the water gas shift reaction and so the observations by Flytzani-Stephanopoulos may be of general significance.

In a recent review, Haruta[5] has reassessed the mechanism of CO oxidation on the basis of the Bond and Thompson and Kung models, i.e. that the CO is activated by adsorption on Au^0 on the surface of the gold nanoparticles and that dioxygen is activated by the atoms at the periphery between the support and the gold nanocrystals (Fig. 4.7). The atoms at the periphery are proposed by Haruta to be cationic in nature, possibly $Au(OH)_3$ or Au(OH) formed by the presence of water vapor that is essential for the observed high activity catalysts.[26] It is clear that the debate will continue for the immediate future. There are two reasons why finding an answer to the key question of the nature of the active site in gold catalysts for CO oxidation. The first is purely scientific

in that the problem poses a significant challenge and it is worthy of close analysis and reflection. Secondly, the oxidation of CO is seen as a crucial aspect of using methanol or hydrocarbons as fuels for fuel cells. At present the reformate from these materials contains traces of CO that must be removed as they poison the electrodes, and gold catalysts may provide a mechanism of removing these trace amounts; this is addressed in the next section.

4.4. COMPETITIVE OXIDATION OF CARBON MONOXIDE IN THE PRESENCE OF HYDROGEN

As noted in the preceding two sections, in recent years there has been considerable interest in the oxidation of CO at relatively low temperatures using gold as a catalyst. One particular application is in fuel cells, especially polymer electrolyte fuel cells (PEFC), which are used in electric vehicles and operate at *ca.* 80 to 100°C. PEFCs operate by the oxidation of hydrogen produced from methanol by steam reforming and water gas shift reactions. Residual CO can poison the Pt anode at the low operating temperature and hence trace amounts of CO have to be removed from the H_2 in the presence of water to ensure long cell lifetimes. Although conceptually simple, the oxidation of CO in the presence of excess moist H_2, without oxidizing the hydrogen, is a particularly difficult reaction which is now attracting considerable research effort. An alternative strategy is to design PEFCs that can tolerate the residual CO, but to date this has also proved to be unsuccessful, so both approaches are being actively pursued at this time.

Considerable effort has been applied to the design of suitable catalysts for the competitive oxidation of CO in the presence of H_2, and the most commonly used partial oxidation catalysts (alumina-supported Pt, Ru and Rh) are unsuitable since they require temperatures in the range 150 to 200°C to be effective,[35–37] and even then significant conversion of H_2 is observed. Haruta and coworkers[38,39] first demonstrated that supported Au nanoparticles could be active at much lower temperatures, but again H_2 was oxidized together with CO at temperatures >70°C. Au/Fe_2O_3 catalysts have also been studied and Kahlich *et al.*[40] used catalysts calcined at 400°C but found that significant H_2 oxidation occurred at 80°C. Most recently, Qiao and Deng[41] have shown that noncalcined Au/Fe_2O_3 catalysts, dried only at 120°C, were very selective for CO oxidation in the presence of H_2 at 25°C, but the selectivity was lost at higher temperatures. To date, some of the best results for this demanding reaction have been reported by Grigorova *et al.*[42] for a Au/CeO_2 catalyst promoted with SnO_2, but even this catalyst gives significant (*ca.* 5%) H_2 conversion at temperatures >70°C with CO conversions of *ca.* 40 to 60%. Recently, Corma and coworkers[43] have reported a nanocrystalline CeO_2-supported gold catalyst that gave appreciable selectivity at 60°C for a dry CO/H_2 mixture. Unfortunately, all these previous studies use dry reactants and consequently are not applicable to the humid conditions prevailing in the fuel cell application which in addition also contains significant quantities of CO_2. However, recently Schubert *et al.*[44] have shown that a calcined Au/Fe_2O_3 can operate under realistic fuel cell conditions in which CO_2 and H_2O are present and reasonable selectivity can be achieved. Given these promising results we can anticipate further progress with this fascinating reaction in the future.

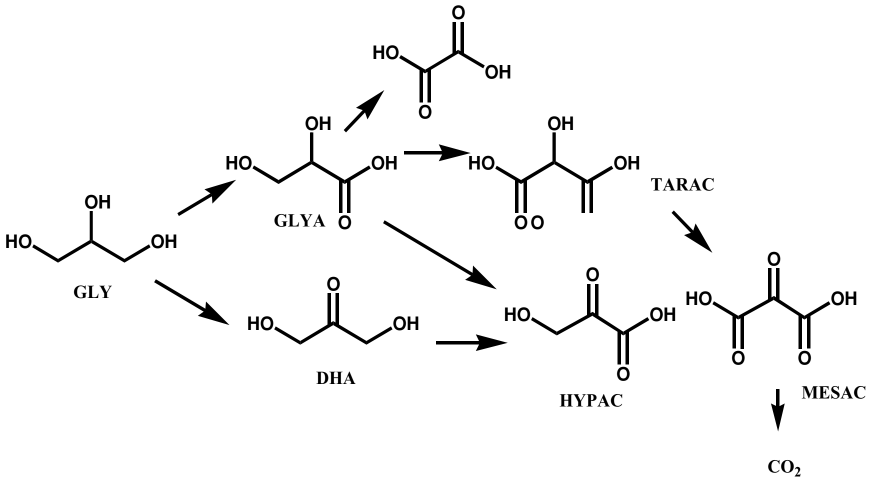

FIGURE 4.8. Reaction scheme for the oxidation of glycerol.

4.5. OXIDATION OF ALCOHOLS

The oxidation of alcohols and polyols to chemical intermediates represents a demanding target. Supported platinum and palladium nanoparticles are generally acknowledged as effective catalysts for the oxidation of polyols, for example in carbohydrate chemistry for the oxidation of glucose to glucinic acid. Glycerol is a highly functionalized molecule that is readily available from biosustainable sources, for example it can be obtained as a by-product of the utilization of rape seed and sunflower crops. This makes glycerol a particularly attractive starting point for the synthesis of intermediates, and a large number of products can be obtained from glycerol oxidation (Fig. 4.8). One of the key problems is the potential complexity of the products that can be formed and so control of the reaction selectivity by a careful design of the catalyst is required. Glycerol oxidation, in aqueous solution, has been extensively studied and in general, palladium catalysts were found to be more selective than platinum, but in all these previous studies using Pt and Pd, mixtures of most of the potential products were formed in addition to nonselective products such as formic acid and carbon dioxide. Hence, glycerol has remained an elusive starting point for the synthesis of chemical intermediates.

Prati and coworkers[45–48] have shown in their seminal studies that supported gold nanoparticles can be very effective catalysts for the oxidation of alcohols, including diols. Recently, the use of supported gold catalysts has been extended to show that Au supported on graphite can oxidize glycerol to glycerate with 100% selectivity using dioxygen as the oxidant under relatively mild conditions (Table 4.1).[49,50] The oxidation of alcohols was recognized by Prati and coworkers to require a base[45–48] which is considered to be essential for the first hydrogen abstraction.[50] Hence NaOH has to be added to observe reaction with supported gold catalysts. This is not the case for supported Pd and Pt catalysts which are active in acidic as well as in alkaline media, but these catalysts are, in general, much less selective when compared with the supported gold catalysts

TABLE 4.1. Oxidation of glycerol using 1 wt.% Au/C catalysts.[a]

Catalyst	Glycerol (mmol)	P_{O2} (bar)	Glycerol/ metal (mol ratio)	NaOH (mmol)	Glycerol Conversion (%)	Selectivity (%)		
						Glyceric Acid	Glyceraldehyde	Tartronic Acid
1 wt.% Au/activated carbon	12	3	538[b]	12	56	100	0	0
1 wt.% Au/graphite	12	3	538[b]	12	54	100	0	0
"	12	6	538[b]	12	72	86	2	12
"	12	6	538[b]	24	58	97	0	3
"	6	3	540[c]	12	56	93	0	7
"	6	3	540[c]	6	43	80	0	20
"	6	3	214[d]	6	59	63	0	12
"	6	3	214[d]	12	69	82	0	18
"	6	6	214[d]	6	58	67	0	33
"	6	6	214[d]	12	91	92	0	6
"	6	6	214[d]	0	0			

[a] 60°C, 3 h, H_2O (and 20 ml), stirring speed 1500 rpm.
[b] 220 mg catalyst.
[c] 217 mg catalyst.
[d] 450 mg catalyst.

used under basic conditions (Table 4.1). It is apparent that the selectivity to glyceric acid and the glycerol conversion are very dependent upon the glycerol/NaOH ratio. In general, with high concentrations of NaOH, exceptionally high selectivities to glyceric acid can be observed. However, decreasing the concentration of glycerol, and increasing the mass of the catalyst and the concentration of oxygen, leads to the formation of tartronic acid *via* consecutive oxidation of glyceric acid. Interestingly, this product is stable with these catalysts. It is apparent that, with careful control of the reaction conditions, 100% selectivity to glyceric acid can be obtained with 1 wt.% Au/C. For comparison, the supported Pd/C and Pt/C always gave other C_3 and C_2 products in addition to glyceric acid and, in particular, also gave some C_1 by-products. In a final set of experiments, catalysts with lower Au concentrations were investigated. For catalysts containing 0.25 or 0.5 wt.% Au supported on graphite, lower glycerol conversions were observed (18% and 26% respectively as compared to 54% for 1 wt.% Au/graphite under the same conditions) and lower selectivities to glyceric acid were also observed. The previous studies for diol oxidation by Prati and coworkers[45–48] have also shown that the conversion is dependent on the Au loading upon the support. This is possibly due to a particle size effect of the Au nanoparticles on the support. As noted earlier in this chapter, for gold as a CO oxidation catalyst, it has been shown that the activity is highly dependent on the particle size, and the optimum size is *ca.* 2 to 4 nm.[1–5] However, the Au supported catalysts that were selective for glycerol oxidation comprised Au particles as small as 5 nm and as large as 50 nm in diameter. The majority, however, were about 25 nm in size and were multiply twinned in character. Decreasing the loading to 0.5 wt.% or 0.25 wt.% did not appreciably change the particle size distribution; the particle number density per unit area was observed to decrease proportionately however, which may be correlated to the decrease in glycerol conversion and selectivity to glyceric acid. The catalysts that

were active and selective for glycerol oxidation were not found to be active for the CO oxidation reaction. Consequently, we consider that different active sites are involved in these two contrasting reactions and this opens up the mechanistic debate still further.

4.6. SELECTIVE OXIDATION OF HYDROGEN TO HYDROGEN PEROXIDE

At present there is significant interest in the design of new heterogeneous catalysts for selective oxidation under ambient conditions, and these typically use hydrogen peroxide as the oxidant.[51–53] At present, hydrogen peroxide is produced by the sequential hydrogenation and oxidation of alkyl anthraquinone[54] and global production is *ca.* 1.9×10^6 tonnes per annum. This process is currently only economic on a large scale ($4–6 \times 10^4$ tpa), whereas it is often required practically on a much smaller scale. Consequently, there is considerable interest in the direct manufacture of hydrogen peroxide from the catalyzed reaction of hydrogen and oxygen.[55,56] At present, some success has been achieved using Pd as a catalyst, especially when halides are used as promoters.[57,58] Supported Au catalysts have been investigated for the oxidation of propene to propene oxide using O_2/H_2 mixtures,[59] and it is considered that a surface hydroperoxy species may be formed as the oxidant. Hutchings and coworkers have found that supported Au catalysts can be very effective for the synthesis of hydrogen peroxide[60,61] and, furthermore, the rate of hydrogen peroxide formation can be significantly enhanced by the use of a supported Au/Pd alloy.

The initial research approach for the design of a direct hydrogen oxidation process for the synthesis of hydrogen peroxide, was to use supercritical CO_2 as a reaction medium. This is because earlier studies with Pd catalysts have indicated that H_2 diffusion is a significant problem and this can be expected to be largely overcome by using supercritical media due to the enhanced solubility of H_2. Au/ZnO, Pd/ZnO and Au:Pd/ZnO catalysts containing 5 wt.% metal were evaluated for the synthesis of hydrogen peroxide using supercritical CO_2 (35°C, 9.7 MPa). The Au/ZnO and Au:Pd/ZnO catalysts exhibited some hydrogen peroxide synthesis, albeit at a low rate. However, the Pd catalyst only generated water as a product. At this temperature it was considered that the hydrogen peroxide formed was relatively unstable with respect to decomposition or hydrogenation (Fig. 4.9). Hence, although using supercritical CO_2 as the reaction medium may have overcome the diffusion limitation, the inherent instability of hydrogen peroxide at the elevated temperature required to achieve supercritical conditions mitigates against the use of this medium.

Subsequently, experiments were conducted at significantly lower temperatures (2°C) and the results, shown in Fig. 4.10, indicate that hydrogen peroxide can be formed at a high rate for the supported Au catalyst. The selectivity for H_2O_2 for the Au/Al_2O_3 catalyst was determined to be 53%. In this case, the catalysts were prepared by impregnation and they were tested for hydrogen peroxide formation at 2°C using methanol as a solvent. The supported Au:Pd (1:1 by wt) catalyst produces significantly more than the pure Au catalyst or the Pd catalyst. It was found that the addition of just a small amount of Pd gave much better effects than the Au:Pd (1:1 by wt) catalyst (Fig. 4.10). This indicates a synergistic effect of Pd acting as a promoter for the Au catalyst. A detailed analysis using STEM-EDX confirmed that the catalysts comprised

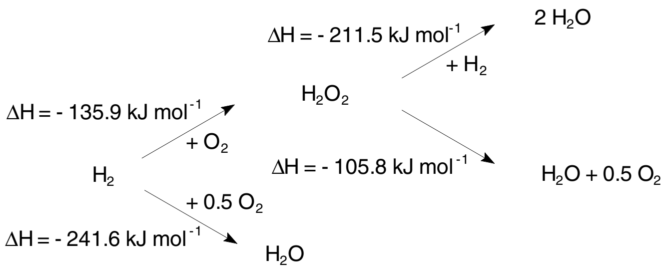

FIGURE 4.9. Reaction scheme for the oxidation of hydrogen to hydrogen peroxide.

Au–Pd alloys with compositions close to that of the bulk components and that particle sizes were *ca.* 25 to 50 nm in diameter. The catalysts that were effective for H_2O_2 synthesis were found to be wholly inactive for CO oxidation at ambient temperature, and catalysts that were effective for low temperature CO oxidation were inactive for H_2O_2 synthesis. This shows that selective oxidation reactions active may utilize very different sites than those for the oxidation of CO.

This preliminary work demonstrates that supported Au catalysts are effective for the direct synthesis of hydrogen peroxide from hydrogen and oxygen. In particular, Au catalysts may provide a significant improvement over Pd catalysts that have been investigated previously.[54–58] This clearly represents an exciting new reaction for which nanocrystalline gold is a highly effective catalyst.

4.7. CONCLUDING COMMENTS

The field of catalysis by gold is now well established. Although most effort to date has been focused on the oxidation of CO it is apparent that this research might

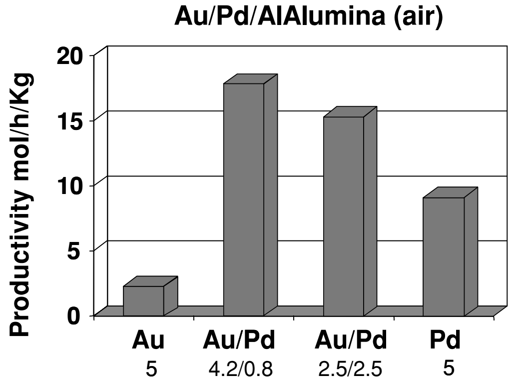

FIGURE 4.10. Production of hydrogen peroxide from the reaction of H_2 and O_2 over Au and Au/Pd catalysts at 2°C in an autoclave reactor using aqueous methanol (CH_3OH,5.6 g; H_2O 2.9 g) as solvent with catalyst (0.05 g), the reactor was purged three times with CO_2 (3 MPa) and then filled with 5% H_2/CO_2 and 25% O_2/CO_2.

find application in fuel cells. There is enormous potential for the use of supported gold nanocrystals for selective oxidation reactions and it is here where we can anticipate the greatest progress in the future.

REFERENCES

1. M. Haruta, Size- and support-dependency in the catalysis of gold, *Catal. Today* **36**(1), 153–166 (1997).
2. M. Haruta, and M. Date, Advances in the catalysis of Au nanoparticles, *Appl. Catal.* A **222**(1–2), 427–437 (2001).
3. M. Haruta, Catalysis of gold nanoparticles deposited on metal oxides, *CATTECH* **6**(3), 102–115 (2002).
4. M. Haruta, When gold is not noble: Catalysis by nanoparticles, *Chem. Rec.* **3**(2), 75–87 (2003).
5. M. Haruta, Gold as a catalyst in the 21st century: Preparation, working mechanism and applications, *Gold Bull.* **37**(1–2), 27–36 (2004).
6. G. C. Bond, and D. T. Thompson, Catalysis by gold, *Catal. Rev. Sci. Eng.* **41**(3–4), 319–388 (1999).
7. G. C. Bond, and D. T. Thompson, Gold-catalysed oxidation of carbon monoxide, *Gold Bull.* **33**(2), 41–51 (2000).
8. D. T. Thompson, Perspective on industrial and scientific aspects of gold catalysis, *Appl. Catal.* A **243**(2), 201–205 (2003).
9. R. Meyer, C, Lemaire, Sh. K. Shaikutdinov, and H.-J. Freund, Surface chemistry of catalysis by gold, *Gold Bull.* **37**(1–2), 72–124 (2004).
10. M. B. Cortie, The weird world of nanoscale gold, *Gold Bull.* **37**(1–2), 12–19 (2004).
11. A. S. K. Hashmi, Homogeneous catalysis by gold, *Gold Bull.* **37**(1–2), 51–65 (2004).
12. G. J. Hutchings, Catalysis: A golden future, *Gold Bull.* **29**(4), 123–130 (1996).
13. G. J. Hutchings, New directions in gold catalysis, *Gold Bull.* **37**(1–2), 3–11 (2004).
14. G. J. Hutchings, Catalysis by gold, *Catal. Today* **100**, 55–61 (2005).
15. G. J. Hutchings, and M. S. Scurrell, Designing oxidation catalysts: Are we getting better?, *CATTECH* **7**(3), 90–103 (2003).
16. M. Haruta, T. Kobayashi, H. Sano, and N. Yamada, Novel gold catalysts for the oxidation of carbon monoxide at a temperature far below 0°C, *Chem. Lett.* **2**, 405–408 (1987).
17. P. A. Sermon, G. C. Bond, and P. B Wells, Hydrogenation of alkenes over supported gold, *J. Chem. Soc., Faraday Trans.* 1 **75**(2), 385–394 (1979).
18. J. E. Bailie, and G. J. Hutchings, Promotion by sulfur of gold catalysts for crotyl alcohol formation from crytonaldehyde hydrogenation, *Chem. Commun.* **21,** 2151–2152 (1999).
19. G. J. Hutchings, Vapour phase hydrochlorination of acetylene: Correlation of catalytic activity of supported metal chloride catalysts, *J. Catal.* **96**(1), 292–295 (1985).
20. K. Shinoda, Vapour-phase hydrochlorination of acetylene over metal chlorides supported on activated carbon, *Chem. Lett.* **3**, 219–220 (1975).
21. B. Nkosi, N. J. Coville, and G. J. Hutchings, Vapour-phase hydrochlorination of acetylene with group VIII and 1B metal chloride catalysts, *Appl. Catal.* **43**(1), 33–39 (1988).
22. B. Nkosi, N. J. Coville, G. J. Hutchings, M. D. Adams, J. Friedl, and F. Wagner, Hydrochlorination of acetylene using carbon-supported gold catalysts: A study of catalyst reactivation, *J. Catal.* **128**(2), 378–386 (1991).
23. B. Nkosi, M. D. Adams, N. J. Coville, and G. J. Hutchings, Hydrochlorination of acetylene using carbon-supported gold catalysts: A study of catalyst deactivation, *J. Catal.* **128**(2), 366–377 (1991).
24. M. Haruta, N. Yamada, T. Kobayashi, and S. Lijima, Gold catalysts prepared by coprecipitation for low-temperature oxidation of hydrogen and of carbon monoxide, *J. Catal.* **115**(2), 301–309 (1989).
25. A. K. Sinha, S. Seelan, S. Tsubota, and M. Haruta, A three-dimensional mesoporous titanosilicate support for gold nanoparticles: Vapour-phase epoxidation of propene with high conversion, *Angew. Chem. Int. Ed.* **43**(12), 1546–1548 (2004).

26. H. H. Kung, M. C. Kung, and C. K. Costello, Supported Au catalysts for low temperature CO oxidation, *J. Catal.* **216**(1–2), 425–432 (2003).
27. M. Valden, X. Lai, and D. W. Goodman, Onset of catalytic activity of gold clusters on titania with the appearance of nonmetallic properties, *Science* **281**(5383), 1647–1650 (1998).
28. H.-G. Boyen, G. Kästle, F. Weigl, B. Koslowski, G. Dietrich, P. Ziemann, J. P. Spatz, S. Rietmüller, T. Hartmann, M. Nöller, G. Smid, M. Garnier, and P. Oelhafen, Oxidation-resistant gold-55 clusters, *Science* **297**(5586), 1533–1536 (2002).
29. N. Lopez, and J. K. Nørskov, Catalytic CO oxidation by a gold nanoparticle: A density functional study, *J. Am. Chem. Soc.* **124**(38), 11262–11263 (2002).
30. R. J. Davis, All that glitters is not Au^0, *Science* **301**(5635), 926–927 (2003).
31. N. A. Hodge, C. J. Kiely, R. Whyman, M. R. H. Siddiqui, G. J. Hutchings, Q. A. Pankhurst, F. E. Wagner, R. R. Rajaram, and S. E Golunski, Microstructural comparison of calcined and uncalcined gold/iron-oxide catalysts for low temperature CO oxidation, *Catal. Today* **72**(1–2), 133–144 (2002).
32. Q. Fu, H. Saltsburg, and M. Flytzani-Stephanopoulos, Active nonmetallic Au and Pt species on ceria-based water-gas shift catalysts, *Science* **301**(5635), 935–938 (2003).
33. M. J. Kahlich, H. A. Gasteiger, and R. J. Behm, Kinetics of the selective CO oxidation in H2-rich gas on Pt/Al2O3, *J. Catal.* **171**(1), 93–105 (1997).
34. S. Özkara, and A. E. Aksoylu, Selective low temperature carbon monoxide oxidation in H2-rich gas streams over activated carbon supported catalysts, *Appl. Catal.* **251**(1), 75–83 (2003).
35. P. V. Snytnikov, V. A. Sobyanin, V. A. Sobyanin, V. D. Belyaev, P. G. Tsyrulnikov, N. B. Shitova, and D. A. Shlyapin, Selective oxidation of carbon monoxide in excess hydrogen over Pt-, Ru-, Pd-supported catalysts, *Appl. Catal.* **239**(1–2), 149–156 (2003).
36. R. M. Torres Sanchez, A. Ueda, K. Tanaka and M. Haruta, Selective oxidation of CO in hydrogen over gold supported on manganese oxides, *J. Catal.* **168,** 125–127 (1997).
37. M. Okumura, S. Nakamura, S. Tsubota, T. Nakamura, M. Azuma, and M. Haruta, Chemical vapor deposition of gold on Al2O3, SiO2, and TiO2 for the oxidation of CO and of H2, *Catal. Lett.* **51**(1–2), 53–58 (1998).
38. M. J. Kahlich, H. A. Gasteiger, and R. J. Behm, Kinetics of the selective low-temperature oxidation of CO in H2-rich gas over Au/α-Fe2O3, *J. Catal.* **182**(2), 430–440 (1999).
39. B. Qiao, and Y. Deng, Highly effective ferric hydroxide supported gold catalyst for selective oxidation of CO in the presence of H2, *Chem. Commun.* **17**, 2192–2193 (2003).
40. B. Grigorova, J. Mellor, A. Palazov, and F. Greyling, Selective catalytic oxidation of CO in presence of H2, *PCT Int.* WO 2000059631 (2000).
41. S. Carrettin, P. Concepción, A. Corma, J. López-Nieto, and V. F. Puntes, Gold catalysts: Nanocrystalline CeO2 increases the activity of Au for CO oxidation by two orders of magnitude, *Angew. Chem. Int. Ed.* **43**(19), 2538–2540 (2004).
42. M. M. Schubert, A. Venugopal, M. J. Kahlich, V. Plzak, and R. J. Behm, Influence of H2O and CO2 on the selective CO oxidation in H2-rich gases over Au/α-Fe2O3, *J. Catal.* **222**(1), 32–40 (2004).
43. L. Prati and M. Rossi, Gold on carbon as a new catalyst for selective liquid phase oxidation of diols, *J. Catal.* **176**(2), 552–560 (1998).
44. F. Porta, L. Prati, M. Rossi, S. Colluccia, and G. Marta, Metal sols as a useful tool for heterogeneous gold catalyst preparation: reinvestigation of a liquid phase oxidation, *Catal. Today* **61**(1–4), 165–172 (2000).
45. C. Bianchi, F. Porta, L. Prati, and M. Rossi, Selective liquid phase oxidation using gold catalysts, *Top. Catal.* **13**(3), 231–236 (2000).
46. L. Prati, and G. Marta, New gold catalysts for liquid phase oxidation, *Gold Bull.* **32**(3), 96–101 (1999).
47. S. Carrettin, P. McMorn, P. Johnston, K. Griffin, and G. J. Hutchings, Selective oxidation of glycerol to glyceric acid using a gold catalyst in aqueous sodium hydroxide, *Chem. Commun.* **7**, 696–697 (2002).
48. S. Carretin, P. McMorn, P. Johnston, K. Griffin, C. J. Kiely, and G. J. Hutchings, Oxidation of glycerol using supported Pt, Pd and Au catalysts, *Phys. Chem. Chem. Phys.* **5**(6), 1329–1336 (2003).

49. M. Besson, and P. Gallezot, Selective oxidation of alcohols and aldehydes on metal catalysts, *Catal. Today* **57**(1–2), 127–141 (2000).
50. R. A. Sheldon, Redox molecular sieves as heterogeneous catalysts for liquid phase oxidations, *Stud. Surf. Sci. Catal.* **110**, 151–175 (1997).
51. G. Jenzer, T. Mallet, M. Maciejewski, F. Eigenmann, and A. Baiker, Continuous epoxidation of propylene with oxygen and hydrogen on a Pd-Pt/TS-1 catalyst, *Appl. Catal.* A **208**(1–2), 125–133 (2001).
52. H. T. Hess, in *Kirk-Othmer Encyclopedia of Chemical Engineering*, Edited by Kroschwitz and M. Howe-Grant (Wiley, New York, 1995)$_m$ vol. 13, p. 961.
53. J. Van Weynbergh, J.-P. Schoebrichts, and J.- C. Colery, Direct synthesis of hydrogen peroxide by heterogeneous catalysis, catalyst for the said synthesis and method of preparation of the said catalyst, *US Pat.* 5447706 (1995).
54. B. Zhou, and L.- K. Lee, Catalyst and process for direct catalystic production of hydrogen peroxide, (H2O2), *US Pat.* 69168775 (2001).
55. J. Wanngard, Method for manufacture of hydrogen peroxide, *Eur. Pat*. 816286 (1998)
56. K. T. Chuang, and B. Zhou, Production of hydrogen peroxide, *US Pat.* 5338531 (1994).
57. T. Hayashi, K. Tanaka, and M. Haruta, Selective vapor-phase epoxidation of propylene over Au/TiO2 catalysts in the presence of oxygen and hydrogen, *J. Catal.* **178**(2), 566–575 (1998).
58. P. Landon, P. J. Collier, A. J. Papworth, C. J. Kiely, and G. J. Hutchings, Direct formation of hydrogen peroxide from H2/O2 using a gold catalyst, *Chem. Commun*. **18,** 2058–2059 (2002).
59. P. Landon, P. J. Collier, A. F. Carley, D. Chadwick, A. J. Papworth, A Burrows, C. J. Kiely, and G. J. Hutchings, Direct synthesis of hydrogen peroxide from H2 and O2 using Pd and Au catalysts, *Phys. Chem. Chem. Phys*. **5**(9), 1917–1923 (2003).
60. G. J. Hutchings, I. H. Stewart, and E. G. Derouane, Catalytic reactions at supercritical conditions, *Curr. Top. Catal*. **2,** 17–38 (1999).
61. G. J. Hutchings, unpublished results.

5

Gold Catalysts Supported on Nanostructured Materials: Support Effects

Wenfu Yan, Steven H. Overbury, and Sheng Dai*

5.1. INTRODUCTION

Although gold in bulk has often been regarded as poorly active as a catalyst, Haruta *et al.* found in the late 1980s and the early of 1990s that the gold particles deposited on selected metal oxides exhibit surprisingly high catalytic activity for CO oxidation at low temperature.[1,2] Now, an extensive body of literature describing the CO oxidation ability of gold nanoparticles supported on various metal oxides, such as TiO_2,[3–15] Fe_2O_3,[1,16] CO_3O_4,[1] NiO,[1] SiO_2,[17] ZrO_2,[18,19] and Al_2O_3,[20] has appeared.[21–30] The catalytic activities of gold catalysts depend on many factors. Among them, the variation in the properties of support oxides gives rise to much of the variability in supported gold catalysts, for example the effect of isoelectronic point (IEP) upon deposition of gold species or the role of the oxide reducibility in effecting the transfer of oxygen between the support and the gold nanoparticles. The focus of this chapter is the review of our recent research on the synthesis and characterization of tailored nanostructured supports for the assembly of ultrasmall gold nanoparticles for catalysis applications.

This chapter is divided into three parts. Firstly, the catalytic activities and stabilities of gold nanoparticles supported on allotropic TiO_2 phases are compared.[4] To understand the mechanism of catalysis of the gold nanoparticles deposited on metal

Chemical Sciences Division, Oak Ridge National Laboratory, Oak Ridge, TN 37831-6201
* To whom correspondence should be addressed. E-mail: dais@ornl.gov

oxides, it is of interest to study the effects of variability of support structures for a single type of oxide. Titania (TiO_2) is a good candidate for such investigation because of the existence of two main allotropic metastable forms: anatase and brookite. Secondly, a surface sol–gel (SSG) method for tailoring mesoporous silica materials for gold catalysis applications is reviewed.[15] The essence of this method is to change the surface IEPs of mesoporous silica through a monolayer surface functionalization with high-IEP oxides (e.g., TiO_2) for the assembly of ultrasmall gold inside mesopores. Thirdly, a building-block approach based on a layer-by-layer SSG process is discussed.[31] Fumed silica materials were modified with a stepwise SSG process for controlled growth of double layers consisting of TiO_2 and Al_2O_3 monolayers with different combinations on silica surfaces. The significant differences in activity of the gold catalysts supported on the silica supports with the different combinations of surface monolayers were observed.

5.2. EXPERIMENTAL SECTION

5.2.1. Preparation of Gold Nanocatalysts Supported on Anatase and Brookite

5.2.1.1. Sonication Synthesis of Anatase.[32] The detailed synthesis protocol has been given previously.[4] Briefly, 100 mL of deionized water was sonicated by employing a direct-immersion titanium horn (Sonics and Materials, VCX-750, 20 kHz, and starting power 100 W/cm^2) followed by the injection of 10 mL of tetraisopropyltitanate (Aldrich) into the sonication cell (glass beaker). The mixture was further sonicated continuously for 1 h. The sonication was conducted without cooling. The white precipitates were separated by centrifugation and washed three times with deionized water and once with ethanol. The product was dried in a desiccater overnight and was ground into a fine powder before the deposition of gold precursor.

5.2.1.2. Hydrothermal Synthesis of Brookite.[33] Typically, NaOH solution (2 M) was added to 5 mL titanium tetrachloride with stirring to adjust the pH value of the solution to 10, producing a basic colloidal solution. The solution obtained was transferred into an autoclave and heated at 200°C for 24 h. The white precipitates were separated by centrifugation and washed three times with deionized water and once with ethanol. The product was dried at 70°C in air overnight and was ground to a fine powder before the deposition of gold precursor on its surface.

5.2.1.3. Deposition–Precipitation (DP) of Gold Precursor Species on Anatase and Brookite. First, weighed amounts of hydrogen tetrachloroaurate(III) trihydrate ($HAuCl_4 \cdot 3H_2O$, 99.9+%, Aldrich) were dissolved into 50 mL deionized water, a process that depends on the gold loading in the gold catalyst. The pH value of the resulting solution was adjusted to 10.0 with vigorous stirring, using a solution of 1.0 M KOH at room temperature to displace Cl^- with hydroxyl on the gold precursor.[34] After pH adjustment, the solution was heated in an 80°C water bath followed by the addition of 1.0 g of TiO_2 powder. The resulting mixture was continually stirred for 2 h to permit the gold precursor to react with and displace surface hydroxyls. Finally, the precipitates were separated by centrifugation and washed three times with deionized water and

once with ethanol to remove Cl^-. The product was dried at 40°C temperature in air overnight to obtain the "as-synthesized" catalyst.

5.2.2. *Preparation of Gold Nanocatalysts Supported on Mesoporous Silica Modified with Oxide Monolayer*

5.2.2.1. Surface Sol–Gel Modification of Mesoporous Silica Materials with TiO_2 Monolayer.[15] The mesoporous material used in this investigation is SBA-15. The SBA-15 silica was prepared using Pluronic P123 (Aldrich) and tetraethylorthosilicate (TEOS, Aldrich) according to the procedure described in the literature.[35] The procedure used for the preparation of one-layer or multilayer titanium oxide on SBA-15 powders was developed according to the method described by Kunitake and coworkers[36] for the preparation of ultrathin films of metal oxides on hydrolyzed surfaces. The homemade apparatus for conducting the surface sol–gel process on the mesopore surfaces of powdered materials consists of two parts: an evacuation system and a fritted reactor. Typically, 1.0 g of pre-dried SBA-15 powder was loaded into the fritted reactor, which was sealed with a rubber septum at one end and connected to a vacuum system at the other end. The initially loaded sample was evacuated at ambient temperature and purged by nitrogen. This cycle was repeated several times. Subsequently, the stop-cock separating the vacuum system and the reactor was closed and 5 mL of titanium(IV) butoxide (Aldrich, 97%) in the mixture of 10 mL anhydrous toluene (Aldrich, 99.8%) and 10 mL anhydrous methanol (Aldrich, 99.8%) was transferred into the reactor through a syringe. After 30 min reaction, the solution was completely removed via vacuum filtration. Anhydrous methanol (5 mL) was injected into the reactor to wash off the unreacted titanium(IV) butoxide. The resulting sample was dried via vacuum evacuation. An excess amount of deionized water was then injected into the glass tube to hydrolyze the monolayer of titanium oxide. The final product can be washed thoroughly with anhydrous methanol and dried for the coating of the second layer. The multilayers of titanium oxide on SBA-15 can be prepared by iteration of the above procedure.

5.2.2.2. Assembly of Ultrasmall Gold Nanoparticles on Surface-Modified Mesoporous Silica. Firstly, 3.0 g of hydrogen tetrachloroaurate(III) trihydrate ($HAuCl_4 \cdot 3H_2O$, 99.9+%, Aldrich) was dissolved into 500 mL deionized water to form the gold precursor solution. Typically, the pH value of the pre-weighed gold precursor solution (20 mL) was adjusted to about 10 with vigorous stirring using a solution of 1.0 M KOH at room temperature. The solution was then heated via an 80°C water bath, and a surface-modified SBA-15 (0.4 g) without any pretreatment was added with stirring. The resulting cloudy solution was continually stirred for 2 h. The precipitates were separated by centrifugation and washed three times with deionized water. The yellow product was dried at 40°C overnight.

5.2.3. *Preparation of Gold Nanocatalysts Supported on Silica Modified with Oxide Double Layers*

5.2.3.1. Surface Sol–Gel Modification of Fumed Silica with TiO_2/Al_2O_3 or Al_2O_3/TiO_2 Double Layer. The basic procedure for functionalization of Cab-O-Sil silica

surfaces with the double layers of TiO_2 and Al_2O_3 was the same as that given in Section 5.2.2.1. Typically, a pre-weighed SiO_2 powder sample (9.8 g) was loaded into a reflux bottle and dried at 125°C for 16 h. The bottle was then sealed with a pre-dried rubber septum. Subsequently, the metal oxide precursor [7.9 g $Ti(OBu^n)_4$ for titania or 7.7 g $Al(OBu^s)_3$ for alumina] and the anhydrous mixture of toluene (100 mL) and methanol (100 mL) were transferred into the bottle through a syringe. The resulting solution was refluxed for 3 h. The final product was filtered, washed several times with anhydrous ethanol, hydrolyzed with deionized water, and dried at 80°C overnight. The iteration of the above sequential condensation and hydrolysis reactions allows the coating of the second monolayer on the one generated in the previous deposition cycle. For comparison, we have also synthesized Cab-O-Sil silica functionalized with TiO_2 or Al_2O_3 monolayer.

5.2.3.2. Deposition–Precipitation (DP) of Gold Precursor on Surface-Modified Amorphous Silica. The gold nanoparticles were deposited on the above surface-modified amorphous silicas by using the same process as that given in Section 5.2.2.2.

5.2.4. Measurements of Catalytic Performance for CO Oxidation

The CO oxidation reaction was carried out in a plug-flow microreactor (AMI 200, Altamira Instruments). Typically, 50 mg of catalyst was packed into a 4-mm-ID quartz U-tube, supported by quartz wool. Sample treatments were carried out on the same instrument, using either 8% O_2/He for oxidations or 12% H_2 mixed with Ar for reductions. For each treatment, gas flow was initiated near room temperature. The temperature was then ramped at 10°C/min to the target, held for 30 min, and then cooled to reaction temperature in the gas. Each pretreatment was followed by activity measurements made as follows. A gas stream of 1% CO balanced with dry air (<4 ppm water) was flowed at ambient pressure through the catalyst at a rate that was adjusted from sample to sample to maintain a constant space velocity of 44,400 mL/(h$\cdot g_{cat.}$), or about 37 cm^3/min. Gas exiting the reactor was analyzed via a Buck Scientific 910 gas chromatograph equipped with a dual molecular sieve/porous polymer column (Alltech CTR1) and using a thermal conductivity detector. Typically, the sample was cooled to low temperature and the exiting gas was analyzed at regular intervals as the sample was slowly warmed. The reaction temperature was varied using an oven or by immersing the U-tube in a Dewar of ice water or cooled acetone, which slowly warmed (typically 0.1 to 0.2°C/min) throughout a period of approximately 10 h. The resulting curve of conversion vs. temperature was used to assess the activity after each treatment.

5.2.5. Characterization Methods

Powder X-ray diffraction (XRD) data were collected via a Siemens D5005 diffractometer with CuKα radiation ($\lambda = 1.5418$ Å). Routine transmission electron microscopy (TEM) and Z-contrast microscopy were carried out using an HITACH HD-2000 scanning transmission electron microscope (STEM) operated at 200 kV. Nitrogen gas adsorption measurements (Micromeritics Gemini) were used to determine the surface area and porosity of the catalyst supports. Inductively coupled plasma (ICP) analysis was performed via an IRIS Intrepid II XSP spectrometer (Thermo Electron Corporation).

5.3. RESULTS AND DISCUSSION

5.3.1. Support Effects from Structural Differences of the TiO_2 Allotropes (Anatase and Brookite)

Previously published work has demonstrated that the photocatalytic efficiency of titania depends upon its crystalline form. This variability has been attributed to differences in the rates of recombination, adsorptive affinity, or band gap between the rutile and anatase phases of titania.[37–39] In titania containing mixed phases of rutile and anatase, such as Degussa P25, enhanced activity for photocatalytic oxidation may also depend on crystallite morphology and interfacial contact.[39] It is therefore of interest to understand how differences in the structure of a titania support may affect other oxidative catalytic processes in gold catalysts. It has been shown that the selectivity in propylene epoxidation is improved by using anatase rather than rutile for catalysts prepared by DP of gold.[40] Higher activity for CO oxidation is observed for anatase compared with rutile when gold is deposited via a rather unconventional ion-cluster beam deposition approach.[41] The contacts at the Au-TiO_2 interfaces are also believed to play an important role in CO oxidation.[42]

Both anatase and brookite are metastable phases that can be readily converted to rutile upon heating at temperatures above 700°C.[43] In both metastable phases, the coordination of titanium is sixfold, with oxygen anions forming a distorted octahedron, and the oxygen atom being shared by three adjacent titanium atoms. However, the different stacking sequences and distortions of the Ti-O octahedral units in these two phases lead to crystallographic differences, thereby resulting in the different arrangement of the Ti–O and Ti–OH bonds on the surface of the corresponding nanoparticles. The structure of the most stable surfaces of anatase has been examined.[44] The (101) surface of anatase exhibits twofold coordinate oxygen anions and fivefold titanium cations, with the oxygen anions being more widely spaced on the anatase surface than on the brookite. The different spacing and symmetry of these Ti–O and –OH bonds on the surface of anatase and brookite can affect the deposition of the gold hydroxyl precursor on the surface of titania particles during the DP process. The systematic study of catalytic reactions on anatase-and brookite-supported gold catalysts can provide new insight into the catalytic mechanism of the gold nanoparticles deposited on metal oxides.

Nanosized anatase ($\leq$10 nm) and brookite ($\sim$70 nm) particles have been successfully synthesized via sonication and hydrothermal methods. Figure 5.1 shows the powder XRD patterns of as-synthesized anatase and brookite nanoparticles. The particle sizes were characterized by XRD and scanning electron microscopy (SEM) (Fig. 5.2).

Gold precursor was deposited on the surface of the nanosized particles of as-synthesized anatase and brookite supports via a DP process. The XRD patterns of the resulting samples (Fig. 5.1) show no metallic gold peaks, indicating that no redox reactions occur during the DP process or that the metallic gold particles are not large enough to generate observable XRD peaks.

Curves (a) and (b) in Fig. 5.3 compare the light-off curves for the gold catalysts supported on anatase and brookite after being treated with O_2 at 300°C. Interestingly, the catalytic activity of the brookite-supported gold catalyst remained highly active, with the onset for 100% CO conversion occurring around −20°C. In contrast, the onset

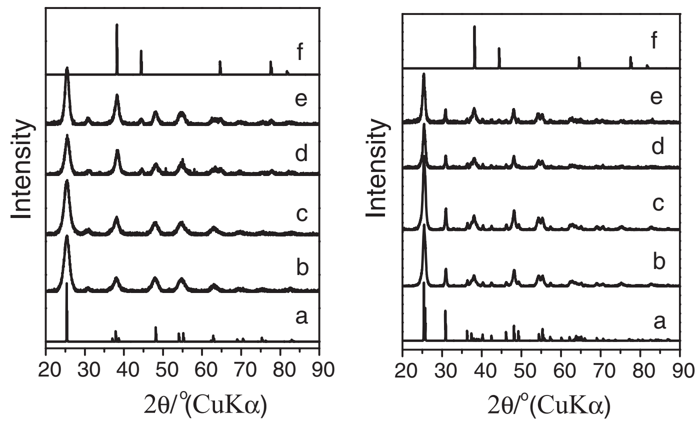

FIGURE 5.1. *Left*: Powder XRD patterns of (a) anatase simulated, (b) anatase as-synthesized, (c) as-synthesized Au-anatase, (d) Au-anatase treated at 300°C in O_2, (e) Au-anatase treated at 500°C in O_2, and (f) Au simulated. *Right*: Powder XRD patterns of (a) brookite simulated, (b) brookite as-synthesized, (c) as-synthesized Au-brookite, (d) Au-brookite treated at 300°C in O_2, (e) Au-brookite treated 500°C in O_2, and (f) Au simulated.

for 100% conversion of CO was obtained at 60°C for the anatase-supported catalyst treated under the same conditions.

The XRD patterns of both catalysts after treatment with O_2 at 300°C are compared in Fig. 5.1 (curves d). Clearly, the Au-anatase catalyst exhibits gold XRD peaks, indicating the formation of large metallic gold nanoparticles (diameter >20 Å) on the anatase support. The XRD pattern of the corresponding brookite-supported catalyst gives no XRD peaks associated with the large metallic gold nanoparticles.

The light-off curves of CO oxidation over Au-anatase and Au-brookite catalysts after treatment at 500°C in O_2 are shown in curves (c) and (d), respectively, in Fig. 5.3. Both catalysts were deactivated by this heat treatment; however, the Au-brookite remains significantly more active than the Au-anatase. The onset of 100% CO conversion for the Au-brookite occurs at approximately 60°C, while the corresponding onset for the Au-anatase occurs at temperatures as high as 160°C. The corresponding XRD patterns of these two samples are shown in Fig. 5.1 [curves (e)]. A very weak gold XRD peak at $2\theta \approx 44.5°$ can be seen in the XRD pattern of Au-brookite treated at 500°C in

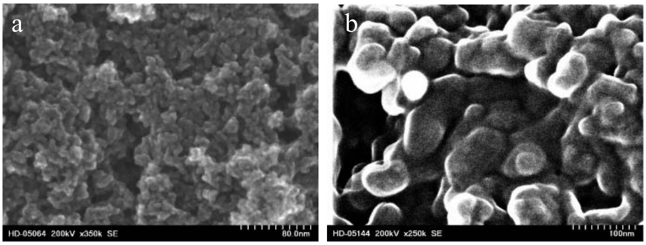

FIGURE 5.2. SEM images of as-synthesized (a) anatase and (b) brookite.

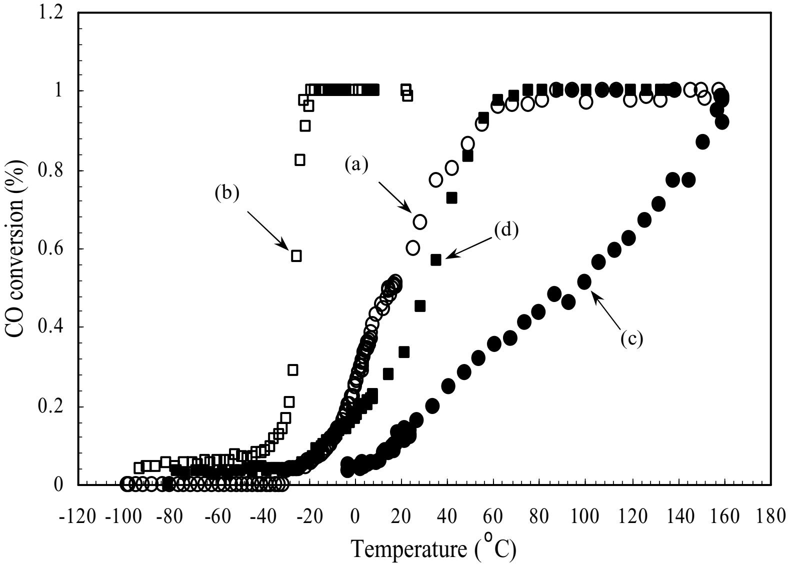

FIGURE 5.3. CO conversion vs. reaction temperature over supported gold catalysts: (a) Au-anatase treated at 300°C in O_2, (b) Au-brookite treated at 300°C in O_2, (c) Au-anatase treated at 500°C in O_2, and (d) Au-brookite treated at 500°C in O_2.

O_2, which indicates the formation via sintering of a small population of gold nanoparticles >3 nm. The gold XRD peaks for Au-anatase after treatment with O_2 at 500°C are more intense than those occurring after treatment with O_2 at 300°C, which indicates a significant increase in the population of large gold nanoparticles (>3 nm). Accordingly, the brookite-supported gold nanoparticles are significantly more stable against the temperature-induced aggregation than the anatase-supported gold nanoparticles.

This assertion about the stability of gold nanoparticles against aggregation on brookite surfaces is also consistent with the microscopy investigation performed using an HD-2000 STEM (probe size ≈ 0.3 nm) operating at 200 kV. Dark-field imaging with a high-angle annular dark-field (HAA-DF) detector provides higher contrast for small clusters of heavy elements in a low-atomic-number matrix as compared with conventional TEM. The nature of gold nanoparticles deposited on anatase and brookite makes these samples well suited to HAA-DF (also known as Z-contrast) STEM imaging. Figure 5.4 shows the comparison of the dark-field STEM images of the gold catalysts supported on anatase and brookite after treatment with O_2 at 300°C followed by treatment at 500°C. As seen in Fig. 5.4, the concentration of the large gold particles (>3 nm) on brookite is lower than that occurring on anatase. However, there is a significant population of small particles (<2 nm) retained on brookite. Thermally induced growth of particles observed in XRD and STEM was further confirmed by X-ray extended absorption spectroscopy, which also clearly indicated that gold supported on anatase sinters more facilely than on brookite.[45] Therefore, the loss of catalytic activity of the gold nanoparticles supported on anatase can be correlated to the higher tendency for the small gold nanoparticles to sinter on anatase during high-temperature O_2 treatment.

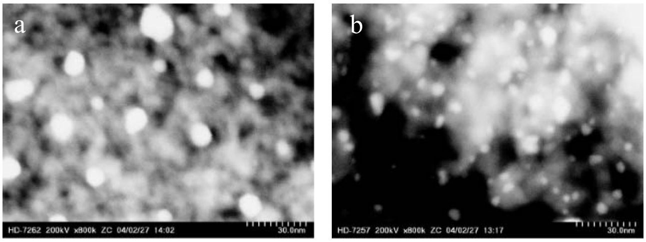

FIGURE 5.4. Dark-field STEM images of the gold catalysts after being treated at 500°C in O_2: (a) Au-anatase and (b) Au-brookite.

Further support for the assertion that gold nanoparticles are more susceptible to sintering on anatase than on brookite comes from the analysis of surface areas and gold loadings. The surface area of as-synthesized anatase is 225 m^2/g, while it is only 106 m^2/g for the as-synthesized brookite. The gold loadings of Au-anatase and Au-brookite determined via inductively coupled plasma-atomic emission (ICP-AE) are 2.8 wt.% and 3.2 wt.%, respectively. Since the surface density of gold is lower on anatase, this catalyst might be expected to be more stable against sintering than for Au on the brookite, if the surface properties of anatase and brookite, as well as the interaction between gold nanoparticles and support, are similar. This is clearly opposite to the above experimental observation. The difference of the sintering tendency of the gold nanoparticles dispersed on the surface of anatase and brookite must come from the different surface properties of these supports. A stronger interaction between gold nanoparticles and brookite surface or a higher barrier for particle coarsening might exist to slow down the kinetics for movement or thickening of the small gold nanoparticles.[46]

In conclusion, the stability of gold nanoparticles against sintering on brookite and anatase is very different. A highly stable catalytic system for CO oxidation based on the brookite-supported gold catalyst has been developed. The high stability of Au-brookite could result from the unique surface property of brookite. The interaction between gold nanoparticles and support plays the important role of stabilizing the catalyst in high-temperature environments. Work is currently under way to explore the applications of the Au-brookite catalyst in other catalytic processes.

5.3.2. Support Effects from Surface-Modified Mesostructured Substrates

The key effect of oxide supports on the catalytic activities of metal particles is exerted through the interface between oxides and metal particles. The key objective of this study is to develop synthesis methodologies for tailoring this interface. Here, an SSG approach was introduced to modify the surface of mesoporous silica materials with ultrathin films of titanium oxide so that the uniform deposition of gold precursors on ordered mesoporous silica materials by DP could be achieved without the constraint of the low IEP of silica. The surface sol–gel process was originally developed by Kunitake and coworkers.[36,47–49] This novel technology enables molecular-scale control of film thickness over a large 2-D substrate area and can be viewed as a solution-based

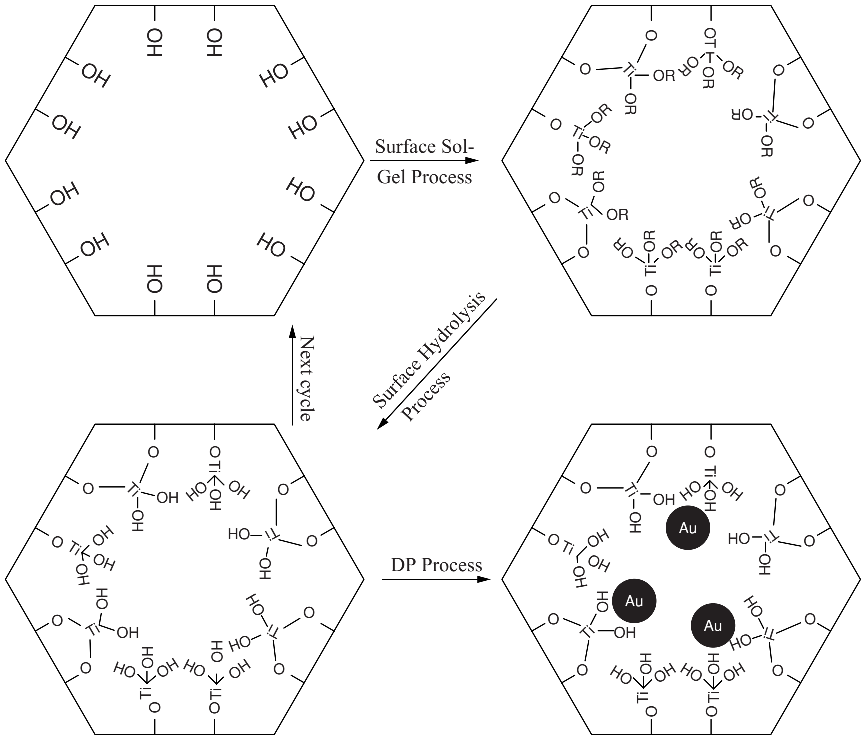

SCHEME 5.1.

methodology for atomic layer deposition (ALD) synthesis.[50–52] The surface sol–gel technique generally consists of two-half reactions: (1) nonaqueous condensation of metal-alkoxide precursor molecules with surface hydroxyl groups and (2) aqueous hydrolysis of the adsorbed metal-alkoxide species to regenerate surface hydroxyls. Iteration of the above sequential condensation and hydrolysis reactions allows the layer-by-layer coating of a selected metal oxide on a hydroxyl-terminated surface. Scheme 5.1 is a schematic diagram of the basic synthesis protocol for ultrathin TiO_2 on SBA-15. The SBA-15 materials have hexagonally packed channels with pore sizes of ~7.4 nm. The large mesopores allow a facile transport of metal-alkoxide reactants inside the mesopores not only for monolayer but also for multilayer functionalization on the internal walls of SBA-15.

Figure 5.5 shows the variation of the pore size distribution as a function of cycles of surface-modification-based N_2 adsorption isotherms. The pore size decreases with the modification cycle number. The reduction of the mesopore size for each cycle should be about twice the single-layer thickness. Accordingly, the effective single-layer thickness is about 6 to 7 Å based on the above BET measurements. This value is close to those estimated from the frequency changes of a quartz crystal balance for ultrathin films prepared by the surface sol–gel process on 2-D substrates.[47–49]

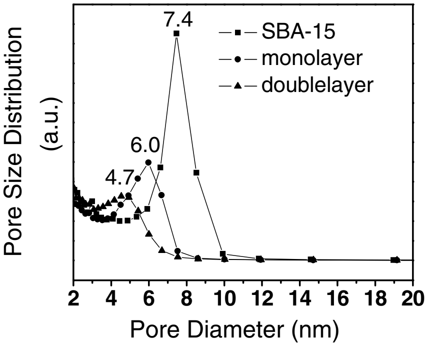

FIGURE 5.5. Pore size distributions as a function of the number of TiO_2 layers.

Another consequence of this surface sol–gel process on SBA-15 is the reduction of the surface silanol groups induced by the condensation reaction with titanium butoxide. The reaction, after hydrolysis, converts surface silanol functionality, $(SiO)_3SiOH$, into Ti-OH functionality. Given the similar electronegativity of silicon (1.8) and titanium (1.7), the expected consequence of this modification in the solid state ^{29}Si NMR is a decrease in the Q^3 band and a corresponding increase in the Q^4 band; that is, the $OTi(OH)_3$ and $OSi(OH)_3$ ligands will cause equivalent NMR shift perturbations on the substituted silicon site.

The solid-state ^{29}Si SPE NMR spectra of SBA-15 and the titania surface-coated SBA-15 (Ti-SBA-15) are in accord with this expectation. The spectrum of SBA-15 displays a broad asymmetric peak at 109 ppm (Q^4 sites) with shoulders at −101 ppm (Q^3 sites) and 90 ppm (Q^2 sites) in the area ratio 79:19:2. The NMR spectrum of Ti-SBA-15 (one layer) shows a reduction of the Q^3 band intensity relative to the Q^4 intensity. The normalized Q^4:Q^3:Q^2 site populations become 85:13:2. No asymmetry is observed in the Q^4 site band. Repetition of the monolayer deposition to form a double layer of titania on silica yields a material whose ^{29}Si NMR spectrum is indistinguishable from that of the Ti-SBA-15 with a monolayer coverage. As expected, the titania-insulated silica resonances are unperturbed by the second titania layer.

The gold precursors were readily introduced via the DP method on the surfaces of the modified mesoporous materials. The subsequent reduction of the surface-immobilized gold precursors with CO successfully led to gold nanoparticles assembled inside ordered mesopores. Figure 5.6 shows the Z-contrast TEM image of the resulting materials. The tiny, highly uniform bright spots (0.8 to 1.0 nm diameter) along the mesopore channels in Fig. 5.6 correspond to the gold nanoparticles. The Z-contrast TEM imaging provides direct proof of the presence of the metallic gold nanoparticles within the channels of SBA-15. The key point with HAA-DF imaging is that the intensity of the Rutherford scattered beams is directly proportional to Z^2, where Z is the atomic number of the scattering element. Thus, heavy atoms (such as gold) stand out very clearly on a light background of silicon and oxygen. The energy-dispersive X-ray (EDX) spectroscopy analysis of the composition of this range in Fig. 5.6 is in agreement with the presence of gold and titanium. The preparation of gold nanoparticles on SBA-15 (without titania monolayer) by the DP method resulted in only a

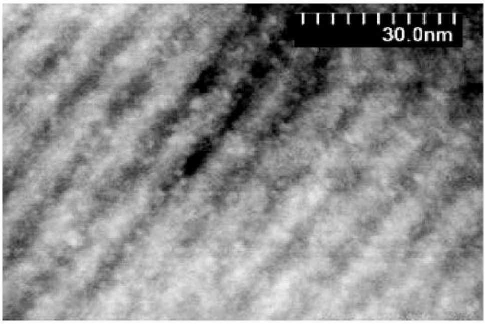

FIGURE 5.6. Z-contrast TEM image of ultrasmall gold nanoparticles on ordered mesoporous materials. The bright spots (0.8∼1.0 nm) correspond to gold nanoparticles.

small population of very large gold nanoparticles aggregated on the external surfaces of SBA-15. This observation clearly demonstrated the importance of TiO_2 surfaces for the immobilization and the stabilization of gold nanoparticles.

The activity of the gold catalysts for CO oxidation was characterized via a plug-flow reactor using 1% CO/dry air at a space velocity at 44,400 $cm^3/(g_{cat}{\cdot}h)$. Comparisons were made between the Au/monolayer TiO_2-SBA-15 and the Au/commercial nanocrystalline titania support (Degussa P25). Comparably high activities (i.e., achieving 50% CO conversion above about −40°C) were found for the as-synthesized gold catalysts. High-temperature (300°C, 30 min) 8%O_2/He treatment dramatically decreased the activity of nanocrystalline TiO_2-supported catalysts, as the light-off curve shifted to high temperature. This deactivation can be attributed primarily to the aggregation of gold nanoparticles.[24] By contrast, the activity of the monolayer catalyst did not change significantly, achieving >50% conversion at −25°C.

5.3.3. Support Effects from the Different Combinations of Oxide Monolayers Sequentially Coated on the Surface of Amorphous Silica

As discussed in the above section, the self-limiting nature of the SSG process is key to the success of the layer-by-layer functionalization. The SSG process is a versatile technique that can be utilized for the functionalization of oxide supports with both single and multiple oxide components. The objective of the current study is to generate more complex multicomponent oxide surfaces via the SSG process for the investigation of the support effects in gold catalysis. The surfaces discussed here consist of two sequential combinations of TiO_2 and Al_2O_3 monolayers on amorphous silica: (1) $Al_2O_3/TiO_2/SiO_2$ (SiO_2 coated with the first layer of TiO_2 and the second layer of Al_2O_3) and (2) $TiO_2/Al_2O_3/SiO_2$ (SiO_2 coated with the first layer of Al_2O_3 and the second layer of TiO_2). For comparison, we have also prepared the same silica sample functionalized by TiO_2 (TiO_2/SiO_2) or Al_2O_3 (Al_2O_3/SiO_2) monolayers.

XRD analyses revealed the amorphous nature of the mono/multilayers of TiO_2 and/or Al_2O_3 on fumed silica. Elemental analyses of the samples of $Au/TiO_2/SiO_2$, $Au/Al_2O_3/SiO_2$, $Au/Al_2O_3/TiO_2/SiO_2$, and $Au/TiO_2/Al_2O_3/SiO_2$ showed that the gold weight loadings for these four samples were 5.1, 7.9, 10.3, and 11.7%, respectively.

Figure 5.7 shows the light-off curves of Au/TiO_2/SiO_2, Au/Al_2O_3/SiO_2, Au/Al_2O_3/TiO_2/SiO_2, and Au/TiO_2/Al_2O_3/SiO_2. These light-off curves were measured from the samples both as-synthesized and pretreated under the following conditions: 150°C in H_2 (50% H_2/He) and 150°C in O_2 (8% O_2/He).

The gold nanoparticles deposited on the surface of unmodified fumed silica with the DP method show no activity for CO oxidation (not shown). No clear improvement of the catalytic activities was observed for the gold nanoparticles on SiO_2 whose surface was modified with an Al_2O_3 monolayer through the SSG process. The as-synthesized Au/Al_2O_3/SiO_2 sample had a very low conversion at high temperature but was quickly deactivated. The initial low activity can be attributed to the reduction of cationic gold species to metallic gold by CO, which disappeared after the cationic gold species were totally consumed. This conjecture is also consistent with the observations that the catalysts pretreated at 150°C (either in H_2 and in O_2) exhibit no activities.

The further surface modification of Al_2O_3-modified fumed silica with a TiO_2 monolayer resulted in a double-layer-coated support (TiO_2/Al_2O_3/SiO_2). The deposition of gold nanoparticles on this double-layer-coated support (Au/TiO_2/Al_2O_3/SiO_2) via DP gave rise to a highly active catalyst for CO oxidation. For the as-synthesized catalyst, a 50% conversion was observed at −22°C (specific rate: 0.085 $mol_{CO}/g_{Au}/h$). The treatment at 150°C (either in O_2 or H_2) slightly decreased its activity. The catalysts treated at 150°C in O_2 and H_2 have 50% conversion temperatures at about −18°C and −11°C (specific rate: 0.085 $mol_{CO}/g_{Au}/h$), respectively.

In contrast to the Al_2O_3-modified fumed silica (Al_2O_3/SiO_2), the TiO_2-modified fumed silica (TiO_2/SiO_2) is a good substrate for the preparation of highly active gold nanocatalysts. The gold nanoparticles deposited on TiO_2/SiO_2 exhibited a high activity for low-temperature CO oxidation. For the as-synthesized catalyst, the 50% conversion temperature (specific rate: 0.194 $mol_{CO}/g_{Au}/h$) is as low as −44°C, which is much lower than that of Au/TiO_2/Al_2O_3/SiO_2. The reduction at 150°C in H_2 decreased the activity, giving rise to a 50% conversion temperature at −32°C. Surprisingly, the treatment at the same temperature in O_2 increased the activity of this catalyst, with a 50% conversion temperature approaching −54°C. The enhanced activity could be attributed to the surface restructuring of cationic gold species on the TiO_2 monolayer to enhance the interaction at the interface.

The further surface modification of the TiO_2-modified fumed silica with an Al_2O_3 monolayer gave rise to another double-layer-coated support (Al_2O_3/TiO_2/SiO_2) whose monolayer functionalization sequence is the reverse of TiO_2/Al_2O_3/SiO_2. A new gold nanocatalyst (Au/Al_2O_3/TiO_2/SiO_2) was prepared through DP of gold precursors on the surface of Al_2O_3/TiO_2/SiO_2. The as-synthesized gold nanocatalyst gave a 50% conversion temperature (specific rate: 0.096 $mol_{CO}/g_{Au}/h$) at −31°C, which is more active than that for Au/TiO_2/Al_2O_3/SiO_2 but less active than that for Au/TiO_2/SiO_2. The treatment at 150°C in O_2 just slightly increased the activity of Au/Al_2O_3/TiO_2/SiO_2, unlike the significant increase in the case of Au/TiO_2/SiO_2. However, the treatment at 150°C in H_2 considerably increased the activity of Au/Al_2O_3/TiO_2/SiO_2. The catalyst treated in H_2 at 150°C is highly active even at −94°C, with 75% conversion (specific rate: 0.144 $mol_{CO}/g_{Au}/h$). In sharp contrast, the Au/TiO_2/SiO_2 catalyst treated in H_2 at 150°C had only 17% conversion (specific rate: 0.066 $mol_{CO}/g_{Au}/h$) at this temperature.

In conclusion, the sequence of activities induced via surface layer structures for the as-synthesized form of these four gold nanocatalysts is: Au/TiO_2/SiO_2 > Au/

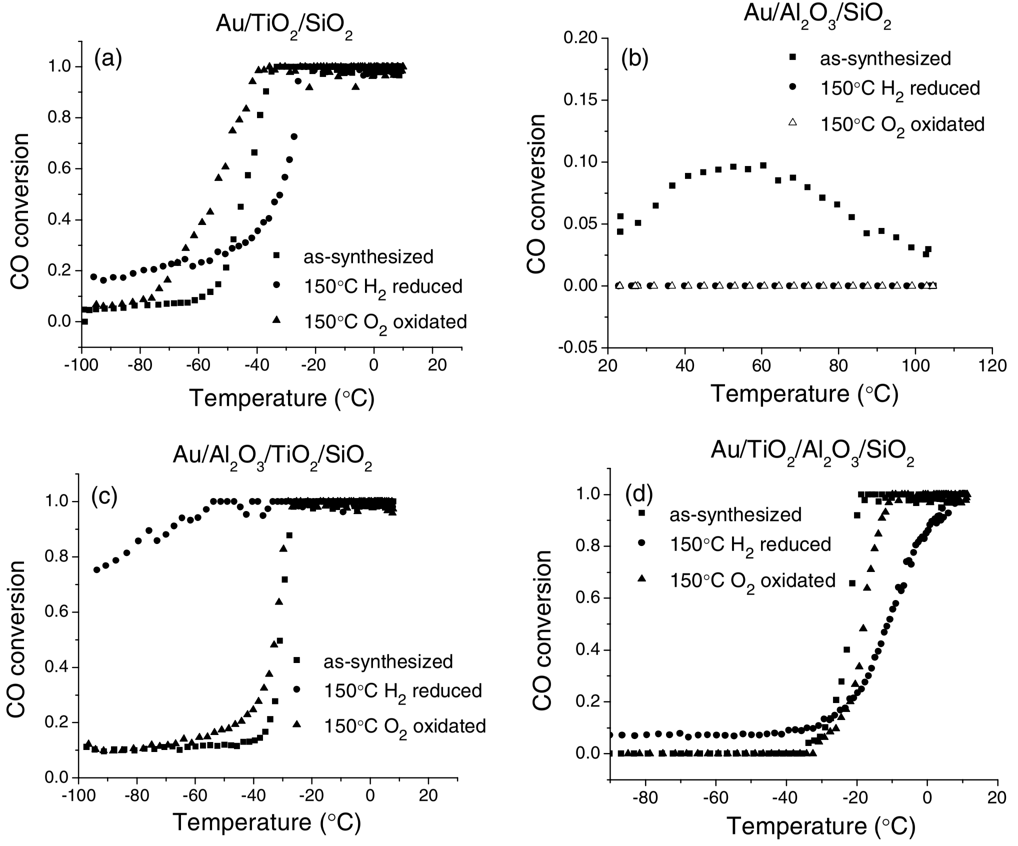

FIGURE 5.7. The light-off curves of as-synthesized $Au/TiO_2/SiO_2$, $Au/Al_2O_3/SiO_2$, $Au/Al_2O_3/TiO_2/SiO_2$, and $Au/TiO_2/Al_2O_3/SiO_2$ and the same samples under treatments of 150°C in H_2 (50% H_2/He) and 150°C in O_2 (8% O_2/He).

$Al_2O_3/TiO_2/SiO_2$ > $Au/TiO_2/Al_2O_3/SiO_2$ >> $Au/Al_2O_3/SiO_2$. However, the Au/$Al_2O_3/TiO_2/SiO_2$ catalyst treated in H_2 at 150°C is the most active in this series based on the layer-by-layer functionalization of silica. The functionalization sequence is an important factor in determining the catalytic activities of the resulting gold catalysts. The activity of $Au/TiO_2/SiO_2$ is higher than that of $Au/TiO_2/Al_2O_3/SiO_2$, indicating that the Al_2O_3 sublayer has a negative effect on the activity of the resulting catalyst. On the other hand, the activity of $Au/Al_2O_3/TiO_2/SiO_2$ is much higher than that of $Au/Al_2O_3/SiO_2$, implying that the TiO_2 sublayer has a positive effect on the resulting catalyst.

5.4. CONCLUSIONS

In summary, the studies on the activity and stability of the gold nanocatalysts supported by TiO_2 anatase and brookite nanoparticles indicate that the stability of gold nanoparticles against sintering on two catalysis systems is very different despite the same chemical composition. The high stability of the brookite-supported gold catalyst could result from the unique surface property of TiO_2 brookite. Another methodology discussed here for tailoring the surface properties of catalyst supports is the generation of amorphous TiO_2 monolayers on mesoporous silica materials. The high catalytic activity and stability of the gold nanoparticles deposited on the TiO_2-modified mesoporous silica surface for low-temperature CO oxidation indicate that the amorphous TiO_2 monolayer on the surface of silica is also a good support for gold catalysts. The significant activity differences among the gold nanocatalysts supported on TiO_2/SiO_2, Al_2O_3/SiO_2, $Al_2O_3/TiO_2/SiO_2$, and $TiO_2/Al_2O_3/SiO_2$ highlight a unique support effect that the sequence of the metal-oxide monolayers on silica surfaces has in determining the activities of supported gold nanocatalysts.

ACKNOWLEDGMENTS

This work was conducted at the Oak Ridge National Laboratory and supported by the Division of Chemical Sciences, Office of Basic Energy Sciences, U.S. Department of Energy, under contract No. DE-AC05-00OR22725 with UT-Battelle, LLC. This research was supported in part by an appointment for W.Y. to the Oak Ridge National Laboratory Postdoctoral Research Associates Program administered jointly by the Oak Ridge Institute for Science and Education and Oak Ridge National Laboratory. We gratefully acknowledge the help from Dr. Bei Chen for the catalytic test, Dr. Zongtao Zhang for the measurement involving SEM, Dr. Shannon M. Mahurin for analyses involving TEM and Z-contrast TEM, and Dr. Edward W. Hagaman for the NMR analysis.

REFERENCES

1. M. Haruta, N. Yamada, T. Kobayashi, and S. Iijima, Gold catalysts prepared by coprecipitation for low-temperature oxidation of hydrogen and of carbon-monoxide, *J. Catal.* **115**(2), 301–309 (1989).

2. M. Haruta, S. Tsubota, T. Kobayashi, H. Kageyama, M. J. Genet, and B. Delmon, Low-temperature oxidation of Co over gold supported on TiO_2, alpha-Fe_2O_3, and Co_3O_4, *J. Catal.* **144**(1), 175–192 (1993).
3. S. D. Lin, M. Bollinger, and M. A. Vannice, Low-temperature CO oxidation over Au/TiO_2 and Au/SiO_2 catalysts, *Catal. Lett.* **17**(3–4), 245–262 (1993).
4. W. F. Yan, B. Chen, S. M. Mahurin, S. Dai, and S. H. Overbury, Brookite-supported highly stable gold catalytic system for CO oxidation, *Chem. Commun.* 1918–1919 (2004).
5. Y. Z. Yuan, A. P. Kozlova, K. Asakura, H. L. Wan, K. Tsai, and Y. Iwasawa, Supported Au catalysts prepared from Au phosphine complexes and As-precipitated metal hydroxides: Characterization and low-temperature CO oxidation, *J. Catal.* **170**(1), 191–199 (1997).
6. J. D. Grunwaldt, C. Kiener, C. Wogerbauer, and A. Baiker, Preparation of supported gold catalysts for low-temperature CO oxidation via "size-controlled" gold colloids, *J. Catal.* **181**(2), 223–232 (1999).
7. G. R. Bamwenda, S. Tsubota, T. Nakamura, and M. Haruta, The influence of the preparation methods on the catalytic activity of platinum and gold supported on TiO_2 for CO oxidation, *Catal. Lett.* **44**(1–2), 83–87 (1997).
8. M. Okumura, K. Tanaka, A. Ueda, and M. Haruta, The reactivities of dimethylgold(III)beta-diketone on the surface of TiO_2—A novel preparation method for Au catalysts, *Solid State Ionics* **95**(1–2), 143–149 (1997).
9. M. A. P. Dekkers, M. J. Lippits, and B. E. Nieuwenhuys, CO adsorption and oxidation on Au/TiO_2, *Catal. Lett.* **56**(4), 195–197 (1998).
10. M. Valden, S. Pak, X. Lai, and D. W. Goodman, Structure sensitivity of CO oxidation over model Au/TiO_2 catalysts, *Catal. Lett.* **56**(1), 7–10 (1998).
11. M. Valden, X. Lai, and D. W. Goodman, Onset of catalytic activity of gold clusters on titania with the appearance of nonmetallic properties, *Science* **281**(5383), 1647–1650 (1998).
12. J. D. Grunwaldt, and A. Baiker, Gold/titania interfaces and their role in carbon monoxide oxidation, *J. Phys. Chem.* B **103**(6), 1002–1012 (1999).
13. G. Mul, A. Zwijnenburg, B. van der Linden, M. Makkee, and J. A. Moulijn, Stability and selectivity of Au/TiO_2 and Au/TiO_2/SiO_2 catalysts in propene epoxidation: An in situ FT-IR study, *J. Catal.* **201**(1), 128–137 (2001).
14. M. Date, Y. Ichihashi, T. Yamashita, A. Chiorino, F. Boccuzzi, and A. Haruta, Performance of Au/TiO_2 catalyst under ambient conditions, *Catal. Today* **72**(1–2), 89–94 (2002).
15. W. F. Yan, B. Chen, S. M. Mahurin, E. W. Hagaman, S. Dai, and S. H. Overbury, Surface sol-gel modification of mesoporous silica materials with TiO_2 for the assembly of ultrasmall gold nanoparticles, *J. Phys. Chem.* B **108**(9), 2793–2796 (2004).
16. F. Boccuzzi, A. Chiorino, M. Manzoli, D. Andreeva, and T. Tabakova, FTIR study of the low-temperature water-gas shift reaction on Au/Fe_2O_3 and Au/TiO_2 catalysts, *J. Catal.* **188**(1), 176–185 (1999).
17. S. H. Overbury, L. Ortiz-Soto, H. G. Zhu, B. Lee, M. D. Amiridis, and S. Dai, Comparison of Au catalysts supported on mesoporous titania and silica: Investigation of Au particle size effects and metal-support interactions, *Catal. Lett.* **95**(3–4), 99–106 (2004).
18. A. Knell, P. Barnickel, A. Baiker, and A. Wokaun, Co Oxidation over Au/ZrO_2 catalysts—Activity, deactivation behavior, and reaction-mechanism, *J. Catal.* **137**(2), 306–321 (1992).
19. J. D. Grunwaldt, M. Maciejewski, O. S. Becker, P. Fabrizioli, and A. Baiker, Comparative study of Au/TiO_2 and Au/ZrO_2 catalysts for low-temperature CO oxidation, *J. Catal.* **186**(2), 458–469 (1999).
20. G. K. Bethke, and H. H. Kung, Selective CO oxidation in a hydrogen-rich stream over Au/gamma-Al_2O_3 catalysts, *Appl. Catal. A-Gen.* **194** 43–53 (2000).
21. G. C. Bond, and D. T. Thompson, Catalysis by gold, *Catal. Rev.-Sci. Eng.* **41**(3–4), 319–388 (1999).
22. G. C. Bond, and D. T. Thompson, Gold-catalysed oxidation of carbon monoxide, *Gold Bull.* **33**(2), 41–51 (2000).
23. A. Wolf, and F. Schuth, A systematic study of the synthesis conditions for the preparation of highly active gold catalysts, *Appl. Catal. A-Gen.* **226**(1–2), 1–13 (2002).

24. M. Haruta, Size- and support-dependency in the catalysis of gold, *Catal. Today* **36**(1), 153–166 (1997).
25. S. Schimpf, M. Lucas, C. Mohr, U. Rodemerck, A. Bruckner, J. Radnik, H. Hofmeister, and P. Claus, Supported gold nanoparticles: in-depth catalyst characterization and application in hydrogenation and oxidation reactions, *Catal. Today* **72**(1–2), 63–78 (2002).
26. A. Zwijnenburg, M. Saleh, M. Makkee, and J. A. Moulijn, Direct gas-phase epoxidation of propene over bimetallic Au catalysts, *Catal. Today* **72**(1–2), 59–62 (2002).
27. M. Haruta, Catalysis of gold nanoparticles deposited on metal oxides, *Cattech* **6**(3), 102–115 (2002).
28. T. V. Choudhary, and D. W. Goodman, Oxidation catalysis by supported gold nano-clusters, *Top. Catal.* **21**(1–3), 25–34 (2002).
29. G. Schmid, and B. Corain, Nanoparticulated gold: syntheses, structures, electronics, and reactivities, *Eur. J. Inorg. Chem.* (17), 3081–3098 (2003).
30. M. C. Daniel, and D. Astruc, Gold nanoparticles: Assembly, supramolecular chemistry, quantum-size-related properties, and applications toward biology, catalysis, and nanotechnology, *Chem. Rev.* **104**(1), 293–346 (2004).
31. W. F. Yan, and S. Dai, Primary- and secondary-support contributions to the activities of Au nanoparticles, to be submitted.
32. W. P. Huang, X. H. Tang, Y. Q. Wang, Y. Koltypin, and A. Gedanken, Selective synthesis of anatase and rutile via ultrasound irradiation, *Chem. Commun.* (15), 1415–1416 (2000).
33. Y. Q. Zheng, S. Erwei, S. X. Cui, W. J. Li, and X. F. Hu, Hydrothermal preparation and characterization of brookite-type TiO_2 nanocrystallites, *J. Mater. Sci. Lett.* **19**(16), 1445–1448 (2000).
34. S.-J. Lee, and A. Gavrilidis, Supported Au catalysts for low-temperature CO oxidation prepared by impregnation, *J. Catal.* **206,** 305–313 (2002).
35. D. Y. Zhao, Q. S. Huo, J. L. Feng, B. F. Chmelka, and G. D. Stucky, Nonionic triblock and star diblock copolymer and oligomeric surfactant syntheses of highly ordered, hydrothermally stable, mesoporous silica structures, *J. Am. Chem. Soc.* **120**(24), 6024–6036 (1998).
36. I. Ichinose, H. Senzu, and T. Kunitake, Stepwise adsorption of metal alkoxides on hydrolyzed surfaces: A surface sol-gel process, *Chem. Lett.* (10), 831–832 (1996).
37. G. Riegel, and J. R. Bolton, Photocatalytic efficiency variability in TiO_2 particles, *J. Phys. Chem.* **99**(12), 4215–4224 (1995).
38. E. Borgarello, J. Kiwi, E. Pelizzetti, M. Visca, and M. Gratzel, Sustained water cleavage by visible-light, *J. Am. Chem. Soc.* **103**(21), 6324–6329 (1981).
39. D. C. Hurum, A. G. Agrios, K. A. Gray, T. Rajh, and M. C. Thurnauer, Explaining the enhanced photocatalytic activity of Degussa P25 mixed-phase TiO_2 using EPR, *J. Phys. Chem.* B **107**(19), 4545–4549 (2003).
40. M. Haruta, B. S. Uphade, S. Tsubota, and A. Miyamoto, Selective oxidation of propylene over gold deposited on titanium-based oxides, *Res. Chem. Intermed.* **24**(3), 329–336 (1998).
41. K. Fukushima, G. H. Takaoka, J. Matsuo, and I. Yamada, Effects on CO oxidation activity of nano-scale Au islands and TiO_2 support prepared by the ionized cluster beam method, *Japan. J. Appl. Phys. Part 1—Regul. Pap. Short Notes Rev. Pap.* **36**(2), 813–818 (1997).
42. Y. Iizuka, T. Tode, T. Takao, K. Yatsu, T. Takeuchi, S. Tsubota, and M. Haruta, A kinetic and adsorption study of CO oxidation over unsupported fine gold powder and over gold supported on titanium dioxide, *J. Catal.* **187**(1), 50–58 (1999).
43. G. V. Samonsov, *The Oxide Handbook*, (IFI/Plenum, New York, 1982).
44. U. Diebold, The surface science of titanium dioxide, *Surf. Sci. Rep.* **48**(5–8), 53–230 (2003).
45. V. Schwartz, D. R. Mullins, W. F. Yan, B. Chen, S. Dai, and S. H. Overbury, XAS study of Au supported on TiO_2: influence of oxidation state and particle size on catalytic activity, *J. Phys. Chem.* B **108**(40), 15782–15790 (2004).
46. C. T. Campbell, Ultrathin metal films and particles on oxide surfaces: Structural, electronic and chemisorptive properties, *Surf. Sci. Rep.* **27**(1–3), 1–111 (1997).
47. I. Ichinose, H. Senzu, and T. Kunitake, A surface sol-gel process of TiO_2 and other metal oxide films with molecular precision, *Chem. Mater.* **9**(6), 1296–1298 (1997).

48. J. G. Huang, and T. Kunitake, Nano-precision replication of natural cellulosic substances by metal oxides, *J. Am. Chem. Soc.* **125**(39), 11834–11835 (2003).
49. J. H. He, I. Ichinose, T. Kunitake, A. Nakao, Y. Shiraishi, and N. Toshima, Facile fabrication of Ag-Pd bimetallic nanoparticles in ultrathin TiO2-gel films: Nanoparticle morphology and catalytic activity, *J. Am. Chem. Soc.* **125**(36), 11034–11040 (2003).
50. M. Leskela, and M. Ritala, Atomic layer deposition chemistry: Recent developments and future challenges, *Angew. Chem. Int. Ed.* **42**(45), 5548–5554 (2003).
51. T. Yasuda, R. Kuse, K. Iwamoto, K. Tominaga, and J. W. Park, Vapor-liquid hybrid deposition process for device-quality metal oxide film growth, *Chem. Mater.* **15**(22), 4157–4159 (2003).
52. J. W. Elam, D. Routkevitch, P. P. Mardilovich, and S. M. George, Conformal coating on ultrahigh-aspect-ratio nanopores of anodic alumina by atomic layer deposition, *Chem. Mater.* **15**(18), 3507–3517 (2003).

6

Highly Effective Nanocatalysts Prepared Through Sol–Gel Technique

Guangshan Zhu[a,b], Ce Wang[a,*], Na Guo[a] and Xiaohui Cai[a,b]

6.1. HIGHLY EFFECTIVE SULFATED ZIRCONIA NANOCATALYSTS GROWN OUT OF COLLOIDAL SILICA AT HIGH TEMPERATURE

6.1.1. Introduction

Catalytic materials are widely used in industrial chemical processes. However, challenges remain to maximize their efficiency, to keep their stability and activity over a long operating period, and to achieve re-usability by regeneration for cost reduction and environmental considerations.[1] Sulfate ion modified metal oxides, such as sulfated zirconia (SZ) and zeolites, are two important solid catalysts in acid-promoted catalytic reactions, such as alkylation, dehydration, isomerization and cracking, etc.[2] In particular, they are the candidates for potential replacement of the liquid acid catalysts, such as hydrofluoric acid or sulfuric acid in commercial gasoline refining processes. Modified complex oxides are good candidates due to their strong acidity. However, such oxides in conventional forms are not effective enough because of the fact that the small specific surface area and their activity decrease quickly after several hours of reaction.[3]

[a] Alan G. MacDiarmid Institute, Jilin University, Changchun, 130012, China
[b] State Key Lab of Inorganic Synthesis & Preparative Chemistry, Jilin University, Changchun, 130012, China
* To whom correspondence should be addressed. Fax: 86-431-5168292; E-mail: cwang@mail.jlu.edu.cn

Although the zeolites possess larger surface areas, the deposition of carbon and the formation of coke in and on them limit their industrial applications as catalysts.[4,5] In order to raise the specific surface area, many metal oxide nanoparticle catalysts have been investigated.[6,7] However, in the process of sulphation at high temperatures of over 500°C, the nanoparticles are agglomerated, leading to a reduction in specific surface area. Silica supported metal oxides, especially SZ over silica (SZ/SiO_2), have attracted particular attention since 1988,[8–12] for their higher thermal stability, bigger specific surface area and lower cost than the SZ.

SZ/SiO_2 is usually prepared by a sol–gel process, and its catalytic activity depends on the reactivity of alkoxide precursors, amount of absorbed sulfuric acid, thermal treatment conditions, and number of active SZ sites on the surface.[13–18] Because of different hydrolysis rates of the ZrO_2 and SiO_2 precursors, a phase separation (colloid agglomeration) occurs during the sol–gel reactions. Consequently, after thermal treatment the SZ nanocatalyst with a large specific surface area cannot be obtained, although SZ is able to partly move onto silica surface during calcination.[19] In addition, the acid strength, as indicated by the concentration of SO_4^{2-}, is not adjustable by the techniques of co-precipitation and impregnation as reported in the literature.[20] It is apparent that the use of silica carrier as described above could not achieve high catalytic efficiency of SZ. Here, we present a novel approach to prepare highly efficient SZ/SiO_2 catalysts with SZ nanocrystals as a shell growing on silica nanoparticles as a core, designated as JML-1 to distinguish from other binary SZ/SiO_2 composite catalysts.

6.1.2. Experimental Section

6.1.2.1. Synthetic Methods

- SiO_2 sol was obtained by hydrolyzing 31.19 g of tetraethoxysilane in a mixture of 21.26 g of THF, 6.74 g of H_2O, and 0.75 g of 2M HCl under a magnetic stirring at 65 to 70°C for 3 h.
- Sulfated zirconia sol was prepared by placing 10 g of ethanol and 10 g of zirconium butoxide (80%) into a flask under magnetic stirring at room temperature, followed by adding a mixture of 6.5 g of ethanol, 1.5 g of distilled water, and 5 g of H_2SO_4 (18 M).
- SZ sol was obtained by gently stirring a solution of 16.5 g of ethanol, 10 g of Zr $(OC_4H_9)_4$ (80 wt.% in butanol), 1.5 g of distilled water, and 5 g of vitriol in a 500-ml flask until the system became a wet gel which was mechanically crushed with intensified stirring to afford a transparent sol.
- The SiO_2 sol was then mixed with the SZ sol at a proper molar ratio, depending on the desired Zr/Si ratio in the final product, under stirring magnetically for 12 to 24 h. Finally, the crosslinking agent HSi $(OC_2H_5)_3$ was added to the system to form a transparent binary gel. The gel was dried at room temperature for 2 days, ground into fine powders and then heated at 50°C for about 5 h, followed by heating to 550°C at a rate of 10°C/h and calcining at 550°C for an additional 3 h. The calcined products were stored in a desiccator for later use.

6.1.2.2. Characterization. The high resolution TEM images were obtained on a JEOL 2010 electron microscope with an acceleration voltage of 200 kV. Measurement of nitrogen adsorption–desorption isotherms was performed on a Micromeritics ASAP

2010 system. Before each measurement, the samples were degassed at 200°C for 2 h. The pore size distribution was calculated by using the Horvath–Kawazoe (HK) method.

IR spectra of the samples with and without pyridine were recorded on an FT-IR spectrometer (PE 430) with a resolution of 1 cm^{-1}. In order to measure the pyridine adsorption, the samples were pressed into thin pellets, and placed into a quartz cell with CaF_2 windows. The sample pellets were evacuated at 400°C for 2 h ($<10^{-5}$ Torr). After cooling down to room temperature, the pellets were exposed to pyridine environment (10 Torr) at 25°C. IR spectra were recorded after adsorption of pyridine for 1 h and evacuation at 150, 250, 350, and 450°C for 1 h.

TPD-NH_3 curves were obtained in a temperature range of 120 to 600°C, at a rate of 15°C/min. The adsorption of ammonia onto the sample was carried out at 25°C. Subsequently, the removal of ammonia was performed at 500 or 550°C for 1 h by purging air or pure nitrogen. Blank runs were carried out under the same conditions but with no NH_3 adsorbed. The TPD-NH_3 curves were obtained after subtraction of the blank run.

6.1.2.3. Catalytic Reactions. The catalytic performance of the samples was evaluated by using GC-8A and GC-17A (Shimazu Co.) instruments equipped with TCD and FID detectors. The catalytic alkylation of isobutane with 1-butene was investigated at 2 MPa by using a stainless-steel apparatus equipped with a one-through stainless-steel flow reactor. A typical reaction was performed with 1 g of JML-1, 12:1 of isobutane: 1-butene (mol/mol), WHSV was 4 h^{-1} at 25°C. A typical reaction of the condensation of diethylene glycol to dioxane was carried out in a reactor with 100 mL diethylene glycol and 20 g catalyst, only the product within 100 to 103°C was collected. After drying with $MgSO_4$, the pure dioxane was finally obtained.

6.1.3. Results and Discussion

In order to anchor SZ nanocrystals onto the surface of silica, the preparation of JML-1 was carried out by the sol–gel process involving the use of a crosslinking agent, triethoxysilane (TrEOS). Thus, tetraethoxysilane (TEOS) was hydrolyzed in a mixture of tetrahydrofuran (THF) and water under HCl catalysis to yield the silica sol. Likewise, i-buthoxyl zirconium Zr $(OC_4H_9)_4$ was hydrolyzed in alcohol/water in the presence of vitriol and sulfuric acid (Zr/S = 1: 2, mol/mol) leading to the SZ sol. The transparent silica and SZ sols were then mixed at desired molar ratios. After stirring at room temperature for 24 h, a certain amount of TrEOS was added to achieve gelation. The binary gel obtained was heated at 50°C for 5 h followed by calcination at a heating rate of 10°C/h up to 550°C to afford JML-1 catalyst. The introduction of TrEOS accelerates the gelation process to a rapid formation of silica network, so that the mobility of ZrO_2 coloidal particles is limited in the network.

Such a hindered mobility would prevent ZrO_2 nanoparticles from self-aggregating in the state of sol and allow for migration from the core to the surface of condensing (shrinking) silica at high temperatures.

At a fixed molar ratio of Zr/Si, the amount of crosslinking agent TrEOS was found to have significant effect on the gel-time, size of SZ nanocrystals, and percentage coverage of SZ on the silica surface that is directly related to the acidity of the catalysts.[21] As the amount of TrEOS was changed from 0.01 to 0.06, and to 0.11 mol% based on SiO_2 for JML-1_{40} (Zr/Si = 40/100, mol/mol), the gel-time was shortened from 24 h

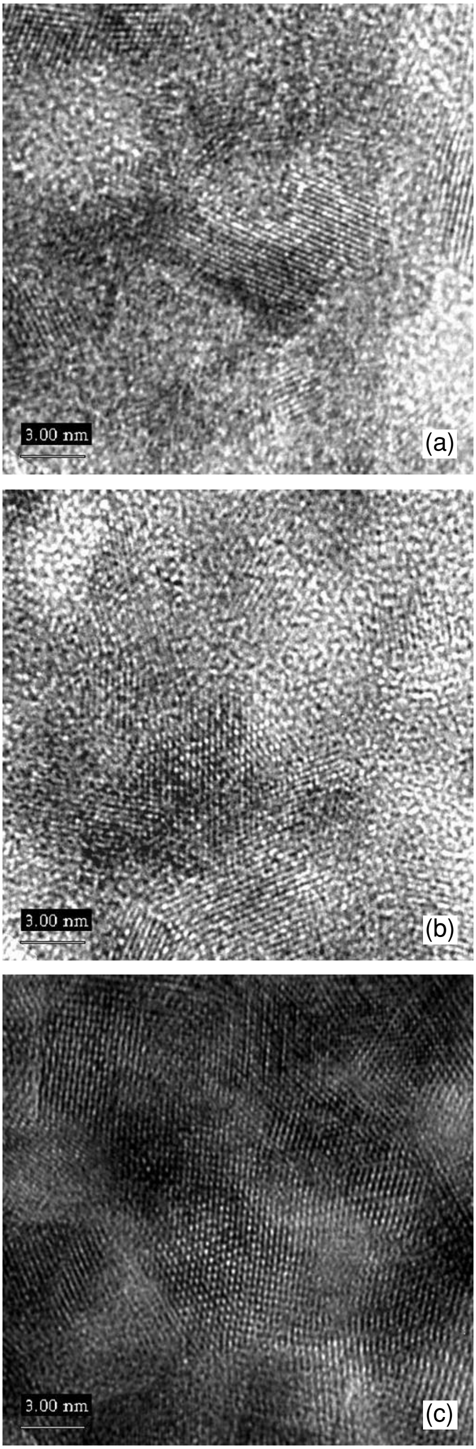

FIGURE 6.1. TEM images of JML-1 catalysts. Molar ratio of $Zr/TrEOS/SiO_2 = 40/0.01/100$ (a); 40/0.06/100 (b) and 40/0.11/100 (c).

to 0.5 h or less. As shown in Fig. 6.1, there are no overlaps between SZ nanocrystals when the Zr/Si mol ratio is lower than 0.4. The average size of SZ nanocrystals with a hexagon structure was also changed from 5.5 × 11 nm (1a) to 3.3 × 7.2 nm (1b), and to 3.5 × 5.5 nm (1c) with a decreasing trend. The percentage coverage decreased from 92% (1a) to 45% (1b) and to 12% (1c). Such a decrease in the SZ coverage with the increase of amount of TrEOS would reduce the effective surface area of SZ. This is understandable because the increase in the amount of crosslinking agent should result in a denser silica network, which would prevent self-aggregation of SZ nanoparticles in the silica matrix but, on the other hand, hinder the migration of ZrO_2 nanoparticles through the network to the surface. Consequently, the percentage coverage of the SZ nanoparticles on the silica surface reduced when the amount of the crosslinking agent was increased. Based on these observations, the TrEOS amount of 0.06 mol% was selected in most of our experiments for a balanced consideration of both SZ nanocrystal size and surface coverage.

During the synthesis of JML-1, it is necessary to get a transparent mixture of the silica and zirconia sols. That is, the two solutions should be mixed homogeneously at the nanometerscale. In the silica matrix, the addition of $HSi(OC_2H_5)_3$ promoted the gelation and condensation of oligosilicates to form a 3-dimensional silica network as shown in Fig. 6.2a. Following the solid phase nucleation mechanism,[22–24] the nuclei of ZrO_2 colloids filled in the network grids were first squeezed from the inside of silica matrix during the calcination. With the out-migration of ZrO_2 nanoparticles under thermodynamic driving forces, the nuclei combined with $SO_4{}^{2-}$ and grew into nanocrystals to form a typical core-shell structure with SZ nanocrystals anchored on/in the silica surface (Fig. 6.2b).

The N_2 adsorption isotherm (Fig. 6.3) suggests a micro-mesoporous structure of the JML sample with a BET surface area of *ca.* 280 m^2/g, which is much larger than that (190 m^2/g) of SZ and non-nanodispersed SZ/SiO_2 catalysts reported.[25] The single pore volume of JML-1_{40} is 0.44 mL/g, and the median pore diameter is 6.3 nm. Temperature-programmed desorption of ammonia (TDP) (Fig. 6.4) showed that JML-1_{40} calcined both under N_2 atmosphere and in air present high acid strength. The high temperature TPD peaks of JML-1_{40}, assigned to ammonia desorbing from the acidic sites, slightly lower than that of superacid sulfated zirconia reported.[26,27]

Surface photovoltage spectroscopy (SPS) in Fig. 6.5 was used to determine the surface acidity of JML-1 by measuring transition of electrons between the interface and the surface. The JML-1_{40} calcined at 550°C exhibited two peaks at 596 nm and 677 nm, whereas the sample without calcination had only one peak at 330 nm. The peak at 330 nm is assigned to the band–band electron transition and those at 596 nm and 677 nm are attributed to the surface-related transitions. The observation of these surface-related transitions indicates the presence of positive charges on the surface of the calcined sample, suggesting that the acidity of JML-1 catalyst is resulted from a large amount of SZ acidic sites on the silica surface.

The pyridine adsorption/desorption infrared spectra (Fig. 6.6) of JML-1_{40} at various temperatures showed that, as the desorption temperature was increased, the intensity of the peak at 1449 cm^{-1} (Lewis acidic site) was almost unchanged, whereas that at 1545 cm^{-1} (Brönsted acidic site) decreased significantly. However, both of these bands still co-existed at 450°C, and the intensity was about 50 to 60% of that at room temperature. These results suggest that both Lewis acid and Brönsted acid coexist in JML-1, and that the Lewis acidic sites are dominant.

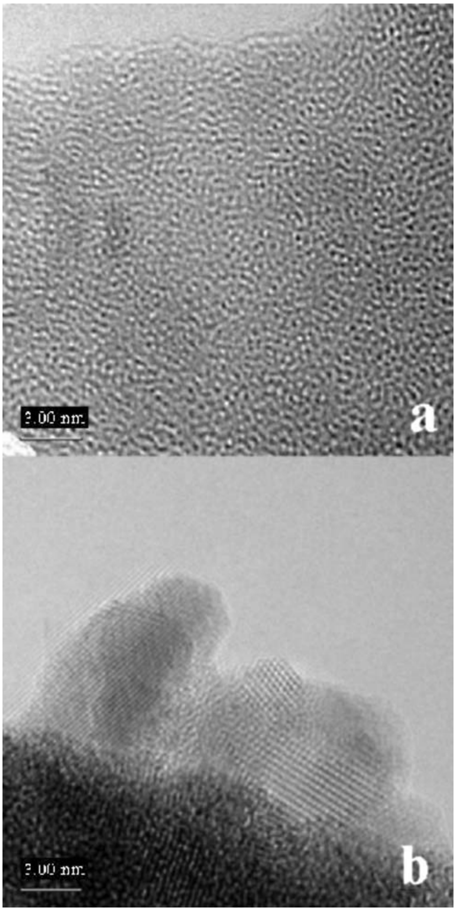

FIGURE 6.2. TEM images of materials prepared at (a) Zr/TrEOS/Si = 0/0.06/100 and (b) Zr/TrEOS/Si = 40/0.06/100 (mol)

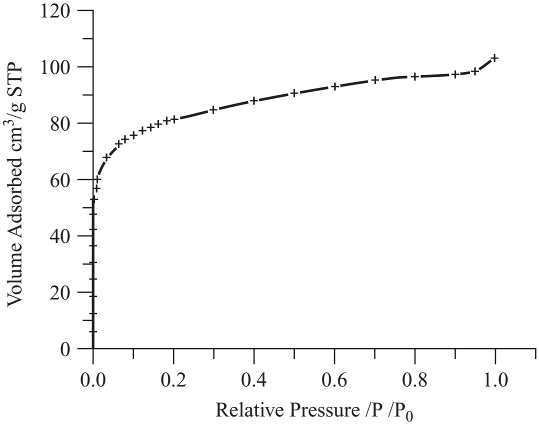

FIGURE 6.3. N_2 adsorption isotherm of JML-1_{50} (calcinated at 550°C under N_2).

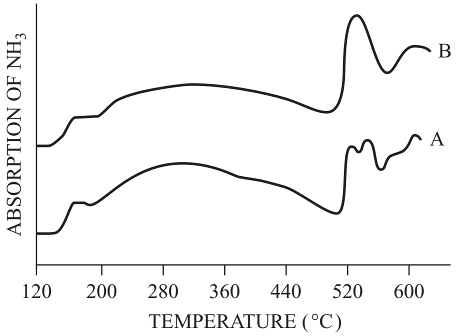

FIGURE 6.4. TPD curves of JML-1_{50} calcinated at 550°C in air (A) and in N_2 (B).

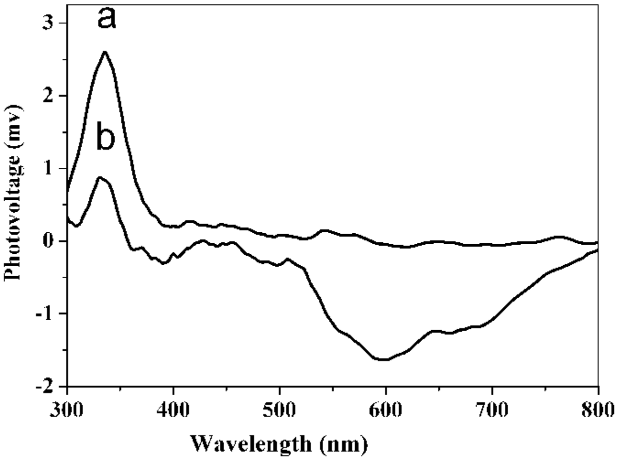

FIGURE 6.5. SPS of JML-1_{50} before (a) and after (b) calcinated at 550°C under N_2.

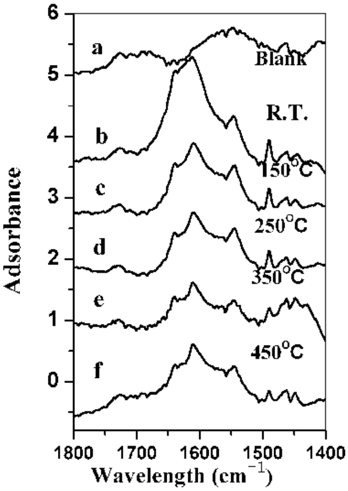

FIGURE 6.6. IR of pyridine adsorbed/desorbed on JML-1_{40}. Adsorption at 450°C (a); desorption at room temperature (b); 150°C (c); 250°C (d); 350°C (e); 450°C (f).

TABLE 6.1. The 1-butene conversion and product distribution after 1 h of alkylation reaction of isobutane on as-prepared JML-1_{50} and zeolite Beta catalysts.

Catalyst	Conversion of 1-butene (wt.%)	Alkylate Distribution (wt.%)			Distribution of C_8 (wt.%)			TMP/DMH Ratio
		C_5–C_7	C_8	C_9+	TMP[a]	DMH[b]	C_{other}	
JLM-1_{50}	97	14.4	59.9	25.7	58.7	4.34	39.2	13.5
Beta	86	29	62	9	73	18	9	4.1

[a] Trimethylpentane.
[b] Dimethylhexane.

The 1-butene conversion and product distribution obtained at 25°C after 1 h of alkylation reaction of isobutane on JML-1_{50} and Beta catalysts are summarized in Table 6.1. The conversion (97%) with JML-1_{50} catalyst is higher than that (86%) with zeolite Beta. The primary products with the above catalysts are C_8 compounds (59.9% with JML-1_{50} and 62% with Beta). The C_8 products mainly consist of trimethylpentanes (TMPs), 58.7% for JML-1_{50} and 73% for zeolite Beta. The TMP/DMH (dimethylhexane) ratios are 13.5 for JLM-1_{50} and 4.1 for Beta, demonstrating that the selectivity of JML-1_{50} is higher than that of zeolite Beta. The yields of alkylate are 6.6 mL and 5.2 mL for JML-1_{50} and Beta zeolite, respectively. The weights of alkylate produced per weight of butene fed to the reactor are 1.13 and 0.95 for JML-1_{50} and zeolite Beta, respectively.

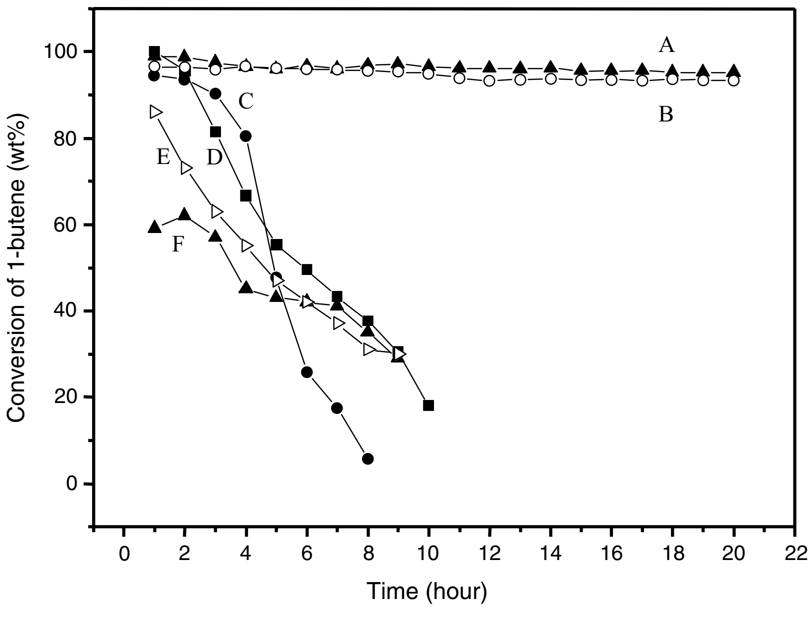

FIGURE 6.7. Catalytic conversion of 1-butene in the alkylation of isobutane with 1-butene (at a mol ratio of 12:1) versus reaction time over various catalysts (1 g each): JML-1_{50} (A); JML-1_{50} regenerated five times by calcination and sulphation (B); SZ(C); SZ/SiO_2 (Zr/Si = 50/100, mol/mol) (D); zeolite Beta (SiO_2/Al_2O_3 = 40) (E); zeolite ZSM-5 (SiO_2/Al_2O_3 = 40) (F).

JML-1 exhibited a higher catalytic activity in many of catalytic reactions over a longer operation time than other catalysts. Alkylation reaction of isobutane with 1-butene (Fig. 6.7) showed that JML-1_{50} (Zr/Si = 50/100 mol/mol) retained an activity of 95% after the catalytic reaction for 20 h. Even after regeneration for five times, it kept its activity at over 90%. In a sharp contrast, the SZ and SZ/SiO_2 (Zr/Si = 50/100, mol/mol) showed very high activities only within the first 2 h of the reaction, and then lost their activity quickly, which are similar to the results of Corma's work.[23,24] For comparison, the initial activities of zeolite Beta and ZSM-5 were 88% and 60%, respectively, in the same alkylation reaction. For the condensation reaction of diethylene glycol to dioxane, JML-1_{40} gave a 92% yield of pure dioxane, while ZSM-5 only afforded 70% yield within 1 h of reaction. Similarly, JML-1_{40} gave much higher yields than zeolite Y and ZSM-5 in the isomerization of n-pentane (Fig. 6.8a) and in the cracking of i-propyl benzene (Fig. 6.8b) at the same given reaction time. The high activity shown by JML-1 catalytic system could be attributed to its unique core-shell structure and high dispersion of discrete SZ nanocrystals on the surface of silica matrix. This allows for the easy diffusion of the reactants and oxygen that leads to the lowest carbon deposition and coke formation. However, in the pentane isomerization, conventional sulphated zirconia performed higher activity than JML-1_{40} (Fig. 6.8a). It was due to the lower surface sulphated zirconia density of JML-1_{40} compared with pure sulphated zirconia.

Due to the special structure, JML-1 prevents the SZ nanocrystals from self-agglomeration, and keeps its stability during the catalytic reaction over a long period of time, even after regeneration by calcination and sulphation many times. The JML-1 nanocatalyst system with high efficiency, long utilizing lifetime with good regeneratability, high catalytic activity and high stability over a long period of reaction time as achieved successfully by this novel sol–gel process would have a great potential for practical applications in solid catalytic reactions.

6.2. AG/SIO_2 COMPOSITE NANOCATALYSTS

6.2.1. Introduction

Metal nanoparticles have been an important and interesting branch in solid-state physics.[28,29] In recent years, the materials based on SiO_2 as carrier and metal particles as functional component attracted the attention of researchers due to their novel physicochemical properties.[30–32]

Silver is especially attractive among all metals. As we all know, the composite silver nanomaterials are used in many application fields, such as photoelectricity science,[33] film separation,[34] catalysis[35], and so on. Composite silver catalyst is usually applied in selective oxidation reaction.[36]

In this part, we prepared and studied the Ag/SiO_2 catalyst by one-step and two-step sol-gel methods. The results show that the Ag/SiO_2 catalyst prepared here is one kind of bulk material which has a high surface area. The Ag/SiO_2 catalyst is made up with functional component of Ag or silver oxide in 20 to 30 nm and carrier SiO_2. Moreover, we found that the different preparation methods have great effect on crystal structure of the samples. The structure of the sample prepared by the one-step method is always a single crystal structure. And the structure of the sample prepared by the two-step method is always a mixed crystal structure.

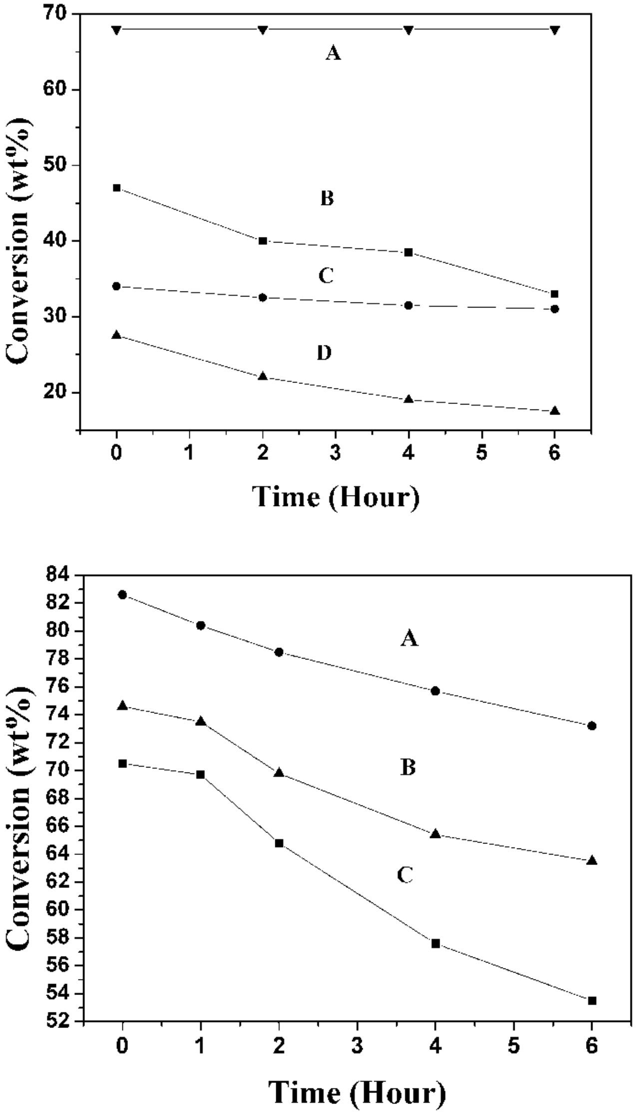

FIGURE 6.8. (a) Isomerization of pentane over sulphated zirconia (A), JML-1_{40} (B), zeolite Y (C) and zeolite ZSM-5 (D); (b) Cracking of iso-propyl benzene over JML-1_{40} (A); zeolite Y (B) and zeolite ZSM-5 (C).

6.2.2. Experimental Section

6.2.2.1. Synthetic Methods

- SiO_2 sol was prepared as 1.2.1 in this chapter.
- Silver sol was prepared by 0.335 g of $AgNO_3$ and 15 ml of ethanol under ultrasonic 1 h, followed by adding 0.965 ml of $(H_3CO)_3$–Si–$(CH_2)_3$–SH, and stirred 1 h at room temperature. Yellow transparent solution was obtained.

- Ag/SiO_2 sol was prepared by two methods:
  1. one-step method
     Silver sol was added to SiO_2 sol and stirred at room temperature for 12 to 14 h.
  2. two-step method
     2.85 g of THF, 0.90 g of distilled water, and 0.10 g of 2 M HCl were added in turn to a 100-ml flask under magnetic stirring at room temperature, followed by adding 4.18 g of TEOS slowly and stirred until the system was homogeneous. The mixture was stirred at 65 to 70°C for 2 to 2.5 h, followed by adding silver sol and stirred additional 3 h.
- Ag/SiO_2 sol was extracted with C_6H_{12}. The obtained wet gel was dried at 50°C for about 2 h and then calcinated at 450 to 550°C for 3 h.

The schematic representation of the preparation of Ag/SiO_2 composite nanocatalyst is shown in Fig. 6.9.

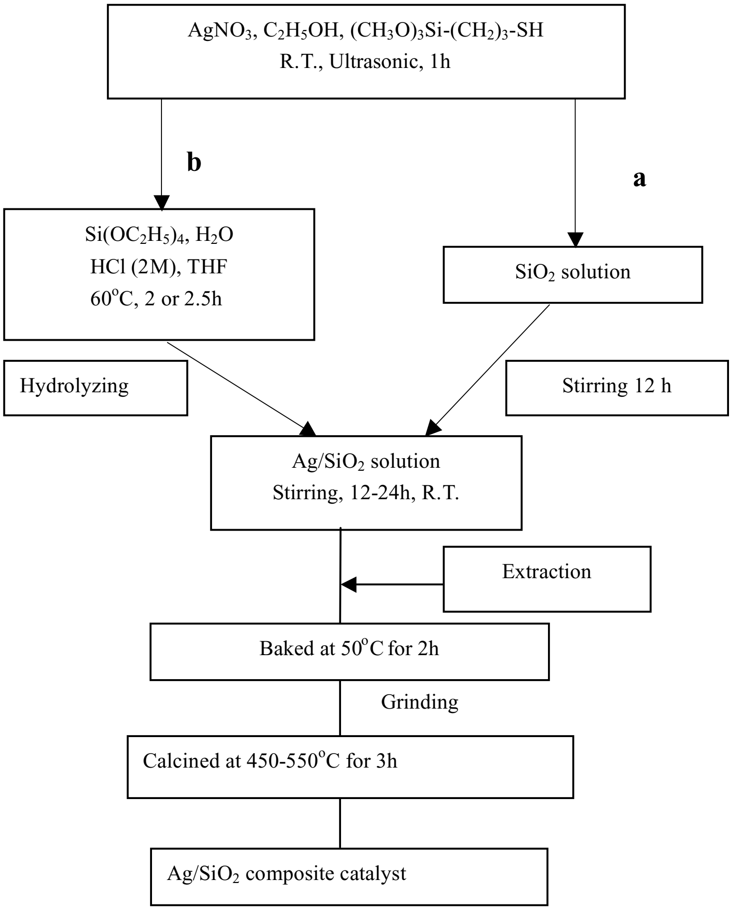

FIGURE 6.9. Scheme of the preparation of Ag/SiO_2 composite nanocatalyst by (a) one-step method, (b) two-step method.

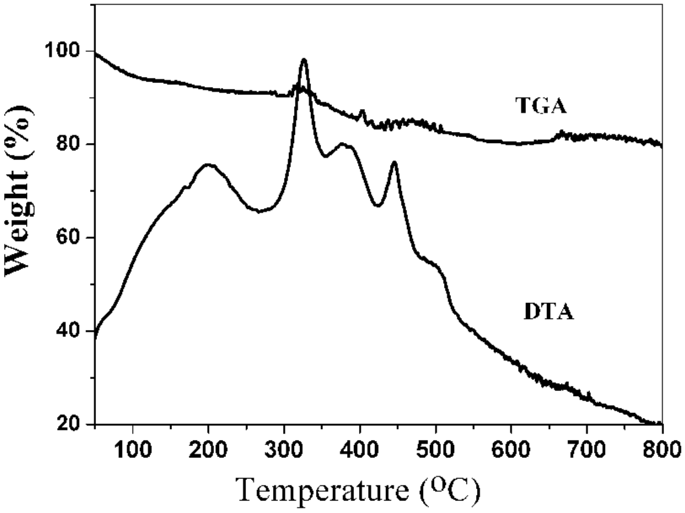

FIGURE 6.10. TGA and DTA curves of the Ag/SiO_2 sample prepared by two-step method.

6.2.2.2. Characterization. IR spectra of the samples were recorded on Nicolit AVATAR360 spectrometer. The TEM images were obtained on Hitachi H-8100IV electron microscope. TGA and DTA analyses were carried out in Du pont 9900 Thermal Analysis System. X-ray diffraction (XRD) measurement was conducted on a Siemens D5005 diffractometer using Cu Kα radiation ($\lambda = 1.54$ Å).

6.2.3. Results and Discussion

Thermogravimetric analysis (TGA) and differential thermal analysis (DTA) curves of the Ag/SiO_2 sample prepared by the two-step method are shown in Fig. 6.10. The TGA curve exhibits two evident weight loses, which are in the range of *ca.* 100 to 250°C and 250 to 550°C, corresponding to the loss of solvent, water, ethanol and THF, and the decomposition of organic silica, respectively. Four evident endothermic peaks can be observed from DTA curve, which centered at *ca.* 200°C, 350°C, 425°C and 480°C, respectively.

These endothermic steps from 250 to 550°C are contributed to the oxidation decomposition of organic functional groups, including decomposition of Ag-(S)-$(CH_2)_3$-Si-$(OCH_3)_3$ and the crystallization of Ag and Ag_2O.

X-ray diffraction patterns for Ag/SiO_2 composite prepared by two-step method (Fig. 6.11) shows that crystal phases are affected by calcined temperature. The structure of the as-synthesized composite is amorphous due to the small Ag cluster dispersed uniformly in carrier SiO_2 when the silver solution and SiO_2 solution are mixed well. After calcination, –(SH) groups encircled Ag particles rupture and the network of SiO_2 carrier shrinks, which makes the Ag cluster squeeze out of the network and form nanocrystal structure. The structure of Ag/SiO_2 composites calcined at 450°C and 550°C are mix-crystals of Ag and the Ag oxide. The structure of the crystal changes accompany with the increasing of calcined temperature.

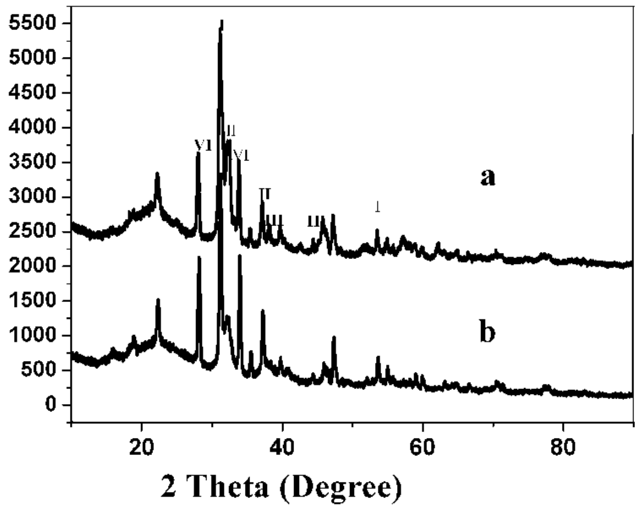

FIGURE 6.11. X-ray diffraction patterns for Ag/SiO_2 samples prepared by two-step method calcined at (a) 550°C, (b) 450°C I: Ag_2O_3 Cubic Primitive (1,1,1) (2,2,0); II: AgO Cubic Face-centered (1,1,1) (2,0,0); III: Ag Cubic Face-centered (1,1,1) (2,0,0); VI: Ag_3O_4 Monoclinic Primitive (0,3,1) (1,1,0).

Figure 6.12 shows the IR spectra of Ag/SiO_2 composites prepared by different methods calcined at 550°C. Because it appears no difference in chemical bond indicates physical structures of the three composite systems are similar. The IR spectra of Ag/SiO_2 composites prepared by the two-step method are shown in Fig. 6.13. The mixture of the silver solution and SiO_2 solution exhibits two peaks at 1382 cm^{-1} and 949 cm^{-1}, which can be attributed respectively to the vibration of $NO_3{}^{-1}$ and the vibration

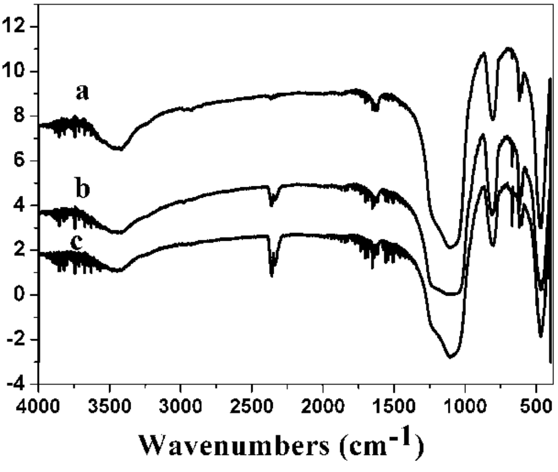

FIGURE 6.12. IR spectra of Ag/SiO_2 samples prepared by different method calcined at 550°C: (a) one-step method, (b) two step method (2.0 h), (c) two step method (2.5 h).

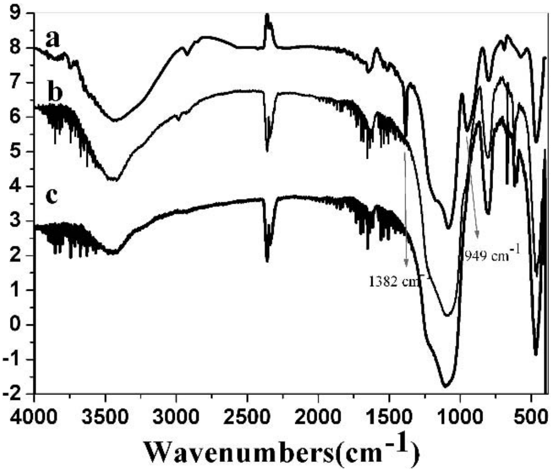

FIGURE 6.13. IR spectra of Ag/SiO_2 samples prepared by two-step method (a) dried at 50°C, (b) calcined at 450°C, (c) calcined at 550°C.

between Ag and –(SH). With the increase of the calcination temperature, the couple of peaks diminish gradually and then disappear. This suggests that NO_3^{-1} and –(SH) combined with Ag particle decompose when the composite was calcined at high temperature. Furthermore, only O–H vibration enhances with the increase of the calcined temperature, which indicates there is no new bond formed between Ag and SiO_2 in Ag/SiO_2 composite.

The TEM images (Fig. 6.14a) show that Ag nanoparticles about 5 nm are dispersed uniformly in SiO_2 carrier before the Ag/SiO_2 composite prepared by the one-step method is calcined. With the increase of the calcination temperature, Ag nanoparticles grow out from the SiO_2 carrier. Ag nanoparticles are about 10 nm and disperse on the surface of the SiO_2 carrier when the composite is calcined at 450°C (Fig. 6.14b).

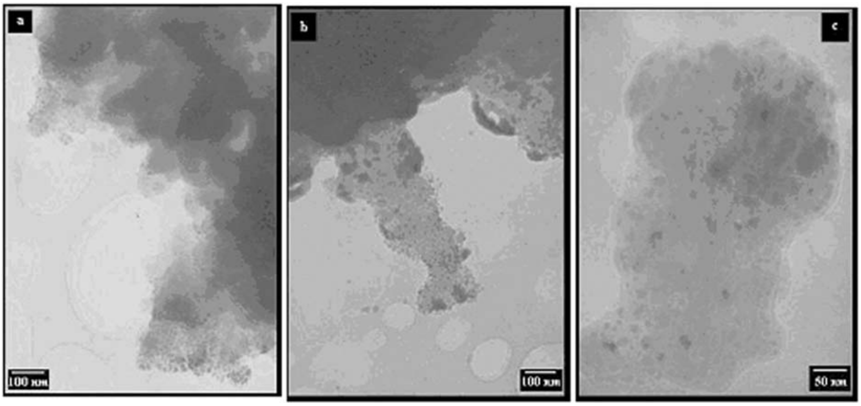

FIGURE 6.14. TEM images of Ag/SiO_2 sample prepared by the one-step method (2.5 h) (a) before calcined, (b) calcined at 450°C, (c) calcined at 550°C.

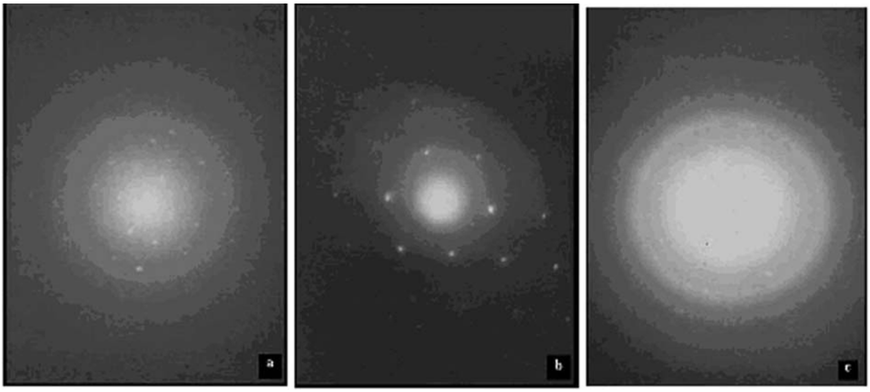

FIGURE 6.15. TEM diffraction images of Ag/SiO_2 sample prepared by different methods: (a) one-step method (2.0 h), (b) one-step method (2.5 h), (c) two-step method.

When the calcination temperature is 550°C, the Ag nanoparticles are 15 to 30 nm in size (Fig. 6.14c).

TEM diffraction images of Ag/SiO_2 sample prepared by different methods, shown in Fig. 6.15, suggest that the different methods result in different types of crystals. The composite prepared by one-step method is evident monoclinic crystal, but the one prepared by the two-step method is a mixture. In the one-step method, $AgNO_3$ solution is added during the process of hydrolyzation of TEOS. The hydrolyzation and condensation of both TEOS and $(H_3CO)_3$–Si–$(CH_2)_3$-SH form a network of SiO_2, which surrounds –SH–Ag clusters. Ag cluster is restricted in the network of SiO_2. During the calcination, Ag cluster is squeezed out of the network of SiO_2 and grows up into a single crystal. In the two-step method, the network of the SiO_2 hydrolyzed from TEOS does not affect Ag clusters owing to the mechanically mixing of the silver solution and the SiO_2 solution. Ag clusters exist freely in the network of SiO_2 and are easy to form mixed phases after calcination.

Ag/SiO_2 composites prepared by the one-step method and two-step methods were characterized by TGA/DTA, FTIR, XRD, and TEM. The results showed that Ag or silver oxide nanoparticles in 20 to30 nm were dispersed on the surface of the carrier SiO_2. The calcination temperature and prepared method affect the crystal phase of the functional component.

In conclusion, the successful preparation of SZ/SiO_2, (JML-1) and Ag/SiO_2 nanocomposites demonstrated that the sol–gel technique is a simple and universal method to prepare nanometer high effective catalysts. The technique can be readily applied to the synthesis of other silica supported metals or metal oxides such as TiO_2/SiO_2, CuO/SiO_2, Pt/SiO_2, Au/SiO_2, etc., for various industrial catalytic reactions.

ACKNOWLEDGMENTS

We thank Dr. B. Zhou, Prof. Dazhen Jiang, and Prof. Tonghao Wu for valuable discussions. We thank Profs. W. Y. Zhang and S. Lin for technical assistance. We are most grateful to the National Natural Science Foundation of China for the financial support.

REFERENCES

1. B. Li and R. D. Gonazalez, Sol-gel synthesis and catalytic properties of sulfated zirconia catalysts, *Ind. Eng. Chem. Res.* **35,** 3141–3148 (1996).
2. D. Farcasiu and J. Q. Li, Preparation of sulfated zirconia catalysts with improved control of sulfur content, III: effect of conditions of catalyst synthesis on physical properties and catalytic activity, *Appl. Catal. A: General* **175,** 1–9 (1998).
3. David J. Zalewski, Saeed Alerasool, Patricia Doolin, Characterization of catalytically active sulfated zirconia, *Catal. Today* **53,** 419–432 (1999)
4. S. Bettina, T. Markus, and K. C. Bettina, Supercritical isomerization of n-butane over sulfated zirconia. Part I: catalyst lifetime, *Ind. Eng. Chem. Res.* **40,** 2767–2772 (2001).
5. P. H. Cuong, B. Christophe, D. Thierry, E. Babrielle, E. Claude, and J. L. Marc, High surface area silicon carbide doped with zirconium for use as catalyst support: preparation, characterization and catalytic application, *Appl. Catal.* A **180,** 385–397 (1999).
6. Y. Y. Huang, B. Y. Zhao, and Y. C. Xie, A novel way to prepare silica supported sulfated titania, *Appl. Catal.* A **171,** 65–73 (1998).
7. H. Althues, and S. Kaskel, Sulfated zirconia nanoparticles synthesized in reverse microemulsions: preparation and catalytic properties, *Langmuir* **18,** 7428–7435 (2002).
8. T. Ishida, T. Yamaguchi, and K. Tanabe, Acid property of sulfur-promoted zirconium-oxide on silica as solid superacid, *Chem. Lett.* 1869–1872 (1988).
9. M. S. Wong, H. C. Huang, and J. Y. Ying, Supramolecular-templated synthesis of nanoporous zirconia-silica catalysts, *Chem. Mater.* **14**(5), 1961–1973 (2002).
10. K. Tomishige, A. Okabe, and K. Fujumoto, Effect of hydrogen on n-butane isomerization over Pt/SO_4^{2-} -ZrO_2 and Pt/SiO_2 + SO_4^{2-}-ZrO_2, *Appl. Catal.* A **194,** 383–393 (2000).
11. J. R. Sohn and H. J. Jang, Characterization of ZrO_2-SiO_2 unmodified or modified with H_2SO_4 and acid catalysis, *J. Mol. Catal.* **64,** 349–360 (1991).
12. T. Lopez, J. Navarrete, R. Gomez, O. Novaro, F. Figueras, and H. Armendariz, Preparation of sol-gel sulfated ZrO_2-SiO_2 and characterization of its surface acidity, *Appl. Catal.* A **125,** 217–232 (1995).
13. C. Morterra, G. Cerrato, and F. Pinna, Preparation and characterization of sulfated zirconia catalysts obtained via various procedures, *Appl. Catal.* A **176**(1), 27–43 (1999).
14. D. Farcasiu, J. Q. Li, and S. Cameron, Preparation of sulfated zirconia catalysts with improved control of sulfur content: III. Effect of conditions of catalyst synthesis on physical properties and catalytic activity, *Appl. Catal.* A **175**(1–2), 1–9 (1998).
15. M. -Trung Tran, N. S. Gnep, G. Szabo, and M. Guisnet, Influence of the calcination temperature on the acidic and catalytic properties of sulphated zirconia, *Appl. Catal.* A **171,** 207–217 (1998).
16. P. Canton, R. Olindo, F. Pinna, G. Strukul, P. Riello, M. Meneghetti, G. Cerrato, C. Morterra, and A. Benedetti, Alumina-promoted sulfated zirconia system: Structure and microstructure characterization, *Chem. Mater.* **13,** 1634–1641 (2001).
17. A. Corma, Inorganic solid acids and their use in acid-catalyzed hydrocarbon reactions, *Chem. Rev.* **95,** 559–614 (1995).
18. X. Song, A. Sayari, Sulfated zirconia-based strong solid-acid catalysts: Recent progress,*Catal. Rev. Sci. Eng.* **38,** 329–412 (1996).
19. C. Ingemar Odenbrand, S. Andersson, L. Andersson, J. Brandin, and G. Busca, Characterization of silica-titania mixed oxides, *J. Catal.* **125,** 541–553 (1990).
20. T. Makoto, The effect of preparation methods on the properties of zirconia/silicas, *J. Mol. Catal.* **94,** 85–96 (1994).
21. H. J. M. Bosman, E. C. Kruissink, J. Spoel Van der, and B. F. Van der, Characterization of the acid strength of SiO_2-ZrO_2 mixed oxides, *J. Catal.* **148,** 660–672 (1994).
22. B. Q. Xu, T. Yamaguchi, and K. Tanabe, Acid-base bifunctional catalysis in the decomposition of alkylamines, *Appl. Catal.* **75,** 75–86 (1991).
23. T. Yamaguchi, T. Jin, T. Ishida, and K. Tnabe, Structural identification of acid sites of sulfur-promoted solid super acid and construction of its structure on silica support,*Mater. Chem. Phys.* **17,** 3–19 (1987).

24. L. M. Kustov, V. B. Kazansky, F. Figueras, and D. Tichit, Investigation of the acidic properties of ZrO_2 modified by $SO_2{}^{-4}$ anions, *J. Catal.* **150,** 143–149 (1994).
25. Y. Parulescu, S. Coman, P. Grange, and V. I. Parvulescu, Preparation and characterization of sulfated zirconia catalysts obtained via various procedures, *Appl. Catal.* A **176,** 27–43 (1999).
26. A. Corma, A. Martinez, and C. Martinez, Influence of process variables on the continuous alkylation of isobutane with 2-butene on superacid sulfated zirconia catalysts, *J. Catal.* **149,** 52–60 (1994).
27. A. Corma, M. I. Juan-Rajadell, J. M. Lopez-Nieto, A. Martinez, and C. Martinez, A comparative study of $SO_4{}^{2-}$ /ZrO_2 and zeolite Beta as catalysts for the isomerization of n-butane and the alkylation of isobutane with 2-butene, *Appl. Catal.* A **111,** 175–189 (1994).
28. G. Mitrikas, C. C. Trapalis, and G. Kordas, Tailoring the particle size of sol–gel derived silver nanoparticles in SiO_2, *J. Non-Crystalline Solids* **286,** 41–50 (2001).
29. W. P. Halperin, Quantum size effects in metal particles, *Rev. Mod. Phys.* **58,** 533–606 (1986).
30. J. R. Martinez, G. Ortega-Zarzosa, O. Dominguez-Espinos, and F. Ruiz, Low temperature devitrification of Ag/SiO_2 and Ag(CuO)/SiO_2 composites, *J. Non-crystalline Solids* **282,** 317–320 (2001).
31. E. M. Vogel., Glasses as nonlinear photonic materials, *J. Am. Ceram. Soc.* **72,** 719–724 (1989).
32. C. Flytzanis, F. Hache., M. C. Klein. D. Ricar., and P. Rossingnol., The impact of quantum confinement on the optical nonlinearities of semiconductor nanocrystals, *Proceedings of SPIE-The International Society for Optical Engineering* (1990), 1319
33. G. De. L. Tapler, G. Battaglin, F. Caccavale, F. Gonella, P. Mazzoldi, and R. F. Haglund. Jr., Formation of copper and silver nanometer dimension clusters in silica by the sol-gel process, *Appl. Phys. Lett.* **68,** 3820–3822 (1996).
34. T. Kokugan, A. Trianto, and H. Takeda, Dehydrogenation of pure cyclohexane in the membrane reactor and prediction of conversion by pseudo equilibrium model, *J. Chem. Eng. Jpn.* **31,** 596–603 (1998).
35. E. Yu. Batyan, S. V. Matveichuk, and G. A. Branitskii, Structural phase transformations in silver-ceramic systems and their relation to catalytic properties in the process of methanol partial oxidation, *Kinet. Catal.* **136,** 816–820 (1995).
36. Konstantin Hadjiivanov, Helmut KnÖzinger, Low-temperature CO adsorption on Ag^+/SiO_2 and Ag-ZSM-5: an FTIR study, *J. Phys. Chem.* B **102,** 10936–10940 (1998).

7

Dendrimer Templates for Supported Nanoparticle Catalysts

Huifang Lang and Bert D. Chandler*

7.1. INTRODUCTION

Catalysis has a tremendous impact on the national economy as one-third of material U.S. GNP involves a catalytic process somewhere in the production chain.[1] Catalytic technologies are well established throughout the economy, particularly in petroleum refining, emissions and pollution control (including energy production), polymers and plastics, pharmaceuticals and fine chemicals, and basic chemicals.[2] The utilization of heterogeneous catalysts in these areas of chemical industry is certain to increase as environmental and economic pressures drive the movement toward clean, selective chemical processes.[2] Similarly, developing new catalysts for more efficient, cost-effective processes will be especially important for growing industries involved in the potential development of a hydrogen economy.[3,4]

An important class of industrial catalysts consists of an active component dispersed in the form of very small particles over high surface area solids.[5] As the field of industrial heterogeneous catalysis has developed, catalyst formulations have evolved such that state-of-the-art catalysts often contain two or more metals and/or main group elements. The additives may promote a desired reaction, prevent undesirable side reactions, or enhance catalyst longevity.[5–7] Bimetallic nanoparticle catalysts in particular are widely

Department of Chemistry, Trinity University, San Antonio, TX 78212
* To whom correspondence should be addressed.

employed in industry and will similarly be vital to the success and economic viability of hydrogen energy technologies,[8] particularly fuel cells and hydrogen production from photochemical and biorenewable resources.[3,4]

7.1.1. *Traditional Routes to Supported Metal Nanoparticle Catalysts*

In spite of the commercial importance of bimetallic catalysts, catalyst formulations, particularly the active sites or phases, are not necessarily well characterized or well understood. This is particularly true for bimetallic catalysts, largely due to the difficulties associated with preparing, characterizing, and proving the presence and activity of well-defined supported bimetallic nanoparticles. Traditional preparative routes involve impregnating metal salts (typically inexpensive chloride complexes) onto high surface area supports, followed by various thermal activation steps.[9] Most important industrial supports can also be employed as separation media; consequently, chromatographic separation of salt precursors as they pass through the support pore structure is unavoidable. Further, nanoparticle preparation via traditional routes depends on the surface and even gas phase mobility of the species present during the thermal treatments.[5,6] These processes vary widely for different metals and are poorly understood, at best.[5,6] Metal salt precursors also introduce ions (K^+, Cl^-) which may inadvertently affect catalyst properties or have deleterious effects on catalyst performance.[10–12]

These *in situ* particle preparation methods offer little control over critical catalyst properties such as particle size and composition. Because the properties of individual particles often vary widely within a given sample, the study of structure–activity relationships is difficult at best. The reliance on these methods also has significant drawbacks in terms of catalyst reproducibility. As pointed out by Ponec and Bond, the "lack of reproducibility of catalytic activity on a sample to sample basis using portions drawn from the same bottle is a humiliating reminder of the lack of control which we have over the complex chemistry involved" in catalyst preparation.[5] The inherent inhomogeneity in traditionally prepared bimetallic catalysts also dramatically complicates their characterization. This, in turn, poses a significant hurdle to evaluating the important features in the best catalysts, understanding how reactions occur over these materials, and learning how to control catalyst properties.

7.1.2. *Molecular Clusters as Precursors to Supported Metal Catalysts*

Ligand-stabilized inorganic and organometallic molecular clusters offer potential advantages over traditional methods for preparing supported bimetallic catalysts.[6] Using well-defined molecular precursors allows for the deposition of particles that are initially consistent in composition and limits the introduction of ions that may adversely affect catalyst performance. The potential for low thermolysis temperatures (e.g. for CO ligands) may also prevent particle agglomeration. Gates and coworkers have a number of excellent reviews detailing the cluster method, particularly as they pertain to preparing extremely well defined supported structures consisting of a few atoms.[6,13] Readers are directed to these reviews for details on the successes of this method; its limitations are outlined below.

Although the molecular cluster route has been known for decades, its potentials have only rarely been realized. A central problem is that under reaction conditions

a cluster is likely to lose its molecular integrity while undergoing a variety of fragmentation and agglomeration processes.[14] Although clusters have played an important role in understanding metallic bonding and selectivity in catalysis,[15] in general, they have not proven to be particularly good models for nanoparticle catalysts and are more appropriately considered as potential precursors to nanoparticle catalysts.[14] As precursors, their potential has been primarily in strict initial compositional control and the possibility of preparing nanoparticles with compositions that are not formed via traditional methods.[6]

Even as catalyst precursors, clusters have drawbacks due to inflexibility in metal stoichiometries. Metal ratios are set by cluster stoichiometry and cannot be systematically varied without an extensive cluster library. Cluster preparation is often time consuming and expensive, so such libraries are seldom available. Further, using clusters (nominally 4 to 12 atoms) to prepare nanoparticles (nominally 10 to 1000 atoms) relies on the same atom/particle mobility that plagues traditional routes, although perhaps to a lesser degree. Essentially, one must hope that cluster precursors stay intact long enough during activation to impart their precise stoichiometry to growing nanoparticles. In terms of understanding the properties of nanoparticles, this situation is less than desirable. Even worse, ligands that stabilize many noble metals often contain elements that can be severe poisons for catalysts (e.g. phosphines, arsines, S donors).[16]

7.1.3. Applying Nanotechnology to the Catalytic Sciences

Colloidal nanoparticles can be employed as heterogeneous catalyst precursors in the same fashion as molecular clusters. In many respects, colloidal nanoparticles offer opportunities to combine the best features of the traditional and cluster catalyst preparation routes to prepare uniform bimetallic catalysts with controlled particle properties. In general, colloidal metal ratios are reasonably variable and controllable. Further, the application of solution and surface characterization techniques may ultimately help correlate solution synthetic schemes to catalytic activity.

Until recently, the available colloidal nanoparticle syntheses generally prepared particles in size ranges (5+ nm) that are not of particular interest to many catalytic scientists. The recent explosion of interest in nanoparticles for nanotechnology applications has fueled the development of several new nanoparticle preparative techniques.[17–19] In some cases, careful syntheses allow control over nanoparticle size, composition, and even morphology. Several synthetic routes to colloidal nanoparticles in the 1 to 5 nm range are now becoming available. For large atoms like platinum, this size range is particularly important for catalysis as it corresponds to dispersions of 95 to 20%, respectively. This not only maximizes the fraction metal on particle surfaces, but also coincides with a transition from large particles with primarily metallic character to nanoparticles composed of tens of atoms that may have characteristics that are more molecular.

Three general preparative schemes are of particular interest due to their success in preparing nanoparticles on the order of 1 to 3 nm. The first, commonly known as the Brust method for preparing thiol stabilized Au nanoparticles, is discussed in detail in the chapter by Zhong *et al.* in Section IV of this book. The second method, which originates from Prof. El-Sayed's group, is noteworthy for preparing particles with extremely well-defined shapes (tetrahedra, cubes, etc).[20,21] The third method,

pioneered by Crooks and coworkers, involves using polyamidoamine dendrimers as nanoparticle templates and stabilizers.[19,22] The synthetic versatility of the dendrimer route to nanoparticle catalysts (see Scheme 7.1) offers substantial promise for the preparation of nanoparticles of interest to catalytic scientists and is the focus of the remainder of this chapter.

7.2. DENDRIMERS AND DENDRIMER ENCAPSULATED NANOPARTICLES (DENs)

Dendrimers are hyperbranched polymers that emanate from a single core and ramify outward with each subsequent branching unit (see Fig. 7.1).[23] They are generally prepared by sequential, alternating reactions of two smaller units, one of which has a point of bifurcation. Several classes of dendrimers are known, including polypropyleneimine (PPI), polyamidoamine (PAMAM), and Fréchet-type polyether dendrimers.[23] Starburst® PAMAM dendrimers (see Fig. 7.1) are a specific class of commercially available dendrimers that have repeating amine/amide branching units. These dendrimers are readily functionalized to terminate in a variety of moieties such as primary amines, carboxylates, hydroxyls, or hydrophobic alkyl chains. The presence of open spaces within the dendrimer interior and the synthetic control over their composition, architecture, and interior/exterior functionalities creates an environment to facilitate trapping guest species.[19,24]

These Dendrimer Encapsulated Nanoparticles (DENs) are prepared via a two-step synthesis (see Scheme 7.2): metal ions (e.g. Cu^{2+}, Pd^{2+}, Pt^{2+}) are complexed to the interior amine groups of a hydroxyl terminated PAMAM dendrimer and then chemically reduced to yield metal nanoparticles with narrow particle size distributions. Several reducing agents are available, depending on the metal and the synthetic conditions.[19,22] Purification is straightforward and reaction byproducts are readily removed with dialysis. DENs are stable for long periods and do not agglomerate because the nanoparticles (NPs) are trapped within the dendrimer framework. Some bimetallic DENs can be prepared via sequential or cocomplexation of metal cations followed by a variety of reduction procedures. Variations on these general schemes can also be used to prepare core-shell bimetallic nanoparticles.[22]

In the typical nomenclature for DENs,[22] the dendrimer is designated by Gx-R where x is the dendrimer generation and R is the surface group (typically –OH or $–NH_2$, see Fig. 7.1). The stoichiometry between the dendrimer and complexed ions or reduced encapsulated nanoparticles is denoted in parentheses after the dendrimer description, e.g. $(M^{c+})_n$ or (M_n). For bimetallic DENs, the metal:metal stoichiometry is typically included, e.g. G5-OH ($Pt_{16}Au_{16}$).

Synthetic methodologies for DEN preparation have been recently reviewed[19,22] and are only briefly described here. In a typical "direct metal loading" preparation, K_2PtCl_4 (5 mM, 4 ml) is added to an aqueous solution of G5-OH (0.01 mM, 20 ml) at room temperature and stirred for 3 days. The initial complexation time and metal:dendrimer stoichiometry vary widely with the metal precursor being used. After purging the solution with N_2 for 30 min, $NaBH_4$ (23 mg) is added and stirred overnight. Dialysis of the dark brown reaction product against water (pH 5.0–6.0, adjusted with HNO_3) over a period of 2 days yields a nanoparticle stock solution.

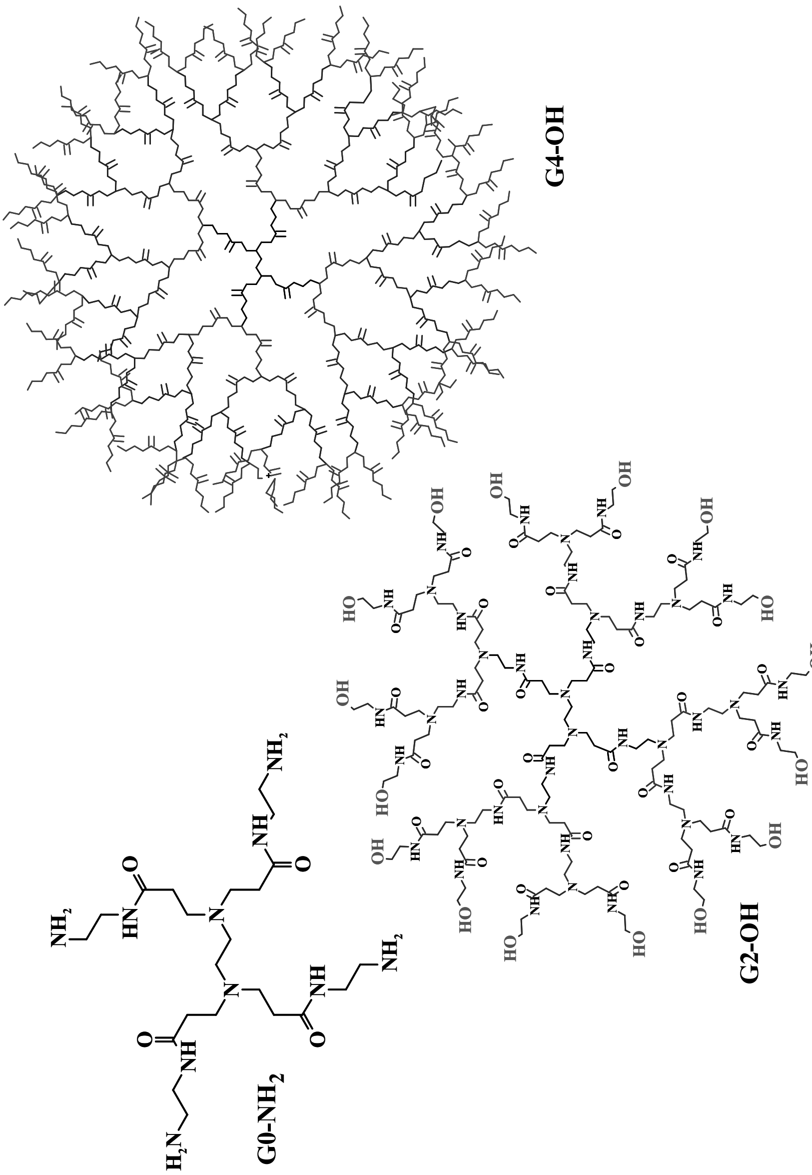

FIGURE 7.1. PAMAM dendrimers.

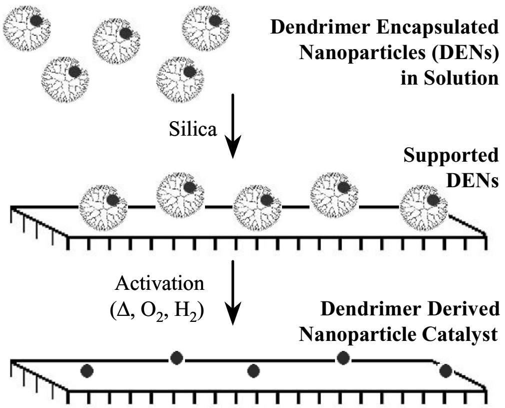

SCHEME 7.1.

Some metals, such as Ag and Au, do not readily form complexes with the interior amine groups of PAMAM dendrimers. However, DENs of these metals can be prepared by reacting the salt of a more noble metal (e.g. $AuCl_4^-$) with a nanoparticle of a less noble metal (e.g. Cu).[19,22] This "Cu displacement" method, pictured in Scheme 7.3, has been particularly useful in preparing bimetallic NPs where the metals are immiscible in the bulk or with substantially different reactivities toward reducing agents such as $NaBH_4$.[25] Cu displacement syntheses are somewhat more challenging than directly loading metal complexes into dendrimer interiors. Cu° nanoparticles are air-sensitive and will oxidize to Cu^{2+} in several hours,[26] so syntheses must be done under inert atmosphere with degassed solvents. Cu^{2+} also readily forms complexes with PAMAM dendrimers, making Cu removal an important consideration. For DENs in solution, dialysis at pH 4 is appropriate for removing residual copper.[27] The dialysis pH must be held low enough to protonate interior dendrimer amine groups.[28] yet not so low that it causes dendrimer degradation, which may lead to particle agglomeration.

The Pt–Au system has been a valuable system to test DENs' potential for preparing NP systems of interest to the heterogeneous catalysis community. It is synthetically challenging, characterized by a wide bulk miscibility gap (18 to 98% Pt),[29,30] and bimetallic NPs within this gap are unavailable by traditional routes.[29,31–33] Nuzzo and coworkers have shown that bulk phase diagrams may not necessarily hold true for NPs[34] and results with the Pt–Au system support this conclusion provided appropriate syntheses are available.[25,33] Utilizing Cu displacement syntheses, these substantial

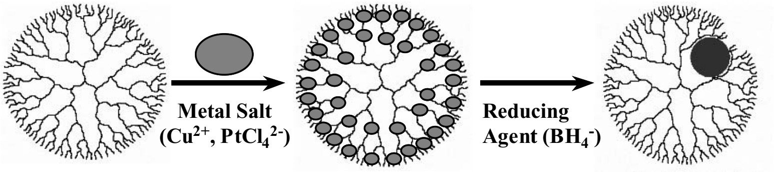

SCHEME 7.2.

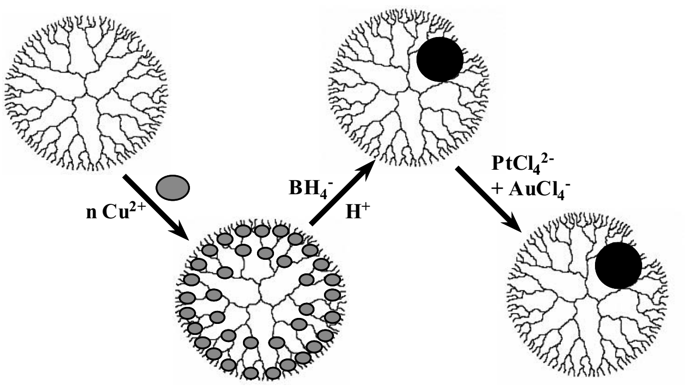

SCHEME 7.3.

synthetic challenges can be overcome to prepare Pt–Au DENs within the bulk miscibility gap.

Cu displacement preparations of Pt–Au NPs are generally accomplished by manipulations under inert atmosphere using standard Schlenk techniques. For example, 20 ml G5-OH (0.01 mM) can be mixed with 1.6 ml $Cu(NO_3)_2$ (5 mM) at pH 7.0 to 7.5 and degassed. A 3-fold molar excess of $NaBH_4$ is then added to prepare (G5-OH$(Cu)_{40}$) nanocomposites. After 30 min, the pH of the resulting brown solution is adjusted to 3.0 with $HClO_4$ and stirred for 1 h to destroy the excess $NaBH_4$. Solutions of K_2PtCl_4 (0.64 ml, 5 mM) and $HAuCl_4$ (1.6 ml, 2 mM) are degassed separately, mixed, and immediately added to the G5-OH$(Cu)_{40}$ nanocomposite solution via cannula transfer. The mixed solution is then stirred for an additional 1 to 2 h before deposition onto a suitable oxide support.

7.3. HOMOGENEOUS CATALYSIS BY DENs

The utilization of DENs in homogeneous catalysis has yielded several results of interest to the heterogeneous catalysis community. Homogeneous catalysis by DENs has been recently reviewed,[22] so only the most pertinent results are summarized here. As homogeneous hydrogenation catalysts, the PAMAM dendrimer surface functions as a size- and shape selective membrane for reactant molecules.[22,35–37] Polypropyleneimine DENs also impart substantial selectivity toward polar substrates in competitive hydrogenation reactions.[37] In a particularly elegant set of experiments, the size selectivity of Pd DENs for alkene hydrogenation, coupled with molecular "rulers" (alkenes tethered to large cyclodextrin "stoppers") has been used to estimate the distance of the Pd nanoparticle from the surface dendrimer surface.[22] This distance (0.7 ± 0.2 nm, on average) indicates that the nanoparticles are substantially displaced from the G4-OH dendrimer center (G4-OH radius ≈ 2.2 nm).[22,38]

The ability to functionalize DENs allows their use as homogeneous catalysts in a variety of reaction media including water, organic solvents, supercritical CO_2, and biphasic fluorous solvents.[22] Pd DENs have been the most widely studied homogeneous

catalysts, especially as carbon–carbon coupling catalysts. In Heck coupling reactions, Pd DENs show higher activities and selectivites relative to other colloidal Pd catalysts.[39] Pd DENs also compared favorably with polymer stabilized nanoparticles for stability in Suzuki couplings, although the DENs exhibited lower TOFs.[40]

Of particular interest to the heterogeneous catalysis community is the possibility of tuning nanoparticle properties by adjusting metal compositions. Homogeneous catalysis by bimetallic DENs has consistently provided control over reaction rates by modifying particle compositions. Better still, synergism between metallic components is a common theme in these studies. Allyl alcohol[41] and cyclohexene[42] hydrogenation by bimetallic Pt–Pd DENs, and 1,3-cyclooctadiene hydrogenation by bimetallic PdRh DENs[43] all exhibited higher intrinsic activities than physical mixtures of monometallic DENs with the same metal composition. Similarly, PdAu DENs prepared with a Au core and Pd shell show higher activity in allyl alcohol hydrogenation than monometallic Pd DENs.[44] The control experiments with physical mixtures of monometallic DENs are extremely important in these studies, and DENs offer the first real opportunities to do comparable control experiments for heterogeneous catalysts (see section 6.2).

7.4. IMMOBILIZATION & DEPOSITION OF DENs

7.4.1. Deposition onto Preformed Supports

For the dendrimer route to heterogeneous catalysts to realize its maximum potential, it is first necessary to prepare site-isolated NPs on a variety of oxide supports. Deposition and activation conditions are critical to preparing site-isolated nanoparticles, which are necessary if catalytic data is going to be meaningfully correlated with solution preparative techniques. DENs tend to agglomerate in solution unless low concentrations ($<50\ \mu$M) are maintained, making solution concentration followed by wetness impregnation far from ideal.[19] Metal yields are typically ca. 70% so it may require 100 mL of solution or more to prepare a gram or two of supported catalysts with relatively low metal loadings.

Simply stirring hydroxyl-terminated DENs with oxides such as silica leads to a small degree of deposition onto the surface. Hydroxyl-terminated PAMAM dendrimers do not spontaneously adsorb onto silica without an encapsulated nanoparticle, suggesting that the adsorption is driven by the introduction of relatively strong metal–support interactions. To an extent, this process can be directed by carefully controlling the solution pH (presumably to maximize the number of deprotonated surface hydroxyl groups) and stirring for several hours. This "slow adsorption" technique has been applied to silica, alumina, and titania using mono or bimetallic Pt- and Au-based DENs and moderate (ca. 0.4 wt%) metal loadings can be achieved without condensing the solution.[45] The slow adsorption method also allows DENs to be deposited immediately after synthesis since the soluble byproducts of synthesis can be readily washed off the support. This allows for the elimination of the dialysis step, substantially reducing preparation time when rapid catalyst screening is a priority. Eliminating the purification step results in slightly broader particle size distributions, however, since dialysis also removes most large particles stabilized by several dendrimers (*inter*dendrimer colloids).

In a typical "slow adsorption" deposition onto silica, the pH of an as-prepared DENs solution is adjusted to 8.5 to 9, SiO_2 is added, and the suspension is stirred overnight. The resulting dark solid can be readily separated from the colorless mother liquor with a fine frit. If the DENs are prepared with the "Cu displacement" route, the wet solid catalysts should be stirred with saturated EDTA solution at pH 7.0 to 8.0 for 15 to 20 min, then filtered and washed with deionized water. This EDTA wash is typically repeated three times to remove any Cu(II) that might remain bound to the dendrimer. The catalyst is then washed several times with deionized water, and dried in a vacuum oven at 50°C overnight. The overall yields for Pt, Au, and Pt–Au DENs are generally about 70 to 75% and residual Cu is nearly always less than 0.01%. This same procedure is readily adapted to other oxide supports by adjusting the deposition pH and stirring time.[45]

7.4.2. Sol–Gel Immobilization

Immobilizing DENs within a sol–gel matrix is another potential method for preparing new supported catalysts. PAMAM and PPI dendrimers can be added to sol–gel preparations of silicas[46–48] and zinc arsenates[49] to template mesopores. In one early report, the dendrimer bound Cu^{2+} ions were added to sol–gel silica and calcined to yield supported copper oxide nanoparticles. Sol–gel chemistry can also be used to prepare titania supported Pd, Au, and Pd–Au nanoparticle catalysts.[50] Aqueous solutions of Pd and Au DENs were added to titanium isopropoxide to coprecipitate the DENs with TiO_2. Activation at 500°C resulted in particles approximately 4 nm in diameter. In this preparation, the PAMAM dendrimers served two roles, templating both nanoparticles and the pores of the titania support.

As prepared and purified G4-OH(Pt_{50}) DENs solutions (ca. 20 μM) can also be used to prepare high surface area sol–gel Pt/silica catalysts. This process can be used to carefully control metal loadings without condensing the solution provided the loadings remain low (less than 0.2 % Pt). The low concentrations do not allow the dendrimer to serve as a porosity template. Further, low loadings combined with delayed introduction of the DENs solution to a preformed sol likely lead to the occlusion of metal nanoparticles within the oxide matrix.[51]

Typical sol–gel silica immobilizations have been based on methods described by Lukehart and coworkers for immobilizing ligand stabilized molecular clusters.[52] In a typical preparation, tetramethoxysilane (TMOS, 2.5 mL) is added to a volume of up to 20 mL aqueous DENs solution in a 150 mL beaker along with a magnetic stir bar. Acetic acid (50 μL) is also added to 19.5 mL H_2O and combined with the first solution. The resulting solution is mixed thoroughly, covered, and stirred slowly for 3 days. The beaker is then placed in a muffle furnace to dry for 48 h at 80°C and resulting monoliths are ground in a mortar and pestle.[51]

7.5. ACTIVATION AND DENDRIMER REMOVAL

7.5.1. Immobilized In-tact DENs

DENs can be immobilized on electroactive substrates to prepare "heterogenized" homogeneous catalysts. Electrochemical grafting of hydroxyl-terminated Pt DENs

yields covalently linked DENs that are active (solution) electrocatalysts. These heterogenized systems are quite robust, withstanding numerous electrochemical cycles and sonification in 0.5 M H_2SO_4. Thiophene terminated PAMAM dendrimers can also be electrocopolymerized with 3-methylthiophene. Coordination of $PtCl_4^{2-}$ and reduction yields DENs within this matrix. Similarly, amine terminated Pt and Pd DENs have been immobilized on planar Au surfaces through self-assembled monolayer (SAM) chemistry. Neither of the latter two systems have proven to be catalytically or electrocatalytically active, although studies are ongoing.

In the absence of a solvent, supported, intact DENs are completely inactive as catalysts and do not bind CO. Presumably, upon drying, the organic dendrimer collapses onto the NP, poisoning the metal surface.[53,54] The activity of immobilized DEN electrocatalysts in water and a recent study by Williams and coworkers have provided the strongest evidence in support of dendrimer poisoning of supported, dried DENs. Using a solid-solution *in-situ* ATR-IR spectroscopy technique, Williams and coworkers have shown that alumina supported intact Pt DENs are capable of binding CO in the presence of water. Control experiments showed that the supported DENs do not migrate into the solution and stay adsorbed on the oxide. The supported DENs were active for CO oxidation in water and showed activity comparable to a Pt/alumina catalyst prepared via wetness impregnation of H_2PtCl_6. This study also showed that the presence of the Pt nanoparticle has a substantial effect on the stretching frequencies associated with the amide bonds that make up the dendrimer backbone.[54]

7.5.2. Activation Conditions

7.5.2.1. High Temperature Activation. Identifying appropriately mild activation conditions for supported DENs is a prerequisite for utilizing them as precursors to heterogeneous catalysts. Ideal activation conditions should be forcing enough to remove or passivate the organic material, yet mild enough not to induce particle agglomeration. Surface particle agglomeration or sintering processes are extremely temperature dependent,[55,56] so minimizing activation temperatures is critical for ultimately correlating supported catalyst properties with synthetic methodologies and particle properties.

Initial work with Pd DENs immobilized on mica showed the importance of carefully determining decomposition protocols as even a short (10 min) treatment at high temperature (630°C) caused substantial particle growth.[57] Thermogravimetric analysis (TGA) studies indicate that that, under the conditions of the TGA experiment, high temperatures (500°C) are required to completely remove organic matter from Pd and Au DENs immobilized in porous sol–gel TiO_2.[50] This treatment resulted in substantial particle agglomeration, although pore templating by the dendrimer mitigated the particle growth.

Similar to the TGA experiments, *in situ* Infrared Spectroscopy has been used to follow the amide bond stretching frequencies while heating under various atmospheres.[53,58–60] These experiments (see Fig. 7.2) suggest that dendrimer removal requires relatively forcing conditions to maximize CO adsorption on supported Pt catalysts prepared from DENs.[50,53,58–60] A variety of activation conditions have been chosen based on these experiments, generally involving some combination of oxygen and/or hydrogen treatments.[53,58–60]

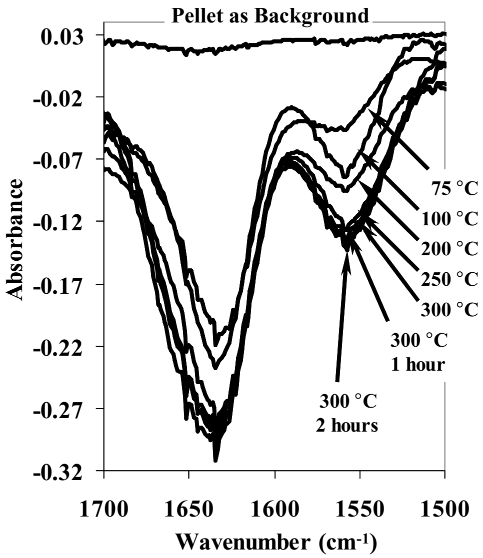

FIGURE 7.2. Typical in-situ dendrimer decomposition experiment in 20% O_2. The supported DENs were pressed into a self-supporting wafer, loaded into the IR cell, and temperature was increased at approximately 5°C/min. The first 5 spectra shown are at intervals of approximately 30°C; the bottom three spectra was collected after soaking at 300°C for 2 h.

The specific activation conditions required for an individual catalyst likely depend on the metal and support, but 300°C appears to be somewhat of a watershed temperature. Activation at temperatures above 300°C generally coincides with loss of Pt metal surface area due to sintering.[53,58,59] The metal loading, dendrimer loading, and metal:dendrimer ratios also impact activation conditions, suggesting that it may be necessary to optimize activation conditions for individual catalysts. Using temperatures at or near 300°C, supported Pt,[45,53,58,61] Au,[45] Pt–Au,[25,62] Pt–Cu,.[63] and Ru[60] nanoparticles have been prepared. In most cases, treatments at 300°C have resulted in little to no particle agglomeration and the ultimate supported nanoparticles have remained in the 1 to 3 nm range (see Fig. 7.3).

The differences in conclusions based on TGA and IR experiments are substantial; however, they are understandable based on conditions of each experiment. Although TGA provides explicit information regarding when removal of organic species is complete, it is most effective for monitoring rapid changes in mass as a function of temperature. Even at a relatively slow temperature ramp (e.g. 1°C/min), standard TGA experiments are ineffective in evaluating decomposition processes that take place over the course of several hours.

In-situ infrared spectroscopy has been used in much the same fashion at TGA, but temperature profiles have been combined with monitoring changes at constant temperature.[53,58–61] IR spectroscopy does not yield the same direct information about the complete removal of organic residues that TGA provides. On the other hand, CO adsorption experiments performed along with dendrimer decomposition experiments provide direct information regarding metal availability. Further, IR experiments provide

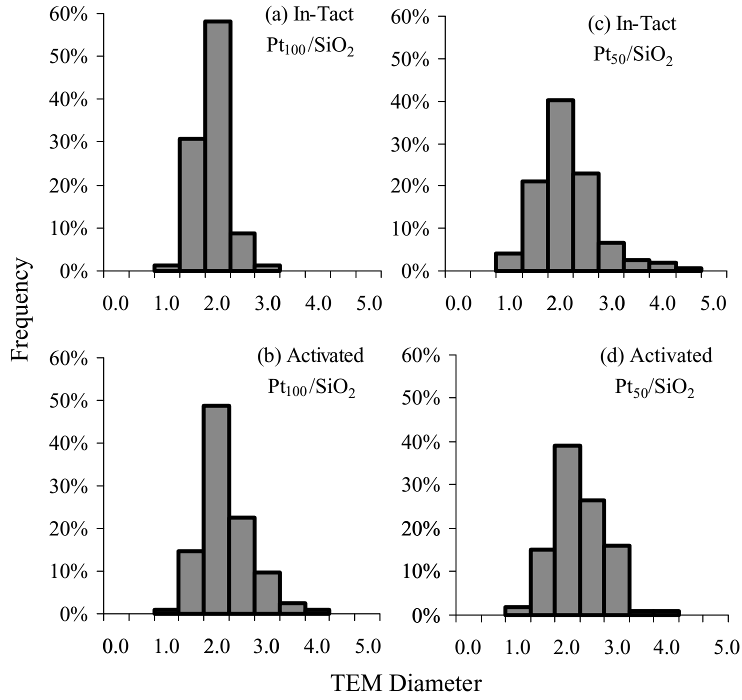

FIGURE 7.3. Transmission Electron Microscopy Data for in-tact (a & c) and activated (b & d) Pt/SiO_2 catalysts. Reprinted with permission from *J. Am. Chem. Soc.* **2003**, 125, 14832–14836. Copyright 2003 American Chemical Society.

important information regarding the dendrimer decomposition products and residues that can act as poisons for supported metal nanoparticle catalysts.

7.5.2.2. Activation Models and Low Temperature Activation. Both TGA and IR experiments show that the PAMAM dendrimer backbone begins decomposing at temperatures as low as 75°C, although more forcing conditions are required to fully activate the catalysts.[50,53,58–60] The low onset temperature of dendrimer decomposition is not surprising given that PAMAM dendrimers can undergo retro-Michael addition reactions at temperature above 100°C.[22] To avoid this, PAMAM dendrimer synthesis and modification are typically carried out at or near ambient temperature using reaction times as long as several days.[64] Further, Bard and coworkers have recently shown that, even in the absence of a nanoparticle catalyst, PAMAM dendrimers are susceptible to oxidation by molecular oxygen in aqueous solution at near ambient temperatures.[65]

Pt and Pd are good oxidation catalysts and have been clearly implicated in catalyzing dendrimer oxidation during decomposition.[50,59,66] Even in the absence of a metal nanoparticle, the dendrimer amide bonds degrade upon heating in He[59,66] Since the dendrimer architecture is relatively unstable upon heating, it is perhaps surprising that such forcing conditions were initially suggested for complete activation of DENs.

The necessity of forcing activation conditions has been attributed to the production of various carbonaceous species during activation. Under oxidizing atmospheres, the appearance of stretching frequencies consistent with the formation of surface carboxylates has been reported.[61] Similarly, several persistent surface bands consistent with coke-type species were identified when activating supported Ru DENs under H_2.[60]

A working model for dendrimer thermolysis during calcination involves the PAMAM dendrimer backbone initially reacting with oxygen (which may or may not be activated by a nanoparticle) in a relatively facile process to generate carboxylates and other surface species.[61] Removal of carbonaceous species closely associated with the nanoparticle is required for complete activation of the catalyst. For Pt DENs, the surface carboxylates may be strongly adsorbed to the nanoparticle surface and extended O_2 treatments are required for deep oxidation of the hydrocarbon to reach reasonably volatile species.[61] Once formed, however, it appears that they can be removed more readily with a hydrogen treatment than with further oxidation.[53]

Given that it may be difficult to remove surface carboxylates from supported DENs, the question arises as to whether it is inherently necessary to remove all organic material to prepare clean, active supported nanoparticles. In a practical sense, except when dealing with freshly calcined supports (e.g. treated overnight at 500°C), carbon species from atmospheric sources are always present on oxide surfaces and C–H stretching vibrations are readily observable in infrared spectra of supports taken directly from a manufacturer's container. The critical species are those directly adsorbed to the metal surface and in close proximity to the nanoparticles. Including strongly adsorbing small molecules such as CO in the treatment feed may effectively protect the metal surface from carboxylates, allowing them to migrate to the support.[61]

7.6. DENDRIMER TEMPLATED HETEROGENEOUS CATALYSTS

7.6.1. Catalysis by Platinum

Silica supported Pt catalysts have been examined in the most depth to identify appropriate activation conditions. The first study with these materials involved catalysts prepared from G5-OH(Pt_{50}) and G5-OH(Pt_{100}), calcined under O_2 at 300°C for four hours and reduced at 300°C for two hours.[53] The resulting catalysts are active for both oxidation and hydrogenation reactions. The turnover requencies (TOFs) for catalytic CO oxidation (see Fig. 7.4) and toluene hydrogenation (at 60°C) by the Pt_{100}/SiO_2 catalyst were indistinguishable from a traditionally prepared catalyst, as was the infrared spectrum of CO adsorbed to Pt_{100}/SiO_2. Beyond an important proof of concept, this study showed that dendrimer-derived catalysts can serve as good models for traditionally prepared or industrial catalysts.

Identifying appropriate deposition and activation conditions has remained a primary goal behind the study of Pt/silica catalysts prepared via the dendrimer route. For Pt/SiO_2 catalysts, calcination at 300°C for 4+ hours has proven to be the best activation protocol thus far. Figure 7.5 shows spectra of CO adsorbed on Pt_{50}/SiO_2 activated with O_2 compared a supported Pt catalyst prepared by wetness impregnation of H_2PtCl_6. The H_2PtCl_6 catalyst is consistent with standard Pt catalysts, and the full coverage CO stretching frequency (2085 cm^{-1}) is consistent with CO linearly adsorbed on Pt.[9,67]

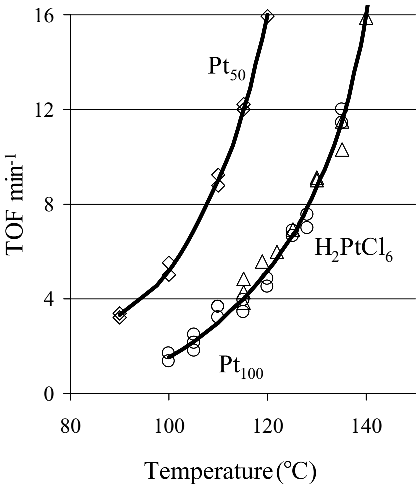

FIGURE 7.4. Co Oxidation by Catalysis by Dendrimer Templated Catalysts. Reprited with permission from *J. Am. Chem. Soc.* **2003**, *125*, 14832–14836. Copyright 2003 American Chemical Society.

Dendrimer derived catalysts have somewhat lower primary stretching frequencies. Fully activated Pt_{20}/SiO_2 catalysts, for example, have a primary stretching frequency near 2068 cm^{-1} with a distinguishable shoulder at 2085 cm^{-1}. These bands remain consistent after a number of activation protocols, including calcination at 300°C for up to 24 h.[61] A number of studies have loosely correlated lower CO stretching frequencies with adsorption onto low coordination edge and corner sites that dominate small nanoparticles.[67] Similarly, high coverage bands near 2085 cm^{-1} have been assigned

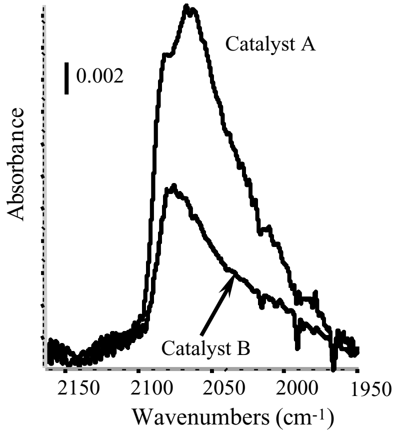

FIGURE 7.5. Infrared spectra of CO adsorbed on two sol–gel immobilized Pt_{50}/SiO_2 catalysts. Catalyst A was prepared by adding the DENs solution at the beginning of the sol–gel preparation. For catalyst B, the DENs solution was added after the sols were allowed to form for 24 hours, but before gellation. Both catalysts were oxidized at 300°C for 16 h and reduced at 300°C for 2 h. Reprinted with permission from *Appl. Catal. A.* **2005,** *292*, 124–129. Copyright 2005 Elsevier.

to terrace or face sites on extended surfaces.[67] The relative intensity of these adsorption bands has also been correlated to the presence of small (<2 nm) supported Pt particles; however, the complexity of factors affecting band intensity (intensity borrowing, dipole coupling, dephasing) makes quantitative interpretation of these bands unreliable.

The consistency of the high (2068 cm^{-1}) and low (2058 cm^{-1}) coverage values for the Pt_{20}/SiO_2 catalyst suggests this is a diagnostic band for fully activated dendrimer derived catalysts. The same 2068 cm^{-1} high coverage band also is found for a Pt_{50}/SiO_2 catalyst prepared with sol–gel chemistry (Fig. 7.5), along with the 10 wavenumber red shift during thermal desorption.[51] Dendrimer-derived catalysts that are not fully activated tend to have slightly blue shifted high coverage CO stretching frequencies. All of these catalysts have relatively similar activities for CO oxidation, indicating that this reaction is relatively fast, even on partially poisoned Pt surfaces. This is consistent with suggestions that the rate limiting step for CO oxidation by smaller nanoparticles involves desorption of a key surface intermediate.[68] In general, toluene hydrogenation appears to be a more sensitive probe reaction for dendrimer-derived catalysts as activity for this reaction is closely tied to the cleanliness of Pt nanoparticle surfaces.[51,53]

7.6.2. Bimetallic Catalysts

One of the most promising areas for dendrimer-derived catalysts is in the controlled preparation of bimetallic catalysts. This is particularly true for catalyst compositions that are unattainable by traditional routes. Using G5-OH, a $Pt_{16}Au_{16}/SiO_2$ catalyst has been prepared via the copper displacement synthesis and characterized. The dendrimer route allows for control experiments that are not available through traditional routes and are rarely available for molecular clusters. Using DENs, it is possible to prepare "cometallic" catalysts composed of monometallic DENS codeposited on a support. Although these catalysts certainly have two metals present, we describe them as "cometallic" to distinguish them from "bimetallic" dendrimer derived catalysts. Hence, "bimetallic" catalysts have been prepared with two metals in intimate contact in individual nanoparticles; "cometallic" catalysts have been prepared so that the two metals intentionally have no interactions prior to activation.

Figure 7.6 shows infrared spectra of adsorbed CO for $Pt_{16}Au_{16}/SiO_2$ compared to Pt_{32}/SiO_2 and a "cometallic" $Pt_{32}{+}Au_{32}/SiO_2$ catalyst. IR spectra of $Pt_{16}Au_{16}$ (Fig. 7.6b) show a high energy absorption band (2113 cm^{-1}), attributed to bound to Au surface sites. The lower energy band (2063 cm^{-1}) is attributable to Pt bound CO[53] and is red shifted 20 cm^{-1} relative to CO on monometallic Pt NPs. This result is also consistent with the presence of a bimetallic surface, where surface Pt atoms are diluted in Au.[31,33,69–71] The physical separation of diluted Pt–CO dipoles would reduce their ability to participate in dipole coupling, resulting in an apparent red shift relative to a pure Pt surface.[67]

During desorption experiments with $Pt_{16}Au_{16}$ (Fig. 7.7), the Au–CO band disappears quickly, and coincides with an increase in the Pt–CO band intensity. Closer inspection of the $Pt_{16}Au_{16}$ desorption experiment suggests that the broad room temperature Pt–CO band may be better described as two bands at 2065 and 2050 cm^{-1}.

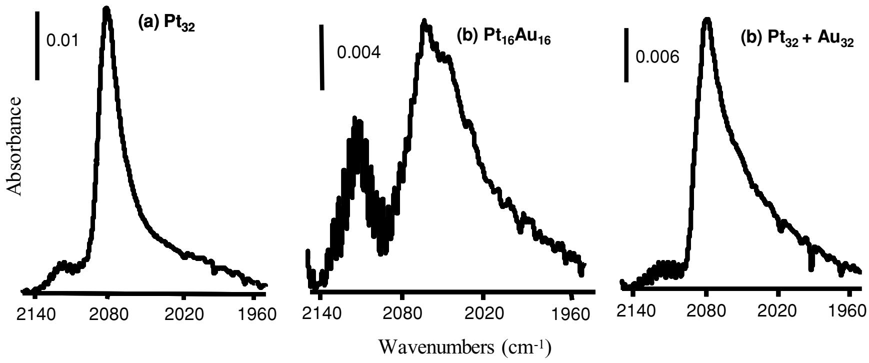

FIGURE 7.6. Infrared Spectroscopy of CO adsorbed at 30°C on (a) Pt_{32}/SiO_2, (b) $Pt_{32}+Au_{32}/SiO_2$ and (c) $Pt_{16}Au_{16}/SiO_2$. Reprinted with permission from *J. Am. Chem. Soc.* **2004**, 126, 12949–12956. Copyright 2004 American Chemical Society.

Changes in the Pt–CO band are due to a substantial increase in the intensity of the 2050 cm^{-1} band. Once CO completely desorbs from Au, the Pt–CO band becomes substantially more symmetric and the 2065 cm^{-1} band is no longer distinguishable. Complete desorption of the 2050 cm^{-1} band also occurs at a higher temperature than

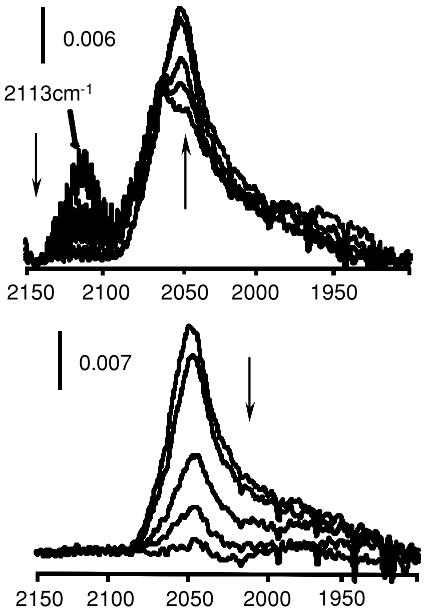

FIGURE 7.7. Infrared Spectroscopy during CO desorption from $Pt_{16}Au_{16}/SiO_2$ (a) 30, 70, 90, &120°C and (b) 120 , 150, 170, 180 & 190°C. As the band at 2113 cm^{-1} decreases, the band at 2055 increases. Once the 2113 band disappears, the 2055 band decreases in intensity, but does not shift. Reprinted with permission from *J. Am. Chem. Soc.* **2004**, 126, 12949–12956. Copyright 2004 American Chemical Society.

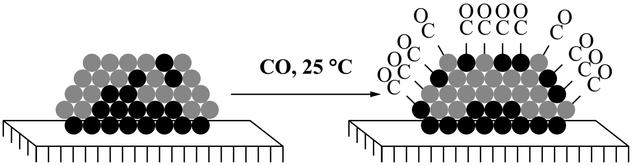

SCHEME 7.4.

with the Pt_{32} or $Pt_{32}+Au_{32}$ samples, suggesting that CO is more strongly bound to the intimately mixed bimetallic NPs.

These IR spectra were explained by a restructuring of the Pt–Au nanoparticles with CO providing a driving force for pulling Pt to the particle surface (see Scheme 7.4).[25,29,72] The mobility of Pt and Au within the bimetallic NPs also explains how the incorporation of Pt anchors Au to the support, preventing the severe particle agglomeration that is so prevalent in monometallic Au/SiO_2 catalysts.[10,31,32,70] TEM data for mono- and cometallic Au based catalysts always show widespread sintering as 100+ nm particles are nearly always observed after these catalysts have been activated. In contrast, Fig. 7.8 shows that bimetallic Pt–Au nanoparticles are primarily 2 to 3 nm in diameter after activation.

CO oxidation catalysis by $Pt_{16}Au_{16}$ also showed synergistic effects upon intimately mixing Pt and Au.[25] Supported Au NPs are well known to be highly active low temperature CO oxidation catalysts;[10,12,73] however, the most active catalysts utilize reducible oxide supports such as TiO_2.[10,73] Silica, being mildly acidic in water and having a low isoelectric point (IP $\approx$ 2), is unsuitable for deposition–precipitation methods because the surface is negatively charged at the pH values required to precipitate

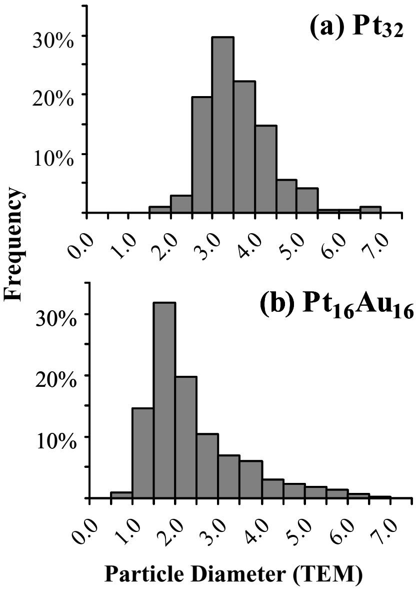

FIGURE 7.8. TEM particle size distributions for Pt_{32}/SiO_2 and $Pt_{16}Au_{16}/SiO_2$. Reprinted with permission from *J. Am. Chem. Soc.* **2004**, 126, 12949–12956. Copyright 2004 American Chemical Society.

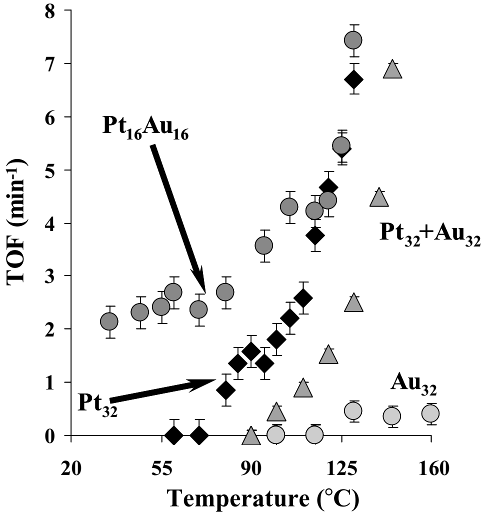

FIGURE 7.9. CO Oxidation Catalysis by $Pt_{16}Au_{16}/SiO_2$. Reprinted with permission from *J. Am. Chem. Soc.* **2004**, 126, 12949-12956. Copyright 2004 American Chemical Society.

$Au(OH)_x$. Additionally, silica does not stabilize gold NPs against agglomeration.[10] It appears that, on silica, one of the primary roles of Pt is to help stabilize small particles. Pt may also add additional functionality to the catalyst by binding O_2 and locating bound or activated O_2 near active Au sites. Alternately, the presence of Pt may affect the surface structure of Au, helping it to adopt a more active geometry.[74]

Dendrimer templated Pt–Au catalysts are also active for the selective catalytic reduction of NO by propylene in the presence of excess O_2. In addition to its commercial importance, this reaction is particularly interesting for the Pt–Au system. Previous work with cluster-derived Pt–Au catalysts has demonstrated that this reaction exhibits structure sensitivity, suggesting that it may be possible to use it as a structural probe for Pt based catalysts.[69,70]

Studies with traditionally prepared and cluster derived Pt_2Au_4 catalysts have shown that Pt is the active metal in this reaction. The primary role of Au appears to be that of a diluent, breaking up large Pt ensembles.[69,70] This mixing has two important results for the catalytic properties of these systems. First, catalytic activity is suppressed at lower temperatures, resulting in a delay in the "light-off curve" for NO and propylene conversion. This is a desirable result, as it allows for higher catalyst operating temperatures. Secondly, cluster derived catalysts show substantially higher selectivities for N_2 production over the undesirable N_2O product. Initial studies with the dendrimer derived Pt/SiO_2, Au/SiO_2, and $Pt_{16}Au_{16}/SiO_2$ catalysts, shown in Fig. 7.10, indicate that they behave similarly and support the conclusion that the dendrimer method is a viable means of templating bimetallic nanoparticles.

7.6.3. Evaluating Support Effects

Another potential advantage of the dendrimer route is the possibility of evaluating support effects. Because DENs are prepared *ex situ* from a support, it is possible to

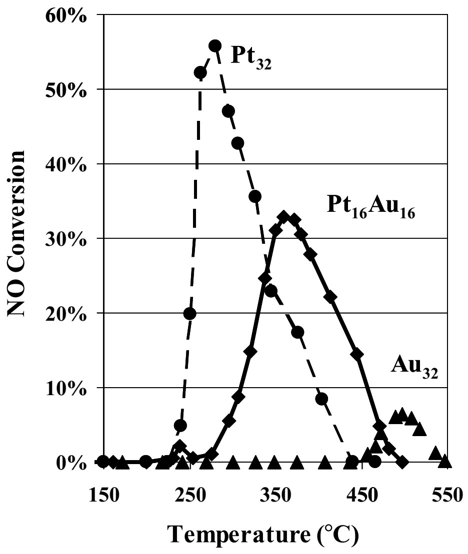

FIGURE 7.10. Selective catalytic reduction of NO with propylene by Pt_{32}/SiO_2, $Pt_{16}Au_{16}/SiO_2$, and Au_{32}/SiO_2.

deposit nanoparticles that, at least initially, are chemically identical on a variety of materials. Monitoring changes in particle size and catalyst properties may allow for eventually evaluating the nature of support effects for a variety of metal systems. Further, the dendrimer route allows for depositing the same set of nanoparticles on well-defined single crystal supports. Although there is only one current surface science study using dendrimer derived catalysts,[66] eventually this may allow for the comparison between catalytic properties of nanoparticles on high surface area and well-defined supports. This should both improve our understanding of dendrimer templated nanoparticles and aid in extrapolating UHV experiments to bench-scale catalysts.

Initial studies on support effects (silica, alumina, amorphous titania, Degussa P-25 titania) for Pt, Au, and Pt–Au bimetallic catalysts are currently underway.[45,62] For monometallic Pt catalysts, high coverage CO stretching frequencies range from 2081 to 2086 cm^{-1} and showed only a slight dependence on the support. Low coverage spectra vary more, from ca. 2053 cm^{-1} (silica and alumina) to 2075 (amorphous titania). CO bound to Au was only observed on Au/TiO_2 and Au/P-25 and occurs at 2119 cm^{-1} for both catalysts. All of the bimetallic $Pt_{16}Au_{16}$ catalysts showed CO bound to Au (2113 to 2119 cm^{-1}) at high coverage and lower Pt–CO stretching frequencies (ca. 2065 cm^{-1}). Additionally, all show an increase in the Pt band intensity during CO desorption from Au as shown in Fig. 7.8. Red shifts during CO desorption from Pt are all around 10 cm^{-1}.

CO oxidation catalysis showed that, for all the supports, the bimetallic catalyst was more active at low temperatures than the corresponing monometallic and cometallic catalysts. Apparent activation energies for monometallic Pt and Au catalysts were very consistent, near 32 and 80 kJ/mole, respectively. The synergism for $Pt_{16}Au_{16}$ catalysts also shows up in the apparent activation energies for these catalysts, which were consistently around 23 kJ/mole.

7.7. SUMMARY AND CONCLUSIONS

Dendrimer encapsulated nanoparticles (DENs) provide new opportunities for studying supported nanoparticle catalysts. A variety of synthetic methodologies now exist for the preparation of mono- and bimetallic DENs with controlled compositions and morphologies. Several methods are available for immobilizing DENs onto oxide and graphitic supports; in some cases, these supported (in-tact) DENs have proven to be active catalysts. The organic dendrimer template can be removed with a variety of thermal treatments, although details of individual treatments depend on the metal and support under study. The amide bonds in PAMAM dendrimers are thermally unstable but thermolysis yields products that are more difficult to remove. It may be possible, however, to protect some metals from the decomposition products by adding a strong ligand (such as CO) to the thermolysis feed. In general, treatement with O_2 at temperatures near 300°C has been required to prepare active catalysts.

Using the dendrimer route, it is possible to prepare supported catalysts not available via traditional routes. Dendrimer derived Pt–Au catalysts having compositions within the bulk miscibility gap can be prepared on several oxide supports. For all the supports studied, the bimetallic catalysts exhibited synergism with respect to mono- and cometallic catalysts for the CO oxidation and hydrocarbon NOx SCR reactions. The bimetallic Pt–Au catalysts also showed evidence of exchanging surface and subsurface atoms in response to strongly binding ligands such as CO.

ACKNOWLEDGMENTS

BDC and HL gratefully acknowledge the Robert A. Welch Foundation (Grant number W-1552) for financial support of this work. Acknowledgement is made to the donors for the American Chemical Society Petroleum Research Fund and to Research Corporation for partial support of this research. We are very grateful to Stephen Maldonado and Prof. Keith Stevenson at the University of Texas at Austin for their assistance in obtaining TEM data. We also thank Samuel Deutsch and Prof. Michael Amiridis at the University of South Carolina for performing the NOx experiments.

REFERENCES

1. A. Bell, The impact of nanoscience on heterogeneous catalysis, *Science* **299,** 1688–1691 (2003).
2. H. Greenblatt, Catalysts: An Innovative Industry Responds to Technological and Competitive Challenges 24-44 (US International Trade Commission, Publication 3602, Washington, DC, 2003).
3. C. S. Song, Fuel processing for low-temperature and high-temperature fuel cells—challenges and opportunities for sustainable development in the 21st century, *Catal. Today* **77,** 17–49 (2002).
4. J. M. Thomas *et al.*, Bimetallic catalysts and their relevance to the hydrogen economy, *Ind. Eng. Chem. Res.* **42,** 1563–1570 (2003).
5. V. Ponec and G. C. Bond, Catalysis by metals and alloys, *Stud. Surface Sci. Catal.* **95**, 23 (1995).
6. O. Alexeev and B. C. Gates, Supported bimetallic cluster catalysts, *Ind. Eng. Chem. Res.* **42,** 1571–1587 (2003).
7. J. H. Sinfelt, *Bimetallic Catalysts* (Wiley, New York, 1985).

8. Argonne National Laboratory, U.S. Department of Energy Report; available at: http://www.sc.doe.gov/bes/ hydrogen.html, (2004).
9. V. Ponec and G. C. Bond (eds.) *Catalysis by Metals and Alloys* (Elsevier, Amsterdam, 1995).
10. A. Wolf and F. Schuth, A systematic study of the synthesis conditions for the preparation of highly active gold catalysts, *Appl. Catal. A—Gen.* **226,** 1–13 (2002).
11. H.-S. Oh *et al.*, Selective catalytic oxidation of CO: Effect of chloride on supported Au catalysts, *J. Catal.* **210,** 375–386 (2002).
12. S. D. Lin, M. Bollinger, and M. A. Vannice, Low temperature CO oxidation over Au/TiO2 and Au/SiO2 catalysts, *Catal. Lett.* **17,** 245 (1993).
13. J. Guzman and B. C. Gates, Supported molecular catalysts: metal complexes and clusters on oxides and zeolites, *Dalton Trans.* **17,** 3303–3318 (2003).
14. A. Brenner, In *Metal Clusters*, edited by M. Moskovits (John Wiley & Sons, New York, 1986), pp. 249–282.
15. D. M. P. Mingos and D. J. Wales, *Introduction to Cluster Chemistry* (Prentice-Hall, London, 1990).
16. B. D. Chandler, L. I. Rubinstein, and L. H. Pignolet, Alkane dehydrogenation with silica supported Pt and Pt–Au catalysts derived from phosphine ligated precursors, *J. Mol. Catal. A: Chem.* **133,** 267–282 (1998).
17. M.-C. Daniel and D. Astruc, Gold nanoparticles: Assembly, supramolecular chemistry, quantum size related properties, and applications toward biology, catalysis, and nanotechnology, *Chem. Rev.* **104,** 293–346 (2004).
18. M. Brust and C. J. Kiely, Some recent advances in nanostructure preparation from gold and silver particles: A short topical review, *Colloids Surf. A: Physicochem. Eng. Aspects* **202,** 175–186 (2002).
19. R. M. Crooks, M. Zhao, L. Sun, V. Chechik, and L. K. Yeung, Dendrimer-encapsulated metal nanoparticles: Synthesis, characterization, and applications to catalysis, *Accounts Chem. Res.* **34,** 181–190 (2001).
20. R. Narayanan and M. A. El-Sayed, Changing catalytic activity during colloidal platinum nanocrystals due to shape changes: Electron-transfer reaction, *J. Am. Chem. Soc.* **126,** 7194–7195 (2004).
21. M. A. El-Sayed, Small is different: Shape-, size-, and composition-dependent properties of some colloidal semiconductor nanocrystals, *Accounts Chem. Res.* **37,** 326–333 (2004).
22. R. W. J. Scott, O. M. Wilson, and R. M. Crooks, Synthesis, characterization, and applications of dendrimer-encapsulated nanoparticles. *J. Phys. Chem.* **109,** 692–704 (2005).
23. M. Fisher and F. Vogtle, Dendrimers: From design to pplication—a progress report, *Angew. Chem. Int. Ed.* **38,** 884 (1999).
24. A. I. Cooper, *et al.*, Extraction of a hydrophilic compound from water into liquid CO_2 using dendritic surfactants, *Nature* **389,** 368–371 (1997).
25. H. Lang, S. Maldonado, K. J. Stevenson, and B. D. Chandler, Synthesis and characterization of dendrimer templated supported bimetallic Pt-Au nanoparticles, *J. Am. Chem. Soc.* **126,** 12949–12956 (2004).
26. M. Q. Zhao and R. M. Crooks, Intradendrimer exchange of metal nanoparticles, *Chem. Mater.* **11,** 3379–3385 (1999).
27. H. Lang and B. D. Chandler, unpublished results
28. Y. Niu, L. Sun and R. M. Crooks, Determination of the intrinsic proton binding constants for poly(amidoamine) dendrimers via potentiometric pH titration, *Macromolecules* **36,** 5725–5731 (2003).
29. R. Bouwman and W. H. M. Sachtler, Photoelectric determination of the work function of gold-platinum alloys, *J. Catal.* **19,** 127 (1970).
30. H. Okamoto and T. B. Massalski, The Au–Pt system, *Bull. Alloy Phase Diagrans* **6,** 46–56 (1985).
31. J. Shen, J. M. Hill, M. W. Ramachandra, S. G. Podkolzin, and J. A Dumesic, Ethylene adsorption on Pt-Au/SiO2 catalysts, *Catal. Lett.* **60,** 1–9 (1999).
32. A. Sachdev and J. Schwank, Microstructure and reactivity of supported bimetallic platinum-gold catalysts, *J. Catal.* **120,** 353–369 (1989).
33. B. D. Chandler, A. B. Schabel, C. F. Blanford, and L. H. Pignolet, The preparation and characterization of supported bimetallic Pt–Au particle catalysts from molecular cluster and chloride salt precursors, *J. Catal.* 367–383 (1999).

34. C. W. Hills, N. H. Mack, and R. G. Nuzzo, The size-dependent structural phase behaviors of supported bimetallic (Pt-Ru) nanoparticles, *J. Phys. Chem.* B **107,** 2626–2636 (2003).
35. M. Zhao and R. M. Crooks, *Angew. Chem. Int. Ed.* **38,** 364–366 (1999).
36. Y. H. Niu, L. K. Yeung, and R. M. Crooks, Size-selective hydrogenation of olefins by dendrimer-encapsulated palladium nanoparticles, *J. Am. Chem. Soc.* **123,** 6840–6846 (2001).
37. M. Ooe, M. Murata, T. Mizugaki, K. Ebitani, and K. Kaneda, Dendritic nanoreactors encapsulating Pd particles for substrate-specific hydrogenation of olefins, *Nano Lett.* **2,** 999–1002 (2002).
38. F. Gröhn, B. J. Bauer, Y. A. Akpalu, C. L. Jackson, and E. J. Amis, *Macromolecules* **33,** 6042–6050 (2000).
39. L. K. Yeung and R. M. Crooks, *Nano Lett.* **1,** 14–17 (2001).
40. Y. Li and M. A. El-Sayed, *J. Phys. Chem.* B **105,** 8938–8943 (2001).
41. R. W. J. Scott, A. K. Datye, and R. M. Crooks, Bimetallic palladium–platinum dendrimer-encapsulated catalysts, *J. Am. Chem. Soc.* **125,** 3708–3709 (2003).
42. Y. M. Chung and H. K. Rhee, Pt–Pd bimetallic nanoparticles encapsulated in dendrimer nanoreactor, *Catal. Lett.* **85,** 159–164 (2003).
43. Y. M. Chung and H. K. Rhee, Partial hydrogenation of 1,3-cyclooctadiene using dendrimer-encapsulated Pd–Rh bimetallic nanoparticles, *J. Mol. Catal.* A—*Chem.* **206,** 291–298 (2003).
44. R. W. J. Scott, O. M. Wilson, S.-K. Oh, E. A. Kenik, and R. M. Crooks, Bimetalic palladium-gold dendrimer encapsulated catalysts, *J. Am. Chem. Soc.* **126,** 15583–15591 (2004).
45. H., Lang, B. Auten, and B. D. Chandler, Support effects on dendrimer templated Pt–Au catalysts I: Deposition and infrared spectroscopy, *J. Catal.*, manuscript in preparation (2004).
46. G. Larsen, E. Lotero, and M. Marquez, Use of polypropylene tetrahexacontaamine (DAB-Am-64) dendrimer as a single-molecule template to produce mesoporous silicas, *Chem. Mater.* **12,** 1513–1515 (2000).
47. G. Larsen and E. Lotero, Amine dendrimers as templates for amorphous silicas, *J. Phys. Chem.* B **104,** 4840–4843 (2000).
48. M. C. Rogers, B. Adisa, and D. A. Bruce, Synthesis and characterization of dendrimer-templated mesoporous oxidation catalysts, *Catal. Lett.* **98,** 29–36 (2004).
49. G. Larsen, R. Spretz, and E. Lotero, Trapping dendrimers in inorganic matrices: DAB-Am-n/ Ainc arsenate composites, *Chem. Mater.* **13,** 4077–4082 (2001).
50. R. W. J. Scott, O. M. Wilson, and R. M. Crooks, Titania-supported Au and Pd composites synthesized from dendrimer-encapsulated metal nanoparticle precursors, *Chem. Mater.* **16,** 5682-5688 (2004).
51. L. Beakley, R. Cheng, S. Yost, and B. D. Chandler, Immobilization of dilute dendrimer encapsulated Pt nanoparticles in a sol-gel silica matrix, *Appl. Catal. A: Gen.* **292,** 124–129 (2005).
52. J. P. Carpenter, C. M. Lukehart, S. R. Stock, and J. E. Wittig, *Chem. Mater.* **7,** 201–205 (1995).
53. H. Lang, R. A. May, B. L. Iversen, and B. D. Chandler, Dendrimer encapsulated nanoparticle precursors to supported platinum catalysts, *J. Am. Chem. Soc.* **125,** 14832–14836 (2003).
54. D. X. Liu, J. X. Gao, C. J. Murphy, and C. T. Williams, In situ attenuated total reflection infrared spectroscopy of dendrimer-stabilized platinum nanoparticles adsorbed on alumina, *J. Phys. Chem.* B **108,** 12911–12916 (2004).
55. P. Forzatti and L. Lietti, Catalyst deactivation, *Catal. Today* **52,** 165–181 (1999).
56. C. H. Bartholomew, Mechanisms of catalyst deactivation, *Appl. Catal. A: Gen.* **212,** 17–60 (2001).
57. L. Sun and R. M. Crooks, Dendrimer-mediated immobilization of catalytic nanoparticles on flat, solid supports, *Langmuir* **18,** 8231–8236 (2002).
58. R. M. Lang, R. A. May, B. L. Iversen, and B. D. Chandler, In *Catalysis of Organic Reactions*, edited by J. Sowa (CRC Press, Boca Raton, FL, 2004) pp. 243–250.
59. S. D. Deutsch, *et al.*, Decomposition and activation of Pt-dendrimer nanocomposites on a silica support, *Catal. Lett.* **97,** 139–143 (2004).
60. G. Lafaye, C. T. Williams, and M. D. Amiridis, Synthesis and microscopic characterization of dendrimer-derived Ru/Al2O3 catalysts, *Catal. Lett.* **96,** 43–47 (2004).
61. A. Singh and B. D. Chandler, Mild thermolysis conditions for the activation of dendrimer encapsulated Pt nanoparticles, *Langmuir*, **21,** 10776–10782 (2005).

62. B. Auten, H. Lang, and B. D. Chandler, Support effects on dendrimer templated Pt–Au catalysts II: CO oxidation catalysis, manuscript in preparation (2004).
63. N. Hoover and B. D. Chandler, Dendrimer routes for the controlled preparation of Pt–Cu catalysts, manuscript in preparation (2005).
64. J. M. J. Fréchet, and D. A. Tomalia (eds.), *Dendrimers and other Dendritic Polymers* (John Wiley & Sons, West Sussex, UK, 2001).
65. W. I. Lee, Y. Bae, and A. J. Bard, Strong blue photoluminescence and ECL from OH-terminated PAMAM dendrimers in the absence of gold nanoparticles, *J. Am. Chem. Soc.* **126,** 8358–8359 (2004).
66. O. Ozturk, *et al.*, Thermal decomposition of generation-4 polyamidoamine dendrimer films: decomposition catalyzed by dendrimer-encapsulated Pt particles, *Langmuir* **21,** 3998–4006 (2005).
67. P. Hollins, The influence of surface defects on the infrared spectra of adsorbed species, *Surf. Sci. Rep.* **16,** 51 (1992).
68. A. Bourane, S. Derrouiche, and D. Bianchi, Impact of Pt dispersion on the elementary steps of CO oxidation by O2 over Pt/Al_2O_3 catalyts, *J. Catal.* **228,** 288–297 (2004).
69. C. Mihut, C. Descorme, D. Duprez, and M. D. Amiridis, Kinetic and spectroscopic characterization of cluster-derived supported Pt–Au catalysts, *J. Catal.* **212,** 125–135 (2003).
70. C. Mihut, B. D. Chandler, and M. D. Amiridis, Bimetallic Pt–Au cluster-derived catalysts for the selective catalytic reduction of NO by propylene, *Catal. Commun.* **3,** 91–97 (2002).
71. B. D. Chandler and L. H. Pignolet, DRIFTS studies of carbon monoxide coverage on highly dispersed bimetallic Pt–Cu and Pt–Au catalysts, *Catal. Today* **65,** 39–50 (2001).
72. G. A. Somorjai, K. S. Hwang, and J. S. Parker, Restructuring of hydrogenation metal catalysts under the influence of CO and H2, *Top. Catal.* **26,** 87–99 (2003).
73. G. C. Bond and D. T. Thompson, Catalysis by gold, *Catal. Rev. Sci. Eng.* **41,** 319–388 (1999).
74. M. S. Chen and D. W. Goodman, The structure of catalytically active gold on titania, *Science* **306,** 252–255 (2004).

8

Tungsten Oxide Nanorods: Synthesis, Characterization, and Application

Erik H. Williamson and Nan Yao

8.1. INTRODUCTION

In recent years, transition metal oxide structures have garnered considerable attention due to their unique properties. Among the numerous transition metal oxides, tungsten oxides have been of special interest because of their distinctive characteristics that have led to a number of applications and promise further developments. Such applications include gas and humidity sensors, optical devices, electrochromatic windows, catalysts, and many more.[1–6] These properties even include high temperature superconductivity—sodium-doped tungsten oxide is thought to be a high temperature superconductor with a $T_c \approx 90$ K.[7] Numerous forms of tungsten oxide have been synthesized, with the stoichiometric formulas for all of forms being WO_x, where $0 < x \leq 3$. Bulk tungsten oxides as well as tungsten oxide films are generally WO_3, with WO_2 forms also possible under some conditions. With the great interest in nanoscience and nanostructured materials over the past 15 years, researchers have developed nanostructured forms of tungsten oxide as well. These have ranged from WO_3 nanocrystals on the order of only a few nanometers to one-dimensional nanorods of nonstoichiometric composition ranging from $WO_{2.5}$ to $WO_{2.9}$ (referred to as nanowires, nanoneedles, or nanowhiskers by some researchers).

Princeton University, Princeton Institute for the Science and Technology of Materials, 70 Prospect Avenue, Princeton, NJ 08540

The nanorod form of tungsten oxide presents both exciting possibilities and some special challenges.[8,9] In particular, tungsten oxide nanorods can be used as a template for the synthesis of WS_2 nanotubes via direct reaction with H_2 and H_2S.[10] These nanotubes have important applications as solid lubricants and as tips for atomic force microscopy.[11] Besides use as a template, the unusual defect structure of $WO_{2.72}$ ($W_{18}O_{49}$) nanorods could be exploited for various applications such as gas sensing and catalysis.[12] Synthesis of these structures, however, has been challenging. Until recently, most methods have involved high temperature vapor or vapor–solid processes.[12,13] Using these processes, it was difficult to achieve a controlled, relatively monodisperse nanorod size. Over the past few years, a number of groups have developed innovative methods to overcome these limitations. Simultaneously, the body of literature on the applications of tungsten oxides has grown, allowing unique insights into the physical processes that govern these applications. This study will review some of these synthetic methods and discuss what these and other studies have elucidated about the structure and properties of tungsten oxide nanorods. The applications of such nanorods will then be addressed, again in light of the literature.

8.2. TUNGSTEN–OXYGEN CHEMISTRY

8.2.1. Oxidation and Reduction of Tungsten and Tungsten Oxides

The chemistry of tungsten and its oxides is well understood for a few compounds, but due to the richness and complexity of the tungsten–oxygen system, this knowledge is far from comprehensive. The complexity of the tungsten–oxygen system is shown in tree representation of the various classes of oxides in Fig. 8.1. In most of these oxides, tungsten is predominately in the W^{+6} oxidation state, with 6 oxygen atoms

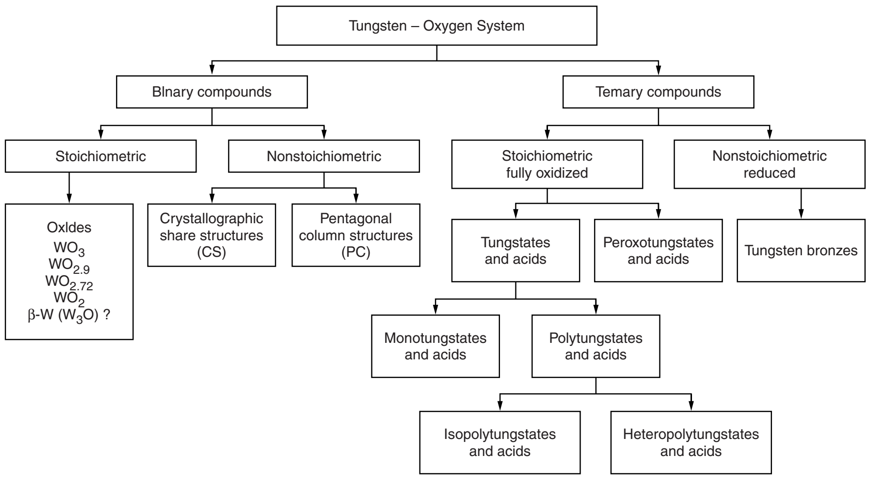

FIGURE 8.1. A summary of the tungsten–oxygen system. From Lassner and Schubert.

surrounding each tungsten atom in an octahedral configuration. In fully oxidized tungsten (WO_3), these octahedra are arranged in a corner-sharing configuration. In reduced oxides (WO_x, $2 < x < 3$), intricate combinations of corner-, edge-, and face-sharing arrangements WO_6 octahedra are frequently present. Further complicating the crystallographic structure of these compounds are the WO_4 tetrahedra and WO_7 pentagonal bipyramids that are frequently found in fully oxidized and partially reduced oxides respectively. With such a vast array of configurations, it is no wonder that several hundreds or thousands of tungsten oxides have been discovered.[14]

Tungsten metal can be easily oxidized in air or oxygen to form oxides. When occurring at temperature up to 327°C, this reaction forms WO_3, with the thickness of the oxide layer dependent on both temperature and humidity. From 327°C to 400°C, a protective oxide layer of oxide is formed, though there is currently some question as to its composition (it has been reported as $WO_{2.75}$, but this figure has been disputed). Above 600°C, a WO_3 layer is produced as the initial protective oxide becomes fully oxidized. WO_3 is quite permeable to oxygen, so the $WO_{2.75}$ layer continues to be oxidized to the trioxide form, with the rate being governed by the diffusion of tungsten ions to the $WO_{2.75}$–WO_3 boundary. Sublimation of WO_3 begins at 750°C, becomes substantial at 900°C, and reaches the rate of oxidation above 1300°C, thus leaving the tungsten surface bare of oxide above this temperature. The log of the rate of oxidation from 700 to 1300°C has been shown to be proportional to $P_{O_2}^{1/2}/T$, where P_{0_2} is the partial pressure of oxygen and T is the absolute temperature.[15]

Oxidation of tungsten with water and reduction of tungsten oxides with hydrogen are quite similar, with the high partial pressure of water or hydrogen driving the reaction in a particular direction. The oxidation reaction has been found to follow this sequence of reactions:

$$W + 2H_2O \rightarrow WO_2 + 2H_2$$
$$W + 3H_2O \rightarrow WO_3 + 3H_2$$
$$WO_3 + xH_2O \rightarrow WO_3 \cdot xH_2O$$

This reaction with water at 38°C is very slow and increases with increasing temperatures and pressures. Reaction with water vapor between 20 and 500°C leads strictly to the formation of WO_3—no other oxides are formed. The rate of this reaction has been found to be dependent on temperature and the ratio of the partial pressure of water to that of hydrogen. However, by adjusting these partial pressures properly, all known oxides can be formed. When both are low, WO_2 is formed. As these pressures increase, the more oxidized forms are produced ($WO_{2.72}$, $WO_{2.9}$, and finally WO_3). Additionally, higher temperatures favor the more oxidized forms. It also must be noted that hydrated oxides can be easily volatilized above about 900°C, with most volatile form being $WO_2(OH)_2$.[15] Such volatile compounds may play a crucial role in the formation of tungsten oxide nanorods.[10,16]

By adding hydrogen to the system, the back reactions are made favorable and tungsten oxide will be reduced rather than oxidized. Because of the volatility described above, the reaction conditions can greatly change the morphology of the final product. For example, when reducing WO_3 to W, changes in the reaction conditions can adjust

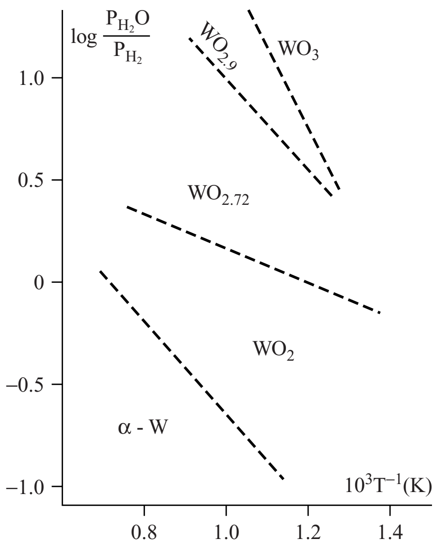

FIGURE 8.2. The stability of various tungsten oxides with respect to the ratio of the partial pressures of H_2O and H_2 and inverse temperature. Increasing this ratio and inverse temperature favor more oxidation.

the average grain size, the grain size distribution, grain shape, agglomeration, and more. With such versatility, it is no wonder this volatility of $WO_2(OH)_2$ is being harnessed to create one-dimensional morphologies. Nonetheless, much of the chemistry of tungsten oxide reduction is still described empirically today.[15] Some quantitative properties of this process will be presented in this chapter to the extent that they are known.

8.2.2. Thermodynamic and Kinetic Properties of WO_x Reactions

Based on the standard Gibbs free energy of the various oxides, three triple points can be calculated: $WO_{2.72}$, $WO_{2.9}$, WO_2 at about 600°C, $WO_{2.9}$, WO_3, WO_2 at about 270°C, and WO_2, $WO_{2.72}$, W at 1480°C. Using this data, a phase diagram can be constructed. The stability of the various oxides is shown in Fig. 8.2 with respect to the partial pressures of H_2O and H_2, and temperature. Because all of these compositions are equilibrium compositions, any of them can be produced simply by annealing W or WO_3 at the given partial pressure ratio and temperature.

As previously mentioned, the hydrated species $WO_2(OH)_2$ is the primary volatile species in the tungsten–oxygen–hydrogen system. This species can be formed from most forms of tungsten and its oxides. For example:

$$WO_3(s) + H_2O(g) \leftrightarrows WO_2(OH)_2(g)$$
$$\frac{1}{2}W_{20}O_{58}(s) + 11H_2O(g) \leftrightarrows 10\,WO_2(OH)_2(g) + H_2(g)$$
$$W_{18}O_{49}(s) + 23H_2O(g) \leftrightarrows 18\,WO_2(OH)_2(g) + 5H_2O(g)$$
$$WO_2(s) + 2H_2O(g) \leftrightarrows WO_2(OH)_2(g) + H_2(g)$$
$$W(s) + 4H_2O(g) \leftrightarrows WO_2(OH)_2(g) + 3H_2(g)$$

It is clear from these expressions that the partial pressure of water vapor should play a central role in determining the partial pressure of the volatile hydrate in the system, and indeed this is found to be the case. The partial pressure can be calculated from thermodynamic data and compared to that of other tungsten oxide species. Such calculations confirm that $WO_2(OH)_2$ is by far the most volatile tungsten-containing species in the tungsten–oxygen–hydrogen system. This volatility leads to chemical vapor transport of tungsten, which in turn can lead to the coarsening of grains in a powder or, under the proper conditions, the formation of nanorods.[15]

The final aspect of tungsten oxide reduction chemistry that needs to be considered is the kinetics of the reactions. Under most circumstances, the reduction of tungsten oxides is a transport limited process limited by the rate of transport of the water vapor product out of the material. Under such conditions, no "shortcuts" in the reduction path may be taken, with the WO_3 oxide being reduced according to the following path:

$$WO_3 \rightarrow WO_{2.9} \rightarrow WO_{2.72} \rightarrow WO_2 \rightarrow W$$

At high temperatures, these reactions occur discreetly, where one step essentially goes to completion before the next starts. This is not the case, however, below 750°C, where there can be overlap of reactions. Due to wide fluctuations in oxygen concentration throughout the reacting sample at these temperatures, some steps can be circumvented in oxygen-deficient regions. These two situations, high temperature and low temperature reduction, are compared in Fig. 8.3 and Fig. 8.4. These oxidation and reduction reactions, as well as their associated processes such as volatization, will play a key role in the discussion of the synthetic routes to $WO_{2.72}$ nanorods.

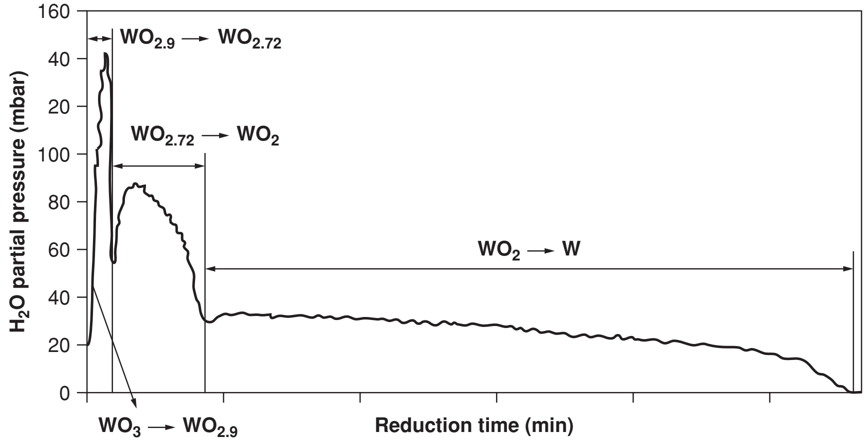

FIGURE 8.3. High temperature reduction of tungsten oxide. H_2O partial pressure is indicative of the rate of reduction. The four reduction steps are distinctly separated, indicating that the material passes through each equilibrium composition as it is reduced. From Lessner and Schubert.

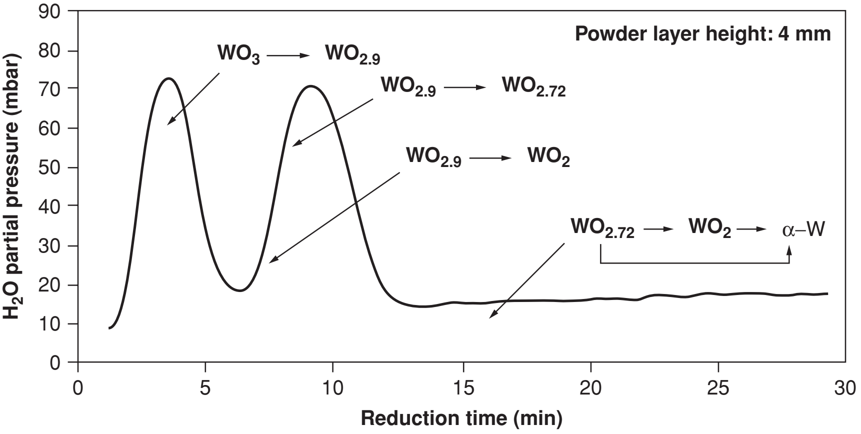

FIGURE 8.4. Low temperature reduction of tungsten oxide. Note that there are only two peaks, indicating that there must be some steps skipped in the $WO_3 \rightarrow W$ reduction. These skipped steps occur because of local variations in oxygen concentration. From Lessner and Schubert.

8.3. SYNTHETIC METHODS TO $WO_{2.72}$ NANORODS

Researchers have employed several strategies to achieve the one-dimensional growth that is necessary to create a nanorod. These strategies fall into several general areas. The simplest of these is relying on an anisotropic crystallographic structure of the desired solid to lead to anisotropic growth. Another route employed involves creating a liquid–solid interface on one face of the growing seed crystal. By reducing the symmetry of the seed so that reaction only takes place on that one face, this interface leads to one-dimensional growth, typically in a direction orthogonal to the interface. A wide variety of templates have also been employed to create one-dimensional nanostructures. These methods have included using solid substrates decorated with grooves or steps to “catch” sputtered, electrochemically plated, or electrodeposited material. Likewise, porous polymer or alumina membranes have been employed as templates for nanorod synthesis of metals, semiconductors, ceramics, and organic polymers. Such a wide variety of products suggest that this may be the most versatile method with respect to nanorod composition. In methods somewhat related to these porous membrane methods, nanorods have been templated against self-assembled rod-shaped micelles of surfactants. Finally, existing nanorods and other one-dimensional nanostructures have also been used to template nanorods. Using this approach, however, frequently results in polycrystalline nanorods, which are generally less desirable than the single crystalline nanorods generally prepared by the other synthetic methods.[9]

Vapor deposition techniques have been extensively studied for the fabrication of metal and metal oxide structures. Indeed, the first reported tungsten oxide nanorods were essentially grown by this method.[17] This groundbreaking synthesis of $WO_{2.72}$ leaves room for improvement, however, as it requires a reaction temperature of 1600°C in an argon atmosphere. Additionally, the researchers found the reaction product to be commingling $WO_{2.72}$ nanorods and WO_3 platelets rather than pure nanorods. Later,

other groups varied the reaction conditions, allowing tungsten oxide nanorods to be grown at lower temperatures (about 800°C).[10,18] Common among all three of these methods, as well as that developed by Liu *et al.*, is that tungsten is oxidized by an oxygen source such as SiO_2 or B_2O_3 that limits the availability of oxygen.[19] For example, the authors propose the following equations to describe the chemistry occurring in their experiments:

$$W + H_2O \rightarrow WO_x + H_2^{10}$$
$$W + SiO_2 \rightarrow WO_x + WSi^{17}$$
$$W + B_2O_3 \rightarrow WO_x + B_2O_2^{19}$$

In each case, an inert atmosphere is employed with the oxidizing agent being supplied in small concentrations. Presumably, the lack of available oxygen results in the substoichiomentric oxide. Indeed, Rothschild *et al.* noted that the aspect ratio of their nanorods declined as the vapor pressure of water in their reaction vessel increased.[20] Because the partial pressure of water directly affects the amount of oxidation, this may be an effect of further oxidation resulting in more isotropic crystal structures. Also, given the variety of oxidizing agents that have been used to produce tungsten oxide nanorods, it is likely that many other oxidizers could be employed as well, allowing the reaction conditions (and perhaps products) to be further optimized.

To allow a simpler, lower temperature route to tungsten oxide nanorods, some groups have turned to colloidal methods that have been used successfully to synthesize nanocrystalline metals and metal calcogenides.[21,22] These methods are generally considered to be cousins of vapor deposition and often called solution–liquid–solid methods.[9] Rather than using vaporized material as the source of tungsten for the oxide, these methods typically rely on dissolved organic tungstates such as $W(CO)_6$ or tungstic acid (H_2WO_4) as a tungsten source.[12,23,24] These methods afford lower reaction temperatures, which may allow better control over the nanorod product as well as lead to easier scale-up.[12,24]

In one such method, Park *et al.* mixed $W(CO)_6$, $Me_3NO{\cdot}2H_2O$, and oleylamine and allowed the slurry to react at about 270°C for about 24 h.[24] The solution eventually turned blue as tungsten oxide nanorods formed, which were precipitated out of the solution by adding ethanol. Unfortunately, the authors do not elaborate on this method and it is unclear what mechanism is at work here. The oleylamine added to the slurry acts as a surfactant, keeping the nanorods dispersed in suspension. While the relatively polar ethanol added to the relatively nonpolar solution presumably disrupts the interaction between the surfactant and the nanorods, allowing them to agglomerate and settle out.[25] No research, however, has investigated the role that the oleylamine surfactant plays in the formation of the nanorods in this particular reaction. It has been used as a surfactant for the size control of other nanoparticles however, suggesting that it is likely that oleylamine guides the formation of the nanorods in this case.[26]

It is worth reviewing how kinetic and thermodynamic factors generally affect the growth of nanostructures under the influence of surfactants. Though they used CdSe and PbS respectively to study the surfactant-assisted synthesis of nanorods, Peng *et al.* and Lee *et al.* have produced a pair of quite complimentary studies.[21,27] Peng *et al.* observed that kinetic control via monomer concentration was the principle factor in their growth

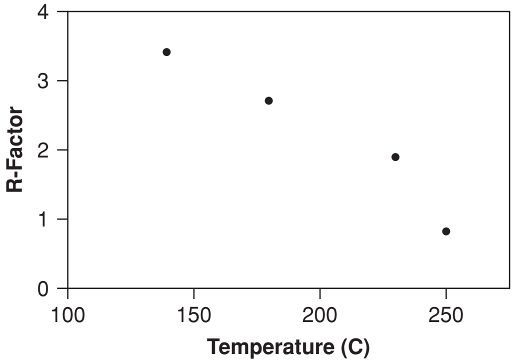

FIGURE 8.5. The effect of synthesis temperature on the anisotropy of PbS nanocrystals. Anisotropy is quantified by the R-factor (r_{100}/r_{111}, the ratio of the central distance of the $\{100\}$ faces to that of the $\{111\}$ faces). The decreasing trend is hypothesized to be due to the increased ability to overcome the activation energy necessary to grow the higher energy faces of the crystal at higher temperature. After Lee *et al.*

of CdSe nanorods. A high concentration of monomer, they found, drove the growth of the anisotropic c-axis at a much faster rate than the other axes (or possibly inhibited the growth of the a-and b-axes—they do not attempt to determine this), leading to high aspect ratio nanorods. Additionally, at high monomer concentrations, the smaller particles grew faster than the larger particles. Thus, by maintaining high monomer concentrations, Peng *et al.* were able to synthesize fairly *monodisperse*, high aspect ratio nanorods. It is clear that the surfactant is directing growth, but without better characterization of the surfactant's behavior in the system it cannot be determined whether rod-shaped surfactant micelles are formed or if the surfactant preferentially adsorbs to particular faces without first forming micelles.

Lee *et al.*[27] expand this research beyond the highly anisotropic crystals of CdSe to the more symmetric crystals of PbS. With such isotropic crystals, more tuning of the reaction conditions was necessary. First, they noted that higher aspect ratio materials result from lower reaction temperatures, as indicated in Fig. 8.5. As the reaction temperature is increased, they argue that the activation barrier to reaction on the less-favored faces is made negligible, and so the crystal grows isotropically. As even higher temperatures and longer reaction times are used, the reaction tends toward the thermodynamic equilibrium of isotropic crystals. Additionally, reducing the concentration of the surfactant led to decreased anisotropy, confirming that the surfactant does indeed block the growth of the crystal in two directions. Instead of the anisotropy of the unit cell contributing to anisotropy of adsorbed surfactant and hence growth, it is simply the difference in surface energy, in this case, between the $\{100\}$ (high energy) and $\{111\}$ (low energy) faces. Because of the complicated nature of these nanocrystals (not only rods but also star-like shapes), it is unlikely that growth is being guided by surfactant micelles.

Lou and Zeng spotted the work of Park *et al.* and sought to improve on it by developing an aqueous synthetic route.[12] In this method, water and sodium sulfate are added to freshly prepared tungstic acid and autoclaved at up to 200°C for up to 24 h (assuming saturated steam conditions, this corresponds to pressures of up to 15.5 bars).

By varying the amount of sodium sulfate and the reaction time, the size of these rods was controlled. Only centrifugation was necessary to collect the nanorods, indicating that rod–rod repulsion was minimal. Though the authors don't offer a detailed explanation for the mechanism of the reaction, they hypothesize that the sulfate ions may adsorb onto side surfaces or modify the ionic strength to allow the formation of nanorods. This will be discussed in the following section.

However, neither of these approaches addresses the issue of making large quantities of tungsten oxide nanorods at high purity that would allow for an efficient and facile scale-up. Walton *et al.* at the University of Sussex sought to address this issue with a novel synthetic method that involves passing water vapor over monocrystalline tungsten powder at 800°C.[10] Though this method requires high temperatures, Walton argues its superiority due to the simple mechanism, high product quality, and absence of harsh chemicals. Perhaps Walton is correct to point this out, but he ignores the work of Lou and Zeng, whose process involves just three inorganic chemicals and temperatures no higher than 200°C.[12] Without further research by scientists more knowledgeable about the scale-up process, a clear "winner" can hardly be declared.

Walton does offer a detailed explanation of a proposed growth mechanism. According to past research, WO_3 powders can be reduced with H_2 to form $WO_{2.72}$ nanorods. If allowed to react further, these continue to reduce to WO_2 agglomerates, as expected based on the general tungsten–oxygen chemistry framework. The presence of water vapor was shown to be the controlling factor in the process.[28] Additionally, another group demonstrated that water vapor is essential for the synthesis of tungsten oxide nanorods via tungsten filament oxidation.[20] Thus, Walton proposes the following two mechanisms—one direct and one indirect:

A. $W + xH_2O \rightarrow WO_x + xH_2$
B. (i) $W + 3H_2O \rightarrow WO_3 + 3H_2$
(ii) $WO_3 + xH_2 \rightarrow WO_{3-x} + xH_2O$

Because Walton started with pure W and observed no WO_3 in the product, he concluded that his method likely follows the direct route. More likely, however, is a two-step oxidation–reduction process that generates volatile $WO_2(OH)_2$ as an intermediate, such as

(i) $W(s) + 2H_2O(g) \rightarrow WO_2(OH)_2(g) + H_2(g)$
(ii) $WO_2(OH)_2(g) + 0.28H_2(g) \rightarrow WO_{2.72}(s) + 1.28H_2O(g)$.

The reaction yielding $WO_2(OH)_2$ is necessary to provide a volatile species to form the nanorod morphology. Without it, mass transport would be exceedingly slow and the nanorod morphology impossible.

The colloidal synthetic routes, however, must follow a reaction path similar to B.(ii) because their reactant is not pure W but an oxidized form. Interestingly, however, neither Park nor Lou indicate that WO_3 is present in their product if produced under optimal conditions even though they note it as a major contaminant when some reaction conditions are used. While this might be expected based on the fact that they are reducing reactants such as WO_4^{2-}, where WO_3 could be an intermediate, it is possible that the reaction conditions do not permit the formation of that phase. This will be discussed further below.

8.4. CRYSTAL STRUCTURE AND GROWTH

Though the synthetic routes vary greatly among these three groups, they do all agree on the crystal structure and growth direction of the nanorods. All three identify their nanorods as $WO_{2.72}$, citing X-ray diffraction (XRD) data that confirms the crystals' monoclinic dimensions in agreement with the literature.[10,12,24] Furthermore, Park compares the intensities of the (010) and (014) peaks to bulk $WO_{2.72}$. Because the intensity of the peak resulting from (010) in the nanorods has increased by 2.25 times the (014) peak, he concludes that $\langle 010 \rangle$ must be the direction of growth. Walton's group cites similar data, while Zeng arrives at this conclusion citing the presence of two strong (0*k*0) rings in the electron diffraction pattern rather than X-ray diffraction data.

This growth direction, incidentally, corresponds to the close-packed plane of the monoclinic $WO_{2.72}$ crystal ($a = 1.828$ nm, $b = 0.3775$ nm, $c = 1.398$ nm, $\beta = 115.14°$).[10,14] Tenne at the Weizmann Institute of Science and his collaborators have published a detailed study of the structure of this material.[29] Tenne describes the crystal as a collection of WO_6 octahedra—the same basic units as WO_3. However, these octahedra form a network of pentagonal columns interspersed with hexagonal channels (see Fig. 8.6). This complicated structure, they report, is not only highly anisotropic but also mechanically strong. For bulk ceramics, the usual mode is crack propagation—an applied stress is concentrated at a crack tip, which propagates through the material (in ductile metals, stresses typically cause defect motion before crack propagation can occur). Nanorods, however, are likely akin to optical fibers in their failure mode—that is, because of their dimensions (and also their growth mechanism) cracks must be formed at the atomic level. Thus, the material must fail by the breaking of chemical bonds, initially unaided by cracks. The energy necessary to "snap" a nanorod—that is, to break it across a plane normal to the growth axis—is the sum of all the chemical

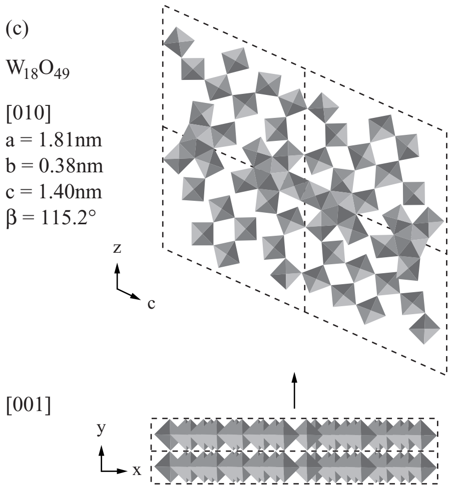

FIGURE 8.6. The crystal structure of $WO_{2.72}$ nanorods, showing the corner- and edge-sharing WO_6 octahedra that form pentagonal columns and hexagonal channels. From Frey *et al.*

bonds that cross that plane. Because of the complicated nature of the $WO_{2.72}$ crystal, many bonds must be broken to accomplish this and the stress in the crystal opposes crack propagation. The durable nature of these nanorods makes them especially suitable for applications such as scanning tunneling microscope (STM) tips and templates for nanotubes.[13]

Tenne is keen to note that the one-dimensional morphology is likely a *result* of the anisotropy of the $WO_{2.72}$ crystal, as has been shown for other materials.[9,29,30] This is ignored by the groups focusing on synthesis when they attempt to devise an explanation for their reactions. The morphology of the nanorods is dictated by the enhanced growth rate along the length of the nanorod. This enhanced growth rate, Tenne argues, is due to the differences in planar spacing of the crystal faces. Citing the Bravais–Friedel—Donnay–Harker (BFDH) law, he submits that the rate of growth should be inversely proportional to the planar spacing, which correctly predicts the morphology of the nanorods.[31] This is reasonable, as it will be energetically favorable to grow in the direction that causes the least increase in surface energy. Thus, the crystal will tend to grow faster in the direction of the shortest planar spacing because each additional plane causes a smaller increase in surface energy than adding a plane of larger spacing, making it more likely to occur. In $WO_{2.72}$, this ratio of planar spacings is about 5:1:1.3, which is in good agreement with the aspect ratio observed in the first reported tungsten oxide nanorods.[17]

Though Zeng recognized this growth direction, his explanation of the effect of the sulfate salt did not appear to be correct in light of the other synthetic methods.[12] He postulated that the salt might adsorb on the side surfaces of the growing nanorods, forcing them to grow into a rod-like morphology. It is more likely, however, that it is the crystal structure of the $WO_{2.72}$ nuclei that cause this morphology, as nanorods can be grown in situations without adsorbed molecules to confine growth (such as the vapor-phase growth described above). More likely is that the sulfate changes the ionic strength of the solution to a condition that favors the formation of the monoclinic $WO_{2.72}$ rather than WO_3 by lowering the activity of water. Figure 8.7 shows the effect of changing salt concentration on the formation of different phases. Because at high enough concentrations of sulfate WO_3 was totally absent in the product, it is probable that the sulfate moderates the rate of nucleation of the two species. By reducing the rate

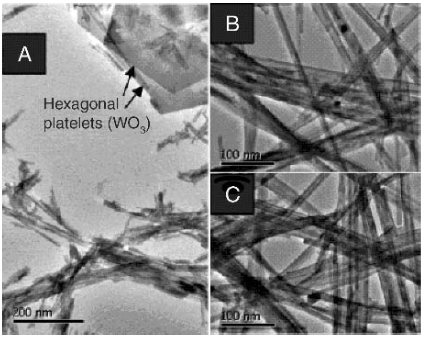

FIGURE 8.7. Effects of Na_2SO_4 content on $WO_{2.72}$ nanorod growth: (a) 2.5 g, (b) 5 g, (c) 10 g. WO_3 platelets contaminate a, but are absent in b and c. From Lou and Zeng.

of nucleation of WO_3 to zero, WO_3 crystals will not form. If sulfate instead controlled the rate of WO_3 growth, WO_3 would likely be present in the product but in the form of smaller crystals. Because this was not observed, sulfate is probably affecting the nucleation rate of WO_3. Perhaps an experiment could address this issue by using WO_3 seed crystals (if WO_3 appears in the product, sulfate controls nucleation) or examining the effects of reaction time on WO_3 formation at various sulfate concentrations (if WO_3 crystal size changes with sulfate concentration, sulfate affects WO_3 growth rate).

Similarly, Park was able to stimulate WO_3 platelet contamination by using elevated reaction temperatures. In this case, it seems clear that temperature is significantly increasing the activity of water, leading to more oxidation. The researchers also note that the temperature of the reaction can be used to control the length of the nanorods obtained, with higher temperatures resulting in longer nanorods with higher aspect ratios. This indicates that more is at work here than simply changing the activity of water. While this activity may control the phase that is formed, it probably doesn't control the aspect ratio. Instead, there must be some effect of temperature that makes the (010) face more reactive. Nonetheless, the resulting nanorods are a stable or metastable state, as longer reaction times do not lead to longer nanorods, indicating this effect is due to changing the thermodynamic equilibrium rather than enhancing the kinetics. This is a different behavior than Lee *et al.* observed when synthesizing the anisotropic PbS crystals described above.[27] In that study, which used surfactants to control the growth direction, they found that increasing temperature reduces the anisotropy. If nothing else, this seems to confirm that Park *et al.*'s $NaSO_4$ does not operate by the same mechanism as surfactants.

8.5. APPLICATIONS OF $WO_{2.72}$ AND OTHER TUNGSTEN OXIDES

8.5.1. Electro-Optical Properties and Quantum Confinement

A number of unique properties result from these characteristics. Some of the more exciting effects involve the nanorods' electrical and optical properties. Park's group noticed that little research had been done on the photoluminescence of nanostructured tungsten oxides.[24] They found that the strongest peaks occur at slightly different wavelengths for different nanorod lengths, with shorter nanorods emitting at shorter wavelengths. These photoluminescence spectra are shown in Fig. 8.8. The group concluded that this effect was the result of quantum confinement—that is, a band-to-band transition. Lou and Zeng also arrived at this same conclusion.[12] Essentially, this indicates that the dimensions of the material do not allow enough orbital–orbital interactions to form continuous valence and conduction bands. Hence, the electrons may only exist at discreet energy levels. The wavelength shift occurs as the electrons fall from the energy level that is the closest approximation to the bulk energy level normally excited by this wavelength.[32] Besides studying the physics of quantum confinement, this has important applications in the field of lasers and other electronics. Solid-state lasers are based on a 2-dimensional confinement (the electrons are free to move in 2 dimensions—a plane), which results in a highly functional but quite inefficient piece of equipment. By moving to lasers based on 1-dimensional confinement (allowing the electrons to move in only 1 dimension) made from, more efficient and powerful lasers may be possible.[32]

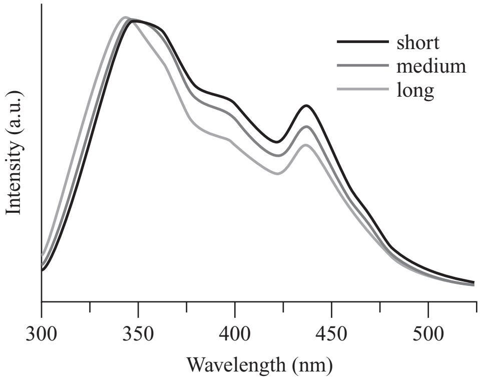

FIGURE 8.8. The photoluminescence spectra for short (25 nm), medium (75 nm), and long (130 nm) $WO_{2.72}$ nanorods. The main peaks are at ~345 nm and 437 nm. The 345 nm peak is likely a result of a band gap while the 437 nm peak is likely a result of oxygen defects. From Lee *et al.*

A higher energy peak was also investigated by Park's group. The wavelength of this peak, at 437 nm, was not dependent on the size of the nanorods used for the study, as shown in Fig. 8.8. Instead, the intensity of the peak was noticeably affected. Based on conclusions made by previous groups while studying the emission of WO_3 films, Park's groups suspects that this peak may originate from the presence of oxygen vacancies or defects.[3] Because longer nanorods were the result of faster growth (the reaction time for all nanorods was the same), it would be reasonable that these nanorods would have incorporated more defects, resulting in their higher intensity 437 nm peak. This justification would also explain why this peak is unaffected by nanorod dimension—presumably, this is because the band structures of the system are irrelevant to the emission.[24] Further study of this peak may lead to a method to analyze the quality of the nanorod crystal with respect to oxygen defects, which would be necessary to evaluate the appropriateness of different synthetic methods to applications such gas sensors, discussed below.

The oxygen defects that Park *et al.* use to explain the photoluminescent emission intensity at 437 nm also play a major role in the conductivity of tungsten oxides. Gillet *et al.* examined the electrical conductivity of annealed WO_3 films.[33] Though these films have a bulk stoichiometry different from $WO_{2.72}$ nanorods, as their surface stoichiometry changes they should fairly accurately model the electrical response of $WO_{2.72}$ nanorods. Indeed, depending on the processing conditions, the researchers found that surface oxygen vacancies could reach 50%, an oxygen concentration substantially less than that in $WO_{2.72}$. Gillet *et al.* found that the activation energy for surface conductivity in WO_3 films changed by a factor of more than two by changing the partial pressure of oxygen in the system from 0.2 mbar to 1 bar. This change in activation energy is manifested as a change in conductivity of about 3 orders of magnitude. The resistivity of these films is shown in Fig. 8.9 with respect to inverse temperature. The increase in oxygen vacancies lowers the activation energy of electrical conductivity—in this case, the ionization energy of the oxygen vacancies—because at higher concentrations the orbitals of the vacancies begin to overlap. This creates a "defect band," reducing the energy necessary to ionize these carriers. As the defect concentration increases, the band widens

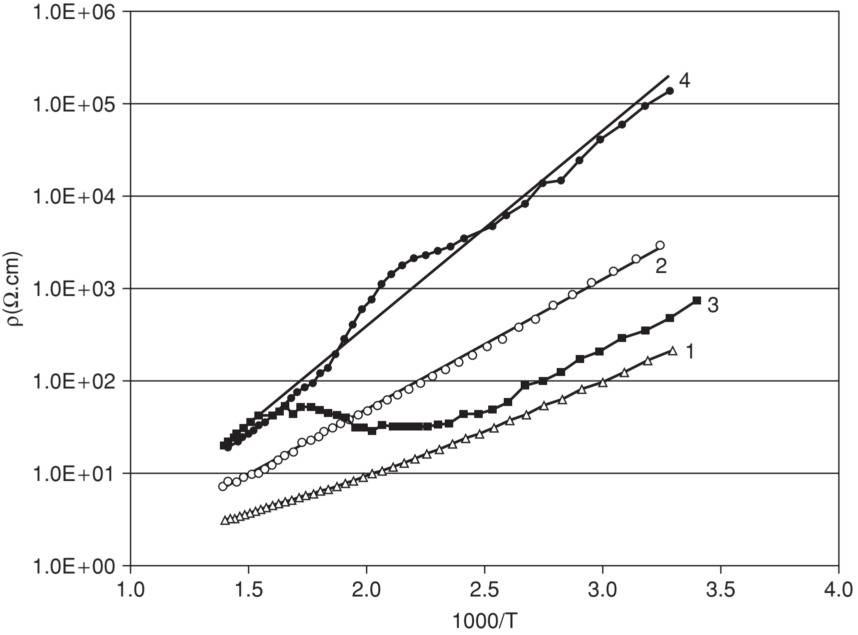

FIGURE 8.9. The resistivity of WO_3 films under various partial pressures of oxygen versus the inverse temperature. Curve 1 is in air, $P = 10$ mbar, curve 2 is in air, $P = 1$ bar, curves 3 and 4 are in oxygen, $P = 1$ bar. Curve 3 was recorded while increasing the temperature while curve 4 was recorded while decreasing the temperature. Note the strong dependence of resistivity on oxygen partial pressure. From Gillet *et al.*

to the point that it eliminates the band gap completely. $WO_{2.72}$ should lie somewhere in this defect range, and its electrical properties may be able to be probed further by testing WO_3 films (which are relatively easy to make) that have been processed so that their surface chemistry is identical to $WO_{2.72}$. Additionally, this study points out the importance of the environmental and processing conditions on tungsten oxides, and these cannot be ignored as studies are expanded to tungsten oxide nanorods.

The results of Gillet *et al.* and Park *et al.* suggest that some knowledge of the tungsten oxide band structure is necessary. Fortunately, in the course of their research on tungsten oxide–titanium oxide heterocatalysts, He *et al.* summarized the known electronic structure of WO_3.[4] The structure is represented graphically in Fig. 8.10, with the conduction-band-forming tungsten orbitals on the left side of the figure and the valence-band-forming oxygen orbitals on the right side. Because of the geometry of the WO_6 octahedra, the 5d orbital of the tungsten splits into a low energy t_{2g} level that points into empty space and a higher energy e_g level that points directly at the electronegative oxygen ion. Likewise, the 2p oxygen orbital splits into a high energy $2p_\pi$ that points into empty space and a lower energy $2p_\sigma$ orbital that points at the electropositive tungsten ion. The tungsten 5d and oxygen 2p orbitals are strongly hybridized. For perfect, defect-free WO_3, these energy levels result in a band gap of about 2.6 eV, but distortion of the crystal lattice by defects widens this gap.[34] However, by adding electrons to the structure, either by applying an electric field as in the case

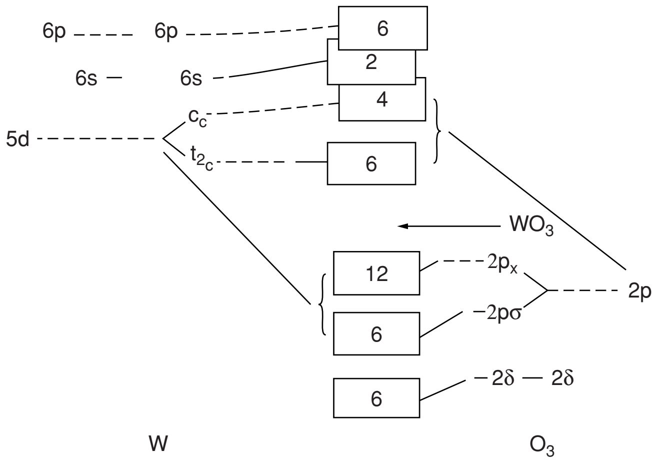

FIGURE 8.10. A representation of the band structure of WO_3. The W5d and O2p orbitals are strongly hybridized and correlated with each other, leading to the delocalization of the e_g and t_{2g} levels. From He *et al.*

with Gillet or by exposing the sample to sufficiently energetic photons, the valence and t_{2g} bands can be filled, resulting in W^{+5}.[4] The band gap of the W^{+5} state is smaller than that of WO_3. Thus, it may be the ease of creating these W^{+5} states that affects the band structure of $WO_{2.72}$ and causes it to appear blue. Because of the presence of W^{+5} in excited WO_3, WO_3 films can interact with visible light and also appear colored. Using this effect, tungsten oxides can be used as catalysts.

8.5.2. Use as Gas Sensors

Because the presence or absence of oxygen within the WO_x crystal lattice can have such a large effect on its conductivity, this material can have many uses as a sensor of oxygen-containing gases. It has even been shown to have the ability to sense H_2S, H_2, CS_2, and numerous hydrocarbons in addition to oxygen-containing compounds.[35] A good gas sensor has two main properties—its conductivity undergoes a large change in the presence of a particular gas due to high rates of adsorption, and the gas also desorbs quickly so that the sensor responds quickly to changing gas concentrations. Operating conditions play a large role in tuning the rates of adsorption and desorption. Sol–gel thin films offer a quick and easy method to make WO_3 thin films, and thus, gas sensors.[36] Galatsis *et al.* constructed WO_3 thin film sensors by this method and compared them to similar TiO_2 and MoO_3 sensors. Though they had inferior response to O_2, the WO_3 sensors excelled at detecting O_3, NO_2, and ethanol.[36] Choi *et al.* performed similar experiments, though they used hydrated tungsten oxide films.[37] They noted that their sensors could detect NO_2 concentrations at and below the environmental standard of 53 ppb.[38] This sensitivity, combined with the films' fast response time of about one minute suggests it as a very capable material for NO_2 sensing. By adjusting the calcination temperature and thus the pore sizes in the film, the group was able to optimize the film for high sensitivity (high calcination temperature) or fast response (low calcination

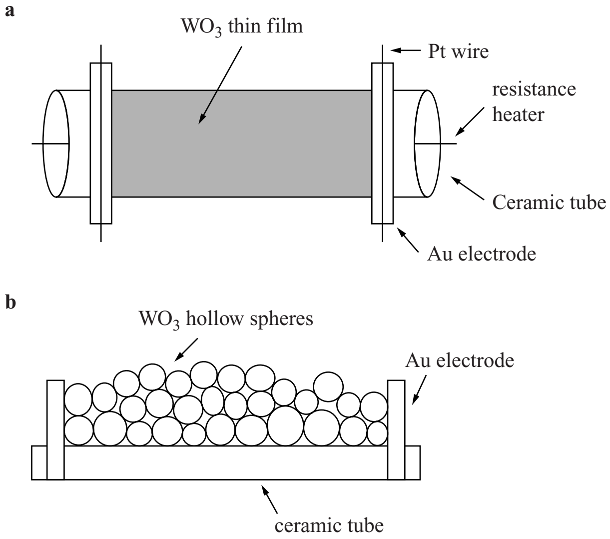

FIGURE 8.11. A schematic representation of the gas sensor designed by Li *et al.* An overview is given in a, while a cross-section is given in b. Tungsten oxide is coated onto an insulating ceramic cylinder and changes in conductivity of the coating are recorded. From Li *et al.*

temperature). A sensor that uses a series of various preparations of tungsten oxide films to quickly detect large concentrations of NO_2 and yet still be sensitive to trace amounts could be easily made.

Though they utilized a novel hollow-sphere form of WO_3 rather than $WO_{2.72}$ nanorods, the work of Li's group in researching tungsten oxide as gas sensors can be applied to the nanorod form.[35] Li's porous, hollow spheres were substituted for tungsten oxide polycrystalline films used in the previous studies by Galatsis *et al.* and Choi *et al.*[36,37] Thus, they overcome the sensitivity and selectivity problems caused by the surface structures and particle size of film approaches. As a result, only intermediate temperatures (~250°C) are required for operation. The spheres were dispersed in a solvent and subsequently applied to an insulating ceramic tube to form a film. Electrodes were connected to the film and a heater was added. A schematic is shown in Fig. 8.11. The sensors were found to be especially sensitive to hydrogen sulfide, ethanol, and acetone, with moderate sensitivity to other organics.

The sensing mechanism was related to changes in conductivity as molecules adsorbed onto the tungsten oxide. The sensitivity to adsorbed organics was hypothesized to be similar to that of the sensing properties of SnO_2 nanobelts. The cited study, by Yang *et al.* at Berkeley, provides good insight into this phenomenon.[39] Yang's tin oxide sensors rely on UV light to generate holes which cause the electron-trapping NO_2 to desorb, which increases the conductivity of the sensor. This prevents the sensor from becoming saturated with NO_2. Interestingly, Li's sensor uses elevated temperature rather than photogenerated holes to cause the adsorbed molecules to desorb. The effect is the same, but it would be interesting to confirm that the same effect can be obtained in tungsten oxide using photogenerated holes. Given that the band structure

can be "tuned" by changing the size of the nanorods and oxygen defects could change the sensitivity, this experimental device may lead to some interesting applications.[24] Additionally, the high aspect ratio of the nanorods affords a high surface to volume ratio, and the synthesis requires none of the complicated template synthesis necessary for Li's hollow spheres. The nanorods also offer an easily controllable platform for testing response to adsorbed molecules by testing the response of individual nanorods as opposed to polycrystalline films.

8.5.3. Tungsten Oxide Nanorods as Field Emitters

Field emitters lie at the heart of many familiar electronic devices. These include cathode ray tubes (such as those in televisions and computer monitors), X-ray generators, and microwave amplifiers.[40] These devices rely on the emission of electrons due to the presence of a large electric field. One-dimensional structures such as nanorods are ideal for such an application, as their "sharp" ends can generate very large electric fields that are difficult to attain in bulk materials, including fields upwards of 3 kV/μm.[41] As such, nanorods show promise for either high flux or low power applications. This potential was first recognized in carbon nanotubes, but investigations have since expanded to include zinc oxide, molybdenum oxide, and indium oxide materials. Armed with a technique to fabricate aligned arrays of $WO_{2.9}$ nanorods, Liu *et al.* sought to expand field emitter research to tungsten oxide materials as well (a method to produce aligned nanorods is essential so that the emitters are all aligned with respect to the applied electric field).[41] These researchers found that $WO_{2.9}$ nanorods had a remarkably low turn-on field (defined as the field necessary to obtain a current density of 10 μA/cm^2) of about 1.2 V/μm, which they report to be comparable to that of carbon nanotubes.

Li *et al.* performed similar experiments on quasialigned $WO_{2.72}$ nanorods, which also appear to be promising field emitters.[42] Using a similar experimental setup as Liu *et al.*, they found that the turn-on voltage was 2.6 V/μm, similar to that of $WO_{2.9}$. The group also investigated the threshold field—that is, the electric field necessary to generate a current density of 10 mA/cm^2. They report this value to be 6.2 V/μm, which is close to that of open-ended carbon nanotubes ($\sim$5 V/μm) and lower than that of SiC nanorods ($\sim$8.5 V/μm) and MoS_2 nanoflowers (7.6–8.6 V/μm). Thus, due to their low turn-on and threshold voltages, $WO_{2.72}$ nanorods appear to be excellent field emitters. However, while these two studies suggest that $WO_{2.9}$ nanorods are better field emitters than $WO_{2.72}$ nanorods because of their lower reported turn-on voltage, the data of Liu *et al.* and Li *et al.* should not be compared directly without some considerations. While this difference may be due to compositional differences, it may also be due to differences in nanorod alignment, measurement distance between the electrodes, and more.[41] Because neither group attempted to quantify these differences, comparisons between the two materials must be limited.

8.5.4. Tungsten Oxide as a Catalyst

Because of their electronic properties, particularly their visible-ultraviolet band gap, tungsten oxides have been the focus of a number of catalysis studies. Kohler and Gopel examined the electrocatalytic properties of $WO_{2.72}$ using spectroscopic surface

analytical techniques.[43] This method allowed them a detailed account of the chemical states present at the surface of $WO_{2.72}$ during aqueous reductions. They found that OH^- ions adsorb to the surface of the material and donate their electron to the surface cations. They observed this by using UPS to reveal that the surface tungsten ions were being reduced to a W5d1 electron state (the same state that was emphasized by Gillet *et al.* and Park *et al.*), which they argue is essential for the formation of adsorbed superoxide radicals.[24,33] Finally, their electromotive force experiments demonstrated that the activity of OH^- determines the activity of the adsorbed superoxide ions, where the tungsten surface acts to transfer an electron from the adsorbed OH^- to the adsorbing oxygen. It is the partially-reduced tungsten sites of the $WO_{2.72}$ electrode that facilitate these reactions.

Lindgren also investigated the electrocatalytic effects of tungsten oxide. In his work he used the more common WO_3 form to oxidize water, paying particular attention to the photoinduced nature of the process.[44] He found the material to be very promising, displaying such desirable characteristics as a low recombination rate of charge carriers and excellent kinetics. These properties resulted in good electron transfer over the WO_3 electrode and a quantum yield of nearly unity. Regardless, there are a number of difficulties that must be overcome. While thicker films tended to have better catalytic behavior, they were also more susceptible to cracking. Also, the band gap of defect-free WO_3 is about 2.6 eV, which is too large for the material to be efficient under solar radiation (silicon solar cells have a band gap of 1.1 eV, while only the largest band gap in a multi-band gap solar cell is 2.6 eV).[45]

Lindgren mentions that a possible solution to the problem of the large band gap is to construct a heterocatalyst of tungsten oxide and another metal oxide semiconductor. These sorts of heterocatalysts have been the focus of the studies of a number of groups. The catalyst is formed from tungsten oxide in conjunction with a common catalytic metal oxide such as those based on tin, zinc, or molybdenum. Of these three, tungsten oxide-zinc oxide catalysts seem to be the most studied, perhaps because of the higher melting point and lower cost of zinc.[46]

Because it also has a large band gap, combining zinc oxide with tungsten oxide will not solve the problem of solar powered oxidation. However, the large band gap does make for a large driving force for catalysis, allowing reactions with larger activation energies. In this case, Sakthivel *et al.* found that the photo-generated electrons created in the zinc oxide reduce sites in the tungsten oxide to a W^{+5} state.[47] This mechanism confirms that proposed by Kohler and Gopel, that reduced W^{+5} acts as the active catalytic site. As a result of this effect combined with enhanced charge carrier separation, Sakthivel *et al.* found that adding WO_3 to zinc oxide significantly enhanced its photocatalytic activity. Torres-Garcia *et al.* also investigated a WO_x–ZnO system for the purpose of oxidative desulfurization of oil refinery products.[48] They report that the stoichiometry of their tungsten oxide appears to be about WO_3 based on Raman spectroscopy. In comparative experiments to investigate the effect of tungsten concentration on the catalyst surface with catalyst activity, Torres-Garcia *et al.* found a direct relationship between high tungsten oxide concentrations and high catalytic activity. Equally important was their characterization of the surface structure and its effect on activity. They discovered that the highly faceted nature of many of the surfaces led to higher activity. This result suggests an important advantage of nanostructured materials over more conventional morphologies such as films: the surfaces

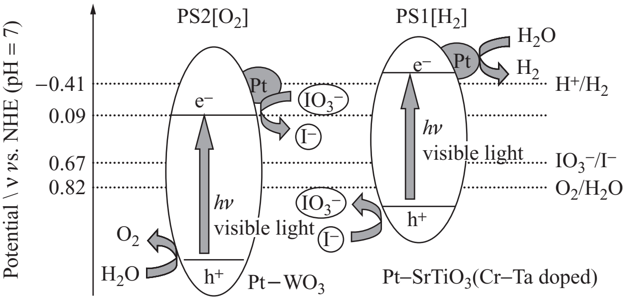

FIGURE 8.12. The speculated mechanism for the stoichiometric splitting of water with visible light using tungsten oxide and titanium oxide. Note the stair-step mechanism. From Sayama *et al.*

of these materials come to approximate these highly faceted surfaces. This effect can be demonstrated by drawing circles of various sizes on a display with discreet pixels. The stair-stepping effect in the display, analogous to faceting of materials, becomes more prevalent with respect to the image as the circle gets smaller. Use of nanorods as catalysts may allow the creation of highly reactive catalysts by taking advantage of this effect.

8.5.5. Tungsten Oxide and Titanium Oxide as a Heterocatalyst

Due to its near-ubiquity in fields ranging from catalysis to colloids to pigments, it is no surprise that titanium oxide has also been a frequent partner for tungsten oxides. In the realm of catalysis, as with pairing with zinc oxide, much of the interest in tungsten oxide–titanium oxide heterocatalysts is for photocatalytic applications. Sayama *et al.* used a system based on this pair of materials to stoichiometrically split water relying solely on visible light ($\lambda > 420$ nm) for the first time.[49] To accomplish this, they relied on the different potentials of the two materials' valence bands. Visible light excited electrons in the tungsten oxide materials. Using a IO_3^-/I^- redox mediator, this energy was shuttled to the titanium oxide material where light excited an electron to the conduction band, which in turn reduced H^+ to H_2. This stair-step mechanism is illustrated in Fig. 8.12. It is possible that the redox mediator could be eliminated if a suitable catalyst could be synthesized with the oxidation and reduction sites adjacent, resulting in a simplified energy diagram as shown in Fig. 8.13. Additionally, the highly active W^{+5} states of $WO_{2.72}$ could help increase the activity of this catalyst.

Lee *et al.* also investigated tungsten oxide–titanium oxide systems for catalysis, focusing on thin films.[50] The group found that this system improved on the photocatalytic properties of titanium oxide alone. The decomposition of methylene blue was used as a model reaction. Once again, the acidic surface of tungsten oxide is credited with the increase in reactivity. This confirms the previously mentioned finding that W^{+5} sites supply the bulk of the reactivity of tungsten oxide. Further evidence suggesting that it is the electronic structure of tungsten oxide that increases the reactivity of the system is the adsorption peak Lee *et al.* found at 410 nm. This peak corresponds well to the band gap of the tungsten oxide system and the effect of cutoff filters used in Sayama *et al.*'s work. Lee *et al.* also make note of the importance of charge carrier separation in the catalytic

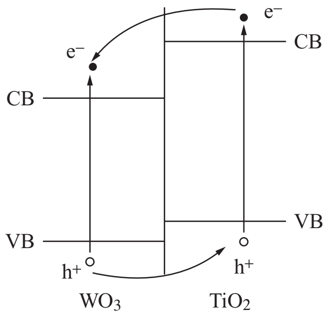

FIGURE 8.13. The energy diagram for the WO_3–TiO_2 system. Note how the energy difference between the lowest valence-band hole and highest conduction band electron is greater than the band gap of either material. From He *et al.*

process, discussing the effect of the traps for electrons and holes that the system generates and how these increase the efficiency of the reaction by preventing recombination.

8.5.6. *Tungsten Oxide and Titanium Oxide as Colloids*

Lee *et al.*'s study also investigates the hydrophilicity of the heterocatalyst. They mention that the highly acidic surface of the material is more hydrophobic than the pure titanium oxide surface. They theorize that this is because the acidic surface results in fewer adsorbed OH^- ions and thus a weaker interaction with water. As expected, this increased hydrophobicity leads to an increase in the stability of dispersions of nanoscale powders of this material.[51] Saltiel *et al.* showed that WO_3-coated titanium oxide powders were much more stable than their uncoated counterparts. Even after agglomeration, the agglomerates of the coated powders were more porous than those of pure titanium oxide (the coated powders had a fractal dimension of 1.55 while the pure titanium oxide powders had a fractal dimension of 1.60).

The effect of electron transfer between tungsten oxide and titanium oxide is also important in photochromatic applications. In an excellent study of aqueous sols, He *et al.* analyze the electronic structure of the tungsten oxide–titanium oxide system, finding that titanium oxide can catalyze the generation of W^{+5}.[4] This W^{+5} state is a colored state and can be generated from $WO_3 \cdot nH_2O$ by the following reactions:

$$WO_3{\cdot}nH_2O + h\nu \rightarrow WO_3{\cdot}(n - x/2)H_2O + xH^+ + xe^- + (x/4)O_2$$

$$WO_3{\cdot}(n - x/2)H_2O + x\,H^+ + xe^- + (x/4)O_2$$
$$\rightarrow W^{6+}{}_{(1-x)}W^{5+}{}_xO_{3-x/2}{\cdot}nH_2O + (x/4)O_2$$

In this case, titanium oxide is used both as a photocatalyst for the production of electrons and as a sink for holes, preventing recombination. This facilitates the reduction and thus the coloring of tungsten oxide. They also observe the effect of quantum confinement, resulting in band gaps in the sol that are greater than those normally observed in the bulk, as well as a blueshifted absorbance band, both results of the lack of orbital

overlap in the valence and conduction bands. These results have been confirmed by other studies.[34]

8.6. CONCLUSION

This chapter provides a detailed discussion on the synthesis, characterization, and applications of tungsten oxide nanorods. This sort of investigation of tungsten oxide, especially with a focus on the nanorod morphology, was previously unavailable. With this information collected, more informed decisions about the direction of tungsten oxide nanorod research can be made. In this course of reviewing the literature, it is clear that there is a relative dearth of characterization studies involving tungsten oxide nanorods (or, for that matter, and tungsten oxide other than WO_3). As a result, much of the discussions of tungsten oxide nanorods had to be inferred from WO_3 data. While this is certainly not ideal, it is immediately clear that WO_3 provides an excellent and well-understood basis for comparison. Thus, tungsten oxide nanorod researchers should be able to arrive at meaningful results and accurate interpretations of those results using the previously reported WO_3 experiments as a guide. The variety of synthetic pathways to tungsten oxide nanorods will hopefully open up synthesis to an equally wide variety of researchers. This will lead to more characterization studies and thus more application-based studies. As tungsten oxide nanorods show promise in a range of applications from gas sensing to catalysis, this will provide the science upon which those technologies can be developed.

REFERENCES

1. M. Stankova, X. Vilanova, E. Llobet, J. Calderer, C. Bittencourt, J. J. Pireaux, and X. Correig, Influence of the annealing and operating temperatures on the gas-sensing properties of rf sputtered WO_3 thin-film sensors, *Sensors Actuators* B **105**(2), 271–277 (2005).
2. S. Sekimoto, H. Nakagawa, S. Okazaki, K. Fukuda, S. Asakura, T Shigemori, and S. Takahashi, A fiber-optic evanescent-wave hydrogen gas sensor using palladium-supported tungsten oxide, *Sensors Actuators* B **66**(1–3), 142–145 (2000).
3. C. Paracchini and G. Schianchi, Luminescence of WO_3, *Physica Status Solidi A—Appl. Res.* **72**(2), K129–K132 (1982).
4. Y. He, Z. Wu, L. Fu, C. Li, Y. Miao, L. Cao, H. Fan, and B. Zou, Photochromism and size effect of WO_3 and WO_3-TiO_2 aqueous sol, *Chem. Mater.* **15,** 4039–4045 (2003).
5. M. A. Gondal, A. Hameed, and A. Suwaiyan, Photo-catalytic conversion of methane into methanol using visible laser, *Appl. Catal.* A **243**(1), 165–174 (2003).
6. C. Martín, G. Solana, V. Rives, G. Marcì, L. Palmisano, and A. Sclafani, Physico-chemical properties ofWO_3/TiO_2 systems employed for 4-nitrophenol photodegradation in aqueous medium, *Catal. Lett.* **49,** 235–243 (1997).
7. A. Shengelaya, S. Reich, Y. Tsabba, and K. A. Müller, Electron spin resonance and magnetic susceptibility suggest superconductivity in Na doped WO_3 samples, *Eur. Phys. J.* B **12**(1), 13–15 (1999).
8. L. Vayssieres, On the design of advanced metal oxide nanomaterials, *Int. J. Nanotechnol.* **1,** 1–41 (2004).
9. Y. Xia, P. Yang, Y. Sun, Y. Wu, B. Mayers, B. Gates, Y. Yin, F. Kim, and H. Yan, One dimensional nanostructures: Synthesis, characterization, and applications, *Adv. Mater.* **15**(5), 353–389 (2003).

10. Y. Z. Jin, Y. Q. Zhu, R. L. D. Whitby, N. Yao, R. Ma, P. C. P. Watts, H. W. Kroto, and D. R. M. Walton, Simple approaches to quality large-scale tungsten oxide nanoneedles, *J. Phys. Chem.* B **108**(40), 15572–15577 (2004).
11. I. Kaplan-Ashiri, S. R. Cohen, K. Gartsman, R. Rosentsveig, G. Seifert, and R. Tenne, Mechanical behavior of individual WS_2 nanotubes, *J. Mater. Res.* **19**(2), 454–459 (2003).
12. X. W. Lou and H. C. Zeng, An inorganic route for controlled synthesis of $W_{18}O_{49}$ nanorods and nanofibers in solution, *Inorganic Chem.* **42**(20), 6169–6171 (2003).
13. G. Gu, B. Zheng, W. Q. Han, S. Roth, and J. Liu, Tungsten oxide nanowires on tungsten substrates, *Nano Lett.* **2**(8), 849–851 (2002).
14. E. Lassner and W.-D. Schubert, *Tungsten - Properties, Chemistry, Technology of the Element, Alloys, and Chemical Compounds* (Kluwer Academic/Plenum Publishers, Norwich, NY, 2004) pp. 133–177.
15. E. Lassner and W.-D. Schubert, *Tungsten - Properties, Chemistry, Technology of the Element, Alloys, and Chemical Compounds* (Kluwer Academic/Plenum Publishers, Norwich, NY, 2004), pp. 85–109.
16. Y. Shingaya, T. Nakayama, and M. Aono, Epitaxial growth of WO_x nanorod array on W(001), *Sci. Technol. Adv. Mater.* **5**(4–5), 647–649 (2004).
17. Y. Q. Zhu, W. Hu, W. K. Hsu, M. Terrones, N. Grobert, J. P. Hare, H. W. Kroto, D. R. M. Walton, and H. Terrones, Tungsten oxide tree-like structures, *Chem. Phys. Lett.* **309**(5–6), 327 (1999).
18. D. Z. Guo, K. Yu-Zhang, A. Gloter, G. M. Zhang, and Z. Q. Xue, Synthesis and characterization of tungsten oxide nanorods, *J. Mater. Res.* **19**(12), 3665–3670 (2004).
19. Z. Liu, Y. Bando and C. Tang, Synthesis of tungsten oxide nanowires, *Chem. Phys. Lett.* **372**(1–2), 179 (2003).
20. A. Rothschild, J. Sloan, and R. Tenne, Growth of WS2 nanotubes phases, *J. Am. Chem. Soc.* **122**(21), 5169–5179 (2000).
21. X. Peng, L. Manna, W. Yang, J. Wickham, E. Scher, A. Kadavanich, and A. P. Alivisatos, Shape control of CdSe nanocrystals, *Nature* **404**(6773), 59–61 (2000).
22. N. R. Jana, L. Gearheart, and C. J. Murphy, Wet chemical synthesis of silver nanorods and nanowires of controllable aspect ratio, *Chem. Commun.* **7**, 617–618 (2001).
23. Y. Koltypin, S. I. Nikitenko, and A. Gedanken, The sonochemical preparation of tungsten oxide nanoparticles, *J. Mater. Chem.* **12,** 1107–1110 (2002).
24. K. Lee, W. S. Seo, and J. T. Park, Synthesis and optical properties of colloidal tungsten oxide nanorods, *J. Am. Chem. Soc.* **125,** 3408–3409 (2003).
25. T. S. Yoon, J. Oh, S. H. Park, V. Kim, B. G. Jung, S. H. Min, J. Park, T. Hyeon, and K. B. Kim, Single and multiple-step dip-coating of colloidal maghemite (g-Fe_2O_3) nanoparticles onto Si, Si_3N_4, and SiO_2 substrates, *Adv. Funct. Mater.* **14**(11), 1062–1068 (2004).
26. F. Dumestre, B. Chaudret, C. Amiens, M. Fromen, M. Casanove, P. Renaud, and P. Zurcher, Shape control of thermodynamically stable cobalt nanorods through organometallic chemistry, *Angew. Chem. Int. Ed.* **41**(22), 4286–4289 (2002).
27. S. M. Lee, Y. W. Jun, S. Cho, and J. Cheon, Single-crystalline star-shaped nanocrystals and their evolution: Programming the geometry of nano-building blocks, *J. Am. Chem. Soc.* **124**(38), 11244–11245 (2002).
28. V. K. Sarin, Morphological changes occurring during the reduction of WO_3, *J. Mater. Sci.* **10**(4), 593–598 (1975).
29. G. L. Frey, A. Rothschild, J. Sloan, R. Rosentsveig, R. Popovitz-Biro, and R. Tenne, Investigations of nonstoichiometric tungsten oxide nanoparticles, *J. Solid State Chem.* **162**(2), 300 (2001).
30. I. Kaplan-Ashiri, S. R. Cohen, K. Gartsman, R. Rosentsveig, G. Seifert, and R. Tenne, Mechanical behavior of individual WS_2 nanotubes, *J. Mater. Res.* **19**(2), 454–459 (2004).
31. J. Prywer, Correlation between growth of high-index faces, relative growth rates and crystallographic structure of crystal, *Eur. Phys. J.* B **25,** 61–68 (2002).
32. G. F. Strauss, *The Basics of Quantum Dots*. (2002) [Available from: http://www.chem.ucsb.edu/~strouse_group/learning.html.
33. M. Gillet, C. Lemire, E. Gillet and K. Aguir, The role of surface oxygen vacancies upon WO_3 conductivity, *Surf. Sci.* **532–535,** 519–525 (2003).

34. T. He, Y. Ma, Y. Cao, X. Hu, H. Liu, G. Zhang, W. Yang, and J. Yao, Photochromism of WO_3 colloids combined with TiO_2 nanoparticles, *J. Phys. Chem.* B **106,** 12670–12676 (2002).
35. X. L. Li, T. J. Lou, X. M. Sun, and Y. D. Li, Highly sensitive WO_3 hollow-sphere gas sensors, *Inorganic Chem.* **43,** 5442–5449 (2004).
36. K. Galatsis, Y. X. Li, W. Wlodarski, E. Comini, G. Sberveglieri, C. Cantalini, S. Santucci, and M. Passacantando, Comparison of single and binary oxide MoO_3, TiO_2 and WO_3 sol-gel gas sensors, *Sensors Actuators* B **83**(1–3), 276–280 (2002).
37. Y. G. Choi, G. Sakai, K. Shimanoe, Y. Teraoka, N. Miura, and N. Yamazoe, Preparation of size and habit-controlled nano crystallites of tungsten oxide, *Sensors Actuators* B **93**(1–3), 486–494 (2003).
38. U.S. Environmental Protection Agency, *National Ambient Air Quality Standards*. (2005).
39. M. Law, H. Kind, B. Messer, F. Kim, and P. Yang, Photochemical sensing of NO_2 with SnO_2 nanoribbon nanosensors at room temperature, *Angew. Chem. Int. Ed.* **41**(13), 2405–2408 (2002).
40. P. Gröning, P. Ruffieux, L. Schlapbach, and O. Gröning, Carbon nanotubes for cold electron sources, *Adv. Eng. Mater.* **5**(8), 541–550 (2003).
41. J. Liu, Z. Zhang, Y. Zhao, X. Su, S. Liu, and E. Wang, Tuning the field-emission properties of tungsten oxide nanorods, *Small* **1**(3), 310–313 (2005).
42. Y. Li, Y. Bando, and D. Golberg, Quasi-aligned single-crystalline $W_{18}O_{49}$ nanotubes and nanowires, *Adv. Mater.* **15**(15), 1294–1296 (2003).
43. H. Kohler and W. Gopel, Catalysis of the oxygen reduction on $W_{18}O_{49}$ electrodes by OH^- induced surface-states—A study based on XPS UPS and electromotive-force measurements, *J. Electrochem. Soc.* **139**(11), 3035–3042 (1992).
44. T. Lindgren, *Photo Induced Oxidation of Water at Thin Film Electrodes: A study of Tungsten Oxide, Hematite, Indium Nitride and Tin Nitride, in Department of Physical Chemistry*. 2001, Uppsala University. p. 80.
45. K. M. Yu, W. Walukiewicz, J. Wu, W. Shan, J. W. Beeman, M. A. Scarpulla, O. D. Dubon, and P. Becla, Diluted II-VI oxide semiconductors with multiple band gaps, *Phys. Rev. Lett.* **91**(24), Art. no. 246403 (2003).
46. United States Geological Survey, *Minerals Information: Commodity Statistics and Information* (2004) [Available from: http://minerals.usgs.gov/minerals/pubs/commodity/.
47. S. Sakthivel, S. U. Geissen, D. W. Bahnemann, V. Murugesan, and A. Vogelpohl, Enhancement of photocatalytic activity by semiconductor heterojunctions:a-Fe_2O_3, WO_3 and CdS deposited on ZnO, *J. Photochem. Photobiol.* A **148,** 283–293 (2002).
48. E. Torres-García, G. Canizal, S. Velumani, L. F. Ramírez-Verduzco, F. Murrieta-Guevara, J. A. Ascencio, and E. Torres-Garcia, Influence of surface phenomena in oxidative desulfurization with WO_x/ZrO_2 catalysts,
Appl. Phys. A—Mater. Sci. Process. **79**(8), 2037–2040 (2004)
49. K. Sayama, K. Mukasa, R. Abe, Y. Abe, and H. Arakawa, Stoichiometric water splitting into H_2 and O_2 using a mixture of two different photocatalysts and an IO_3^-/I^- shuttle redox mediator under visible light irradiation, *Chem. Commun.* **23,** 2416–2417 (2001).
50. Y. C. Lee, Y. P. Hong, H. Y. Lee, H. Kim, Y. J. Jung, K. H. Ko, H. S. Jung, and K. S. Hong, Photocatalysis and hydrophilicity of doped TiO_2 thin films, *J. Colloid Interface Sci.* **267,** 127–131 (2003).
51. C. Saltiel, Q. Chen, S. Manickavasagam, L. S. Schadler, R. W. Siegel, and M. P. Menguc, Identification of the dispersion behavior of surface treated nanoscale powders, *J. Nanopart. Res.* **6,** 35–46 (2004).

9

Catalysis by Metal and Oxide Nanoparticles, Single Metal Atoms and Di-Nuclear Oxo-Ions in Zeolites

Wolfgang M. H. Sachtler

9.1. INTRODUCTION

Nanoparticles of precious metals have been routinely used in heterogeneous catalysis for more than half a century. Zeolites with a well-defined regular network of nanopores and nanocages were introduced by the Mobil company in 1964[1] because their superior acidity enables them to better catalyze hydrocarbon conversions involving carbenium ion intermediates, such as isomerization, dehydrocyclyzation, and cracking. The high acidity of zeolites in their H-form is a consequence of their structure: As shown by van Santen *et al.*, the energy required to remove a proton from an OH-group is lower if flexibility of the lattice accommodates the charge of the resulting O^{-} ion.[2] Unusual stereoselectivity in alkylation of aromatic molecules has been achieved by Csicsery with acid zeolites, because these solids act as molecular sieves, favoring diffusion of small linear molecules over that of more bulky or branched isomers. In addition, the finite volume of nanocages in zeolites favors transition states which are compatible with the cage dimensions.[3] A well-known process exploiting this feature is the methanol-to-gasoline process which converts methanol to high octane gasoline over an acid zeolite

Department of Chemistry and Institute for Environmental Catalysis, Northwestern University, Evanston, IL; E.mail: wmhs@northwestern.edu

of MFI structure. While acid catalyzed polymerization and dehydro-condensation can produce unsaturated olefins or aromatic compounds of any size, the pores in the MFI framework limit this process to products of the size of tetra-methyl benzene.

The use of very small metal particles in supported catalysts is now common industrial practice. More recently, it has been found that catalytic oxidation of organic molecules is highly selective over catalysts that expose small oxo-ions of a transition metal rather than multiatomic oxide particles.[4] This chapter will focus on supported metal catalysts and zeolite-supported transition metal oxides. The fundamental principles which distinguish the catalytic propensities of these systems from those of their macroscopic counterparts will be sketched and illustrated by a few examples. The techniques used to prepare such catalysts and protect nano- and subnano particles against agglomeration will be described. Extreme examples of heterogeneous catalysts with nanoparticle sites are a Pt/mordenite catalyst exposing isolated Pt atoms and an Fe/MFI catalyst with oxo-ions as the sites catalyzing oxidation.

9.2. SUPPORTED METAL CLUSTERS

A crucial invention was made in 1947 by V. Haensel and his associates at Universal Oil Products. They developed a catalyst for the conversion of predominantly straight chain paraffinic hydrocarbons to high octane gasoline.[5] Their catalyst converted 90% of a low octane gasoline into a product with an octane rating above 80 and had an astonishingly long life. The support was alumina; presumably this was the first bifunctional catalyst, exposing both platinum atoms and acid sites. It was soon found that performance could be substantially improved by chemical treatments that produce even stronger acidic sites on the alumina.

Using a catalyst with an expensive metal for producing a cheap commodity challenged conventional economic wisdom. (The price of gasoline in the United States was roughly 8¢ per gallon at the time). It was demonstrated that long life and *in situ* regeneration of the catalyst justify a high initial price. To keep that price within acceptable limits, it was crucial to minimize the amount of platinum by maximizing its dispersion. The Pt content of the catalyst was 0.1%. Hydrogen adsorption indicated that 50% or more of the Pt atoms were surface atoms. The inventors coined the new word "platforming" for the new process. The term "nanoparticle" did not yet exist.

High metal dispersion results in exposure of metal sites of enhanced catalytic activity. I. Stranski *et al.* used the Gibbs–Wulff principle[6–8]

$$\Sigma(\sigma_{\mathrm{hkl}} A_{\mathrm{hkl}}) = \mathrm{Minimum} \qquad [\sigma = \text{specific surface energy; A = surface area}) \quad (1)$$

to estimate the equilibrium shape of metal crystals and showed not only, why polyhedra are formed with atomically close-packed crystal faces, but also that with metals the sharp edges and corners of perfect polyhedra will be blunted, so that segments of less stable crystal faces become exposed. Regions of "blunted" edges and corners expose coordinatively unsaturated metal atoms. Such crystallographical regions have a lower electronic work function than close-packed crystal faces; the first evident confirmation of Stranski's conclusions was provided by the invention of the field emission microscope. This instrument uses electron emission from the sharp tip of a needle-shaped emitter; the bright regions in the resulting image clearly show the presence of atomically

"open" faces. Moreover, electron microscopic images of such tips show their edge-less and corner-less shape in contrast to the polyhedra of macroscopic crystals.

The difference between the close-packed crystal faces, such as (110) in bcc or (111) in fcc crystals, and the "open" faces that prevail in the surface of nano particles, is of relevance to heterogeneous catalysis, because most adsorbates are more strongly bonded to the "coordinatively unsaturated" metal atoms in the "open" faces.

Sabatier and Balandin had predicted a relationship between catalytic activity and heat of adsorption. If a solid adsorbs the reactants only weakly, it will be a poor catalyst, but if it holds reactants, intermediates or products too strongly, it will again perform poorly. The ideal catalyst for a given reaction was predicted to be a compromise between too weak and too strong chemisorption. Balandin transformed this concept to a semiquantitative theory by predicting that a plot of the reaction rate of a catalytic reaction as a function of the heat of adsorption of the reactant should have a sharp maximum. He called these plots "*volcano-shaped curves*."[9] This prediction was confirmed by Fahrenfort *et al.*[10,11] An example of their "volcano-shaped curve" is reproduced in Fig. 9.1. They chose the catalytic decomposition of formic acid

$$HCOOH \Longrightarrow CO_2 + H_2 \tag{2}$$

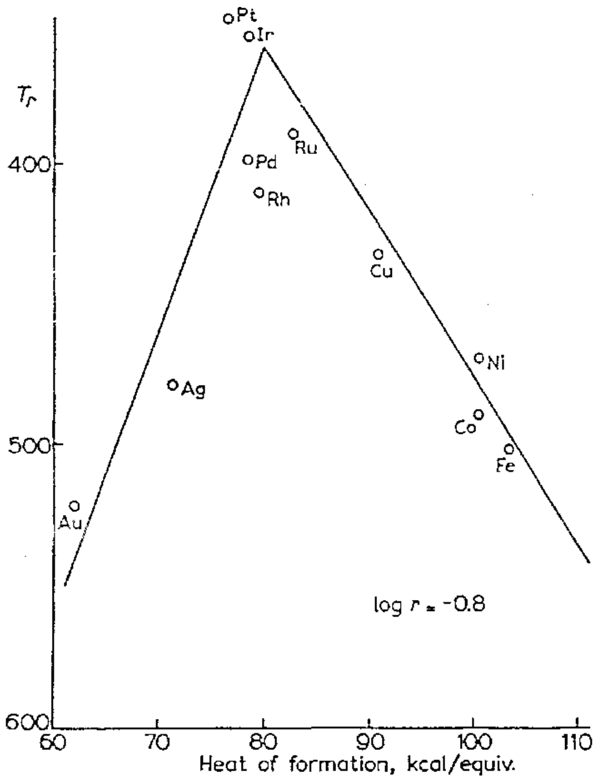

FIGURE 9.1. "Volcano Plot" of formic acid decomposition. Abscissa: Calculated Δ Hads of HCOOH; Ordinate: Temperature at which rate of HCOOH decomposition reaches the same value for all metals.

as the probe reaction, because it is catalyzed by a large number of metals, including gold and silver on the ascending branch of the volcano, while iron and tungsten with high heats of chemisorption are located on the descending branch of the plot. Although Fig. 9.1 has been reproduced in review papers and textbooks, a short explanation might be useful.

There were not many calorimetric data on the heat of adsorption available at the time of its first publication in 1959. However, the data that were available showed that enthalpies of chemisorption, ΔHads, tend to be proportional to the enthalpies of formation of the enthalpies of formation of the corresponding bulk compounds, ΔHform; moreover the heats of formation of oxides, nitrides, hydrides and formates are, in first approximation, proportional to each other. When only a relative ranking of metals is required as is the case with Balandin's theory, it is permitted to make use of these relationships where no direct calorimetric data are available. A second remark pertains to the measured catalytic activity. As the reaction rates differ by several orders of magnitude between the most active metals at the top of the volcano and the least active ones at the two feet, most authors who measure catalytic rates use equipment optimized for a certain range of reaction rates and adjust the temperature of the catalyst accordingly. In order to avoid risky extrapolations from the measured data, we decided not to plot the rate at a given temperature, but the temperature at which a given rate was attained. As the most active catalyst attains this prefixed rate at a lower temperature than a poor catalyst, the concept is best illustrated by using an inverted linear temperature scale at the ordinate axis of Fig. 9.1, so that the most active catalyst will appear at the top of the volcano.

Upon considering that heats of chemisorption will generally be higher on nanocrystals than on metals in their macroscopic form, this concept leads to two consequences:

(1) For the metals on the left leg of the volcano plot, an increase of the heat of adsorption will ensue enhanced catalytic activity. This consequence applies most obviously to gold which in its standard state is a poor catalyst because heats of adsorption of most molecules are very low on gold. Indeed, Haruta and other authors confirmed that gold becomes very active when present as nanoparticles.[12]

(2) For the metals on the right leg of the volcano plot, where heat of adsorption is high, the surface structure is no longer that of the stable polyhedron under vacuum as considered in the calculations by Stranski *et al.* In 1966 Holscher and Sachtler showed that strong chemisorption is *corrosive*, which means that surface atoms leave their original positions and arrange themselves with the adsorbed entities to a two-dimensional compound.[13] This phenomenon, later called *surface reconstruction*, has been confirmed for a large number of metal/adsorbate systems.

The heat of chemisorption is, of course, the energy difference between the chemical bonds formed and those broken. One of the strongest bonds to be broken in dissociative chemisorption on metals is the N–N bond of N_2. This chemisorption is known to be rate limiting in ammonia synthesis. Brill *et al.* reported in 1967 field emission results indicating that N_2 adsorption on Fe is strongest on the (111) face.[41] Their suspicion that this might be the initial step in ammonia synthesis over Fe catalysts

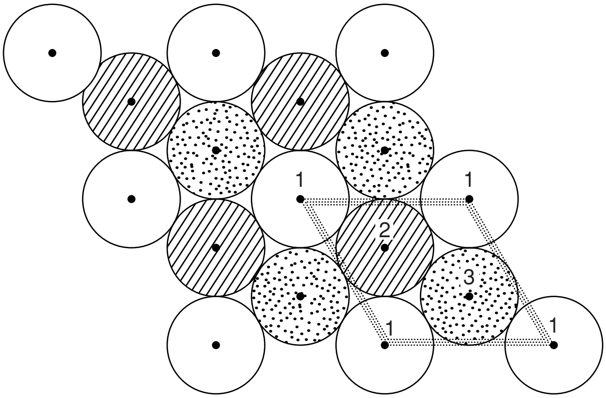

FIGURE 9.2. Surface topography of (111) face of bcc metal with probable sites for dissociative chemisorption of N_2 on bcc Fe.

was confirmed by H. Topsøe who showed that the measured synthesis activity correlates with the area of the (111) face.[14] Inspecting the microtopography of this crystal face reveals that the outermost Fe atoms are widely spaced creating hollow sites of 6 Fe atoms located in three parallel (111) planes, as illustrated in Fig. 9.2. It stands to reason that these are the sites where N_2 molecules are dissociatively chemisorbed. The ammonia synthesis is thus another example for a catalytic reaction depending on crystal faces with a very open structure. This illustrates the need for surface science to focus on nanoparticles, because the atomically close-packed faces that prevail on macroscopic metal crystals are of limited relevance to heterogeneous catalysis.

9.3. CHEMICAL ANCHORING AND DE-ANCHORING

For metal atoms the state of lowest Gibbs Free Energy is achieved when they are organized in a macroscopic polyhedron. High dispersion on a support requires strong chemical interaction between metal and support, conventionally called "*chemical anchoring*." The formation of solid particles either from the vapor or from an adsorbed precursor is dominated by two kinetic processes:

(1) Nucleation
(2) Growth

The interplay of these two basic rates determines the size of the resulting particles. For instance, the reason that snow flakes reach sizes of several cm at lower latitudes but arrive as extremely small crystals, called "diamond dust" in Antarctica, is that the nuclei that are formed in a cloud, will grow during their voyage to earth by adsorbing water molecules. Obviously, this growth will be more important in the moist atmosphere at low latitudes than in the extremely dry atmosphere above Antarctica. The same interplay of nucleation and growth determine the size of metal particles that are formed on a support by chemical reduction of adsorbed precursors, such as metal ions. Here

the rate of growth of the nuclei is determined by the transport of the precursor ions over the surface of the support. Fully ligated metal ions are usually quite mobile at moderate temperatures, but if ligands and surface hydroxyl groups are removed by thermal treatment, the oxide ions of the support surface will act as ligands to the adsorbed metal ions and slow down its movements. Needless to say, very small metal particles will be obtained if the rate of nucleation is large and the rate of growth is small.

As an aside, we should mention that the same principles apply to the formation of bimetallic clusters on a support. In the case of Pt–Re on Al_2O_3 it has been shown that hydroxylation of the surface favors the ability of Re ions to migrate toward the Pt nuclei and thus the formation of alloy particles, whereas fixing the Re ions onto a dehydroxylated alumina surface creates mainly separated Re particles. As catalytic activity and selectivity of the bimetallic particles differ vastly from those of a physical mixture of monometallic particles, the catalytic performance of the reduced catalyst depends significantly on the protocol used during its formation.[15–17] The bimetallic Pt–Re catalysts have been identified by comparison with preparations in which gaseous Re carbonyl was decomposed on conventionally prepared Pt/Al_2O_3 catalysts.[18]

Chemical anchoring of catalytically active metal clusters onto a support is of practical importance to stabilize catalysts against loss of activity by *Ostwald ripening*, i.e. metal agglomeration. Documented examples include Pt, Pd, or Rh supported on acidic oxides, in particular zeolites in their H-form.[19–22] Three types of anchors have been described in the literature: (a) Brønsted acid sites, (b) Lewis acid sites, (c) transition metal ions. The interaction of metal atoms with a strong Brønsted acid site leads to formation of proton–metal adducts that are of importance in bifunctional catalysts, such as Pt, Pd, or Rh supported on an acidic oxide, in particular a zeolite in its acidic form.[23–25] Recently, Zhang *et al.* have reported on hydrodechlorination of CCl_4 over Pt/Al_2O_3 catalysts.[22] Whereas Pt nanoparticles deactivate rapidly due to HCl poisoning, larger Pt particles are remarkably stable. Controlled agglomeration of primary nanoclusters to stable particles was achieved in an atmosphere of NH_4Cl. The mechanism of this controlled growth is ascribed to de-anchoring by Cl adsorption of the Pt clusters.

De-anchoring is understood as the action of an adsorbate that forms a chemical bond with a surface metal atom that is stronger than the bond which held this metal atom when anchored to its site. This phenomenon has been demonstrated with palladium atoms that were held onto the cage walls of a Y zeolite as palladium proton adducts. Once this system was exposed to carbon monoxide, Pd formed Pd–CO bonds that are much stronger than the original Pd–H bonds. As a result, the Pd–CO complex become mobile at low temperature and will oligomerize with other Pd–CO entities to Pd carbonyl clusters.[26] These are identified by their very characteristic IR spectrum with C–O vibrations giving much sharper IR bands than those usually observed with CO on Pd or other supported transition metals. Figure 9.3 shows an example.

The identification of these carbonyl clusters was achieved by comparison with the spectra of $Pd_{13}(CO)_n$ clusters that have been unambiguously characterized by XRD and other techniques. As the IR bands can be assigned to linear, bridging and triple-bridging CO it is assumed that the carbonyl cluster responsible for the spectrum in Fig. 9.3 has a core of 13 Pd atoms of icosahedral structure. Interestingly, these neutral complexes can only be observed in zeolite cages, where they are entrapped inside cages which prevent their agglomeration to larger clusters. Both the size of the cage and the width of the windows are essential for the (meta-) stability of these compounds. Spectra obtained

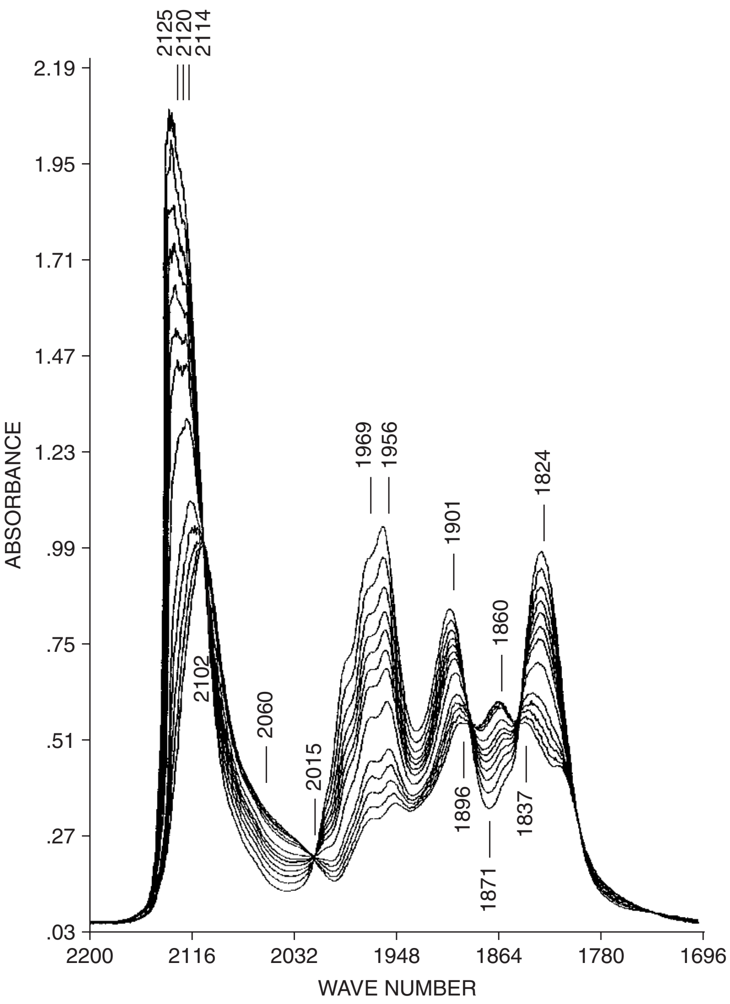

FIGURE 9.3. FTIR spectrum of Pd carbonyl cluster in zeolite cages.

after exposure to higher temperature, form larger Pd particles, positioned outside the zeolite cages and more reminiscent of the IR spectral normally obtained with CO on less well-defined Pd clusters.

9.4. MONOATOMIC PLATINUM IN ZEOLITES

The extreme case of an ultrananoparticle consists of one single atom. Such monoatomic Pt sites have been realized in Pt/H-zeolites that are prepared at low temperature. They are identified by their unique selectivity in catalyzing the H/D exchange between cyclopentane and D_2. Numerous data in the literature show that over conventional Pt

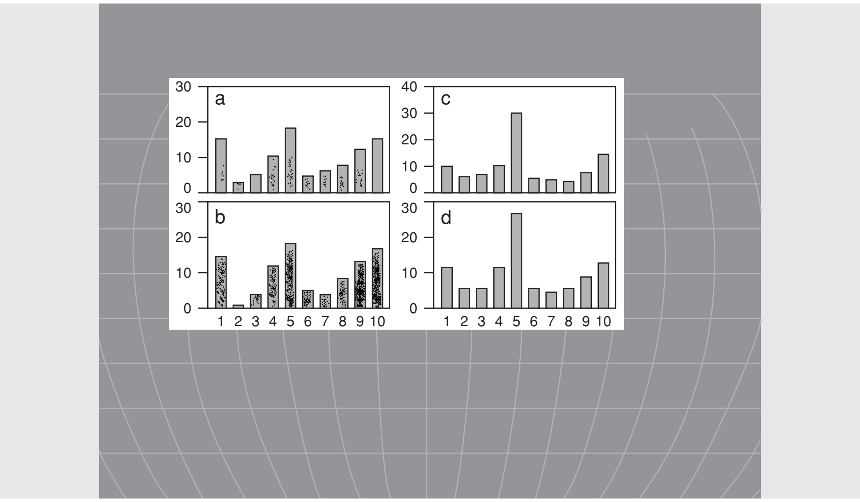

FIGURE 9.4. Distribution patterns of deuteron cyclopentanes Multiple exchange after H/D exchange over conventional Pt catalysts with Pt_n particles. Abscissa: Value of x in $C_5H_{(10-x)}D_x$ fraction; ordinate: rel. abundance.

catalysts, exposing multiatomic Pt_n sites, this reaction follows the "*multiple-exchange*" pathway, i.e. more than one H atom of cyclopentane is exchanged during a residence of the molecule on a Pt_n site. All five H atoms at the same side of the C_5 ring can be easily exchanged while the molecule is adsorbed. In the presence of an excess of D_2 this leads to the preferential formation of $C_5H_5D_5$.[27–29]

Some adsorbed molecules are able to "flip over"; they then exchange also the H atoms at the other side of the ring and leave the catalyst as C_5D_{10} molecules. A typical product pattern, as obtained with a conventional catalyst, is shown in Fig. 9.4. At low extent of exchange the pattern shows three predominant peaks, one at $C_5H_9D_1$, one at $C_5H_5D_5$, and one at C_5D_{10}. It is also known that multiple exchange of alkanes requires the ability of the molecule to form adsorption bonds through two vicinal C atoms, leading to H/D exchange of two H atoms positioned in $\alpha - \beta$ positions. That conclusion is based on the observation that the only alkane which shows negligible multiple exchange is neo-pentane, $(CH_3)_4C$, which contains 12 H atoms but no pair in $\alpha - \beta$ positions.

It is not exactly known how large a Pt_n ensemble must be which can catalyze the multiple H/D exchange with D_2 of alkanes such as cyclopentane, but it stands to reason that at least two adjacent Pt atoms are required (probably more). It follows that a catalyst which has its Pt atoms predominantly isolated from each other should NOT show this product pattern, but give a product distribution typical of *stepwise* exchange. Such a product should follow the binomial law; i.e. no predominant peak at $C_5H_5D_5$; the concentrations of the $C_5H_{10-x}D_x$ products at low exchange should show a monotonous decrease with x.

To test this hypothesis a Pt/mordenite catalyst was prepared from H-mordenite by exchanging a small amount of Pt and reducing at low temperature, so that Pt–H adducts could be formed and most Pt atoms were located in the *side pockets* of the

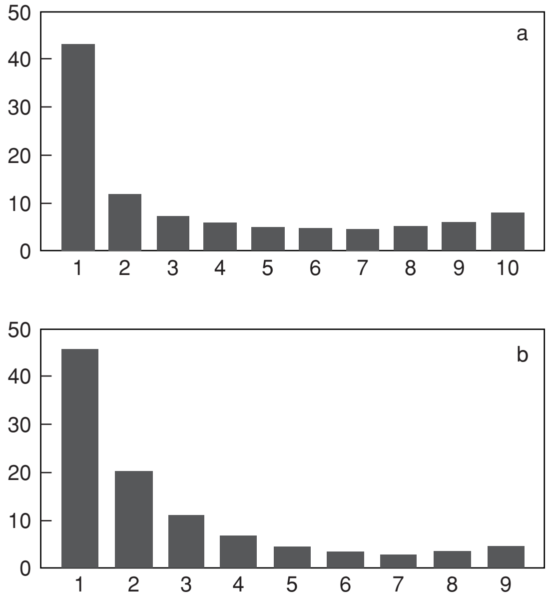

FIGURE 9.5. H/D stepwise exchange over Pt_1 in H-MOR. a. Cyclopentane b. Neopentane.

mordenite channels.[30] Exchange of cyclopentane with D_2 over this catalyst led to the product distribution shown in Fig. 9.5a.

Indeed, a monotonously decreasing abundance of exchanged molecules is found, peaks at $x = 5$ and $x = 10$ do not deviate from the pattern. For comparison the distribution of neo-pentane exchanged over the same catalyst is included in Fig. 9.5b. Both figures clearly show prevailing *stepwise* exchange. For neopentane this is typical because the molecule is lacking H pairs in $\alpha - \beta$ position; for *cyclo*-pentane this result clearly indicates Pt sites that are different from those in all conventional catalysts which have been used in the numerous published studies of this exchange. The results indicate that in the Pt/H-mordenite catalyst as prepared and probed here, isolated Pt atoms, present as $Pt–H^+$ adducts, are the prevailing sites.

9.5. TRANSITION METAL OXIDES AND OXO-IONS

Most industrially desirable oxidation processes target products of partial, not total oxidation. Well-investigated examples are the oxidation of propane or propene to acrolein, butane to maleic acid anhydride, benzene to phenol, or the ammoxidation of propene to acrylonitrile. The mechanism of many reactions of this type is adequately described in terms of the Mars and van Krevelen model[31]: A molecule is chemisorbed at the surface of the oxide and reacts with one or more oxygen ions, lowering the electrochemical oxidation state of the metal ions in the process. After desorption of the product, the oxide reacts with O_2, re-oxidizing the metal ions to their original oxidation state. The selectivity of the process is determined[33] by the relative chances of

a partially oxidized intermediate to either jump to the gas phase or react further with the oxide, finally leaving it as $CO_2 + H_2O$. Selectivity thus depends on the steepness of the curve relating the Gibbs Free Energy of removing oxygen from the solid to the extent of its reduction.[33] This gradient will depend on the size of the entity from which one or more oxygen atoms have to be removed. All other parameters being equal, this model leads us to expect that very small particles should be more selective oxidation catalysts than macroscopic oxides.

The selectivity for partial oxidation thus is basically controlled by the energy difference, for a given domain of the catalyst, to release either one oxygen atom rather than become deeply reduced. A small domain will release more easily one oxygen rather than a larger number, which would cause a very large change in oxidation number of the cations in the domain. Obviously, the domain size in small articles will be limited by the size of the oxide particle. The ability to release oxygen is not limited to neutral oxide particles, also oxo-ions such as RhO^+ or $[HO\text{-}Fe\text{-}O\text{-}Fe\text{-}OH]^{2+}$ can release part of their oxygen and thus act as active sites in catalytic oxidation. If linked to an appropriate support, their positive charge protects them against agglomeration.

An interesting variant of selective oxidation catalysis is the catalytic reduction of nitrogen oxides by ammonia or hydrocarbons. In this case the reducing molecule should specifically react with NO or NO_2, that are present in very low concentrations, rather than become oxidized to $CO_2 + H_2O$ by reacting with O_2 that is present in much higher concentration. The distinction between oxo-ions and oxide particle is most convenient if these entities are present on a zeolite support. Techniques have been developed to study the interconversion by IR spectroscopy:

(a) agglomeration to large oxide particles by chemically neutralizing oxo cations,
(b) redispersion of such oxide particles to oxo-ions by protons, e.g.

$$Fe_2O_3 + 2H^+ \rightarrow [HO\text{-}Fe\text{-}O\text{-}Fe\text{-}OH]^{2+} \quad (3)$$

and registering the resulting change in catalytic performance, using the reduction of NO_x with *iso*-butane as the test reaction.

Work with the objective of comparing oxo-ions with oxide particles in order to test the validity of this reasoning has been reported by Chen *et al.* who used a catalyst that initially contains Fe oxo-ions, $[HO\text{-}Fe\text{-}O\text{-}Fe\text{-}OH]^{2+}$. These sites were first converted to Fe_2O_3 particles by a simple chemical treatment. This was followed by another treatment, which redispersed these Fe_2O_3 particles back to oxo-ions.[34] The change in particle size was monitored by a spectroscopic method based on the observation that in zeolites metal ions and oxo-ions, that are attached to the wall of a cage, give rise to a typical IR band caused by the perturbation of the vibrations of the zeolite lattice.[35]

In these tests, the NO_x was present in very low concentration and O_2 in large excess. The "selectivity" is thus defined by the preference of the *iso*-C_4 for reducing the minority partner NO_x to N_2 rather than the majority partner O_2 to $CO_2 + H_2O$. In Fig. 9.6 the yield of N_2 by reducing NO_x with *iso*-butane while increasing the temperature is depicted for an Fe/MFI catalyst treated in this manner. The curve of the highest yield is the original Fe/MFI catalyst exposing a high concentration of $[HO\text{-}Fe\text{-}O\text{-}Fe\text{-}OH]^{2+}$ sites. The curve labeled Fe,Na/MFI shows the N_2 yield after treating this catalyst with NaOH to induce agglomeration. As a result, the maximum N_2 yield drops

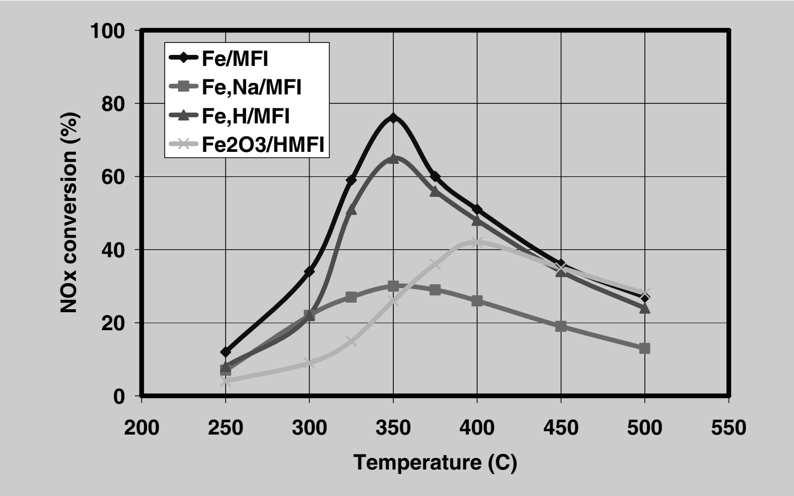

FIGURE 9.6. N_2 yield of NO_x reduction with *iso*-butane over Fe/MFI in the presence of excess O_2 Fe/MFI: as prepared with large concentration of {HO-Fe-O-Fe-OH} ions Fe, Na/MFI: same after NaOH treatment Fe, H/MFI: same after exchanging Na^+ against NH_4^+ and transforming NH_4^+ to H^+ Fe_2O_3/HMFI: catalyst prepared by incipient wetness impregnation of HMFI with Fe salt.

from 76% to 30%. The curve labeled Fe,H/MFI shows the N_2 yield after exchanging the Na^+ ions against NH_4^+ ions and calcining it to regenerate the H^+ sites. This treatment brings the N_2 yield to 65%, i.e. almost back to the value over the original catalyst. The same graph also shows the N_2 yield over another Fe/MFI catalyst with nearly the same Fe content that was prepared by impregnation and thus contained most of the iron as Fe_2O_3 particles. Over this catalyst the maximum yield is only 26%. These results clearly demonstrate superior performance of oxo-ions over Fe_2O_3 particles, though the size of the latter is still inside the nanoregime.

Another example of heterogeneous catalysis by oxo-ions is the one-step oxidation of benzene to phenol with nitrous oxide, N_2O. Fe/MFI catalysts have, again been found to be very active. This catalysis was discovered by Iwamoto[36] and has been extensively studied by the group of G. Panov in Novosibirsk.[37–38] Preparations of Fe/MFI which appear highly active for this reaction display poor activity for NO_x reduction and those which are optimum for that process, are poor for benzene oxidation. This shows that different sites are used. Work by Jia *et al.* revealed that the active sites for benzene oxidation appear to be Fe-oxo-ions containing only one Fe ion.[39] This does not necessarily mean that the sites are mononuclear. A recent work by Zhu *et al.* has rather suggested that the site consists of one Fe^{2+} and one Al^{3+} ion, the latter ion having left the zeolite framework.[40]

9.6. CONCLUSIONS

For metal catalysts used for hydrogenations and, in combination with acid functions, in hydrocarbon "reforming" reactions, the advantage of nano-size metal particles has been well known. More recently it has been demonstrated that metals on

the ascending branch of the “volcano shaped curves”, in particular gold, display high catalytic performance when present as nano-size particles on an appropriate support. With platinum it has been demonstrated that single atoms in zeolite cages are efficient sites displaying a catalytic activity that is distinctly different from that of multiatom particles exposing sites consisting of “ensembles.” For catalytic oxidations and reductions, recent work demonstrates the great advantages of fine-tuning the size of entities that consist of a small number of transition metal ions combined with oxide or hydroxide ions. Extremely high selectivity has been achieved with oxo-ions of Fe in the selective reduction of nitrogen oxides to N_2 and the one step oxidation of benzene to phenol.

REFERENCES

1. H. Heinemann, Development of industrial catalysis, Handbook of Catalysis, edited by B. G. Ertl, H. Knözinger, and J. Weitkamp (Verlag Chemie, Weinheim) 1997, vol. 1, p. 35.
2. S. R. Blaszlowski and R. A. van Santen, Quantum chemical studies of zeolite proton catalyzed reactions, *Top. Catal.* **4,** 145–156 (1997).
3. S. M. Csicsery, Shape selective catalysis in zeolites, *Zeolites* **4,** 202–213 (1984).
4. J. Jia, K. S. Pillai, and W. M. H. Sachtler, One-step oxidation of benzene to phenol with nitrous oxide over Fe/MFI catalysts, *J. Catal.* **221,** 119–126 (2004).
5. C. Remsberg and H. Higdon, Ideas for rent (UOP, Des Plaines, IL) (Publ) p. 259 (1994).
6. I. N. Stranski and R. Kaischew, Gleichgewichtsform und Wachstumsform der Kristalle, *Ann. Phys.* **21,** 330 (1935).
7. I. N. Stranski, Zur Berechnung der spezifischen Oberflächen-, Kanten-, und Eckenenergien an kleinen Kristallen, *Monatshefte Chem.* **69,** 234 (1936).
8. I. N. Stranski and R. Kaischew, Kristallwachstum und Kristallkeimbildung, *Phys. Z.eitschr.* **36.** 393 (1936).
9. A. A. Balandin, Structural and energy factors in the theory of catalyst selection, *Sci. Select. Catal.* (1968).
10. J. Fahrenfort, L. L. van Reijen, and W. M. H. Sachtler, The decomposition of HCOOH on metal catalysts, *The Mechanism of Heterogeneous. Catalysis* (Elsevier, Amsterdam) pp. 23–48 (1960).
11. W. M. H. Sachtler and J. F. Fahrenfort, Catalytic decomposition of HCOOH vapour on metals, Actes du 2ième Congrès Intern. de Catalyse 1960, (Editions Technip., Paris) pp. 831–863 (1961).
12. M. Haruta, Catalysis of gold nanoparticles deposited on metal oxides, *CatTech* **6,** 102 (2002).
13. A. A. Holscher and W. M. H. Sachtler, Chemisorption and surface corrosion in the tungsten + carbon monoxide system, as studied by field emission and field on microscopy, *Dis. Faraday Soc.* **41,** 29 (1966).
14. H. Topsøe, N. Topsøe, H. Bohlbro, and J. A. Dumesic, Supported iron catalysts: Particle size dependence of catalytic and chemisorptive properties, *Proc. 7th Int. Congress Catalysis*, edited by T. Seyama, K. Tanabe (Kondansha, Tokyo), p. 247 (1981).
15. S. M. Augustine and W. M. H. Sachtler, Catalytic probe for alloy formation in supported PtRe catalysts, *J. Catal.* **106,** 417–427 (1987).
16. S. M. Augustine and W. M. H. Sachtler, Variation of catalytic activity over PtRe/Al_2O_3, *J. Phys. Chem.* **91,** 5935–5956 (1987).
17. S. M. Augustine and W. M. H. Sachtler, On the mechanism for the platinum catalyzed reduction of rhenium in PtRe/γ-Al_2O_3, *J. Catal.* **116,** 184–194 (1989).
18. C. M. Tsang, S. M. Augustine, J. B. Butt, and W. M. H. Sachtler, Synthesis and characterization of bimetallic $PtRe_x$ clusters prepared by sublimation of $Re_2(CO)_{10}$ onto Pt/NaY, *Appl. Catal.* **46,** 45–56 (1989).
19. Y. Z. Zhang, T. T. Wong, and W. M. H. Sachtler, The effect of Ca^{2+} and Mg^{2+} ions on the formation of electron-deficient palladium-proton adducts in zeolite, *J. Catal.* **128,** 13–22 (1991).

20. X. L. Bai and W. M. H. Sachtler, Methylcyclopentane conversion catalysis by zeolite encaged palladium clusters and palladium-proton adducts, *J. Catal.* **129,** 121–129 (1991).
21. T. J. McCarthy, G.-D. Lei, and W. M. H. Sachtler, Methylcyclopentane conversion catalysis over zeolite Y encaged rhodium; a test for the metal-proton adduct model, *J. Catal.* **159,** 90–98 (1996).
22. Z. C. Zhang, J. Hare, and B. Beard, Basicity of nanosized noble metal clusters in catalysis, 13th Int. Congr. Catalysis, Paris Abstract, 2-017 (2004).
23. Y. Z. Zhang, T. T. Wong, and W. M. H. Sachtler, The effect of Ca^{2+} and Mg^{2+} ions on the formation of electron-deficient palladium-proton adducts in zeolite, *J. Catal.* **128,** 13–22 (1991).
24. X. L. Bai and W. M. H. Sachtler, Methylcyclopentane conversion catalysis by zeolite encaged palladium clusters and palladium-proton adducts, *J. Catal.* **129,** 121–129 (1991).
25. T. J. McCarthy, G.-D. Lei, and W. M. H. Sachtler, Methylcyclopentane conversion catalysis over zeolite Y encaged fhodium; a test for the metal-proton adduct model, *J. Catal.* **159,** 90–98 (1996).
26. W. M. H. Sachtler and Z. Zhang, Zeolite supported transition metal catalysts, *Adv. Catal.* **39,** 129–220 (1993).
27. F. C. Gault, J. J. Rooney, and C. Kemball, Catalytic exchange with deuterium of polymethylcyclopentanes on metal films: Evidence for π-bonded intermediates, *J. Catal.* **1,** 225 (1962).
28. C. Kemball, The catalytic exchange of hydrocarbons with deuterium, *Adv. Catal.* **11,** 233 (1970).
29. R. L. Burwell, Jr., Use of deuterium on the study of heterogeneous catalysis, *Catal. Rev.* **7,** 25 (1972).
30. G.-D. Lei and W. M. H. Sachtler, H/D exchange of cyclopentane on Pt/mordenites: Probing for monoatomic Pt sites, *J. Catal.* **140,** 601–611 (1993).
31. P. Mars and D. W. van Krevelen, Oxidations carried out by means of vanadium oxide catalysts, *Chem. Eng. Sci. (Special Suppl.)* **3,** 41 (1954).
32. H.-Y. Chen, X. Wang, and W. M. H. Sachtler, Reduction of NO_x over zeolite MFI supported iron catalysts: Nature of active sites, *Phys. Chem., Chem. Phys.* **2,** 3083–3090 (2000).
33. W. M. H. Sachtler, G. J. H. Dorgelo, J. Fahrenfort, and R. J. H. Voorhoeve, Correlations between catalytic and thermodynamic parameters of transition metal oxides, *Proceedings 4th Int. Congress Catalysis,* Moscow, 1968 (Akad. Kiado, Budapest) vol 1971, pp. 454–465.
34. H.-Y. Chen, X. Wang, W. and W. M. H. Sachtler, Reduction of NO_x over zeolite MFI supported iron catalysts: nature of active sites, *Phys. Chem., Chem. Phys.* **2,** 3083–3090 (2000).
35. J. Sárkány and W. M. H. Sachtler, Redox chemistry of Cu/Na-ZSM-5; detection of cuprous ions by FTIR, *Zeolites* **14,** 7 (1994).
36. M. Iwamoto, K. Matsukami, and S. Kagawa, Catalytic oxidation by oxide radical ions. 1. One-step hydroxylation of benzene to phenol over group 5 or 6 oxides supported on silica gel, *J. Phys. Chem.* **87,** 903 (1983).
37. G. I. Panov, A. S. Kharitonov, and V. I. Sobolev, Oxidative hydroxylation using dinitrogen monoxide: a possible route for organic synthesis over zeolites, *Appl. Catal.* A **98,** 1 (1992).
38. G. I. Panov, A. K. Uriarte, M. A. Rodkin, and V. I. Sobolev, Generation of active oxygen species on solid surfaces. Opportunity for novel oxidation technologies over zeolites, *Catal. Today* **41,** 365 (1998).
39. J. Jia, K. S. Pillai, and W. M. H. Sachtler, One-step oxidation of benzene to phenol with nitrous oxide over Fe/MFI catalysts, *J. Catal.* **221,** 119–126 (2004).
40. Q. Zhu, R. M. van Teeffelen, R. A van Santen, and E. J. M. Hensen, Effect of high-temperature treatment on Fe/ZSM-5 prepared by chemical vapor deposition of $FeCl_3$: II. Nitrous oxide decomposition, selective oxidation of benzene to phenol, selective reduction of nitrous oxide by *iso*-butane, *J. Catal.* **221,** 575–583 (2004)
41. R. Brill, E.-L. Richter, and E. Ruch, Adsorption of nitrogen on iron, *Angew. Chem. Int. Ed.* **6,** 882–883 (1967).

10

A Dual Catalytic Role of Co Nanoparticles in Bulk Synthesis of Si-Based Nanowires

Ting Guo

10.1. BACKGROUND

10.1.1. Overview

Nanotechnology has been employed in catalysis for many years. For example, Sinfelt *et al.* have carefully developed and analyzed composite nanoparticles employed in petroleum refining.[1−3] Goodman *et al.* have examined the roles of nanoparticles in catalysis under well-controlled environment.[4] Gates and others have employed molecular nanoparticles in catalysis.[5] The benefits of applying nanotechnology to catalysis include improved activity, lifetime, resistance to poisoning, and other novel abilities such as catalyzing the growth of carbon nanotubes. These improvements and novelties cannot always be achieved with catalysts prepared by other methods.

An example of expanding the catalytic capabilities of regular catalysts through nanoscale manipulation is cobalt-based catalysis. Co nanoparticle catalysts may be influenced by their size and structure and by other additional components such as Si, Ni, and Mg. For example, Co or Co oxide nanostructures are known to be effective catalysts.[6−8] Adding trace amounts of Si has been known to counter the aging problem of Fe or Co catalysts. Mixing with Ni increases the catalytic ability of Co nanoparticles in producing single-walled carbon nanotubes by more than 10-fold.[9] Surface

Chemistry Department, University of California, One Shields Ave., Davis, CA 95616. E-mail: tguo@ucdavis.edu

segregation in these Co–Ni bimetallic nanoparticles was discovered by Guo *et al.*, a surface science phenomenon that was carefully studied by Somorjai and others in the 1970s.[10] Hence, nanotechnology can help improve catalysts by fine-tuning their existing features or enabling new properties.

Carbon fibers and silicon whiskers catalyzed by metal particle catalysts were investigated by Bacon, Tibbets, and Dresselhaus *et al.*, and by Ellis *et al.* between the 1960s and 1980s.[11–14] Ijima *et al.* and Bethune *et al.* discovered that single-walled carbon nanotubes were made in the presence of transition metal nanoparticles.[15,16] These important discoveries were followed by other work that helped produce higher quality and larger quantity single-walled carbon nanotubes. Guo *et al.* and Thess *et al.* made laser vaporization a powerful method to produce high quality single-walled carbon nanotubes that made many critical measurements possible.[9,17] Dai *et al.* used chemical vapor deposition (CVD) on premade nanoparticles to make these nanotubes.[18] Lieber *et al.* used the laser vaporization method to make Si and Ge nanowires, with the help of gold nanoparticle catalysts.[19,20] Recently, nanoparticle catalysts have found important applications in catalyzing the growth of nanowires of various compositions.[21]

10.1.2. Silicon-Based Nanowires

10.1.2.1. Methods. The results mentioned above have led to the establishment of a general field of manufacturing nanostructures using metal nanoparticle catalysts. More recently, silicon-based nanowires (SiNW or SiNWs) have been produced, including those composed of amorphous and crystalline silicon, amorphous silicon dioxide, crystalline silicon core with an amorphous silicon dioxide sheath, and SiO_x. Morales *et al.* used the laser vaporization method to make 15-nm Si nanowires at 1200°C. Holmes *et al.* used a solution phase synthesis to make 5-nm SiNW in supercritical carbon dioxide at 500°C.[22] Ti catalysts were employed to make SiNW by Kamins *et al.*,[23] though the nanowires produced in their work were short. Of a special mention is the use of Ga as a low temperature catalyst to make SiNW. Pan *et al.* and Sunkara *et al.* used Ga to help catalyze the growth of SiNW at temperatures as low as 400°C.[24,25] Hence, it seems that the synthesis using Ga catalysts is the most convenient method. However, the nanowires made with this method were not as long and uniform as those produced at higher temperatures where high quality Si-based nanowires free of additional amorphous coating and up to centimeter long were made. Pure SiNW without a SiO_2 sheath were made by Yan *et al.* in which hydrogen was used to prevent the formation of a SiO_2 surface layer.[26] However, it is unclear whether the sample would be stable in air after exposure to oxygen. SiO_x nanowires were made by Tang *et al.*,[27] and SiO was suggested as the catalyst in that work.

Ni thin films were used as catalysts by Jin *et al.* and Yan *et al.* to produce amorphous SiNW at 1200°C.[28,29] No external supplies of Si were needed, but hydrogen gas was used. It was unclear whether the nanowires were amorphous silicon nanowires covered with silica layers, or silica nanowires.

10.1.2.2. Growth Mechanisms. Growth mechanisms have been investigated, and several theories have been proposed. There are two general models that are used to explain catalytic synthesis of nanowires or nanotubes. The first is called tip growth, in which

gas-phase reaction feedstock such as silane (SiH_4) deposits on nanoparticle tips on growing nanowires. The breakdown and dissolution of silane and subsequent migration and precipitation of Si after saturation in the metal catalyst leads to the formation of SiNW. Many images have shown that metal nanoparticles are at the tip of nanowires or nanotubes.[30,31] The second model is termed root growth. In this case, Si feedstock, either coming directly from the substrate or coming from the gas phase, migrates and diffuses to the locations of nanoparticle catalysts on the surface or substrate. The feedstock is then converted to SiNW by the catalysts. In both cases, the size of the nanoparticles has to be comparable to the diameter of the nanowires so that nanoparticles can efficiently absorb feedstock. For root growth, nanoparticles are found near the root or anchor of the nanowires, as contrasted to tip growth in which nanoparticles are found at the suspended end of the nanowires growing in space.

It is also possible to categorize growth of SiNW based on the source of feedstock. In CVD and laser vaporization methods, gaseous stock materials are used, which lead to the well-known vapor–liquid–solid (VLS) growth mechanism, referring to the gas feedstock, liquid catalysts and solid nanowires. In solution synthesis, the Si feedstock comes from the solution, leading to the solution–liquid–solid growth model. This should not be confused with the solid–liquid–solid model, which suggests that bulk solid materials are used to produce nanostructures via catalytic processes, as in the Ni case.[28] Recently, solid forms of nanoparticle catalysts have been observed.[21]

Most of the aforementioned methods use gas-phase feedstock, including CVD via the VLS mechanism in the presence of metal catalysts, evaporation at high temperatures without the use of metal catalysts, or laser vaporization in the presence of metal catalysts. Solution–liquid–solid methods have been explored in the presence of metal catalysts and under supercritical conditions. These two mechanisms can result in either tip or root growth, meaning that the catalysts can be either suspended in space at the tips of the growing nanowires, or anchored at the surface of the substrate, depending on the strength of interactions between the nanoparticles and the substrate.

On the other hand, the work by Yan *et al.* and Jin *et al.* using silicon wafers and Ni as catalysts has suggested that bulk silicon would diffuse through the nanoparticles to produce SiNW. In this case, solid silicon in the wafer reacts with Ni catalysts to directly make SiNW. If this is true, it falls into the category of root growth. However, as we will illustrate below, the use of hydrogen in the presence of metal catalysts may activate a new reaction pathway that converts Si in the substrate into silane. As a result, the suggested solid–liquid–solid model may actually be the VLS model at work.

During growth, Co or Co silicide nanoparticles are considered molten. Molten metal catalysts are considered to be spherical or near spherical because of the surface tension. They may also take in silicon feedstock more readily than solid form catalysts. The melting point of metal nanoparticles is size dependent. For example, 2 to 3-nm gold nanoparticles can produce SiNW at 500°C.[22] For larger gold nanoparticles, the reaction temperatures are higher, and the diameters of the SiNW are bigger.[32] For transition metal nanoparticles of medium sizes (10 to 50 nm), the lowering of the melting temperature due to the size effect may not be significant, and growth temperatures are generally close to the eutectic temperatures of their respective alloys with Si. For example, 1035°C is needed for Co catalysts to produce SiNW (*vide infra*), whereas bulk Co–Si binary alloys melt at ~1230°C.[33]

When Si in Co nanoparticles becomes supersaturated, it will precipitate out. For small size nanoparticles (<100 nm), the interactions between Co nanoparticles and the Si substrate may not be strong enough to hold the nanoparticles onto the Si surface, as results have shown that these nanoparticles are at the tip of SiNW. The precipitation of Si then pushes the nanoparticles in the opposite direction to the growth of the SiNW, resulting in tip growth. This may be why small nanoparticles are usually involved in tip growth. When nanoparticles are larger, the growth rate is slower and the interaction between nanoparticles and the substrate is stronger, and most likely the growth of nanowires will not cause the nanoparticles to move. Most of the results on SiNW have shown tip growth, and they often yield 15-nm diameter nanowires. Experimentally, it is still unproven that thin nanowires (<50 nm) can be formed directly from solid, with nanoparticles still attached to the substrate during the growth of SiNW.

Thus it is clear that the VLS model can enable either tip or root growth mechanisms, whereas the solid–liquid–solid model only applies to the root growth mechanism.

Other mechanisms have also been proposed. For example, SiO has been used to produce SiNW. In this case, disproportionation reactions between SiO nanoparticles produce Si and SiO_2 nanoparticles. These nanoparticles then coalesce to form SiNW.

10.1.2.3. Morphology of Si-Based Nanowires. The overall diameters of SiNW produced so far range from 3 nm to 100 nm, and many methods have yielded a frequently occurring diameter of 15 nm when they are made between the temperature of 1100 and 1200°C. This size of nanowires, as speculated at the end of this chapter, may be determined by the selected growth temperature.

Pure silicon nanowires can be made when the nanowires are reduced by hydrogen while growing. However, it has been shown that these pure Si nanowires are generally more difficult to make or preserve because Si in those nanowires is readily oxidized in air. Therefore, Si nanowires are normally covered with SiO_2. Under special conditions, SiO_x ($x < 2$) nanowires can be made. These nanowires possess very intense photoluminescence (PL) due to oxygen vacancies compared to that of pure SiO_2. In contrast, crystalline silicon nanowires possess little PL because silicon has an indirect band gap. Although amorphous Si nanowires in principle should photoluminesce, no direct evidence is available yet. On the other hand, Raman emission from SiO_2 nanowires is weak, but is intense for silicon nanowires. These characteristics are important because they help define both applications and methods of characterization of these nanowires.

SiNW (made of silicon, silicon-covered with silica, or silica) can be either crystalline or amorphous. The interaction of silicon and metal catalysts, the evolution of silicon precipitating out of the catalysts, and the reactions followed the precipitation determine the morphology and crystallinity of SiNW. In many cases, SiNW have been observed with a silicon core covered with an amorphous silicon dioxide sheath.[34,35] The crystalline core can make SiNW either fairly straight, or coiled or curly. It was discovered that CH_4 may affect the helicity.[36] This may be caused by a more complicated phase diagram that involves carbon, silicon, and metal.

Other morphologies have also been made and observed for SiNW. Although straight nanowires dominate, other forms such as string beans (strings of pearls), shells,

cones, nanoflowers, and elongated volcanoes have been reported.[37] Coiled nanowires represent another category, and have been reported by several groups.[38,39]

Milligram quantity SiNW have been obtained, although no stand-alone materials have been generated for easy handling. In general, nanowires so produced are attached to the substrate, and removal has been difficult or nearly impossible due to the small quantities available.

10.1.2.4. Catalysts. The catalysts employed in SiNW synthesis include Au, Ti, Fe, Co, Ni, and Ga, all in the form of nanoparticles whose size determines or has a correlation with the diameter of the nanowires. Among these catalysts, Ga tends to make multiple-branched nanowires, probably due to its low melting point and the subsequent propensity for nanoparticle agglomeration. On the other hand, transition metals such as Ni and Co, when used in the form of nanoparticles, can produce long nanowires of small diameters. Au has also been used to make very thin Si-based nanowires in heated supercritical solution. In general, as long as the particle size is small, the diameter of the nanowires can be kept small, demonstrating a loose correlation between the two. SiO_x has been considered as a catalyst as well.[35] It is suggested that SiO_x nanoparticles are formed first, and annealing of strings of these nanoparticles would eventually lead to the production of nanowires. Free energy considerations may also play a role in controlling the conversion from SiO nanoparticles to SiNW.

In many cases, metal silicides may very well be the catalysts. For example, $FeSi_2$ is being considered to be the catalyst in Fe-assisted nanowire synthesis.[20] This is similar to the silicon mono-oxide case, although it is much easier to understand the mechanisms in the $FeSi_2$ case. It is also possible that during the catalytic processes that silicon diffuses relatively freely through the metal catalyst and consequently, the observed silicides at the end of reaction may be different from those during the catalytic reaction. No direct evidence is available to show whether metal or metal silicide nanoparticles are the true catalyst.

Like the growth of carbon nanotubes, SiNW can be grown with and without catalysts.[40] However, it is generally easier to produce these nanowires with catalysts. For example, with catalysts, the reaction temperature can be as low as 300 to 400°C. The diameter of the nanowires is more controllable with the use of catalysts. The difference between the diameters of long SiNW and the catalysts forming them is comparable to that between long carbon nanotubes and the corresponding catalysts, and the correlation between the two in both cases is strong. The extent of correlation is also temperature and catalyst dependent.

The identification of catalysts has been straightforward. In most cases, they are metal nanoparticles that are found either at the tip of the nanowires, or are enclosed at the tip of or along the nanowires, suggesting tip growth. When SiO_x was used as a catalyst, no alien nanoparticles were found at the tip of the nanowires. Strings of SiO nanoparticles were found in the sample, providing critical information regarding the growth mechanisms.[41] Similar results have been observed when Si precursors were laser vaporized.[38]

10.1.2.5. Correlation between Sizes of Catalysts and SiNW. A loose correlation exists between the nanowire diameter and the size of the catalysts. The size of

nanoparticles is generally larger than the diameter of the SiNW for the reasons stated above. In some cases, the nanoparticles are smaller and sometimes are even seen trapped in the middle of nanowires.[42] The catalytic processes involved in those productions are unclear. One possibility is that an outer layer grows on top of the initial fast-grown thinner SiNW, and the nanoparticles then migrate freely along the nanowires as they do along carbon nanotubes.[43] The other possibility is that the observed nanoparticles at the end of synthesis are not the same as the catalysts during synthesis, as small nanoparticles such as Au or Au silicides have much lower melting points than the growth temperature (1000 to 1100°C) of SiNW made in the process.

10.1.2.6. Applications. SiNW can be used in many different applications. For example, PL from nanowires can be used to make blue light-emitting nanoscale devices.[44,45] One possible origin of the PL from these nanowires is the oxygen vacancies in SiO_2.[46] The nanowires can also be made as optical read head or nanoscale optical fibers. Although the PL from silicon nanowires is relatively weak, silicon nanowires possess unique electronic properties for device making. The diversity of SiNW in their compositions and morphologies thus help drive forward the progress in both synthesis and applications.

Improved morphology and compositions of SiNW can further enable many new applications. For example, SiO_x nanowires usually possess the most intense blue PL.[47,48] And in a recent study, long wavelength PL from oxygen vacancies in SiO_2 has been achieved.[49]

SiNW can also be used as sensors.[50] In this case, SiNW of a silicon core without or with a very thin SiO_2 sheath are preferred. Since oxygen in the air normally reacts with Si, thin Si nanowires will eventually become SiO_2 nanowires if no protective layers are in place.

10.1.3. Outline of This Chapter

In this chapter, we will present results on SiNW by reacting H_2 gas with silicon wafers in the presence of Co nanoparticles. We will demonstrate that Co nanoparticles are indispensable to the growth under the conditions specified here. Furthermore, we will show that $CoSi_2$ may also play a role, not by directly catalyzing nanowire growth, but by producing gaseous silicon feedstock as the supply of Si to Co nanoparticle catalysts to form SiNW. Hydrogen is believed to be crucial to the formation of gaseous silicon compounds. An experiment has been designed to prove that large quantities of silicon or silicon compounds were airborne during growth. We will show that our method can be used to make large quantity SiNW which may be used as photon scatterers, photoluminescent materials, chemical sensors, templates for making other nanostructures, and as light guides.

10.2. EXPERIMENTAL DETAILS

In the following, experimental details will be given. The methods of synthesizing nanoparticles, nanostructures, and silicon-based nanowires will be discussed. The analytical tools will be briefly described.

10.2.1. Nanoparticle Synthesis

10.2.1.1. Chemicals and Nanoparticles. All chemicals were used without further treatment. Anhydrous solvents and chemicals were stored in a drybox and used under dry nitrogen gas.

Nanoparticles were prepared on the basis of our previous report.[51] In brief, Co nanoparticles were synthesized via a high-temperature thermo-decomposition method.[52] Three-, five-, and twelve-nanometer Co nanoparticles in dichlorobenzene (DCB) solutions were made and used to make self-aligned nanostructures (SAN) and SiNW.

Gold nanoparticles were synthesized according to the literature procedure.[53] Fifteen-nanometer Au nanoparticles were made and used for SiNW production.

10.2.1.2. Synthesis of SAN. Piranha solution (1:4 H_2O_2 (30%): H_2SO_4 (conc.)) cleaned Si (100) wafers (5 mm × 5 mm to 1 cm × 4 cm, Virginia Semiconductor) were immersed in the nanoparticle solutions for a short time. The wafers were then retrieved and rinsed with DCB and dried with Ar gas. All wafers were coated with nanoparticles in an identical manner, and approximately the same number of nanoparticles was assumed to be deposited on each of the wafers. The wafers were then set in a high temperature furnace (Lindberg/Blue) to react for a certain time, during which Ar (99.997%, Praxair) and H_2 (99.95%, Praxair) were fed through the furnace. The flow rates for SiNW growth were 600 SCCM for Ar and 400 SCCM for H_2. The apparatus is shown in Fig. 10.1. Piranha solution was used to remove residual Co materials from the original SAN samples. Both original and cleaned SAN samples were studied with X-ray absorption spectroscopy.

10.2.1.3. Synthesis of SiNW. SiNW were made by reacting Co nanoparticles with Si wafers in H_2 and Ar between 1000 and 1100°C.[54] After nanoparticle deposition, the

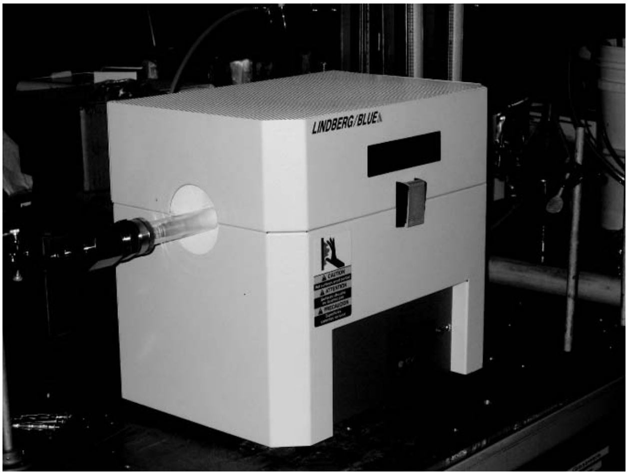

FIGURE 10.1. Apparatus used to grow silicon-based self-aligned nanostructures and nanowires. A quartz tube was placed in a high temperature furnace (shown here). Ar, H_2 and CH_4 selectively flowed through the tube.

Si wafers were either cleaned in Piranha solution, washed with deionized water and dried with Ar gas, or used without cleaning. The samples were then inserted into the high temperature tube furnace. Since SAN can form extremely fast, we believe that SAN existed in all samples. When the furnace temperature was set between 1035 and 1100°C, SiNW were formed.

The apparatus was identical to that shown in Fig. 10.1. The gases were Ar (99.997%, Praxair), H_2 (99.95%, Praxair), and CH_4 (99.99%, Quadren Cryogenic Processing LTD). CH_4 was not necessary to produce either SAN or SiNW. The flow rates were the same as for the growth of SAN. Only small amounts of CH_4 were used.

10.2.2. Analytical Methods

10.2.2.1. Electron Microscopy. The nanowires were inspected by scanning electron microscopy (SEM, FEI XL-30 SFEG), transmission electron microscopy (TEM, TOP-CON, JEOL 002B), energy-dispersive X-ray analysis (SEM-EDX), and TEM-EDX. For SEM-EDX, the excitation electron energy was set to 15 keV. For TEM-EDX, the electron energy was set to 200 keV. TEM samples were prepared by scraping SiNW off the wafers onto Lacey carbon TEM grids.

High resolution TEM (CEM300) was used to study the morphology of SiNW, and *in situ* TEM (JEOL 3010) experiments were performed at the National Center for Electron Microscopy (NCEM) to study migration of nanoparticles on Si wafers as a function of temperature.

10.2.2.2. Raman Spectroscopy. Raman spectra were collected using a frequency-doubled Nd:YAG pumped laser. The central wavelength was set to 532 nm, and the bandwidth of the laser was ~1.0 nm. The laser beam was sent into a homemade inverted microscope equipped with a Raman filter (Omega Optical, 538 AELP). The light was focused onto the sample by a microscope objective (Ziess Acroplan 0.8 NA 63×) after the dichroic Raman filter. The light backscattered by the sample was collected using the same objective. This light was then focused into a fiber, which coupled the light into a spectrometer (Acton, SpectraPro 300i). The signal was detected by a charge-coupled device (Roper Scientific, EEV-1024). Spectra resolution was estimated at 15 to 20 cm^{-1}. The power at the sample was 10 to 15 mW, and the focal spot size was ~3 μm. Raman spectra were collected for 100 s of each acquisition, and subsequently summed using WinSpec32 (Roper Scientific, version 2.5.12.0) to equal a 500-s total acquisition time.

Raman samples were prepared by peeling SiNW thin films off the silicon wafers to avoid Raman signals from the silicon substrate. A razor blade was used to shave the thin films on top of the silicon wafers. The thin films were mounted on a carbon tape for SEM and Raman inspection, or on a transparent Mylar film for Raman measurements.

10.2.2.3. X-Ray Absorption Spectroscopy (XAS). The XAS measurements were similar to those described elsewhere.[55] Grazing incidence (GI)-XAS measurements were performed at beamline 11-2 at Stanford Synchrotron Radiation Laboratory (SSRL). A double Si(220) crystal spectrometer was used to select the energy of the synchrotron X-rays, and the beam size was set to 400 $\mu m \times 2$ mm. The bandwidth of the spectrometer was about 1 eV. Routine procedures were used to optimize the positions of the samples so that the angle of incidence was about 0.17°, with the X-ray

beam covering most of the 4-cm length of the SAN samples. A 29-channel Ge detector was used to detect the X-ray fluorescence from Co in SAN. The detector was positioned about 20 cm away from the samples. Program SUPER was used to configure the detector, and program XAS was used to collect the EXAFS and XANES data. Normally five sweeps were used for measuring a sample. All the channels in each sweep were summed and all sweeps were added for each measurement. EXAFSPAK and FEFF software programs were used to process and fit the EXAFS data.[56]

An FEFF8 package was used to simulate both XANES and EXAFS patterns of $CoSi_2$, CoSi, and Co_2Si. Crystal structures in the literature were used for these calculations. Program ATOMS was used to generate the coordinates for FEFF8, which was then used to calculate the XAS patterns. In EXAFS calculations, an *ab initio* self-consistent real space multiple scattering code was used to obtain the scattering potentials, the scattering phase shifts, the relativistic dipole matrix elements, and X-ray absorption cross sections. The maximum scattering path length was set to be 11 Å. The Debye–Waller constants for Co–Si and Co–Co obtained from the experimental values in this study were used. In XANES simulations, full multiple scattering (FMS) calculations were used, which was implemented in FEFF8 through Green's function theory. The radius for FMS was set to 6 Å.

10.2.2.4. Growth on Al_2O_3 Substrates. The setup of the Al_2O_3 experiment is shown in Fig. 10.2. The Al_2O_3 wafer (Valley Design, CA) was separated from the Si substrate by two 0.66-mm Al_2O_3 spacers. Co nanoparticles were deposited on both Al_2O_3 and Si wafers. Reaction gas H_2 and buffer gas Ar were fed into the reaction quartz tube as described above. The goal of this experiment was to test whether a significant amount of silicon could become airborne and reach the Al_2O_3 wafer during reaction.[54]

10.3. RESULTS

10.3.1. Nanoparticle Deposition on Si and Al_2O_3 Wafers

The optimal densities of nanoparticle deposition for the formation of SAN and SiNW were different. For SAN formation, low-density deposition of Co nanoparticles was preferred. In contrast, high-density deposition was needed to produce high yield SiNW.

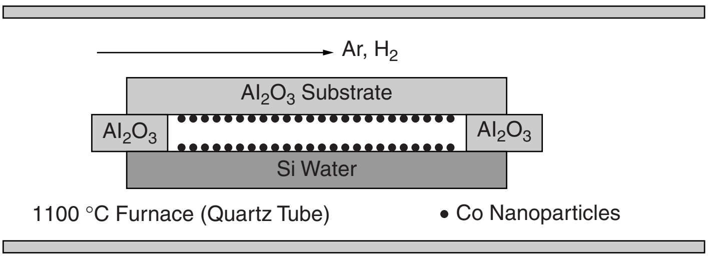

FIGURE 10.2. Schematic of the two-substrate experiments. An alumina plate was positioned above a Si wafer, separated by 0.66 mm. The whole assembly was placed in the middle of the quartz tube. [Chem Comm 2005]—Reproduced by permission of The Royal Society of Chemistry. (ref 54)

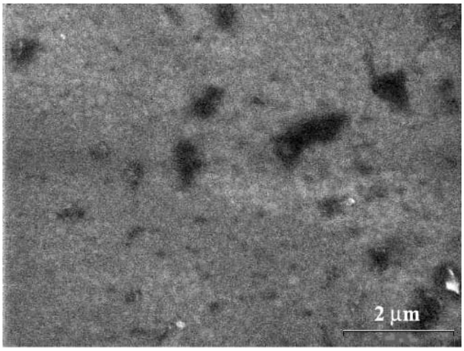

FIGURE 10.3. Nanoparticle deposition for SiNW production. High-density deposition of nanoparticles was used.

Figure 10.3 shows a Co nanoparticle deposition prior to SiNW growth. The average size of the nanoparticles used in this deposition was 12 nm. The standard deviation was 5 nm. As shown in Fig. 10.3, no individual nanoparticles were detected by SEM. The nanoparticles were embedded in large amounts of organic solvents or hydrocarbons such as oleic acid (OA) and tri-octylphosphine oxide (TOPO).

Under the optimum condition for SAN formation, where the samples prior to high temperature synthesis were washed with DI-water and DCB, the nanoparticle density was much lower. In this case, fewer SiNW were produced at 1100°C. An SEM image of the sample before growth is shown in Fig. 10.4. The cleanliness of the surface was due to the DI-water wash and the DCB rinse. Individual and strings of nanoparticles are clearly seen.

10.3.2. Nanowires Formation

10.3.2.1. Temperature Effect. When the sample shown in Fig. 10.3 was treated at high temperatures, nanoparticles began to move around on the Si wafer at approximately

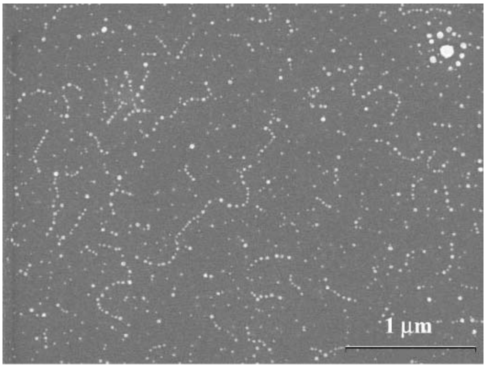

FIGURE 10.4. Nanoparticle deposition for SAN production. Low-density deposition was used, and individual nanoparticles are clearly visible.

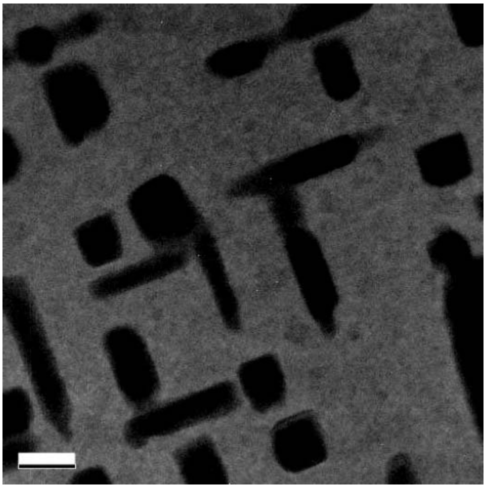

FIGURE 10.5. *In situ* TEM image on migration of nanoparticles deposited on an ion-milled Si wafer at 500°C. The scale bar is 200 nm.

450°C. We performed *in situ* TEM studies to track the movement of the nanoparticles. The result is shown in Fig. 10.5. In this case, the temperature was 500°C. As shown, the nanoparticles already migrated to align to the silicon (100) wafer substrate. At a much higher temperature such as 1000°C, these patches would break up to form nanoparticles again, although the diameters of these newly formed nanoparticles were different from those as deposited, as the former often had larger than 12-nm diameters and a larger size distribution. It is unknown whether these piles were pure Co or Co silicide.

Figure 10.6 shows the result of growth from a low-density deposition at 900°C in Ar and H_2. In this case, SAN were produced.[51] The SAN were 3 to 6 nm wide and hundreds of nanometers long.

Figure 10.7 shows the results of growth at 1000°C from a sample with a moderately high-density nanoparticle deposition. In this case, the sample was still dominated by SAN, although their morphology was more diverse than SAN grown at 900°C. Thicker SAN, as much as 10 to 20 nm, were made.

At 1100°C, SiNW dominated. Figure 10.8 shows SiNW grown at 1100°C for 5 s. Reaction time was also a factor for SAN formation. Reaction times of 30 min and a few seconds produced similar results, although longer times generally produced more SiNW. Long SiNW fully covered the Si wafers after a few hours. The nanowires were between 5 and 50 nm in diameter, and microns to millimeter long.

10.3.2.2. Effect of Co and Au Nanoparticles. We found that Co nanoparticles were indispensable to growth of SiNW. To further demonstrate the importance of Co nanoparticles for SiNW growth, we designed and performed a simple experiment in which a fingerprint was used to modify the surface of the wafer to promote binding of Co nanoparticles to the substrate through ligand interactions.

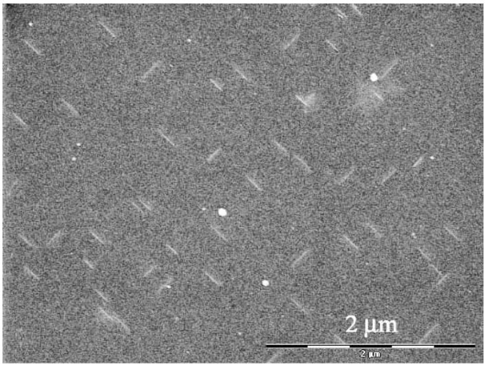

FIGURE 10.6. SAN growth at 900°C. Some Co nanoparticles are visible after the reaction. The average length of SAN is 250 nm.

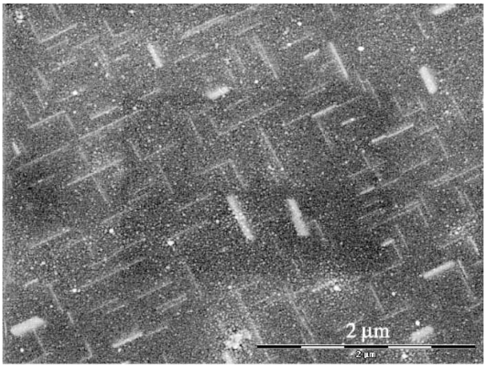

FIGURE 10.7. Samples of SAN produced at 1000°C. Both thin (3 nm wide) and thick SAN (10–20 nm wide) are present.

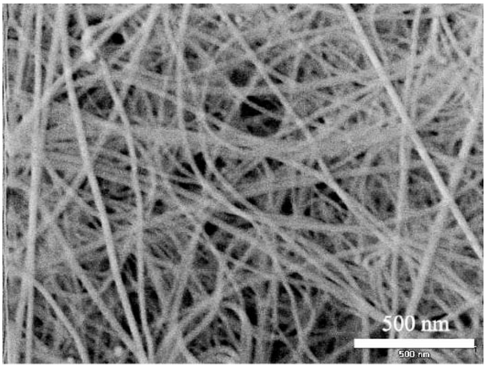

FIGURE 10.8. Samples of SiNW grown at 1100°C. The SiNW are microns to millimeters long, and have an average diameter of 16 nm.

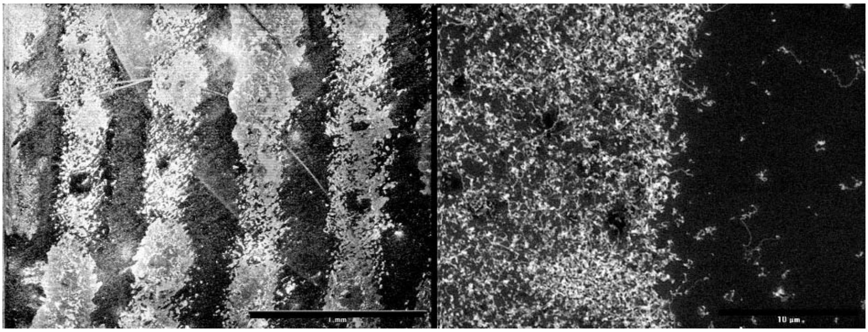

FIGURE 10.9. A SiNW sample produced with the finger printing technique (see text). The scale bar on the left is 1mm, and 10 μm on the right. The darker regions are bare Si surfaces. [Chem Comm 2005]-Reproduced by permission of The Royal Society of Chemistry. (ref 54)

In this experiment, a finger touched a cleaned Si wafer before Co nanoparticle deposition. Because the greasy fingerprint was left on the wafer, it presented a pattern of hydrophobic surface with which the hydrophobic ligands on Co nanoparticles could interact. After the deposition, the wafer was thoroughly washed with DCB to remove most of the nanoparticles that were only weakly bound to the surface. Because of interactions of the hydrophobic surfactants with the fingerprint, Co nanoparticles remained attached to the greasy areas of the wafer after cleaning and washing. Figure 10.9 shows the fingerprint results. High magnification pictures (right panel, Fig. 10.9) showed that SiNW were grown in the regions where the fingertip contacted the Si wafer.

10.3.2.3. Effect of Hydrogen, Methane, and Substrate. We found that H_2 was necessary for the growth of SiNW. Although previous results had shown that H_2 may aid in the growth of long, thin Si nanowires, this is the first time that H_2 was shown to be critical to the formation of SiNW. Figure 10.10 shows the results. As can be seen, there are hardly any SiNW after 30 min growth if H_2 was absent.

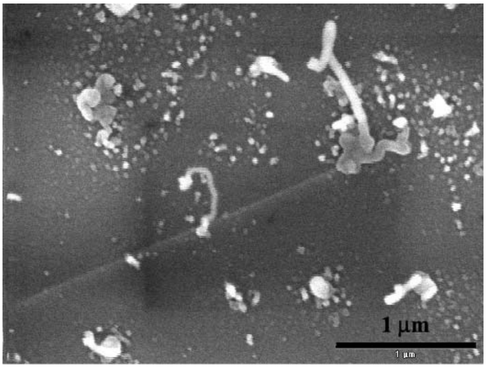

FIGURE 10.10. SiNW grown on a Si wafer coated with Co nanoparticles at 1100°C, with H_2. Several short SiNW are visible under SEM.

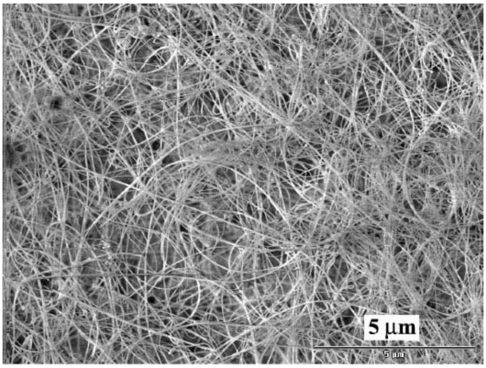

FIGURE 10.11. SiNW grown on a Si wafer coated with Co nanoparticles at 1100°C. Large quantities of SiNW are visible under SEM. [Chem Comm 2005] - Reproduced by permission of The Royal Society of Chemistry. (ref 54)

We also found that addition of methane did not yield any SiNW at up to 1100°C. This may be caused by an increase in the melting point of cobalt carbide nanoparticles when methane was added.

The substrate also played an important role in controlling the movement of nanoparticles at moderate temperatures before the nanoparticles melt. This can be clearly seen in Fig. 10.5 where nanoparticles are aligned with the atomic lines on Si (001). In addition, H_2 and SAN together may play an even more important role in the catalysis of SiNW, as shown below.

The nanowires in Fig. 10.5, straight and coiled, are believed to be SiNW. Experiments were performed to verify that they were not carbon nanotubes or metal nanorods. One method to prove this was by using a substrate other than Si. In this case, Al_2O_3 wafers replaced Si as the substrate to avoid interference from the Si substrate for characterization. The SiNW grown on Si are shown in Fig. 10.11, and those grown on the Al_2O_3 wafer are shown in Fig. 10.12. Characterization of these nanowires yielded that they were SiNW.

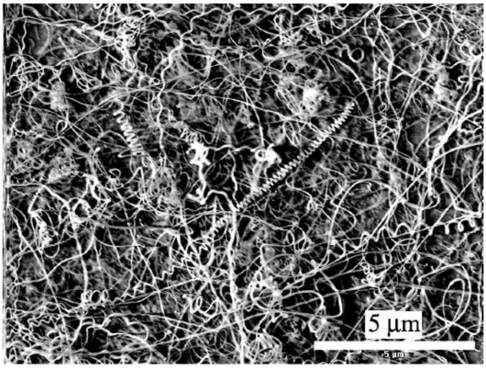

FIGURE 10.12. SiNW grown on an Al_2O_3 wafer coated with Co nanoparticles at 1100°C. Large quantities of coiled SiNW are visible under SEM. [Chem Comm 2005] - Reproduced by permission of The Royal Society of Chemistry. (ref 54)

This experiment also proved that the Si source became airborne and migrated from the Si wafer to the Al_2O_3 substrate because initially there was no Si on the Al_2O_3 substrate. Therefore, silicon in the silicon wafer had to move across the space between the two wafers to enable the growth of SiNW on the Al_2O_3 wafer.

Oxidized Si wafers were prepared by placing them in a furnace in the presence of air at 1100°C for 45 min. They were then coated with Co nanoparticles for SiNW growth as discussed above. It was found that almost no SiNW were made, and the Si wafers were covered with either cracks or short wires with Co nanoparticles at their tips.

10.3.2.4. Effect of SAN. We also investigated the contribution of SAN to the growth of SiNW. In these experiments, extra Co left on the substrate after the synthesis of SAN was removed from the SAN samples by washing it in Piranha solution. The Co in those washed samples was in the form of almost pure $CoSi_2$, as verified by XAS measurements (*vide infra*). These cleaned samples were then used to grow SiNW at 1100°C. It was found that moderate yields of SiNW were produced.

Although it was clear that SAN did not play a role in the growth of SiNW when the Al_2O_3 substrates were used, as discussed later SAN or Co silicides might still play an alternative role in assisting the growth of SiNW: SAN on the Si wafers might be needed for producing SiH_4, which was likely the source of Si for SiNW grown on Al_2O_3 wafers.

10.3.3. Composition of Nanowires

10.3.3.1. Raman Spectroscopy. As seen in Fig. 10.13a, the Raman peak at 520 cm^{-1} (at 547 nm) that is typically associated with crystalline Si was barely visible (see the inset). Instead, fluorescence at 700 nm dominated, which implies that the material was SiO_2 with some O vacancies.[49] The sample also contained some crystalline Si, possibly due to the presence of some Si chips removed from the substrate by the razor blade. However, there were only a few spots where the 520 cm^{-1} peak was significant,

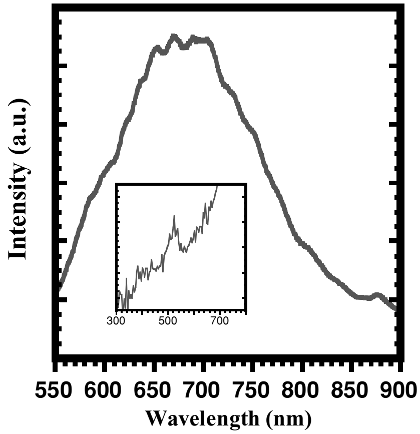

FIGURE 10.13a. Raman measurements of the SiNW thin film on the Mylar thin film. A peak at 700 nm was found. The intensity was nearly twice the regular Raman intensity at 520 cm^{-1} for silicon The Inset shows the weak peak at 520 cm^{-1}.

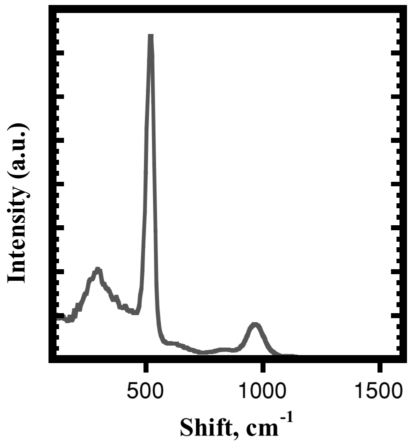

FIGURE 10.13b. Raman measurements of the SiNW thin film on the Mylar thin film, except the sample was scanned to maximize the peak at 520 cm^{-1}. This shows that the sample may contain crystalline chips carried over during the removal process.

as shown in Fig. 10.13b. No carbon peaks (at 1300 and 1600 cm^{-1}) were detectable, and no amorphous Si peak at 480 cm^{-1} was detected.[57] This clearly demonstrated that the nanowires were not carbon nanotubes or amorphous silicon. The Raman results shown in Fig. 10.13 confirm that the stand-alone samples peeled off silicon wafers contained mostly amorphous silicon oxide nanowires rather than silicon nanowires. HRTEM results further confirmed this finding. It is possible that any Si nanowires initially formed were oxidized into SiO_2 nanowires after exposure to air.

10.3.3.2. EDX. The composition of the nanowires was studied with energy dispersive X-ray (EDX) analysis with both TEM and SEM. Figure 10.14 shows a TEM image of SiNW that were removed from a Si wafer with a razor blade, and a TEM-EDX result on a section of a SiNW deposited on a Lacey carbon TEM grid. The EDX showed pure Si from those wire segments. The Cu signal came from the Cu in the TEM grids. The spot in Fig. 10.14 (top panel) shows the location of the electron beam.

EDX-SEM results measured on a thin-film sample on a carbon tape showed that the nanowires contained Si and O (Fig. 10.15). The ratio of Si to O was approximately 1.5–2:1, suggesting that the nanowires were made of SiO_2 with O vacancies. This also agreed with the results from the PL and Raman experiments. No carbon signal from the carbon tape was observed because the film was too thick for the e-beam to penetrate.

10.3.3.3. XAS. In order to better understand the catalytic processes, we investigated Co nanoparticle catalysts in SAN and SiNW with grazing incidence X-ray absorption spectroscopy (GI-XAS). Figure 10.16 shows the results of EXAFS measurements. FT of the EXAFS of both SAN and SiNW samples are shown.

Two coordination shells were found for Co in SAN, one at 2.33 and the other at 3.50 Å (phase corrected). These two peaks correspond to Co–Si direct bonds (first coordination shell) and Co–Co scattering (second coordination shell). Only one major

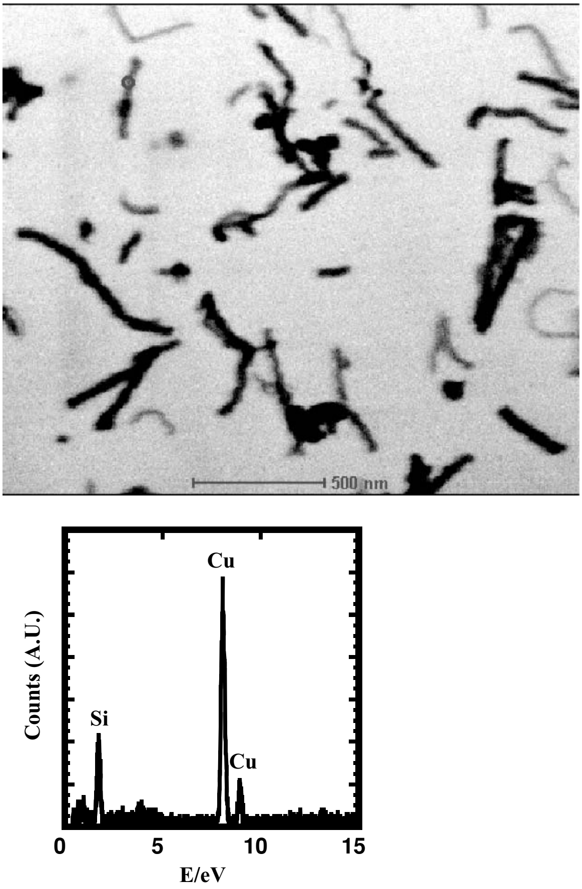

FIGURE 10.14. TEM-EDX of SiNW scraped from a Si wafer with a razor blade. The EDX spectrum is shown in the lower panel. The data was taken from the circled area shown in the top panel.

coordination shell was found for SiNW, corresponding to Co–Si direct bond (first shell) at 2.33 Å. This shows that Co in SiNW likely adopted Si-rich forms, which were not $CoSi_2$ because the former lacked the second Co–Co coordination shell at 3.50 Å. Further experiments with higher accuracy and more analysis are needed to conclusively determine the structure. This result also excluded the possibility of having pure Co nanoparticles as catalysts.

XANES spectra were also obtained, as shown in Fig. 10.17. The spectrum of Co in SiNW differs from Co in SAN and CoO.[58] It shows a feature near 7706 eV that was very close to that of Co metal. However, the other features associated with SiNW were different from that of Co metal, as shown by the peak at 7722 eV. These results suggest that Co in SiNW was different from Co metal and $CoSi_2$.

10.3.3.4. HRTEM of Si-Based Nanowires. High resolution TEM images of SiNW showed amorphous structures for all the nanowires inspected. Although it is difficult

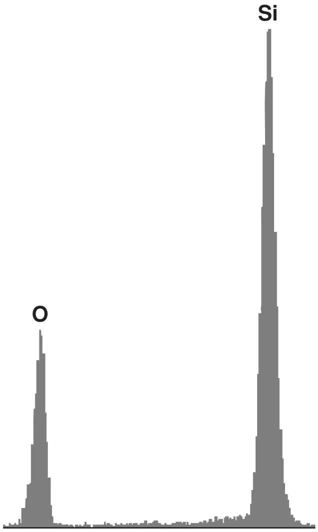

FIGURE 10.15. SEM-EDX of SiNW grown on an Al_2O_3 substrate.

to conclusively state that ALL nanowires were amorphous, it is evident that based on the Raman, XAS, and TEM measurements that most of these nanowires were made of amorphous silicon oxides.

10.3.4. Growth of Nanowires

10.3.4.1. Evidence for Tip Growth. The evidence for tip growth can be found from the images which directly show that nanowires are connected to metal catalysts. Figures 10.18 and 10.19 show two types of SiNW, one straight and one coiled. This clearly indicates that nanowires were grown from the tip.

If the nanowires are coiled, one likely reason is that they were crystalline, as evidenced by coiled nanowires in ZnO case.[39] The crystalline nanowires that were originally coiled could become amorphous after they were exposed to air, but they

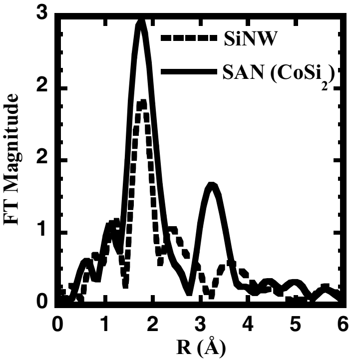

FIGURE 10.16. EXAFS results after Fourier transformation. Results of both SAN and SiNW are shown for comparison purpose.

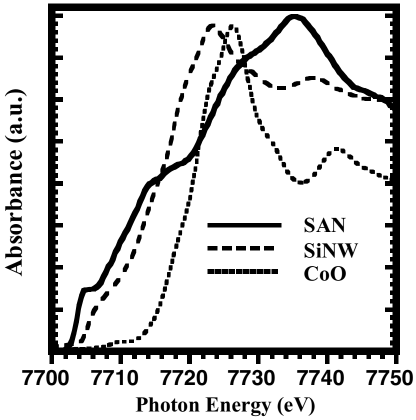

FIGURE 10.17. XANES results of the same samples. CoO reference was used for comparison purpose. SAN and SiNW both have a similar peak at 7706 eV that resembles the bulk Co metal.

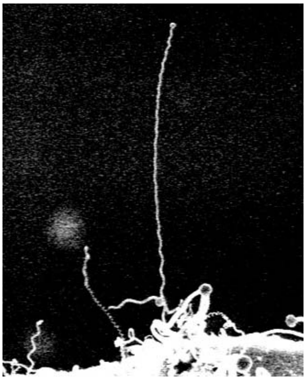

FIGURE 10.18. A single SiNW pointing into space with a nanoparticle catalyst on its tip. The nanowires are slightly coiled to maintain its straightness over a long distance. [Chem Comm 2005]—Reproduced by permission of The Royal Society of Chemistry. (ref 54)

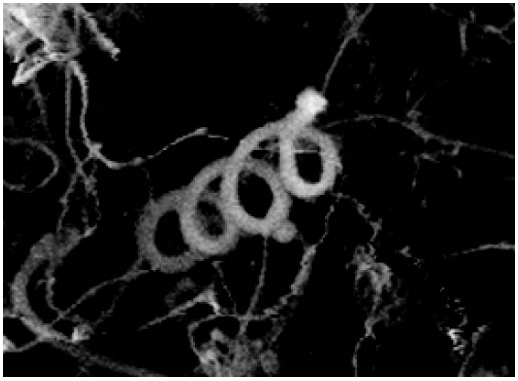

FIGURE 10.19. A heavily coiled SiNW with a nanoparticle on its tip. The radius of curvature is about 100 nm, and diameter of the nanowires is about 20 nm. [Chem Comm 2005]—Reproduced by permission of The Royal Society of Chemistry. (ref 54)

would maintain the coiled geometry. The nanoparticles responsible for the growth of those coiled nanowires could also be crystalline, and the registration between the two crystalline materials may produce coiled nanowires.

Another possibility is that the growth rates of SiNW from catalysts were nonuniform across SiNW cross sections. This can be true if the catalysts are close to melting, but not quite fully molten. At much higher temperatures, catalysts are all well molten and adopt a spherical shape. At near-melting temperatures, they may not be spherical, and therefore the SiNW produced under this condition may have nonsymmetric growth with respect to its nanowire axis, which will lead to the growth of coiled nanowires.

The statistics of the morphologies of these SiNW can be obtained. High resolution SEM picture (e.g., based on Fig. 10.10) showed that the crystalline SiNW were 5 to 50 nm in diameter, with an average diameter of 16 nm. It was generally difficult to find the ends of the SiNW, as these nanowires can be extremely long, in the order of millimeters or even longer. In the cases where tips were visible, nanoparticles were often found at the end of the SiNW. We consider this a strong indication of tip growth.

10.3.4.2. Bulk Growth and Manipulation. Under good growth conditions, high yield or blanket-like thin films (sometimes with a tongue as shown in Fig. 10.20) were made and removed from substrates (Fig. 10.21). The thickness of the films was estimated to be in the order of a fraction of millimeter. This showed that it is possible to produce thin films of nanowires for various applications by stripping them directly from Si wafers. The films could be peeled off from the substrate, as shown in Fig. 10.21, and used for various measurements such as PL, Raman, and electron microscopy.

Since the ends of SiNW were generally difficult to be found, one can estimate that these wires were at least millimeters long. The quality of those wires was high as they were free of non-nanowire amorphous materials. Since no hydrocarbons were used during growth, no amorphous carbon was visible on the surface of the SiNW. When CH_4 was used, almost no SiNW were made. Under optimal growth conditions, the density of the nanowires was high, the thickness of the SiNW layer was significant, and the Si substrate was completely covered with the wires.

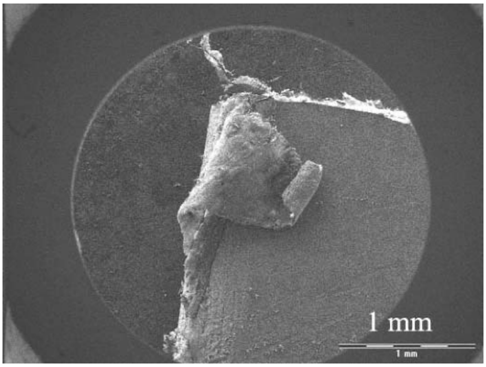

FIGURE 10.20. A rolled up corner of SiNW thin film on Si wafer. The scale bar is 1 mm. The thickness of the film/blanket is a fraction of one mm.

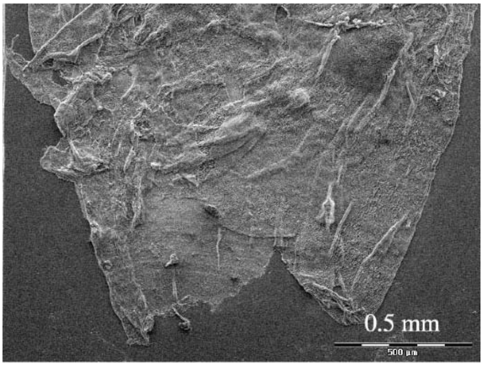

FIGURE 10.21. A thin film of SiNW that was separated from the Si wafer with a razor blade. Ethanol was sprayed onto the film during the removal.

We also observed growth of SiNW from Au nanoparticles. In this case, H_2 was also necessary. Although Au silicides can form at moderate temperatures and can also be reduced by hydrogen to Au nanoparticles and silane, the growth temperature for SiNW was still above 1000°C. It seems that silane was produced in both Au and Co catalytic growth cases.

Figure 10.22 shows the two wafers, one on the left with SAN on it, and the other on the right with SiNW on it. The appearance of the SiNW covered Si wafers is dramatically different from that of SAN or unreacted Si wafers. The latter are highly reflective, while the SiNW-covered ones are highly scattering. Thus the dull color of the SiNW sample (the wafer on the right) was caused by the strong scattering of the SiNW on the substrate. The dimensions of the strips were approximately 1/4 inch × 2 inch.

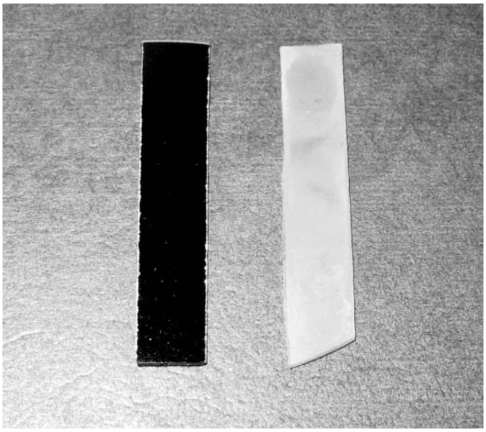

FIGURE 10.22. Samples of SAN and SiNW (right). The size of the wafers is 1/4″ × 2″. The left wafer shows the SEM image of SAN, and right one shows the SEM image of SiNW. [Chem Comm 2005]—Reproduced by permission of The Royal Society of Chemistry. (ref 54)

10.4. DISCUSSION

As presented above, we have observed SiNW with nanoparticles at their ends, suggesting tip growth. The Co in the samples seemed to have a composition different from Co metal and crystalline $CoSi_2$, as suggested by the XAS experimental results. Undetectable amounts of carbon were found in those SiNW, and large quantities of SiNW can be made with the current method. Thin films of SiNW can now be separated from the substrate, making it possible to directly handle mass quantity SiNW.

However, it is unclear what the growth mechanisms are because no Si feedstock was fed in the gas form, which is required for the tip-growth model to work. In the following, we will discuss the composition and growth mechanisms of the nanowires made in this work, and show that the Co nanoparticles may play a dual-catalytic role by helping form gaseous silicon species and catalyze the growth of Si-based nanowires.

10.4.1. Composition and Morphology of the Silicon Nanowires

HRTEM results showed that SiNW were made of amorphous materials. EDX of the nanowires showed both Si and O peaks, with the ratio ranged from $SiO_{1.5}$ to SiO_2. The observation that SiNW were amorphous materials was further supported by the Raman measurements, in which very small amounts of crystalline Si was detected. Even the amorphous Si peak at 480 cm^{-1} was undetectable due to the presence of high PL signal. On the basis of the information presented here, we concluded that the majority of the SiNW are made of amorphous silicon dioxide, with a certain amount of oxygen deficiencies.

It is possible that the as-made nanowires contain some crystalline Si core, and subsequent reaction with oxygen in the air results in the formation of silica nanowires. Since hydrogen gas was used in the reaction, pure silicon nanowires were probably made first, followed by oxidation in air. In the following discussion, for simplicity reason we will assume that amorphous SiNW were made during catalytic reactions.

10.4.2. Growth Mechanisms

10.4.2.1. Growth Conditions. Since Co or Co silicide nanoparticles need to be molten or very close to melting during the growth of SiNW to allow efficient growth via migration of Si through nanoparticle catalysts, there is only a small temperature window below 1100°C for this to occur. Our experimental results have shown that only at temperatures above 1035°C could SiNW be produced at good yields. Based on the phase diagram of Co–Si, the lowest melting temperature for the bulk alloy is 1239°C, where the composition is close to Co_3Si.[33] This means that the quantum size effect lowering the melting temperature for 15-nm median diameter SiNW is small. In the cases where nanoparticles are much smaller, in the order of 1-5 nm, as much as a 50% decrease in the melting temperature has been predicted.[59] The small difference observed here implies that the size of Co or Co silicide nanoparticles responsible for the growth of SiNW is large, as supported by the results of SEM and TEM.

Even when small nanoparticles (<10 nm) are used, they may first coalesce to form larger ones at a temperature below the synthetic temperature of SiNW and the temperature at which the small nanoparticle catalysts begin to melt. This may be why

thin SiNW (<5 nm) are seldom made at high temperatures. It will be critical to eliminate the coalescence of nanoparticles if small-diameter SiNW are to be made.

We also attempted to produce SiNW from oxidized Si wafers. However, as shown earlier, only a small number of SiNW were produced. This indicates that a thick SiO_2 layer may not allow the formation of SiNW, even in the presence of H_2 and Co nanoparticles. Since Si is oxidized and becomes amorphous, no SAN would form under this condition. This result perhaps implies that SAN may contribute to SiNW growth (e.g., via the production of silane gas). Also, since H_2 can reduce SiO_2 to Si or SiO, and SiO can be evaporated at 1200°C, oxidized Si in the presence of H_2 may, in principle, produce SiNW without the use of catalysts. However, the negative result shown here implies that Co nanoparticles may not react well with SiO_2 to form $CoSi_2$ and thus H_2 cannot affect the growth of SiNW.

The phase diagram of Co–Si shows that Co–Si alloys of any compositions have a relatively uniform melting point of about 1250°C. This means that at high temperatures, it is not important for Co and Si to adopt a certain composition. When the temperature is lowered, Co may form $CoSi_2$ because this is one of the most stable forms for Si-rich alloys, as supported by the observation made by Morales *et al.*[20]

10.4.2.2. Analysis of the Growth Conditions. It is intriguing that nanowires can be grown at a very high rate without silicon vapor from the substrate, as silicon vapor pressure is negligible (1×10^{-4} mm Hg) at 1100°C.[60] Our tests have shown that it only takes a few seconds to produce high yields of SiNW at 1100°C. With no additional Si fed, and with growth that follows the tip-growth model as shown earlier, the exact identity of the silicon source is unclear.

Several possibilities exist. First, it is possible that the growth model is really root growth, as in the Ni case presented by Yan *et al.* and Jin *et al.*[29] However, their explanation was largely a hypothesis. In order for SiNW to grow, silicon has to dissolve in metal catalysts and precipitate out upon saturation. If the growth model is based on root growth, and silicon from the wafer has to migrate through metal nanoparticles to form nanowires, the driving force for root growth model would disappear when Co or Co silicide nanoparticle catalysts are lifted off the silicon substrate as the nanoparticles will no doubt be pushed as Si diffuse through it at a high rate. As shown in this work, many nanowires have metal nanoparticles on their tips, suggesting that Co or Co silicide catalysts leave the substrate during reaction and the growth is tip-based, thus countering the idea of root growth. Furthermore, although it is also possible that Si vapor may come from small Si nanostructures created at such a high temperature, the facts that H_2 is needed and that oxidized Si wafers did not grow SiNW indicate that it is not small silicon nanoparticles or islands that cause SiNW to grow, as small Si particles exist in both cases.

Our experiments have shown that hydrogen is critical for growth. The required presence of both hydrogen and metal catalysts, and the virtual absence of silicon vapor suggest that totally new reaction paths assist in the growth of these nanowires under the conditions studied. If silicon does not come directly from the wafer substrate, then it is required to become airborne in some form, as in the CVD production of SiNW, thus enabling tip growth.

This leaves to only one possibility, namely that Si gets first into the gas phase to enable the catalytic growth of nanowires via Co or Co silicide nanoparticles. For silicon

Co nanoparticles migration (450 °C);

Co nanoparticles + Si → Co silicides (500 °C);

Co nanoparticles + Co nanoparticles → Co silicides SAN (900 °C);

Co silicides + 2 H_2 (gas) → Co + SiH_4 (gas);
Co + Si → Co silicides;

SiH_4 (gas) + Co nanoparticles or Co silicides nanostructures → Si nanowires + 2 H_2.

SCHEME 10.1. Formation of silane and SiNW by a series of reactions involving Co nanoparticles, hydrogen, and silicon wafers.

to become airborne from a silicon wafer, gas-producing reactions have to happen. In our experiment, Co or Au nanoparticles are present. As shown in our earlier work, Co nanoparticles can react with the silicon substrate to produce Co silicides such as CoSi, Co_2Si, and $CoSi_2$. $FeCo_2$ itself has been suggested as the catalyst.[20] On the basis of our experiments, we speculate that Co silicides may react with hydrogen to form silane. Co in the silicides is reduced by hydrogen to cobalt metal, which then reacts with more silicon in the wafer to form Co silicides again so that the catalytic process can continue, as illustrated in Scheme 10.1. In the same way, Au silicides may also be reduced to provide silane. We suspect the Ni catalysts would undergo the same reactions.

We further suggest that silane is produced and becomes airborne, which then reacts with metal or metal silicide nanoparticles that have not reacted with silicon or with Co silicide nanostructures to produce SiNW, as shown in Scheme 1. We are looking into how to directly prove the existence of silane.

Other reports have supported the notion that SiO can evaporate at 1200°C. This source of Si is not present in our work when using pure silicon wafers. In the case of oxidized wafers, the question is whether hydrogen can reduce SiO_2 to become SiO, which can then become airborne. Our tests using oxidized wafers suggest that this is unlikely as no SiNW were produced from these wafers.

Because Si needs to migrate through Co or Co silicide nanoparticle catalysts to form SiNW, it is conceivable that at the end of the growth stage, all catalyst nanoparticles are in the form of Co silicides as a result of Co reacting with Si in the silicon-rich regions. This theory was partially supported by the EXAFS results, which suggest a Si-rich composition in the Co-containing species after the catalytic growth. As we stated before, the quality of the EXAFS data needed to be improved before these claims can be confirmed.

10.4.2.3. Proposed Growth Models. Summarizing the results given above, the growth mechanisms are proposed as follows. Because of the location of nanoparticles at the tips of SiNW, we conclude that growth must occur in the gas phase. More precisely, we think that Co silicide SAN play a role here. They help convert Si and H_2 into SiH_4 (gas). Unreacted Co nanoparticles left on the surface, possibly due to the

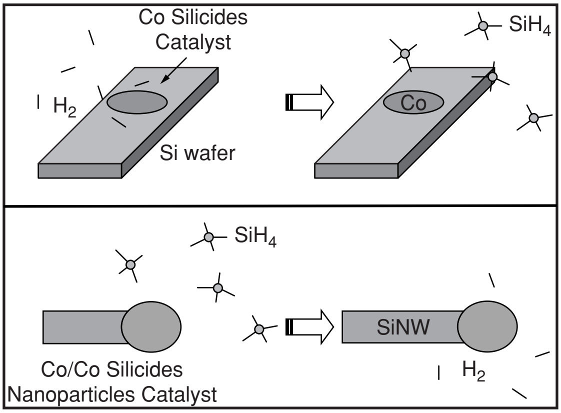

FIGURE 10.23. Proposed catalytic processes to make SiNW from Co nanoparticles and hydrogen. Si wafers act as the source of silicon. Silane is produced, which then reacts with Co or Co silicide catalysts to make SiNW. [Chem Comm 2005]—Reproduced by permission of The Royal Society of Chemistry. (ref 54)

slow diffusion rate of Co in Si, then catalyze the SiNW growth. The feedstock is SiH_4, which is made *in situ*. We thus term this method *in situ* CVD, or iCVD.

A schematic of the proposed growth model is shown in Fig. 10.23. In this model, Co nanoparticles play a dual catalytic role. On the one hand, they catalyze silane formation by reacting first with silicon to form Co silicides, and then react with hydrogen to form silane while being reduced to Co metal. The second role of Co nanoparticles is their classic catalytic ability of making nanowires by first dissolving the silane and precipitating out Si nanowires.

The proposed growth mechanisms can also help explain the often seen 15-nm average diameter SiNW. At high temperatures, approximately 15-nm diameter Co or Co silicide nanoparticles breakaway from patches of Co thin films formed from deposited Co nanoparticles. Some of these newly formed nanoparticles will form SAN or other Co silicides, and catalyze the formation of SiH_4. The rest may remain as Co-rich nanoparticles and act as SiNW catalysts in the presence of SiH_4. Once the nanoparticle catalysts are lifted off the wafer surface, they have little chance to react with each other to form larger nanoparticles. Therefore, only the temperature at the growth stage of SiNW is important; the original size of the Co nanoparticles matters little in determining the SiNW diameter. As a result, only medium-sized (15 nm in this case) nanowires are made from those 15 to 20 nm Co or Co silicide nanoparticles. At low density deposition, this explanation does not apply, and SiNW may very well follow the morphology of Co nanoparticles as deposited.

10.4.2.4. Applications. We have shown here that bulk quantity SiNW can be made in the form of thin films. These films can be used as (1) templates for making other nanostructures because of the large surface area offered by those nanowires; (2) PL devices; and (3) nanoelectronic and chemical sensor devices or fuel cells because the silicon oxide nanowires may be passivated before they are oxidized. We are pursuing all these options in our lab.

10.5. FUTURE WORK

10.5.0.5. Fischer–Tropsch. Other benefits from learning and applying these synthetic approaches and reactions include gaining a better understanding of several important industrial catalytic reactions such as the Fischer–Tropsch process in which hydrocarbon chains are formed from CO and hydrogen.[61] In hopes of producing hydrogen fuels and reducing pollution in developing countries, it is critical to develop nanotechnology that can eventually help such processes.[6,62] All the important ingredients, hydrogen, Co nanoparticles, and Si are in the reactions studied here.

10.5.0.6. In Situ Characterization. As a result of this study, it is clear that Co or other metals may play a dual catalytic role catalyzing both the growth of nanowires and the production of airborne Si species, such as silane, which acts as a silicon source. An *in situ* characterization method will eventually be needed.

Other experiments are underway to further identify, both *ex situ* and *in situ*, the structure of nanoparticle catalysts responsible for the growth of SiNW.

The results presented here also indicate the need to measure the melting temperature of Co nanoparticles at high temperatures. Our group is working toward achieving this goal using synchrotron sources.

ACKNOWLEDGMENTS

I would like to thank my graduate students Joshua D. Carter, Yongquan Qu, and Rhiannon Porter for their contribution to this work. I also thank C. Echer and C. Song at the National Center for Electron Microscope (NCEM), and J. Rogers and the excellent staff at the Stanford Synchrotron Radiation Laboratory (SSRL) for experimental support. I am also grateful to DOE for support of both facilities. Acknowledgment is made to the Donors of The Petroleum Research Fund, administrated by the American Chemical Society, for partial support of this research. This work is also partially supported by the Camille and Henry Dreyfus Foundation and the National Science Foundation (CHE-0135132).

REFERENCES

1. J. H. Sinfelt, Bimetallic catalysts, *Sci. Am.* **253,** 90–98 (1985).
2. J. H. Sinfelt, In *Bimetallic Catalysts: Discoveries, Concepts, and Aapplications*, (Wiley, New York 1983), pp. 164.
3. J. H. Sinfelt, From the 1950s to the 1990s—My years as a scientist in an industrial laboratory, *Catal. Today* **53,** 305–309 (1999).
4. M. Valden, X. Lai, and D. W. Goodman, Onset of catalytic activity of gold clusters on titania with the appearance of nonmetallic properties, *Science* **281,** 1647–1650 (1998).
5. B. C. Gates, Supported metal cluster catalysts, *J. Mol. Catal. A: Chem.* **163,** 55–65 (2000).
6. W. Yang, H. Gao, H. Xiang, D. Yin, Y. Yang, J. Yang, Y. Xu, and Y. Li, Cobalt supported mesoporous silica catalyst for Fischer–Tropsch synthesis, *Acta Chim. Sinica* **59,** 1870–1877 (2001).
7. V. Kesavan, D. Dhar, Y. Koltypin, N. Perkas, O. Palchik, A. Gedanken, and S. Chandrasekaran, Nanostructured amorphous metals, alloys, and metal oxides as new catalysts for oxidation, *Pure Appl. Chem.* **73,** 85–91 (2001).

8. S. Son, S. Lee, Y. Chung, S. Kim, and T. Hyeon, The first intramolecular Pauson–Khand reaction in water using aqueous colloidal cobalt nanoparticles as catalysts, *Organ. Lett.* **4,** 277–279 (2002).
9. T. Guo, P. Nikolaev, A. Thess, D. T. Colbert, and R. E. Smalley, Catalytic growth of single-walled nanotubes by laser vaporization, *Chem. Phys. Lett.* **243,** 49–54 (1995).
10. S. H. Overbury, P. A. Bertrand, and G. A. Somorjai, The surface composition of binary systems: Prediction of surface phase diagram of solid solutions, *Chem. Rev.* **75,** 547–560 (1975).
11. R. Bacon, Growth, structure, and properties of graphite whiskers, *J. Appl. Phys.* **31,** 283–290 (1960).
12. G. G. Tibbetts, Why are carbon filaments tubular? *J. Cryst. Growth* **66,** 632–638 (1984).
13. J. S. Speck, M. Endo, and M. S. Dresselhaus, Structure and intercalation of thin bezene derived carbon fibers, *J. Cryst. Growth* **94,** 834–848 (1989).
14. R. S. Wagner, and W. C. Ellis, Vapor–liquid–solid mechanism of single crystal growth. *Appl. Phys. Lett.* **4,** 89–90 (1964).
15. S. Iijima, and T. Ichihashi, Single-shell carbon nanotubes of 1-nm diameter (Vol 363, Pg 603, 1993), *Nature* **364,** 737 (1993).
16. D. S. Bethune, C. H. Kiang, M. S. Devries, G. Gorman, R. Savoy, J. Vazquez, and R. Beyers, Cobalt-catalysed growth of carbon nanotubes with single-atomic-layerwalls, *Nature* **363,** 605–607 (1993).
17. A. Thess, R. Lee, P. Nikolaev, H. J. Dai, P. Petit, J. Robert, C. H. Xu, Y. H. Lee, and S. G. Kim *et al.*, Crystalline ropes of metallic carbon nanotubes, *Science* **273,** 483–487 (1996).
18. H. J. Dai, A. G. Rinzler, P. Nikolaev, A. Thess, D. T. Colbert, and R. E. Smalley, Single-wall nanotubes produced by metal-catalyzed disproportionation of carbon monoxide, *Chem. Phys. Lett.* **260,** 471–475 (1996).
19. M. S. Gudiksen, L. J. Lauhon, J. Wang, D. C. Smith, and C. M. Lieber, Growth of nanowire superlattice structures for nanoscale photonics and electronics, *Nature* **415,** 617–620 (2002).
20. A. M. Morales, and C. M. Lieber, A laser ablation method for the synthesis of crystalline semiconductor nanowires, *Science* **279,** 208–211 (1998).
21. A. Persson, M. Larsson, S. Stenstrom, B. Ohlsson, L. Samuelson, and L. Wallenberg, Solid-phase diffusion mechanism for GaAs nanowire growth, *Nature Mater.* **3,** 677–681 (2004).
22. J. D. Holmes, K. P. Johnston, R. C. Doty, and B. A. Korgel, Control of thickness and orientation of solution-grown silicon nanowires, *Science* **287,** 1471–1473 (2000).
23. T. Kamins, X. Li, and R. Williams, Thermal stability of Ti-catalyzed Si nanowires, *Appl. Phys. Lett.* **82,** 263–265 (2003).
24. Z. Pan, Z. Dai, C. Ma, and Z. Wang, Molten gallium as a catalyst for the large-scale growth of highly aligned silica nanowires, *J. Am. Chem. Soc.* **124,** 1817–1822 (2002).
25. M. K. Sunkara, S. Sharma, R. Miranda, G. Lian, and E. C. Dickey, Bulk synthesis of silicon nanowires using a low-temperature vapor–liquid–solid method, *Appl. Phys. Lett.* **79,** 1546–1548 (2001).
26. X. Q. Yan, D. F. Liu, L. J. Ci, J. X. Wang, Z. P. Zhou, H. J. Yuan, L. Song, Y. Gao, L. F. Liu, *et al.* H_2-assisted control growth of Si nanowires, *J. Cryst. Growth* **257,** 69–74 (2003).
27. Y. H. Tang, Y. F. Zhang, N. Wang, W. S. Shi, C. S. Lee, I. Bello, and S. Lee, T. Si nanowires synthesized from silicon monoxide by laser ablation, *J. Vac. Sci. Technol.* B **19,** 317–319 (2001).
28. S. Jin, Q. Li, and C. Lee, Direct growth of amorphous silicon oxide nanowires and crystalline silicon nanowires from silicon wafer, *Phys. Status Solidi A—Appl. Res.* **188,** R1–R2 (2001).
29. H. Yan, Xing, Y., Hang, Q., Yu, D., Wang, Y., Xu, J., Xi, Z. and Feng, S. Growth of amorphous silicon nanowires via a solid–liquid–solid mechanism, *Chem. Phys. Lett.* **323,** 224–228 (2000).
30. J. Westwater, D. P. Gosain, and S. Usui, Si nanowires grown via the vapour–liquid–solid reaction, *Phys. Status Solidi A—Appl. Res.* **165,** 37–42 (1998).
31. S. Helveg, C. Lopez-Cartes, J. Sehested, P. Hansen, B. Clausen, J. Rostrup-Nielsen, F. Abild-Pedersen, and J. Norskov, Atomic-scale imaging of carbon nanofibre growth. *Nature* **427,** 426–429 (2004).
32. S. Hofmann, C. Ducati, Neill, R., S. Piscanec, A. Ferrari, J. Geng, R. Dunin-Borkowski, and J. Robertson, Gold catalyzed growth of silicon nanowires by plasma enhanced chemical vapor deposition, *J. Appl. Phys.* **94,** 6005–6012 (2003).

33. T. B. Massalski, H. Okamoto, P. R. Subramanian, and L. Kacprzak, In *Binary Alloy Phase Diagrams*, (ASM International, Materials Park, OH 1990).
34. Q. Hu, S. Verghese, R. Wyss, T. Schapers, J. delAlamo, S. Feng, K. Yakubo, M. Rooks, M. Melloch, *et al.* High-frequency (f similar to 1 THz) studies of quantum-effect devices, *Semicond. Sci. Technol.* **11,** 1888–1894 (1996).
35. Y. F. Zhang, Y. H. Tang, C. Lam, N. Wang, C. S. Lee, I. Bello, and S. T. Lee, Bulk-quantity Si nanowires synthesized by SiO sublimation, *J. Cryst. Growth* **212,** 115–118 (2000).
36. H. F. Zhang, C. M. Wang, E. C. Buck, and L. S. Wang, Synthesis, characterization, and manipulation of helical SiO2 nanosprings, *Nano Lett.* **3,** 577–580 (2003).
37. Y. Zhu, W. Hsu, M. Terrones, N. Grobert, H. Terrones, J. Hare, H. Kroto, and D. Walton, 3D silicon oxide nanostructures: From nanoflowers to radiolaria, *J. Mater. Chem.* **8,** 1859–1864 (1998).
38. Y. Tang, Y. Zhang, N. Wang, C. Lee, X. Han, I. Bello, and S. Lee, Morphology of Si nanowires synthesized by high-temperature laser ablation, *J. Appl. Phys.* **85,** 7981–7983 (1999).
39. R. S. Yang, Y. Ding, and Z. L. Wang, Deformation-free single-crystal nanohelixes of polar nanowires, *Nano Lett.* **4,** 1309–1312 (2004).
40. T. Guo, P. Nikolaev, A. G. Rinzler, D. Tomanek, D. T. Colbert, and R. E. Smalley, Self-assembly of tubular fullerenes, *J. Phys. Chem.* **99,** 10694–10697 (1995).
41. N. Wang, Y. Tang, Y. Zhang, C. Lee, I. Bello, and S. Lee, Si nanowires grown from silicon oxide, *Chem. Phys. Lett.* **299,** 237–242 (1999).
42. C. Li, N. Wang, S. Wong, C. Lee, and S. Lee, Metal silicide/silicon nanowires from metal vapor vacuum arc implantation, *Adv. Mater.* **14,** 218–221 (2002).
43. B. Regan, S. Aloni, R. Ritchie, U. Dahmen, and A. Zettl, Carbon nanotubes as nanoscale mass conveyors, *Nature* **428,** 924–927 (2004).
44. D. P. Yu, Q. L. Hang, Y. Ding, H. Z. Zhang, Z. G. Bai, J. J. Wang, Y. H. Zou, W. Qian, G. C. Xiong, *et al.* Amorphous silica nanowires—Intensive blue light emitters, *Appl. Phys. Lett.* **73,** 3076–3078 (1998).
45. Z. Liu, S. Xie, L. Sun, D. Tang, W. Zhou, C. Wang, W. Liu, Y. Li, X. Zou, *et al.* Synthesis of alpha-SiO_2 nanowires using Au nanoparticle catalysts on a silicon substrate, *J. Maert. Res.* **16,** 683–686 (2001).
46. H. Nishikawa, T. Shiroyama, R. Nakamura, Y. Ohki, K. Nagasawa, and Y. Hama, Photoluminescence from defect centers in high-purity silica glasses observed under 7.9-eV excitation, *Phys. Rev.* B **45,** 586–591 (1992).
47. G. Meng, X. Peng, Y. Wang, C. Wang, X. Wang, and L. Zhang, Synthesis and photoluminescence of aligned SiO_x nanowire arrays, *Appl. Phys. A—Mater. Sci. Process.* **76,** 119–121 (2003).
48. Y. Wang, C. Liang, G. Meng, X. Peng, and L. Zhang, Synthesis and photoluminescence properties of amorphous SiO_x nanowires, *J. Mater. Res.* **12,** 651–653 (2002).
49. Y. F. Zhang, Y. H. Tang, N. Wang, C. S. Lee, D. P. Yu, I. Bello, and S. T. Lee, Silicon nanowire: A new shape of crystalline silicon, *Mater. Res. Soc. Symp. Proc.* **507,** 993 (1998).
50. O. Elibol, D. Morisette, D. Akin, J. Denton, and R. Bashir, Integrated nanoscale silicon sensors using top–down fabrication, *Appl. Phys. Lett.* **83,** 4613–4615 (2003).
51. J. D. Carter, G. Cheng, and T. Guo, Growth of self-aligned crystalline cobalt silicide nanostructures from Co nanoparticles, *J. Phys. Chem.* B **108,** 6901–6904 (2004).
52. V. F. Puntes, K. M. Krishnan, and A. P. Alivisatos, Colloidal nanocrystal shape and size control: The case of cobalt, *Science* **291,** 2115–2117 (2001).
53. M. Brust, M. Walker, D. Bethell, D. J. Schiffrin, and R. Whyman, Synthesis of thiol-derivatised gold nanoparticles in a 2-phase liquid–liquid system, *J. Chem. Soc.—Chem. Commun.* 801–802 (1994).
54. J. D. Carter, Y. R. P. Qu, L. Hoang, D. J. Masiel, and T. Guo, Silicon-based nanowires from silicon wafers catalyzed by cobalt nanoparticles in hydrogen environment, *Chem. Commun.* 2274–2276 (2005).
55. J. D. Carter, F. Shan, and T. Guo, Determination of $CoSi_2$ self-aligned nanostructures (SAN) with grazing incidence X-ray absorption spectroscopy, *J. Phys. Chem.* B **109,** 4118–4122 (2004).
56. G. N. George, and I. J. Pickering, EXAFSPAK: A suite of computer programs for analysis of X-ray absorption spectra, (1995).

57. M. Khayyat, G. Banini, D. Hasko, and M. Chaudhri, Raman microscopy investigations of structural phase transformations in crystalline and amorphous silicon due to indentation with a Vickers diamond at room temperature and at 77 K, *J. Phys. D—Appl. Phys*. **36,** 1300–1307 (2003).
58. G. Cheng and T. Guo, Surface segregation in Ni/Co bimetallic nanoparticles produced in single-walled carbon nanotube synthesis, *J. Phys. Chem.* B **106,** 5833–5839 (2002).
59. F. Ercolessi, W. Andreoni, and E. Tosatti, Melting of small gold particles—Mechanism and size effects, *Phys. Rev. Lett*. **66,** 911–914 (1991).
60. A. Tseplyaeva, Y. Priselkov, and V. Karelin, The Measurement of the saturated vapor pressure of silicon, *Vestmik Moskovskogo Universiteta*. **Ser 11 15**, 36–38 (1960).
61. G. Bian, T. Mochizuki, N. Fujishita, H. Nomoto, and M. Yamada, Activation and catalytic behavior of several Co/SiO_2 catalysts for Fischer–Tropsch synthesis, *Energy Fuels* **17,** 799–803 (2003).
62. R. Vijay, R. Hendershot, S. Rivera-Jimenez, W. Rogers, B. Feist, C. Snively, and J. Lauterbach, Noble metal free NO_x storage catalysts using cobalt discovered via high-throughput experimentation, *Catal. Commun*. **6,** 167–171 (2005).

11

Influence of Particle Size and Interaction with the Support on Redox and Catalytic Properties of Metals, Metal Oxides, and Metal Complexes

Darbha Srinivas and Paul Ratnasamy*

11.1. INTRODUCTION

The importance of particle size on the catalytic properties of metals was recognized from the early days of catalysis when the concept of active sites ("particular atoms or groups of atoms on the surface of solids responsible for their catalytic activity and selectivity of") was introduced in 1925 by H. S. Taylor.[1,2] It was recognized that the coordination number and concentration of such active sites may depend on the type of crystallographic planes exposed which may, in turn, depend on the size of the particle. The electronic energy levels of an atom on the surface of a solid are likely to be modified both by its surface coordination number and, to a lesser extent, the type of support. The particle size influences both the surface coordination number and the extent of particle–support interaction.[3,4] Smaller particles, especially in the nanometer range, expose more edges, corners and kinks (per unit weight) than larger particles. Hence,

National Chemical Laboratory, Pune 411 008, India
* To whom correspondence should be addressed. Fax: +91-020-25902633; E-mail: p.ratnasamy@ncl.res.in

structure-sensitive reactions which require a large *ensemble* of surface atoms of a particular configuration, are less likely to occur on nanosized particles. Structure-insensitive reactions, on the other hand, may be expected to be facilitated by the greater dispersion of the active sites that occurs when metal particle size is reduced to the nanorange. Superimposed on this first-order effect of the size of the particle on the concentration of the active sites, interactions with the support (charge transfer, geometric, confinement effects when active sites are encapsulated in the spatially constrained environment in the cavities and channels of molecular sieves etc.), may also contribute to the observed catalytic activity and selectivity. The nature of the support material, the preparation method, and the activation procedure are expected to influence the structure and reactivity of the supported metal species. The influence of particle size, in the nanometer range, and the nature of the support on the structural and catalytic properties of a few systems (metals, metal oxides, and metal complexes encapsulated in molecular sieves) in oxidation reactions that were recently investigated in our laboratory is described in this chapter. It is shown that while the size of the nanocrystallites has a dominant influence in the case of the metal/metal oxide catalysts, active site–support interactions are responsible for the enormous enhancement of oxidation activity observed when transition metal complexes are encapsulated in the cavities of molecular sieves and zeolites. The support can influence catalytic activity either indirectly by modifying the particle size of the metal/metal oxide dispersed on its surface (Sections 11.2 and 11.3) or directly by changing the relative electronic energy levels of the metal ions in metal complexes encapsulated in the geometrically constrained environment of the molecular sieves (Section 11.4).

11.2. SUPPORTED METALS

Che and Bennett[3] reviewed the influence of particle size on the catalytic properties of supported metals. The physical and catalytic properties of many metals start to change when the particle size is reduced below about 2 nm. At and below this particle size, the spacing between adjacent electronic levels becomes larger than the thermal energy, kT. The levels begin to behave independently and the particle begins to lose its metallic properties. As a consequence of this electronic effect, the catalytic properties, especially in redox reactions, are expected to vary. In such nanoparticles, the proportion of surface atoms will be very large. Their coordination numbers will also be different (usually lower) from those of the bulk structure. Many of the precious metal catalyst systems (like the Pt(Re)-chlorided-alumina used for aromatics production), wherein the metal content in the catalyst is below 1 wt.%, do indeed contain metal particles of about 1 to 2 nm in diameter.[5] However, in the majority of the base metal catalysts (like the Ni and Cu-based catalysts described below for steam reforming and preferential CO oxidation, respectively), wherein the base metal content is much higher (necessitated by their lower intrinsic activity), there is a distribution of metal particle sizes. In such cases, the catalytic activity will be a complex function of particle size distribution depending on the relative fraction of metal atoms residing in the nano range vs. the larger particles. In such cases, the support may play an indirect but decisive role in determining catalytic activity by its influence on the dispersion of the metal particles.

11.2.1. Ni–CeO_2–ZrO_2 for Steam Reforming

Steam reforming and autothermal reforming of hydrocarbons have been receiving renewed interest in recent years for generation of hydrogen for use in fuel cells.[6–10] Conventional steam reforming catalysts, e.g. Ni supported on oxides like SiO_2, Al_2O_3, MgO, calcium aluminates, $MgAl_2O_4$ or their mixtures, are (1) not sufficiently active as they operate at gas hourly space velocities of around 10,000 to 15,000 h^{-1} thereby requiring a large volume of catalyst, (2) require high steam-to-carbon ratios (1.5 to 3.0 mol), (3) undergo catalytic deactivation due to sintering of the Ni crystallites and carbon deposition, and (4) are pyrophoric when exposed to air inadvertently during operation leading to unacceptable safety risks for fuel cell operations.[11–19] They also require deep desulphurization (to less than 0.1 ppm S). Their relatively low catalytic activities require large volumes of catalysts which is difficult for adoption in "on-board" hydrogen generation for fuel cells in automobiles. Hence, worldwide efforts are in progress to develop novel, more active and more stable catalysts. While a major role of the support (apart from improving the mechanical and thermal resistance of the catalyst) is the initial dispersion of the metal and sustaining that dispersion for long periods of time, an equally important function is the supply of oxygen-containing species (like the OH^- anion) to the metal particle to remove the carbon as CO or CO_2 thereby suppressing the formation of carbon:

$$\text{M—C} + \text{OH}^- \Rightarrow \text{M—H} + \text{CO}$$

The CO generated can undergo further reaction with the H_2O present in the system to form CO_2 and H_2 (the water gas reaction):

$$CO + H_2O \Rightarrow CO_2 + H_2$$

KOH is added to conventional supports such as α-alumina or calcium aluminate to supply the OH^- anion. A problem with KOH addition is that K ions are volatile under the reaction conditions of steam or autothermal reforming and tend to migrate downstream of the catalyst bed during operation. Hence, metal oxide supports, which can dissociate H_2O and generate surface hydroxyl groups, have been extensively investigated during the past decade. Ceria-zirconia and yttria-stabilized zirconia mixed oxides are some of the most promising catalyst systems for this task.[20–22]

11.2.1.1. Synthesis of Nanoparticle Ni–CeO_2(Y_2O_3)–ZrO_2 Catalysts. Table 11.1 lists the nanoparticle Ni–CeO_2 (Y_2O_3)–ZrO_2 catalysts prepared by different methods. CeO_2 and CeO_2–ZrO_2 are used as supports for Pt, Pd, Rh in three-way catalysts for automobile exhaust pollution control.[23–28] Ceria promotes the stability of the catalysts and Pt-dispersion. Ceria's ability to store and release oxygen is a crucial feature in its superior performance. The materials have large specific surface areas and pore sizes in the mesopore range (3 to 7 nm). The method of preparation (hydrothermal synthesis with the template, cetyltrimethylammonium bromide, coprecipitation and digestion methods) has a great influence on the textural, structural and catalytic properties of the catalysts.[20,22]

Coprecipitation Synthesis (Method-A): In this method of preparation for a 5 g batch of sample **6A**, $Ni(NO_3)_2 \cdot 8H_2O$ (7.787 g), $Ce(NO_3)_3$ (3.7842 g) and

TABLE 11.1. $NiO–Y_2O_3–ZrO_2$ and $NiO–CeO_2–ZrO_2$ catalysts investigated in steam reforming reactions[21–22]

Sample No.	Catalyst Composition (in wt.%)	Preparation Method
1A	NiO(1)–CeO_2(49.5)–ZrO_2(49.5)	**A**: Coprecipitation
2A	NiO(5)–CeO_2(47.5)–ZrO_2(47.5)	**A**: Coprecipitation
3A	NiO(10)–CeO_2(45)–ZrO_2(45)	**A**: Coprecipitation
4A	NiO(20)–CeO_2(40)–ZrO_2(40)	**A**: Coprecipitation
5A	NiO(30)–CeO_2(35)–ZrO_2(35)	**A**: Coprecipitation
6A	NiO(40)–CeO_2(30)–ZrO_2(30)	**A**: Coprecipitation
7A	NiO(40)–CeO_2(5.4)–ZrO_2(54.6)	**A**: Coprecipitation
7B	NiO(40)–CeO_2(5.4)–ZrO_2(54.6)	**B**: Coprecipitation + digestion
7C	NiO(40)–CeO_2(5.4)–ZrO_2(54.6)	**C**: Hydrothermal synthesis with template
8A	NiO(40)–CeO_2(60)	**A**: Coprecipitation
9B	NiO(40)–Y_2O_3(6)–ZrO_2(54)	**B**: Coprecipitation + digestion
10D	NiO(20)–Al_2O_3(20)–Y_2O_3(6)–ZrO_2	**D**: Coprecipitation along with template

$ZrO(NO_3)_2 \cdot xH_2O$ (3.329 g) were dissolved separately in distilled water and then mixed together to make a total volume of about 150 mL. The solution was then divided into eight equal portions in eight Teflon-lined SUS304 steel autoclaves. To these, KOH solution (20 wt.%; about 4.3 mL per each portion) was added dropwise while stirring. The pH of the solution was maintained at about 10. All the cations were precipitated in the form of their hydroxides. The reactors were then closed and placed in the rotating hydrothermal (30 rpm) unit at 353 K for 72 h. At the end of the synthesis, the autoclaves were cooled to 298 K, and the precipitates obtained were washed with distilled water several times to remove potassium. The precipitates were initially dried in air for 48 h and then dried in an air oven, at 363 K, overnight. The dried materials were crushed and further calcined in air at 773 K for 12 h, to get the final powders. Catalysts, **1A–5A**, **7A** and **8A**, were prepared in a similar manner.[22]

Coprecipitation + Digestion Synthesis (Method-B): In this method for samples **7B**, and **9B**, $ZrO(NO_3)_2 \cdot xH_2O$, $Ce(NO_3)_3$, $Y(NO_3)_3{\cdot}5H_2O$ and $Ni(NO_3)_2 \cdot 8H_2O$ aqueous salt solutions were taken in a round bottom flask and stirred while heating at 353 K. Then, 20% KOH solution was added dropwise to precipitate the cations (Zr, Y (or Ce) and/or Ni) in the form of their hydroxides (pH $\approx$ 10). The precipitate thus obtained was digested under reflux (353 to 363 K) for 72 h. The precipitate obtained was filtered and washed with distilled water till the pH of the washings was 7. The precipitate was air-dried for 48 h and further dried in a static air oven at 373 K overnight. Finally the samples were calcined in air at 773 K for 12 h.

Hydrothermal Synthesis with Template (Method-C): In the preparation of sample **7C** by this method,[20] $ZrO(NO_3)_2{\cdot}xH_2O$, $Ce(NO_3)_3$, $Ni(NO_3)_2{\cdot}8H_2O$ and cetyltrimethylammonium bromide (CTABr) and tetramethylammonium hydroxide pentahydrate (TAOH) (Aldrich) were used as starting materials. The molar composition of the gel was as follows: 0.839Ni:0.085CeO_2:0.978ZrO_2:0.086$(NH_4)_2O$: 0.089$(CTMA)_2O$:0.155$(TMA)_2O$:40H_2O. The gel (pH $\approx$10) was allowed to crystallize at 383 K for 6 days, filtered, washed, and dried at 353 K overnight. The template was removed by calcining the samples at 823 K for 12 h.

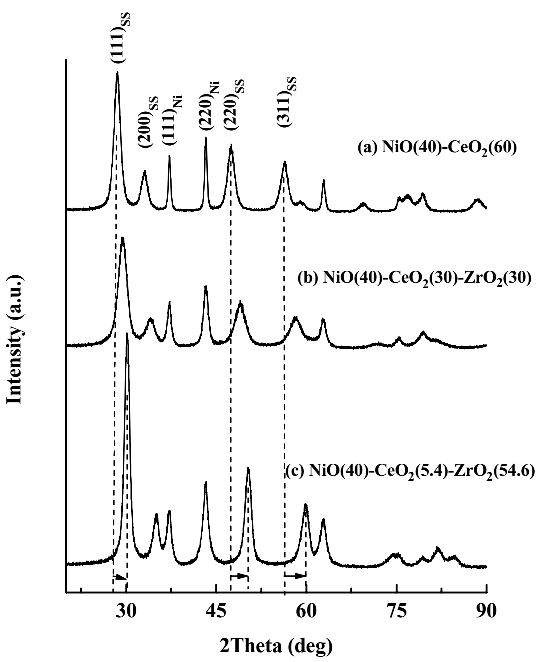

FIGURE 11.1. XRD patterns of NiO–CeO_2-ZrO_2 with varying Ce/Zr composition. Peaks marked as SS correspond to CeO_2–ZrO_2 crystallites and those denoted as Ni correspond to NiO crystallites.[22]

Coprecipitation Synthesis with Template (Method-D): In the preparation of sample **10D**, $Ni(NO_3)_2 \cdot 8H_2O$, $ZrOCl_2 \cdot 8H_2O$, and YCl_3(2) were dissolved in distilled water to get a clear solution. CTABr template was then added and the resulting solution was stirred for 30 min. Then, ammonia (70%; 10 mL diluted to 105 mL with distilled water) was added to get a white gelatinous precipitate. The pH was maintained at around 9. The contents were stirred for 1 h and the precipitate was aged for 16.5 h, then filtered and calcined at 773 K for 1 h in a static air oven.

11.2.1.2. Structural and Textural Properties of Ni–CeO_2(Y_2O_3)–ZrO_2

X-Ray Diffraction: ZrO_2 forms solid solutions with CeO_2 and Y_2O_3 (X-ray diffraction studies; Fig. 11.1) with a cubic, fluorite structure.[23] NiO is supported on CeO_2–ZrO_2 and CeO_2–Y_2O_3 solid solutions. A small amount of nickel substitution in CeO_2–ZrO_2 lattice, however, cannot be excluded (EPR studies; *vide infra*).

With a change in Ce/Zr composition, a marked shift (indicated by arrows in Fig. 11.1) of the XRD peaks (of CeO_2–ZrO_2 solid solutions) was observed. This shift corresponds to a change in the unit cell parameter (from 0.510 to 0.542 nm) as a consequence of the solid solution formation (Table 11.2). In the samples containing 5 wt.% or more nickel, a separate NiO phase (unit cell parameter = 0.591 nm) was detected, the concentration of which increased with the nickel content. The average crystallite size of CeO_2–ZrO_2 decreased with increasing NiO-content (Fig. 11.2a). The size of NiO crystallites also decreased from 10.4 to 7.3 nm with increasing Ni-content

TABLE 11.2. Physicochemical characteristics of stabilized zirconia-based catalysts[20,22]

Sample Nono.	Unit Cell Parameter (nm)	Average CeO_2/ZrO_2 Crystallite Size (XRD) (nm)	S_{BET} (m^2/g)	Pore Volume (mL/g)	Average Pore Diameter (Å)	NiO Crystallite Size (XRD) (nm)	Ni Dispersion (wt.%)
1A	0.526	5.9	84	–	–		–
2A	0.526	5.6	95	–	–		–
3A	0.526	5.1	95	–	–		–
4A	0.527	4.7	107	–	–	10.3	–
5A	0.527	4.7	89	–	–	10.4	–
6A	0.526	4.6	92	–	–	9.9	–
7A	0.510	7.9	86	–	–	7.3	–
7B	0.519	7.1	233	0.22	40	8.2	7.6
7C	0.519	5.5	272	0.19	29	21.4	–
8A	0.542	6.4	71	–	–	17.2	
9B	0.513	8.5	302	0.22	40		11
10D	0.512	5.1	148	0.34	68	21.3	18

in samples **4A–7A** (Table 11.2). Sample **8A** having no Zr has the largest NiO crystallites (17.2 nm) (Table 11.2). NiO peaks (denoted as Ni in Fig. 11.1) were narrower in sample **8A** (containing no Zr) than in **6A** and **7A** (containing Ce and Zr in 1 : 1 and 1 : 9 ratio, respectively) (see Fig. 11.1; compare trace (a) with traces (b) and (c)). For a particular NiO, composition (40 wt.%), in the catalysts prepared by different methods, there appears a linear relation between the crystallite sizes of NiO and the support oxide (Fig. 11.2b). The crystallite size of NiO also varies (from 7.3 to 17.2 nm) with the Ce/Zr ratio. Incorporation of Ce in ZrO_2 enhances NiO dispersion (Table 11.2).

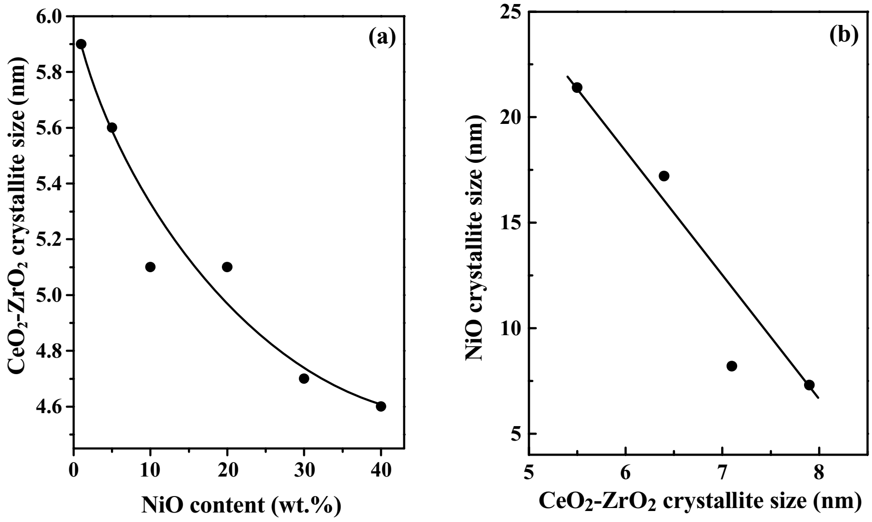

FIGURE 11.2. (a) Influence of NiO content on the crystallite size of CeO_2–ZrO_2. (b) Correlation of crystallite size of CeO_2–ZrO_2 with that of NiO in samples containing 40 wt.% NiO and prepared by different methods.

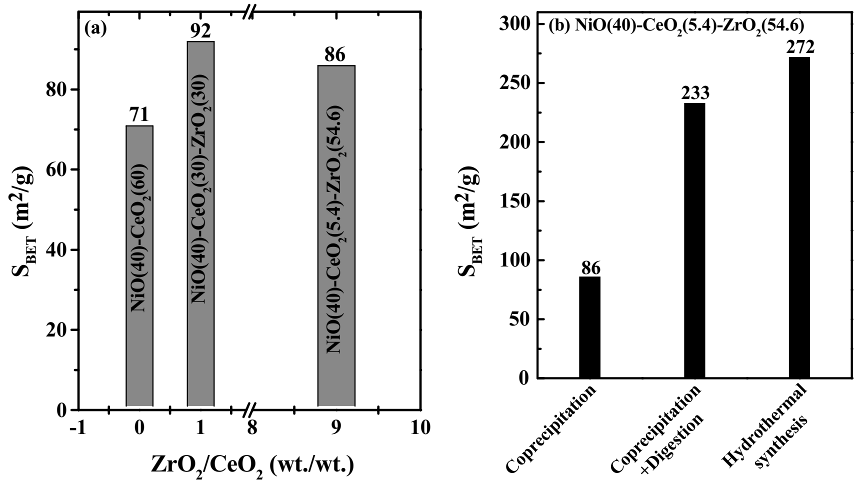

FIGURE 11.3. Influence of (a) ZrO_2/CeO_2 composition and (b) a method of preparation on the specific surface area (S_{BET}) of CeO_2–ZrO_2 crystallites.

Surface Area: Our methods of preparation yielded CeO_2/ZrO_2 composites with a large specific surface area, S_{BET} (Table 11.2). Samples prepared with the template have a lower crystallite size and higher surface area than those prepared without the template. The presence of ZrO_2 led to an increase in the surface area (Fig. 11.3a). Further, the method of preparation affects S_{BET} (Fig. 11.3b). NiO(40)–CeO_2(5.4)–ZrO_2(54.6) prepared by hydrothermal synthesis with template (method C) has the highest S_{BET}. Hence, there exists an interdependency of the crystallite sizes of Ni and Ce/Zr with their composition and method of preparation (Fig. 11.2).

The NiO phase could be reduced to metallic Ni by hydrogen treatment (723 K, 1 h). The crystallite size of Ni metal (estimated from XRD pattern of the reduced sample) is similar to that of the NiO in the unreduced sample (e.g., for **7B**, the Ni metal crystallite size is 8.2 nm). The textural characterization studies reveal that for the samples prepared by coprecipitation + digestion and hydrothermal synthesis (methods B and C) the pore sizes are in the mesopore range (2.9 to 6.8 nm) (Table 11.2).

11.2.1.3. In Situ Spectroscopy—Electronic Structure and Redox Behavior of Nickel

X-ray Photoelectron Spectroscopy: Table 11.3 lists the X-ray photoelectron spectroscopy (XPS) parameters. The main and satellite lines of Ni $2p_{3/2}$ and $2p_{1/2}$ were observed at about 857 and 876 eV, respectively. Zr $3d_{5/2}$ and $3d_{3/2}$ lines were observed at 182.2 and 184.6 eV, respectively. The lines corresponding to Ce appeared in the range of 882 to 918 eV. The spectral parameters are consistent with a +2 oxidation state for Ni and +4 oxidation state for Zr and Ce. Samples reduced in hydrogen (at 723 K for 1 h) showed a low BE feature close to 853 eV attributable to Ni metal.[29] Figure 11.4 depicts the spectra of NiO(40)–CeO_2(6)–ZrO_2(54) (**7B**)

TABLE 11.3. XPS parameters of nickel-containing Y_2O_3–ZrO_2 and CeO_2–ZrO_2 samples[20]

	Binding Energy (eV)		Ni/Zr Ratio	
Sample No.	Ni ($2p_{3/2}$)	Zr ($3d_{5/2}$)	Surface	Bulk
7B	855.2	182.2	5.35	0.8
7B (reduced)	855.2, 853.0	182.2	2.64	0.8
7C	854.9	182.6	15.9	0.8
9B	855.0	182.2	2.66	0.8
9B (reduced)	855.8, 853.2	181.9	2.66	0.8
10D	855.3	181.8	2.16	0.4

and NiO(40)–Y_2O_3(6)–ZrO_2(54) (**9B**) before and after reduction with hydrogen. The spectra reveal that the extent of Ni^{2+} reduction to Ni metal is more in **7B** than in **9B** suggesting that Ce promotes nickel reduction in **7B**. Sample **7C** (prepared by the hydrothermal synthesis method with template) is more surface-enriched in nickel than **7B** (prepared by coprecipitation followed by digestion). While the spectrum of Ni in **7C** is typical of a NiO phase segregated on the surface of ceria-zirconia, that of **7B** corresponds to a composite oxide phase. Table 11.3 reveals that among the four-nickel samples (**7B**, **7C**, **9B,** and **10D**), the Ni surface area is more in the ceria-containing than in the yttria-containing samples. The surface Zr concentration is lower in **7C** than in the other samples perhaps due to nickel oxide segregation on the surface in the former.

DRIFT-IR Spectroscopy—Study of Surface Hydroxyl Groups: DRIFT-IR spectroscopy at 298 K of self-supported wafers in the region 3500 to 3900 cm^{-1} indicated the presence of four different types of terminal and bridged hydroxyl groups

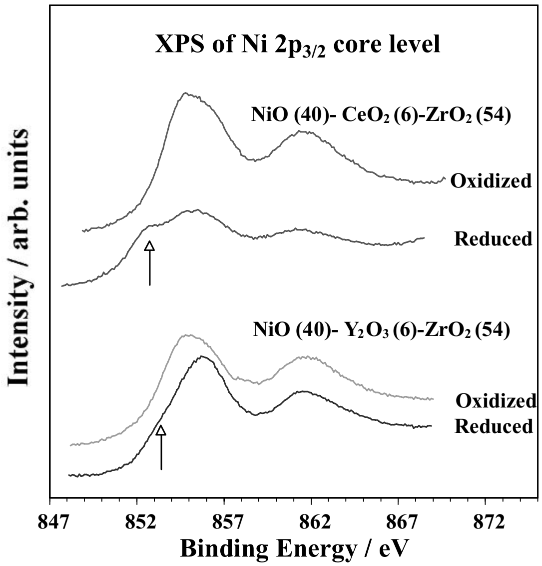

FIGURE 11.4. Influence of support on the reduction of NiO.

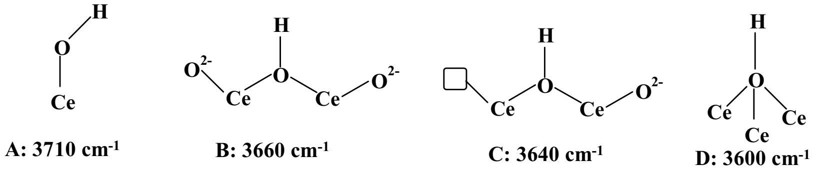

SCHEME 11.1. Surface OH groups

(Scheme 11.1).[30] IR peak positions of different hydroxyl groups for CeO_2 sample are also given in Scheme 11.1. After passing hydrogen and then water at 873 K, the sample was evacuated and the IR spectrum was measured. The intensity of the OH groups on different supports increased in the order: Al_2O_3 < CeO_2–ZrO_2/Al_2O_3 < NiO(20)–Al_2O_3(20)–CeO_2(6)–ZrO_2(54). Significant amount of surface OH groups were present under reaction conditions. In addition to increasing the total concentration of OH groups on ceria, ZrO_2 also increases the *relative* concentration of the mono-coordinated, basic OH groups. The availability of higher amount of OH groups during the reaction conditions is, perhaps, the cause for the lower deactivation of the CeO_2–ZrO_2 catalysts.

Diffuse Reflectance UV–Visible Spectroscopy: Samples **1A–6A** (activated at 473 K) showed an intense, asymmetric diffuse reflectance UV band with a maximum at 240 nm and a shoulder around 310 nm. The former dominated in samples with higher Ni-content, indicating its origin from O→Ni charge transitions.[31] The shoulder is due to O → Ce/Zr transitions.[32,33] Additionally, weak d–d bands of octahedrally coordinated Ni^{2+} were also observed at 724, 649, and 400 nm.[31,34] The intensity of these bands increased with increasing Ni-content. The Ce/Zr ratio considerably affected the DRUV-visible spectra (Fig. 11.5). Sample **8A** (activated at 473 K) showed an additional, asymmetric broad band in the region 400 to 650 nm attributable to the d–d transitions of Ni^{+} ions.[34] The DRUV–VIS data also support the conclusions drawn earlier from XPS, namely, that ceria promotes the reduction of NiO to Ni metal. On treating with dry H_2, the intensity of the charge transfer band was reduced considerably and the d–d bands disappeared. The samples became black and the reflectance was considerably lower. A broad absorption beyond 350 nm appeared. All these features suggest that Ni^{2+} ions in the original samples were reduced to metallic nickel.[35,36]

EPR Spectroscopy-Defect Sites and Oxygen—Centered Radicals: EPR spectra of pure CeO_2 reduced with dry hydrogen revealed the presence of two types of paramagnetic species, A, due to Ce^{3+} ($g_{\perp} = 1.965$ and $g_{||} = 1.940$) and B, due to $O_2^{-\bullet}$ ions[23–25] ($g_1 = 2.030$, $g_2 = 2.016$, and $g_3 = 2.011$), the concentration of which depended on the reduction temperature (T_r). Pure ZrO_2 did not form these paramagnetic species when reduced in hydrogen. CeO_2–ZrO_2 behaved in a manner similar to pure CeO_2. Upon reoxidation by exposure to air at 298 K, the signals due to species A disappeared and of B decreased and broadened. Specie A and B could be generated, repeatedly, in several cycles indicating the facile redox behavior of CeO_2 and CeO_2–ZrO_2 supports.

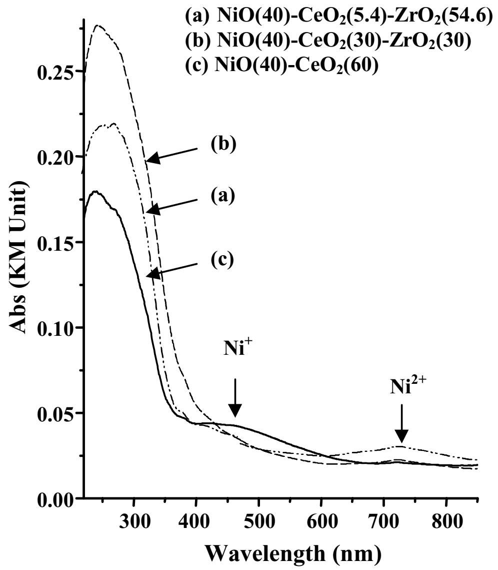

FIGURE 11.5. Diffuse reflectance UV–visible spectra of NiO–CeO_2–ZrO_2.[22]

Temperature-programmed reduction experiments also indicated that the reduction of ceria is facilitated in the presence of zirconia. The reduction of ceria occurred at 620 K in CeO_2–ZrO_2 compared to 658 K in CeO_2. In NiO-containing samples, signals due to O^- ($g = 2.008$) and a broad feature due to Ni^+ species[37,38] ($g = 2.21$ for **1A–6A** and 2.36 for **8A**) were observed additionally. Interestingly, sample **7A** containing less CeO_2 did not show this signal, indicating that CeO_2 promotes the reduction. Samples **7C** and **10D,** prepared with a template showed broader features ($g = 2.24$, $\Delta H_{pp} = 907$ G for **7C** and $g = 2.16$, $\Delta H_{pp} = 1140$ G for **10D**) than **7B** or **9B** prepared without a template ($g = 2.22$, $\Delta H_{pp} = 352$ G for **7B** and $g = 2.22$, $\Delta H_{pp} = 436$ G for **9B**). Nickel ions are probably better dispersed in materials prepared with template (**7C** and **10D**) and the signals are dipolar-broadened.

EPR of Ni-Reduction with Hydrogen, Hydrocarbons, and Alcohols: Sample **1A,** reduced in dry hydrogen (for 1 h at elevated temperatures) showed two types of Ni signals: Species I was characterized by sharp signals at $g_{||} = 2.08$ and $g_{\perp} = 2.009$ whose intensity did not change with the reduction temperature (T_r). Species II was characterized by a broad signal ($\Delta H_{pp} = 340$ G) at $g = 2.20$ whose intensity increased with the reduction temperature (Fig. 11.6a). Sample **2A** when reduced in hydrogen showed three types of species (species III in addition to species I and II observed in sample **1A**). The spectra of **2A** at different reduction temperatures are shown in Fig. 11.6b. Species III was characterized by a very broad signal on which the signals due to species I and II were superimposed. Species I was observed at 573 to 798 K, species II (with significant intensity) was seen above 748 K and species III from 673 K onward. The signal intensity of III did not change significantly beyond 773 K, but that of II increased continuously with the reduction temperature.

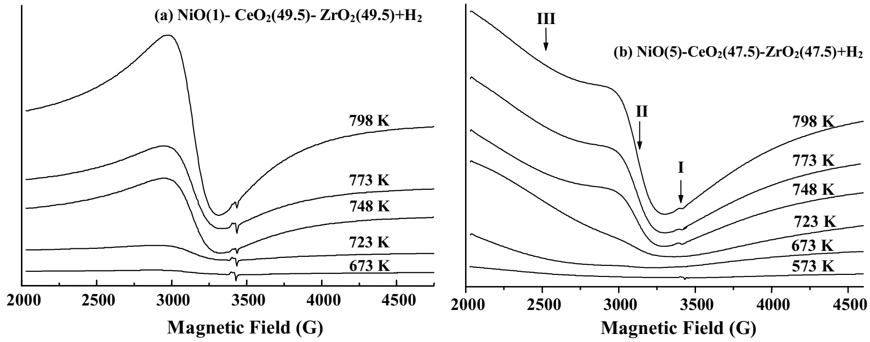

FIGURE 11.6. EPR spectra of (a) NiO(1)–CeO_2(49.5)–ZrO_2(49.5) and (b) NiO(5)–CeO_2(47.5)–ZrO_2(47.5) reduced in hydrogen at different temperatures. Signals due to species I, II, and III are marked.[22]

The spectra of samples **6A, 7A**, and **8A** (containing 40 wt.% NiO) reduced in hydrogen were mainly due to species III. Species II was not present. Species I was present, but the signals were weak and masked by the intense, broad signal of species III. The CeO_2–ZrO_2 composition affected both the signal position (g value) and the line width at $T_r = 798$ K; for example: Sample 6A – g value = 3.1 (line width = 1660 G), 7A – 3.1 (2130 G), and 8A – 2.4 (1850 G) respectively. The shift in the EPR signal with T_r was smaller (100 G) in sample **7A** (containing more ZrO_2 than CeO_2) than in **6A** (320 G; Ce:Zr = 1:1) and **8A** (600 G; containing only CeO_2). Reduction of Ni (species III) occurred at lower temperatures (573 K) in CeO_2 containing samples. In other words, CeO_2 facilitated the reduction of Ni.

When Ce^{4+} (coordination number = 8 in the CeO_2 lattice) is substituted for a six-coordinated Zr^{4+} ion in the ZrO_2 lattice, defect centers are created. Also, doping ceria with zirconia promotes formation of Ce^{3+} ions due to the smaller size of Zr^{4+} cations that take part in removing the strain associated with the increase of ionic size accompanying the Ce^{4+} to Ce^{3+} transition. These defects in solid CeO_2–ZrO_2 superlattice and the redox properties of Ce and Zr ions at temperatures above 873 K are responsible for the superior oxygen storage capacity and the ion transport properties. EPR spectroscopy has identified three types of paramagnetic defects in CeO_2–ZrO_2 oxides viz., electrons, "quasi-free" or trapped in anion vacancies (signals at $g = 1.965$ and 1.943), O^- ions (signal at $g = 2.008$) and O_2^- ions (signals at $g = 2.083$, 2.033, and 2.001).[23–25,37] These species arise by the following interactions:

$$Ce^{3+} + O_2 \rightarrow Ce^{4+}(O_2^{-\bullet})$$
$$Ni^{+} + O_2 \rightarrow Ni^{2+}(O_2^{-\bullet})$$
$$Ce^{4+} + O^{2-} \rightarrow Ce^{3+}(O^{-})$$

The oxygen storage capacity of CeO_2–ZrO_2 catalysts was correlated in the past to the concentration of these oxide ion species.[23–25] Samples **8A** and **6A** showed signals at $g = 2.36$ and 2.21, respectively, due to a small amount of Ni substituted in the

CeO_2–ZrO_2 solid lattice. The latter is reduced to a Ni^+ species:

$$Ce^{4+}\text{–}O^{2-}\text{–}Zr^{4+} \leftrightarrow Ce^{3+}\text{–}O^{-}\text{–}Zr^{4+}$$
$$Ce^{3+} + Ni^{2+} \rightarrow Ce^{4+} + Ni^{+}$$
$$Ni^{+}_{surf} + O_2 \rightarrow Ni(O_2^{-\bullet})$$

Part of the Ni^+ ions, subsequently, react with oxygen and form Ni^{2+} ($O_2^{-\bullet}$) species.

The reduction experiments have revealed at least three types of Ni-species in our NiO–CeO_2–ZrO_2 samples: (I) Ni substituted in the lattice forming Ni($O_2^{-\bullet}$) ions (signals at $g_{||} = 2.028$ and $g_{\perp} = 2.009$),[37] (II) nanosize crystallites of NiO, forming superparamagnetic metallic Ni ($g = 2.195$; linewidth = 340 G)[39], and (III) larger particles of NiO containing ferromagnetic Ni.[40] Sample **1** (1 wt.% Ni) contained species I and II, sample **2** (5 wt.% Ni) contained all the three species, while samples **6A–8A** (40 wt.% Ni) contained species I and III. The reducibility of these species decreased in the order: I > III > II. Reduction experiments at steam reforming conditions in the presence of both H_2 and hydrocarbons have shown an increased reducibility of nickel ions in the presence of hydrocarbons and long-chain alcohol.

11.2.1.4. Catalytic Activity of NiO–CeO2–ZrO2—Influence of Ni Crystallite Size and Support Composition

Hydrogenation of Benzene: Benzene hydrogenation is a "facile" reaction and is indicative of the number of surface Ni atoms available for catalysis. The activity of the catalysts in the benzene hydrogenation reaction was investigated at 453 K.[22] Cyclohexane was the only product of the reaction. Benzene conversion (Table 11.4) increased with increasing Ni content (samples **2A–4A**) up to 20 wt.%.

A marked effect of the CeO_2/ZrO_2 composition (in samples containing 40 wt.% NiO) on the catalytic activity was noticed. The catalysts with Ce:Zr = 1:1 (**6A**) were not only more active (than **7A** and **8A**) but were also stable during the reaction. Sample **8A** containing no zirconia in the support showed a low activity. The NiO crystallite size (Table 11.2) in these compositions varied in the order: **7A** < **6A** < **8A**. It may be recalled that on ceria-based catalysts the crystallite size of nickel metal was similar to that of NiO. The higher activity for **6A** than **7A** indicates that in addition to accessibility of

TABLE 11.4. Benzene hydrogenation[a]

Sample No.	Catalyst	Benzene Conversion (wt.%)[b]	TOF[c]
2A	NiO(5)–CeO_2(47.5)–ZrO_2(47.5)	0.6	0.9
3A	NiO(10)–CeO_2(45)–ZrO_2(45)	0.9	0.7
4A	NiO(20)–CeO_2(40)–ZrO_2(40)	9.2	3.5
6A	NiO(40)–CeO_2(30)–ZrO_2(30)	18.1	3.5
7A	NiO(40)–CeO_2(5.4)–ZrO_2(54.6)	11.4	2.2
8A	NiO(40)–CeO_2(60)	8.1	1.6

[a] Reaction conditions: catalyst = 1 g, benzene : H_2 = 1:4, temperature = 453 K, time = 1 h.
[b] Reaction with thiophene (20 ppm)-containing benzene feed.
[c] TOF = turnover frequency (number of moles of benzene converted per mole of Ni per hour).

TABLE 11.5. Steam reforming of n-octane

Catalyst	H_2 Yield (Relative)	$\%H_2$ (v/v) in Dry Gas	CO/CO_2
10D	1.0	46	2.5
7B	1.0	30	1.2
7C	7.7	85	14

nickel, the reducibility–reoxidizability as well as the oxygen storage-release capacity of the support plays crucial roles determining catalytic activity.

Steam Reforming of n-Decane: Sample **7C**, prepared by hydrothermal synthesis in the presence of CTABr and TAOH templates, has the highest catalytic activity (H_2 yield) in the steam reforming of n-decane (Table 11.5). Even though samples **7B** and **7C** have identical bulk composition (Table 11.1), a similar surface area, and porosities (Table 11.2), accessible nickel metal on the surface is much higher on **7C** (Table 11.3) accounting for the higher catalytic activity of the latter. Template molecules present during the synthesis of $NiO–CeO_2–ZrO_2$ reduce the particle size and enhance the accessibility of nickel. It is interesting to note that the concentration of CO_2 (produced by the water gas shift) follows the reverse trend. The crystallites of Ni in **7C** (larger than those in **7B)** are less active, as expected, in the water–gas shift reactions. **10D** having a smaller concentration of surface nickel is also less active. Consequently, catalyst deactivation decreased in the order: **10D** > **7B** > **7C**.

Steam Reforming of Ethanol: Even though all the samples containing 20 wt.% or above of Ni exhibited similar activity and selectivity (Table 11.6), their stability over a 500 h duration run varied; sample **6A**, with 40% Ni and a CeO_2/ZrO_2 ratio of 1 was the most stable. The Ce/Zr ratio has a marked effect on the catalytic *stability* of these materials.

11.2.2. Au and Au–Pt Bimetallic Nanoparticles in MCM-41 for Preferential Oxidation of CO in the Presence of H_2

Supported noble metals such as Au and Pt are active for CO oxidation. Since Pt-based catalysts operate at relatively higher reaction temperatures (403 to 473 K), they are not very selective for CO oxidation in hydrogen-rich streams.[41] Au catalysts,

TABLE 11.6. Steam reforming of ethanol[a]

Sample No.	Catalyst	H_2 in Dry Gas (vol.%)	CH_4 (vol.%)	CO (vol.%)	CO_2 (vol.%)
8A	$NiO(40)–CeO_2(60)$	67.9	7.4	3.0	21.7
7A	$NiO(40)–CeO_2(5.4)–ZrO_2(54.6)$	68.0	6.7	3.2	22.1
6A	$NiO(40)–CeO_2(30)–ZrO_2(30)$	68.0	6.5	2.9	22.6
5A	$NiO(30)–CeO_2(35)–ZrO_2(35)$	69.0	6.0	3.7	21.3
4A	$NiO(20)–CeO_2(40)–ZrO_2(40)$	67.5	6.5	3.7	22.3

[a] Reaction conditions: catalyst = 0.677 g, feed—ethanol:water = 1:8 (mol), LHSV = 6; temperature = 823 K, time on stream = 5 h. Conversion of ethanol was above 95% in all cases.

on the other hand, are reported to be active at very low temperatures (at or below room temperatures) and, hence, selectively oxidize CO without consuming much hydrogen in the process.[42] However, the Au loadings (~5%) in these catalysts are high. Any reduction in this amount brought about by better dispersion is welcome. There are three factors that govern the performance of the gold catalysts, viz., (1) the type of support, (2) the size of the gold particles, and (3) the strength of interaction between the gold particle and the support.[43,44] It is reported that gold catalysts are active at lower temperatures only if they are supported on reducible oxide supports such as the oxides of Mn, Ti, and Fe.[45,46] While gold catalysts, supported on the above metal oxides, show good activity and selectivity toward CO oxidation, they deactivate after a few hours in gas streams that contain CO_2. This deactivation is attributed to the build-up of surface carbonate species on the basic oxide supports. We have used amine-functionalized MCM-41 material in the entrapment of $PtCl_6^-$ and $AuCl_4^-$ anions via electrostatic interactions with the pendant amine groups.[47] Reduction of the above anions, *in situ* at room temperature, resulted in the formation of mono- as well as bimetallic nanoparticles of well-defined dimensions. These catalysts show excellent catalytic activity in the preferential oxidation of CO_2.[47]

11.2.2.1. Synthesis of Au, Pt, and Au–Pt Bimetallic Nanoparticles in MCM-41. For preparing Au, Pt, and Au–Pt nanoclusters, freshly calcined MCM-41 (surface area 1100 m^2/g) was refluxed with 3-aminopropyl triethoxy silane (APTES) in toluene for 5 h. It was filtered and washed with toluene and diethyl ether to remove any adsorbed APTES and was vacuum dried. This amine-functionalized MCM-41 was suspended in a solution of (10^{-4} M) $HAuCl_4$ and H_2PtCl_6 for 12 h. The solid was then filtered, washed, and vacuum dried. These samples were then reduced, to form nanoparticles, using 10^{-4} M $NaBH_4$ solutions. The catalyst compositions with total metal contents (wt.% of MCM-41 given in parentheses) are as follows: Au–MCM-41 (0.081), Pt–MCM-41 (0.098), Au_1Pt_{19}–MCM-41 (0.15), Au_1Pt_5–MCM-41 (0.17), AuPt–MCM-41 (0.060), and $Au_{22}Pt$–MCM-41 (0.090). The nanoscopic size (2 to 4 nm) of the metal particles was confirmed by transmission electron microscopy. A representative TEM micrograph of Au_1Pt_{19}–MCM-41 catalyst is shown in Fig. 11.7.

11.2.2.2. Preferential Catalytic Oxidation of CO. CO oxidation experiments ($O_2/CO = 1$) were conducted in a simulated gas stream of composition: CO (9600 ppm) + H_2 (73.36 vol.%) + CO_2 (23.75 vol.%) + CH_4 (1.93 vol.%) (Table 11.7). The Pt catalyst is more active but less selective. The catalysts that contain more Pt were more active. A combination of Pt with Au forming a bimetallic catalyst enables preferential CO oxidation. It should be noted that the Pt–Au–MCM-41 catalysts are not deactivated in CO_2.

11.2.3. Pt- and Pd-TS-1 for Selective Oxidation

Titanosilicates molecular sieves, especially TS-1, have been widely studied for the selective oxidation of a variety of organic substrates, using aqueous H_2O_2.[48–50] Recently, there have been attempts to substitute aqueous H_2O_2 by a mixture of H_2 and O_2 in the presence of metals such as Pd, Pt, Au, etc.[51–57] Selectivities of 99% for propylene oxide formation from propylene were observed by Haruta and co-workers[56] over Au-containing catalysts. We had also found that the epoxide *selectivity* in the epoxidation

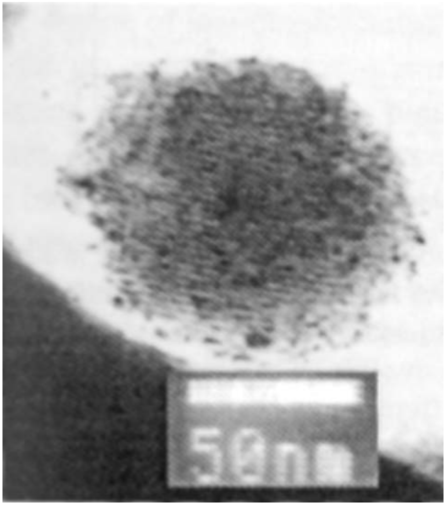

FIGURE 11.7. Transmission electron micrograph of Au–Pt bimetallic nanocatalyst Au_1Pt_{19}–MCM-41.[47]

of allyl alcohol over Pd-TS-1 is higher when using ($H_2 + O_2$) than H_2O_2.[58] However, the observed catalytic *activities* were much lower. The catalytic activity was dependent on the amount of Pd. Apparently the activity is dependent predominantly on the formation of H_2O_2 from H_2 and O_2 over the metal centers; the epoxidation of the substrate by the H_2O_2 formed *in situ* proceeds rapidly and almost quantitatively. Efforts should, hence, be made to enhance the yield of H_2O_2 from H_2 and O_2 over the metals in metal–TS-1 systems. Reactive oxygen species (superoxides, hydroperoxide, and peroxides of Ti) are generated during the oxidation process. Their type and concentration influence the activity and selectivity of the titanosilicate molecular sieves. Pt and Pd influence the reducibility of Ti^{4+} ions and the type of oxo-titanium species formed in the presence of H_2O_2 or $H_2 + O_2$.[58,59]

11.2.3.1. Preparation of Titanosilicate Molecular Sieves. TS-1 and TiMCM-41 were prepared according to the reported procedures.[58] In the preparation of Pd(n)-TS-1 (n refers to the Pd content in wt.%),[58] an aqueous solution (15 mL) containing the required amounts of $[Pd(NH_3)_4]Cl_2{\cdot}H_2O$ or $Pd(CH_3COO)_2$ (Aldrich) was added

TABLE 11.7. Preferential CO oxidation over Au–Pt bimetallic catalysts[47]

Catalyst	Reaction Temperature (K)	Gas Composition			
		CO (ppm)	H_2 (vol.%)	CO_2 (vol.%)	CH_4 (vol.%)
Au–MCM-41	423	4200	73.07	24.53	1.98
Pt–MCM-41	423	0.9	71.30	26.69	2.01
Au_1Pt_{19}–MCM-41	353	0.3	71.76	26.18	2.05
Au_1Pt_5–MCM-41	423	157	71.55	26.43	2.02
AuPt–MCM-41	473	169	70.90	27.00	2.09
$Au_{22}Pt$–MCM-41	448	3940	72.26	25.25	2.10

to TS-1 (3 g) taken in a 50 mL round bottom flask. The slurry was stirred at 353 K for 20 to 24 h under N_2 atmosphere. The contents were then dried over a rotavapor (338 K) and then in a vacuum oven (348 K) for 15 h. The resultant solids were heated in nitrogen flow at 423 K for 2 h. Pt(0.015)-TS-1 was prepared similarly, except that $[Pt(NH_3)_4]Cl_2 \cdot H_2O$ was used.

11.2.3.2. EPR Studies of Oxo-Titanium Species. A known quantity of titanosilicate (40 mg) was taken in 4.5 mm o.d. Suprasil quartz EPR tubes. Aqueous hydrogen peroxide (50%, 0.1 mL) was added to it in amounts adequate to wet the solid completely. In the experiments on solvent effects, the titanosilicate samples were initially activated at 373 K in static air, cooled to 298 K and then soaked in the desired solvent (0.4 mL). H_2O_2 was added, and the EPR spectra were recorded. In the experiments with urea–hydrogen peroxide adducts (UHP), 50 mg of titanosilicate was physically mixed (without grinding) with 100 mg of UHP. In the experiments involving solvents, this mixture was then exposed to solvent vapor (water, methanol, acetone, and acetonitrile) for 5 to 15 min before recording the spectra. In the experiments with $H_2 + O_2$, the titanosilicates (40 mg) were initially evacuated at 423 K, for 2 h. Then the samples were reacted with dry hydrogen (20 mL/min), at 323 to 343 K, for 4 h and subsequently with molecular oxygen (20 mL/min) for 15 min. The sample temperature was quenched to 80 K and the EPR spectra were recorded.

In Pd(n)-TS-1, part of the Pd is in +2 oxidation state and the remaining in the zero oxidation state. The samples were EPR silent, consistent with the +4 oxidation state of Ti in the silicate structures. Upon interaction with H_2O_2 or UHP, the color of TS-1 and TiMCM-41 changed from white to yellow. The samples became paramagnetic showing sharp EPR signals attributable to Ti(IV)-superoxo radical species ($Ti(O_2^{-\bullet})$). Spectral simulations revealed the presence of two types of $Ti(O_2^{-\bullet})$ species, A and B (A being preponderant) in TS-1 in the presence of H_2O_2. Only species B was present in TiMCM-41. UHP on interaction with TS-1 generated four types of $Ti(O_2^{-\bullet})$ species, A′, A, B, and C. Only species B was detected in the TiMCM-41 + UHP system. The g-values of the various $Ti(O_2^{-\bullet})$ species differ mainly in their g_z parameter. At least six different $Ti(O_2^{-\bullet})$ species (A, A′, A″, B, B′, and C) were detected in Pd(n)-TS-1. The Ti sites adjacent to Pd ions are magnetically different than the other Ti ions accounting for the greater variety of $Ti(O_2^{-\bullet})$ species.

In the absence of H_2, exposure of TS-1 or TiMCM-41 or Pd-TS-1 or Pt-TS-1 to O_2 alone does not generate the superoxide species. When Pd(Pt)-TS-1 samples are contacted with $H_2 + O_2$, Ti^{4+} is reduced to Ti^{3+} by H_2.[59] The Ti^{3+} ion generates $Ti(O_2^{-\bullet})$ species on interaction with O_2. The EPR signals due to Ti^{3+} and $Ti(O_2^{-\bullet})$ (Fig. 11.8) are well separated and can be differentiated. This reduction and reoxidation of Ti ions which requires 673 K or above in TS-1 is facilitated by Pd or Pt even at 323 K (Fig. 11.8, compare traces I and (d)). The superoxo species generated are more of A and A′ type on the Pd- and Pt-containing TS-1. The extent of Ti reduction and $Ti(O_2^{-\bullet})$ formation depends on the Pd content, the concentration of the paramagnetic Ti-oxo species reaching maximal values of 2 (wt.%) Pd (Fig. 11.9).

In situ EPR experiments in the presence of different substrates (allyl alcohol, benzene, phenol, or toluene) reveal that type A species is involved in epoxidation reactions. Species B is more active than A in ring hydroxylation reactions. A comparison of the toluene results with those of phenol/benzene suggests that while species B is involved in ring hydroxylations, the A-type species are possibly involved in

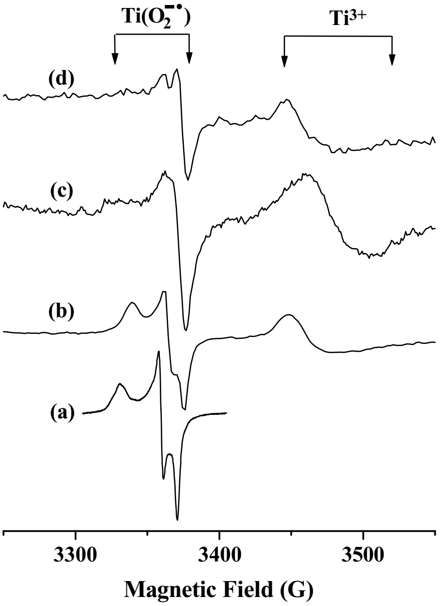

FIGURE 11.8. EPR spectra of $Ti(O_2^{-\bullet})$ and Ti^{3+} ions at 80 K. (a) Pd(2)-TS-1 + H_2O_2, (b) Pt(0.015)-TS-1 + H_2 + O_2 (treated at 673 K), (c) Pd(2)-TS-1 + H_2 + O_2 (treated at 323 K) and (d) TS-1 + H_2 + O_2 (treated at 673 K). For clarity curves (c) and (d) are shown at four and five times the actual gain. Spectral regions corresponding to $Ti(O_2^{-\bullet})$ and Ti^{3+} ions are marked.[58]

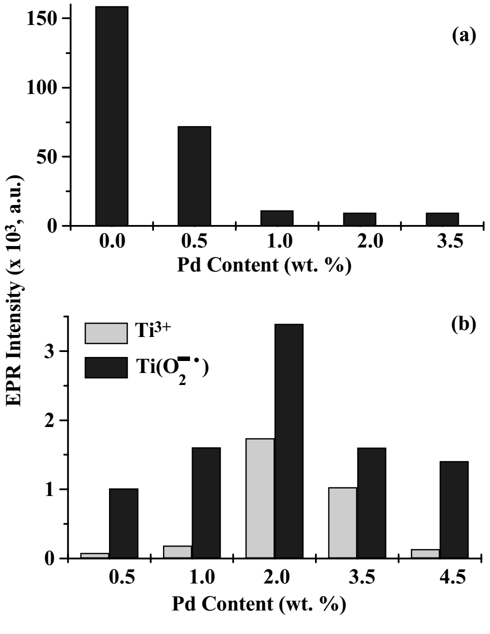

FIGURE 11.9. (a) EPR spectral intensity of $Ti(O_2^{-\bullet})$ ions as a function of Pd content in Pd(n)-TS-1 samples on reaction with H_2O_2. (b) EPR spectral intensity of Ti^{3+} and $Ti(O_2^{-\bullet})$ ions as a function of Pd content in Pd(n)-TS-1 reacted with H_2 + O_2.[58]

TABLE 11.8. Epoxidation of allyl alcohol over TS-1 and Pd(n)-TS-1 catalysts[a]

Catalyst	Oxidant	TOF[b]	H_2O_2 Efficiency (%)	Conversion (wt.%)	Epoxide Selectivity (wt.%)
TS-1	H_2O_2	15.3	42.8	77.0	96.1
Pd(0.5)-TS-1	H_2O_2	12.3	34.2	61.5	95.6
Pd(2)-TS-1	H_2O_2	10.5	28.8	51.7	90.4
Pd(3.5)-TS-1	H_2O_2	7.6	20.7	37.1	82.8
Pd(4.5)-TS-1	H_2O_2	6.2	16.7	30.0	74.0
Pd(2)-TS-1	$H_2 + O_2$	2.1	—	10.5	99.0

[a] Reaction medium: catalyst (100 mg) + allyl alcohol (0.5 g) + acetone (10 g) + H_2O_2 (50%, 0.9 mL); temperature: 333 K; run time: 8 h.
[b] Turnover frequency (TOF): moles of allyl alcohol converted per mole of Ti per hour.

the side chain oxidation. The catalytic activity data using ($H_2 + O_2$) as the oxidant, over Pd(2)-TS-1 (Table 11.8) confirm the correlation between the epoxidation selectivity and the concentration of type A species. Higher epoxide selectivities were observed also in the TS-1+UHP system[60] where species A′ was predominant. Our *in situ* studies suggest that the different oxo species lead to different products. Allyl alchol conversions of 77% and epoxide selectivities of 96% were obtained over TS-1 catalysts at 333 K. Over Pd(n)-TS-1 catalysts, the conversion and selectivity decreased with increasing Pd-content (Table 11.8) consistent with the lower $Ti(O_2^{-\bullet})$ signal intensities at higher Pd content (Fig. 11.9a). Pd catalyzes the decomposition H_2O_2 into H_2O and O_2 and leads to lowered H_2O_2 efficiency for epoxidation. Even though, similar oxo species are formed over all the titanosilicates in the presence of either H_2O_2 or $H_2 + O_2$, their relative concentration determines the catalytic activity and selectivity. A schematic representation of the possible role of Pd is shown in Fig. 11.10.

11.3. SUPPORTED METAL OXIDES

11.3.1. CuO–CeO$_2$–ZrO$_2$ for Preferential Oxidation of CO

Typical effluents from steam/autothermal reforming followed by water gas shift reaction contain about 0.3 to 1.0% of CO in a large excess of H_2 (40 to 75%) and about 20 to 25% CO_2. CO levels, however, have to be reduced to below 100 and, preferably, below 10 ppm for use in PEM fuel cells.[61–63] Preferential oxidation of CO to CO_2 without simultaneously oxidizing H_2 to H_2O (PROX) is a major challenge. Some of the known catalysts, especially those based on Au, which were very active at very low temperatures (even below 373 K) exhibited activity decay in long-term studies probably due to the strong adsorption of CO_2 (an "acid gas") and H_2O on some of the basic oxides used as supports for Au.[64] On Pt-Al_2O_3, Korotkikh and Farrauto[65] reported that CO_2 does not affect CO oxidation; H_2O, however, decreased CO oxidation by about 10%. Hence, it is desirable to develop a catalyst, which does not get deactivated in CO_2 and H_2O and, at the same time, is active at low temperatures. CuO supported on CeO_2–ZrO_2 mixed oxide system exhibits good activity using a feed composition more representative of the feed to a PROX reactor in a PEM fuel cell.[66] The influence of the crystallite and particle size of cerium and zirconium oxides on the dispersion,

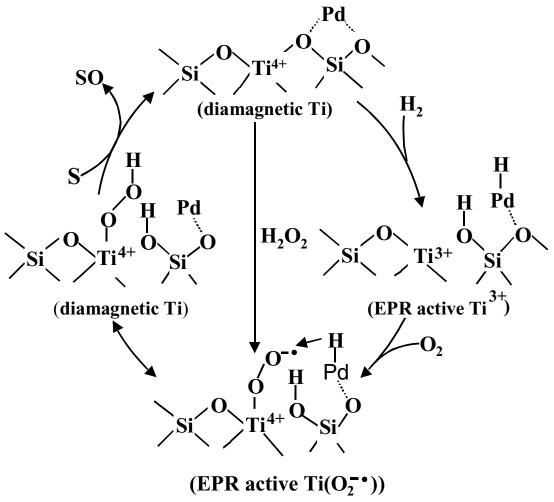

FIGURE 11.10. A role of Pd in the *in situ* generation of H_2O_2 from $H_2 + O_2$ over Pd(n)-TS-1 catalysts. S denotes the substrate and SO the oxygenated product.[58]

oxidation states, magnetic properties, and catalytic activity, in PROX reactions, of copper catalysts supported on the CeO_2–ZrO_2 support is described in this section.

Synthesis of Nanosize CuO–CeO_2–ZrO_2 Catalysts: A series of CuO–CeO_2, CuO–ZrO_2 and CuO–CeO_2–ZrO_2 with varying CuO concentrations (1 to 10 wt.%) were prepared by the coprecipitation followed by a digestion method (Table 11.9).[66] In a typical preparation of CuO(1 wt.%)–CeO_2(99 wt.%), 12.48 g of $Ce(NO_3)_3 \cdot 6H_2O$ was dissolved in 288 mL of distilled water and 0.152 g of $Cu(NO_3)_2 \cdot 3H_2O$ was dissolved in 6.3 mL of distilled water. These solutions were mixed together and added dropwise to a continuously stirred solution of KOH (0.1 M) taken in a 2-L round-bottom flask,

TABLE 11.9. Structural parameters (from XRD) and BET surface area of CuO–CeO_2–ZrO_2 composites[66]

Catalyst[a]	Unit Cell Parameter of the Support Oxide (nm)	Average Crystallite Size of the Support Oxide (nm)	Average Crystallite Size of CuO (nm)	S_{BET} (m^2/g)
CuO(1)–CeO_2(99)	0.547	6.6	–	117
CuO(5)–CeO_2(95)	0.545	7.8	–	129
CuO(10)–CeO_2(90)	0.542	8.4	4.1	124
CuO(1)–CeO_2(49.5)–ZrO_2(49.5)	0.532	4.4	–	168
CuO(5)–CeO_2(47.5)–ZrO_2(47.5)	0.533	4.2	–	148
CuO(10)–CeO_2(45)–ZrO_2(45)	0.530	3.8	3.2	136
CuO(1)–ZrO_2(99)	b	b	b	161
CuO(5)–ZrO_2(95)	b	b	b	153
CuO(10)–ZrO_2(90)	b	b	b	161

[a] Values in parentheses indicate composition in wt.%.
[b] XRD peaks were broad and hence the parameters could not be determined with precision.

placed in a heating mantle and fitted with a pH electrode, water-cooled condenser and burette containing additional 0.1 M KOH solution. During addition, the temperature of the flask was maintained at 353 K and pH 10. The cations were precipitated in the form of their hydroxides. The mixture was digested at 353 K for 3 h and then cooled to 298 K. The precipitate was separated and washed copiously with distilled water until all the potassium ions were removed. It was then dried in an air-oven, at 393 K, for 8 h. Later, the dried material was powdered and calcined in air, at 773 K, for 5 h, to get the final product. Potassium is an effective element for preferential oxidation of CO in H_2-rich streams.[67] The CuO–ZrO_2 catalysts were prepared in a similar manner. In a typical preparation of CuO(1 wt.%)–ZrO_2(99 wt%), 9.28 g of $ZrO(NO_3)_2 \times xH_2O$ dissolved in 400 mL distilled water and 0.152 g of $Cu(NO_3)_2 \cdot 3H_2O$ dissolved in 6.3 mL distilled water were used. In the preparation of CuO(1 wt%)–CeO_2(49.5 wt%)–ZrO_2(49.5 wt%), 6.24 g of $Ce(NO_3)_3{\cdot}6H_2O$ dissolved in 144 mL of distilled water, 4.64 g of $ZrO(NO_3)_2{\cdot}xH_2O$ dissolved in 200 mL of distilled water and 0.152 g of $Cu(NO_3)_2{\cdot}3H_2O$ dissolved in 6.3 mL of distilled water were used. The Ce:Zr ratio in these catalysts is 1:1 wt%.

Structural Characteristics of CuO–CeO_2–ZrO_2: No separate phase due to CuO or Cu_2O was detected, except in the samples with 10 wt.% CuO. The presence of zirconium decreased the crystallite size of ceria as well as that of CuO (Table 11.9). The crystallite size of ceria decreased from 8.4 (in CuO(10)–CeO_2(90)) to 3.8 nm (in CuO(10)–CeO_2(45)–ZrO_2(45)). The corresponding decrease for CuO was from 4.1 to 3.2 nm. Incorporation of CuO, in turn, influenced the crystallite size of the support ceria and ceria-zirconia, respectively. In the case of CuO–CeO_2–ZrO_2 samples, the crystallite size of the support decreased from 4.4 nm to 3.8 nm while in the case of CuO–CeO_2 samples, the crystallite size of CeO_2 *increased* from 4.9 to 8.4. S_{BET} values increased in the series: $CeO_2 < CeO_2–ZrO_2 < ZrO_2$ (Table 11.9). When CuO was also present, the CuO–CeO_2 samples showed a marked decrease in surface area (from 150 to 117 m^2/g). The decrease is not significant in CuO–CeO_2–ZrO_2 (Table 11.9). Zirconia incorporation in the support, hence, increases the surface area of the samples. A similar observation was found also in the case of NiO–CeO_2–ZrO_2 (Table 11.2 and Fig. 11.3a).

Temperature-Programmed Reduction: CuO(5)–ZrO_2(95) showed overlapping reduction peaks at 465 K and 450 K (Fig. 11.11), respectively. In ceria-containing CuO(5)–CeO_2(95), these peaks appeared at lower temperatures, 445 and 425 K, respectively (Fig. 11.11). In CuO(5)–CeO_2(47.5)–ZrO_2(47.5), they occurred at still lower temperatures, 435 and 398 K, respectively (Fig. 11.11). The reducibility of CuO increased in the order: $ZrO_2 < CeO_2 < CeO_2–ZrO_2$. The TPR of CuO supported on CeO_2 and ZrO_2 was investigated by several groups.[68–70] They observed CuO reduction peaks in the range 398 to 448 K and above 473 K. The former were attributed to dispersed copper oxide clusters, strongly interacting with the support while the latter (above 473 K) was assigned to discrete CuO particles. The TPR peaks (Fig. 11.11) reveal that the latter type of bulk CuO particles is not present in our catalysts.

Electronic Spectroscopy: CuO–CeO_2/ZrO_2 catalysts showed a broad, d–d band in the visible region. This band shifted from 780 (Cu^{2+} in six-fold coordination) to 680 nm (Cu^{2+} in four-fold coordination) with a change in the support from ZrO_2 to CeO_2–ZrO_2 to CeO_2, respectively.[71–73] A similar shift (from 800 to 763 nm in

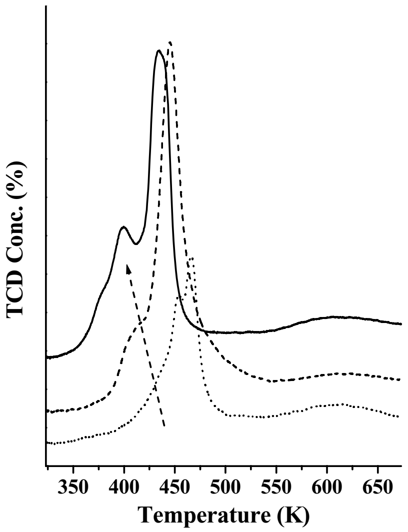

FIGURE 11.11. Temperature programmed reduction (hydrogen) profiles of $CuO(5)–ZrO_2(95)$ (· · · · ·), $CuO(5)–CeO_2(95)$ (- - - - -) and $CuO(5)–CeO_2(47.5)–ZrO_2(47.5)$ (—).[66]

$CuO–ZrO_2$, 768 to 645 nm in $CuO–CeO_2–ZrO_2$ and 670 to 650 nm in $CuO–CeO_2$) was observed with an increase (from 1 to 10 wt.%) in the CuO content indicating that the type of copper species in these catalysts is influenced by both the support and concentration.

EPR Spectroscopy: At least four types of paramagnetic copper species (I–IV) could be identified by EPR in $CuO(1)–CeO_2(99)$ (Fig. 11.12, curve a). Types I and II

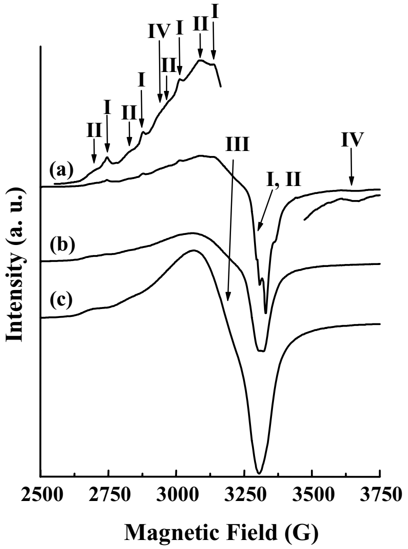

FIGURE 11.12. EPR spectra of CuO(1%) supported on (a) CeO_2, (b) $CeO_2–ZrO_2$, and (c) ZrO_2. Signals due to different copper species (I, II, III, and IV) are indicated.[66]

correspond to isolated, monomeric Cu^{2+} species characterized by axial spectra with resolved Cu hyperfine features in the parallel and perpendicular regions.[74,75] These species are different in their $g_{||}$ and $A_{||}(Cu)$ values (type 1: $g_{||} = 2.300$, $A_{||}(Cu) = 126.4$ G; type 2: $g_{||} = 2.339$, $A_{||}(Cu) = 124.8$ G). Their $g_{\perp}$ (2.049) and $A_{\perp}$ (Cu) (10.0 G) values are similar. The line width of species I is smaller than that of species II (curve a). The spin Hamiltonian parameters indicate that the geometry around Cu^{2+} is distorted octahedral. These species (I and II) are perhaps located in the lattice and surface sites of ceria crystallites, respectively.[74] Type III species characterized by a broad signal (line width = 210 G) centered at $g_{av} = 2.10$ is attributed to dipolar, interacting Cu^{2+} ions forming a nanosized two-dimensional structure.[74] The relative concentration of type III species increased with copper content. The visible band at 645 to 680 nm in the diffuse reflectance spectrum corresponds to this species. Type IV species showed two signals at 3017 and 3716 G corresponding to single-quantum, perpendicular transitions of Cu^{2+}–Cu^{2+} dimers at the surface.[75] The exchange coupling constant (J) for these dimers (type IV) was –52.5 cm^{-1} and the Cu–Cu separation was 3.4 Å.[75] If the two copper ions of the dimer were to occupy adjacent Ce^{4+} locations in the fluorite lattice, their Cu–Cu separation would have been 5.41 Å. It was, hence, proposed that these interacting, Cu^{2+}–Cu^{2+} dimers in copper oxo species are at the surface of ceria.[74,75]

CuO(1)–ZrO_2(99), on the other hand, contained only two types of Cu^{2+} species viz., isolated Cu^{2+} ions (II) and interacting Cu^{2+} ions (III) (Fig. 11.12, curve c). The spin Hamiltonian parameters of these species are different from CuO(1)–CeO_2(99). Unlike in CuO(1)–CeO_2(99) (Fig. 11.12, curve a), the perpendicular Cu-hyperfine features could not be resolved in CuO(1)–ZrO_2(99) (Fig. 11.12, curve c). Type III species of CuO–ZrO_2 showed a signal at $g_{av} = 2.12$.

CuO(1)–CeO_2(49.5)–ZrO_2(49.5) showed spectra (Fig. 11.12, curve b) intermediate in shape to that of CuO(1)–CeO_2(99) and CuO(1)–ZrO_2(99). Cu species, types I, II, and III were detected. Similar to CuO(1)–CeO_2(99), type I species of CuO(1)–CeO_2(49.5)–ZrO_2(49.5) showed resolved Cu-hyperfine features at parallel and perpendicular regions. Signals of CuO(1)–CeO_2(49.5)–ZrO_2(49.5) were broader. Cu^{2+}–Cu^{2+} dimers (type IV) could not be detected. Thus, different types and amounts of CuO species were present on CeO_2, ZrO_2, and CeO_2–ZrO_2.

The reducibility of CuO on various supports increased in the order: CuO–ZrO_2 < CuO–CeO_2 < CuO–CeO_2–ZrO_2 (Fig. 11.13). When CuO–CeO_2 and CuO–CeO_2–ZrO_2 were reduced at 573 K, almost all the copper was reduced. Reoxidation by exposing the samples to air regenerated the EPR spectrum of types I, II, and IV species. Type III species could not be regenerated. The reduction–reoxidation of types I, II, and IV species (isolated/dispersed copper) could be repeated several times. A similar observation was noted also on CeO_2–ZrO_2 supports. While 39.7% of total intensity could be regenerated upon reduction followed by reoxidation in CuO–CeO_2, it was only 31.4% in CuO–CeO_2–ZrO_2. Hence, the amount of reactive copper oxide that could be reduced and reoxidized is more on CeO_2 than on CeO_2–ZrO_2 support. The facile redox behavior and the abundance of the reactive copper species influence the CO oxidation activity of these catalysts (vide supra).

Magnetic Susceptibility: The support influences the dispersion and magnetic state of copper significantly. From the linear increase in magnetic susceptibility, it may be concluded that the concentration of isolated, noninteracting Cu^{2+} ion increases with the copper content in CeO_2–ZrO_2 (Fig. 11.14). The presence of Cu^{1+} and *interacting*

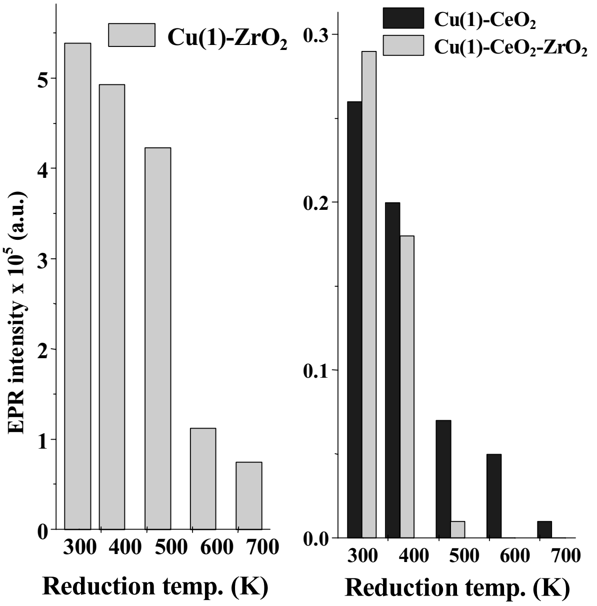

FIGURE 11.13. Variation of Cu^{2+} (EPR) signal intensity as a function of reduction temperature: Cu(1)–ZrO_2(99) (left panel); CuO(1)–CeO_2(99) and CuO(1)–CeO_2(49.5)–ZrO_2(49.5) (right panel).[66]

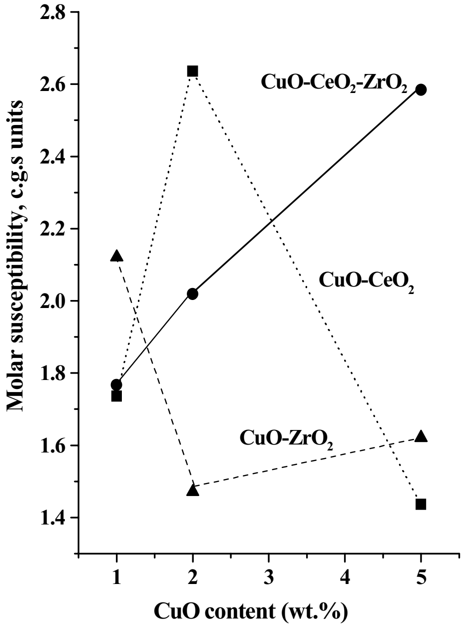

FIGURE 11.14. Magnetic susceptibility (χ_M) as a function of CuO content in CuO–CeO_2, CuO–ZrO_2 and CuO–CeO_2–ZrO_2.[66]

TABLE 11.10. Preferential oxidation of CO over $CuO–CeO_2–ZrO_2$ catalysts.[66] Reaction conditions: catalyst = 1.5 g, feed—H_2 (74.17%) + CO(0.49%) + CO_2(23.26%) + H_4(2.08%); O_2/CO = 1.25, GHSV = 5000 h^{-1}; temperature = 423 K, run time = 4 h

	Feed with Water[a]				
	CO		H_2		
Catalyst	Comp. (ppm)	Conv. (%)	Comp. (v%)	Conv. (%)	Sele. (%)[b]
CuO(1)–CeO_2(99)	3070	37.3	73.1	1.4	14.6
CuO(2)–CeO_2(98)	1620	66.9	73.3	1.2	26.2
CuO(5)–CeO_2(95)	17	99.7	73.4	1.0	39.0
CuO(10)–CeO_2(90)	80	98.4	73.4	1.0	38.6
CuO(5)–CeO_2(47.5)–ZrO_2(47.5)	495	89.9	73.4	1.0	35.2
CuO(5)–ZrO_2(95)	3500	28.6	73.1	1.5	11.2

[a] p(H_2O) = 200 torr.
[b] Selectivity of oxygen toward CO oxidation = (oxygen consumed in CO oxidation) × 100/(total oxygen consumed in CO + H_2 oxidation).

Cu^{2+} ions (at high concentrations) in CeO_2 and ZrO_2 probably account for their lower χ_M values at the CuO content above 2 wt.%. In other words, in samples containing more than 2 wt.% CuO, larger amounts of interacting Cu^{2+} ions/bulk CuO-like phases are formed on ZrO_2 and CeO_2 supports compared to CeO_2–ZrO_2. Apparently, CeO_2–ZrO_2 promotes a better and more stable dispersion of copper oxide.

Catalytic Activity–Preferential Oxidation of CO: PROX selectivity is defined as (oxygen consumed in CO oxidation) × 100/(oxygen consumed in the oxidation of CO and H_2). At our reaction conditions oxidation of CH_4 was not observed. Oxygen conversion was more than 99.8%. CO oxidation increased with CuO content reaching a maximum at 5 wt.% (Table 11.10; rows 1 to 4). CuO supported on CeO_2 exhibited superior activity than CuO–CeO_2–ZrO_2 and CuO–ZrO_2 (Table 11.10; compare rows 3, 5, and 6). With a water-containing feed (p(H_2O) = 200 torr), a decrease in the CO oxidation activity was observed. This decrease is more significant with ZrO_2-containing catalysts.

The CO oxidation activity/selectivity increased with temperature reaching a maximum at 448 to 478 K due either to increased H_2 oxidation at higher temperatures and/or the growth of CuO particles above around 470 K.[76] The support has a marked effect on the catalytic activity (Fig. 11.15). With water-containing feed (p(H_2O) = 200 torr), the CO oxidation activity decreased in the order: CuO–CeO_2 > CuO–CeO_2–ZrO_2 > CuO–ZrO_2. Copper-free supports also catalyzed the oxidation of CO and H_2, but their activities were considerably lower than the copper-containing catalysts. H_2 oxidation, takes place on both the metal and support. CuO–CeO_2 and CuO–CeO_2–ZrO_2 samples exhibited a stable activity in long-term (18 h) experiments.

Table 11.11 illustrates the PROX activity for a feed consisting of the effluent from a fuel processor (steam reformer-cum-high temperature (HTS)-cum-low temperature water gas shift (LTS) reactors combination). Indian LPG (liquefied petroleum gas), comprising mostly of C_3 and C_4 hydrocarbons (both saturates and olefins), was the feed to the steam reformer. 40%NiO–30%CeO_2–30%ZrO_2 was the steam reforming catalyst operating at 923 K, GHSV = 20,000 h^{-1} and steam/carbon = 3.0.[20] Both the HTS

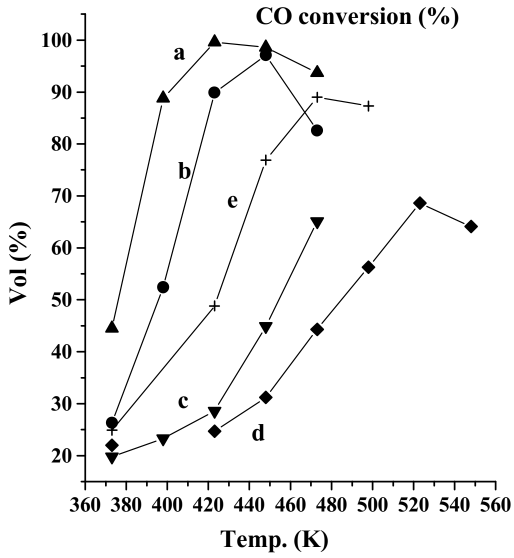

FIGURE 11.15. Influence of support and temperature on the conversion of CO to CO_2. Reaction conditions: catalyst (1.5 g, feed—(H_2(74.17%) + CO(0.49%) + CO_2(23.26%) + CH_4(2.08 v%)) + water (p(H_2O) = 200 torr), O_2/CO = 1.25, GHSV = 5000 h^{-1}; run time = 4 h): (a)—CuO(5)-CeO_2(47.5)-ZrO_2(47.5); (b)—CuO(5)-CeO_2(95); (c)—CuO(5)-ZrO_2(95); (d)—CeO_2; (e)—CeO_2(50)-ZrO_2(50).[66]

(Fe–Cr oxides) and LTS (CuO–ZnO–Al_2O_3) catalysts were commercial samples from Sud-Chemie (India) operated at conditions recommended by the catalyst manufacturer. With this realistic feed, CuO–CeO_2–ZrO_2 exhibited higher PROX *selectivity* than CuO–CeO_2 and CuO–ZrO_2. Long-term experiments with this feed (27 h) also confirmed the stability of this catalyst even in the presence of realistic amounts of CO_2 and H_2O. The CO content in the effluent from the PROX reactor was consistently below 10 ppm for CuO–CeO_2 and 50 ppm for CuO–CeO_2–ZrO_2.

Both the PROX activity and selectivity of the CuO are significantly affected by interactions with the underlying support. Bera *et al.*[14] attributed the promoting effect of CeO_2 in the CuO–CeO_2–ZrO_2 system for CO oxidation to the lowering of the redox potentials of the Cu^{2+}/Cu^{1+} and Cu^{1+}/Cu^{0} couples in a CeO_2 matrix in relation to CuO

TABLE 11.11. Preferential oxidation of CO in the effluent from LTS on CuO–CeO_2–ZrO_2

Catalyst	Conversion of CO (%)	Conversion of H_2 (%)	Selectivity[a]
CuO(5)–CeO_2(95)	99.95	2.8	20.3
CuO(5)–CeO_2(47.5)–ZrO_2(47.5)	99.5	0.8	47.0
CuO(5)–ZrO2(95)	53.0	0.8	32.1

Reaction conditions: average feed composition: 5000 ppm CO + 20% CO_2 + 70% H_2 + balance H_2O + CH_4; GHSV = 20,000 h^{-1}, catalyst = 1.5 g, O_2/CO = 1.25, temperature = 423 K.

[a] Selectivity of oxygen toward CO oxidation = (oxygen consumed in CO oxidation) × 100/(total oxygen consumed in CO + H_2 oxidation).

and $CuO–ZrO_2$. In agreement with our results (TPR and EPR) they also observed that the Cu species in a $CuO–CeO_2$ matrix require less energy to be reduced and reoxidized than in the case of pure CuO and $CuO–ZrO_2$. The oxidation of CO on metals is known to obey a single site Langmuir–Hinshelwood kinetic model[77] where CO and O_2 compete for the same sites. In the case of a metal-reducible oxide system (like our reduced $Cu–CeO_2–ZrO_2$), we may expect that while CO may adsorb on copper sites, O_2 (and H_2 and H_2O) may adsorb on both the metal (Cu) and support ($CeO_2–ZrO_2$). The availability of additional surface oxygen and the consequent higher activity of $CuO–CeO_2$ and $CuO–CeO_2–ZrO_2$ in CO oxidation are, thus, understandable.

Both the XRD and magnetic susceptibility data indicate that the dispersion of supported CuO decreases in the series $CeO_2–ZrO_2 > CeO_2 > ZrO_2$. EPR and magnetic susceptibility data indicate that while a small amount of copper is incorporated in the CeO_2/ZrO_2, fluorite lattice (forming a solid solution), most of it is present on the surface as isolated, monomeric copper as well as dimeric copper oxo species containing magnetically interacting copper ions, nanosized copper oxide clusters and a bulk, CuO-like phase. While the isolated and dispersed CuO species exhibit reversible reduction–oxidation behavior, the bulk CuO-like phase exhibits irreversible reduction behavior. The amount of reducible and reoxidizable CuO content is more on CeO_2 (39.7%) than on $CeO_2–ZrO_2$ catalysts (31.4%) (EPR). The concentration of the bulk-like CuO phase decreases in the series: $ZrO_2 > CeO_2 > CeO_2–ZrO_2$. The PROX *selectivity* of these samples correlated with the concentration of the *dispersed* nanosized CuO species.

11.4. METAL COMPLEXES ENCAPSULATED IN MOLECULAR SIEVES

In addition to the size of the metal and metal oxide particles in which the active sites are located, the underlying support can also exert an influence on their geometric and electronic properties. This effect is especially predominant as the size of the supported particles diminishes to the nanorange. In the limit, when they attain molecular dimensions, as is the case when molecular complexes of transition metals are deposited, grafted or encapsulated in molecular sieves, the support can influence the electronic properties of the active site, either directly or indirectly by modifying the symmetry and geometric configuration of the molecular complex and thereby the relative electronic energy levels of the metal cation of the complex. Such changes in the electronic energy levels are expected to affect the redox and catalytic properties of the metal especially in oxidation reactions. In this section, we will demonstrate this phenomenon with copper acetate dimeric complexes and transition metal salens encapsulated in zeolites.

11.4.1. Dimeric Copper Acetate Complexes

Transition metal complexes encapsulated in the cavities of zeolites and mesoporous materials exhibit enhanced catalytic activity, compared to their “neat” analogs.[78–87] We had earlier found that Cu(II)-acetate exhibited enhanced regioselective *ortho*-hydroxylation of phenols using atmospheric oxygen as the oxidant on encapsulation in molecular sieves Y, MCM-22 or VPI-5.[88,89] Rao *et al.*[90] had also found a similar enhancement for encapsulation in Al-MCM-48.

TABLE 11.12. Hydroxylation of phenol using molecular oxygen as the oxidant (pH = 6.5, temperature = 298 K, reaction time = 19 h)[88]

Catalyst	Phenol Conversion (mol%)	*Ortho*-Benzoquinone (mol%)	Others (mol%)	TOF (h^{-1})
Cu(acetate) – "neat"	5.1	4.9	0.2	3.6
Cu(acetate)-Y	11.5	11.5	–	60.9
Cu(chloroacetate) – "neat"	1.0	1.0	–	0.9
Cu(chloroacetate)-Y	12.0	11.9	0.1	227.1

Turnover frequency (TOF): Number of molecules of phenol converted per atom of Cu per hour.

The turnover frequency increases from 3.6 for "neat" copper acetate to 60.9 for the encapsulated complex (Table 11.12). The corresponding values for copper chloroacetate are 0.9 and 227.1, respectively. In their catalytic activity for regioselective *ortho*-hydroxylation of phenols to catechols and further oxidation of the catechols to *ortho*-benzoquinones, the dimeric copper acetates resemble the copper monoxygenase enzyme tyrosinase[89–91] which regioselectively *ortho*-hydroxylates tyrosine to L-dopa. Interestingly, this enzyme also contains a dicopper site as the active center. Why do the intrinsic catalytic activities (turnover frequencies) of copper acetates increase upon encapsulation in zeolites such as zeolite, Y? We had probed the origin of this enhancement in the oxidation activity of copper acetates using FT-IR, UV–visible and, especially EPR, spectroscopies. Isolated dimeric copper acetate units are present in copper acetate monohydrate in the solid state. The Cu–Cu separation in these dimeric units is 0.261 nm which is only slightly longer than the separation in copper metal, i.e., 0.254 nm. Our spectroscopic and thermogravimetric studies had revealed[88] that the dimeric acetato and chloroacetato complexes of Cu(II) are encapsulated in the *supercages* of zeolite Y. The dimensions of these dimeric Cu(II) complexes are more than 0.85×0.1 nm while the size of the window for the supercage is only about 0.74 nm. Hence, these complexes, once formed, are truly encapsulated and cannot come out of the supercages of the zeolite. Encapsulation has a significant effect on the geometric and electronic structure of the complexes as revealed by FTIR and EPR spectroscopies. Even though, the stoichiometric integrity of the complex is conserved upon encapsulation the shift in the vibrational and electronic band positions[88] clearly reveal changes in the carboxylate bridge coordination. The symmetry of the Cu(II) ions in copper chloroacetate changes from C_{4v} to C_{2v} upon encapsulation. The lowering of symmetry of the encapsulated copper chloroacetate complexes is probably due to the greater geometric constraints on the larger copper chloroacetate dimeric complexes upon encapsulation. In addition to the changes in the molecular symmetry, the variation in the EPR spectral intensities in the range of 77 to 298 K[88] indicates that the Cu–Cu antiferromagnetic exchange interaction increases upon encapsulation due to the compression of the Cu–Cu separation to 0.240 nm from 0.264 nm for the "neat" copper acetate complex. The corresponding decrease for copper chloroacetate is from 0.292 nm (neat) to 0.273 nm (encapsulated). Geometric constraints imposed by the cavities of the zeolite probably cause the observed geometric changes in the structure of these encapsulated complexes.

The EPR spectra of phenol adsorbed on the encapsulated copper acetate in the presence of O_2 clearly indicated[88] the formation of an axially coordinated copper–phenol

adduct. The labile coordination of phenol and the enhanced catalytic activity of the encapsulated dimeric copper acetate could both be attributed, perhaps, to the shorter Cu–Cu distance and consequent greater interaction between the two copper ions in the encapsulated state compared to the neat complex. The short Cu–Cu distance and the consequent greater, lateral, overlap of the copper orbitals would facilitate the transfer of electron density from the phenolate ligand to the anti-bonding LUMO of the complex, thereby weakening the O—O and Cu—O bonds. Weakening of these bonds would, in turn, make it easier for the cleavage and the transfer of one of the two oxygens of the peroxide ligand to the position *ortho* to the phenolate bond. Due to the greater Cu–Cu bonding, the strength and lability of the Cu-phenolate and Cu-dioxygen bonds are modified by a *trans*-axial ligand effect, leading to the enhanced reactivity of the encapsulated complex. There is, hence, a direct relationship between the shortening of the internuclear Cu–Cu distance upon encapsulation and the enhanced reactivity of the resultant, structurally modified complex. Analogous rhodium complexes having direct overlap of the metal orbitals also exhibit such *trans*-axial lability and consequent enhanced catalytic activity.[92]

A qualitative and preliminary picture (Fig. 11.16) of the mechanism of oxidation that emerges from our studies is the following: Under the reaction conditions (pH = 6.5), the phenols exist in the phenolate form. Two phenolate ions coordinate to the two Cu(II) ions of the copper acetate dimer, reducing them to the Cu(I) oxidation state. Next, dioxygen reacts with the copper–phenolate adduct. The latter undergoes an O–O bond scission concomitant with the hydroxylation of the substrate. The acetate

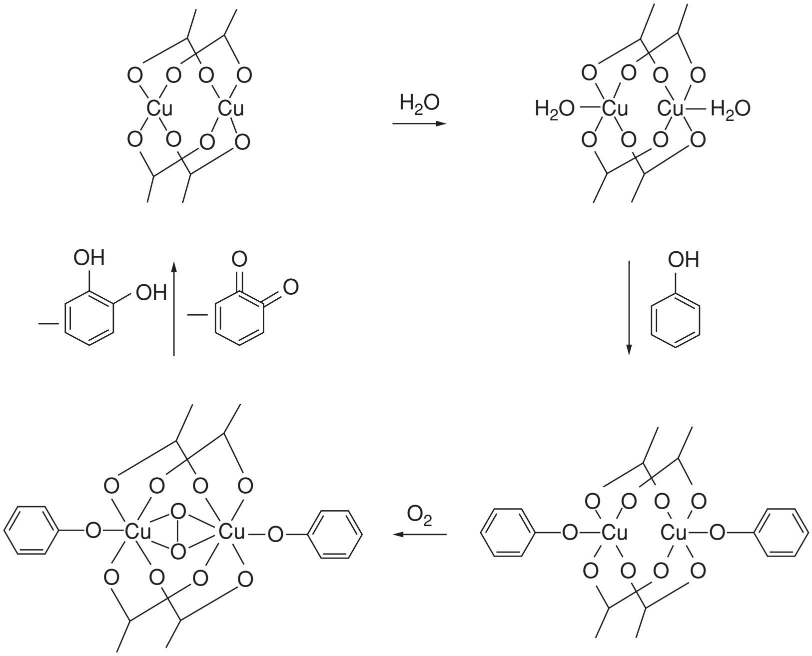

FIGURE 11.16. A possible mechanism for the *ortho*-hydroxylation of phenol over copper acetate dimers.[88]

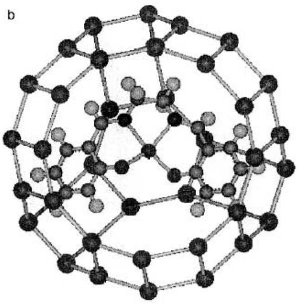

FIGURE 11.17. Structural model of "neat" and zeolite-Y-encapsulated Cu(salen) complex.

group can change its mode of coordination from a bidentate to a monodentate type as a consequence of forming the dioxygen adduct. Such a coordination lability is common in the enzymatic reactions. Hence, by varying the substituent groups on the acetate ligand and the size and shape of the zeolite cavity, one should be able, at least in principle, to design suitable solid catalysts for selective oxidation reactions at low temperatures in the liquid phase.

11.4.2. Transition Metal Salen Complexes

Transition metal salen complexes, where salen is N, N′-ethylenebis(salicylidenaminato), are functional mimics of metalloproteins in dioxygen binding and oxidation of olefins and aromatic compounds using hydrogen peroxide, iodosylbenzene, NaOCl, etc.[78,82,93] The Schiff base salen complexes are conformationally flexible and adopt a variety of geometries, viz., planar, umbrella-type and stepped conformations, to generate various active site environments for the different oxidation reactions.[94,95] This flexibility, similar to that observed in metalloproteins, is a key factor for the biomimetic activity of these molecules. Heterogenization of these metal salen complexes by encapsulating inside the pores and supercages of zeolites (Fig. 11.17) and zeolitic materials leads to more efficient solid catalysts. For example, copper salen complexes encapsulated inside the supercages of zeolite-Y exhibit catalase activity with rates of decomposition of H_2O_2 (to H_2O) or *tert.*-butyl hydroperoxide (TBHP) (to *tert.*-butanol) approaching those of natural catalase enzymes.[86] Substitution of the aromatic hydrogen atoms of salen ligand by electron withdrawing groups, such as Cl, Br, and NO_2, enhances the catalytic activity. The encapsulated complexes exhibit higher turnover frequencies (TOF) by several orders of magnitude than the corresponding "neat" complexes. Similar enhancements in the activity were observed also for the oxidation of styrene and aerobic oxidation of *para*-xylene (to mainly *para*-toluic acid) with these complexes.[86] Table 11.13 shows the catalytic activity data of "neat" and zeolite-Y-encapsulated copper salen complexes for certain chosen reactions. Thus, dispersion and supporting of active model complexes on zeolite surfaces enhances the catalytic activity. In fact, significant enhancement in the intrinsic activity compared to the "neat" complexes is a strong indication that it is the catalytic behavior of the isolated copper salens inside the cavities of the zeolite that is responsible for

the observed enhancement. The catalytic activity of the leached complexes, if any, would have been lower similar to solutions of the "neat" complex. An additional point is

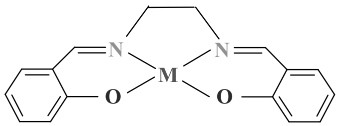

that the turnover frequencies (TOF) have been calculated on the basis of the total copper ions present in the solid and represent the minimum values since only a fraction of the copper ions encapsulated in the zeolite are expected to contribute to the observed activity due to diffusional and other constraints on those located deeper in the core of the zeolite particle. The "true" TOF values may be significantly higher. What could be the origin for efficient functional activity of the metal salen complex when they are encapsulated and supported on zeolite surfaces? Spectroscopic investigations, EPR in particular, showed that the molecular and electron structures are considerably altered due to zeolite-entrapment and support interactions.

The "neat" copper salen complexes showed broad EPR spectra[96] corresponding to nearest-neighbor spin–spin interaction. Salen molecules adsorbed on the external surface exhibit spectra similar to "neat" complexes. Since copper salens adsorbed on the external surface had carefully been washed away during the preparation of our catalyst samples, the remaining metal salens encapsulated in the supercages as mononuclear complexes exhibited well-resolved metal hyperfine features similar to spectra of these complexes in dilute frozen solutions indicating the encapsulation of monomeric salen complexes in zeolite cavities (Fig. 11.18). The catalytic data in Table 11.13, thus, refer to truly encapsulated copper salens. EPR spectroscopy can, thus, be used as an analytical tool to distinguish transition metal complexes encapsulated in zeolites from those which are merely adsorbed on their external surface. The intermolecular interactions (leading to line broadening in the case of the "neat" complex) are avoided due to site isolation in the zeolite cavities and thereby resolved metal hyperfine features are observed even in the solid state in encapsulated metal complexes. From quantitative, EPR intensity measurements, it was estimated that one molecule of the copper

TABLE 11.13. Catalytic activity of "neat" and zeolite-encapsulated substituted Cu(salen)[96]

	Catalytic Activity			
Catalyst	*Para*-Xylene Oxidation (wt.%)	Phenol Oxidation (wt.%)	TBHP Conv. (TOF, h^{-1})	H_2O_2 Conv. (TOF, h^{-1})
Cu(salen)	3.4	6.2 (21)	53	36
Cu(5-Cl-salen)	4.6	7.7 (31)	108	64
Cu(salen)-Y	45.1	5.4 (40)	1,704	232,506
Cu(5-Cl-salen)-Y	48.9	6.8 (88)	29,377	454,949

Values in parentheses refer to TOF, h^{-1} values. TOF, h^{-1} = moles of substrate converted per mole of copper (in the solid catalyst) per hour.

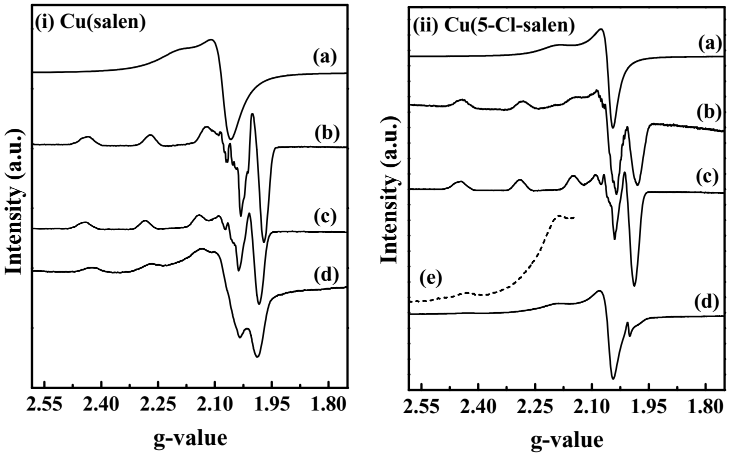

FIGURE 11.18. EPR spectra of (i) Cu(salen) and (ii) Cu(5-Cl-salen) at 77 K: (a) "neat" polycrystalline sample, (b) frozen $CHCl_3/CH_3CN$ (3:1) solution, (c) frozen DMF solution and (d) zeolite-Y-encapsulated complexes. Dotted line (e) is a blown-up trace of curve (d).

complex is encapsulated in every seven supercages of Na-Y for Cu(salen) and in every nine supercages for Cu(5-Cl-salen).

"Neat" Cu(salen) in the *solid* state is dimeric and the copper complex has a tetragonally elongated square pyramidal configuration with the donor atoms, N_2O_2, forming a perfect basal plane.[96] However, in the dissolved state and in noncoordinating solvents, the complex exists as a monomer with square planar geometry. Our EPR results and geometry minimization studies[96] indicate that in the encapsulated complex, Cu(salen) is present as monomers (as in the dissolved state) in the supercages of zeolite Y. Further, the geometry is distorted square planar. Cu(5-Cl-salen) possesses a distorted square planar configuration in both 'neat' and encapsulated states. From the EPR spin Hamiltonian parameters and UV-visible spectral data, electronic structure and ground-state wave function of the copper salen complexes in frozen state and when encapsulated in zeolites were estimated. The MO coefficients are modified considerably on encapsulation. The coefficient α, characteristic of in-plane σ-bonding increases while β, characteristic of in-plane π bonding, decreases on encapsulation (Table 11.14). These results highlight the structural changes in the Schiff base complexes on encapsulation, These changes are apparently more for Cu(salen) than for Cu(5-Cl-salen) (Table 11.14). The higher in-plane covalency as indicated by a smaller α value and lower hyperfine coupling constant for Cu(5-Cl-salen) indicates larger depletion of electron density at the site of copper. *Encapsulation in zeolites, hence, leads to depletion of electron density at the copper site.* The higher observed catalytic activity (especially for the decomposition of TBHP and H_2O_2) of "neat" Cu(5-Cl-salen) vis-à-vis Cu(salen), (Table 11.13) is probably due to the depletion of electron density at copper by the electron-withdrawing chlorine. Our earlier result[94] that the Cu(II)/Cu(I) couple appears at less negative potentials for Cu(5-Cl-salen) than for Cu(salen) also supports the electron depletion by Cl. The encapsulated complexes are, hence, present in a distorted tetrahedral conformation. A tetrahedral distortion of the square planar complex

TABLE 11.14. Ground-state molecular orbital coefficients and d–d transition energies for substituted Cu(salen) complexes[96]

		MO Coefficients				d–d Transition Energies (cm^{-1})	
System	State	α^2	α'^2	β^2	δ^2	$\Delta(E_{xy} - E_{x^2-y^2})$	$\Delta(E_{xz,yz} - E_{x^2-y^2})$
Cu(salen)	Encapsulated	0.839	0.245	0.588		17,391	
	$CHCl_3/CH_3CN$	0.826	0.260	0.596		17,730	
	DMF	0.805	0.284	0.645		17,361	
Cu(5-Cl-salen)	Encapsulated	0.811	0.278	0.588		17,391	
	$CHCl_3/CH_3CN$	0.807	0.282	0.664	0.880	17,731	24,390
	DMF	0.799	0.290	0.666	0.779	17,361	23,810

will increase the Cu(II)/Cu(I) reduction potential leading to a further enhancement of the oxidation reaction. It may be borne in mind that while Cu(II) complexes prefer square planarity, tetrahedral symmetry is favored by Cu(I) complexes. Changes in the Cu(II)/Cu(I) reduction potentials of the copper salen complexes (brought about either by substitution of electron-withdrawing groups or geometric distortion in the cavities of supports such as zeolites) are, thus, responsible for their catalytic activity.

11.5. SUMMARY AND CONCLUSIONS

The influence of particle size and support-interactions on the redox behavior and catalytic properties are investigated for three classes of solid catalysts: (1) supported metals, (2) supported metal oxides, and (3) zeolite-encapsulated metal complexes, for a few industrially important catalytic transformations. The metals included (1) Ni on CeO_2–ZrO_2 for steam reforming, (2) Au and Au–Pt on MCM-41 for preferential oxidation of CO and (3) Pt- and Pd on TS-1 for selective oxidations, respectively. The influence of the ceria support on the electronic and catalytic properties (preferential oxidation of CO) of copper oxide was investigated. Finally, two groups of metal complexes, viz., (i) dimeric copper acetates and (ii) metal salens, respectively, were encapsulated in zeolite-Y and their spectral and catalytic activities in selective oxidation reactions were studied. Structural characterizations of the catalysts before, during and after the reaction were carried out using IR, UV–VIS and EPR spectroscopic techniques. The studies reveal that the support exerts a significant influence on the size and dispersion of the metal/metal oxide particles and the geometric and electronic structure of the encapsulated complexes thereby modifying the redox and catalytic properties of the active sites located on the metal/metal oxide/complex. Incorporation of CeO_2 in ZrO_2 enhances nickel dispersion and reduction in Ni–CeO_2–ZrO_2 catalysts. Samples prepared by hydrothermal synthesis with organic templates have a larger surface area. In addition, there is an enrichment of nanoparticles of nickel on the surface of these samples than in those samples prepared by coprecipitation and digestion. Au and Au–Pt bimetallic nanoparticles could be dispersed on amine-functionalized MCM-41 supports. A bimetallic nanoparticle composition of Au_1Pt_{19} was found to be highly

active and selective for preferential oxidation of CO in the presence of H_2 as compared to pure Au or Pt as well as other Au–Pt bimetallic compositions. In the case of Pt- and Pd-TS-1 systems, reduction and reoxidation of Ti ions, which requires 673 K or above in pure TS-1, occurred at a much lower temperature (323 K) when Pd or Pt is present. The noble metals facilitate the reduction of Ti^{4+} ions. A mixture of ($H_2 + O_2$), instead of aqueous H_2O_2, could be used as oxidant in the case of Pd-TS-1 catalysts for the epoxidation of allyl alcohol. The amount and dispersion of Pd exerts a profound influence on catalytic activity and selectivity. At a Pd loading of 2%, a large amount of reactive oxo-Ti species (such as Ti-OOH and Ti-$OO^{-\bullet}$) is formed, contributing to the enhanced catalytic activity. Both the activity and selectivity of CuO in the preferential oxidation of CO in the presence of H_2 are significantly affected by interactions with the underlying support. The dispersion of CuO is modified by the crystallite and particle sizes of the support CeO_2–ZrO_2. CuO–CeO_2–ZrO_2 exhibited a higher selectivity than CuO–CeO_2 or CuO–ZrO_2. Metal complexes (e.g., dimeric copper acetate and metal salens), when encapsulated inside the supercages of zeolite-Y showed enhanced catalytic activity/selectivity in selective *ortho*-hydroxylation of phenols. EPR spectroscopic studies reveal that encapsulation modifies the electronic properties of the metal active site, either directly or indirectly by modifying the geometric configuration of the metal complex in the cavities of the zeolite. In the case of dimeric copper acetate, the Cu–Cu separation is shortened. Upon encapsulation in zeolite-Y, the geometry of metal salen complexes is distorted, the ground-state electronic configuration is considerably modified and the electron density at the metal active site is depleted.

The catalytic properties of metals, metal oxides, and metal complexes in oxidation reactions are controlled by the redox potential of the metal atoms. The latter, in turn, is influenced by the local geometric and electronic environment around the metal atoms on the surface. The coordination number and, consequently, the energy levels (and redox potentials) of such surface metal atoms vary with their particle size, especially, in the nanorange. Particle sizes can be modulated by proper choice of the support. In addition, the support can also influence the electronic state of the metal atoms by direct, support–metal interactions. This phenomenon is most evident when transition metal complexes are encapsulated in zeolites. Variations in the symmetry of the metal complexes due to geometric distortion in zeolitic cavities and the consequent changes in the redox potential (and catalytic activity) of the metal ion active site are significant examples of the importance of the support in the design of heterogeneous catalysts.

REFERENCES

1. H. S. Taylor, A theory of the catalytic surface, *Proc. R. Soc.* A **108,** 105–111 (1925).
2. H. S. Taylor, Fourth report of the committee on contact catalysis, *J. Phys. Chem.* **30,** 145–171 (1926).
3. M. Che, and C. O. Bennett, The influence of particle size on the catalytic properties of supported metals, *Adv. Catal.* **36,** 55–172 (1989).
4. G. L. Haller, and D. E. Resasco, Metal–support interaction: Group VIII metals and reducible oxides, *Adv. Catal.* **36,** 173–235 (1989).
5. P. Ratnasamy, A. J. Leonard, L. Rodrique, and J. J. Fripiat, Structure and surface properties of supported platinum catalysts, *J. Catal.* **29,** 374–384 (1973).

6. B.C.H. Steele, and A. Heinzel, Material for fuel-cell technologies, *Nature* **414,** 345–352 (2001).
7. L. Schlapbach, and A. Zuttel, Hydrogen-storage materials for mobile applications, *Nature* **414,** 353–358 (2001).
8. R. J. Gorte, S. Park, J. M. Vohs, and C. Wang, Anodes for direct oxidation of dry hydrocarbons in a solid-oxide fuel cell, *Adv. Mater.* **12,** 1465–1469 (2000).
9. R. J. Farrauto, and R. M. Heck, Environmental catalysis into the 21st Century, *Catal. Today* **55,** 179–187 (2000).
10. S. C. Singhal, Status of solid oxide fuel cells, *Adv. Sci. Technol.* **24,** 3–14 (1999).
11. M. Mamak, N. Coombs, and G. Ozin, Mesoporous yttria–zirconia and metal–yttria–zirconia solid solutions for fuel cells, *Adv. Mater.* **12,** 198–202 (2000).
12. M. Mamak, N. Coombs, and G. Ozin, Self-assembling solid-oxide fuel cell materials: mesoporous yttria–zirconia and metal—yttria–zirconia solid solutions, *J. Am. Chem. Soc.* **122,** 8932–8939 (2000).
13. M. Mamak, N.Coombs, and G. Ozin, Mesoporous nickel-yttria-zirconia fuel cell materials, *Chem. Mater.* **13,** 3564–3570 (2001).
14. P. Bera, S. Mitra, S. Sampath, and M. S. Hegde, Promoting effect of ceria in a Cu/CeO_2 catalyst: Lowering of redox potentials of Cu species in the CeO_2 matrix, *Chem. Commun.* **10,** 927–928 (2001).
15. A. Martinez-Arias, J. M. Coronado, R. Cataluna, J. C. Conesa, and J. C. Soria, Influence of mutual platinum-dispersed ceria interactions on the promoting effect of ceria for the CO oxidation reaction in a Pt/CeO_2/Al_2O_3 catalyst, *J. Phys. Chem.* B **102,** 4357–4365 (1998).
16. D. Skarmoutsos, F. Tietz, and P. Nikolopoulos, Structure–property relationships for Ni/YSZ and Ni/(YSZ + TiO_2) cermets, *Fuel Cells* **1,** 243–248 (2001).
17. T. Takeguchi, S.-n. Furukawa and M. Inoue, Hydrogen spillover from NiO to the large surface area CeO_2–ZrO_2 solid solution and activity of the NiO/CeO_2–ZrO_2 catalysts for partial oxidation of methane, *J. Catal.* **202,** 14–24 (2001).
18. J. Sfeir, P. A. Buffat, P. Möckli, N. Xanthopoulos, R. Vasquez, H. J. Mathieu, J. Van herle, and K. Ravindranathan Thampi, Lanthanum chromite based catalysts for oxidation of methane directly on SOFC anode, *J. Catal.* **202,** 229–244 (2001).
19. N. Kiratzis, P. Holtappels, C. E. Hatchwell, M. Mogensen, and J. T. S. Irvine, Preparation and characterization of copper/yttria titania zirconia cermets for use as possible solid oxide fuel cell anodes, *Fuel Cells* **1,** 211–218 (2001).
20. P. Ratnasamy, D. Srinivas, H. S. Soni, A. J. Chandwadkar, H. S. Poddar, C. S. Gopinath, and B. S. Rao, Crystallite, mesoporous NiO–ZrO_2-based solid oxide fuel cell catalysts, *Stud. Surf. Sci. Catal.* **135,** 1270–1277 (2001).
21. P. Ratnasamy, Crystalline, mesoporous ceria–zirconia based reforming catalysts for PEM fuel cells, *Preprints Symp.–Am. Chem. Soc., Div. Fuel Chem.* **46,** 635–640 (2001).
22. D. Srinivas, C. V. V. Satyanarayana, H. S. Poddar, and P. Ratnasamy, Structural studies on NiO–CeO_2–ZrO_2 catalysts for steam reforming of ethanol, *Appl. Catal. A: General* **246,** 323–334 (2003).
23. A. Martínez-Arias, M. Fernández-García, V. Ballesteros, L.N. Salamanca, J.C. Conesa, C. Otero and J. Soria, Characterization of high surface area Zr–Ce (1:1) mixed oxide prepared by a microemulsion method, *Langmuir* **15,** 4796–4802 (1999).
24. A. Martínez-Arias, M. Fernández-García, L.N. Salamanca, R.X. Valenzuela, J.C. Conesa, and J. Soria, Structural and redox properties of ceria in alumina-supported ceria catalyst supports, *J. Phys. Chem.* B **104,** 4038–4046 (2000).
25. A. Martínez-Arias, M. Fernández-García, C. Belver, J. C. Conesa, and J. Soria, EPR study of oxygen handling properties of ceria, zirconia and Zr–Ce (1:1) mixed oxide samples, *Catal. Lett.* **65,** 197–204 (2001).
26. E. Mamontov, T. Egami, R. Brezny, M. Koranne, and S. Tyagi, Lattice defects and oxygen storage capacity of nanocrystalline ceria and ceria–zirconia, *J. Phys. Chem.* B **104,** 11110–11116 (2000).
27. H. Vidal, S. Bernal, J. Kašpar, M. Pijolat, V. Perrichon, G. Blanco, J. M. Pintado, R.T. Baker, G. Colona and F. Fally, Influence of high temperature treatments under net oxidizing and reducing

conditions on the oxygen storage and buffering properties of a $Ce_{0.68}Zr_{0.32}O_2$ mixed oxide, *Catal. Today* **54,** 93–100 (1999).
28. Y. Nagai, T. Yamamoto, T. Tanaka, S. Yoshida, T. Nonaka, T. Okamoto, A. Suda, and M. Sugiura, X-ray absorption fine structure analysis of local structure of CeO_2–ZrO_2 mixed oxides with the same composition ratio (Ce/Zr = 1), *Catal. Today* **74,** 225–234 (2002).
29. C. D. Wagner, W. M. Riggs, L. E. Davis, J. F. Moulder, and G. F. Muilenberg, In *Handbook of X-ray Photoelectron Spectroscopy* (Perkin-Elmer Corporation, USA 1979).
30. A. Badri, C. Binet and J.-C. Lavalley, An FT-IR Study of Surface Ceria Hydroxyl Groups During a Redox Process with H_2, *J. Chem. Soc. Faraday Trans.* **92,** 4669–4673 (1996).
31. V. Rives, and S. Kannan, Layered double hydroxides with the hydrotalcite-type structure containing Cu^{2+}, Ni^{2+} and Al^{3+}, *J. Mater. Chem.* **10,** 489–495 (2000).
32. A. Bensalem, F. Bozon-Verduraz, M. Delamar, and G. Bugli, Preparation and characterization of highly dispersed silica-supported ceria, *Appl. Catal. A: Gen.* **121,** 81–93 (1995).
33. A. Bensalem, J. C. Muller, and F. Bozon-Verduraz, From bulk CeO_2 to supported cerium–oxygen clusters: A diffuse reflectance approach, *J. Chem. Soc. Faraday Trans.* **88,** 153–154 (1992).
34. A.B.P. Lever, In *Inorganic Electronic Spectroscopy*, 2nd edn, (Elsevier, Amsterdam 1984).
35. B. Scheffer, J.J. Heijeinga, and J.A. Moulijn, An electron spectroscopy and X-ray diffraction study of nickel oxide/alumina and nickel oxide/tungsten trioxide/alumina catalysts, *J. Phys. Chem.* **91,** 4752–4759 (1987).
36. M. Lo Jacono, M. Schiavello, and A. Cimino, Structural, magnetic and optical properties of nickel oxide supported on η- and γ-aluminas, *J. Phys. Chem.* **75,** 1044–1050 (1971).
37. Z. Chang, Z. Zhu, and L. Kevan, Electron spin resonance of Ni(I) in Ni-containing MCM-41 molecular sieves, *J. Phys. Chem.* B **103,** 9442–9449 (1999).
38. J. E. Wertz, and J. R. Bolton, In *Electron Spin Resonance: Elementary Theory and Practical Applications*, (McGraw-Hill, New York 1972).
39. M. Che, M. Richard, and D. Olivier ferromagnetic resonance study of dispersed nickel particles prepared by reduction of nickel ion-exchanged X-zeolites by hydrogen molecules or hydrogen atom beams, *J. Chem. Soc. Faraday Trans.* I **76,** 1526–1534 (1980).
40. B. R. Loy, and C.R. Noddings, A ferromagnetic resonance study of chemisorbed hydrogen on a nickel catalyst, *J. Catal.* **3,** 1–6 (1964).
41. C. D. Dudfield, R. Chen, and P. L. Adcock, A carbon monoxide PROX reactor for pem fuel cell automotive application, *Int. J. Hydrogen Energy* **26,** 763–775 (2001).
42. M. Haruta, and M. Daté, Advances in catalysis of Au nanoparticles, *Appl. Catal. A. Gen.* **222,** 427–437 (2001).
43. G. C. Bond, and D. T. Thompson, Catalysis by gold, *Catal. Rev.—Sci. Eng.* **41,** 319–399 (1999).
44. M. Haruta, Size- and support-dependency in the catalysis of gold, *Catal. Today* **36,** 153–166 (1997).
45. M. M. Schubert, S. Hackenberg, A. C. van Veen, M. Muhler, V. Plzak, and R. J. Behm, CO oxidation over supported gold catalysts—"Inert" and "active" support materials and their role for the oxygen supply during reaction, *J. Catal.* **197,** 113–122 (2001).
46. D. Brunel, N. Bellocq, P. Sutra, A. Cauvel, M. Laspéras, P. Moreau, F. Di Renzo, A. Galarneau, and F. Fajula, Transition-metal ligands bound onto the micelle-templated silica surface, *Coord. Chem. Rev.* **180,** 1085–1108 (1998).
47. C. Satyanarayana, J. Trissa, M. Sachin, D. Chinmay, S. B. Halligudi, B. S. Rao, M. Sastry, and P. Ratnasamy, Au and Au–Pt bimetallic nanoparticles in MCM-41 materials: Applications in CO preferential oxidation, Stud. Surf. Sci. Catal. **146,** 573–576 (2003).
48. B. Notari, Microporous crystalline titanium silicates, *Adv. Catal.* **41,** 253–334 (1996).
49. G. N. Vayssilov, Structural and physicochemical features of titanium silicates, *Catal. Rev.—Sci. Eng.* **39,** 209–251 (1997).
50. P. Ratnasamy, D. Srinivas, and H. Knözinger, Active sites and reactive intermediates in titanium silicate molecular sieves, *Adv. Catal.* **48,** 1–169 (2004).
51. J. D. Jewson, C. A. Jones, and R. M. Dessau, Direct epoxidation process of olefins using palladium–titanosilicate catalyst containing gold promoter, PCT Int. Appl. WO 2001062380 A1 30 Aug 2001.

52. R. Meiers, U. Dingerdissen, and W. F. Hölderich, Synthesis of propylene oxide from propylene, oxygen and hydrogen catalyzed by palladium—platinum–containing titanium silicate, *J. Catal.* **176,** 376–386 (1998).
53. R. Meiers, and W. F. Hölderich, Epoxidation of propylene and direct synthesis of hydrogen peroxide by hydrogen and oxygen, *Catal. Lett.* **59,** 161–163 (1999).
54. G. Jenzer, T. Mallat, M. Maciejewski, F. Eigenmann, and A. Baiker, Continuous epoxidation of propylene with oxygen and hydrogen on a Pd-Pt/TS-1 Catalyst, *Appl. Catal. A: Gen.* **208,** 125–133 (2001).
55. E. E. Stangland, K. B. Stavens, R. P. Andres, and W. N. Delgass, Characterization of gold–titania catalysts viz., oxidation of propylene to propylene oxide, *J. Catal.* **191,** 332–347 (2000).
56. C. Qi, T. Akita, M. Okumura, and M. Haruta, Epoxidation of propylene over gold catalysts supported on non-porous silica, *Appl. Catal. A: Gen.* **218,** 81–89 (2001).
57. T. A. Nijhuis, B. J. Huizinga, M. Makkee, and J. A. Moulijn, Direct epoxidation of propene using gold dispersed on TS-1 and other titanium-containing supports, *Ind. Eng. Chem. Res.* **38,** 884–891 (1999).
58. V. N. Shetti, P. Manikandan, D. Srinivas, and P. Ratnasamy, Reactive oxygen species in epoxidation reactions over titanosilicate molecular sieves, *J. Catal.* **216,** 461–467 (2003).
59. R. Bal, K. Chaudhari, D. Srinivas, S. Sivasanker, and P. Ratnasamy, Redox and catalytic chemistry of Ti in titanosilicate molecular sieves: An EPR investigation, *J. Mol. Catal. A: Chem.* **162,** 199–207 (2000).
60. D. Srinivas, P. Manikandan, S. C. Laha, R. Kumar, and P. Ratnasamy, Reactive oxo-titanium species in titanosilicate molecular sieves: EPR investigations and structure–Activity correlations, *J. Catal.* **217,** 160–171 (2003).
61. D.L. Trimm and Z. I. Önsan, Onboard fuel conversion for hydrogen-fuel-cell-driven vehicles, *Catal. Rev. Sci. Tech.* **43,** 31–84 (2001).
62. T. V. Choudhary, and D.W. Goodman, CO-free fuel processing for fuel cell applications, *Catal. Today* **77,** 65–78 (2002).
63. J. R. Rostrup-Nielson, and T. Rostrup-Nielson, Large-scale hydrogen production, *Cattech* **6,** 150–159 (2002).
64. R. M. Sanchez, K. Ueda, K. Tanaka, and M. Haruta, Selective oxidation of CO in hydrogen over gold supported on manganese oxide, *J. Catal.* **168,** 125–127 (1997).
65. O. Korotkikh, and R.Farrauto, Selective catalytic oxidation of CO in H_2: Fuel cell applications, *Catal. Today* **62,** 249–254 (2000).
66. P. Ratnasamy, D. Srinivas, C. V. V. Satyanarayana, P. Manikandan, R. S. Senthil Kumaran, M. Sachin, and V. N. Shetti, Influence of the support on the preferential oxidation of CO in hydrogen-rich stream reformates over the $CuO–CeO_2–ZrO_2$ system, *J. Catal.* **221,** 455–465 (2004).
67. H. Tanaka, S.-I. Ito, S. Kameoka, K. Tomishige, and K. Kunimori, Promoting effect of potassium in selective oxidation of CO in hydrogen-rich stream on Rh catalysts, *Catal. Commun.* **4,** 1–4 (2003).
68. W. Liu, and M. Flytzani-Stephanopoulos, Transition metal-promoted oxidation catalysis by fluorite oxides: A study of CO oxidation over $Cu–CeO_2$, *Chem. Eng. J.* **64,** 283–294 (1996).
69. L. Kundakovic, and M. Flytzani-Stephanopoulos, Reduction characterization of copper oxide in cerium and zirconium oxide systems, *Appl. Catal. A: Gen.* **171,** 13–29 (1998).
70. G. Wrobel, C. Lamonier, A. Bennani, A. D'Huysser, and A. Aboukais, Effect of incorporation of copper or nickel on hydrogen storage in ceria: Mechanism of reduction, *J. Chem. Soc. Faraday Trans.* **92,** 2001–2009 (1996).
71. H. Praliaud, S. Mikhailenko, Z. Chajar, and M. Primet, Surface and bulk properties of Cu-ZSM-5 and Cu/Al_2O_3 solids during redox treatments: Correlation with the selective reduction of nitric oxide by hydrocarbons, *Appl. Catal. B. Environ.* **16,** 359–374 (1998).
72. S. Velu, K. Suzuki, M. Okazaki, M. P. Kapoor, T. Osaki ,and F. Ohashi, Oxidative steam reforming of methanol over CuZnAl(Zr)-oxide catalysts for the selective production of hydrogen for fuel cells: Catalyst characterization and performance evaluation, *J. Catal.* **194,** 373 (2000).

73. P. I. Paulose, G. Jose, V. Thomas, G. Jose, N. V. Unnikrishnan, and M. K. R. Warrier, Spectroscopic studies of Cu^{2+} ions in sold–gel derived silica matrix, *Bull. Mater. Sci.* **25,** 69–74 (2002).
74. P. G. Harrison, I. K. Ball, W. Azelee, W. Daniell, and D. Goldfarb, Nature and surface redox properties of copper(II)-promoted cerium(IV) oxide CO oxidation catalysts, *Chem. Mater.* **12,** 3715–3725 (2000).
75. A. Aboukais, A. Bennani, C. F. Aïssi, G. Wrobel, M. Guelton, and J. C. Vedrine, High resolved electron paramagnetic resonance spectrum of copper(II) ion pairs in CuCe Oxide, *J. Chem. Soc. Faraday Trans.* **88,** 615–620 (1992).
76. M. M. Günter, T. Ressler, R. E. Jentoft, and B. Bems, Redox behavior of copper oxide catalysts in the steam reforming of methanol studied by *in situ* X-ray diffraction and absorption spectroscopy, *J. Catal.* **203,** 133–149 (2001).
77. R.J. Farrauto, and C. Bartholomew, In *Introduction to Industrial Catalytic Processes* (Chapman & Hall, London, UK 1997) Chapters 1, 38, 39.
78. K. J. Balkus, Jr., and A. G. Gabrielov, Zeolite encapsulated metal complexes, *J. Incl. Phenom. Mol. Recog. Chem.* **21,** 159–184 (1995).
79. K. J. Balkus, Jr., A. G. Gabrielov, S. L. Bell, S. Bedioui, L Roué, and J. Devynck, Zeolite encapsulated cobalt(II) and copper(II) perfluorophthalocyanines: Synthesis and characterization, *Inorg. Chem.* **33,** 67–72 (1994).
80. N. Herron, Toward Si-based life: Zeolites and enzyme mimics, *Chemtech* **19,** 542–548 (1989).
81. B. T. Holland, C. Walkup, and A. Stein, Encapsulation, stabilization and catalytic properties of flexible metal porphyrin complexes in MCM-41 with minimal electronic perturbation by the environment, *J. Phys. Chem.* B **102,** 4301–4309 (1998).
82. C. Bowers, and P. K. Dutta, Olefin oxidation by zeolite-encapsulated $Mn(salen)^+$ complexes under ambient conditions, *J. Catal.* **122,** 271–279 (1990).
83. R. F. Parton, C. P. Bezoukheanova, J. Grobet, P. J. Grobet, and P. A. Jacobs, Synthesis, characterization and catalytic performance of nitro-substituted Fe-phthalocyanines on zeolite-Y, *Stud. Surf. Sci. Catal.* **83,** 371–378 (1994).
84. R. Raja, and P. Ratnasamy, Direct conversion of methane to methanol, *Appl. Catal.* A **158,** L7–L15 (1997).
85. C. R. Jacob, S. P. Varkey, and P. Ratnasamy, Zeolite encapsulated copper (X_2-Salen) complexes, *Appl. Catal.* A **168,** 353–364 (1998).
86. C. R. Jacob, S. P. Varkey, and P. Ratnasamy, Selective oxidation over copper and manganese salens encapsulated in zeolites, *Microporous Mesoporous Mater.* **22,** 465–474 (1998).
87. R. Raja, and P. Ratnasamy, Oxidation of cyclohexane over copper phalocyanines encapsulated in zeolites, *Catal. Lett.* **48,** 1–10 (1998).
88. S. Chavan, D.Srinivas, and P. Ratnasamy, Structure and catalytic properties of dimeric copper(II) acetato complexes encapsulated in zeolite-Y, *J. Catal.* **192,** 286–295 (2000).
89. R. Raja, and P. Ratnasamy, Activation of dioxygen by copper complexes incorporated in molecular sieves, *J. Mol. Catal.* A **100,** 93–102 (1995).
90. M. Eswaramoorthy, S. Neeraj, and C. N. R. Rao, High Catalytic Efficiency of Transition Metal Complexes Encapsulated in a Mesoporous Phase, *J. Chem. Soc. Chem. Commun.* **5,** 615–616 (1998).
91. E. I. Solomon, and M. D. Lowery, Electronic structure contributions to function in bioinorganic chemistry, *Science* **259,** 1575–1581 (1993).
92. T. R. Felthouse, The chemistry, structure and metal–metal bonding in compounds of rhodium(II), *Prog. Inorg. Chem.* **29,** 73–166 (1982).
93. K. J. Balkus, Jr., A. A. Welch, and B. E. Gnade, The preparation and characterization of rhodium(III) salens complexes encapsulated in zeolites X and Y, *zeolites* **10,** 722–729 (1990).
94. M. M. Bhadbhade, and D. Srinivas, Effects on molecular association, chelate conformation and reactivity toward substitution in Cu(5-X-salen) complexes, $salen^{2-}$ = N,N′-ethylenebis (salicylidenaminato), X = H, CH_3O and Cl: synthesis, X-ray structures and EPR investigations, *Inorg. Chem.* **32,** 5458–5466 (1993).

95. M. M. Bhadbhade, and D. Srinivas, Spin crossover in substituted N, N′-ethylenebis (salicylidenamine) iron(III) complexes: variable temperature EPR and X-ray structures of [Fe(5-CH_3O-salen)$(Im)_2$]Y, where Y = ClO_4^- and Cl^-, *Polyhedron* **17,** 2699–2711 (1998).
96. S. Deshpande, D.Srinivas, and P. Ratnasamy, EPR and catalytic investigation of Cu(salen) complexes encapsulated in zeolites, *J. Catal.* **188,** 261–269 (1999).

12

Thermo-Catalytic Oxidation of Dihydroxybenzenes in the Presence of Nanoparticle Iron Oxide

Eun-Jae Shin[a,c], Mohammad R. Hajaligol[b,*], Donald E. Miser[b], and W. Geoffrey Chan[b]

12.1. INTRODUCTION

During the pyrolysis and gasification of fossil and nonfossil materials such as coals and biomass, various organic compounds are produced. Many of these decomposition products have been considered a source of major concern for plant operations and product utilization, especially their emission into the environment which is seen as a major public concern.[1–5] Examples of these organic compounds are organic acids, aldehydes, ketones, and phenols. As a class of compounds, phenols, such as catechol, hydroquinone, and their methylated derivatives, are found among the products of thermo-chemical conversion processes of biomass[4,5] as well as in cigarette smoke.[6–10] Pyrolytic formation of phenolic compounds from polyphenols in biomass[6–10] and the decomposition behavior of phenolic compounds under homogeneous[11–17] and heterogeneous[4,5,18–22] conditions have been studied. These studies have shown that with heterogeneous

[a] Philip Morris USA Postgraduate Research Program, VA
[b] Philip Morris USA Research Center, 4201 Commerce Road, Richmond, VA 23234, USA
[c] Current address: Colorado School of Mines, Department of Chemical Engineering, Golden, CO 80401
[*] To whom correspondence should be addressed. E-mail: mohammad.r.hajaligol@pmusa.com

gas–solid reactions, using reagents such as freshly formed calcium oxide[4,5] or iron oxide nanoparticles,[21–23] the decomposition temperature is significantly lowered, when compared to homogeneous conditions.[15–17]

Previous studies in conventional reactor setups at Philip Morris USA have demonstrated the significant effectiveness of nanoparticle iron oxide on the oxidation of carbon monoxide when compared to the conventional, micron-sized iron oxide,[21,24,25] as well as its effect on the combustion and pyrolysis of biomass[21] and biomass model compounds.[21,22] These effects are derived from a higher reactivity of nanoparticles that are attributed to a higher BET surface area as well as the coordination of unsaturated sites on the surfaces. The chemical and electronic properties of nanoparticle iron oxide could also contribute to its higher reactivity. In this work, we present the possibility of using nanoparticle iron oxide as a catalyst for the decomposition of phenolic compounds.

The objective of this work is to understand the cracking and oxidation of the phenolic compounds under a mildly oxidative atmosphere over nanoparticle iron oxide. In particular, we estimated the kinetics of the cracking reaction for catechol and hydroquinone. As a long-term goal, we want to understand the chemical pathways and develop parameters that are effective in reducing phenolic compounds in thermo-catalytic reactions. Hence, we first characterized the materials that were exposed to various reaction conditions. We collected the iron oxide nanoparticles that had been preheated at 200, 300, and 350°C, measured their BET surface areas, and average particle sizes, and determined the phases present by high-resolution transmission electron microscopy (HRTEM). We also collected the iron oxide nanoparticles after being exposed to the vapor of a starting material, such as hydroquinone, and analyzed the solid phase changes that could be related to the deactivation of the catalyst. Characteristics of the nanoparticle iron oxide changed with the reaction conditions but the variations were not significant. Nanoparticle iron oxide remained active after being exposed to the vapor of reactants without any carbon deposition. We present here the results of catechol, 3-methylcatechol, hydroquinone, 2-methylhydroquinone, and 2,3-dimethylhydroquinone cracking in the presence of the iron oxide nanoparticles under partially oxidative conditions that are relevant to practical applications of biomass and coal derived materials. The conversions and product distributions generated from different reactants are compared, reaction pathways leading to the formation of cracking products are considered, and characteristics of the iron oxide under different conditions are described. For the experimental work, we used a flow tube reactor setup in a batch mode which was coupled with a molecular beam mass spectrometer (MBMS) for direct and real time sampling and measurement from the reaction system. Multivariate factor analysis[26–29] was employed to simplify the data and to extract groups of products that behaved similarly as a function of reaction severity. This approach provides an efficient way of handling the complex data that resulted from mass spectrometric analysis of high-temperature chemical processes.

12.2. EXPERIMENTAL

12.2.1. Material and Characterization Procedure

The nanoparticle iron oxide in this study is a commercial product sold as Nanocat® iron oxide, purchased from Mach I Inc., (King of Prussia, PA). Nanocat® has a particle

diameter of about 3 nm with a BET surface area of 250 m^2/g. It seemed prudent to fully characterize the materials of interest. Although the material was originally characterized in 1993[31–33] and determined to most likely be a nanoparticle form of lepidocrocite, it was not an iron oxide *per se*, but instead, an iron oxy-hydroxide. This leaves to question the role, if any, for catalysis involving the hydroxyl groups or the change in structure, both surfacial and lattice, associated with the presence of these groups. Similarly, changes during preparation or catalysis in the chemistry or structure of the catalyst itself might also affect the mechanism or leave clues to the mechanism of catalysis. Thus, in order to verify the results previously reported and to insure consistency between lots manufactured at widely separated times, the authors have presented their own characterizations.[21,25,30] The newer characterizations include data from X-ray diffraction (XRD), Fourier transform infrared spectroscopy (FTIR), energy dispersive spectroscopy (EDS), electron energy loss spectroscopy (EELS), selected area electron diffraction (SAED), transmission electron microscopy (TEM), high-resolution (atomic imaging) field emission transmission electron microscopy (HRTEM), and extended edge X-ray absorption fine structure spectroscopy (EXAFS).

For this study, the bed of the nanoparticle iron oxide was preheated to reach the reaction temperature before any cracking study was conducted. During preheating, the nanoparticle iron oxide dehydrated and tended to coarsen, which led to the growth of particles. We collected the iron oxide nanoparticles preheated at 200, 300, and 350°C, measured their particle sizes, determined the phases present, and their surface areas by (HRTEM), EELS, and measured their BET surface area. We also collected the iron oxide nanoparticles after being exposed to the vapor of a substrate, hydroquinone, and analyzed phase changes that could be related to the deactivation of the catalyst. While phase changes of the iron oxide resulting from the exposure to air before characterization by HRTEM was a concern, the identification of the relatively unstable compounds magnetite (Fe_3O_4) and maghemite (γ-Fe_2O_3) from very similar, previously performed experiments[22,30] suggested that the stability of these phases was sufficient under the conditions of the experiment to allow direct interpretation of the phases present during reaction.

For HRTEM analysis the sample catalyst was physically dislodged from the quartz chips (see the following section), suspended in methanol, and applied to "lacey" carbon grids. The transmission electron microscope used was a Philips-FEI Tecnai F20 equipped with a Schottky field emission gun operating at 200 kV accelerating potential. Energy dispersive spectra (EDS) were collected by an EDAX thin window detector using Emispec software for the analysis. Images and EELS spectra were collected digitally by a Gatan imaging filter (GIF). Fourier transforms of the high resolution images were performed by Gatan Digital Micrograph software. This software was also employed in the measurements of lattice spacings and interplanar angles from the transformed images. More detailed procedure for the phase analysis can be found elsewhere.[30]

12.2.2. Reactor Setup and Procedure for Oxidative Cracking

The experimental setup and procedures used in this study was described previously in more detail.[21,22] Briefly, all experiments were carried out in a flow tube reactor

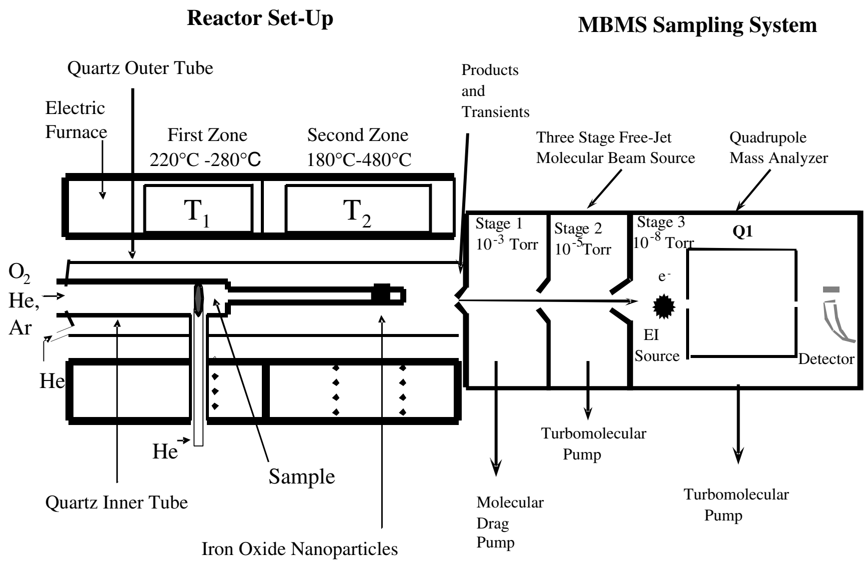

FIGURE 12.1. Schematic of tubular reactor setup for pyrolysis/catalytic/oxidation studies coupled to a molecular-beam mass spectrometer sampling system.

under 3% of oxygen in helium. The flow tube reactor was made of quartz and consisted of inner and outer tubes, with reactions occurring in the inner tube and the flow from the outer tube used for diluting the reaction products at the end of the reactor, where it was coupled to a molecular beam mass spectrometer (MBMS) for product detection, as shown in Fig. 12.1. An electric furnace with two independently controlled temperature zones was used to heat and control the temperatures in the reactor. The first zone was set at 220°C for hydroquinones and 280°C for catechols so that a slow and steady sublimation of the starting materials could be obtained. The temperature in the second zone was varied in the range of 180°C to 480°C to study its effect on the reactant conversion and product distributions. The feed rate of the starting material was fixed at about 18×10^{-3} mmol/min and was calculated by dividing a given weight of a starting material sublimed completely into the reactor by the time it takes to sublime. The conversion is defined as the difference between the total amounts of the starting materials fed to the system (measured under the conditions with no conversion) and the amount that exited the system, divided by the total amount fed. The estimate of unreacted starting material was done by monitoring a single ion (m/z 110 for catechol and hydroquinone, m/z 124 for 3-methylcatehol and 2-methylhydroquinone, and m/z 138 for 2,3-dimethylhydroquinone) as a function of evolution time by MBMS. The monitoring was done in such a way that the integrated area of the steady-state evolution of the single ion resulting from various reaction conditions was subtracted from that resulting from a controlled condition where no reaction was observed. Due to a small particle size of 3 nm, the iron oxide (2.5 mg) must be mixed with quartz chips (1 g) before being placed into the reactor. A bed of nanoparticle iron-oxide/quartz chips mixture was placed at the end of the inner tube between two pieces of clean quartz wool and was preheated to a given reaction temperature before any reactant was fed through the reactor.

The average size and surface area of quartz chips were 50 to 70 mesh and 0.29 g/m^2 respectively. The effect of the quartz chips on the reaction were already discussed in a previous work.[23] A flow rate of 10 mL/min of argon (1%) in helium was used as an internal standard to obtain the semi-quantitative data.

Catechol, 3-methylcatechol, hydroquinone, 2-methylhydroquinone, and 2,3-dimethylhy-droquinone with 99% purity were purchased from Acros Organics (Pittsburgh, PA) and used as received. Each sample was loaded into a quartz holder "boat" and was inserted into the first heated zone, after the catalyst had been preheated to a given temperature while the carrier gas, composed of 3% oxygen, 1% argon, with a balance of helium was flowing through the setup. Estimated residence time for the vapors in this zone was about 0.5 s. The vapors formed in this zone passed through the bed of the nanoparticle iron oxide and the products exiting the reactor (inner tube) were diluted with the helium flowing in the outer tube. Before condensing, the product mixture was introduced directly into the orifice of the MBMS for sampling. Finally, factor analysis was used to deconvolute the complex chemistry of the dihydroxybenzene conversion.[26–29]

12.3. RESULTS AND DISCUSSION

12.3.1. Characterization of the Iron Oxide Before and After Use

The iron oxide preheated at 200, 300, and 350°C were separately collected and characterized using HRTEM and BET surface area measuring techniques. At these temperatures Nanocat® showed a progressive increase in the amount of hematite (α-Fe_2O_3) present. The starting material was found to consist of grains, typically of 3 nm diameter, consistent with earlier findings. It was variable in structure, however, with most of the material having a weakly crystalline lattice or no lattice at all. A few percent of material consisted of well crystallized γ-Fe_2O_3. As such, the powder could not be considered a single phase material, but instead a mixture of crystalline and amorphous (glassy) phases. Larger d-spacings, determined from Fourier transforms of lattice images that would be expected from lepidocrocite, were not generally found. Indeed d-spacings normally associated with any of the commonly cited hydroxides of iron, such as goethite or bernalite, could not be found. Instead, the lattice, when present, appeared to be a modification of a body-centered cubic lattice that could not be associated with any known phase. The presence of hydroxyl groups were verified by FTIR, EELS, and EDS analyses. Composition determinations suggested Fe/O ratios intermediate between FeOOH (iron oxyhydroxide) and $Fe(OH)_3$ (bernalite), and suggested that the sample was a mixture of these materials. At 200°C, the phase of the iron oxide was essentially the same as the starting material (before preheating), i.e. iron oxy-hydroxide with minor γ-Fe_2O_3.[30] However, at higher temperatures, it dehydrated and coarsened to the extent that it gave a lower BET surface area and larger particle sizes than those of the starting material. At 300°C, minor amounts of hematite (Fe_2O_3) were observed and appeared as coherent diffraction maxima in the selected area electron diffraction (SAED) patterns. By 350°C the diffuse rings, indicating incoherent diffraction that remained in the 300°C patterns, were completely replaced by intense coherent maxima representing hematite.

The TEM images of the iron oxide at three temperatures, 200°C (Fig. 12.2a), 300°C (Fig.12.2e) and 350°C (Fig. 12.2i) are shown in Fig. 12.2. At 200°C, as stated above, the phase of iron oxide is essentially the same as the room temperature sample. At 300°C, the hydroxylated phase was poorly crystalline to amorphous, as evidenced by the presence of the many defects in the high-resolution image and the presence of incoherent diffraction "rings" in the selected area electron diffraction (SAED) pattern, shown in Fig. 12.2b and f. However, by 350°C the material had coarsened, became more crystalline, and had largely experienced a phase change between these two temperatures. The SAED of the 350°C sample, shown in Fig. 12.2j, showed strong maxima corresponding to the rhombohedral phase hematite (α-Fe_2O_3) as well as a quantity of poorly organized material.

The iron oxide was also collected and characterized after it was used once, having been exposed to vapors of hydroquinone, at reaction temperatures of 200°C, 300°C, and 350°C. The catalysts exposed to vapors of the dihydroxybenzene displayed the same structural and chemical transformations as in the absence of these vapors, but the transformation to α-Fe_2O_3, as monitored by electron diffraction, occurred at slightly lowered temperatures. At 200°C, the material was substantially the same as the starting materials (Figs. 12.2a and b and 12.3a and b). However, Fourier transforms of lattice images indicated that the glassy component was found to be in greater quantity than that found in the absence of hydroquinone and the minor amounts of γ-Fe_2O_3, found in the starting material, were not generally observed. Instead, minor amounts of hematite were found. SAED patterns (Fig. 12.3b) indicated only the diffuse rings associated with the carbon substrate and iron oxide glass with little to no coherent diffraction maxima associated with crystalline iron phases. Broad peaks and prominent shoulders in the EELS spectra for the L2 and L3 absorption lines as well as in the O–K line attested to the structural variability of the powder (Figs. 12.2c and d and 12.3c and d). These shoulders and peak broadening were more pronounced than in the samples that were not exposed to hydroquinone. This is consistent with the observation of more glassy materials in the sample. Minor coarsening was apparent to the extent that it gave a lower BET surface area and larger particle sizes than that of the starting material.

By 300°C, considerable changes occurred with respect to the crystallinity of the sample as shown in Figs. 12.2e and f and 12.3e and f. SAED patterns shown in Figs. 12.2f and 12.3f showed an increase in the amount of intense coherent maxima, which correspond to α-Fe_2O_3, in the sample exposed to hydroquinone. TEM photomicrographs indicated slight grain growth ranging in excess of 5 nm and larger. Larger crystals of hematite had grown among the smaller, defect-rich and poorly organized crystals. Intense lattice lines are apparent throughout the images with local disruption restricted to grain boundaries. Incipient crystal faces often developed with at least some on $\{11.0\}$ of hematite. EELS spectra (Figs. 12.2g and h and 12.3g and h) were sharper when exposed to hydroquinone with four peaks visible (one as a shoulder on the higher energy peak) for the oxygen-K region and slightly skewed L3 and L2 peaks of iron. Fourier transforms of the lattice images revealed spinel spacings, despite their absence from electron diffraction patterns, which would correspond to γ-Fe2O3.

By 350°C, considerable grain growth had occurred when exposed to the vapors and the sample was mostly hematite as shown by comparing Figs. 12.2i and j and 12.3i

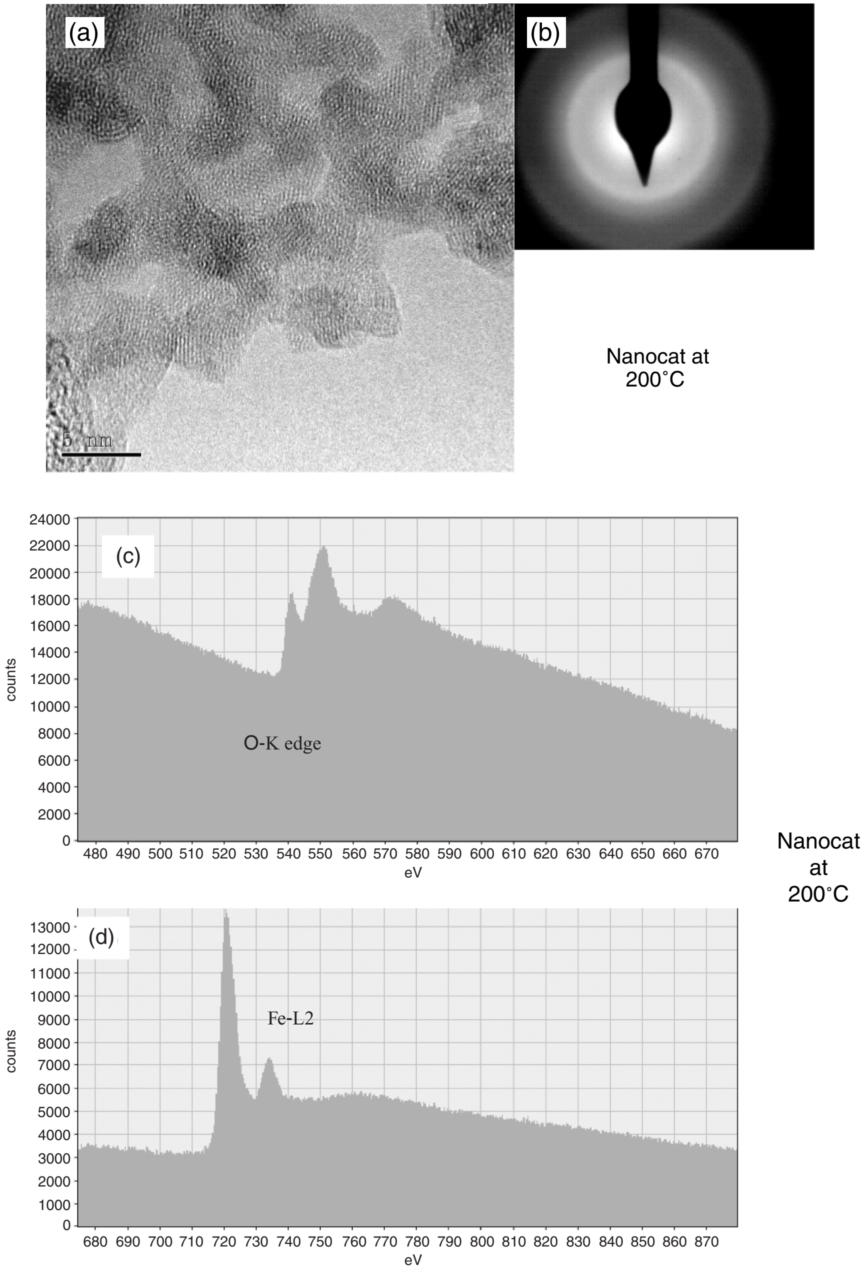

FIGURE 12.2. (a) HRTEM image of Nanocat heated to 200°C; (b) SAED of iron oxide heated to 200°C; (c) EELS spectrum of Oxygen-K edge from Nanocat heated to 200°C; (d) EELS spectrum of Fe-L edge from Nanocat heated to 200°C; (e) HRTEM image of Nanocat heated to 300°C; (f) SAED of iron oxide heated to 300°C; (g) EELS spectrum of Oxygen-K edge from Nanocat heated to 300°C; (h) EELS spectrum of Fe-L edge from Nanocat heated to 300°C; (i) HRTEM image of Nanocat heated to 350°C; (j) SAED of iron oxide heated to 350°C; (k) EELS spectrum of Oxygen-K edge from Nanocat heated to 350°C; (l) EELS spectrum of Fe-L edge from Nanocat heated to 350°C.

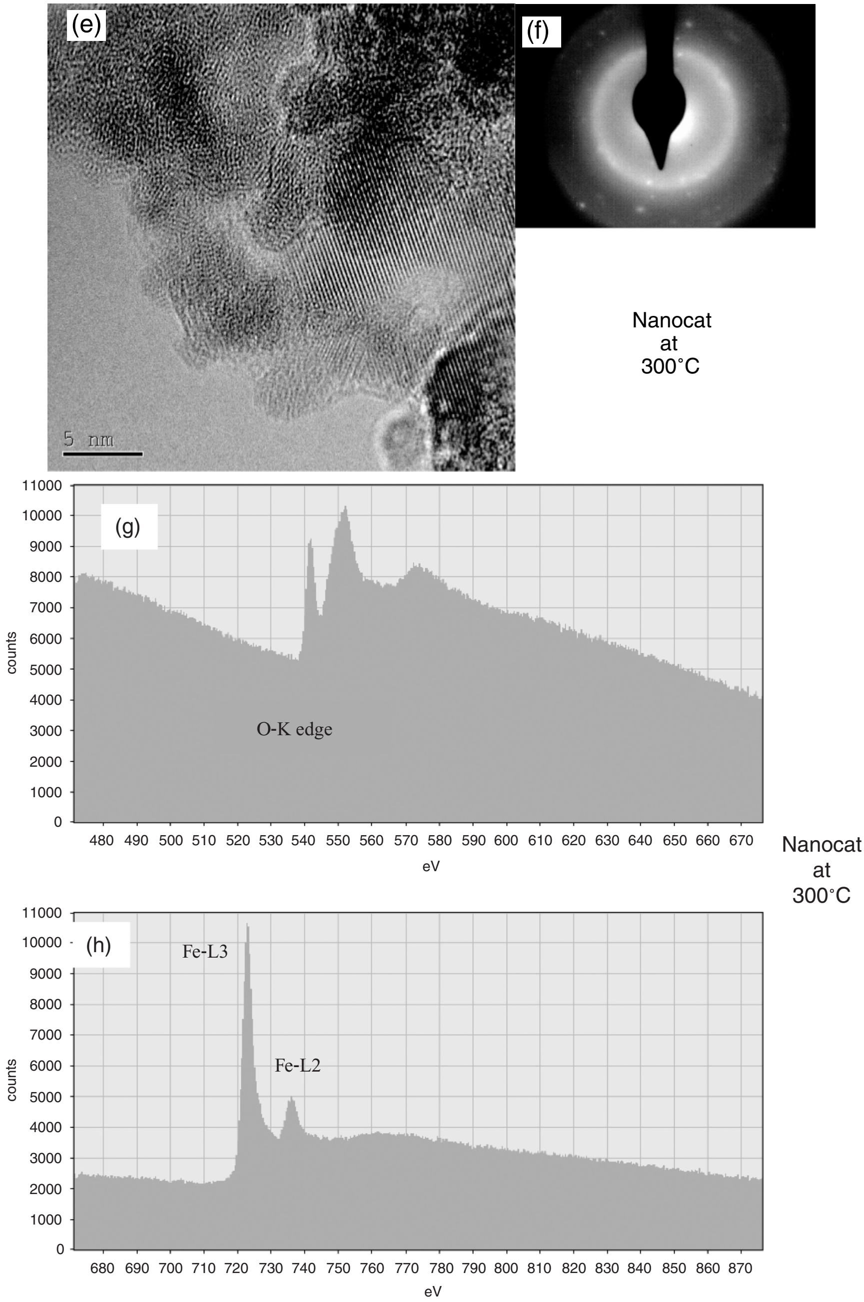

FIGURE 12.2. (*Continued*)

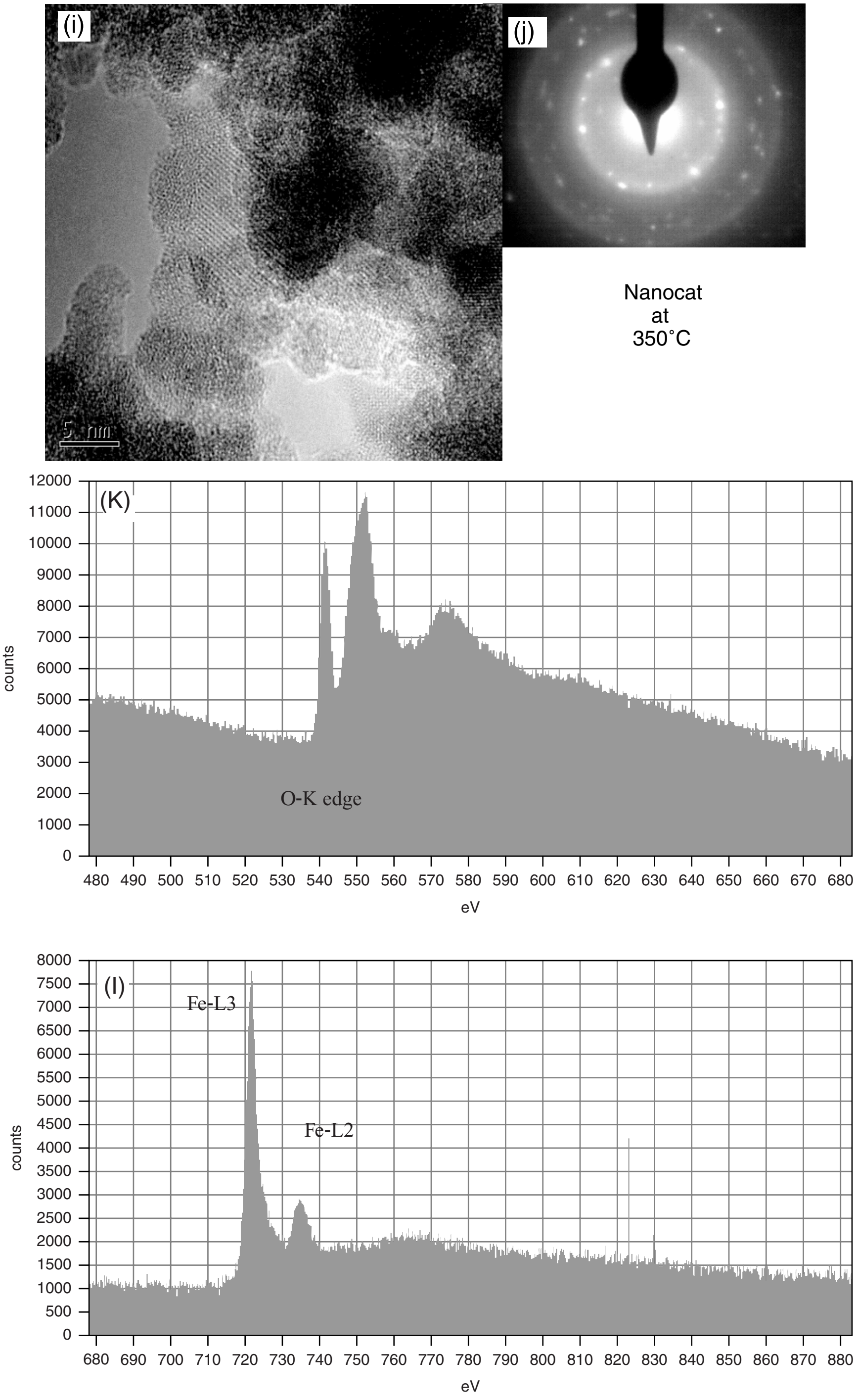

FIGURE 12.2. (*Continued*)

and j. Electron diffraction patterns displayed entirely hematite reflections. EELS spectra shown in Figs. 12.2k and l and 12.3k and l were also correspondingly sharp and intense. The relative intensity of the first O–K peak was much stronger than the peak at lower temperatures. At 350°C, the catalyst "product" was similar to that formed at 300°C, however, regions of the sample existed where glassy material occurred as massive, separate grains and as a coating on the iron oxide. These probably originated from the glass wool used in the tube furnace. Much of the sample consisted of large grains that had grown as cements, rather than as fused grains or simply as grain growth. Fourier transforms of lattice images from both the cement and original grains indexed as hematite. No detectable deactivation of the iron oxide was observed while it was being exposed to the vapors of hydroquinone. When the same amount of reactant feed was introduced repeatedly for the same catalyst bed, there was also no detectable deactivation of the iron oxide. This could be attributed to a diluted reactant feed, i.e. 18×10^{-3} mmol/min, and a continuous flow of 3% oxygen in helium, which could have continuously oxidized any carbon deposition, if any, on the surfaces of the iron oxide. Figure 12.3 showed the TEM images of the iron oxide that was used for hydroquinone cracking with 3% of oxygen at 300°C (Fig. 12.3e) and 350°C (Fig. 12.3i). At both of these temperatures there were more coherent diffraction maxima present than in those samples that were never exposed to hydroquinone (compare with Fig. 12.2e and 12.2i). In fact the SAED of the 350°C (Fig. 12.3j) sample showed no diffuse rings, indicating that there was no amorphous or poorly crystalline phases present within the sampled area. There was also no evidence of carbon deposition. The samples of the iron oxide after the experiments showed similar phases to those observed in the absence of reactant, i.e. poorly crystalline FeOOH and/or $Fe(OH)_3$ with minor hematite at 300°C and nearly all α-Fe_2O_3 at 350°C. Furthermore, the catalyst showed consistency in its retained reactivity for subsequent experiments. Identification of the active site from the used catalyst was seemingly hampered by the lack of crystal faces, especially in the higher temperature experiments. As previously mentioned, {11.0} faces are apparent in the lower temperature experiments but they seem to have disappeared in the coarser crystals of the 350°C experiment. This is another difference between the used catalyst and the fresh catalyst. Not only has the phase transformation been more complete when exposed to catechol, but the absence of crystal faces precludes a fixed distance between atoms on the surface of the catalyst. This should have made the binding of molecules to the surface more general thereby allowing a range of reactions possible.

→

FIGURE 12.3. HRTEM image of Nanocat heated to 200°C in the presence of hydroquinone; (b) SAED of iron oxide heated to 200°C in the presence of hydroquinone; (c) EELS spectrum of Oxygen-K edge from Nanocat heated to 200°C in the presence of hydroquinone; (d) EELS spectrum of Fe-L edge from Nanocat heated to 200°C in the presence of hydroquinone; (e) HRTEM image of Nanocat heated to 300°C in the presence of hydroquinone; (f) SAED of iron oxide heated to 300°C in the presence of hydroquinone; (g) EELS spectrum of Oxygen-K edge from Nanocat heated to 300°C in the presence of hydroquinone; (h) EELS spectrum of Fe-L edge from Nanocat heated to 300°C in the presence of hydroquinone; (i) HRTEM image of Nanocat heated to 350°C in the presence of hydroquinone; (j) SAED of iron oxide heated to 350°C in the presence of hydroquinone; (k) EELS spectrum of Oxygen-K edge from Nanocat heated to 350°C in the presence of hydroquinone; (l) EELS spectrum of Fe-L edge from Nanocat heated to 350°C in the presence of hydroquinone.

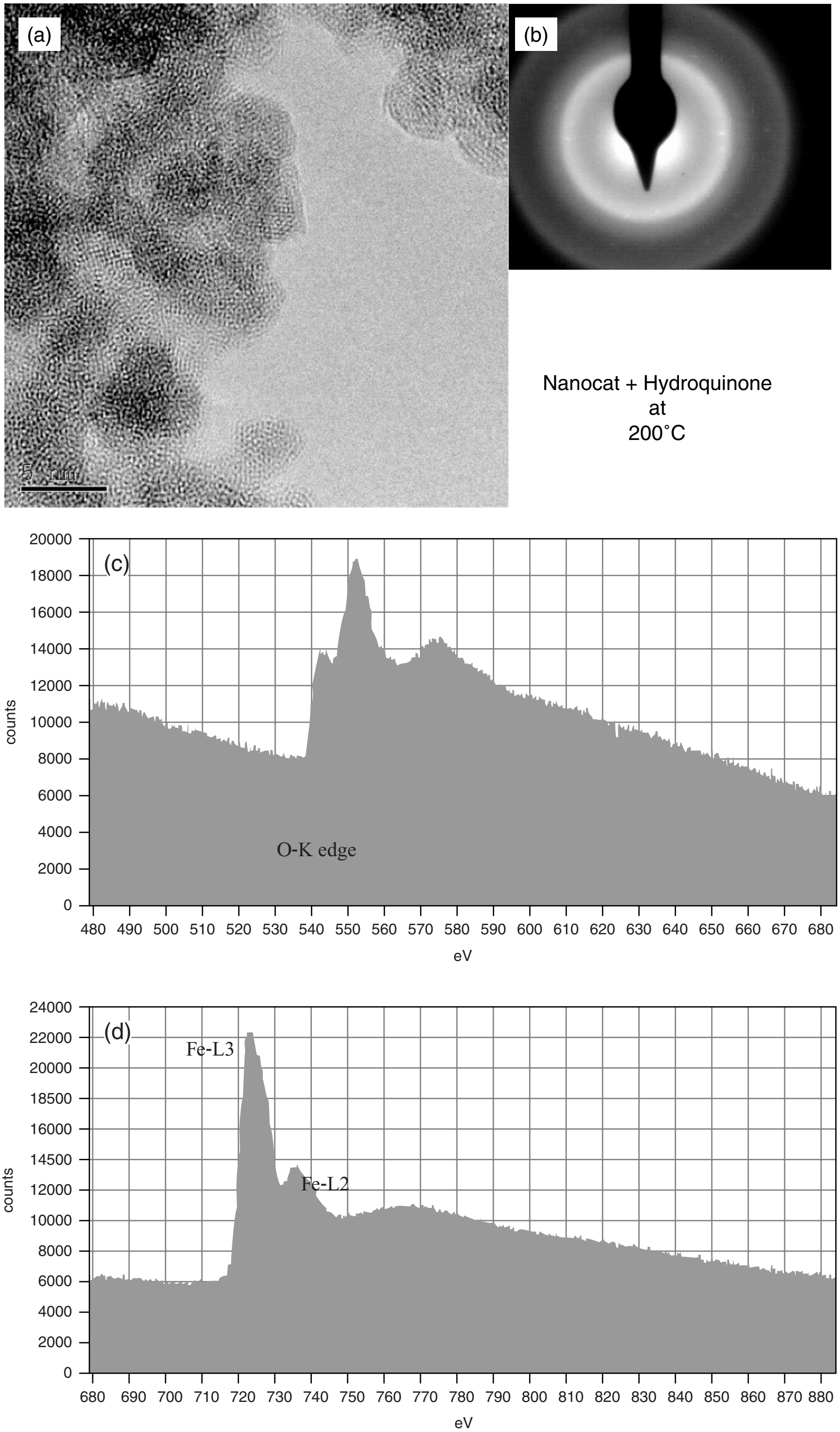

FIGURE 12.3. (See Caption in facing page)

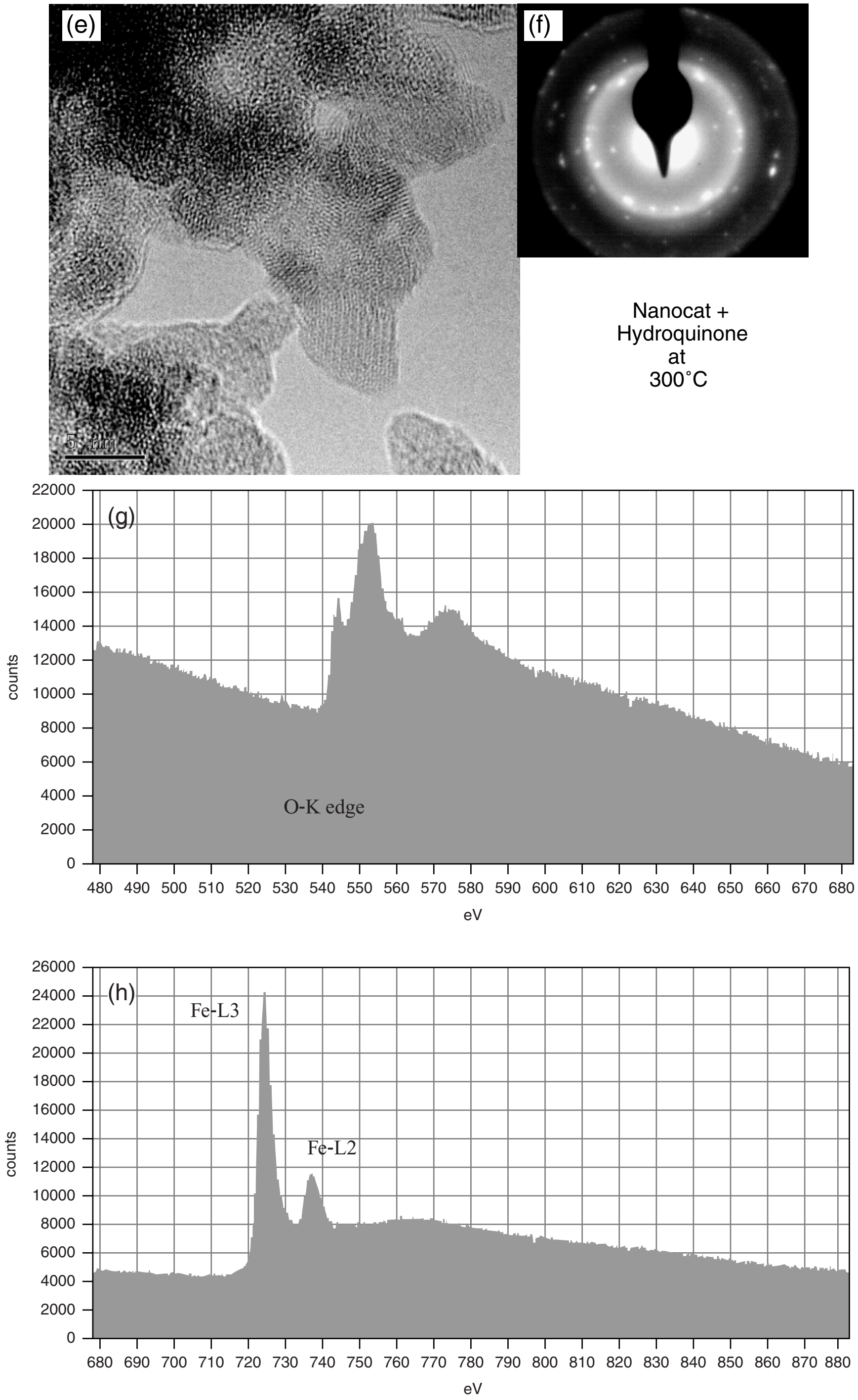

FIGURE 12.3. (*Continued*)

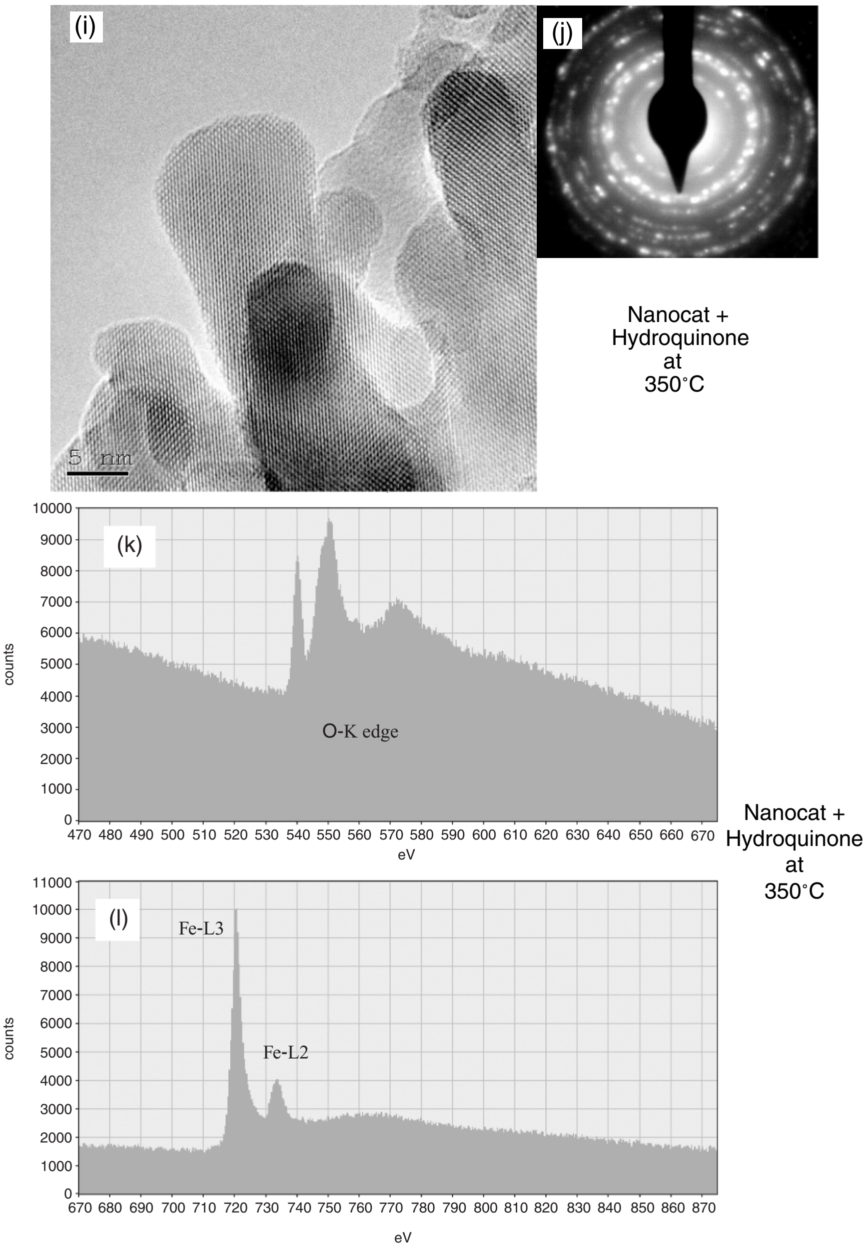

FIGURE 12.3. (*Continued*)

TABLE 12.1. Characteristics of the iron oxide at different conditions

		Before Use[a]	After Use[b]
25°C	BET surface area (m^2/g)	250	
	Particle size (nm)	3 nm	
	Dominant phases	$FeOOH/Fe(OH)_3$	
	BET surface area (m^2/g)	170	–
200°C	Particle size (nm)	4	4-7
	Dominant phases	$FeOOH/Fe(OH)_3$	$FeOOH/Fe(OH)_3$
	BET surface area (m^2/g)	170	–
	Particle size (nm)	5 to 16$FeOOH/Fe(OH)_3 + \alpha$-	5 to 16
300°C	Dominant phases	Fe_2O_3	$FeOOH/Fe(OH)_3 + \alpha$-Fe_2O_3
	BET surface area (m^2/g)	140	–
	Particle size (nm)	6 to 20	4-35
350°C	Dominant phases	α-Fe_2O_3	α-Fe_2O_3

[a] After preheating.
[b] After preheating and exposure to hydroquinone cracking.

The properties of the iron oxide at different reaction conditions are summarized in Table 12.1. As the results shows, these properties varied with the reaction conditions, and one might assume that the experimental data were obtained from the iron oxide with different properties at different reaction conditions. While we recognize these variations, we also emphasize that the variation in particle sizes and surface areas in the temperature range employed in this study is not significant, i.e., the BET surface area of 170 and 140 m^2/g at 200 and 350°C, respectively. Furthermore, for the purpose of this work, the variation in the properties did not seem to be significant. Thus the "active sites" for catalysis of dihydroxybenzene decomposition associated with trivalent iron from a hydroxide appeared to be similar to the "active sites" from anhydrous trivalent iron from hematite. This iron oxide has had appreciable effects on various reactions based on previously studies.[21–23,25,30] Therefore, using the iron oxide, even though its characteristics are not constant in the temperature range used in this work, is justified according to the objective of this work.

12.3.2. Decomposition of the Reactants

The total conversions of catechol, 3-methylcatechol, hydroquinone, 2-methylhydroquinone, and 2,3-dimethyldhydroquinone were compared in the presence and absence of the nanoparticle iron oxide in quartz chips beds. It is evident that the presence of nanoparticle iron oxide lowered the temperature for a given conversion by about 180°C for all starting materials. In Fig. 12.4, representative results of the comparison are shown for catechol and hydroquinone over nanoparticle iron oxide/quartz mixture and quartz only, as a function of temperature. Each data point in Fig. 12.4 represents the averaged result of more than two experiments under the same conditions and a fresh catalyst was used for each new experiment. Catechol showed lower reactivity (50% conversion) than hydroquinone (100% conversion) at 260°C in the presence of the catalyst. This could be attributed to two phenomena. When the dihydroxybenzenes approach the catalyst surface in a co-planar fashion, intermolecular hydrogen bonding will lower the adsorption of catechol onto the catalyst surface and its interaction

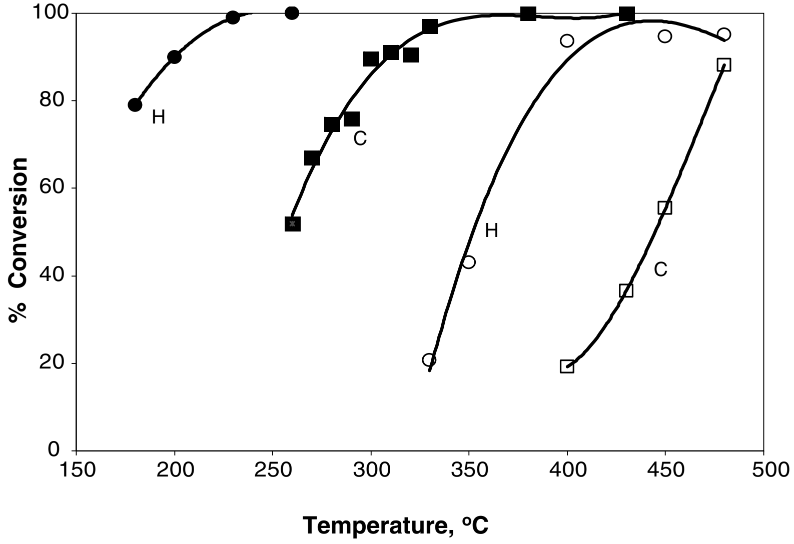

FIGURE 12.4. Conversion of catechol (C) (■,□) and hydroquinone (H) (●,○) over the nanoparticle iron oxide/quartz chips (■,●) and quartz chips (□,○) as a function of temperature with a feed rate of 18 × 10^{-3} mmol/min and an oxygen concentration of 3%.

with active site and/or oxygen relative to that of hydroquinone. On the other hand if the dihydroxybenzenes approach the catalyst surface in a perpendicular fashion, the intramolecular hydrogen bonding between the adjacent hydroxyl groups in catechol may not allow both groups to have significant interaction with the active site of the catalyst. Either of these effects can be supported by the lower melting point of catechol (105°C), resulting from intramolecular hydrogen bonding, compared to that of hydroquinone (170°C), resulting from intermolecular hydrogen bonds.

In order to show that the oxidative decomposition of dihydroxybenzenes is a result of their interaction with iron oxide surface and not of the quartz, we conducted similar experiments with the beds of quartz chips only. The results clearly indicated that under the conditions where hydroquinone or catechol was fully decomposed in the presence of iron oxide no decomposition was observed with quarts chips. However, as we increased the temperature to about 400°C, both catechol and hydroquinone began to show decomposition as shown in Fig. 12.4. The temperature of decomposition in the presence of quarts chips, though higher than with iron oxide, was still somewhat lower than expected for decomposition under homogeneous conditions where catechol and hydroquinone begin to decompose at temperatures above 500°C.[12] This could be attributed to the surface effect induced by quartz, which must have led to limited reactions to initiate decomposition at lower temperatures. In addition, the anhedral surface of quartz, like that of the more active iron oxide nanoparticles, would provide a wide range of interatomic distances to which any molecule could bind, thus producing a range of active sites. This range of sites could lead to a relative lack of specificity, as was evidenced by the mass spectral data (shown in the next section).

TABLE 12.2. Arrhenius parameters for the decomposition of catechol and hydroquinone in the presence and absence of iron oxide, assuming pseudo first-order kinetics

	Ea (kcal/mol)	*A* (s^{-1})	Correlat. Coeff.
Catechol			
Iron Oxide/Quartz	15.5	3.6×10^7	0.96
Quartz	30.2	3.3×10^{10}	0.99
Homogeneous Cracking[14]	34.4	8.7×10^7	–
Hydroquinone			
Iron Oxide/Quartz	10.0	5.0×10^4	0.96
Quartz	25.3	9.51×10^{10}	0.98

The effect of temperature can be effectively described in term of the global activation energy for the decomposition. Based on the assumption of a pseudo-first-order reaction, kinetic parameters resulted from two different conditions for catechol and hydroquinone are compared in Table 12.2 where homogeneous reaction data for catechol[14] were also included. The energy barrier for hydroquinone cracking in both cases was lower than that for catechol as evidenced by Fig. 12.4. It is noteworthy that the preexponential factor (A) is about 10^3 higher for catechol over quartz only, when compared to the result from the homogeneous reaction of catechol. This may be attributed to the surface reactivity of quartz that enhances the number of collisions, and depicted in the preexponential factor. In addition, the preexponential factor for catechol over quartz is about 10^3 higher than that over iron oxide. This is not surprising as the reaction over quartz starts at much higher temperature where the number of collisions would be much higher; i.e., the number of collisions is proportionally higher at higher temperatures. As is expected from the role of catalysts, the activation energy for catechol over the nanoparticle iron oxide was a factor of about 2 lower than that for homogeneous reaction, suggesting a strong effect of the nanoparticle iron oxide on the cracking reactions.

The effects of oxygen concentration with a catechol feed rate of 18×10^{-3} mmol/min and the effect of catechol feed rate with 3% oxygen on the cracking of catechol over nanoparticle iron oxide were studied at 280°C temperature. There was an increase in the conversion of catechol with an increase in oxygen concentration and a decrease in catechol feed rate (lower concentration) as illustrated in Fig. 12.5.

12.3.3. Product Distributions

As we presented above, the presence of quartz in the temperature range studied had no effects on the decomposition of dihyroxybenzenes. To further investigate this point and show the different effects of iron oxide and quartz on the product distribution, we present the product distribution for two cases of nanoparticle iron-oxide mixed with quartz chips and only quartz chips. Comparison in product distribution over nanoparticle iron oxide/quartz mixture and quartz was carried out with 3% of oxygen and 18×10^{-3} mmol/min of feed rate for starting materials, and at reaction temperatures that resulted in a comparable conversion of dihydroxybenzenes (e.g., 80%). Figure 12.6 shows the average spectra of the products obtained from MBMS for two cases with about 80% catechol conversion that was achieved at 300°C in the presence of iron oxide

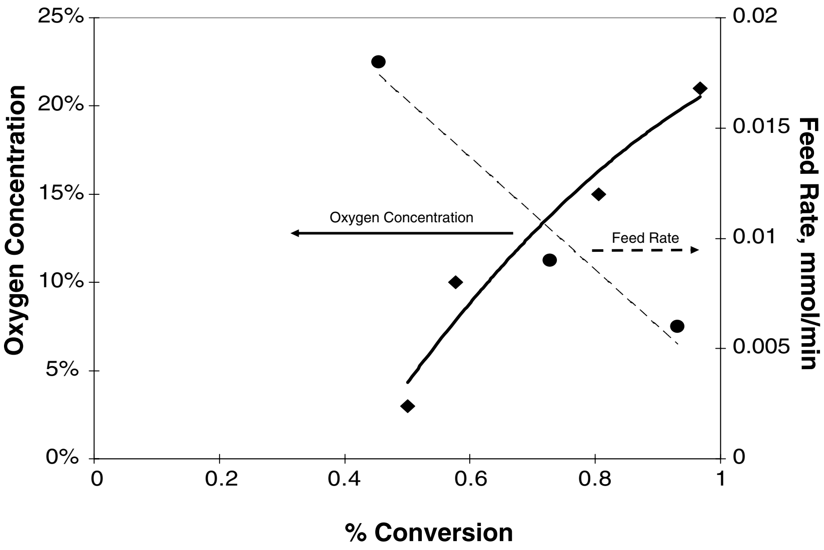

FIGURE 12.5. Effects of oxygen concentration and feed rate on catechol conversion over iron oxide/quartz chips at 280°C.

and at 480°C in the absence of iron oxide. For the catalytic oxidation over the iron oxide as shown in Fig. 12.6a, the peak at m/z 110 represents catechol. The major products from cracking of catechol were found at m/z 52 (assigned as C_4H_4, i.e., vinyl acetylene), m/z 80 (C_5H_4O, i.e., cyclopentadienone) and m/z 108 ($C_6H_4O_2$, i.e., o-benzoquinone). The cracking of catechol over nanoparticle iron oxide was complete at temperatures above 380°C. At 430°C temperature, catechol was totally oxidized to carbon dioxide (m/z 44), a minor amount of carbon monoxide (m/z 28), and water (not shown in Fig. 12.6). Product distribution of catechol cracking at 480°C temperature over quartz chips is shown in Fig. 12.6b where products observed were comprised of the same chemical species as seen in the iron oxide case as well as a new group of products, especially some aromatic compounds that were newly formed over quartz. Possible identities of the aromatic compounds are benzene (m/z 78), styrene (m/z 104), indene (m/z 116), and indanone (m/z 132). Benzene is one of the major products in the pyrolysis of phenolic compounds such as phenol,[15–17] cresols,[4,5] and catechol.[12–14] The formation of higher molecular weight compounds has been observed by others.[12–17] Nonetheless, it is surprising to observe this level of reactivity with quartz at this temperature and this could be attributed to the surface effect induced by quartz, which must have led to limited reactions to produce more aromatic compounds.

These patterns in product distribution were also observed with methyl-substituted catechol, such as 3-methylcatechol. In Fig. 12.7, products formed from 3-methylcatechol cracking under two similar conditions as above (e.g., 80% conversion) were compared. In the presence of nanoparticle iron oxide shown in Fig. 12.7a, the starting material was represented by m/z 124 with its fragment ions, m/z 78 and m/z 106. Major peaks for products were found at m/z 66 (C_5H_6, pentenyne), m/z 94 (C_6H_6O, methylcyclopentadienone), and m/z 122 ($C_7H_6O_2$, methylbenzoquinone). Figure 12.7b shows

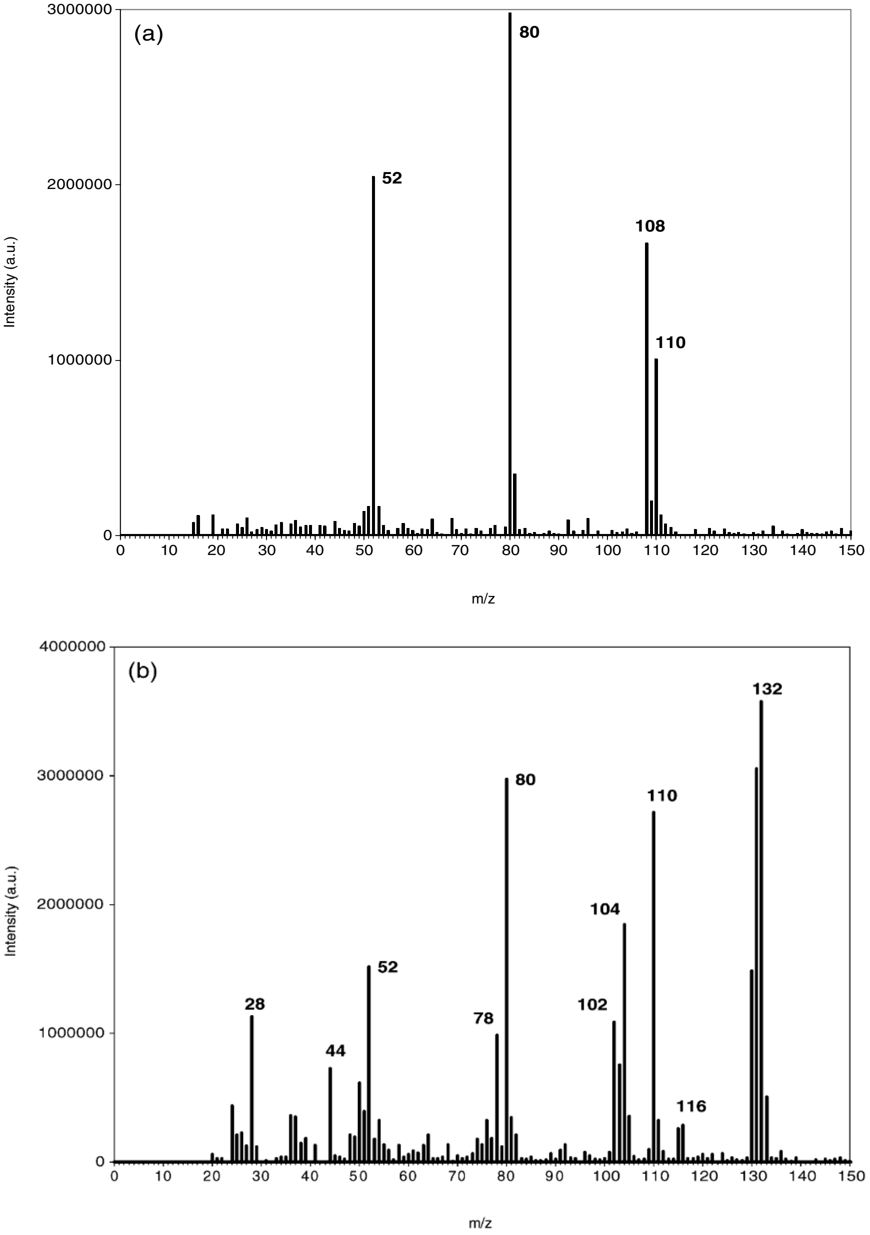

FIGURE 12.6. Product distribution resulting at 80% conversion of catechol over (a) iron oxide/quartz chips at 300°C and (b) only quartz chips at 480°C with 18×10^{-3} mmol/min and 3% of oxygen.

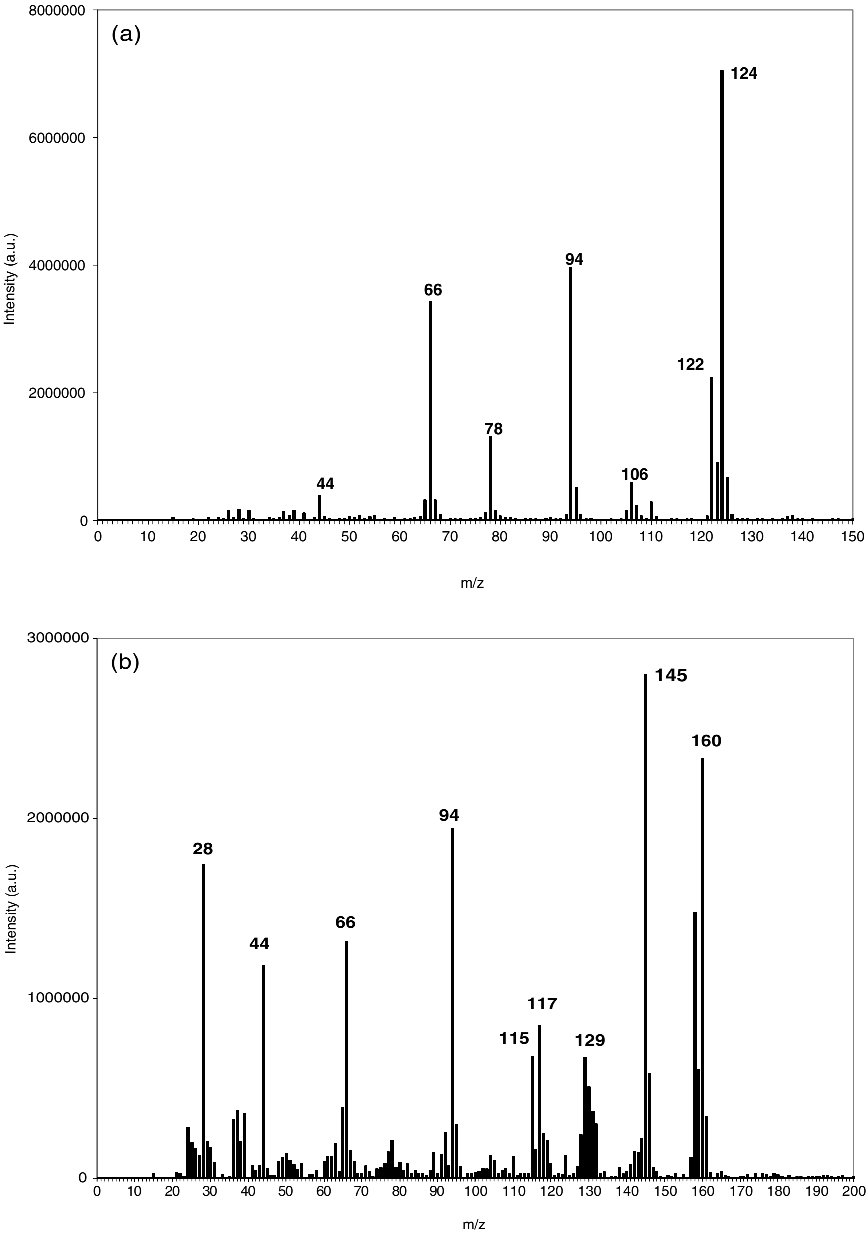

FIGURE 12.7. Product distribution resulting at 80% conversion of 3-methylcatechol over (a) iron oxide/quartz chips at 300°C and (b) only quartz chips at 480°C with 18×10^{-3} mmol/min and 3% of oxygen.

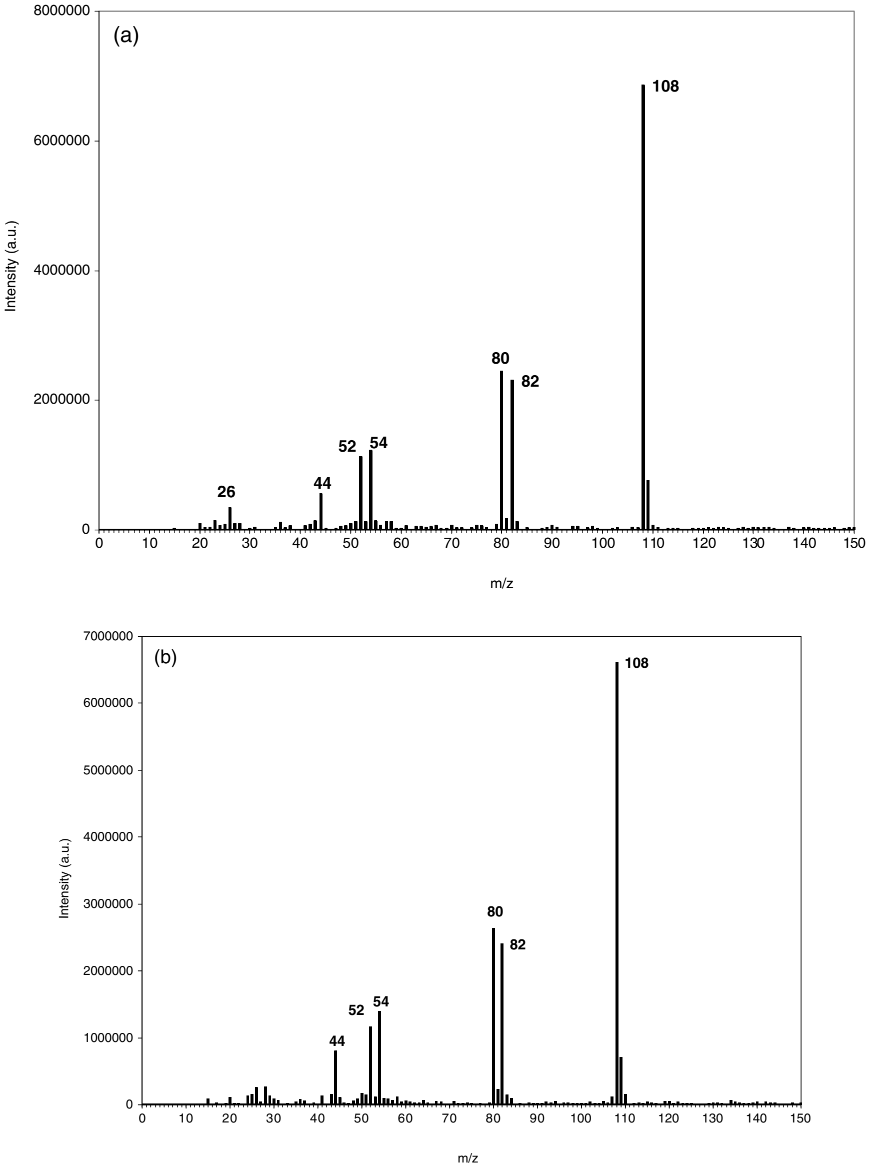

FIGURE 12.8. Product distribution resulting at 80% conversion of hydroquinone over (a) iron oxide/quartz chips at 300°C and (b) only quartz chips at 480°C with 18×10^{-3} mmol/min and 3% of oxygen.

product distributions generated with quartz chips in the absence of iron oxide. Again, we observed new products in addition to what we observed in Fig. 12.7a. Two dominant compounds are found at m/z 160 and m/z 145 and more carbon monoxide (m/z 28) and carbon dioxide (m/z 44) were formed. These results indicate that not only the activity of both materials, e.g., iron oxide and quartz, differ significantly (Fig. 12.4), but the nature of the active sites on these two materials are different as can be seen from the product distributions (Figs. 12.6–12.7).

The same comparison was made for hydroquinone for a given conversion of 80%, which is exhibited in Fig. 12.8. Unlike catechol and 3-methycatechol, products resulting from hydroquinone cracking in the presence and absence of iron oxide are identical. A peak found at m/z 110 is probably hydroquinone and its fragment ions are at m/z 39, 55, and 81. The identities of some of the products (Fig. 12.8a and b) are likely to be as follow: acetylene (m/z 26), vinyl acetylene (m/z 52), butadiene (m/z 54), cyclopentadienone (m/z 80), and 1,4-benzoquinone (m/z 108). To confirm the differences in chemistry between catechols and hydroquinones, 2,3-dimethyhydroquinone was subjected to the same comparison.

Figure 12.9 shows the products distribution generated from 2,3-dimethylhydroquinone cracking with 80% conversion under two different thermal conditions. Despite its two substituted methyl groups, it followed the same trend as found with hydroquinone, i.e. the product distributions were identical in both cases, which again was different from the chemistry of catechol. A peak of the starting material is found at m/z 136 (dimethylbenzoquinone) and possible identities of other peaks are methylpentenyne (m/z 80) and butadiene (m/z 54).

It is necessary to point out that our off-line pyrolysis data with GC/MS analysis of the resultant pyrolysates showed no interconversion between catechol and hydroquinone, and each dihydroxybenzene gave the corresponding benzoquinone. In addition, the analysis confirmed that the peak found at m/z 132 was indeed indanone (C_9H_8O). Nevertheless, the identities of other products should be confirmed by off-line experiments. This should be applied also to the following discussion.

12.3.4. Effects of Oxygen

The effect of oxygen concentration on the cracking of catechol over nanoparticle iron oxide was studied at 280°C and 330°C temperatures and a feed rate of 18×10^{-3} mmol/min. At 280°C, the conversion of catechol was promoted with an increase in oxygen concentration (Fig. 12.5), but as Fig. 12.10 shows, the product distribution was not affected, i.e. major products were the secondary products I (see the following section). The effect of oxygen concentration was even less at 330°C, where the catechol conversion was almost 100% with the secondary products I as major products under 3% of oxygen. The effect of catechol feed rate on the cracking reaction over nanoparticle iron oxide was studied at 280°C with 3% of oxygen. Again, product distribution was not affected by varying the feed rate of catechol at this condition, i.e., the secondary products I remained the major products (data not shown), while the conversion of catechol was promoted with a decrease in catechol concentration (Fig. 12.5). The presence of water should always be a concern during rate analyses since it could function as a flux or as an oxidant. However, the only source of water in the reaction setup, outside of residual atmospheric moisture, would come from decomposition of

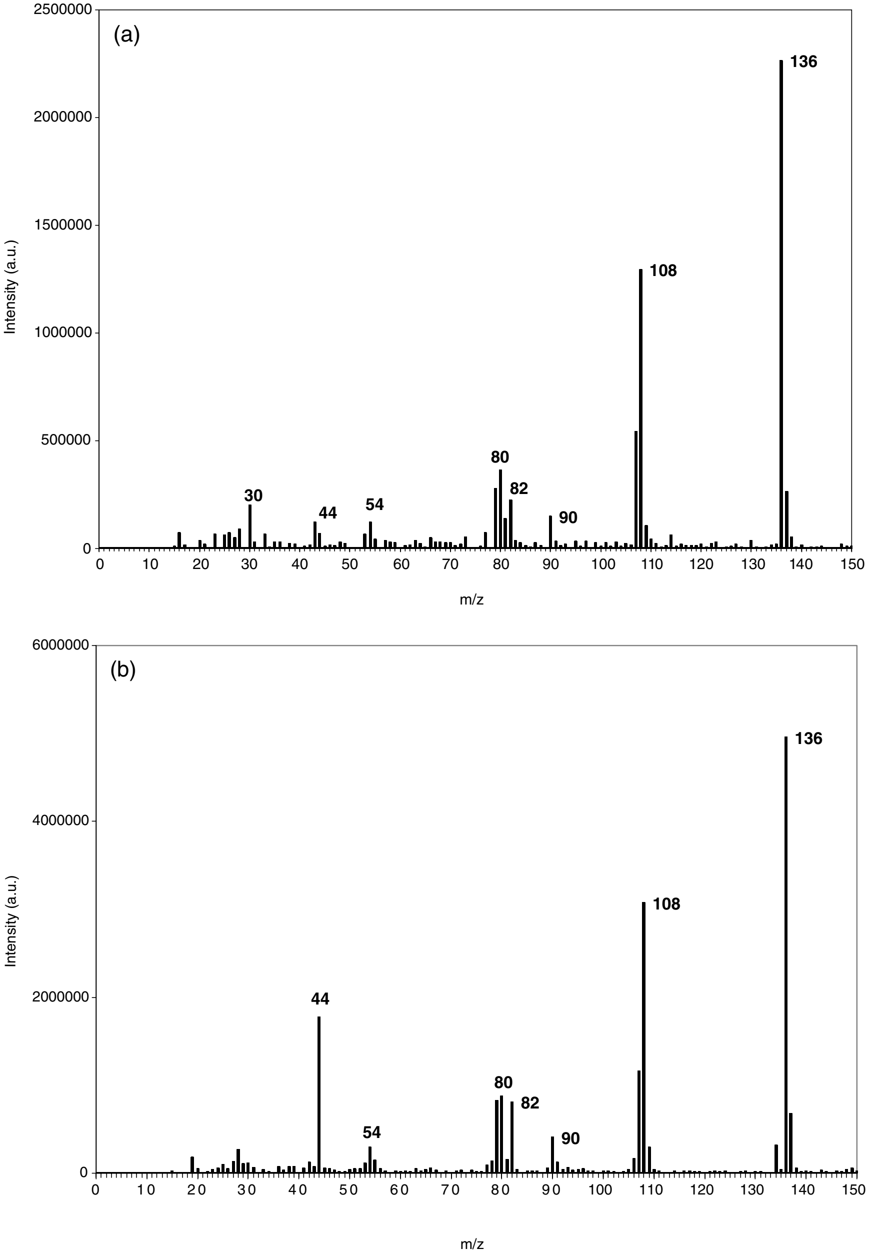

FIGURE 12.9. Product distribution resulting at 80% conversion of 2,3-dimethylhydroquinone over (a) iron oxide/quartz chips at 300°C and (b) only quartz at chips 480°C with 18 $\times$ 10^{-3} mmol/min and 3% of oxygen.

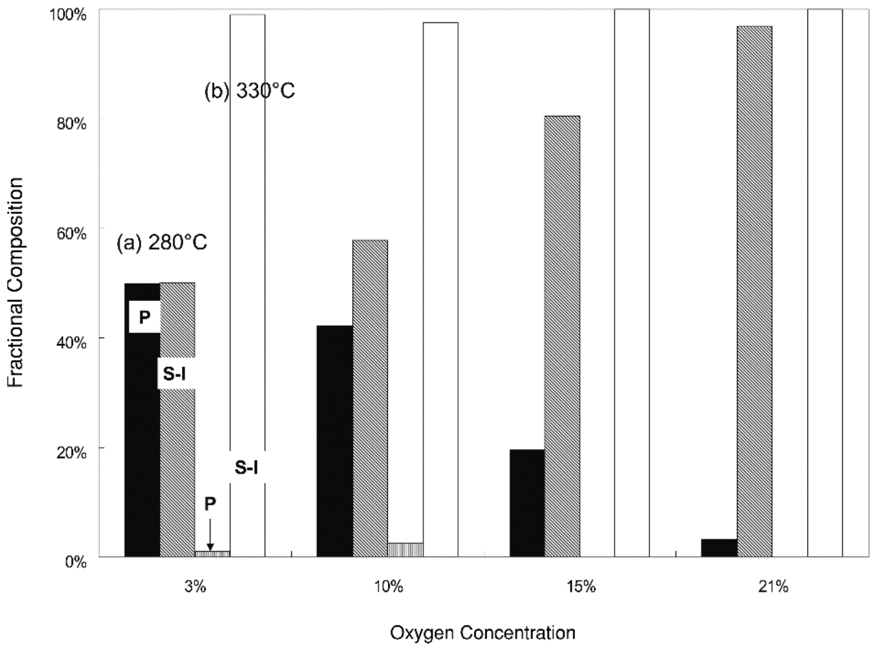

FIGURE 12.10. Effect of oxygen concentration on the fractional concentration of products resulting from catechol cracking over iron oxide/quartz chips with a feed rate of 18 × 10^{-3} mmol/min at (a) 280°C and (b) 330°C for primary (P) and secondary I (S-I)products that are derived by factor analysis.

the dihydroxybenzenes. Since the residence time of this water is so short, it has been neglected as a significant rate determining variable.

12.3.5. Factor Analysis

To uncover the underlying changes in chemistry as a function of process parameters, factor analysis was applied to the mass spectra obtained from MBMS under various reaction conditions. From catechol cracking reactions, the factor analysis extracted four classes of products that were correlated with the reaction conditions. These four classes of products were used to qualitatively and quantitatively reveal trends of conversion and product distributions in the heterogeneous cracking of catechol. Figure 12.11 represents the four classes of products derived from the factor analysis. Figure 12.11a represents the mass spectrum that belongs to the pure catechol without any contribution from cracking products. This class of product(s) is generally referred to as primary products(s). As catechol undergoes cracking with partial oxidation, a few major products are formed as presented in Fig. 12.11b that are clustered separately from another group of aromatic compounds presented in Fig. 12.11c. These products shown in Fig. 12.11b and c must have been derived from the cracking of catechol and subsequent reactions of cracking products, so these products are referred to as secondary products I and II as given in Fig. 12.11b and c, respectively. Finally, thermally

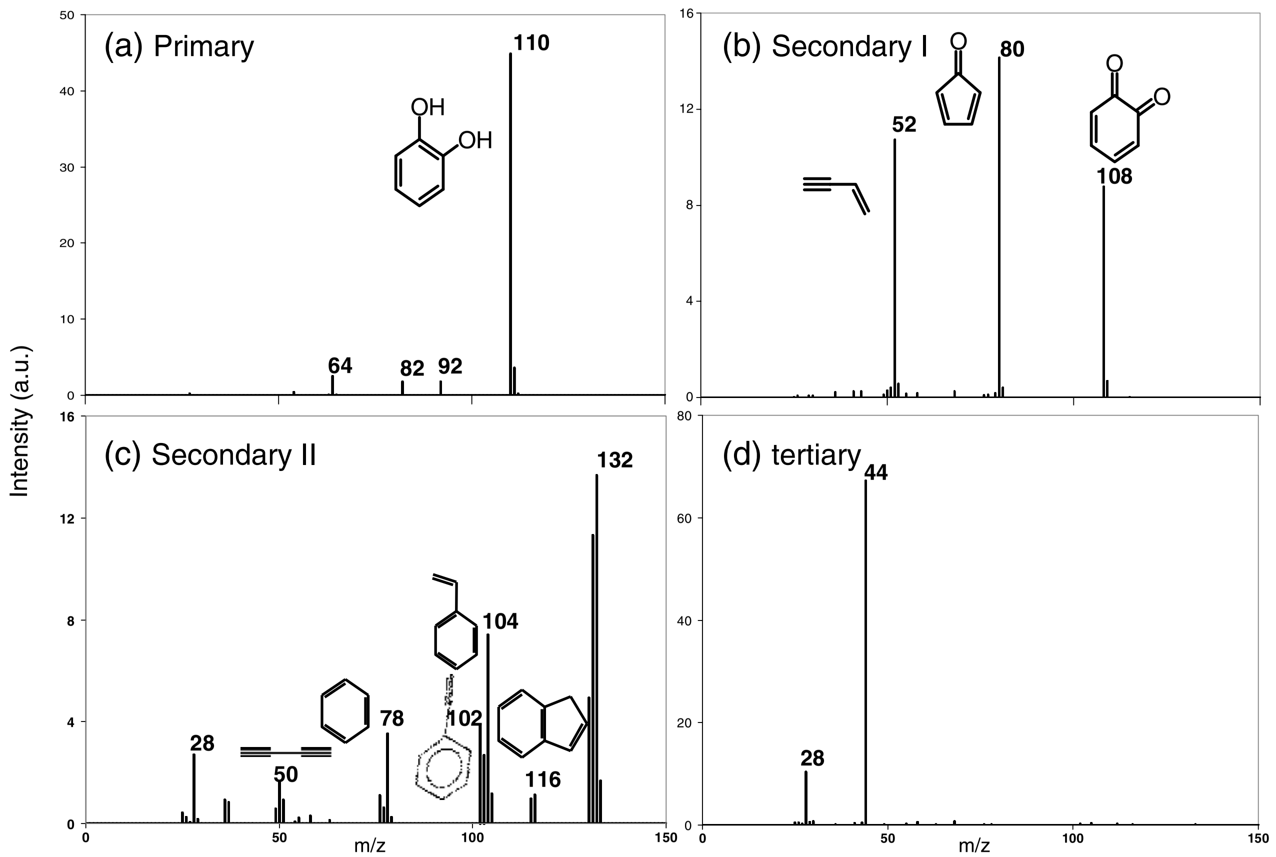

FIGURE 12.11. Four classes of possible products from catechol cracking over 280 to 480°C temperature range: (a) primary, (b) secondary I, (c) secondary II, and (d) tertiary products that are derived by factor analysis.

stable products, carbon dioxide and carbon monoxide, are illustrated in Fig. 12.11d and they could be derived from further cracking and oxidation of the secondary products and they are called tertiary products. Water (m/z 18) must have formed but it was not included in our scan range because of the uncertainty of measuring background water in using the MBMS technique. The conversion and product distribution of catechol cracking over the iron oxide/quartz chips mixture and only quartz chips, determined by the factor analysis, are given in Fig. 12.12 where the variation of conversion and the formation of classes of products as a function of temperature for a constant catechol (18×10^{-3} mmol/min) and oxygen (3%) concentrations are exhibited. This clearly shows the trend of the formation of each class of products.

In the cracking of 3-methylcatechol over quartz chips, four groups of products, namely primary, secondary I, secondary II, and tertiary, were extracted from the MBMS data by factor analysis and are given in Fig. 12.13. Likely identities are as follows: The primary product (Fig. 12.13a) was the starting material, 3-methylcatechol (m/z 124), with its fragment ions (m/z 78 and m/z 106). Major peaks for the secondary products I (Fig. 12.13b) were found at m/z 66 (C_5H_6, pentenyne), m/z 94 (C_6H_6O, methylcyclopentadienone), and m/z 122 ($C_7H_6O_2$, methylbenzoquinone). The secondary products II contained two dominant compounds, m/z 160 and m/z 145 (Fig. 12.13c); where tertiary products were identified as carbon dioxide and carbon monoxide as shown in Fig. 12.13d.

For the cracking of catechol and 3-methylcatechol in the presence of iron oxide, reaction pathways for the secondary products appeared to follow the same trend based on the assumption that the possible identities of the products we proposed above were correct. As presented in Scheme 12.1, catechol and 3-methylcatechol were oxidized to their corresponding quinones, 1,2-benzoquinone, and methylbenzoquinone, respectively. This was followed by an expulsion of CO to form cyclopentadienones; and further followed by one more CO expulsion to form possibly vinyl acetylene from catechol and pentenyne from 3-methylcatechol. These products were eventually converted to the tertiary products. The formation of quinones was also observed in other studies where the oxidation of catechols was carried out.[18,19] The formation of secondary products I in our study is in agreement with the previous studies (e.g., Wornet *et al.*[13,14]). Therefore, it is reasonable to propose the reaction pathways described above for the formation of the secondary products I that we detected with the MBMS.

Factor analysis extracted three groups of products from hydroquinone cracking in the presence and absence of iron oxide as shown in Fig. 12.14. The primary product

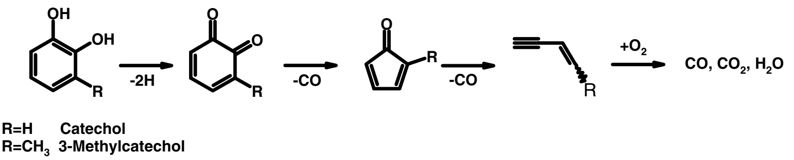

SCHEME 12.1.

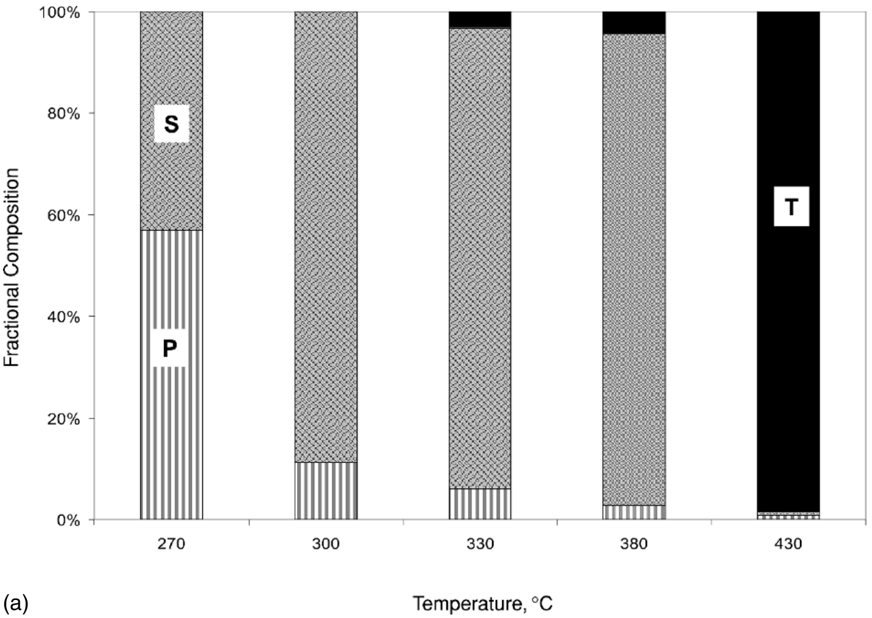

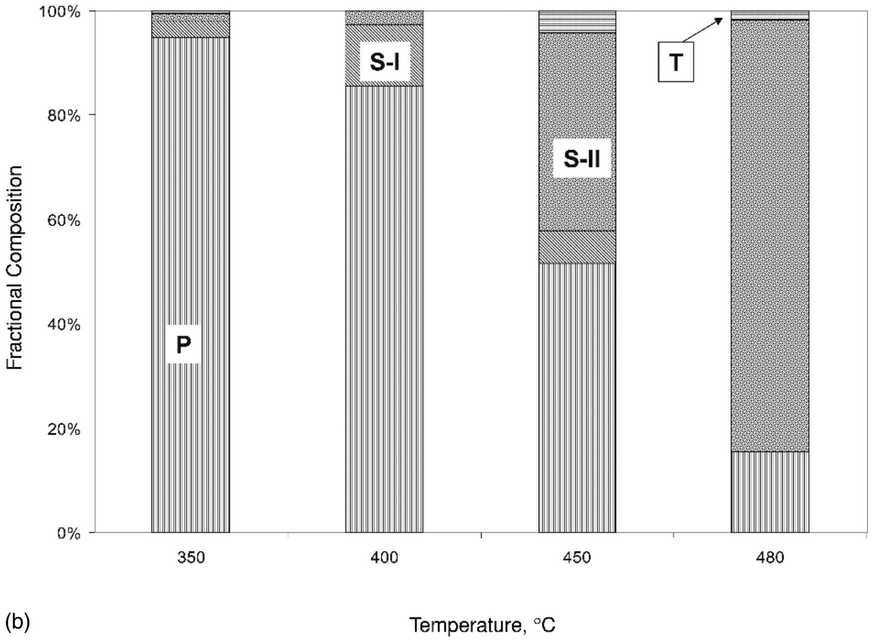

FIGURE 12.12. Fractional concentration of four classes of products from catechol cracking, resulting from factor analysis as a function of temperature over (a) iron oxide/quartz chips and (b) only quartz chips, primary (P), secondary I (S-I), secondary II (S-II), and tertiary (T) products at a feed rate and oxygen concentration of 8×10^{-3} mmol/min and 3%, respectively.

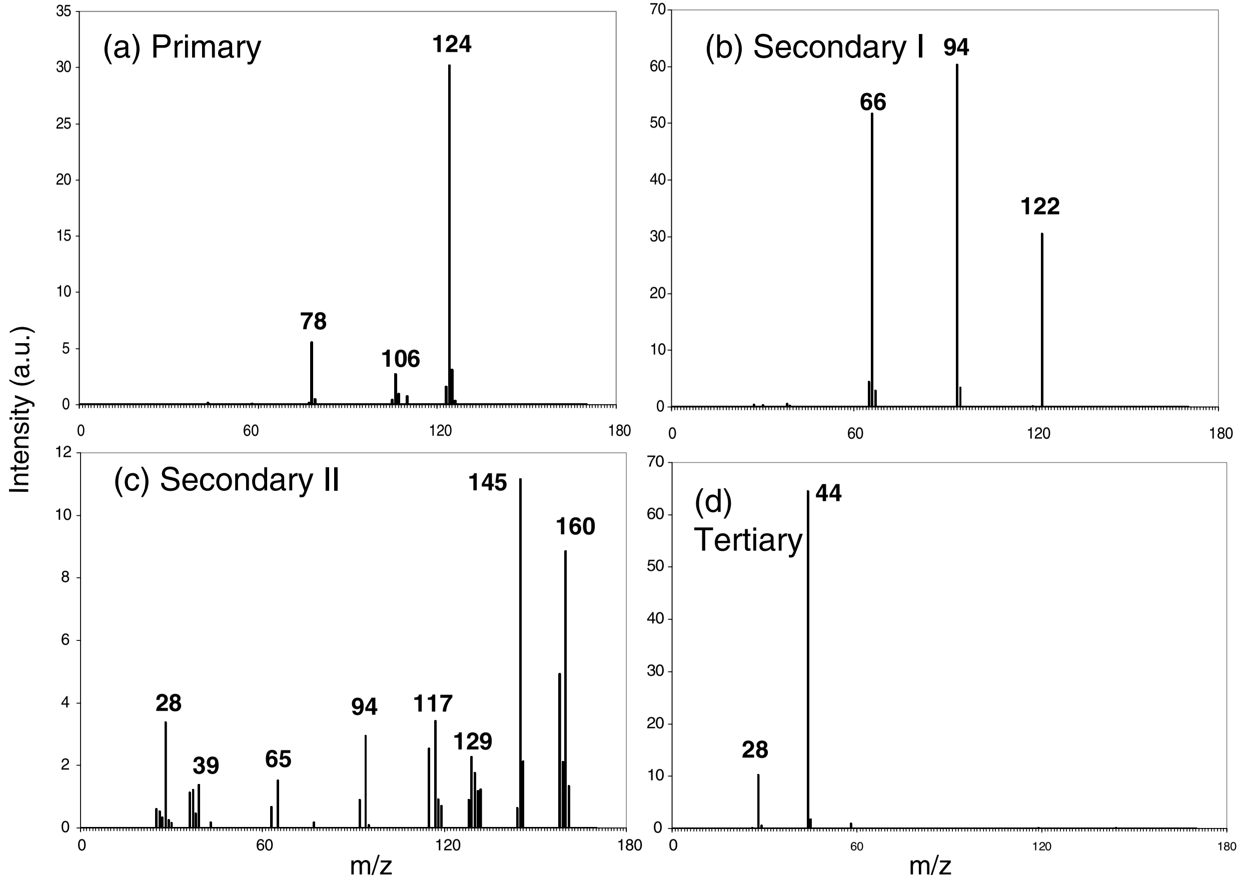

FIGURE 12.13. Four classes of possible products from 3-methycatechol cracking over quartz chips in the temperature range of 280 to 480°C: (a) Primary, (b) secondary I, (c) secondary II, and (d) tertiary products that are derived by factor analysis.

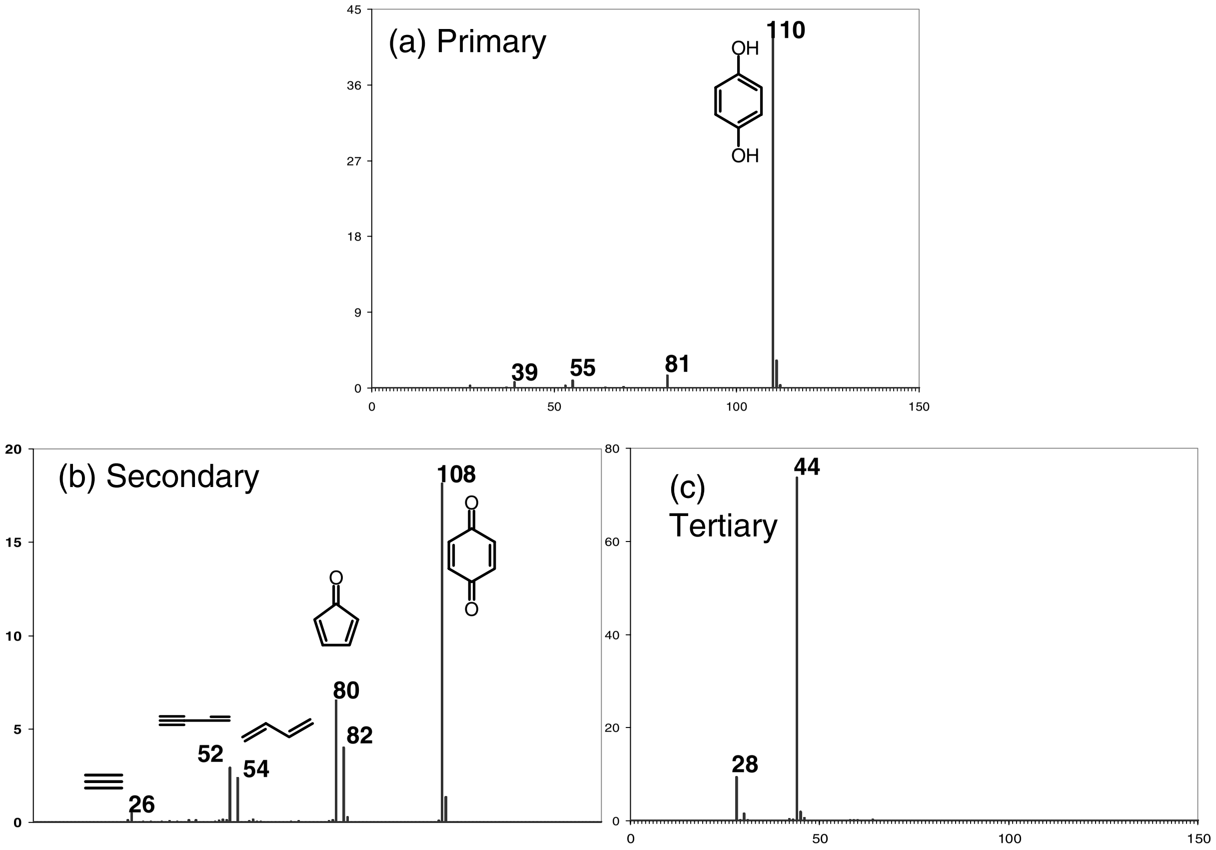

FIGURE 12.14. Three classes of possible products from hydroquinone cracking over 280 to 480°C temperature range: (a) Primary, (b) secondary, and (c) tertiary products that are derived by factor analysis.

was hydroquinone with m/z 110 (Fig. 12.14a) and its fragment ions at m/z 39, 55, and 81. The identities of some of the secondary products (Fig. 12.14b) are likely to be as follow: acetylene (m/z 26), vinyl acetylene (m/z 52), butadiene (m/z 54), cyclopentadienone (m/z 80), and 1,4-benzoquinone (m/z 108). The observation of 1,4-benzoquinone is consistent with the result from a previous study where the oxidation of hydroquinone was investigated.[20] Tertiary products were carbon dioxide and carbon monoxide. The variations of these products resulting from the presence of iron oxide are exhibited in Fig. 12.15a where the secondary products were the only products at temperatures below 330°C. The formation of the tertiary products was promoted at temperatures above 330°C at the expense of the secondary products, and became the only products at 430°C. In the absence of iron oxide, the secondary products were dominant in the temperature range shown in Fig. 12.15b (i.e. 350°C to 480°C). At 480°C, the highest temperature that was employed in this work, the tertiary products started to form with further decomposition of the secondary products.

The cracking of the substituted hydroquinones, 2-methyhydroquinone, and 2, 3-dimethylhydroquinone, were also studied. As discussed above, three groups of products were extracted for the pyrolysis of each compound using factor analysis. The sequence of reaction pathways appeared to follow the same trend: Primary to secondary and then tertiary products. Therefore, only secondary products from two substituted hydroquinones cracking are compared in Fig. 12.16. The secondary products from 2-methylhydroquinone (m/z 124) cracking (Fig. 12.16a) include possible methylbenzoquinone (m/z 122), methylcyclopentadienone (m/z 94), pentenyne (m/z 66), and butadiene (m/z 54). In Fig. 12.16b where the secondary products from 2,3-dimethylhydroquinone (m/z 138) are displayed, peaks were found at m/z 136 (dimethylbenzoquinone), m/z 108 (dimethylcyclopentadien-one), m/z 80 (methylpentenyne), and m/z 54 (butadiene). Again, the identities of these and other peaks in the mass spectra needs to be confirmed by separate off-line pyrolysis experiments. However, it is fair to say that the general trend for reaction pathways of the secondary products observed with catechol cracking may apply to the hydroquinones reaction as presented in Scheme 12.2, i.e. oxidization of hydroquinones to their corresponding quinones and two subsequent stepwise CO expulsions. All of these species were then oxidized to the final products, i.e. tertiary products (Fig. 12.14c).

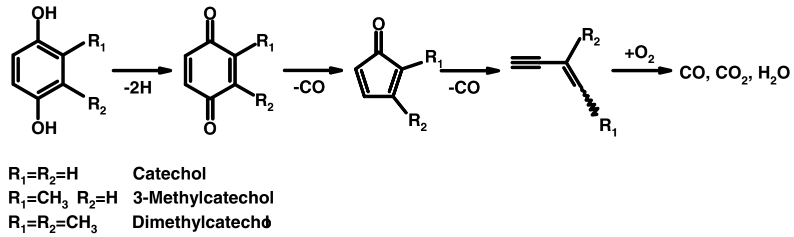

SCHEME 12.2.

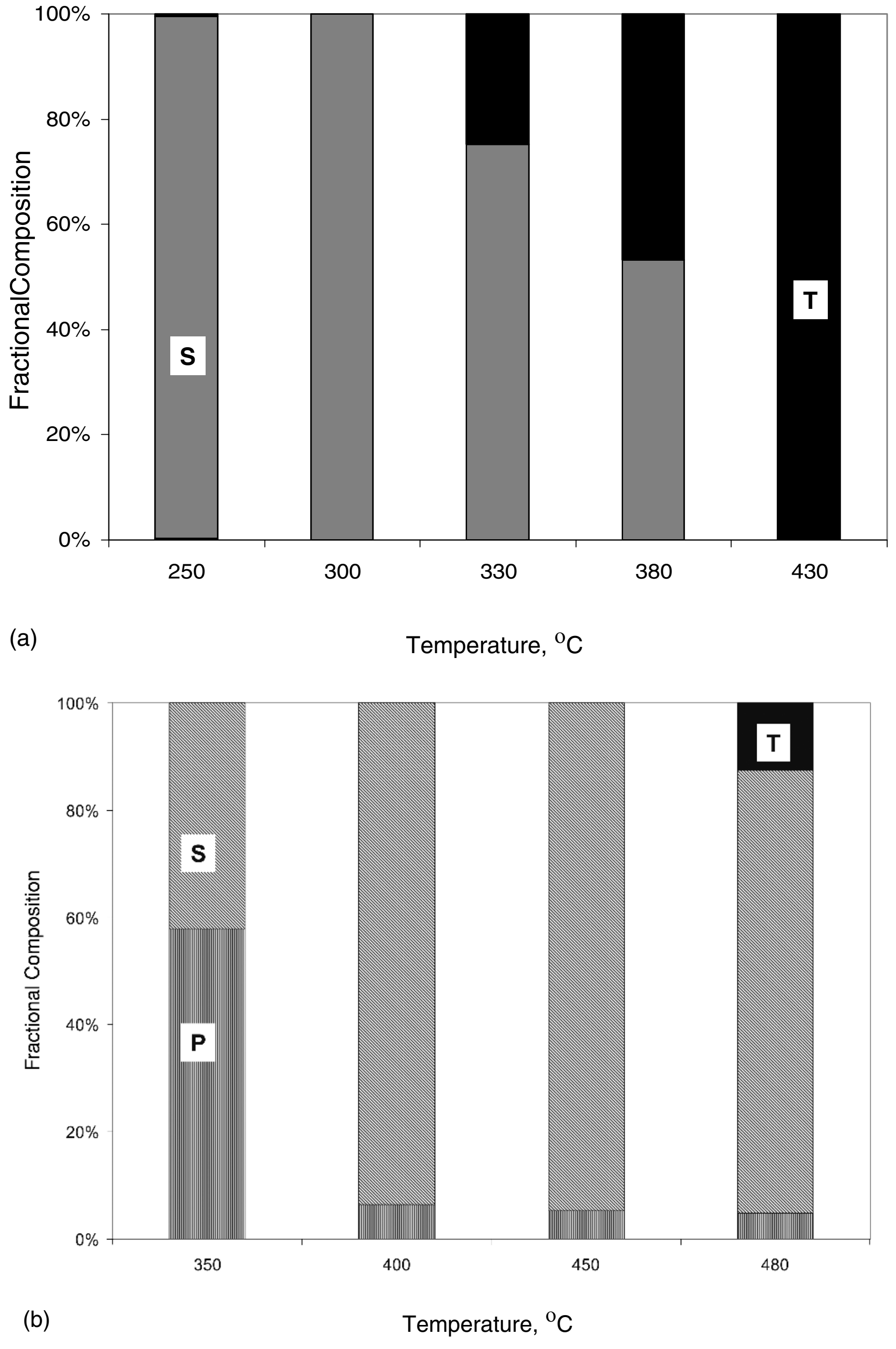

FIGURE 12.15. Fractional concentration of three classes of products from hydroquinone cracking, resulting from factor analysis as a function of temperature over (a) iron oxide/quartz chips and (b) only quartz chips, primary (P), secondary I (S), and tertiary (T) products at a feed rate and oxygen concentration of 8x10-3mmol/min and 3%, respectively.

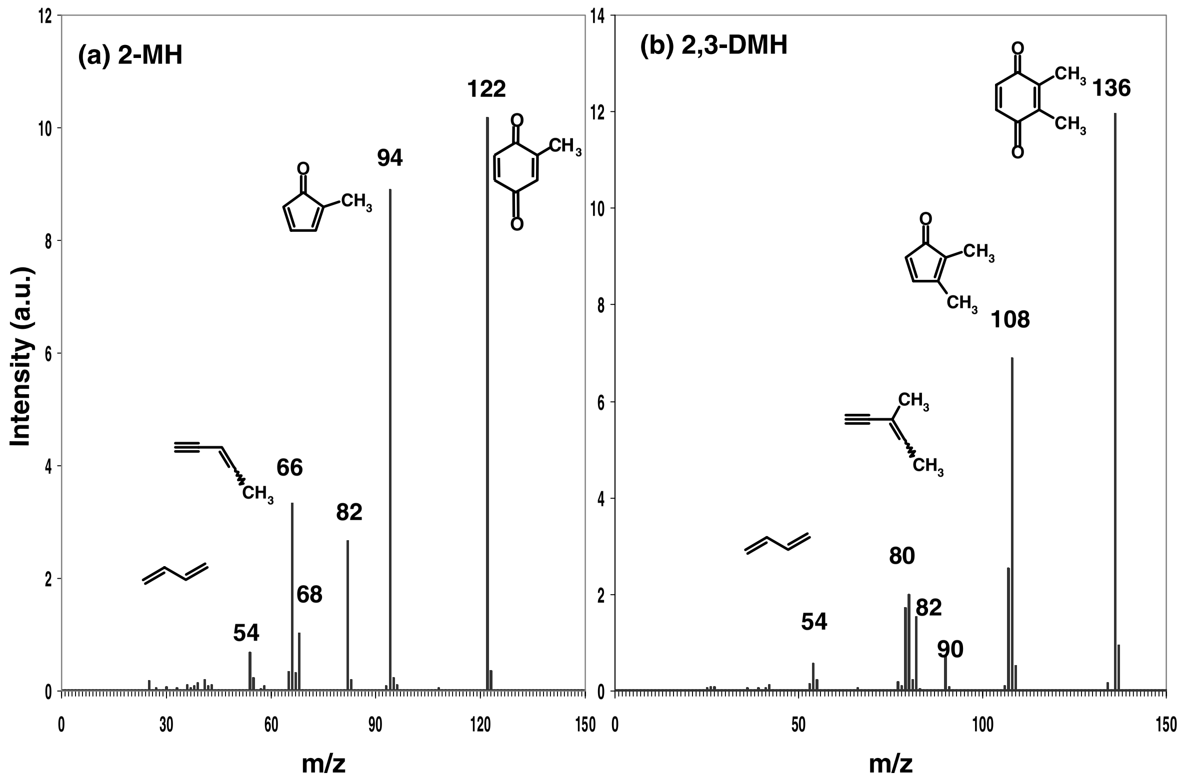

FIGURE 12.16. Possible secondary products from the cracking of (a) 2-methylhydroquinone (2-MH) and (b) 2,3-dimethylhydroquinone (2,3-DMH) derived by factor analysis.

12.4. CONCLUSION

A significant cracking of dihyroxybenzenes was observed at temperature as low as 180°C using a nanoparticle iron oxide catalyst and a partially oxidative atmosphere. Reaction products were classified into four or three groups for the cracking of all catechol and hydroquinone samples, respectively. In the absence of iron oxide, the chemistry for catechols was quite different from that for hydroquinones. However, the presence of iron oxide steered the reaction pathway for both catechol and hydroquinones along a similar pathway i.e., primary product to correspondingly more oxidized species (secondary products I), which followed the same trend in reaction pathway for all the reactants. All of these products eventually were converted to tertiary products, mainly carbon dioxide and water. The presence of the iron oxide certainly enhanced the conversion of the dihydroxybenzenes to less toxic products at much lower temperatures compared to the vapor phase cracking. Derived global kinetic data indicated a strong catalytic effect of the nanoparticle iron oxide on catechol and hydroquinone cracking. Under the conditions of diluted reactant concentrations and 3% of oxygen, the nanoparticle iron oxide retained its reactivity after successive exposures to the reactants.

ACKNOWLEDGEMENTS

The authors would like to thank Dr. Firooz Rasouli and Dr. Hoongsun Im for technical discussions and Felecia Logan for experimental work. Special thanks to Dr. Weizhong Zhu for BET surface area measurements. Dr. Weizhong Zhu and Dr. Hoongsun Im were participants in the Philip Morris USA Postgraduate Research Program.

REFERENCES

1. P. Hasler, and T. Nussbaumer, Sampling and analysis of particles and tars from biomass gasifiers, *Biomass Bioenergy* **18**(1), 61–66 (2000).
2. R. J. Evans, and T. A. Milne, Chemistry of tar formation and maturation in the thermochemical conversion of biomass, *Fuel Energy Abstract* **39**(3), 197 98/02189 (1998).
3. E. J. Shin, M. Nimlos, and R. J. Evans, The formation of aromatics from the gas-phase pyrolysis of stigmasterol: Kinetics, *Fuel* **80**(12 Special Edition S1), 1681–1688 (2001).
4. C. S. Lai, P. Chen, J. P. Longwell, and W. A. Peters, Thermal reactions of *m*-cresol over calcium oxide between 350 and 600 °C, *Fuel* **66**(4), 525–531 (1987).
5. D. L. Ellig, C. K. Lai, D. W. Mead, J. P. Longwell, and W. A. Peters, Pyrolysis of volatile aromatic hydrocarbons and *n*-heptane over calcium oxide and quartz, *Ind. Eng. Process Des. Dev.* **24,** 1080–1087 (1985).
6. C. J. Smith, T. A. Perfetti, M. J. Morton, A. Rodgman, R. Garg, C. D. Selassie, and C. Hansch, The relative toxicity of substituted phenols reported in cigarette mainstream smoke, *Toxicological Sci.* **69,** 265–278 (2002).
7. R. K. Sharma, T. S. Fisher, and M. R. Hajaligol, Effect of reaction conditions on pyrolysis of chlorogenic acid, *J. Anal. Appl. Pyrolysis* **62,** 281–296 (2002).
8. W. S. Schlotzhauer, R. M. Martin, M. E. Snook, and R. E. Williamson, Pyrolytic studies on the contribution of tobacco leaf constituents to the formation of smoke catechols, *J. Agric. Food Chem.* **30,** 372–374 (1982).

9. S. G. Carmella, S. S. Hecht, T. C. Tso, and D. Hoffmann, Roles of tobacco cellulose, sugars, and chlorogenic acid as precursors to catechol in cigarette smoke, *J. Agric. Food Chem.* **32**(2), 267–273 (1984).
10. W. S. Schlotzhauer, M. E. Snook, O. T. Chortyk, and R. E. Wilson, Pyrolytic evaluation of low chlorogenic acid tobaccos in the formation of the tobacco smoke co-carcinogen catechol, *J. Anal. Appl. Pyrolysis* **22**(3), 231–238 (1992).
11. T. Sakai, and M. Hattori, Thermal decarbonylation of catechol, hydroquinone and resolinol, *Chem. Lett.* **11,** 1153–1156 (1976).
12. M. J. Wornat, E. B. Ledesma, and N. D. Marsh, Polycyclic aromatic hydrocarbons from the pyrolysis of catechol (ortho-dihydroxybenzene), a model fuel representative of entities in tobacco, coal, and lignin, *Fuel* **80,** 1711–1726 (2001).
13. E. B. Ledesma, N. D. Marsh, A. K.Sandrowitz, and M. J. Wornat, Global kinetic rate parameters for the formation of polycyclic aromatic hydrocarbons [PAH] from the pyrolysis of catechol: A model compound representative of solid fuel moieties, *Energy Fuels* **16**(6), 1331–1336 (2002).
14. E. B. Ledesma, N. D. Marsh, A. K.Sandrowitz, and M. J. Wornat, Experimental study on the thermal decomposition of catechol, *Proc. Combust. Inst.* **29,** 2299–2306 (2002).
15. A. B. Lovell, K. Brezinsky, and I. Glassman, The gas phase pyrolysis of phenol, *Int. J. Chem. Kinetic.* **21,** 547–560 (1989).
16. Y. Z. He, W. G. Mallard, and W. Tsang, Kinetics of hydrogen and hydroxyl radical attack on phenol at high temperatures,*J. Phys. Chem.* **92,** 2196–2201 (1988).
17. A. J. Colussi, F. Zabel, and S. W. Benson, Very low-pressure pyrolysis of phenyl ethyl ether, phenyl allyl ether, and benzyl methyl-ether and enthalpy of formation of phenoxy radical,*Int. J. Chem. Kinetic*. **9**(2), 161–178 (1977).
18. D. Nematollahi, and Z. Forooghi, Electrochemical oxidation of catechols in the presence of 4-hydroxy-6-methyl-2-pyrone, *Tetrahedron* **58**(24)**,** 4949–4953 (2002).
19. A. Naidja, and P. M. Huang, Significance of the Henri–Michaelis–Menten theory in abiotic catalysis: Catechol oxidation by δ-MnO_2, *Surf. Sci.* **506**(1–2)**,** L243–L249 (2002).
20. Y. Tsuji, T. Ohta, T. Ido, H. Minbu, and Y. Watanabe, Ruthenium-catalyzed oxidation of alcohols and catechols using t-butyl hydroperoxide**,** *J. Organometallic Chem*. **270**(3)**,** 333–341 (1984).
21. P Li, E. J. Shin, D. Miser, M. R. Hajaligol, and F. Rasouli, The catalytic/oxidative effects of iron oxide nanoparticles on carbon monoxide and the pyrolytic products of biomass model compounds, In *Nanotechnology in Catalysis*, edited by B. Zhou, S. Hermans, and G. A. Somorjai (Kluwer Academic/Plenum Publishers, New York 2004) pp. 515–542.
22. E. J. Shin, M. R. Hajaligol, and F. Rasouli, Heterogeneous cracking of catechol under partially oxidative conditions, *Fuel* **83**(11–12), 1445–1453 (2004).
23. E. J. Shin, F. Rasouli, W. G. Chan, and M. R. Hajaligol, Thermal reaction of catechol over nanoparticle iron oxide and quartz, *Fuel Chem. Preprints, ACS*, **48,** 616–617 (2003).
24. J. S. Walker, G. I. Straguzzi, H. Manogue, and G. C. A. Schuit,Carbon monoxide and propene oxidation by iron oxides for auto-emission control**,** *J. Catal*.**110**(2), 298–309 (1988).
25. P. Li, D. Miser, S. Rabiei, R. Yadav, and M. R. Hajaligol, The removal of carbon monoxide by iron oxide nanoparticles, *Appl. Catal. B: Environ.* **43**(2), 151–162 (2003).
26. W. Windig, J. L.Lippert, M. J. Robbins, K. R. Kresinske, J. P. Twist, and A. P Snyder, interactive self-modeling multivariate analysis,*Chemometrics Intell. Lab. Syst.* **9**(1), 7–30 (1990).
27. W. Windig, and H. L. C. Meuzelaar, Nonsupervised numerical component extraction from pyrolysis mass spectra of complex mixtures, *Anal. Chem.* **56**(13), 2297–2303 (1984).
28. W. Windig, P. G. Kistenmaker, and J. Haverkamp, Chemical interpretation of differences in pyrolysis—Mass spectra of simulated mixtures of biopolymers by factor analysis with graphical rotation, *J. Anal. Appl. Pyrolysis* **3**(3), 199–212 (1981/1982)
29. W. Windig, J. Haverkamp, and P. G. Kistenaker, Interpretation of sets of pyrolysis mass spectra by discriminant analysis and graphical rotation,*Anal. Chem.* **55**(1), 81–88 (1983) .
30. D. Miser, E. J. Shin, M. R. Hajaligol, and F. Rasouli, HRTEM characterization of phase changes and the occurrence of maghemite during catalysis by an iron oxide, *Appl. Catal. A: Gen.* **258**(1), 7–16 (2004).

31. G. P. Huffman, B. Ganguly, J. Zhao, K. R. P.M. Rao, N. Shah, Z. Feng, F. E. Huggins, M. M. Taghiei, F. Lu, I. Wender, V. R. Pradhan, J. W. Tierney, M. M. Seehra, M. M. Ibrahim, J. Shabtai, and E. M. Eyring, Structure and dispersion of iron- based catalysts for direct coal liquefaction, *Energy Fuels* **7,** 285–296 (1993).
32. J. Zhao, F. E. Huggins, Z. Feng, F. Lu, N. Shah, and G. P. Huffman, Structure of a nanophase iron oxide catalyst, *J. Catal.* **143**(2), 499–509 (1993).
33. F. Zhen, J. Zhao, F. E. Huggins, and G. P. Huffman, Agglomeration and phase transition of a nanophase iron oxide catalyst, *J. Catal*. **143**(2), 510–519 (1993).

13

Synthesis of Palladium-Based Supported Catalysts by Colloidal Oxide Chemistry

Blaise Didillon[a], Thierry Pagès[c], Stephan Verdier[b], and Denis Uzio[c,*]

13.1. INTRODUCTION

In the field of heterogeneous catalysis, the control of the characteristics of supported particles is one of the main objectives of all researchers who want to establish relationships between structure and reactivity. Catalysts with the same macroscopic composition may exhibit very different catalytic performances because of large variations of the active site properties at the nanometer scale. Because of the structure sensitive nature of most of the phenomena involved in heterogeneous catalysis, future improvements of heterogeneous catalysts, in terms of reaction rate, selectivity, stability in operation or sensitivity to poisons, will necessarily be obtained through the nanoscaled control of the physical and chemical characteristics of active sites. For this purpose, many sophisticated preparation methods have been explored including controlled surface reactions such as redox reactions, electrochemical methods, and surface grafting or physical techniques such as vapor deposition of metallic precursors. Chemical methods to prepare supported heterogeneous catalysts generally use the different possible

[a] RHODIA, PPD, P.O. Box 9837 Oldbury, West Midlands, B69 4WD, UK
[b] RHODIA, CRA 52, rue de la Haie Coq 93308 Aubervilliers Cedex, France
[c] IFP Solaize BP no. 3, 69390 Vernaison, France
[*] To whom correspondence should be addressed. E-mail: denis.uzio@ifp.fr

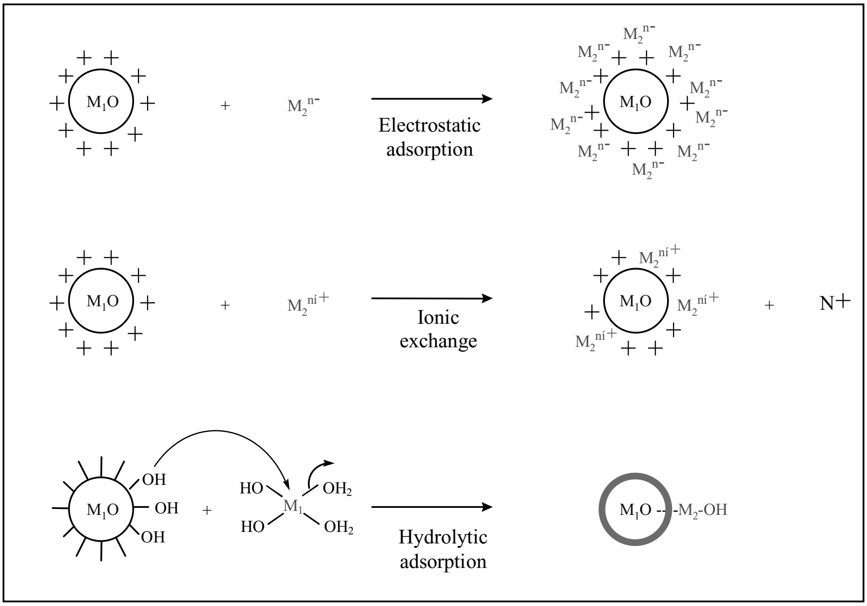

FIGURE 13.1. Different modes of adsorption between metallic precursor and the oxide surface.

interactions between metallic precursors such as ionic complexes (chlorides, amino, sulfates), alkoxides (ethoxy, acetylacetonate), organometallics (allyls, carbonyls) and the surface of an inorganic carrier's hydroxyl groups or Lewis acid sites (uncoordinated sites CUS).[1,2] Ionic exchange, electrostatic interaction, and hydrolytic adsorption may be generated by choosing the right candidates and the appropriate operating conditions, especially pH (Fig. 13.1).

Chemical interactions, often called "grafting," between the surface sites of a carrier and an organometallic or alkoxide compound govern the final particle size distribution for very small particles.[3–5]

However, it is much more difficult to design a supported catalyst with larger particles (i.e. more than 1 nm in diameter) keeping a monomodal particle size distribution. Post treatments, such as drying, calcinations, and reduction steps under different atmospheres (wet, reductive, and oxidative) have also been widely studied in order to control sintering and ultimately the characteristics of the supported particles.[16,17] Using thermal sintering, even under optimized conditions, it is very difficult to obtain a monomodal particle size distribution or a homogeneous composition along with a controlled metal–support interaction.

Various catalytic reactions are known to be structure sensitive as proposed by Boudart[6] and studied by many authors.[7–9] Examples are the selective hydrogenation of polyunsaturated hydrocarbons, hydrogenolysis of paraffins, and ammonia or Fischer–Tropsch synthesis. Controlled surface reactions such as oxidation–reduction reactions[10–13] or surface organometallic chemistry (SOMC)[14,15] are two suitable methods for the synthesis of mono- or bimetallic particles. However, for these techniques,

the redox potential and the availability or reactivity of the organometallic precursors may be a limitation for some elements.

Concerning catalytic applications, such as selective hydrogenation of polyunsaturated hydrocarbons, an eggshell repartition of the active phase is often required for mass-transfer considerations, combined to a well-defined particle size (around 20 to 50 Å depending on the substrate) because of the aforementioned structure sensitive phenomena. Furthermore, most of the catalysts designed for these applications contain more than one element and obviously an association at a nanometer scale of the principal element to the promoter is targeted. All these characteristics involve a very high level of control, which is quite difficult to achieve mainly if aqueous and one-pot synthesis is required for environmental, economic, and scaling up considerations. In this area, colloidal oxide synthesis also appears to be an alternative route able to meet the requirements of the most sophisticated supported catalysts produced in industrial manufacturing processes. The scientific bases of this method have been extensively studied and applied for a long time in the synthesis of new oxide solids that are well-defined in terms of size, crystalline structure, and morphology.[18,19] As an example, it has been successfully applied to the synthesis of various metal oxides ($\alpha-Fe_2O_3$, β-FeOOH, Co_3O_4, ZrO_2, Cr_2O_3, ZnO).[20] Less attention has been given to the last series group VIII metals, and more particularly, to the noble metals used in catalysis for refining and petrochemical applications. Synthesis of metallic colloidal nanoparticles has been identified as a powerful preparation method in order to prepare mono- and bimetallic supported catalysts. Nucleation of reduced atoms activated by various methods (photoreduction, radiolysis, or chemical reduction) produces well-calibrated particles, which can be further deposited on different supports.[21–23] These studies have demonstrated the great interest to control the parameters related to the particles such as size, distribution, and morphology.[24] However, most of the work deals with organic solutions and colloidal particles generated via a chemical, radiolytic, or reduction process. In spite of the obvious advantages of using aqueous instead of organic solutions, due to safety and economic aspects, the synthesis of supported metal catalysts from oxide colloidal suspensions has not until recently received significant attention. Moreover, all options offered by the sol–gel chemistry have not yet been entirely explored to produce designed supported nanoparticles.

Unlike most of the industrial preparation methods, colloidal oxide synthesis does not make use of the chemistry between metallic ions in solution and the surface sites of the oxide carrier (hydroxyl or Lewis acid sites). Indeed, the strategy disconnects the steps corresponding to the formation of particles, synthesized previously in solution, and to the subsequent deposition and activation on the oxide carrier.

Covering monometallic (Pd, Sn) and multimetallic (Pd–Sn, Pd–Ag) systems, several examples are presented in this chapter to illustrate the possibility offered by this chemistry to control the particle size distribution and the bimetallic interaction at a molecular level. This work is supported by a multitechnique characterization approach using: ^{119}Sn Mössbauer spectroscopy, X-ray photoelectron spectroscopy (XPS), low-energy ion spectroscopy (LEIS), and transmission electron microscopy (TEM). Catalytic performances in hydrogenation of different unsaturated hydrocarbons (phenylacetylene, butadiene) are finally discussed in order to establish structure–reactivity relationships.

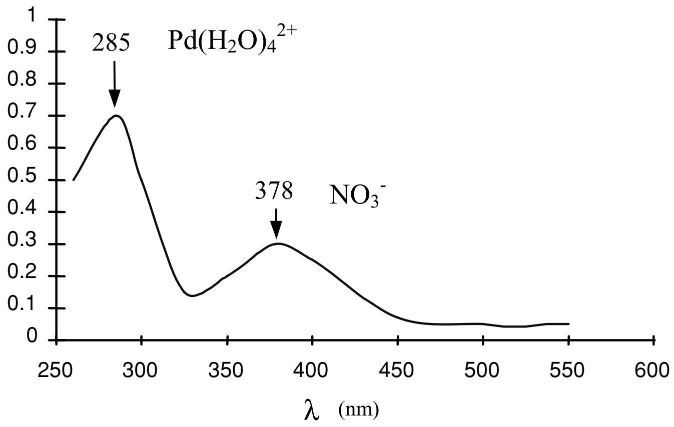

FIGURE 13.2. UV–visible spectrum of the initial $Pd(NO_3)_2$.

13.2. SYNTHESIS OF MONOMETALLIC CATALYSTS

13.2.1. Synthesis of Palladium Oxide Hydrosols

Oxide hydrosols synthesis relies on the destabilization of a true solution by a pH change. In order to prepare palladium oxide colloidal particles, two experimental routes can be carried out: the neutralization of an acidic (basic) solution by an alkaline (acidic) solution, or thermohydrolysis of the palladium precursor solution.

The different molecular species present in a palladium nitrate solution can be easily identified by UV–visible spectroscopy (Fig. 13.2). Two absorption peaks are generally observed at $\lambda = 285$ nm and $\lambda = 378$ nm, the latter being ascribed to free nitrate ions corresponding to the electronic transition from the σ to the π^* state in the NO_3^- ions, as observed in the case of an aqueous solution of $NaNO_3$. The other absorption band at $\lambda = 285$ nm is assigned to a d–d transition in the aquo complex $Pd(H_2O)_4^{2+}$.[26] These UV–visible results show the noncomplexant behavior of nitrate ions toward palladium metallic centers. The palladium containing species in the starting solution is then the planar tetra-aquo complex $Pd(H_2O)_4^{2+}$.

The water molecule in the Pd cationic complex $Pd(H_2O)_4^{2+}$ brings an electric charge of $+0.37$, calculated according to the partial charge model as described by Jolivet and Hiemstra et al.[27,28] This positive charge indicates that the aquo ligand has an electrophilic character. As a consequence, condensation of aquo cationic complexes cannot occur spontaneously. The charge calculation is thus in agreement with UV–visible results which show monomolecular stable Pd species in the acidic solution.

The formation of palladium oxide colloidal particles from an acidic palladium nitrate solution can be achieved by addition of an alkaline solution. The different steps, describing the chemistry involved in such a process are[29]

- nucleophilic attack of hydroxyl ions leading to the substitution of hydroxo ligands and formation of a complex with no electric charge: $Pd(OH)_2(H_2O)_2$,

TABLE 13.1. Partial charge of the hydroxo ligand and metallic center for different metallic precursors.

Metallic Salts	Complex in Solution	Corresponding Hydroxyl Complex	δ(Pd)	$\delta(H_2O)$	δ(OH)
$Pd(NO_3)_2$	$Pd(H_2O)_4{}^{2+}$		0.49	0.37	
		$Pd(OH)(H_2O)^+$	0.46		0.00
		$Pd(OH)_2(H_2O)_2$	0.35		−0.19
Na_2PdCl_4	$PdCl_3(H_2O)^-$		0.19	−039	
	$PdCl_3(OH)^{2-}$		0.01		−0.75
		$Pd(H_2O)_2Cl\ (OH)$	0.34		−0.19
$K_2Pd(NO_2)_4$	$Pd(NO_2)_4{}^{2-}$	$Pd(NO_2)OH(H_2O)$	0.43		−0.05
$Pd(NH_3)_4(NO_3)_2$	$Pd(NH_3)_4{}^{2+}$	$Pd(NH_3)_2(OH)_2$	0.29		−0.29

- inorganic polymerization or condensation by olation reactions between these complexes and formation of nuclei, and
- growth of these nuclei by olation reactions.

In the case of the $Pd(OH)_2(H_2O)_2$ complex, the partial charge model predicts condensation because of the nucleophilic character of the hydroxo ligand toward the metallic center (Table 13.1). The partial charge of the nucleophilic group ($\delta_{OH} = -0.19$) and the electrophilic center ($\delta_{Pd} = +0.35$) meet the R. Anderson principle ($\delta_{OH} < 0$ and $\delta_{Pd} > +0.3$). This criterion is not filled for every molecular precursor (for ex. $Pd(NH_3)_4(NO_3)_2$, $K_2Pd(NO_2)_4$) depending on the stabilization effect of the ligand.

Finally, PdO particles are spontaneously formed from palladium hydroxide $Pd(OH)_2$ via dehydration by internal oxolation in agreement with the positive value of the partial charge of the water molecule ($\delta_{H2O} = 0.03$). Figure 13.3 summarizes the overall mechanism leading to the formation of PdO colloidal particles.

Figure 13.4 shows the titration curve of a palladium nitrate solution [Pd] = 5 g/L by soda [NaOH] = 0.1 N. Three regions can be clearly distinguished, corresponding to a true solution (starting point until addition of about 14 mL of soda), to the formation of colloidal PdO particles (from 14 to 24 mL added), and to the flocculation of particles with segregation of liquid and solid phases (above 25 mL).

The preparation of colloidal particles can be performed by the addition of a well-defined amount of soda corresponding to the second intermediate zone. The neutralization process corresponds to simultaneous titrations of free acidity brought by nitric acid and a palladium complex according to the following reactions:

$$HNO_3 + NaOH \rightarrow NaNO_3 + H_2O \quad (1)$$

$$Pd(H_2O)_4{}^{2+} + 2\,NO_3{}^- + 2\,NaOH \rightarrow 2\,NaNO_3 + Pd(OH)_{2+}4\,H_2O. \quad (2)$$

It is worth noticing that for pH > 2, reaction (2) is complete as shown by the absence of the molecular complex $Pd(H_2O)_4{}^{2+}$ in the solution analyzed by UV–visible spectroscopy. X-ray diffraction diagrams of dried suspensions after neutralization confirm

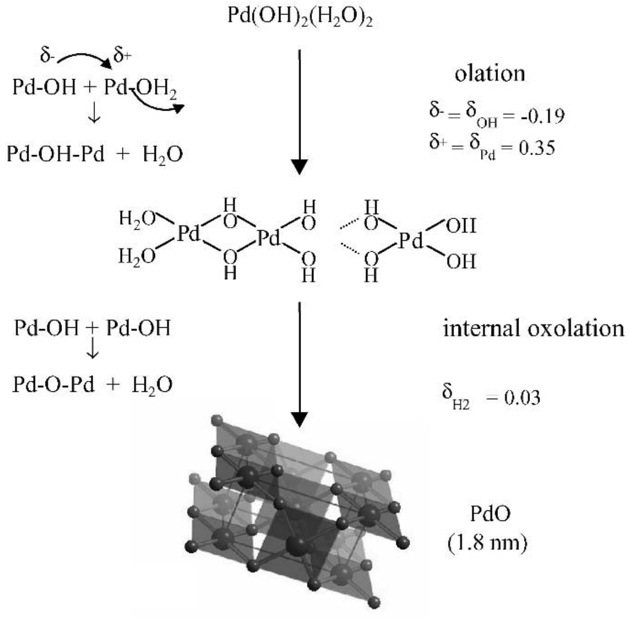

FIGURE 13.3. Reaction mechanisms involved during the synthesis of PdO colloidal particles from palladium hydroxo complexes.

the exclusive formation of palladium oxide identified by comparisons to the JCPDS database (Fig. 13.5).

Using the multisite complexation model (MUSIC),[30] the surface of palladium oxide has been modeled providing useful data on the nature, number, and the acid–base strength of the hydroxyl groups present on the different faces (1 1 1) and (1 0 0) of

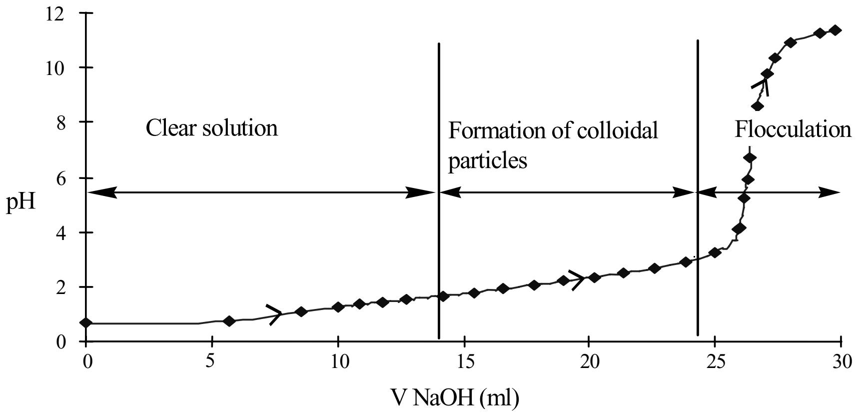

FIGURE 13.4. Neutralization curve of a palladium nitrate solution [Pd] = 5 g/L by addition of soda [NaOH] = 0.1 N.

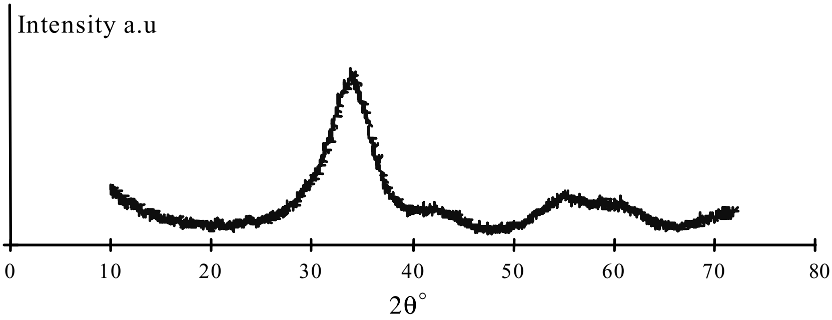

FIGURE 13.5. X-ray diffraction pattern of dried suspension after neutralization by soda.

the PdO crystal (Fig. 13.6). One can see the good agreement between the value of the isoelectric point given by this model and the value of 4.5 determined experimentally by the potentiometric titration method described in Ref. 31.

Particle size distributions of both hydrosols determined using a statistical image analysis of transmission electron microscopy (Jeol TEM 120 CX) micrographs are presented in Fig. 13.7. These hydrosols were prepared at different neutralization levels (pH = 2 and 2.8). Both particle size distributions are centered around 18 to 19 Å and are extremely sharp as shown by the low values of the standard deviation σ.

The reverse operation, i.e. the addition of palladium nitrate solution to soda, can also be used to prepare colloidal suspensions. Figure 13.8 presents the corresponding titration curve of a soda ([NaOH] = 0.2 N) by a palladium nitrate solution ([Pd] = 5 g/L).

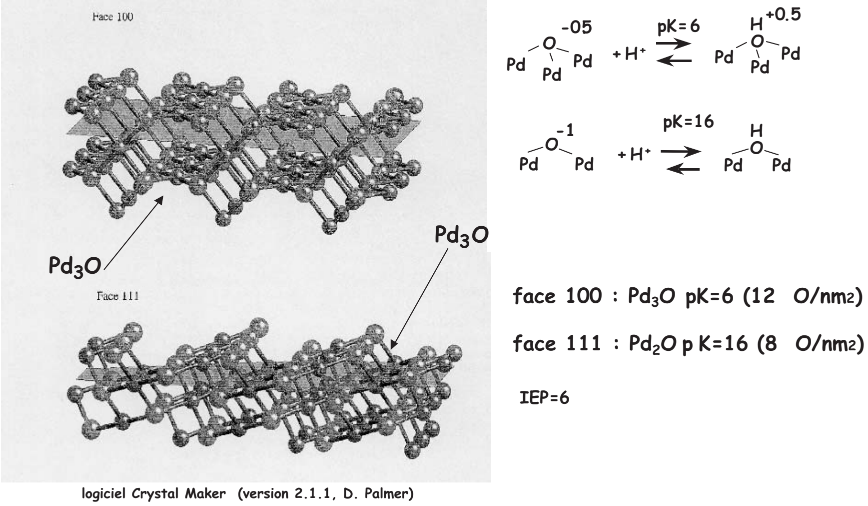

FIGURE 13.6. Molecular modeling of the surfaces of PdO (111) and PdO (100) by CristalMaker. Calculation made by J. Hernandez and C. Froidefond (LCMC, UPMC PARIS VI).

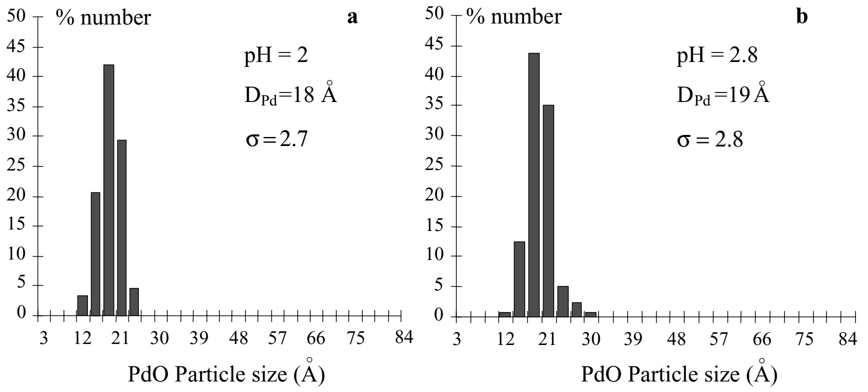

FIGURE 13.7. PdO particle size distributions obtained by neutralization of palladium nitrate solution by soda at different pH determined by transmission electron microscopy.

Particle size distributions obtained via direct (pH = 1.8) or reverse procedure (pH = 12) are very narrow and both centered around 17 to 18 Å (Fig. 13.9).

Micrographs of replica (Fig. 13.10) obtained by vitrification in liquid propane (performed at the biology laboratory IFR 2062, Paris VI University, F. Gaill.) reveals the presence of large three-dimensional aggregates for the hydrosol prepared in basic pH (12.3).

For the formation of the different species (oxides or hydroxylated), one must take into account both kinetic and thermodynamic aspects. In Fig. 13.11, one can see that despite the stable character predicted by the thermodynamic diagram (Fig. 13.12) of the $Pd(OH)_2(H_2O)_2$ at pH = 12.6, only $Pd(OH)_4^{2-}$ (band at 368 nm[32]) is formed in the previous stage of the synthesis. This complex is slowly converted into $Pd(OH)_2$ and then into PdO after a few minutes as shown by the disappearance of the absorption band of the $Pd(OH)_4^{2-}$ complex.

For catalytic purposes, it is generally important to optimize the exposed surface area of active sites, and as a consequence one must control the degree of aggregation of the colloidal particles. These suspensions are metastable thermodynamic systems

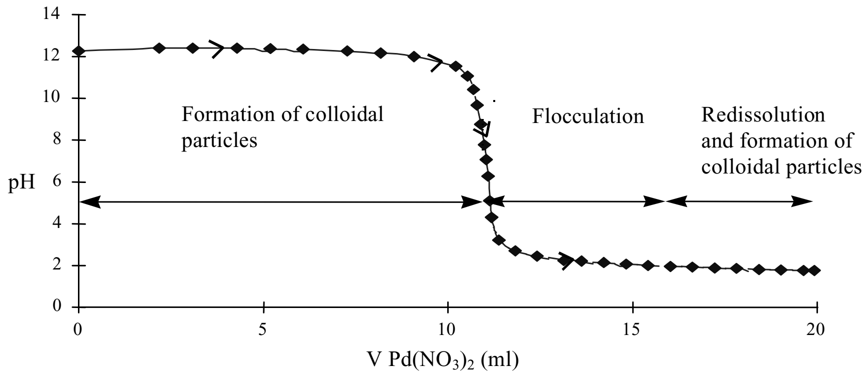

FIGURE 13.8. Neutralization curve of soda [NaOH] = 0.1 N by addition of a palladium nitrate solution [Pd] = 5 g/L.

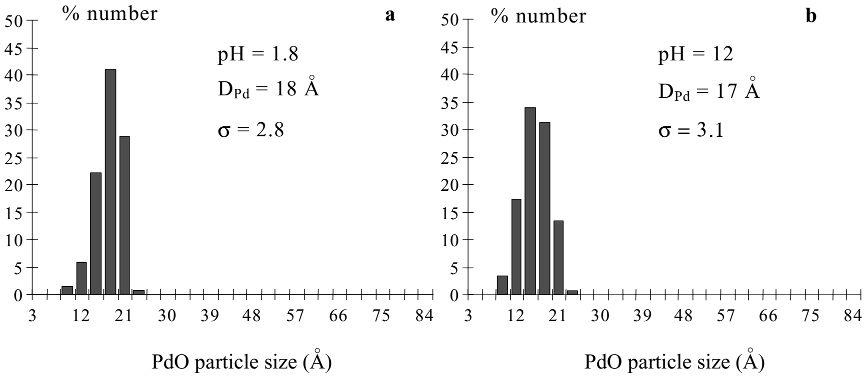

FIGURE 13.9. PdO particle size distributions for different pH by neutralization of palladium nitrate by soda (a) and soda by palladium nitrate (b) as determined by TEM.

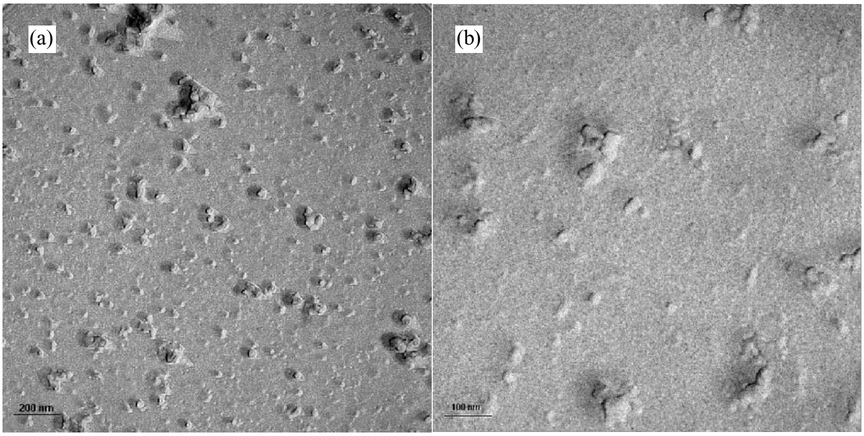

FIGURE 13.10. Micrographs after vitrification in liquid C_3H_8 of a basic hydrosol.

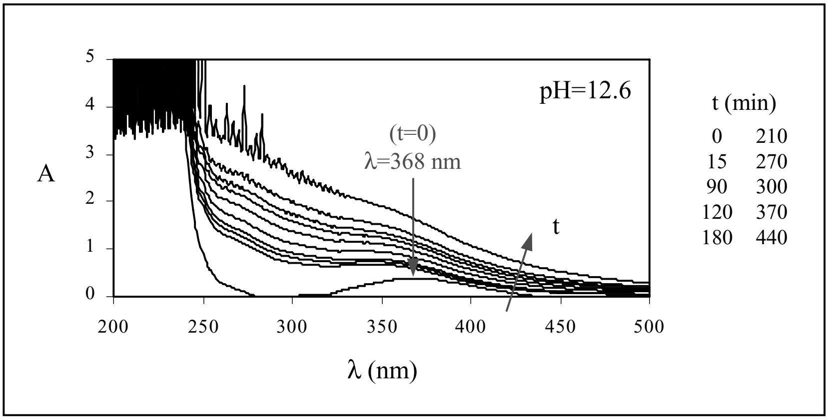

FIGURE 13.11. UV–visible spectra of the SB PdO hydrosol (pH = 12.6) ([Pd] = 3.40 g/L) versus time.

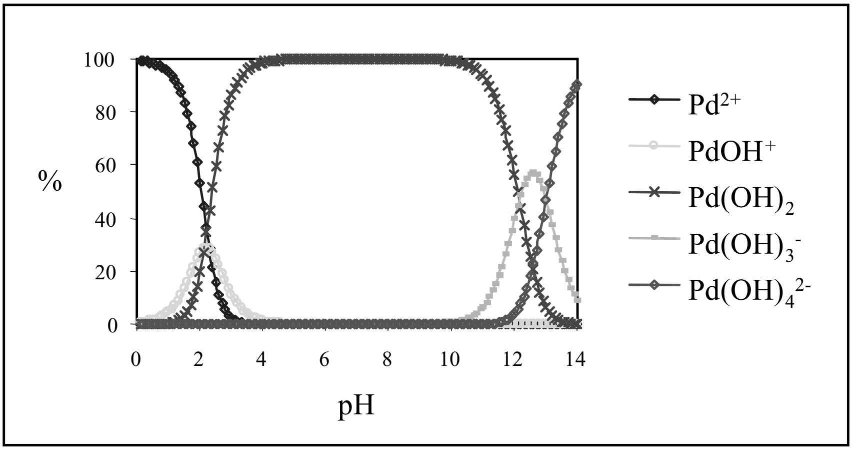

FIGURE 13.12. Stable existing species as a function of pH ([Pd] = 10 g/L = 9.4×10^{-2} M and I = 1 M) from Ref. 35.

and various operating parameters have a strong influence on the physical stability of the sol: ionic strength, addition of a stabilizing agent (surfactant, polymers, complexant), the pH of the medium, and temperature. Aggregation phenomena (or desaggregation which is generally the objective for catalytic applications), are closely related to the solubility of the oxide phase in the medium. Experimental data clearly shows that isolated particles are more easily obtained for pH conditions where solubility of the oxide solid phase is not zero. On the other hand, aggregation is more favored when solubility of the solid phase is very low. As an example, isolated PdO particles can be obtained for an acidic pH (for example with a reacidification at pH < 2), whereas highly aggregated PdO particles are observed for basic pH (typically pH > 12), resulting in a low solubility of PdO. In this case, physical phenomena like electrostatic interaction seem to play a minor role with respect to chemical solubility. Variations of $|pH\text{-}PIE_{PdO}|$, which is the driving force for the repulsive interaction between particles (2.5 for the acidic medium when pH = 2, and 7.5 in basic medium when pH = 12), and the ionic strength values are not able to explain the aggregation–desaggregation process.

The same results were observed for other oxide-colloidal systems such as SnO, SnO_2, and NiO. It is interesting to note that this tendency seems to be a general feature of oxides in solution as it has been observed for other systems.[33,34] Using the quasielastic light scattering (QELS) technique (Fig. 13.13), it is possible to follow the size of the PdO aggregates in the colloidal suspensions, while changing the operating conditions (in this case, the pH, but the concentration of Pd and time could be varied as well).

We have seen that direct and reverse neutralization lead to the same average particle size. In order to explain this result, one must consider the chemical reactions occurring during both preparations. Although several monomolecular species are thermodynamically predicted (Fig. 13.12), the determination of the partial charge of the hydroxo ligand in different complexes shows that this ligand is the only one exhibiting

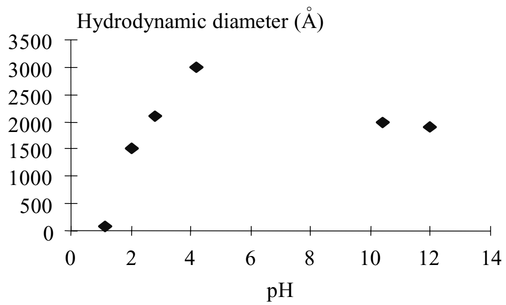

FIGURE 13.13. Hydrodynamic diameters of colloidal particles determined by QELS as a function of the hydrosol pH.

the nucleophilic character necessary for the condensation mechanism (Table 13.1). For pH < 12, the anionic species $Pd(H_2O)(OH)_3^-$ and $Pd(OH)_4^{2-}$ are not present. Thus, both types of neutralization, addition of soda to nitric acid and the reverse, lead to the same complex, i.e. $Pd(H_2O)_2(OH)_2$ which is the only complex able to generate nuclei by polycondensation. It has been verified by UV–visible measurements that for pH < 12, no molecular complex was observed.

For direct neutralization (addition of soda into palladium nitrate) different hydrolyzed intermediate species can be formed from $Pd(H_2O)_4^{2+}$ (Fig. 13.14): $Pd(H_2O)_2(OH)_2$, $Pd(H_2O)_3(OH)^+$. In the reverse method, i.e. the addition of $Pd(H_2O)_4^{2+}$ in a NaOH solution at pH = 12, the only complex produced is the neutral complex $Pd(H_2O)_2(OH)_2$, in agreement with UV–visible measurements. In this case, the cloudy solution appears in the initial stage of the experiment with the first drops of palladium nitrate solution.

Moreover, the formation of $Pd(H_2O)_2(OH)_2$ by substitution of aquo groups by hydroxo groups is very fast ($k = 10^{10}$ mol^{-1} s^{-1}), and as a consequence, the concentration

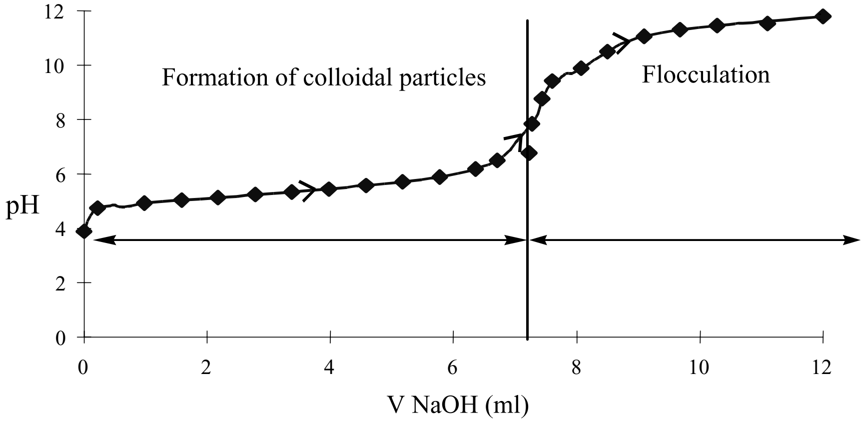

FIGURE 13.14. Neutralization curve of a palladium chloride solution [Pd] = 5 g/L by addition of soda [NaOH] = 0.1 N.

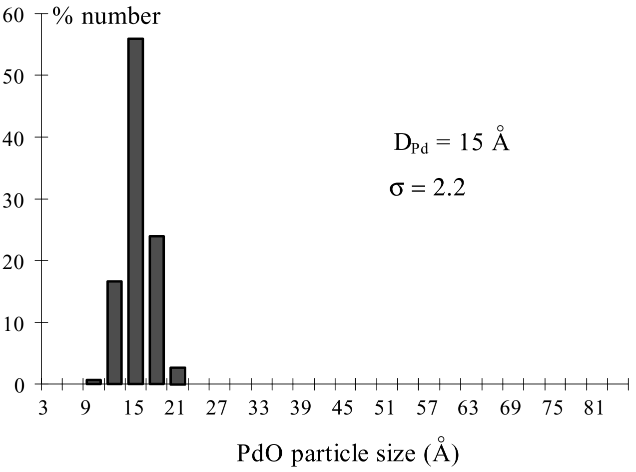

FIGURE 13.15. PdO particle size distributions obtained by neutralization at pH = 7 of Na_2PdCl_4 solution by soda determined by transmission electron microscopy.

of this complex is very high for all preparations. This fast reaction is responsible for the high sursaturation values defined by the ratio of the concentration of metallic precursor $Pd(H_2O)_2(OH)_2$ in the solution to the solubility of the solid PdO phase. At room temperature and solutions with a pH ranging from 3 to 12, high sursaturation values are reached as well due to the very low value of the pKs of the solid precursor ($\sim 1.1 \times 10^{-29}$). This high value of sursaturation favors the nucleation rate with respect to the growth rate from a kinetic point of view. This "explosive" nucleation step governs the final PdO particle size. In the case of the Pd nitrate precursor, no growth above a size of about 2 nm of the particles has been achieved varying the other operating parameters of pH, ionic strength, nature of the counter ion of hydroxides, or metal concentration.

One way to modify the final particle size is to generate a different precursor of condensation. As an example, Na_2PdCl_4 in acidic solution contains the $PdCl_3(H_2O)^-$ complex as seen by UV–visible measurements. Neutralization by soda leads to the formation of two types of neutral complexes: $Pd(H_2O)_2ClOH$ and $Pd(H_2O)_2(OH)_2$. According to the partial charge model, these two complexes are able to polymerize ($\delta_{OH} = -0.19$ and $\delta_{Pd} = +0.34$ in the case of $Pd(H_2O)_2ClOH$ complex, Table 13.1). By inductive effect, the chloride ligand affects the kinetics of the nucleation rate versus growth of the entities. As a result, the final particle size is slightly lower than compared to the results obtained starting with palladium nitrate solution (Fig. 13.15).

This effect, moderated by the presence of $Pd(H_2O)_2(OH)_2$, is clearly related to the properties of the $Pd(H_2O)_2ClOH$ complex. The reverse neutralization (addition of Na_2PdCl_4 or $PdCl_3(H_2O)^-$ under its hydrolyzed form, to soda) gives rise only to $Pd(H_2O)_2(OH)_2$ formation due to the instability of $PdCl_3(H_2O)^-$ at high pH values.[36] For these conditions, the consecutive condensation reactions generate palladium oxide particles with the same average size as in preparations using palladium nitrate precursor.

Thermohydrolysis is another reaction which can be used to prepare colloidal suspensions of palladium oxide particles, and has been proven for other oxides.[37–40]

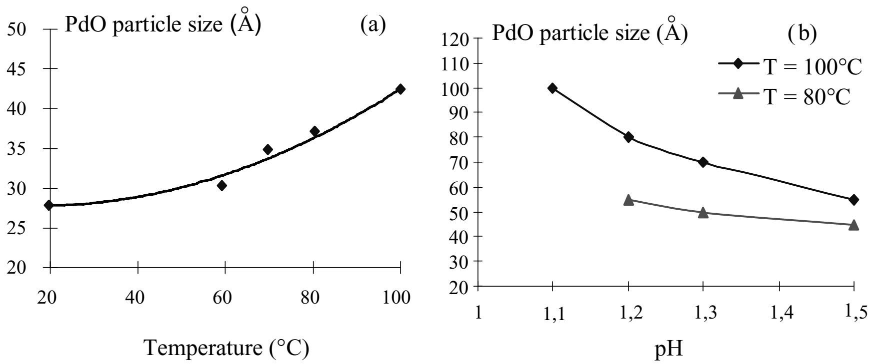

FIGURE 13.16. Evolution of PdO particle size with temperature and pH (a: starting $Pd(NO_3)_2$ solution [Pd] = 5 g/L and b: [Pd] = 1 g/L).

In this case, the reaction of water molecules with palladium complexes is promoted by heat, so no addition of soda is required. The global chemical reaction is expressed by Eq. (3):

$$[Pd(OH_2)_4]^{2+} + 2NO_3{}^- + hH_2O \rightarrow [Pd(OH)_h(OH_2)_{4-h}]^{(2-h)+} + 2NO_3{}^- + hH_3O^+. \quad (3)$$

In comparison with the neutralization methods previously described, lower sursaturations are obtained with thermohydrolysis because the solubility of $Pd(H_2O)_2(OH)_2$ increases with temperature. Thermohydrolysis is then more favorable to particle growth. Figures 16a and b present the influence of temperature and the initial pH of the solution on the average PdO particle size determined by X-ray diffraction on the solid phase after precipitation.

PdO particle growth may have two origins: A thermodynamic phenomenon due to the spontaneous evolution in order to minimize surface energy of the system by Ostwald ripening, or a kinetic control of nucleation and condensation reaction rates. In our case, no variation of the final particle size was observed between the first 18 h at 100°C under reflux. So, the evolution of average particle size is probably more related to a kinetic effect. Lowering the pH displaces the equilibrated reaction (3) to the left, depressing the formation of the neutral precursor $Pd(H_2O)_2(OH)_2$ ($h = 2$). Moreover, at low pH values, the solubility of PdO oxide is enhanced, decreasing the sursaturation of the medium. The nucleation rate, which is greatly dependent on the concentration of the nuclei, is then lower and the nuclei are less numerous and may grow by condensation reactions. The effect of temperature may also be explained in terms of kinetic control of the formation of solid nuclei, increasing their solubility and lowering the sursaturation of the solution.

13.2.2. Synthesis of Tin Oxide Hydrosols

Using the same experimental procedure as previously described, destabilization of a chloride stannic ($SnCl_4$, $5H_2O$) solution by the addition of soda easily forms a colloidal suspension. Figure 13.17 presents a TEM micrograph of a colloidal SnO_2

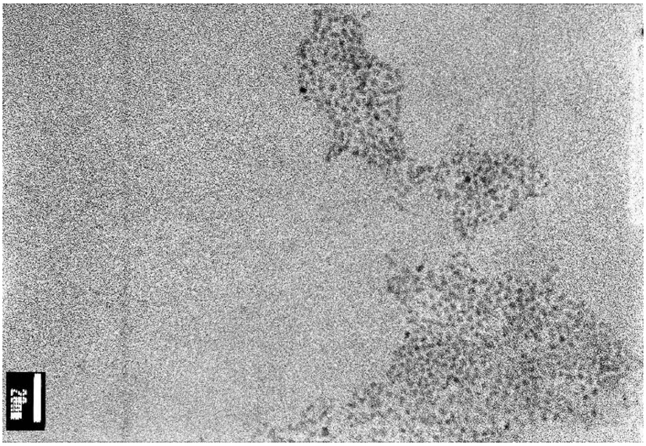

FIGURE 13.17. TEM micrograph of SnO_2 hydrosol (pH = 0.5) diluted 100 times with water.

(pH = 0.5) suspension deposited on a grid. Monomodal particle size distributions are obtained with an average size close to 2 nm.

The X-ray diffraction pattern of the solid phase obtained by complete neutralization of an acidic solution of $SnCl_4{\cdot}5H_2O$ is presented in Fig. 13.18. Cassiterite SnO_2 (rutile-type structure) was identified and Laue–Scherrer's law gives an average particle size of 2 ± 0.2 nm in good agreement with transmission electron microscopy observations.

Figure 13.19 summarizes the reaction mechanism starting from $Sn(OH)^{3+}$ or $Sn(OH)_6{}^{2-}$ in acidic media in alkaline media. As in the case of Pd, SnO_2 oxide is spontaneously formed by dehydration due to an internal oxolation reaction promoted by a strong polarization of the O–H bond of the hydroxide. Thermodynamically stable species with respect to pH are presented in Fig. 13.20. Various molecular cationic species with different hydroxylated levels are possible in an acidic medium, whereas only $Sn(OH)_6{}^{2-}$ is expected for a basic pH.

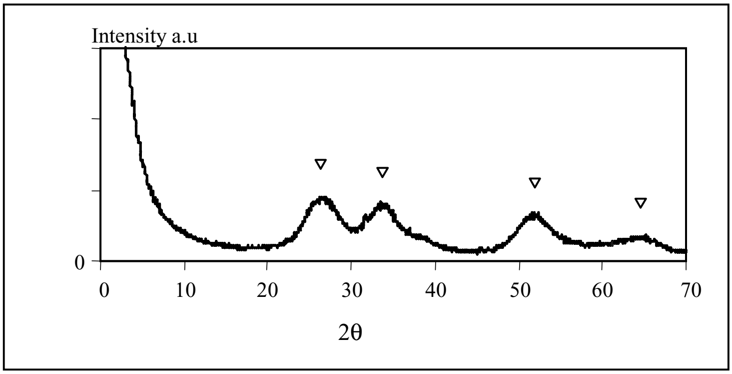

FIGURE 13.18. X-ray diffraction diffractogramm of the solid phase obtained by complete neutralization of a $SnCl_4{\cdot}5H_2O$ acid solution ∇SnO_2.

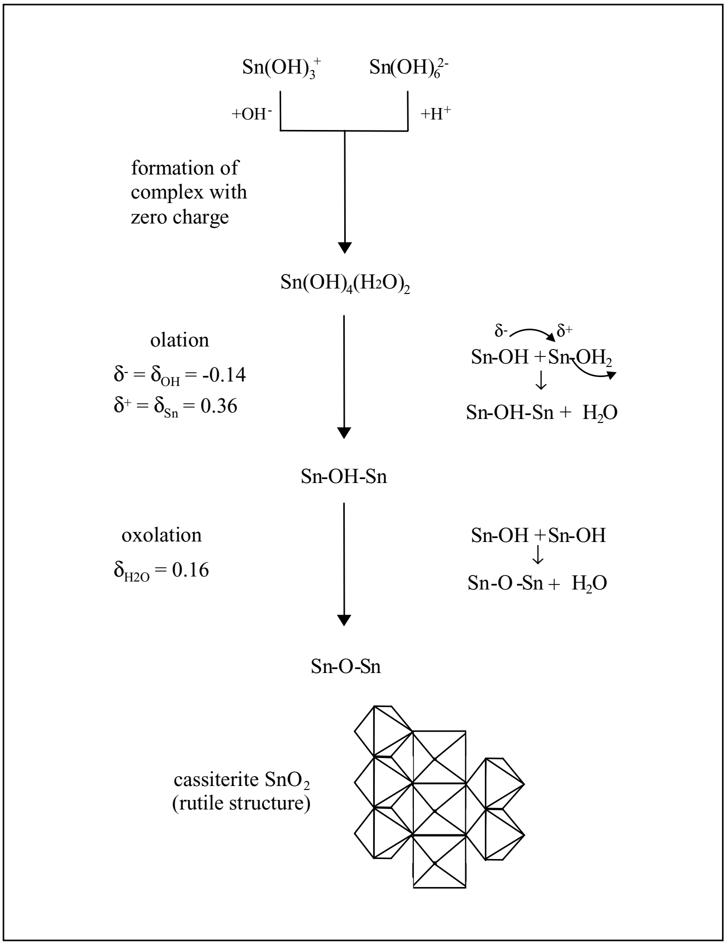

FIGURE 13.19. Schematic mechanism of the formation of SnO_2 (Cassiterite).

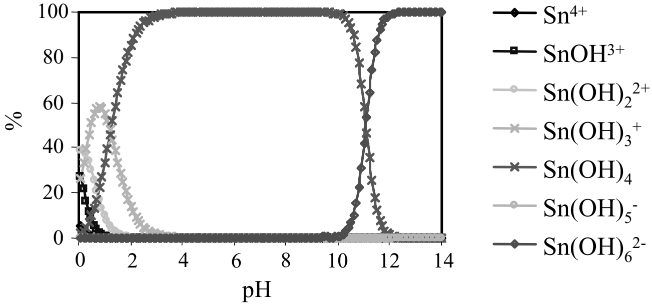

FIGURE 13.20. Repartition diagram of Sn^{IV} species ([Sn] = 10 g/L and I = 1 M).

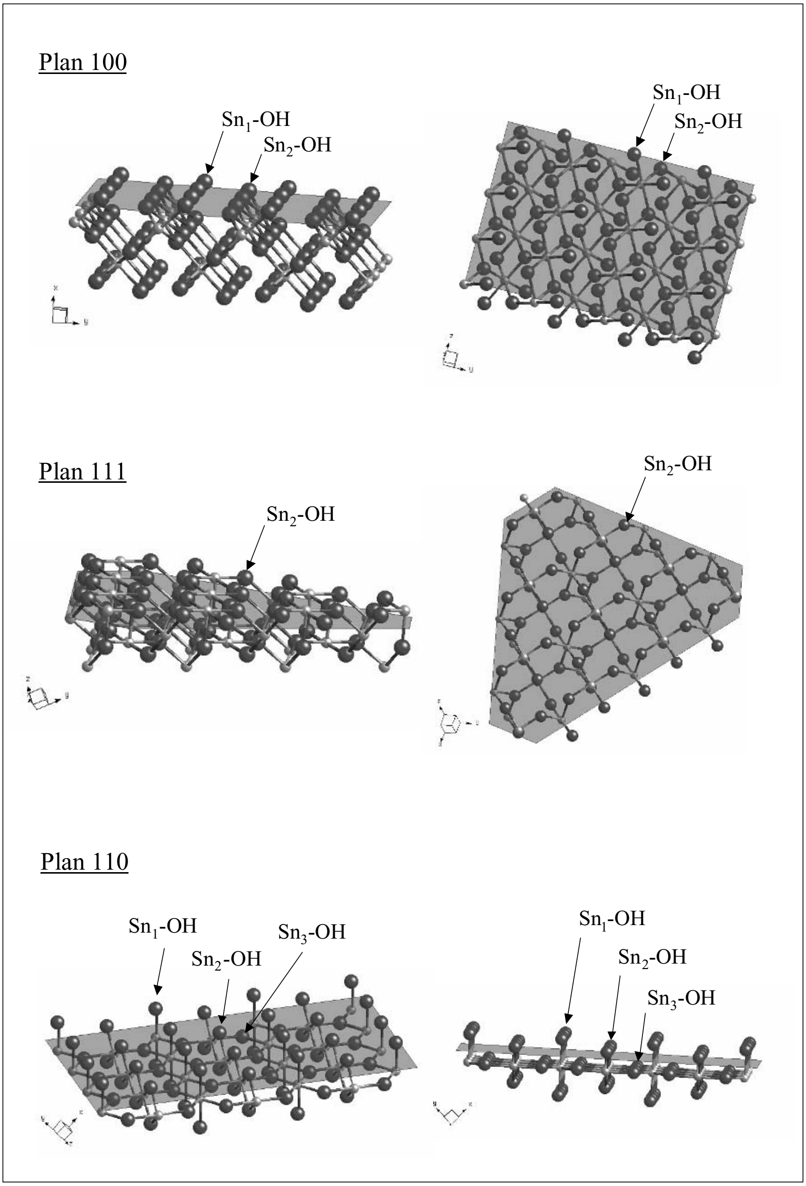

FIGURE 13.21. Surface sites of SnO_2 crystal (cassiterite) obtained with CrystalMaker 2.1.1 software.

The surface structure and characteristics (density and acidity) of the hydroxyl groups presented in Fig. 13.21 (using CrystalMaker 2.1.1 software) give very useful information to understand the reactivity of the surface of the particles, particularly when adsorption of another complex is desired to synthesize a bimetallic catalyst, or to control the interaction with an oxide carrier (the deposition step). The isoelectric point calculated with the model (5.9) is in fair agreement with the experimental value (4.3).

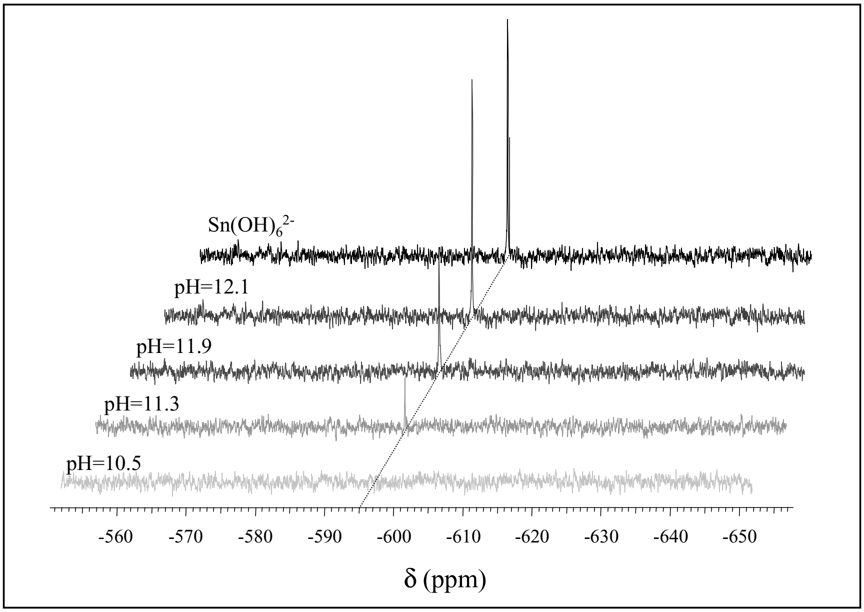

FIGURE 13.22. [119]Sn NMR spectra of hydrosol of SnO_2 and of the solution $Sn(OH)_6{}^{2-}$ ([Sn] = 3.67 g/L).

Using [119]Sn NMR spectroscopy, it is possible to follow the dissolution of SnO_2 and the formation of $Sn(OH)_6{}^{2-}$ (Fig. 13.22). During the hour long preparation, this complex is formed for pH > 11.3 (signal at 595 ppm) in agreement with the thermodynamic diagram in Fig. 13.20. The optimal OH/metal ratio must be determined to neutralize all the initial precursors without promoting dissolution.

13.2.3. Alumina-Supported Palladium Catalyst

The colloidal suspensions obtained by the neutralization or thermohydrolysis procedures described previously have been used to prepare supported Pd catalysts. The support is impregnated with a volume of colloidal oxide suspension corresponding exactly to the porous volume of the solid, according the well-known incipient wetness impregnation.

Various supports have been used, but the results reported here have been exclusively obtained with δ-Al_2O_3 with a specific surface area of 130 m^2/g and a porous volume of 1.04 cm^3/g. The palladium loading is about 0.1% by weight. After impregnation, the samples are dried overnight at 393 K.

Figures 13.23a and b show the PdO particle size distribution of PdO-supported catalysts prepared from an acidic hydrosol (neutralization of palladium nitrate solution by addition of soda) and a basic one (neutralization of soda by addition of palladium nitrate). Comparisons with the corresponding histograms of the initial suspensions (Figs. 7b and 9b), show that the distributions are not significantly modified. Only a very slight increase of the standard deviation of the dispersion values is observed

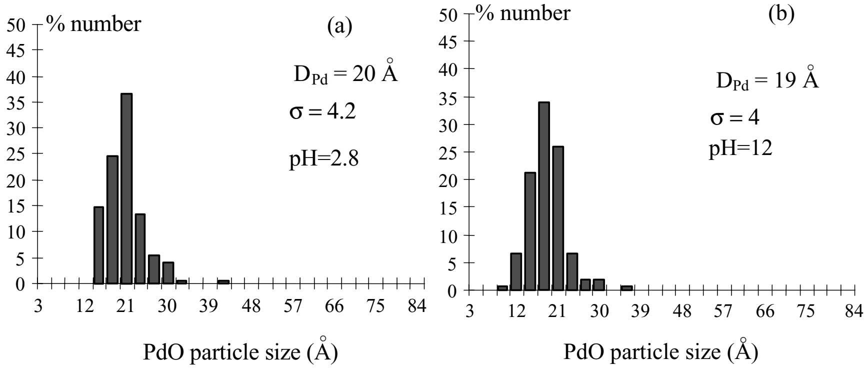

FIGURE 13.23. PdO particle size distributions for samples prepared from an acidic hydrosol pH = 2.8 (a) and a basic one pH = 12 (b).

(σ = 4 to 4.2 instead of σ = 2 to 3 for hydrosols), with the same average sizes of PdO particles.

Transmission electron microscopy micrographs (Fig. 13.24) also indicate an important characteristic of the supported particles. As in the case of suspensions, they are either aggregated or isolated. Support surface properties may be an important factor governing this aggregation. After deposition on the support, we observed that samples prepared from acidic hydrosols are characterized by the presence of aggregated particles constituting flocculates ranging from 10 to 200 nm, whereas samples prepared via basic hydrosols contain only isolated particles. The opposite was observed when hydrosols were concerned. These final states of the supported particles may be controlled

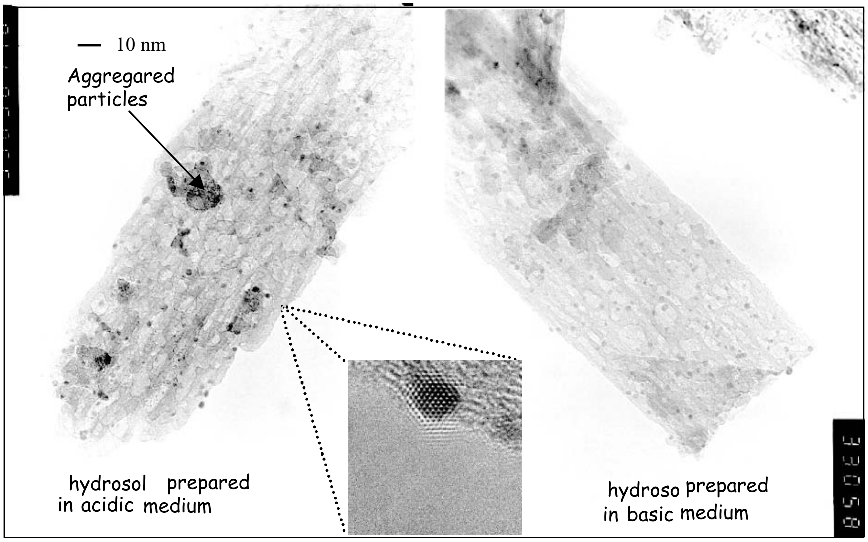

FIGURE 13.24. TEM micrographs of supported PdO catalysts prepared via "acid" and "basic" hydrosols.

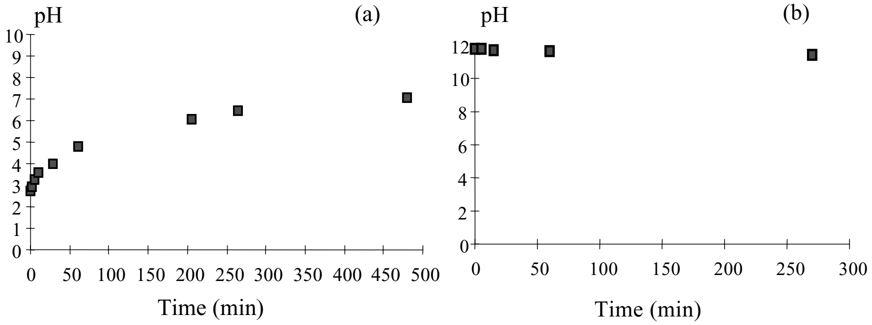

FIGURE 13.25. Evolution of pH of an acidic suspension (a: pH = 2.8) and basic suspension (b: pH = 12) in contact with δ-Al_2O_3.

via the pH of the suspension and its adequation with the isoelectric point of the solids (PdO particles and support), or the addition of a dispersing agent in the hydrosol before the impregnation step.

In the case of the impregnation of the acidic hydrosol (pH = 2.8), the surface of alumina is positively charged and the protonation of the surface hydroxyl groups is rather slow but significant when compared to the duration of preparation (around 30 min). After 200 min, the equilibrium is reached at a pH of approximately 7 (Fig. 13.25a). Keeping in mind that the IEP value of the palladium oxide is 4.5 in these conditions, both the support and PdO particles are initially positively charged and have a repulsive interaction favoring an isolated state at pH = 2.8. The progressive increase of pH due to the alumina protonation destabilizes the PdO particles repulsion leading to aggregated particles.

Impregnating a basic colloidal suspension (pH = 12) on alumina does not induce proton liberation, thus the pH is constant (Fig. 13.25b). The system keeps its initial properties, i.e. negative charges for alumina support and PdO particles. Repulsive interactions are created between the alumina surface and the PdO particles so that the particles deposited on the support are redispersed, and finally isolated from each other.

The aggregation state of particles can also be controlled by addition of dispersing agents to the hydrosol. As shown by transmission electron microscopy, samples stabilized by nitrite or chloride anions contain isolated particles for a very long period. The oxide particles, stabilized by the formation of Pd–NO_2 bonds, are isolated in the hydrosol. Because this bond is stable at the high pH values obtained during the deposition on alumina, the isolated state is retained for the final PdO supported catalyst. Since the stabilization by a strong ligand may also lead to redissolution of palladium oxide particles, one must precisely adjust the quantity of stabilizing agent. The use of steric stabilization may also be successfully employed with a cationic surfactant such as cethyl triammonium bromide (CTAB).

Reduction of PdO particles to metallic Pd° does not significantly modify the size of the particle to the extent shown by the BIOSYM calculation (Fig. 13.26). This important result means that the optimization of the size of the PdO particle, carried out during the preparation of the suspension, should remain even after activation, i.e. reduction under hydrogen, necessary for catalytic purposes to produce metallic active sites.

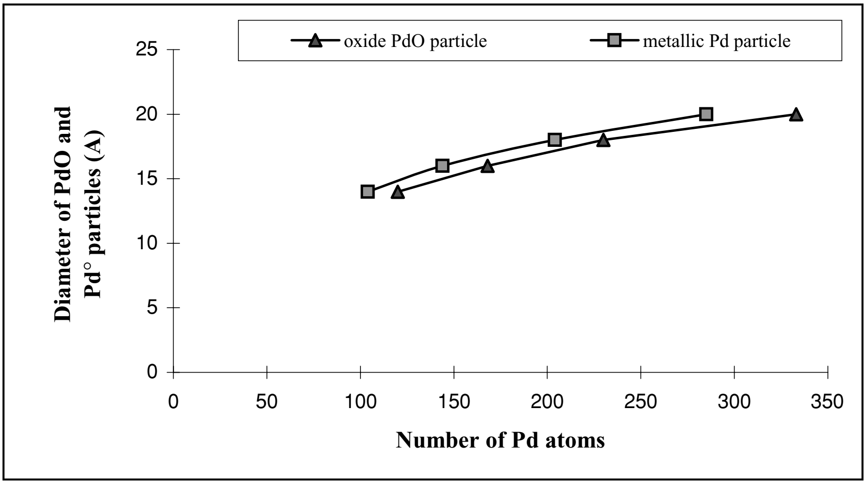

FIGURE 13.26. Number of Pd atoms in a spherical particle PdO and Pd° for different sizes.

13.3. BIMETALLIC CATALYSTS PREPARED BY COLLOIDAL SYNTHESIS

13.3.1. Palladium–Tin Catalysts

As mentioned in the introduction, the idea is to first synthesize a hydrosol (PdO, SnO_2), and then contacting it with a stannate (or palladate) complex aqueous solution. The initial oxide suspension acts as a "nano" carrier for the second element.

In the following section, we describe the case of adsorption of a Sn^{IV} complex onto a palladium oxide suspension. In an alkaline medium (a basic PdO hydrosol), chlorides in the $SnCl_4$ complex are substituted in the coordination sphere of tin(IV) by hydroxo anions, which are in excess, yielding the stannate $Sn(OH)_6{}^{2-}$ complex. The ^{119}Sn Mössbauer spectroscopy spectrum of a bimetallic sol (frozen in liquid nitrogen) is compared with a true stannic solution. At the same tin concentration, it shows the changes in the Sn environment due to adsorption onto the PdO surface (Fig. 13.27). The isomer shift δ is found to be close to zero for the stannate solution and increases when contacted with the PdO suspension, indicating a modification of the coordination sphere of tin. The increase in δ can be correlated to an increase in the core level electronic density of tin. The quadrupole splitting Δ, is related to a modification of the symmetry of the close environment of tin, due to adsorption of $Sn(OH)_6{}^{2-}$ complexes onto the PdO colloidal nanoparticles.

At pH close to 12, the surface of palladium oxide is negatively charged (point of zero charge: PIE $= 4.5$) excluding an electrostatic adsorption of the stannate anion to form an outer sphere complex. According to the multisite complexation model (MUSIC), in the investigated range of alkaline pH values, two surface hydroxyl groups are supposed to coexist, Pd_2–OH^0 (μ^2 sites) and Pd_3–$O^{-0.5}$ (μ^3 sites), yielding a negatively charged surface. Adsorption is suggested to proceed via chemisorption

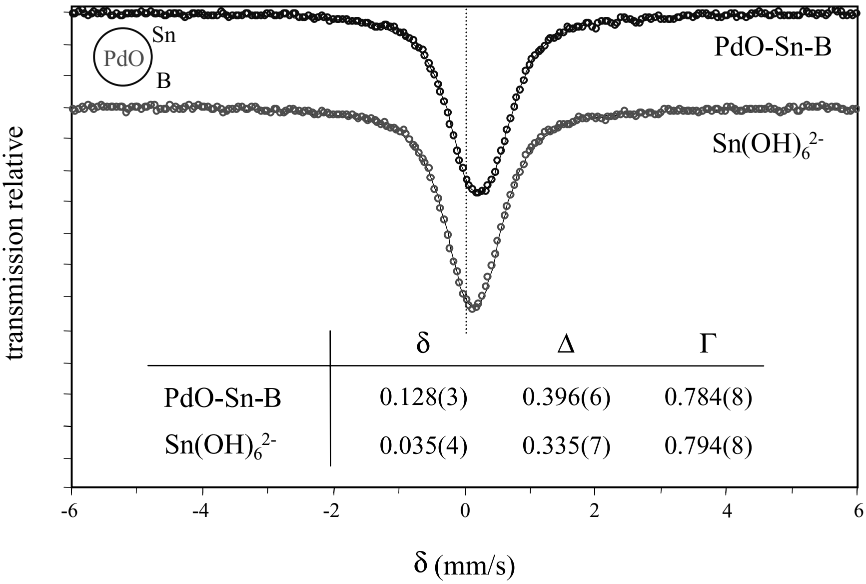

FIGURE 13.27. [119]Sn Mössbauer spectra at –193°C of (•) the $Sn(OH)_6{}^{2-}$ solution and of (○) the bimetallic *PdOSn* sol (PdO sol+$Sn(OH)_6{}^{2-}$) at the same tin concentration ([Sn] $= 1.3 \times 10^{-2}$ mol/L).

(hydrolytic adsorption) of stannate, leading to the formation of an inner sphere complex[41], as described in Eq. (4):

$$Pd_2{-}OH^0 + HO{-}Sn(OH)_5{}^{2-} \quad \rightarrow \quad Pd_2{-}O{-}Sn{-}(OH)_5{}^{2-} + H_2O. \qquad (4)$$

After deposition on the alumina support using a classical incipient wetness impregnation, only isolated particles are observed by TEM (Fig. 13.28). When compared to the starting PdO particles (mean particle size = 1.8 nm), the mean particle size slightly increases to 2.9 nm but the standard deviation of the distribution is kept constant.

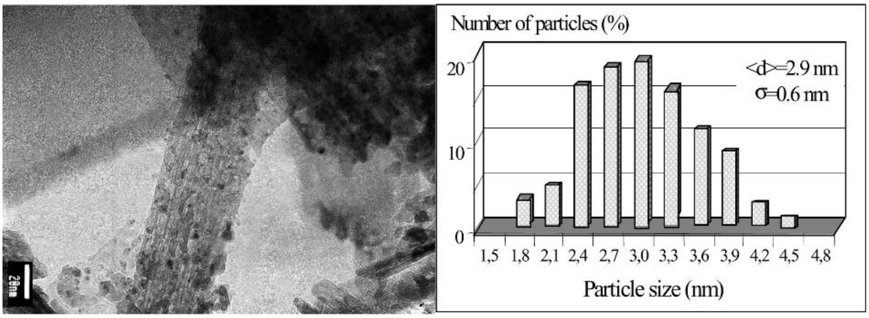

FIGURE 13.28. TEM micrograph and histogram of the *PdOSn* catalyst and particle size distribution.

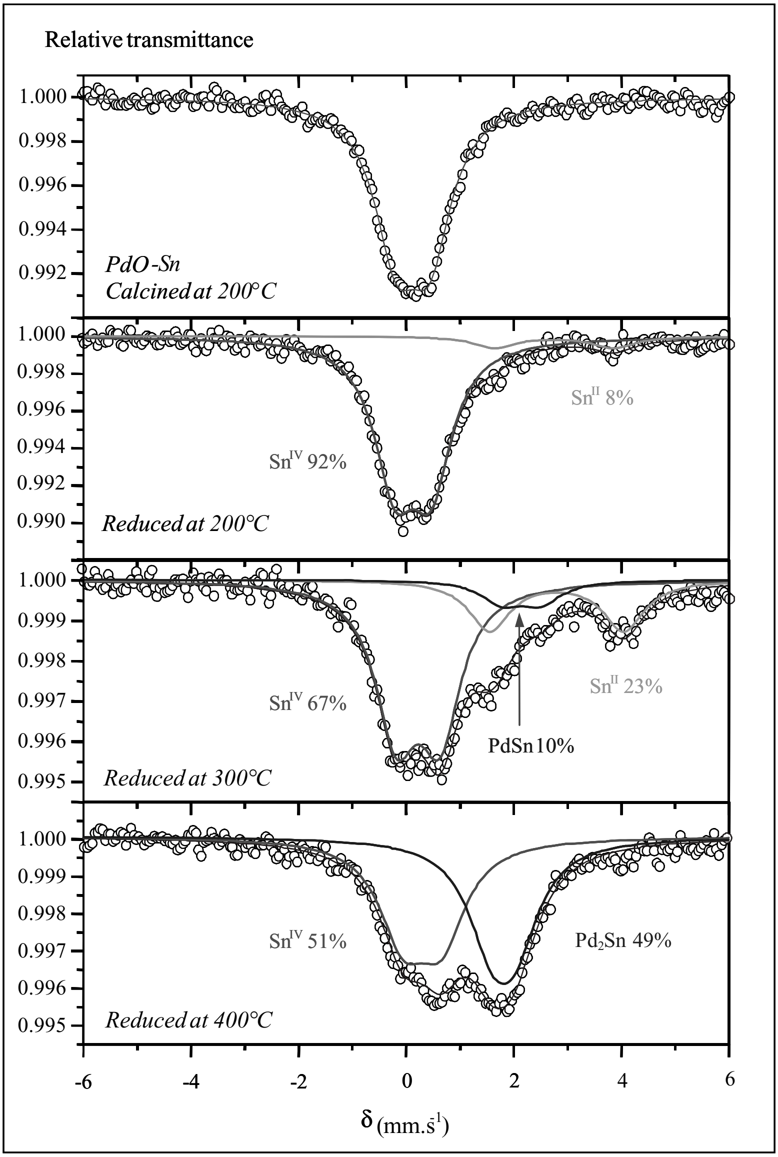

FIGURE 13.29. ^{119}Sn Mössbauer spectra of the *PdOSn* catalyst calcined at 200°C (top) and reduced at 200°C, 300°C, and 400°C (bottom).

The ^{119}Sn Mössbauer spectra of the supported catalyst (*PdOSn)* after low temperature calcination (200°C) under airflow and reduction treatments performed at different temperatures are presented in Fig. 13.29. The corresponding hyperfine parameters (δ and Δ) are reported in Table 13.2. For a reduction temperature of 200°C, the tin reduction is initiated as demonstrated by the presence of 8% of Sn^{II}. Formation of bimetallic species (presence of Pd° and Sn°) starts at around 300°C and increases with reduction

TABLE 13.2. Hyperfine parameters of refined spectra of the *PdOSn* catalyst after calcination at 200°C and reduction at various temperatures.

Sample	δ (mm/s)	Δ(mm/s)	Γ (mm/s)	RC (%)	Sn species
PdOSn	0.02 (1)	0.62 (1)	0.98 (2)	100	Sn^{IV}
Calcined at 200°C					
PdOSn	0.02 (1)	0.67 (1)	0.94 (2)	92	Sn^{IV}
Reduced at 200°C	2.64 (9)	2.2 (1)	1.0 (2)	8	Sn^{II}
PdOSn	0.12 (1)	0.80 (1)	0.94 (3)	67	Sn^{IV}
Reduced at 300°C	2.05 (8)	0.7 (1)	0.94 (3)	10	PdSn
	2.69 (4)	2.49 (6)	0.94 (3)	23	Sn^{II}
PdOSn	0.19 (2)	0.71 (3)	1.09 (4)	51	Sn^{IV}
Reduced at 400°C	1.70 (3)	0.44 (5)	1.09 (4)	49	Pd_2Sn

temperature: 10% of PdSn at 300°C and 49% of the expected Pd_2Sn alloy at 400°C with a molar Pd/Sn ratio close to 2. Hence, the maximum amount of Pd_2Sn observed (49%) approximately corresponds to 50% of the total amount of palladium. Stannous tin is an intermediate species between stannic tin and reduced tin and acts as a precursor of the bimetallic Pd–Sn species. As tin is supposed to migrate easily on alumina because of its ability to reoxidize via formation of tin aluminate,[42] its incorporation into palladium demonstrates that the stannate anions adsorbed on the PdO particles in the initial hydrosol is not significantly disturbed by the deposition process onto the support.

Casting microprobe analysis (Fig. 13.30) shows the very pronounced eggshell repartition of Pd and Sn across the diameter of the alumina beads. This is an important feature in the case of intragranular limited reactions such as selective hydrogenations. The thickness of the shell is very small (about 50 μm) and both elements are located in the same zone, which is a necessary condition for an interaction between the two metals.

Surface concentrations deduced from low-energy ion scattering (LEIS) spectra analysis showed that as erosion increases with time, the concentration of palladium increases whereas that of tin decreases. This result is in agreement with a pronounced surface enrichment by tin with respect to palladium according to the principle of the preparation method.

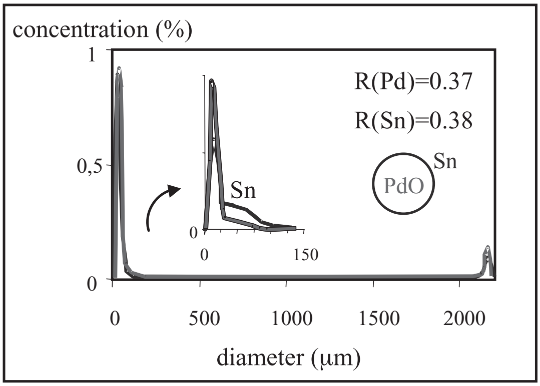

FIGURE 13.30. Repartitions of Pd and Sn obtained by casting μ probe analysis for the PdOSn catalyst (PdO—Sn).

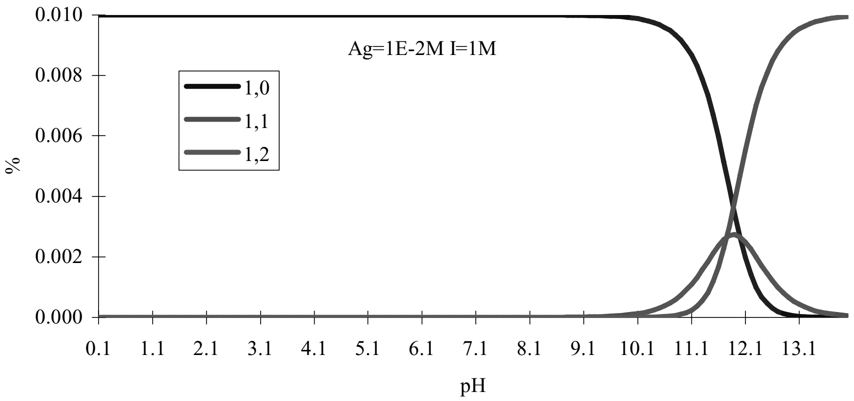

FIGURE 13.31. Predominance diagram of Ag(I): [Ag(I)] = 0.01 M I = 1 M.

13.3.2. Palladium–Silver Catalysts

Adsorption of Ag on the surface of PdO is also an interesting option offered by colloidal oxide synthesis. Silver is a well-known promoter for the improvement of catalytic properties, primarily selectivity, in various reactions such as hydrogenation of polyunsaturated compounds.[43] The more stable oxidation state of silver is +1.[44] Aquo soluble precursors are silver nitrate (halide precursors are all insoluble), and some organics such as acetate or oxalate with limited solubility may also be used.[45] Ag^+ is a d^{10} ion and can easily form linear AgL_2 type complexes according to crystal field theory. Nevertheless, even for a concentrated solution of $AgNO_3$, Ag^+ does not form aquo complexes.[46] Although a solvation sphere surrounds the cation, no metal–water chemical bonds have been observed.

The diagram presented in Fig. 13.31 is rather simple and is quite independent to the concentration of metallic precursor or ionic strength. It was obtained from the literature data[47] resolving Eq. (5.2), which was obtained from Eq. (5.1).

$$C_0 = [Ag^+] + [AgOH] + [Ag(OH)_2{}^-], \quad (5.1)$$

$$C_0 = [Ag^+] \cdot \left(1 + \frac{Q_{11}}{h} + \frac{Q_{12}}{h^2}\right), \quad (5.2)$$

where

$$Q11 = \frac{[Ag(OH)][H^+]}{[Ag^+]}, \quad \text{and} \quad Q12 = \frac{[Ag(OH)_2{}^-][H^+]^2}{[Ag^+]}.$$

If one considers now different options to generate interaction in solution between Ag^+ and the PdO surface, Fig. 13.32 shows that in the pH = 5 to 10 range electrostatic adsorption is expected to take place. In this pH range, deprotonated hydroxyl groups of the PdO surface have a negative charge and can interact with the Ag^+ cations.

Despite that thermodynamics predicts the coexistence of molecular Ag^+ and PdO oxide particles over a rather large pH domain, AgOH is readily formed at $5 < pH < 13$.

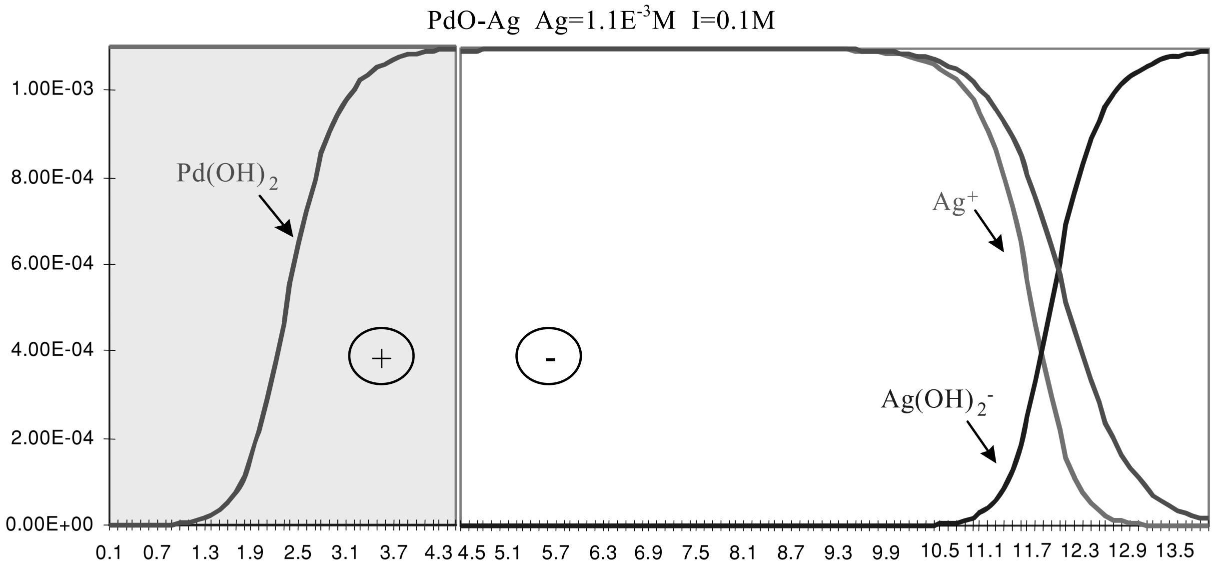

FIGURE 13.32. A predominance diagram of silver and palladium species as a function of pH.

In fact, adsorption of Ag^+ can be successfully performed by an ionic exchange mechanism for pH ≤ 5. A negatively charged PdO surface is able to adsorb Ag^+ in this acidic medium. Such a solution was impregnated onto α-Al_2O_3 and results of the catalytic tests are presented in Section 13.4.3.

13.4. APPLICATION TO CATALYSIS: SELECTIVE HYDROGENATION REACTIONS

13.4.1. Hydrogenation of Phenylacetylene on Pd Monometallic Catalysts

This section presents the result of the catalytic performances in the case of phenylacetylene hydrogenation reaction. The catalytic evaluation was performed in a classical well-stirred stainless steel reactor operating in batch mode under constant H_2 pressure (10 bar) at 17°C using n-heptane as the solvent. As mentioned in Section 13.2.2, no modification of the particle size distribution has been observed by transmission electron microscopy before or after reduction of colloidal oxide particles.

For all catalysts, the hydrogenation mechanism performed under our conditions (liquid phase and low hydrogen pressure) is consistent with an Horiuti–Polanyi mechanism.[48] We found that the phenylacetylene (PhAc) hydrogenation reaction was zero order with respect to hydrocarbon reactants up to 80% of conversion, in agreement with several other studies devoted to the hydrogenation of polyunsaturated compounds.[49]

Constant rates k (mol/s·gPd^{-1}) have been determined from the slope of the experimental curves plotting acetylenic molar concentration versus time. Turn over numbers (TONs = mol/s·atom Pd^{-1}) were calculated from the following equation:

$$\mathrm{TON} = \frac{kM}{D},$$

where M is the atomic weight of Pd, D is the dispersion defined as the fraction of exposed Pd atoms (the ratio between the number of surface atoms and the total number of atoms) obtained from CO chemisorption measurements

Catalytic results reported in Table 13.3 show a comparison between a "colloidal" catalyst and a more conventional preparation procedure using palladium acetylacetonate as a precursor.[50] These two catalysts have nearly the same dispersion, but the colloidal-based catalyst is roughly six times more active for PhAc hydrogenation.

Particle size distribution of the catalysts prepared from acetylacetonate (Fig. 13.33) reveals a much larger distribution than that of the catalyst prepared from the colloidal route (Fig. 13.23b). This difference may explain the relatively poor specific activity

TABLE 13.3. Characteristics and catalytic activity of samples prepared from the colloidal method and conventional preparation method.

	Particle Size (Å) (TEM)	Particle Size Distribution (TEM)	Dispersion % by CO Chemisorption	k PhAc mol/s^{-1}·gPd^{-1}	TON PhAc mol/s·atom Pd^{-1}
"Colloidal" catalyst	19	Narrow $\sigma = 4$	63	0.052	8.8
Preparation using $Pd(Acac)_2$	23	Broad $\sigma = 8.1$	66	0.008	1.3

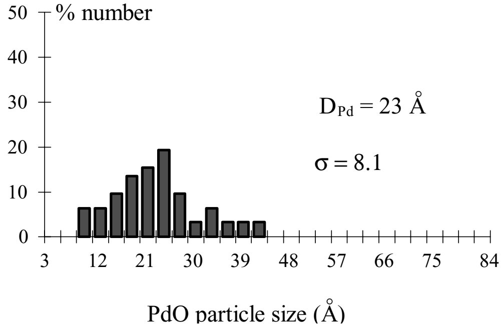

FIGURE 13.33. Particle size distribution obtained by TEM analysis of the $Pd(Ac)_2$ catalyst.

of the catalyst containing small particles (<10 Å), which have a low activity for such a highly structure sensitive reaction, and large particles (>30 Å), which have a low fraction of accessible atoms. Thus, the highest hydrogenation activity is obtained for particle sizes between 10 and 30 Å.

Regarding the degree of aggregation, a comparison of the catalytic activity of the two "colloidal" catalysts is given in Table 13.4. It appears that the aggregation of particles lowers the specific activity of the catalyst but the turn over number is significantly higher for the catalyst having aggregated particles (Fig. 13.34). The same observation has been made for butadiene hydrogenation.

An infrared study of adsorbed CO showed that particle aggregation occurred mainly at unsaturated atoms sites such as corners and edges. These low coordination atoms are then blocked to the reactants, which can only be activated by atoms located on planes. Moreover, the binding energy of the $3d_{5/2}$ core level, determined by X-ray photoelectron spectroscopy (XPS) of aggregated particles ($El_{3d5/2} = 334.4$ eV), is smaller than that of isolated particles of 20 Å in size ($El_{3d5/2} = 334.8$ eV) (Fig. 13.34). In summary, aggregation phenomenon promotes geometric and electronic effects in such a way that an increase of the TON is observed due to a favorable organization of the particles on the surface of the support, leading to the blocking of the unsaturated atoms having a lower intrinsic hydrogenation activity.[51]

13.4.2. Hydrogenation of Butadiene on Bimetallic Palladium–Tin Catalysts

A colloidal suspension prepared according to the method described in Section 13.2.3 was contacted with a porous alumina carrier to obtain a bimetallic palladium–tin catalyst. Evaluation of the catalytic properties of this system is detailed

TABLE 13.4. Characteristics and catalytic activity of samples prepared from colloidal suspensions.

Particle Size (Å) (by TEM)	TEM Observation	Dispersion % by CO Measurements	k PhAc mol/s·gPd^{-1}	TON PhAc mol/s ·atom Pd^{-1}
20	Aggregated particles	12	0.033	29.3
19	Isolated particles	63	0.052	8.8

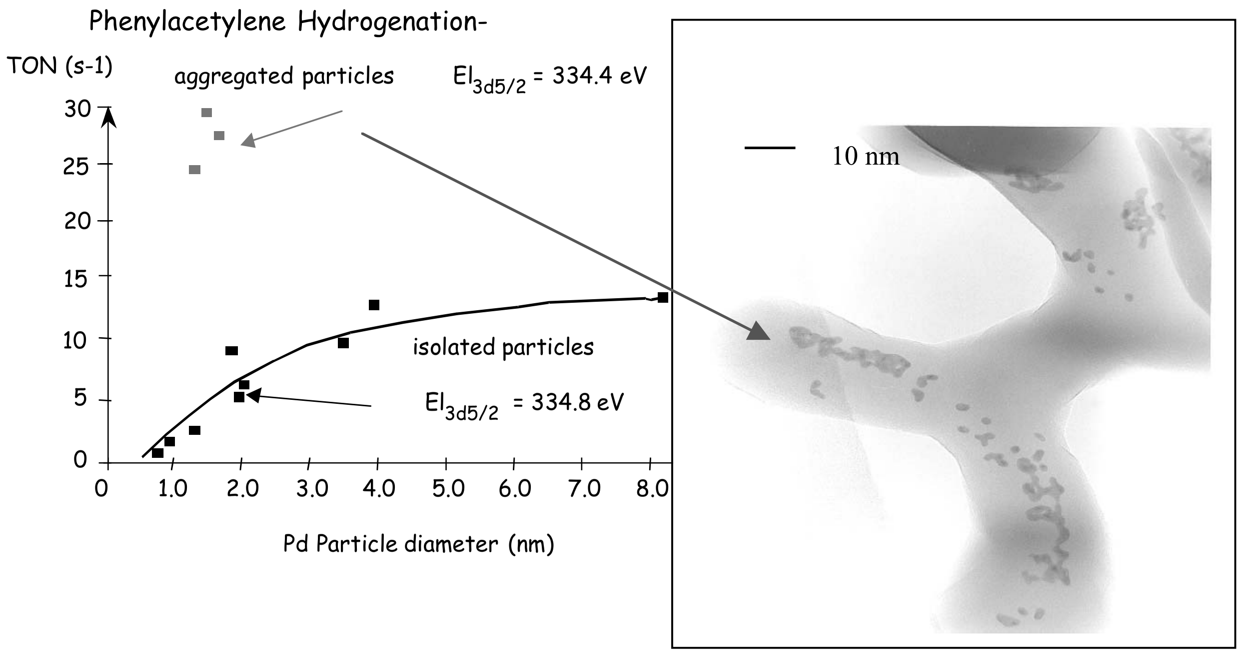

FIGURE 13.34. Comparison of phenylacetylene hydrogenation TON for aggregated and isolated Pd on α-Al_2O_3 particles.

TABLE 13.5. Intrinsic kinetic constant k_i (mol/s·mol$_{\text{surface Pd}}{}^{-1}$) and kinetic selectivity r for different catalysts after reduction at 200°C.

T_{red} = 200°C	PdO	PdSn	PdOSn
k_1 (BD→B1)	5.8	8.2	11.6
k_2 (BD→B2)	3.6	2.4	6.6
k_3 (B1→BA)	2.6	7.3	2.3
k_4 (B1→B2)	4.7	8.9	2.5
$K_{BD}/K_{Butenes}$	22.0	11.2	80.9
r	17.3	5.7	194.4

hereafter in the case of buta-1,3-diene hydrogenation in liquid phase, and compared to a bimetallic catalyst obtained via a standard procedure of coimpregnation of palladium and tin precursors.

Buta-1,3-diene (BD) hydrogenation is a widely used model reaction to investigate surface modification by promoters or alloy formation.[52] The reaction is usually described as a consecutive mechanism[53,54] without direct hydrogenation of buta-1, 3-diene to butane (BA).[55]

From the kinetic and adsorption constants, the kinetic selectivity r is defined as

$$r = \frac{k_1.K_{BD}}{(k_3 + k_4).K_{B1}} \quad \text{for the reaction mechanism} \quad BD \xrightarrow{k_1} B1 \begin{cases} \xrightarrow{k_3} BA \\ \xrightarrow{k_4} B2 \end{cases}$$

More details concerning calculation of the kinetic parameters are given in Ref. 56.

In the results presented in Table 13.5, the addition of tin affects the kinetic selectivity r differently, depending on the catalyst preparation method. When compared to the monometallic PdO catalyst, r slightly decreases for the coimpregnated PdSn catalyst, but it sharply increases for the PdOSn catalyst prepared via the colloidal oxide synthesis. As the intrinsic kinetic constant rates k_i do not show significant discrepancies between the different catalysts, the main contribution of the variation of the kinetic selectivity is ascribed to the adsorption constant ratio $K_{BD}/K_{Butenes}$. In the case of the PdOSn catalyst, formation of but-1-ene is favored compared to its consumption because the $K_{BD}/K_{Butenes}$ ratio increases, indicating that olefin adsorption is much more destabilized than diene adsorption. Thus, the olefin easily desorbs before being hydrogenated into butane.

In short, it has been observed that aggregation of particles plays an important role for the catalytic properties. For the same reduction temperature (T_{red} = 200°C) aggregated particles are much more selective (r = 194 versus 27) for the same amount of Pd_2Sn phase (around 40%). In this case, the change of selectivity cannot be related to the amount of Pd_xSn_y alloy. This shows that the degree of aggregation of the supported particles plays a major role in controlling the kinetic selectivity of the catalyst through the adsorption constant ratio $K_{BD}/K_{Butenes}$. On the other hand, the aggregation state does not modify the intrinsic constant rates k_i.

In the case of isolated particles, the kinetic selectivity increases with the reduction temperature (Fig. 13.35). In this case, the $K_{BD}/K_{Butenes}$ ratio remains almost constant, but the intrinsic kinetic constants relative to the hydrogenation and double bond

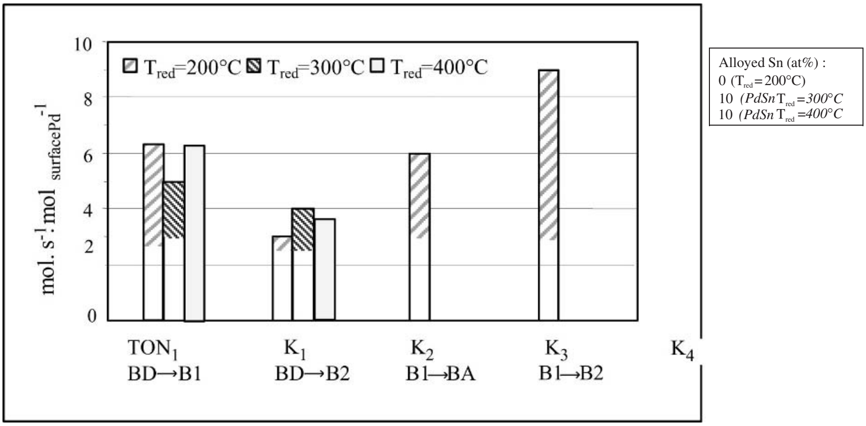

FIGURE 13.35. Effect of reduction temperature on kinetic constants and % of alloyed phases determined by ^{119}Sn Mössbauer spectroscopy.

isomerization of but-1-ene (k_3 and k_4 respectively) decreases sharply. When the reduction temperature increases, the aggregation state does not vary; the supported metallic particles remain isolated without sintering. Thus, the modification of the chemical steps relative to but-1-ene can be associated with the increasing proportion of Sn° incorporated in the alloyed phase changing the electronic properties of active sites as shown by different characterization techniques (XPS and IR of adsorbed CO).[56]

13.4.3. Hydrogenation of Acetylene on Bimetallic Palladium–Silver Catalysts

A supported PdAg/α-Al_2O_3 bimetallic catalyst prepared according to the colloidal method described in Section 13.3.2 was characterized and tested for acetylene/ethylene hydrogenation in typical tail end gas phase conditions ($P_{tot} = 25$ bar, $H_2/C_2H_2 = 1.5$ mol/mol, 2% C_2H_2 in C_2H_4, WHSV $= 3000$ h^{-1}). Figure 13.36 shows the increase in the time corresponding to the breakthrough of acetylene compared to a Pd monometallic catalyst and a PdAg catalyst with the same composition prepared with a conventional incipient wetness coimpregnation method.

High bimetallic character at a nanometer scale is probably the reason of this spectacular change in performance. As proposed in reference[57], the formation of heavy oligomers (green oil), which is the main deactivation factor and responsible of the acetylene breakthrough, is strongly inhibited on the surface of the bimetallic catalyst due to the isolation of adsorption sites. The probability of coupling between carbene or carbyne fragments covering the metallic surface is much lower on a bimetallic surface, increasing the cycle length and ethylene yields.

13.5. CONCLUSION

In this chapter, we discussed some general results obtained using a new route of preparation method of metallic supported catalysts by using colloidal oxide chemistry

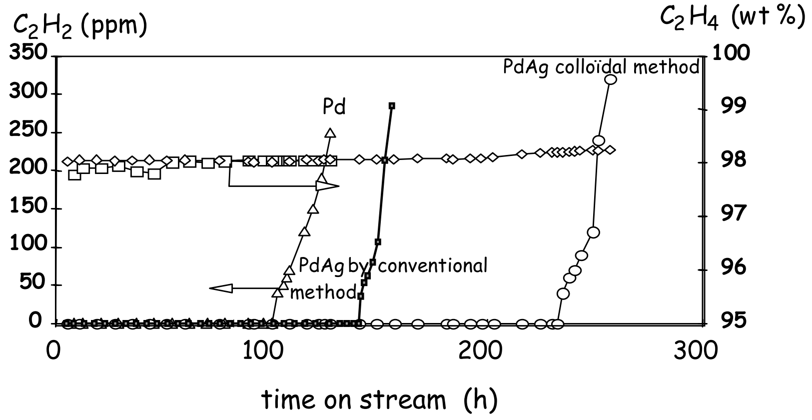

FIGURE 13.36. Yields in C_2H_2 and C_2H_4 versus time on stream for a Pd monometallic and PdAg bimetallic catalysts.

in aqueous phase. It has been shown that this method can be successfully applied to control the physical and chemical characteristics of supported particles at a nanometer scale, including particle size distribution, repartition on the support, and the interaction between metals in the case of multimetallic formulations. The fundamental bases of this chemistry follow the general principles already described for other oxides, but a real predictive approach of the phenomenon needs to take into account the kinetic factors governing the different reactions involved (nuclei formation and growth, dissolution, and aggregation), and which are specific of each system (nature of the metal, precursors, pH, metal concentration).

The catalytic performances of the supported catalysts clearly demonstrated the improvement in terms of activity or selectivity by such optimized catalytic systems. This improvement is related to a nanometer control of the critical characteristics of the active sites. Enhancement of the catalytic performances and the understanding of structure–reactivity relationships can only be achieved by advancing the understanding of different preparation methods, eventually leading to better control over the characteristics of the active sites at a nanometer scale. Moreover, new properties of these solids may be found, which could have a great impact on catalytic reactions.

REFERENCES

1. M. Che, O Clause, and Ch. Marcilly, Deposition of active component In *Preparation of Solid Catalysts*, edited by G. Ertl, H. Knözinger, and J. Weitkamp (Wiley-VCH, Weinheim 1999) pp. 315–340.
2. C. Louis, and M. Che, Anchoring and grafting of coordination metal complexes onto oxide surfaces In *Preparation of Solid Catalysts* edited by G. Ertl, H. Knözinger, and J. Weitkamp (Wiley-VCH, Weinheim 1999) pp. 341–371.
3. J. A. Rob van Veen, G. Jonkers, and W. H. Hesselink, Interaction of transition-metal acetylacetonates with γ-Al_2O_3 surfaces, *J. Chem. Soc. Faraday Trans.* 1 **85**(2), 389–413 (1989).
4. YU. I. Yermakov, Supported catalysts obtained by interaction of organometallic compounds of transition elements with oxide supports, *Catal. Rev. Sci. Eng.* **13**(1), 77–120 (1976).

5. M. Schreier, and J. R. Regalbuto, A fundamental study of Pt tetra ammine impregnation of silica 1: The electrostatic nature of platinum adsorption, *J. Catal.* **225,** 190–202 (2004).
6. M. Boudart, Catalysis by supported metals, In *Advances in Catalysis*, vol. 20, (Academic Press, San Diego 1969) pp. 153–166.
7. P. W. Jacobs, and G. A. Somorjai, Conversion of heterogeneous catalysis from art to science: The surface science of heterogeneous catalysis, *J. Mol. Catal. A Chem.* **131,** 5–18 (1998).
8. M. Che, and C. O. Bennett, The influence of particle size on the catalytic properties of supported metals, In *Advances in Catalysis*, vol. 36, (Academic Press , San Diego 1989) pp. 55–172.
9. V. Ponec, anjd G. C. Bond, Catalysis by metals and alloys, *Stud. Surf. Sci. Catal.* **95,** 317 (1995).
10. E. Lamy-Pitara, and J. Barbier, Platinum modified by electrochemical deposition of adatoms, *Appl. Catal.* A **149,** 49–87 (1997).
11. C. Micheaud, P. Marécot, M. Guérin, and J. Barbier, Preparation of alumina supported palladium-platinum catalysts by surface redox reactions: Activity for complete hydrocarbon oxidation, *Appl. Catal.* A **171,** 229–239 (1998).
12. J. Barbier, Redox method of bimetallic catalysts, In *Handbook of Heterogeneous Catalysis* edited by G. Ertl, H. Knözinger, and J. Weitkamp (Wiley-VCH, Weinheim 1997) pp. 257–264.
13. J. Margitfalvi, S. Szabó, and F. Nagy, Supported bimetallic catalysts prepared by controlled surface reactions, *Stud. Surf. Sci. Catal.* **27,** 373–409 (1983).
14. Y. A. Ryndin, and Y. I. Yermakov, Reactions of organometallic compounds with surfaces of supported and unsupported metals, In *Surface Organometallic Chemistry: Molecular Approaches to Catalysis* edited by J. -M. Basset, B. C. Gates, J.-P. Candy, A. Choplin, M. Lecomte, F. Quignard, and C. Santini (Kluwer, Dordrecht 1998) pp. 127–141.
15. J. P. Candy, B. Didillon, E. L. Smith, T. M. Shay, and J. M. Basset, Surface organometallic chemistry on metals: A novel and effective route to custom-designed bimetallic catalysts, *J. Mol. Catal.* **86,** 179–204 (1994).
16. A. Goguet, M. Aouine, F. J. Cadete Santos Aires, A. De Malmann, D. Schweich, and J. P. Candy, Preparation of a Pt/SiO_2 catalyst, *J. Catal.* **209,** 135–144 (2002).
17. N. Yao, C. Pinckney, S. Lim, C. Pak, and G. L Haller, Synthesis and characterization of Pt/MCM-41 catalysts *Microporous Mater.* **44–45,** 377–384 (2001).
18. J. Livage, and C. Sanchez, Sol–gel chemistry *J. Non Crystalline Solids* **145**(1–3), 11 (1992).
19. C. J. Brinker, and G. W. Scherer, Sol–gel science: The physics and chemistry of sol–gel processing, In *Sol–Gel Science*, (Academic Press, San Diego 1990) pp. 907, 108.
20. J. P Jolivet, In *De la Solution à l'oxyde* edited by CNRS, (1994).
21. L. N. Lewis, and N. Lewis, Platinum catalyzed hydrosilylation—Colloid formation as the essential step, *J. Am. Chem. Soc.* **108,** 7228–7231 (1986).
22. H. Bonnemann, W. Brijoux, R. Brinkmann, E. Dinjus, T. Jouben, R. Fretzen, and B. Korall, Highly dispersed metal clusters and colloïds for the preparation of active liquid-phase hydrogenation catalysts, *J. Mol. Catal*. **74,** 323–333 (1992).
23. J. Belloni, Metal nanocolloids, *Colloid Interface Sci.* **1**(2), 184–196 (1996).
24. A. Rakai, D. Tessier, and F. Bozon-Verduraz, Palladium-alumina catalysts: A diffuse reflectance study, *New J. Chem.* **16,** 869–875 (1992).
25. L. I. Elding, and L. F. Olsson, Electronic absorption spectra of square-planar chloro-aqua and bromo-aqua complexes of palladium (II) and platinum (II), *J. Phys. Chem.* **82**(1), 69–74 (1978)
26. P. B. Critchlow, and S. D. Robinson, A review of platinum metal nitrato complexes, *Coord. Chem. Rev.* **25**(1), 69–102 (1978)
27. J. P. Jolivet, In *De la solution à l'oxyde* edited by CNRS, (1994) pp. 219—254.
28. T. Hiemstra, W. H. van Riemsdijk, and G. H. Bolt, Multisite proton adsorption modeling at the solid/solution interface of (hydr)oxides: A new approach: I. Model description and evaluation of intrinsic reaction constants, *J. Colloid Interface Sci.* **133**(1), 99–104 (1989).
29. J. P. Jolivet, In *De la solution à l'oxyde* edited by CNRS, (1994) pp. 52—64.
30. J. P. Jolivet, In *Metal Oxide Chemistry and Synthesis, from Solution to Solid State* edited by Wiley & Sons, (Wiley & Sons, New York 2000), p. 223.
31. R. Sprycha, Surface charge and adsorption of background electrolyte ions at anatase/electrolyte interface, *J. Colloid Interface Sci.* **102**(1), 173 (1984).

32. B. N. Ivanov-Emin, B. E. Zaitsev, L. P. Petrishcheva, T. M. Ivanova, and R. V. Lin'ko, Study of alkaline solutions of palladium (II) oxide hydrate, *Russ. J. Inorg. Chem.* **30,** 1786 (1985).
33. S. Desset, O. Spalla, and B. Cabane, Redispersion of alumina particles in water, *Langmuir* **16,** 10495–10508 (2000).
34. D. Fauchadour, *PhD Thesis* Orléans University (2000).
35. B. I. Nabivanets, L. V. Kalabina, State of palladium (II) and platinum (IV) in inorganic acid solutions, *Russ. J. Inorg. Chem.* **15,** 818 (1970).
36. C. F. Baes, R.E. Mesmer, In *The Hydrolysis of Cations*, edited by John Wiley & Sons (Wiley & Sons, New York 1976).
37. E. Matijevic, Production of monodispersed colloidal particles, *Ann. Rev. Mater. Sci.* **15,** 483–516 (1985).
38. E. Matijevic, Monodispersed colloids: Art and science, *Langmuir* **2**(1), 12–20 (1986).
39. E. Matijevic, Preparation and properties of monodispersed colloidal metal hydrous oxides, *Pure Appl. Chem.* **50**(9–10), 1193–1210 (1978).
40. E. Matijevic, Preparation and properties of uniform size colloids, *Chem. Mater.* **5**(4), 412–426 (1993).
41. J.P. Jolivet, In *Metal Oxide Chemistry and Synthesis, from Solution to Solid State*, edited by John Wiley & Sons, (Wiley & Sons, New York 2000) p. 286.
42. T. Cholley, *PhD Thesis* University Paris VI (1997).
43. V. Ponec, and G. C. Bond, Catalysis by metals and alloys, *Stud. Surf. Sci. Catal.* **95,** 488 (1995).
44. C. F. Baes, and R. E. Mesmer, In *The Hydrolysis of Cations*, edited by John Wiley & Sons, (John Wiley & Sons, New York 1976) p. 274.
45. Gmelin's Handbook of Inorganic Chemistry, Ag [B5], p. 130.
46. Gmelin's Handbook of Inorganic Chemistry, Ag [A3], p. 70.
47. C. F. Baes, R.E. Mesmer, In *The Hydrolysis of Cations*, edited by John Wiley & Sons, (John Wiley & Sons, New York 1976) p. 276.
48. J. Horiuti, and T. Nakamura, Stoichiometric number and the theory of steady reaction, *Z. Phys. Chem.* Neue Folge **11,** 358–365 (1957).
49. G. C. Bond, In *Catalysis by Metals Chapter 12–14,* (Academic Press, London 1962) pp. 281–352.
50. J. P. Boitiaux, J. Cosyns, and S. Vasudevan, Hydrogenation of highly unsaturated hydrocarbons over highly dispersed palladium catalyst: Part I. Behaviour of small metal particles, *Appl. Catal.* **6,** 41–51 (1983).
51. Z. Karpinski, Catalysis by supported, unsupported and electron-deficient palladium, *Adv. Catal.* **37,** 45–100 (1981).
52. V. Ponec, and G. C. Bond, Catalysis by metals and alloys, *Stud. Surf. Sci. Catal.* **95,** 500 (1995).
53. J. P. Boitiaux, J. Cosyns, M. Derrien, and G. Léger, Proper design of butadiene selective hydrogenation process for maximum 1-butene yield by using comprehensive kinetic model, *AIChE National Meeting* (*Houston, March 24, 1984*).
54. J. Goetz, D. Y. Murzin, M. Ulischenko, and R. Touroude, Kinetics of buta-1,3-diene hydrogenation over palladium catalysts, *Chem. Eng. Sci.* **51**(11), 2879–2884 (1996).
55. J. P. Boitiaux, J. Cosyns, and E. Robert, Hydrogenation of unsaturated hydrocarbons in liquid phase on palladium, platinum and rhodium catalysts, *Appl. Catal.* **35,** 193 (1987).
56. S. Verdier, B. Didillon, S. Morin, and D. Uzio, PdSn/Al_2O_3 catalysts from colloidal oxide synthesis: II. Surface characterization and catalytic properties for buta-1,3-diene selective hydrogenation, *J. Catal.* **218,** 288–295 (2003).
57. B. Didillon, P. Sarrazin, J. P. Boitiaux, P. Vance, and Ch. Cameron, Advanced catalyst design for high ethylene production and maximized cycle lengths, *AIChE Spring Meeting* (*Houston, TX, March 19—23, 1995*), Symposium Hydroprocessing IV.

14

Gold-Based Nanoparticle Catalysts for Fuel Cell Reactions

Chuan-Jian Zhong*, Jin Luo, Derrick Mott, Mathew M. Maye, Nancy Kariuki, Lingyan Wang, Peter Njoki, Mark Schadt, Stephanie I-Im. Lim, and Yan Lin

14.1. INTRODUCTION

Hydrogen fuel cells and direct methanol fuel cells are becoming increasingly attractive power sources because of the high conversion efficiencies and low pollution and the use for mobile and stationary applications such as on-board electric power sources for advanced propulsion systems, nonpolluting electric vehicles, and portable devices. In proton exchange membrane fuel cells (PEMFCs), hydrocarbon fuels must be converted to pure hydrogen by reforming, and the overall conversion requires a complex process technology. Direct methanol fuel cells (DMFCs) offer a simpler solution and require no reformer. Currently, the energy density (~2000 Wh/kg) and operating cell voltage (0.4 V) for methanol fuel cells are much lower than the theoretical energy density (~6000 Wh/kg) and the thermodynamic potential (~1.2 V) due to poor activity of the anode catalysts and "methanol cross-over" to the cathode electrode,[1,2] which lead to a loss of about one-third of the available energy at the cathode and another one-third at the anode. Pt-group metals are extensively studied for both anode and cathode catalysts, but a major problem is the poisoning of Pt by CO-like intermediate species.[3–5] On the cathode, the kinetic limitation of the oxygen reduction reaction (ORR) is a problem of interest in proton exchange membrane fuel

Department of Chemistry, State University of New York at Binghamton, Binghamton, NY 13902
* To whom correspondence should be addressed. E-mail: cjzhong@binghamton.edu

cells operating at low temperature (<100°C) and in DMFCs.[2,6] The rate of breaking O=O bond to form water strongly depends on the degree of its interaction with the adsorption sites of the catalyst, and competition with other species in the electrolyte (e.g., CH_3OH). There is also strong adsorption of OH forming Pt–OH, which causes inhibition of the O_2 reduction. The binary PtRu nanoparticle catalyst on carbon support is currently one of the most-studied catalysts[7,8] showing a bifunctional catalytic mechanism in which Pt provides the main site for the dehydrogenation of methanol and Ru provides the site for hydroxide (OH) and for oxidizing CO-like species to CO_2.

The exploration of gold nanoparticles in catalysis[9–22] has recently shown potential applications in fuel cell related catalytic reactions.[23,24] The effects of gold substrate and gold-core has also been studied in catalytic activities.[25–27] We have recently investigated gold and alloy nanoparticles as electrocatalysts fuel cell reactions such as CO and methanol oxidation reaction[28–37] and oxygen reduction reaction (ORR).[34–37] The surface properties are essential for the adsorption of oxygen and the catalytic reaction of gold at nanoscale sizes.[22,23,27,38,39] Bimetallic AuPt composition may produce a synergistic catalytic effect that involves the suppression of adsorbed poisonous species and the change in electronic band structure to modify the strength of the surface adsorption for ORR. While AuPt was a known electrocatalyst for oxygen reduction in alkaline fuel cells, the study of AuPt nanoparticles with controllable size and composition for fuel cell catalyst applications[24] is important because the metal nanoparticles (1 to 10 nm) undergo a transition from atomic to metallic properties, and the bimetallic composition could produce synergistic effect. For example, for the adsorption of OH-ads in alkaline medium the presence of Au in Pt catalysts could reduce the strength of the Pt–OH formation.[22,27] The understanding of how the synergistic catalytic effect operates at the nanoscale gold and gold–platinum surface remain elusive. Recently, the unique properties of gold at nanoscale sizes were found to show unprecedented catalytic activities for CO oxidation[9–11,13,23,24,40–45] and the electrocatalytic activity for CO and methanol oxidation.[19,36,37,46–48] For methanol oxidation reaction (MOR) at the anode in methanol oxidation fuel cells, the study of nanoscale gold-based bimetallic materials could potentially provide a synergistic catalytic effect. For example, the synergistic catalytic effect of gold–platinum (AuPt) nanoparticles could involve the suppression of adsorbed poisonous species and the change in an electronic band structure to modify the strength of the surface adsorption. While bimetallic AuPt is a known electrocatalyst for oxygen reduction in alkaline fuel cells,[24] there have been few reports on the utilization of AuPt nanoparticles with controllable size and composition in fuel cell catalyst applications. With such a bimetallic system, Pt could function as main hydrogenation or dehydrogenation sites, whereas the use of Au together with Pt could speed up the removal of the poisonous species. The decrease of activation energy for facilitating oxidative desorption and suppressing the adsorption of CO was previously considered to lead to sufficiently-high adsorptivity to support catalytic oxidation in alkaline electrolytes.[49–52] A recent study[53] showed that catalysts prepared by impregnation from Pt and Au precursors are similar to those of monometallic Pt catalysts, suggesting that the presence of Au did not affect the catalytic performance of Pt in any significant way. This was attributed to a phase-segregation of the two metals due to their miscibility gap.[54] As a result, only Pt participates in the adsorption of CO and the catalytic

reaction. How the bimetallic catalytic properties depend on nanoparticle preparation and composition is an important question that must be answered for the development of bimetallic catalysts with new or improved properties. To our knowledge, little has been reported about the phase properties of the AuPt bimetallic nanoparticles with different compositions.

In view of the fact that the catalytic property is highly dependent on the atomic arrangement of the binary components on the surface, the ability to probe the surface binding sites is essential for understanding the unique catalytic properties of gold-based alloy nanoparticles and catalysts. Intensive research has been carried out to study the catalytic activity of gold and oxide-supported gold in a restricted nanoscale size range. The origin of the catalytic activity of nanosized gold and the synergistic catalytic effect of gold-based bimetallic catalysts remain elusive. Because CO adsorption is highly sensitive to the surface sites and the sensitivity leads to diagnostic CO stretching bands at different frequencies,[53] there have been a number of reports on FTIR characterizations of CO adsorption on oxide supported gold and platinum catalysts.[53,55–61] For example, using gold catalysts supported on silica prepared by a cation-exchange method using gold chloride salt precursors, CO stretching bands were observed between 2050 and 2175 cm^{-1}.[57,58] FTIR studies of platinum catalysts supported on silica[59] prepared by insipient wetness impregnation[55,59–61] have shown bands in this region but with different relative intensities. Recently, an FTIR study of CO adsorption on Pt–Au bimetallic catalysts prepared using dendrimer-stabilized nanoparticles was reported.[55] The bimetallic composition was within the bulk miscibility gap of this binary system, and the major CO stretching band was observed at 2063 cm^{-1} for Au–Pt catalysts supported on silica. While there have been several FTIR studies of CO adsorption on oxide-supported gold and bimetallic catalysts,[55] relatively little is known about the correlation between the catalyst preparation or treatment conditions and the surface adsorption properties.

We have recently investigated the morphological, structural, and phase properties of carbon-supported gold and gold–platinum catalysts with different bimetallic compositions. The bimetallic catalysts are prepared by two-phase synthesis with organic monolayer encapsulation on the nanocrystal core, and followed by an assembly on carbon support materials and thermal calcination. The alloy property for some of the bimetallic AuPt nanoparticles prepared was in sharp contrast to the miscibility gap known for the bulk counterparts of the bimetallic metals. Moreover, the finding of CO adsorption on the bimetallic catalysts with CO stretching bands different from those for the monometallic Au and Pt nanoparticle catalysts is also significant because it has further substantiated the alloy character of the surface of the bimetallic nanoparticle catalysts.

For the study of the electrocatalytic reduction of oxygen and oxidation of methanol, our approach to the preparation of catalysts by two-phase protocol[62–65] provides a better controllability over size, composition or surface properties[62,66] in comparison with traditional approaches such as coprecipitation, deposition–precipitation, and impregnation.[3,4,17] The electrocatalytic activities were studied in both acidic and alkaline electrolytes. This chapter summarizes some of these recent results, which have provided us with further information for assessing gold-based alloy catalysts for fuel cell reactions.

14.2. EXPERIMENTAL

Gold (Au) and gold–platinum (AuPt) nanoparticles of 2-nm core size encapsulated with an alkanethiolate monolayer shell were synthesized by a modified two-phase method.[33,35,62,65] Briefly $AuCl_4^-$ and $PtCl_6^{2-}$ were first transferred from aqueous solution of $HAuCl_4$ and H_2PtCl_6 into toluene solution using a phase transfer reagent (tetraoctylammonium bromide). Thiols (e.g., decanethiol, DT) or amines (e.g., oleylamine, OAM) were added to the organic solution as capping agents. An excess of aqueous $NaBH_4$ was slowly added for the reduction reaction. The resulting DT/OAM-encapsulated AuPt nanoparticles in toluene were collected by removing the solvent, and cleaned using ethanol. The nanoparticle product was dissolved in hexane. The bimetallic composition of the AuPt nanoparticles was determined by direct current plasma—atomic emission spectroscopy (DCP-AES).

Au and AuPt nanoparticles were assembled on carbon black (XR-72C) or silica powders with a controlled weight ratio of the metals (Au or AuPt) vs. the support materials. The actual loading was determined by thermogravimetric analysis (TGA) and DCP-AES analysis.

The carbon or silica-loaded nanoparticles were treated in a tube-furnace under controlled temperature and atmosphere. A typical protocol involved shell removal by heating at 300°C under 20% O_2/N_2 for 1 h and calcination at 400°C under 15% H_2/N_2 for 2 h. The carbon-loaded Au or AuPt nanoparticles are denoted as Au/C or AuPt/C. The silica-loaded AuPt nanoparticles are denoted as $AuPt/SiO_2$.

The calcined Au/C and AuPt/C powders were mixed with Nafion solution (0.25 wt.%), and were quantitatively transferred to the surface of the polished glassy carbon (GC) disk electrode.

14.3. CHARACTERIZATIONS OF NANOSTRUCTURED CATALYSTS

The nanostructured bimetallic catalysts were characterized using several techniques, and some of the main results are summarized in this section. We first describe the size and composition of the AuPt nanoparticles determined from TEM and DCP-AES analysis. This description is followed by discussion of the phase properties based on XRD results. We further discuss the FTIR provbing of CO adsorption on the bimetallic nanoparticle catalysts.

14.3.1. Size and Composition

Bimetallic Au_mPt_{100-m} nanoparticles with different atomic compositions ranging from $m = 10$ to 90% Au have been obtained in our laboratory. On the basis of the correlation between the synthetic bimetallic feeding and the nanoparticle bimetallic composition as determined by DCP-AES, the composition of the nanoparticles is controllable. In this subsection, the results for the size and composition of selected catalysts are described.

Figure 14.1 shows a representative TEM micrograph and size distribution for decanethiolate-capped $Au_{72}Pt_{28}$ nanoparticles. The nanoparticles display a relatively high monodispersity (±0.4 nm), with an average size of 1.8 nm. As evidenced by

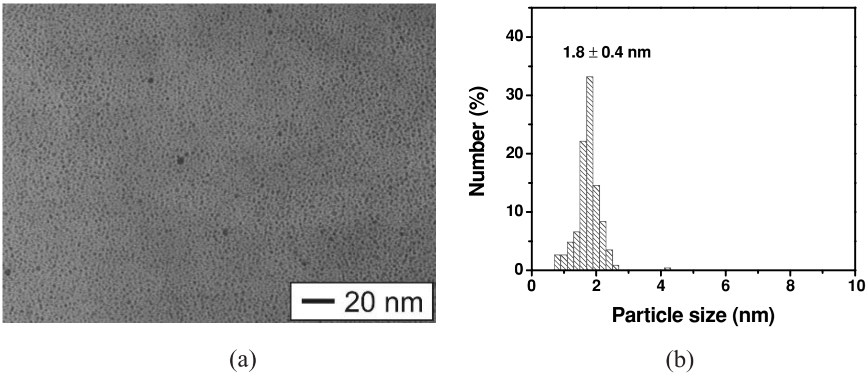

FIGURE 14.1. TEM micrograph (a) and particle size distribution (b) for $Au_{72}Pt_{28}$ nanoparticles.

the uniform interparticle spacing, the particles seem to be well separated from each other, which is consistent with the presence of the capping organic monolayer. The presence of such a capping layer is supported by FTIR data showing vibrational bands characteristic of the stretching bands of methyl and methylene groups of the capping molecules.

The $Au_{72}Pt_{28}$ nanoparticles assembled onto carbon black support materials were found to show very good dispersion. Typically, the loading amount of metallic nanoparticles was determined by TGA. A metal loading range from 1 to 40 (wt.%) can be easily controlled by adjusting the relative feed ratio of the nanoparticles and the carbon support material.[33,35] Importantly, the average size of the particles shows little change upon loading, suggesting that the capping shells remain intact while interacting with the carbon support.

While the dispersion of the $Au_{72}Pt_{28}$ nanoparticles supported on carbon remains relatively high after the calcination treatment, the average size of the particles was found to increase slightly with the calcination temperature. For example, the average size of $Au_{72}Pt_{28}$ nanoparticles increased to 4.6 ±1.0 nm after treatment at 400°C (Fig. 14.2).

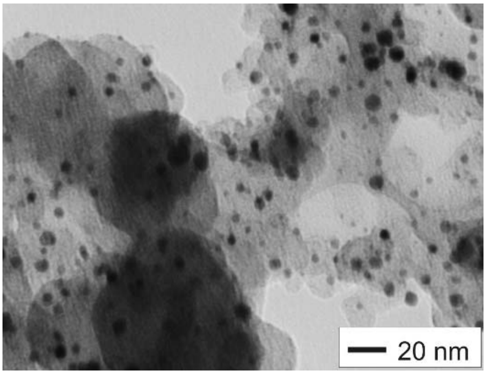

FIGURE 14.2. TEM micrographs for $Au_{72}Pt_{28}$/C catalysts after calcination at 400°C.

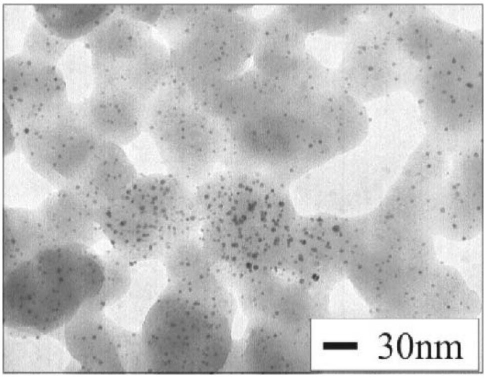

FIGURE 14.3. TEM micrograph of bimetallic catalysts $Au_{72}Pt_{28}/SiO_2$ after calcination treatment at 400°C.

Figure 14.3 shows a representative TEM micrograph for $Au_{72}Pt_{28}/SiO_2$ after the calcination at 400°C. It is evident that the nanoparticles are well dispersed on the silica support materials after the calcination treatment of the silica-supported nanoparticles. Similar dispersion and loading have also been observed for other nanoparticle catalysts. The average particle diameters determined from the TEM data were 2.6 ± 0.7 nm for $Au_{72}Pt_{28}/SiO_2$ catalysts. In this case, the high dispersion and monodispersity remain largely unchanged. The average sizes of the nanoparticles showed a small increase (~0.8 nm) in comparison with the observation for the nanoparticles on carbon support materials. This difference is attributed to the stronger adhesion of the particle to silica than that for the particle to carbon.[67]

In addition, our FTIR and XPS analyses of the nanoparticle samples showed that the removal of the capping shells from the surface of the bimetallic nanocrystalline core was very effective by the calcination treatment. The vibrational bands characteristic of the capping molecules in the C–H stretching region ($\nu_a(CH_3)$: 2955 cm^{-1}; $\nu_s(CH_3)$: 2872 cm^{-1}; $\nu_a(CH_2)$: 2917 cm^{-1}; $\nu_s(CH_2)$: 2848 cm^{-1}) were not detected by FTIR for samples after calcination. XPS analysis of the calcined samples also showed no bands that can be associated with the presence of sulfur species (S(2p1/2) ~163.8 eV, and S(2p3/2) ~162.5 eV) on the nanoparticles surface.

14.3.2. XRD Characterization

To determine the phase properties of the calcined bimetallic nanoparticles, a detailed x-ray diffraction (XRD) study was carried out. The XRD data of AuPt/C showed that the diffraction patterns for the carbon-supported nanoparticles show a series of broad Bragg peaks, a picture typical for materials of limited structural coherence. Nevertheless, the peaks are defined well enough to allow a definitive phase identification and structural characterization. The diffraction patterns of Au/C and Pt/C could be unambiguously indexed into an fcc-type cubic lattice occurring with bulk gold and platinum. We estimated the corresponding lattice parameters by carefully determining

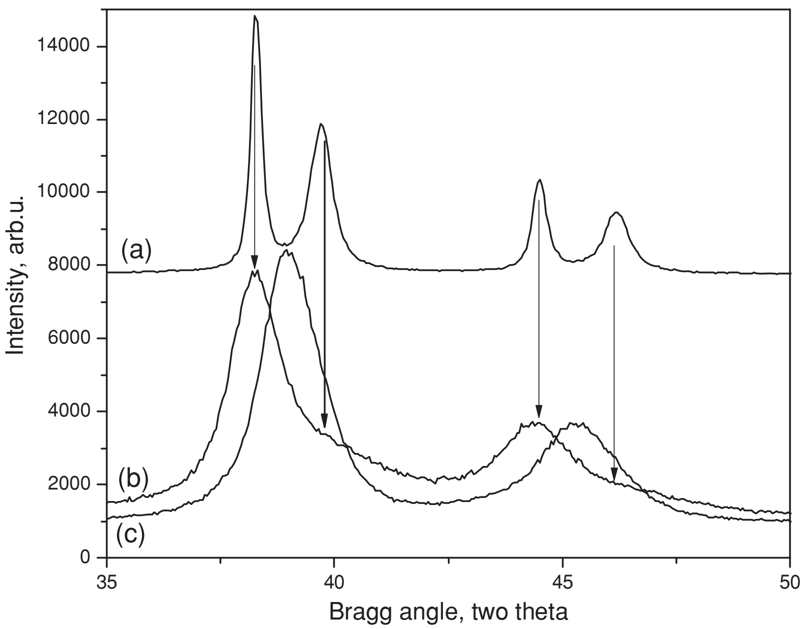

FIGURE 14.4. XRD patterns for $Au_{68}Pt_{32}/C$ (a) and $Au_{60}Pt_{40}/C$ (c) treated at 500°C. The pattern (b) for a mixture of Au/C and Pt/C is included for comparison. The diffraction peaks originating from the presence of two different nanophases, Au (the lower-angle peak) and Pt (the higher-angle peak), are marked with arrows (from Ref. 68).

the positions of all Bragg peaks seen in the diffraction patterns. For gold on carbon we obtained a lattice parameter a = 4.077(2) Å, which is practically identical to the literature value of 4.078 Å. Clearly, the Au nanoparticles have the lattice parameter of bulk gold. For platinum on carbon we obtained a lattice parameter a = 3.927(2) Å. It is shorter than the lattice parameter of bulk platinum: a = 3.97 Å. It may be due to the fact that Pt/C nanoparticles are rather small (~1–2 nm). For comparison, the average size of Au/C nanoparticles is ~3–4 nm as shown by our TEM analyses. The diffraction patterns of Au_mPt_{100-m}/C nanoparticles also show Bragg peaks that are characteristic of the fcc-type lattice.[68] Moreover, those patterns show a smooth transition from a Au/C-like pattern to a Pt/C-like pattern with the increase of Pt content. This observation indicates that Au_mPt_{100-m}/C nanoparticles bear the characteristics of an alloy-type compound involving Au and Pt.

To verify the above assumption we carefully examined the shape of the Bragg peaks in the diffraction patterns of the Au_mPt_{100-m}/C catalysts. Representative results are shown in Fig. 14.4. One of the diffraction patterns shown (Fig. 14.4a) is from $Au_{68}Pt_{32}/C$ sample which was influenced by the "burning effect" discussed earlier. These nanoparticles are rather large (20 to 30 nm) and exhibit well-defined Bragg peaks clearly originating from two different phases: Nanocrystalline Au (the lower-angle peak) and nanocrystalline Pt (the higher-angle peak). The peaks in the diffraction pattern of a physical mixture of Au/C and Pt/C nanoparticles not affected by the

"burning effect" (Fig. 14.4b) are rather broad reflecting the small particle size but highly asymmetric again revealing the presence of two distinct phases. The peaks in the diffraction patterns for the $Au_{60}Pt_{40}/C$ catalyst not affected by the "burning effect" (Fig. 14.4c) are also rather broad but fairly symmetric. These peaks fall well in between the peaks of Au/C and Pt/C nanophases. The peaks can be perfectly fitted with a single analytical function suggesting that $Au_{60}Pt_{40}/C$ catalyst is indeed a single-phase nanomaterials, i.e. an alloy. Most of Au_mPt_{100-m}/C catalysts prepared under the experimental conditions described above turned out not to be affected by "burning" of the support, and showed diffraction patterns of the type presented in Fig. 14.4c. This observation allowed us to determine the lattice parameters of the corresponding alloys with good accuracy.

The lattice parameters were found to scale linearly with the relative Au/Pt content. In other words, they follow a Vegard's type law that is frequently observed with binary metallic alloys. This is an important finding because it shows that the correlation between the phase property and the bimetallic composition for nanoscale materials is different from their bulk counterparts. Bulk Au–Pt metals show a miscibility gap[54] and the linear correlation between the lattice parameter and the composition breaks in a very wide composition range extending from ~10 to ~80% Au. Within the miscibility gap, the lattice parameters corresponding to bulk crystalline Au–Pt samples are independent of the composition.

Using Scherrer's equation relating the coherently scattering domains with Bragg peak widths, and the measured full width at half maximum of the peak in radians and the Bragg angle, we estimated the average size of the AumPt100-*m*/C nanoparticles studied. The equation was applied to the major (111) peak in the corresponding powder diffraction patterns. The average size of the AumPt100-*m*/C nanoparticles turned out to be ~4.0 (±0.5) nm, in close agreement with the findings of the TEM experiments. This observation indicated that the nanoparticles are more or less homogeneous at the atomic scale and not partitioned into smaller fragments that are substantially misoriented with respect to one another.

14.3.3. FTIR Characterization of CO Adsorption

Because the vibrational band of CO is very sensitive to the surface binding sites for CO adsorption, a detailed FTIR study of the CO adsorption was carried out. Figure 14.5 shows a representative set of FTIR spectra for CO adsorption on $Au_{72}Pt_{28}/SiO_2$ calcinated at 400°C. The spectra were collected immediately following the purging of the CO-filled cell with N_2 at the indicated time intervals. The catalyst calcination and sample preparation conditions were found to be important in the resulting spectral characteristics. For the sample calcined and prepared under normal conditions, two CO bands are detected at 2115 cm^-1 and 2066 cm^{-1} (Figure 5A). These two bands are attributed to CO adsorption on Au-atop sites in a Au-rich surface environment and on Pt-atop sties alloyed in the bimetallic nanocrystal, respectively. Both bands disappeared after 5-15 min purging with N_2. For the sample calcined under normal condition but sample preparation under humidified (60~70%RH) environment, subtle differences in the CO bands were observed (Figure 5B). At 1 min, the spectrum shows two strong peaks between 2200 and 2100 cm^{-1} for gas-phase CO left in the chamber. As evidenced

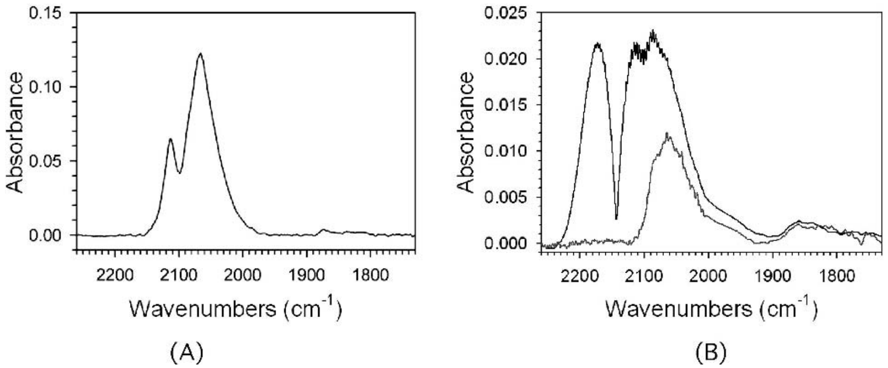

FIGURE 14.5. FTIR spectra for CO adsorption on $Au_{72}Pt_{28}/SiO_2$ catalyst calcined at 400°C under two different sample preparation conditions (A and B). N_2-purging times: 0 min (the spectrum was corrected by subtracting the gas-phase CO spectrum) (A), and 1 min (top) and 52 min (bottom (the gas-phase CO is absent)) (B).

by the subsequent spectra in which these peaks quickly disappear as the chamber is continuously purged with N_2, these peaks are from gas-phase CO molecules. After a few minutes of purging, the bands remaining are due to CO adsorbed on the catalyst surface, which are identified at 2070 and 1850 cm^{-1} with shoulder bands at 2080 and 1990 cm^{-1}. None of these bands was completely purged away with nitrogen, even at an extended period of time. An overlapped shoulder band appears at 2080 cm^{-1}, which is higher than the primary band (2070 cm^{-1}). The small difference is indicative of a subtle difference in binding strength of the catalytic sites to the CO molecules. The higher wavenumber is characteristic of weakening of the C≡O bond by the adsorption sites to a less extent. The small shoulder band at 1990 cm^{-1} is quite broad with a significant tailing feature. A weak and broad band was also observed at 1850 cm^{-1}.

The FTIR spectra for the adsorption of CO on $Au_{82}Pt_{18}/SiO_2$ catalyst calcined at 400°C show bands at 2060 and 1850 cm^{-1} with a shoulder band at 1990 cm^{-1} after the disappearance of the bands for gas-phase CO as a result of the initial purging with N_2. This finding is remarkable, demonstrating that the subtle increase of Au component in the bimetallic nanoparticles has significantly modified the surface binding properties at the nanocrystals. We note that the observation of a broad shoulder band at 1990 cm^{-1} was similar to those for the previous $Au_{72}Pt_{28}/SiO_2$ sample, but the broad band at 1850 cm^{-1} has a relatively smaller absorbance.

The differences in the CO bands on different catalysts suggest that the surface binding sites of the catalyst is dependent on the bimetallic composition and the calcination temperature. The CO bands at the higher wavenumbers are likely associated with CO species weakly bound to the catalyst whereas the bands at the lower wavenumbers are associated with CO species strongly bound to the catalytic sites. Based on these findings and the control experiment with mixed Au and Pt catalysts, we believe that the surface sites of our bimetallic $Au_{72}Pt_{28}/SiO_2$ and $Au_{82}Pt_{18}/SiO_2$ catalysts are characteristic of alloy properties, not phased-segregated metals. The calcination temperature was also found to strongly affect the surface binding properties and catalytic activity of the bimetallic catalysts.

14.4. ELECTROCATALYTIC ACTIVITY OF NANOSTRUCTURED CATALYSTS

The electrocatalytic activity of the nanostructured catalysts was investigated for electrocatalytic reduction of oxygen and oxidation of methanol. Several selected examples are discussed in this section. The results from electrochemical characterization of the oxygen reduction reaction (ORR) are first described. This description is followed by discussion of the results from electrochemical characterization of the methanol oxidation reaction (MOR).

14.4.1. Electrocatalytic Reduction of Oxygen

The nanostructured Au and AuPt catalysts were found to exhibit electrocatalytic activity for ORR reaction. The cyclic voltammetric (CV) curves at Au/C catalyst reveal an oxidation–reduction wave of gold oxide at ∼+200 mV in the alkaline (0.5 M KOH) electrolyte but little redox current in the acidic (0.5 M H_2SO_4) electrolyte. Under saturated with O_2, the appearance of the cathodic wave is observed at –190 mV in the alkaline electrolyte and at +50 mV in the acidic electrolyte. This finding indicates that the Au catalyst is active toward O_2 reduction in both electrolytes. From the Levich plots[69] of the limiting current vs. rotating speed data, one can derive the electron transfer number (n). We obtained $n = 3.1$ for ORR in 0.5 M KOH electrolyte, and 2.9 for ORR in 0.5 M H_2SO_4 electrolyte. The intermittent n-value between 2 and 4 indicates that the electrocatalytic ORR at the Au/Ccatalyst likely involved mixed $2e^-$ and $4e^-$ reduction processes.

Figure 14.6 shows a typical set of CV curves obtained at $Au_{81}Pt_{19}$/C catalyst (24wt.% metals) in acidic (0.5 M H_2SO_4) electrolytes. There are two important pieces

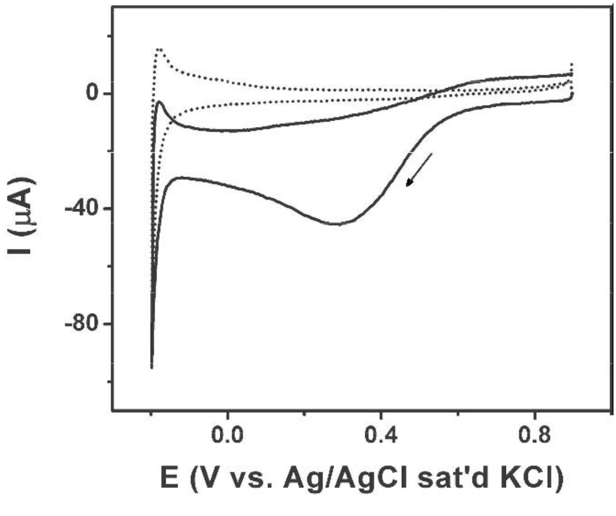

FIGURE 14.6. Cyclic voltammetric curves for a $Au_{81}Pt_{19}$/C catalyst (24 wt.%) on GC electrode (0.07 cm^2) in 0.5M H_2SO_4 electrolytes saturated with O_2 (solid curves) and Ar (dash curves). Scan rate: 50 mV/s (from Ref. 35).

TABLE 14.1. Electrocatalytic activities of several different catalysts for ORR (saturated O_2) in terms of peak potential (E_{pa}) and peak current (i_{pa}) (from Ref. 35).

Catalyst	Wt.% Mt	0.5 M KOH		0.5 M H_2SO_4	
		E_{pc} (mV)	i_{pc} (mA/cm^2/mg)	E_{pc} (mV)	i_{pc} (mA/cm^2/mg)
Au/C	17 Au	−145	1744	+23	903
AuPt/C	24 $Au_{72}Pt_{28}$	−135	1147	+280	677
AuPt/C	39 $Au_{68}Pt_{32}$	−172	530	+454	540

Scan rate: 50 mV/s; ref electrode: Ag/AgCl, Sat'd KCl; Mt: total metals.

of evidence supporting the presence of both Au and Pt on the surface of the nanoparticle catalyst. First, similar to the CV curve for the Au/C catalyst in the absence of oxygen, the observation of the oxidation–reduction wave of gold oxide at ~200 mV at the $Au_{81}Pt_{19}$/C catalyst in the O_2-free alkaline electrolyte is a clear indication of the presence of Au on the catalyst. Second, the observation of the hydrogen reduction–oxidation currents at –200 mV in the O_2-free acidic electrolyte, which is characteristic of hydrogen adsorption and reduction at Pt electrodes, is strong evidence for the presence of Pt on the catalyst surface.

In comparison with the data for Au/C catalysts, there are two important observations for the electrocatalytic activity of the AuPt nanoparticle catalysts. First, the ORR wave at the $Au_{81}Pt_{19}$/C catalyst is observed at about the same potential (+190 mV) as that for the Au/C in the alkaline electrolyte. We also note that a very small wave is detectable at –450 mV for the AuPt/C catalyst. Second, the ORR waves are highly dependent on the nature of the electrolyte. This wave for $Au_{81}Pt_{19}$/C is observed at +350 mV in the acidic electrolyte, which is much more positive than that for the Au/C in the same electrolyte. In this case, the ORR currents detected at below +50 mV are characteristic of hydrogen adsorption–reduction at Pt electrodes. The result thus suggests that there is a significant fraction of Au on the bimetallic catalyst which keeps the nanoscale gold property unchanged in basic condition, but modifies the catalytic property of Pt in the acidic electrolyte.

The dependence of the electrocatalytic activity on the relative bimetallic composition of the catalyst was further examined. Table 14.1 summarizes some electrocatalytic data to quantitatively compare ORR activities for different catalysts. Two important changes are observed from the CV curves obtained at $Au_{68}Pt_{32}$/C catalyst. First, while the ORR peak potential at –190 mV remains largely unchanged, a significant wave component of the ORR is evident at –400 mV in the alkaline electrolyte, which showed an increase for the $Au_{68}Pt_{32}$/C in comparison with that for the previous $Au_{81}Pt_{19}$/C. Second, the ORR wave for the $Au_{68}Pt_{32}$/C showed a shift of the peak potential to a much more positive potential (~+500 mV) than that for the $Au_{81}Pt_{19}$/C in the acidic electrolyte. Both findings suggest that the electrocatalytic activity of Au and Pt metal components in the nanoparticle catalysts is dependent on the nature of the electrolyte. It appears that the catalysis at the individual Au or Pt surface site is operative in the alkaline electrolyte, whereas the catalysis of the bimetallic surface sites is operative in the acidic electrolyte.

To further evaluate the electrocatalytic properties, rotating disk electrode (RDE) experiments were performed to characterize the number of electrons transferred in the

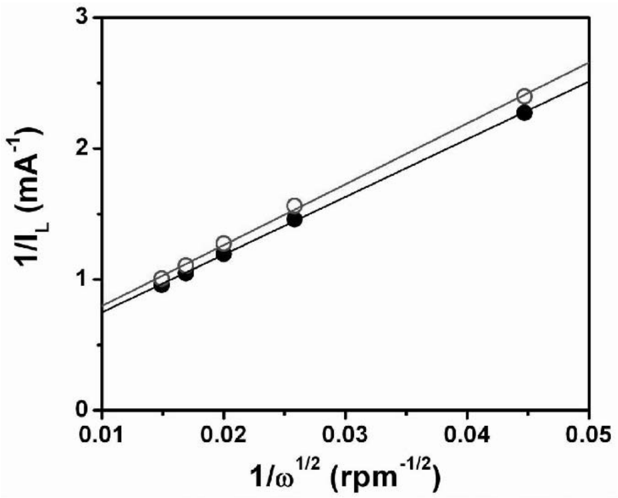

FIGURE 14.7. Levich plots of the limiting current from RDE curves for a $Au_{81}Pt_{19}$/C catalyst (24 wt.%) on GC electrode (0.2 cm^2) in alkaline (closed circles: 0.5 M KOH) and acidic (open circles: 0.5 M H_2SO_4) electrolytes saturated with O_2 (from Ref. 35).

electrocatalytic ORR process. From the Levich plots (Fig. 14.7), one derives the value for the electron transfer number (n). We found that n = 3.6 in 0.5 M KOH and 3.4 in 0.5 M H_2SO_4 ($\sim \pm 0.4$ error bar) for ORR at the $Au_{81}Pt_{19}$/C catalyst. There is a noticeable increase in the n value for the bimetallic AuPt/C catalyst in comparison with that for the monometallic Au/C catalyst. The fact that the determined n values are very similar for both acidic and alkaline electrolytes and are close to $4e^-$ reduction process is interesting in view of the relatively large difference in reduction potential.

In comparison with the Pt/C data, the n values obtained with our Au/C and AuPt/C catalysts are in between 3.0 and 3.6, displaying an increase in n with increasing Pt composition in the bimetallic nanoparticles. The fact that the obtained n values fall in between n = 2 and 4 likely suggests that both $2e^-$ reduction to H_2O_2 and $4e^-$ reduction to H_2O processes are operative with the catalysts. Two possible origins include the presence of large-sized particles in the calcined catalysts and the presence of possible surface segregation of the two metals on the bimetallic surface. A further delineation of the surface composition, particle size, and calcination condition is in progress, which should provide more insights into the detailed catalytic mechanism.

14.4.2. Electrocatalytic Oxidation of Methanol

The electrocatalytic activity of the nanostructured Au and AuPt catalysts for MOR reaction is also investigated. The CV curve of Au/C catalysts for methanol oxidation (0.5 M) in alkaline electrolyte (0.5 M KOH) showed an increase in the anodic current at $\sim$0.30 V which indicating the oxidation of methanol by the Au catalyst. In terms of peak potentials, the catalytic activity is comparable with those observed for Au nanoparticles directly assembled on GC electrode after electrochemical activation.[28–30,32] We note however that measurement of the carbon-supported gold nanoparticle catalyst did not reveal any significant electrocatalytic activity for MOR in acidic electrolyte. The

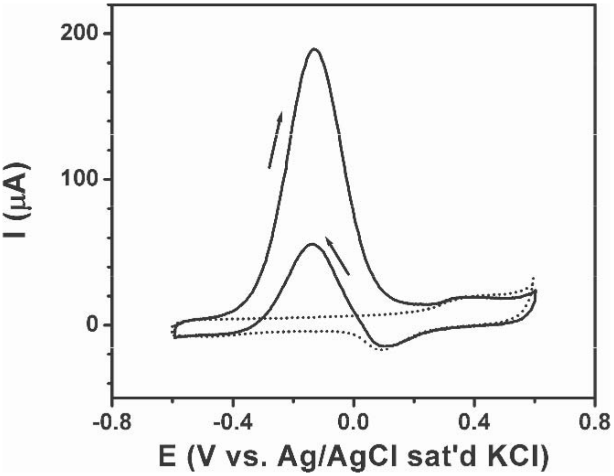

FIGURE 14.8. Cyclic voltammetric curves for a 24% $Au_{81}Pt_{19}/C$ catalyst (on GC electrode, 0.07 cm^2) in 0.5 M KOH electrolyte with (solid curves) and without (dash curves) 0.5 M methanol. Scan rate: 50 mV/s (from Ref. 33).

results thus indicate that Au nanoparticle catalysts are active only in the presence of hydroxides.

Figure 14.8 shows a typical set of CV curves obtained for methanol oxidation at $Au_{81}Pt_{19}/C$ catalysts in alkaline electrolyte. Electrocatalytic activity of $Au_{68}Pt_{32}/C$ catalyst was also characterized and is shown in Table 14.2.

In comparison with the data from the control experiment (dashed lines), there is a large anodic wave at –0.13 V, corresponding to the oxidation of methanol. This peak potential is clearly shifted negatively by about 500 mV in comparison with that observed for a Au/C catalyst. The magnitude of the anodic current increases with an increase in the relative Pt composition of the AuPt nanoparticles. Furthermore, a smaller anodic wave is observed at the same potential on the reverse sweep for the $Au_{81}Pt_{19}/C$ catalyst, arising from the oxidation of methanol on re-activated catalyst surface.[70] For the $Au_{68}Pt_{32}/C$ catalyst, the anodic wave on the reverse sweep is apparently split into two much smaller waves at –0.13 V and –0.35 V, respectively. We also note that peak splitting for the anodic wave was observed for AuPt nanoparticles directly assembled on the GC electrode surface, which is attributed to the phase segregation of the two metals.[34,71] For example, with 1,9-nonanedithiol(NDT)-linked AuPt nanoparticles

TABLE 14.2. Electrocatalytic activities of several different catalysts catalysts for MOR in terms of peak potential (E_{pa}) and peak current (i_{pa}) (from Ref. 33).

Catalyst	Wt.% Mt	0.5 M KOH E_{pc} (mV)	0.5 M KOH i_{pc} ($mA/cm^2/mg$)	0.5 M H_2SO_4 E_{pc} (mV)	0.5 M H_2SO_4 i_{pc} ($mA/cm^2/mg$)
Au/C	17 Au	+357	349	–	–
AuPt/C	24 $Au_{72}Pt_{28}$	–131	2820	~ +609	~ 113
AuPt/C	39 $Au_{68}Pt_{32}$	–136	5643	+693	304

Scan rate: 50 mV/s; ref electrode: Ag/AgCl, Sat'd KCl; Mt: total metals.

assembled on a planar glassy carbon electrode after thermal activation, two anodic waves were observed for methanol oxidation. These two waves, A (0.28 V) and B (–0.08 V), correspond to the reaction sites of Au and Pt, respectively. The current density for wave-B was found to increase with the relative amount of Pt component. In this case, the two metal components in the nanoparticles are likely phase-segregated, which are in contrast to the bimetallic composition for the AuPt nanoparticles supported on carbon black materials. The observation of the single anodic wave character in the forward sweep and the differences in the reverse sweep likely reflect a cooperative bimetallic effect of the AuPt nanoparticles on the catalytic reaction.

In acidic electrolyte, the catalytic activity is found to be highly dependent on the alloy composition. For example, while the $Au_{81}Pt_{19}$/C catalyst showed little activity, the $Au_{68}Pt_{32}$/C catalyst showed clear catalytic activity. A detailed correlation between the electrocatalytic activity and the bimetallic composition and the phase properties is part of our on-going work.

The electrocatalytic activities data indicate that there is a major enhancement in comparison with that of Au/C catalysts in terms of the peak potential (by ~-500 mV) and the peak current (by ~20×). The presence of a small fraction of Pt in the Au-based bimetallic nanoparticles significantly modified the catalytic properties. While a detailed characterization is needed, it is clear that the bimetallic AuPt composition played a significant role in the observed modification of the catalytic properties.

On the basis of the combined weight of the above results, we believe that bifunctional electrocatalytic properties may be operative for both MOR and ORR on the AuPt bimetallic nanoparticle catalysts depending on the nature of the electrolyte. For ORR in acidic electrolyte, the approaching of both the reduction potential and the electron transfer number for the bimetallic catalyst with less than 25%Pt to those for pure Pt catalyst is indicative of a synergistic effect of Au and Pt in the catalyst. For MOR in alkaline electrolyte, the similarity of both the oxidation potential and the current density for the bimetallic catalyst with less than 25%Pt to those for pure Pt catalyst is suggestive of the operation of bifunctional mechanism. Such a bifunctional mechanism may involve the following reactions:

$$Pt + CO \Rightarrow Pt\text{—}CO_{\mathrm{ad}} \qquad (1)$$

$$Au + H_2O \Rightarrow Au\text{—}OH_{\mathrm{ad}} + H^+ + e^- \qquad (2)$$

$$Pt\text{—}CO_{\mathrm{ad}} + Au\text{—}OH_{\mathrm{ad}} \Rightarrow CO_2 + Pt + Au + H^+ + e^{-} \qquad (3)$$

The formation of Au–OH_{ad} or surface oxides on gold in alkaline electrolyte was in fact proposed to explain some of the electrocatalytic properties observed for a gold electrode (e.g., incipient hydrous oxide/adatom mediator model[72]). Our previous measurement of the interfacial mass change also indicated the formation of Au oxides (Au_2O_3, AuOHorAu$(OH)_3$) on gold nanoparticle surfaces.[73] A detailed delineation of the catalytic mechanism is part of our on-going work.

14.5. CONCLUSION

In conclusion, bimetallic AuPt nanoparticles prepared by two-phase synthesis, assembly on carbon, and thermal calcination were shown to display alloy properties,

which is in sharp contrast to the bimetallic miscibility gap known for the bulk counterpart of the bimetallic AuPt metals. This finding is one of the first examples demonstrating the difference of the physical and chemical properties for nanoscale materials from the bulk crystalline state. Further work along this line is in progress to achieve an in-depth understanding of the physics and chemistry of binary or ternary metal materials structured at the nanoscale. Such understanding will help us gain full control over the bimetallic AuPt nanoparticles with improved catalytic properties. The CO binding properties of the bimetallic nanocrystal surface is highly dependent on the bimetallic composition, the calcination temperature, and the preparation condition. The findings further substantiated the alloy character of the surface binding sites of our bimetallic nanoparticle catalysts. The bimetallic AuPt composition significantly modifies the electrocatalytic ORR properties of both Au and Pt. This finding has important implications to finding effective catalysts for improving fuel cell cathode reactions. The catalytic activity is dependent on the composition and calcination temperature. The combined results from the study of MOR electrocatalysts revealed the dependence of the morphology and the surface binding properties of the bimetallic nanoparticles on the calcination temperature.

Our on-going work aimed at a detailed delineation of the activity correlation with composition, size, and calcination conditions via spectroscopic and microscopic characterizations. A further comparison of our catalysts and commercial catalysts in a commercial fuel cell will provide the basis for us to evaluate the practical viability in both qualitative and quantitative ways. In view of the fact that there is a miscibility gap over a wide composition range for bulk bimetallic AuPt metals,[54] the understanding of how phase segregation is operative in the nanoscale AuPt under different temperatures and the ability to control it is another area of our research to manipulate the electrocatalytic ORR activities. A further correlation between the catalytic activity and the bimetallic surface composition for bimetallic catalysts prepared or characterized under different conditions, including a wide range of different compositions, adsorption at higher temperatures, and calcination at different reducing/oxidizing atmospheres will provide information for the better design and processing of the gold-based bimetallic nanoparticle catalysts.

ACKNOWLEDGMENTS

This work was supported in part by the National Science Foundation (CHE 0316322), the Petroleum Research Fund administered by the American Chemical Society (40253-AC5M), the G.R.O.W. of World Gold Council (RP03-03), and the 3M Corporation.

REFERENCES

1. X. M. Ren, P. Zelenay, S. Thomas, J. Davey, and S. Gottesfeld, Recent advances in direct methanol fuel cells at Los Alamos National Laboratory, *J. Power Sources* **86,** 111–116 (2000).
2. D. Chu, and R. Jiang, Novel electrocatalysts for direct methanol fuel cells, *Solid State Ion.* **148,** 591–599 (2002).
3. U. A. Paulus, U. Endruschat, G. J. Feldmeyer, T. J. Schmidt, H. Bonnemann, and R. J. Behm, New PtRu alloy colloids as precursors for fuel cell catalysts, *J. Catal.* **195,** 383–393 (2000).

4. E. Antolini, Formation of carbon-supported PtM alloys for low temperature fuel cells: A review, *Mater. Chem. Phys.* **78,** 563–573 (2003).
5. G. Q. Lu, and A. Wieckowski, Heterogeneous electrocatalysis: A core field of interfacial science, *Curr. Opin. Coll. Interf. Sci.* **5,** 95–100 (2000).
6. L. Xiong, A. M. Kannan, and A. Manthiram, Pt–M (M = Fe, Co, Ni and Cu) electrocatalysts synthesized by an aqueous route for proton exchange membrane fuel cells, *Electrochem. Commun.* **4,** 898–903 (2002).
7. E. Reddington, A. Sapienza, B. Gurau, R. Viswanathan, S. Sarangapani, E. S. Smotkin, and T. E. Mallouk, Combinatorial electrochemistry: A highly parallel, optical screening method for discovery of better electrocatalysts, *Science* **280,** 1735–1737 (1998).
8. R. X. Liu, and E. S. Smotkin, Array membrane electrode assemblies for high throughput screening of direct methanol fuel cell anode catalysts, *J. Electroanal. Chem.* **535,** 49–55 (2002).
9. M. Haruta, Size- and support-dependency in the catalysis of gold, *Catal. Today* **36,** 153–166 (1997).
10. M. Haruta, and M. Date, Advances in the catalysis of Au nanoparticles, *Appl. Catal.* A **222,** 427–437 (2001).
11. G. C. Bond, and D. T. Thompson, Gold-catalysed oxidation of carbon monoxide, *Gold Bull.* **33,** 41–51 (2000).
12. G. C. Bond, Gold: A relatively new catalyst, *Gold Bull.* **34,** 117–140 (2001).
13. C. W. Corti, R. J. Holliday, and D. T. Thompson, Developing new industrial applications for gold: Gold nanotechnology, *Gold Bull.* **35,** 111–136 (2002).
14. A. Ueda, and M. Haruta, Nitric oxide reduction with hydrogen, carbon monoxide, and hydrocarbons over gold catalysts, *Gold Bull.* **32,** 3–11 (1999).
15. D. Andreeva, Low temperature water gas shift over gold catalysts, *Gold Bull.* **35,** 82–88 (2002).
16. R. Grisel, K. J. Weststrate, A. Gluhoi, and B. E. Nieuwenhuys, Catalysis by gold nanoparticles, *Gold Bull.* **35,** 39–45 (2002).
17. D. T. Thompson, New advances in gold catalysis, *Gold Bull.* **31,** 111–118 (1998) & **32,** 12–19 (1999).
18. L. D. Burke, and P. F. Nugent, The electrochemistry of gold: II. The electrocatalytic behaviour of the metal in aqueous media, *Gold Bull.* **31,** 39–50 (1998).
19. C. J. Zhong, and M. M. Maye, Core-shell assembled nanoparticles as catalysts, *Adv. Mater.* **13,** 1507–1511 (2001).
20. M. S. El-Deab, T. Okajima, and T. Ohsaka, Electrochemical reduction of oxygen on gold nanoparticle-electrodeposited glassy carbon electrodes, *J. Electrochem. Soc.* **150,** A851–A857 (2003).
21. M. S. El-Deab, and T. Ohsaka, Electrocatalysis by nanoparticles: Oxygen reduction on gold nanoparticles-electrodeposited platinum electrodes, *J. Electroanal. Chem.* **553,** 107–115 (2003).
22. M. S. El-Deab, and T. Ohsaka, Hydrodynamic voltammetric studies of the oxygen reduction at gold nanoparticles-electrodeposited gold electrodes, *Electrochim. Acta* **47,** 4255–4261 (2002).
23. *Gold 2003: New Industrial Applications for Gold*, Proceeding Volume, (World Gold Council, 2003).
24. D. Cameron, R. Holliday, and D. Thompson, Gold's future role in fuel cell systems, *J. Power Sources* **118,** 298–303 (2003).
25. Y. D. Jin, Y. Shen, and S. J. Dong, Electrochemical design of ultrathin platinum-coated gold nanoparticle monolayer films as a novel nanostructured electrocatalyst for oxygen reduction, *J. Phys. Chem.* B **108,** 8142–8147 (2004).
26. M. Van Brussel, G. Kokkinidis, A. Hubin, and C. Buess-Herman, Oxygen reduction at platinum modified gold electrodes, *Electrochim. Acta* **48,** 3909–3919 (2003).
27. M. Van Brussel, G. Kokkinidis, I. Vandendael, and C. Buess-Herman, High performance gold-supported platinum electrocatalyst for oxygen reduction, *Electrochem. Commun.* **4,** 808–813 (2002).
28. Y. Lou, M. M. Maye, L. Han, J. Luo, and C. J. Zhong, Gold–platinum alloy nanoparticle assembly as catalyst for methanol electrooxidation, *Chem. Commun.* 473–474 (2001).

29. J. Luo, M. M. Maye, Y. Lou, L. Han, M. Hepel, and C. J. Zhong, Catalytic activation of core-shell assembled gold nanoparticles as catalyst for methanol electrooxidation, *Catal. Today* **77,** 127–138 (2002).
30. J. Luo, Y. B. Lou, M. M. Maye, C. J. Zhong, and M. Hepel, An EQCN assessment of electrocatalytic oxidation of methanol at nanostructured Au–Pt Alloy nanoparticles, *Electrochem. Commun*. **3,** 172–176 (2001).
31. J. Luo, V. W. Jones, M. M. Maye, L. Han, N. N. Kariuki, and C. J. Zhong, Thermal activation of molecularly-wired gold nanoparticles on a substrate as catalyst, *J. Am. Chem. Soc*. **124,** 13988–13989 (2002).
32. M. M. Maye, J. Luo, Y. Lin, M. H. Engelhard, M. Hepel, and C. J. Zhong, X-Ray photoelectron spectroscopic study of the activation of molecularly-linked gold nanoparticle catalysts, *Langmuir* **19,** 125–131 (2003).
33. J. Luo, M. M. Maye, N. N. Kariuki, L. Wang, P. Njoki, Y. Lin, M. Schadt, H. R. Naslund, and C. J. Zhong, Electrocatalytic oxidation of methanol: Carbon-supported gold–platinum nanoparticle catalysts prepared by two-phase protocol, *Catal. Today* **99,** 291–297 (2005).
34. M. M. Maye, J. Luo, L. Han, N. Kariuki, and C. J. Zhong, Synthesis, processing, assembly and activation of core-shell structured gold nanoparticle catalysts, *Gold Bull*. **36,** 75–82 (2003).
35. M. M. Maye, N. N. Kariuki, J. Luo, L. Han, P. Njoki, L. Wang, Y. Lin, H. R. Naslund, and C. J. Zhong, Electrocatalytic reduction of oxygen: Gold and Gold-platinum nanoparticle catalysts prepared by two-phase protocol, *Gold Bull*. **37,** 217–223 (2004).
36. C. J. Zhong, M. M. Maye, J. Luo, L. Han, and N. N. Kariuki, In *Nanoparticles: Building Blocks for Nanotechnology*, edited by V. M. Rotello (Kluwer Academic Publishers, 2004) Chapter 5, pp. 113–144.
37. C. J. Zhong, J. Luo, M. M. Maye, L. Han, and N. N. Kariuki, In *Nanotechnology in Catalysis*, edited by B. Zhou, S. Hermans, and G. A. Somorjai, vol. 1, (Kluwer Academic/Plenum Publishers, New York 2004) Chapter 11, pp. 222–248.
38. Y. D. Kim, M. Fischer, and G. Gantefor, Origin of unusual catalytic activities of Au-based catalysts, *Chem. Phys. Lett*. **377,** 170–176 (2003).
39. Y. Xu, and M. Mavrikakis, Adsorption and dissociation of O_2 on gold surfaces: Effect of steps and strain, *J. Phys. Chem.* B **107,** 9298–9307 (2003).
40. M. Valden, X. Lai, and D. W. Goodman, Onset of catalytic activity of gold clusters on titania with the appearance of nonmetallic properties *Science* **281,** 1647–1650 (1998).
41. D. R. Rolison, Catalytic nanoarchitectures—The importance of nothing and the unimportance of periodicity *Science* **299,** 1698–1701 (2003).
42. T. F. Jaramillo, S. H. Baeck, B. R. Cuenya, and E. W. McFarland, Catalytic activity of supported au nanoparticles deposited from block copolymer micelles, *J. Am. Chem. Soc*. **125,** 7148–7149 (2003).
43. B. B. Blizanac, M. Arenz, P. N. Ross, and N. M. Markovic, Surface electrochemistry of CO on reconstructed gold single crystal surfaces studied by infrared reflection absorption spectroscopy and rotating disk electrode, *J. Am. Chem. Soc*. **126,** 10130–10141 (2004).
44. S. Kandoi, A. A. Gokhale, L. C. Grabow, J. A. Dumesic, and M. Mavrikakis, Why Au and Cu are more selective than Pt for preferential oxidation of CO at low temperature? *Catal. Lett*. **93,** 93–100 (2004).
45. G. Avgouropoulos, T. Ioannides, C. Papadopoulou, J. Batista, S. Hocevar, and H. K. Matralis, A comparative study of Pt/gamma-Al2O3, Au/alpha-Fe2O3 and CuO-CeO2 catalysts for the selective oxidation of carbon monoxide in excess hydrogen, *Catal. Today* **75,** 157–167 (2002).
46. Z. Borkowska, A. Tymosiak-Zielinska, and R. Nowakowski, High catalytic activity of chemically activated gold electrodes towards electro-oxidation of methanol, *Electrochim. Acta* **49,** 2613–2621 (2004).
47. H. Tang, J. H. Chen, M. Y. Wang, L. H. Nie, Y. F. Kuang, and S. Z. Yao, Controlled synthesis of platinum catalysts on Au nanoparticles and their electrocatalytic property for methanol oxidation, *Appl. Catal. A—Gen.* **275,** 43–48 (2004).

48. M. Umeda, H. Ojima, M. Mohamedi, and I. Uchida, Methanol electrooxidation at Pt—Ru–W sputter deposited on Au substrate, *J. Power Sources* **136,** 10–15 (2004).
49. K. Nishimura, K. Kunimatsu, and M. Enyo, Electrocatalysis on Pd + Au alloy electrodes: 3. IR spectroscopic studies on the surface species derived from CO and CH3OH in NaOH solution, *J. Electroanal. Chem.* **260,** 167–179 (1989).
50. M. Morita, Y. Iwanaga, and Y. Matsuda, Anodic-oxidation of methanol at a gold-modified platinum electrocatalyst prepared by RF-sputtering on a glassy-carbon support, *Electrichim. Acta* **36,** 947–951 (1991).
51. A. B. Anderson, E. Grantscharova, and S. Seong, Systematic theoretical study of alloys of platinum for enhanced methanol fuel cell performance, *J. Electrochem. Soc.* **143,** 2075–2082 (1996).
52. L. D. Burke, J. A. Collins, M. A. Horgan, L. M. Hurley, and A. P. O'Mullane, The importance of the active states of surface atoms with regard to the electrocatalytic behaviour of metal electrodes in aqueous media, *Electrochim. Acta* **45,** 4127–4134 (2000).
53. C. Mihut, C. Descorme, D. Duprez, and M. D. Amiridis, Kinetic and spectroscopic characterization of cluster-derived supported Pt-Au catalysts, *J. Catal.* **212,** 125–135 (2002).
54. *Catalysis by Metals and Alloys*, edited by V. Ponec and G. C. Bond (Elsevier, Amsterdam 1995).
55. H. Lang, S. Maldonado, K. J. Stevenson, and B. D. Chandler, Synthesis and characterization of dendrimer templated supported bimetallic Pt–Au nanoparticles, *J. Am. Chem. Soc.* **126,** 12949–12956 (2004).
56. R. Meyer, C. Lemire, S. K. Shaikhutdinov, and H.-J. Freund, Surface chemistry of catalysis by gold, *Gold Bull.* **37,** 72–124 (2004).
57. D. Yates, Spectroscopic investigations of gold surfaces, *J. Colloid Interf. Sci.* **29,** 194–204 (1969).
58. J. Lee, and J. Schwank, Infrared spectroscopic study of NO reduction by H_2 on supported gold catalysts, *J. Catal.* **102,** 207–215 (1986).
59. M. Kim, J. Ebner, R. Friedman, and M. Vannice, Dissociative N_2O adsorption on supported Pt, *J. Catal.*, **204,** 348–357 (2001).
60. P. Fanson, W. Delgass, and J. Lauterbach, Island formation during kinetic rate oscillations in the oxidation of CO over Pt/SiO_2: A transient Fourier transform infrared spectrometry study, *J. Catal.* **204,** 35–52 (2001).
61. J. Lauterbach, G. Bonilla, and T. Pletcher, Non-linear phenomena during CO oxidation in the mbar pressure range: a comparison between Pt/SiO_2 and Pt(1 0 0), *Chem. Eng. Sci.* **54,** 4501–4512 (1999).
62. M. Brust, M. Walker, D. Bethell, D. J. Schiffrin, and R. Whyman Synthesis of thiol-derivatized gold nanoparticles in a 2-phase liquid–liquid system, *J. Chem. Soc., Chem. Commun.* 801–802 (1994).
63. M. M. Maye, W. X. Zheng, F. L. Leibowitz, N. K. Ly, and C. J. Zhong, Heating-induced evolution of thiolate-encapsulated gold nanoparticles: A strategy for size and shape manipulations, *Langmuir* **16,** 490–497 (2000).
64. M. M. Maye, and C. J. Zhong, Manipulating core-shell reactivities for processing nanoparticle sizes and shapes, *J. Mater. Chem.* **10,** 1895–1901 (2000).
65. M. J. Hostetler, C. J. Zhong, B. K. H. Yen, J. Anderegg, S. M. Gross, N. D. Evans, M. D. Porter, and R. W. Murray, Stable, monolayer-protected metal alloy clusters, *J. Am. Chem. Soc.* **120,** 9396–9397 (1998).
66. M. J. Hostetler, J. E. Wingate, C. J. Zhong, J. E. Harris, R. W. Vachet, M. R. Clark, J. D. Londono, S. J. Green, J. J. Stokes, G. D. Wignall, G. L. Glish, M. D. Porter, N. D. Evans, and R. W. Murray, Alkanethiolate gold cluster molecules with core diameters from 1.5 to 5.2 nm: Core and monolayer properties as a function of core size, *Langmuir* **14,** 17–30 (1998).
67. J. Luo, V. W. Jones, L. Han, M. M. Maye, N. Kariuki, and C. J. Zhong, AFM probing of thermal activation of molecularly-linked nanoparticle assembly, *J. Phys. Chem.* B **108,** 9669–9677 (2004).
68. J. Luo, M. M. Maye, V. Petkov, N. N. Kariuki, L. Wang, P. Njoki, D. Mott, Y. Lin, and C. J. Zhong, Phase properties of carbon-supported gold–platinum nanoparticles with different bimetallic compositions, *Chem. Mater.* in press

69. U. A. Paulus, A. Wokaun, G. G. Scherer, T. J. Schmidt, V. Stamenkovic, V. Radmilovic, N. M. Markovic, and P. N. Ross, Oxygen reduction on carbon–supported Pt–Ni and Pt–Co alloy catalysts, *J. Phys. Chem.* B **106,** 4181–4191 (2002).
70. T. Page, R. Johnson, J. Hormes, S. Noding, and B. Rambabu, A study of methanol electro-oxidation reactions in carbon membrane electrodes and structural properties of Pt alloy electro-catalysts by EXAFS, *J. Electroanal. Chem*. **485,** 34–41 (2000).
71. M. M. Maye, J. Luo, W.-B. Chan, L. Han, N. Kariuki, H. R. Naslund, M. H. Engelhard, Y. Lin, R. Sze, and C. J. Zhong, In *Solid-State Ionics-2002 (MRS Symposium Proceedings Volume 756)*, edited by P. Knauth, J.-M. Tarascon, E. Traversa, and H. L. Tuller (Materials Research Society, 2003), FF6.2.
72. L. D. Burke, Scope for new applications for gold arising from the electrocatalytic behaviour of its metastable surface states, *Gold Bull*. **37**(1–2), 125–135 (2004).
73. J. Luo, M. M. Maye, L. Han, C. J. Zhong, and M. Hepel, Probing mass transport characteristics in nanostructured gold catalysts, *J. New Mater. Electrochem. Syst.* **5,** 237–242 (2000).

15

Carbon-Supported Core-Shell PtSn Nanoparticles: Synthesis, Characterization and Performance as Anode Catalysts for Direct Ethanol Fuel Cell

Luhua Jiang[a,b], Gongquan Sun[b], Suli Wang[a,b], Qin Xin[a,c,*], Zhenhua Zhou[d], and Bing Zhou[d,*]

15.1. INTRODUCTION

In recent decades, direct alcohol fuel cells (DAFCs) have been extensively studied and considered as possible power sources for portable electronic devices and vehicles in the near future.[1] The application of methanol is limited due to its high volatility and toxicity,[2,3] although it is relatively easily oxidized to CO_2 and protons. So other short chain organic chemicals especially ethanol, ethylene glycol, propanol, and dimethyl

[a] Graduate School of the Chinese Academy of Sciences, Beijing 100039, CAS, People's Republic of China

[b] Direct Alcohol Fuel Cell Laboratory, Dalian Institute of Chemical Physics, P.O. Box 110, Dalian, 116023, People's Republic of China

[c] State Key Laboratory of Catalysis, Dalian Institute of Chemical Physics, P.O. Box 110, Dalian, 116023, People's Republic of China

[d] Headwaters NanoKinetix Inc., 1501 New York Avenue, Lawrenceville, NJ 08648, USA

* To whom correspondence should be addressed. E-mail: xinqin@dicp.ac.cn (Q. Xin), Zhou@htinj.com (B. Zhou)

oxalate have also been investigated as fuels for DAFCs.[3–5] As a green fuel, ethanol is much safer and has higher energy density than methanol. Most of all, ethanol is a renewable energy source and can be easily produced in great quantity by fermentation of sugar-containing raw materials. Thus ethanol is more attractive than methanol for direct alcohol fuel cells.

However, the complete oxidation of ethanol to CO_2 involves the cleavage of the C–C bond and transferring 12 electrons from one molecule. The process is very difficult at low temperature ($<100°C$) and many adsorbed intermediates and byproducts are produced. It is now urgent to develop novel electrocatalysts with high electrocatalytic activity for ethanol oxidation. Pt is a suitable electrocatalyst for oxidation of many small-molecule chemicals because of its high activity and stability under acidic environment. However, it is well known that pure platinum is not a good anode catalyst for ethanol at room or moderate temperatures because it is readily poisoned by the strongly adsorbed intermediates,[6] such as CO_{ads}. Other than the oxidative removal of intermediates such as CO_{ads}, the cleavage of the C–C bond is a key step to completely electrooxidize ethanol to CO_2. Most of previous research on ethanol fuel cells focused on identification of intermediates of ethanol electrooxidation on the state-of-the-art PtRu catalyst, since it is the best catalyst for methanol electrooxidation.[7–10] However, PtRu gave low activity for ethanol electrooxidation. Recent research[11–15] showed that PtSn catalysts outperformed PtRu for ethanol oxidation, and the improvement varied with the preparation procedure, the particle size, and the composition of PtSn catalysts. In 1998, Arico *et al.*[16] found that PtSn showed promising activity for ethanol electrooxidation at high temperature (170°C). Later Lamy *et al.*[17] reported DEFCs working at lower temperature ($<100°C$) and showed that the performance of a DEFC is improved to 35 mW/cm^2 at 90°C by applying bimetallic PtSn/C as the anode catalyst. By adopting a polyol preparation method to prepare carbon-supported PtSn catalysts, Zhou *et al.*[13] significantly improved DEFC performance to near 60 mW/cm^2. The above achievements indicate that ethanol is a promising fuel for low temperature fuel cells.

In this chapter, two carbon-supported PtSn catalysts with core-shell nanostructure were designed and prepared to explore the effect of the nanostructure of PtSn nanoparticles on the performance of ethanol electro-oxidation. The physical (XRD, TEM, EDX, XPS) characterization was carried out to clarify the microstructure, the composition, and the chemical environment of nanoparticles. The electrochemical characterization, including cyclic voltammetry, chronoamperometry, of the two PtSn/C catalysts was conducted to characterize the electrochemical activities to ethanol oxidation. Finally, the performances of DEFCs with PtSn/C anode catalysts were tested. The microstructure and composition of PtSn catalysts were correlated with their performance for ethanol electrooxidation.

15.2. EXPERIMENTAL DETAILS

15.2.1. Chemicals

All chemicals were analytically pure and used as received. $H_2PtCl_6{\cdot}6H_2O$ and $SnCl_2{\cdot}2H_2O$ were used as precursors of PtSn catalysts. The solid electrolyte was

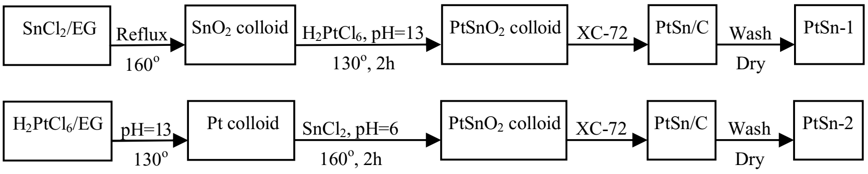

FIGURE 15.1. Synthesis routes of $PtSnO_2$ nanocomposites with different microstructures.

Nafion®-115 purchased from DuPont Corporation. The activated carbon of Vulcan XC-72R with a specific surface area (BET) of about 250 m^2/g (Cabot Corp.) was used as a support for all catalysts.

15.2.2. Preparation of Catalyst

Two PtSn/C catalysts were prepared for comparison. The preparation scheme is shown in Fig. 15.1. PtSn-1 was prepared via the following procedure: $SnCl_2{\cdot}2H_2O$ was first added to ethylene glycol (EG) to form a clear solution with a Sn concentration of 0.5 mg/mL, and then the solution was heated to 160°C at a rate of 10°C/min and kept at this temperature until the solution changed to pale yellow colloid. After the colloid cooled down to room temperature, the required amount of $H_2PtCl_6{\cdot}6H_2O$ was added and stirred for half hour. Then the pH value of the solution was adjusted to above 13 with sodium hydroxide and the solution was heated to 130°C and kept at this temperature for 2 h to obtain brown–black colloid. Carbon support was then added to the above sol and stirred for another 2 h. The obtained black product was filtered, washed and dried. Conversely, PtSn-2 was prepared by depositing SnO_2 onto the as-synthesized Pt nanoparticles. The required amount of H_2PtCl_6 was added to EG to obtain a mixture with 1 mg metal/mL solvent. The mixture was stirred for 0.5 h at room temperature to obtain a homogeneous solution. Sodium hydroxide was then added to modify the pH value of the solution to $>$13. Then the mixture was heated to 130°C at a rate of 10°C/min in an oil bath and kept at this temperature for 2 h to obtain brown–black colloid. After the colloid cooled down to room temperature, the stoichiometric amount of $SnCl_2$ was added and stirred for 2 h to form a homogeneous mixture. Then the mixture was heated to 160°C and kept at this temperature for 2 h to form tin oxide coating on the surface of the above Pt nanoparticles in acidic condition. After the mixture cooled down, the needed amount of Vulcan XC-72R was added and stirred for another 2 h to deposit metal particles onto the carbon surface. The black mixture was filtered, washed, and dried at 80°C for 10 h in a vacuum oven. The nominal Pt loading of the two catalysts was 20 wt.% (the nominal atomic ratio of Pt to Sn was 3 to 1).

15.2.3. Physical Chemical Characterizations

XRD patterns were recorded with a Rigaku Rotalflex (RU-200B) X-ray diffractometer using Cu Kα radiation with a Ni filter. The tube current was 100 mA with a tube voltage of 40 kV. The 2θ angular regions between 15 and 85° were explored at a scan rate of 5° min^{-1}. The Pt (220) peak (64 to 72°) was scanned at 1° min^{-1} to obtain

the Pt particle size by using the Scherrer formula. For all XRD tests, the resolution in the 2θ scans was kept at 0.02°.

Transmission electron microscopy (TEM) investigations of Pt colloid and SnO_2 colloid were carried out using a JEOL JEM-2000EX microscope operating at 120 kV. A drop of as-prepared Pt colloid or SnO_2 colloid was applied directly onto clean holey copper grids and dried in air. TEM and EDX analyses of PtSn/C catalysts were taken on JEOL JEM-2010F operating at 200 kV. Specimens were prepared by ultrasonically suspending the catalyst powder in ethanol. A drop of the suspension was then applied onto copper grids and dried in air. The size distribution and the mean particle size of each sample were obtained by measuring 300 particles from bright-field micrographs.

X-ray photoelectron spectroscopy characterization of catalysts was performed on a VG ESCA LABMKII X-ray photoelectron spectrograph under a vacuum of 10^{-9} Pa. Mg Kα ray was used as excitation source ($h\nu = 1253.6$ eV). C_{1s} was used as the internal standard to calibrate the binding energy results.

15.2.4. Electrochemical Characterization

Electroactivities of PtSn/C electrodes towards methanol oxidation were measured by cyclic voltammetry, and chronoamperometry using an EG&G model 273A potentiostat/galvanostat in a three-electrode test cell at room temperature. The working electrode was a thin layer of Nafion® impregnated PtSn/C composite cast on a vitreous carbon disk electrode. The detailed preparation method has been described previously.[18,19] A 5.0 mg catalyst sample were suspended in 1.0 mL of ethanol, and 10.0 wt.% Nafion® was added as adhesive and proton conductor. The mixture was sonicated for 10 min to form a homogeneous ink. Then 25 μL of ink were pipeted on a 4 mm diameter vitreous electrode to act as the working electrode. The supporting electrolyte was 0.5 M H_2SO_4 or 0.1 M $HClO_4$+0.5 M CH_3CH_2OH. The counter electrode was a Pt wire. The reference electrode was a saturated calomel electrode (SCE). All experiments were carried out at room temperature.

15.2.5. Single-Cell Performance Tests

The membrane electrode assemblies (MEAs), in which the cathode was a commercial Pt/C catalyst (20 wt.%) with a Pt loading of 1.0 mg/cm^2, were fabricated by pressing the electrodes onto both sides of Nafion®-115 membranes at 130°C for 90 s.[20] The anode included the different in-house carbon-supported PtSn catalysts with a Pt loading of 1.5 mg/cm^2. The MEAs were fastened between two stainless steel polar plates with a parallel flow field and fixed on an in-house single-cell test apparatus. Two stainless wire nettings were placed between the bipolar plates and the MEAs to collect currents. In the DEFCs, unhumidified oxygen with 2 bar (abs.) backpressure was directly fed to the cathode side and 1.0 mol/L of ethanol solution without backpressure at a flow rate of 1.0 mL/min was directly fed to the anode side. Every single cell has been operated for at least 3 days. On the first day, the single cell was fed only by distilled water to the anode at 75°C for at least 4 h in order to fully hydrate the electrolyte membrane in the MEAs and remove any low molecular weight organic impurity on the anode firstly. Then the anode was fed with an aqueous solution of ethanol. The cell voltage–current density data were collected on the second day. The

power density–current density data were obtained from the multiplication of the cell voltage and the corresponding current density.

15.3. RESULTS AND DISCUSSION

TEM images of the as-prepared tin oxide and platinum colloid are shown in Fig. 15.2. It can be seen that both the tin oxide and platinum nanoparticles are uniform and well distributed. Based on the measurements of 300 particles in random regions, the

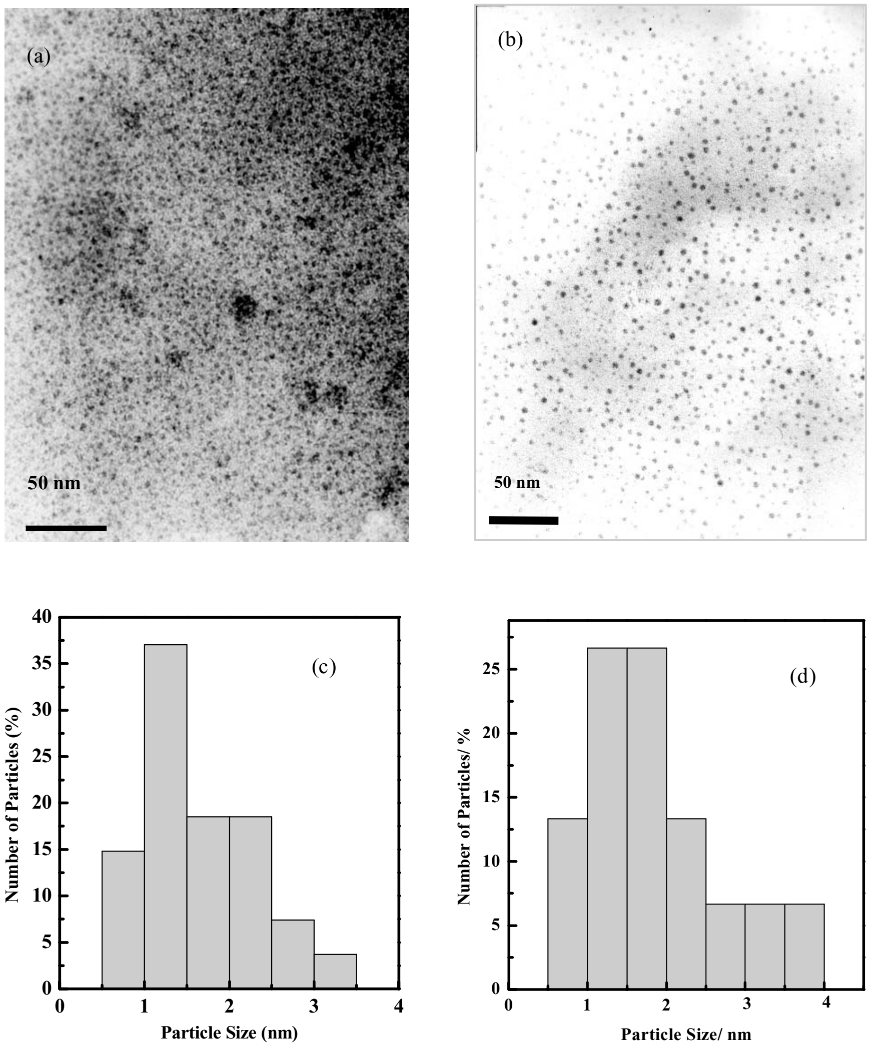

FIGURE 15.2. TEM images of (a) as-prepared tin oxide, (b) Pt colloid and the corresponding histograms of (c) tin oxide, (d) Pt colloid.

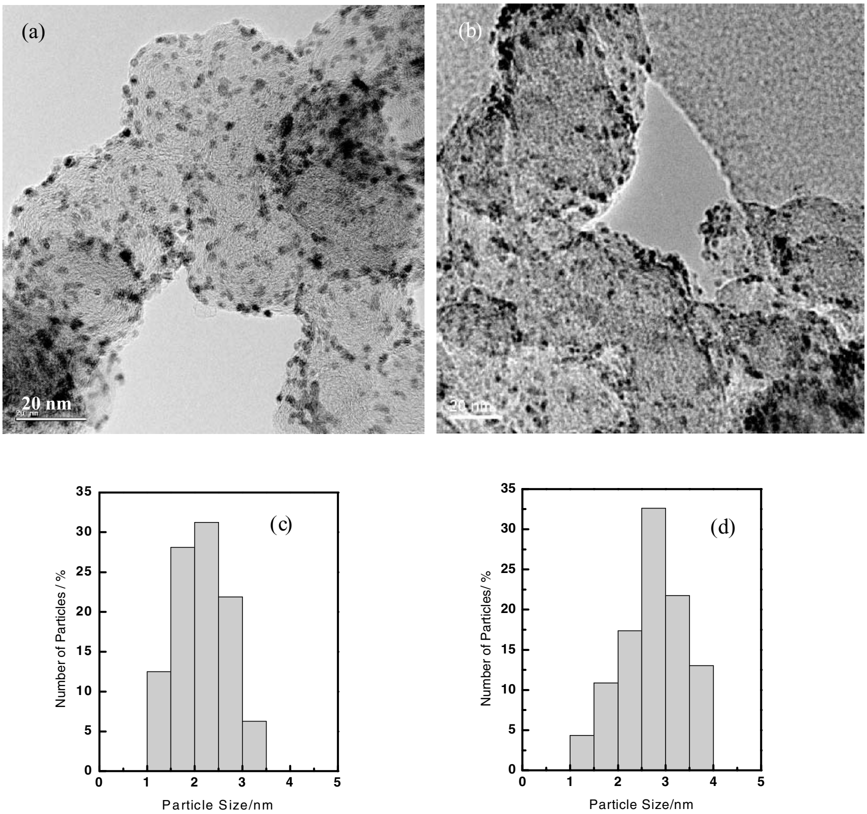

FIGURE 15.3. TEM images of (a) PtSn-1, (b) PtSn-2 and the corresponding histograms of (c) PtSn-1, (d) PtSn-2.

average particle size of tin oxide and platinum was estimated to be 1.2 and 1.5 nm, respectively. The corresponding histograms (Fig. 15.2c and d) reveal that the particle size distribution is rather narrow and that the majority of Pt and SnO_2 particles are mostly concentrated at the smaller particle diameters with a tail toward the large-particle side. After coating Pt and SnO_2 on the surface of the as-prepared SnO_2 and Pt colloid, and followed by depositing the composite particles on the carbon support, respectively, PtSn-1 and PtSn-2 were obtained and their TEM images are shown in Fig. 15.3. The corresponding histogram of PtSn-1 and PtSn-2 are also displayed in Fig. 15.3. It can be clearly observed that the nanoparticles are spherical in shape with sharp size distribution, and no agglomerations are observed. However, it also can be seen that the mean particle size of PtSn-1 and PtSn-2 increased relative to corresponding colloidal precursors, with the average particle size of 1.2 (SnO_2 colloid) and 1.5 nm (Pt colloid) increasing to 2.3 and 2.8 nm, respectively, for the supported particles. The particle size distribution of PtSn-1 and PtSn-2 also shifted to the direction of larger particles.

XRD patterns of the two PtSn catalysts are displayed in Fig. 15.4. The diffraction peak at 20 to 25° observed in both XRD patterns is attributed to the (002) plane of carbon. The diffraction peaks at around 39°, 46°, 68°, and 81° are attributed to Pt

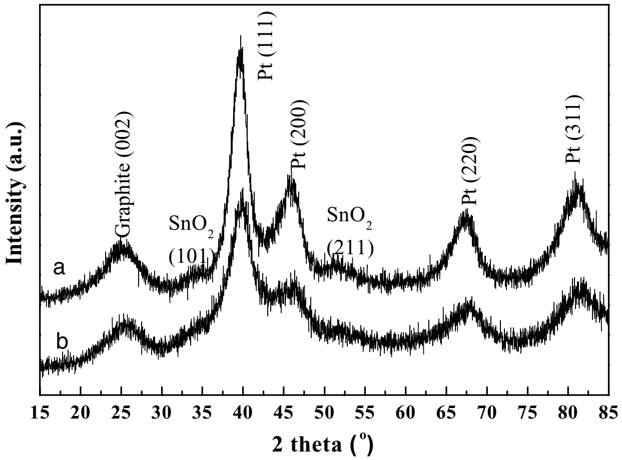

FIGURE 15.4. XRD patterns of (a) PtSn-1 and (b) PtSn-2.

(111), (200), (220), and (311) crystalline plane (JCPDF-040802), respectively, which represents the typical character of a crystalline Pt with face-centered cubic (fcc) structure. Apart from the obvious four peaks relative to Pt, the diffraction peaks of SnO_2 (101) and (211) at around 34° and 52° (JCPDF-411445) were also observed in the two samples, though these peaks were weaker for PtSn-2 compared to PtSn-1. The fcc lattice parameters and average particle size for PtSn catalysts were evaluated according to the full width at half-maximum (FWHM) and the angular position of the Gaussian-fitted (220) peaks, respectively. The relevant data are listed in Table 15.1. The (220) peak positions of both PtSn catalysts (67.5° for PtSn-1 and 67.2° for PtSn-2), compared with that of single Pt (67.4°), varies slightly. The lattice parameters for PtSn-1 and PtSn-2 catalysts are 3.928 and 3.936 Å, which are increased slightly compared with that of the pure Pt (3.923 Å). In our previous research[13] on co-reduction of Pt and Sn, it was found that the peak positions of Pt in PtSn/C catalysts, compared with Pt/C, shifted significantly to lower angle and the Pt lattice parameter of PtSn catalysts clearly increased. The shift of the peak position and the dilation of Pt lattice parameter reflect the degree of alloying of the two metals. Thus, it can be confirmed that PtSn catalysts prepared by the successive reduction method described here are less alloyed than those prepared by the coreduction method.[13] In Table 15.1, both catalysts show similar mean nanoparticle sizes whether from both XRD and TEM results.

EDX analyses were carried out for random areas of the samples and the results are shown in Table 15.2. For PtSn-1, two clusters with a diameter of 10 and 20 nm and

TABLE 15.1. Data calculated by the Sherrer formula.

			Mean Particle Size (nm)	
Catalyst	$2\theta_{max}$(°)	Lattice Parameter (Å)	XRD	TEM
PtSn-1	67.5	3.928	2.7	2.3
PtSn-2	67.2	3.936	2.1	2.8

TABLE 15.2. Microanalysis of PtSn catalysts by EDX (atomic ratio).

Analysis	Pt	Sn	Beam (nm)	Remarks
		PtSn-1		
Particle 1	73.4	26.6	10	Cluster 20 nm
Particle 2	74.0	26.0	10	Particle 2.5 nm
Particle 3	78.9	21.1	10	Cluster 10 nm
Average	75.4	24.6		
		PtSn-2		
Particle 1	79.2	21.8	10	Particle 3 nm
Particle 2	70.4	29.6	10	Cluster 10 nm
Particle 3	71.6	28.4	30	Bulk
Average	73.7	26.3		

one particle with a diameter of 2.5 nm were analyzed. In Table 15.2, it can be seen that the atomic ratios of Pt/Sn in the analyzed clusters and particle are very close to the nominal ratio. The distributions of Pt and Sn are uniform. For PtSn-2, apart from the bulk analysis of the element distribution, one particle with a diameter of 3 nm and a cluster with a diameter of 5 nm were analyzed. It can be seen that whether in one particle or in bulk the distributions of Pt and Sn are all uniform. Based on the above results, the average Pt/Sn atomic ratios for PtSn-1 and PtSn-2 are 75.4 to 24.6 and 73.7 to 26.3, respectively. This indicates that the distribution of Pt and Sn is uniform in both catalysts. It is noteworthy that the electron beam size employed herein was 10 nm, well above the average particle size, so that the analysis on one single particle may be affected by its neighboring particles. Thus, regardless of the beam size, the Pt/Sn ratio was always the same and in reasonable agreement with the nominal composition of the catalyst.

To clarify the valence state of metals in both of the PtSn catalysts, XPS analyses were carried out. Sn 3d and Pt 4f spectra for PtSn catalysts are shown in Fig. 15.5. All spectra have been deconvoluted into different components. The binding energies of Pt and Sn in various catalysts as obtained from their XPS spectra are given in Table 15.3

TABLE 15.3. Comparison of binding energies of Pt $4f_{7/2}$ and Sn $3d_{5/2}$ between the literature and experiment.

References	Data in the Literature			Experimental Data	
	PtO_2	PtO	Pt	PtSn-1	PtSn-2
		$Pt_{4f}^{7/2}$			
[21]	74.5	73.6	70.9	71.1	71.1
[22]	74.5	72.93	71.55		
	SnO_2	SnO	Sn	PtSn-1	PtSn-2
		$Sn_{3d}^{5/2}$			
[21]	486.4	486.6	484.6	487.0	486.7
[22]	486.87–487.10[a]		485.26–485.65[a]		

[a] These data change slightly because of the contents of Sn and total metal loadings.

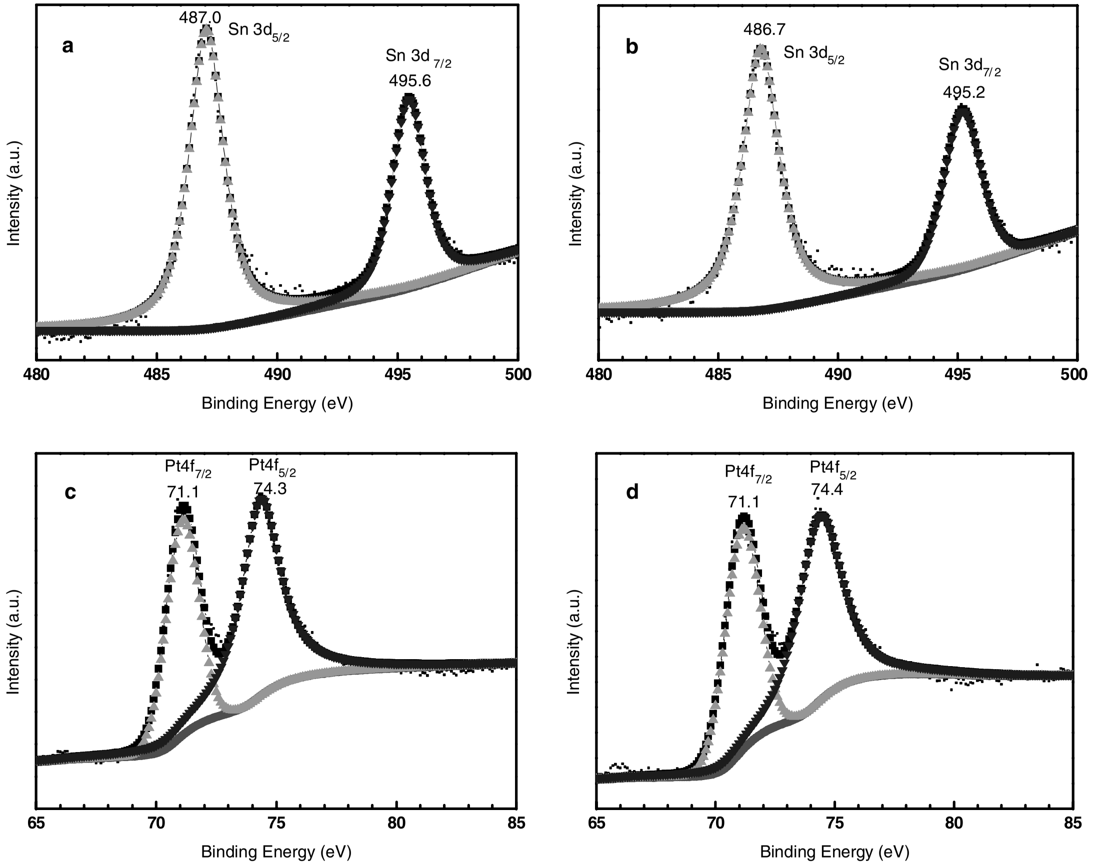

FIGURE 15.5. XPS spectra of (a) Sn 3d in PtSn-1, (b) Sn 3d in PtSn-2, (c) Pt 4f in PtSn-1, and (d) Pt 4f in PtSn-2.

along with corresponding data from the literature.[21,22] In the entire Pt spectra, the $4f_{7/2}$ signal at around 71.1 eV in both catalysts is assigned to zero-valent Pt. The slight shift from the value of 70.9 eV for bulk Pt-metal is attributed to a contribution from the metal–metal interaction or small cluster-size effects.[22] The comparison with literature data suggests that most of the Pt in the two PtSn catalysts is in the metallic state. The binding energies of Sn in both catalysts (487.0 and 486.7 eV, respectively) are slightly higher than the reference data, due to the electronic effect between Sn and Pt, or due to small cluster-size effects. From the experimental results, it is confirmed that the main part of Sn is in the oxidized state. Based on the design of these experiments, it was expected that the surface of the PtSn-1 catalyst would be rich in Pt, and that the surface of PtSn-2 would be rich in Sn, but the XPS detected both elements on each catalyst. However, considering the metal particle is only 2 to 3 nm in size, and that the penetration ability of X-ray photoelectrons is 1 to 2 nm, it follows that the results of the XPS analyses are representative of the bulk composition of the nanoparticles rather than their surface. Therefore, the XPS method is unable to resolve the nanostructure of these catalyst particles.

Cyclic voltammograms of PtSn microelectrodes in 0.5 M sulfuric acid solution are shown in Fig. 15.6. The potential range was –200 to 800 mV (vs. SCE) and the scan rate was 100 mV/s. It can be seen clearly that hydrogen desorption from the PtSn-2 electrode is seriously inhibited compared with that from the PtSn-1 electrode. From the hydrogen desorption peak areas in the CV curves and the Pt single crystallite hydrogen desorption constant of 210 $\mu C/cm^2$ Pt, the electrochemical surface areas (ESA) for PtSn-1 and PtSn-2 were calculated to be 391 and 49 cm^2/mg, respectively. However, it is evident from XRD and TEM results that the two catalysts have similar particle size and so they should possess the similar physical surface area. The difference

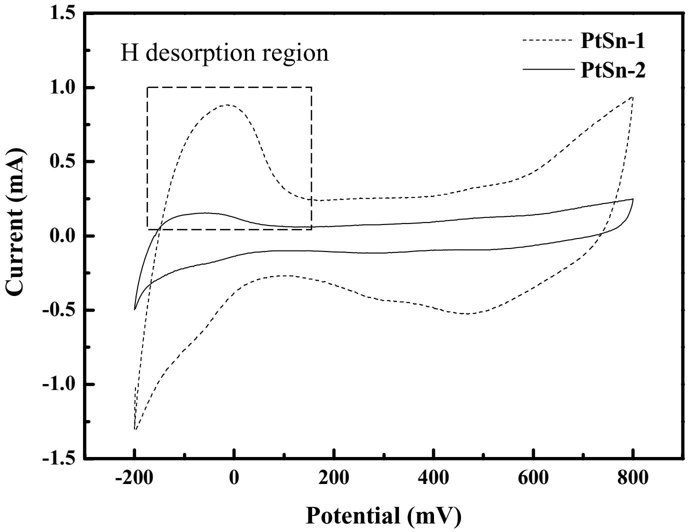

FIGURE 15.6. Cyclic voltammograms of PtSn-1 and PtSn-2 in 0.5M H_2SO_4 at room temperature, scan rate: 100 mV/s.

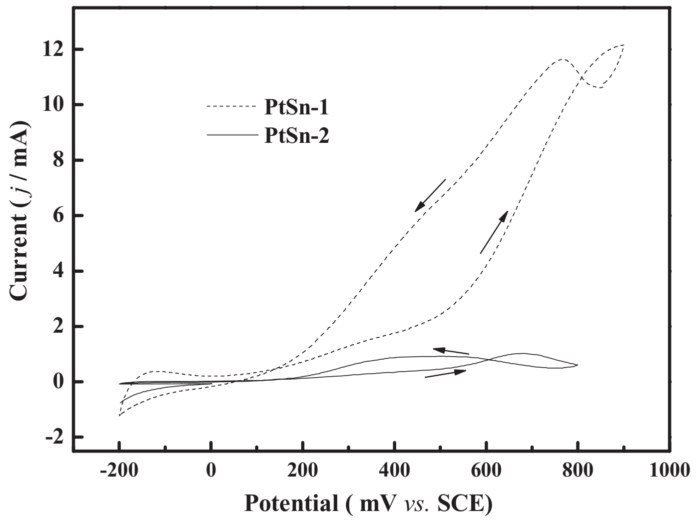

FIGURE 15.7. Cyclic voltammograms of PtSn electrodes in 0.5 M CH_3CH_2OH/0.1 M $HClO_4$ electrolyte at room temperature. Scan rate: 50 mV/ s.

of the electrochemical surface area (ESA) between the two catalysts may be due to differences in the nanostructure of particles arising from the different order in which the components were precipitated during the preparation process. The CV results strongly support a Sn core-Pt shell structure for PtSn-1, and a reverse structure for PtSn-2. SnO_2 surface enrichment for the PtSn-2 catalyst may be responsible for the lower ESA of PtSn-2. By the same argument, PtSn-1 may retain a reasonable level of hydrogen adsorption/desorption ability due to a Pt-rich shell structure.

The catalytic activities of the two catalysts for ethanol electro-oxidation were characterized by cyclic voltammetry and chronoamperometry on half-cells. Figure 15.7 shows the cyclic voltammograms of ethanol oxidation under acidic conditions (0.5 M CH_3CH_2OH/ 0.1 M $HClO_4$) catalyzed by the PtSn catalyst. The potential range was –200 to 900 mV (vs. SCE) for PtSn-1. Considering the risk of dissolving the relatively soluble SnO_2-rich surface, the potential range for PtSn-2 was narrowed to –200 mV to 800 mV (vs. SCE). The scan rate was 50 mV/s. The voltammetric features are in good agreement with our previously published work.[13,14] The current peak at about 900 mV (vs. SCE) in the forward scan is attributed to ethanol electro-oxidation on the PtSn/C catalysts. Compared with previous results,[13] this peak position is shifted slightly to higher potential, which may be related with the scan rate. In general, faster scan rate is expected to lead to lag of the current peak. The onset of oxidative current peak and the maximum oxidative current are related to the ethanol electro-oxidation activity of the catalysts. The onset of oxidative current on the PtSn-1 catalyst is about 100 mV (vs. SCE), while the oxidative current on PtSn-2 starts from nearly 200 mV indicating that PtSn-1 can oxidize ethanol at a much lower potential. Figure 15.7 clearly shows that the oxidation current peak on the PtSn-1 catalyst is significantly higher than on the PtSn-2. The peak oxidative current is 12.1 mA at nearly 900 mV (vs. SCE) on PtSn-1

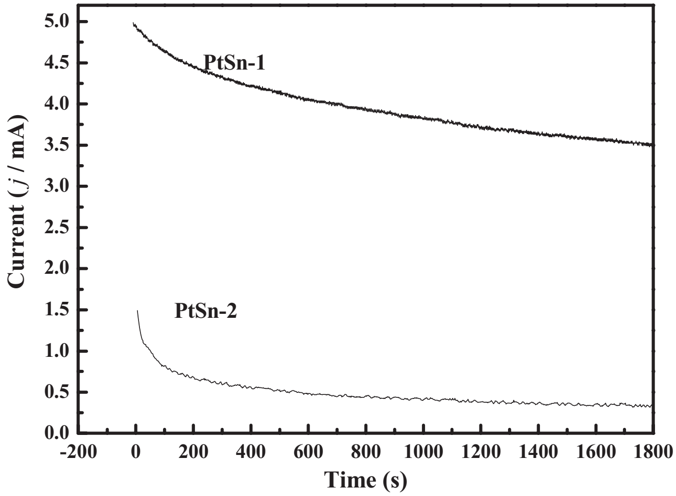

FIGURE 15.8. Current density–time dependence measured by the CA method in 0.5 M CH_3CH_2OH + 0.1 M $HClO_4$ solution for PtSn electrodes.

catalyst, while PtSn-2 give lower activities for ethanol oxidation according to the peak oxidation currents (1.0 mA at 670 mV).

From a practical point of view, data obtained by CA methods are more useful. Figure 15.8 shows examples of the CA curves obtained in 0.5 M ethanol solution in 0.1 M $HClO_4$ at an anodic potential of 600 mV vs. SCE. In both of the CA curves there is a sharp initial current drop in the first 5 min, followed by a slower decay. The sharp decrease might be related to a double layer thus indicating that the catalysts differ mainly in their active area based on the above CV experiments in acid solution. In longer runs it was found that the current ($j$after 30 min polarization at 600 mV vs. SCE) obtained on PtSn-1 electrodes is higher than that on PtSn-2. The quasi-steady-state current density stabilized for both the catalysts within 0.5 h at the potential hold. The final current densities on PtSn-1 and PtSn-2 electrodes after holding the cell potential at 600 mV vs. SCE for 30 min were 3.5 and 0.3 mA, respectively.

Ultimately, the catalyst performance of a real fuel cell is of the greatest importance. The DEFC polarization curves for the two PtSn anode catalysts are tested and shown in Fig. 15.9. The characteristic data are summarized in Table 15.4. The PtSn-1 catalyst shows a strongly enhanced electron-oxidation reaction (EOR) activity and much better performance in both the activation-controlled region (low-current density region) and

TABLE 15.4. Summary of performances of DEFCs adopting PtSn-1 or PtSn-2 as an anode catalyst.

Catalyst	Open Circuit Voltage (V)	Current Density (mA/cm^2)					Maximum Power Density (mW/cm^2)
		0.7 V	0.6V	0.5 V	0.4V	0.3V	
PtSn-1	0.819	63.4	116.9	158.3	188.4	212.5	79.5
PtSn-2	0.785	5.7	17.1	31.0	52.2	72.0	22.5

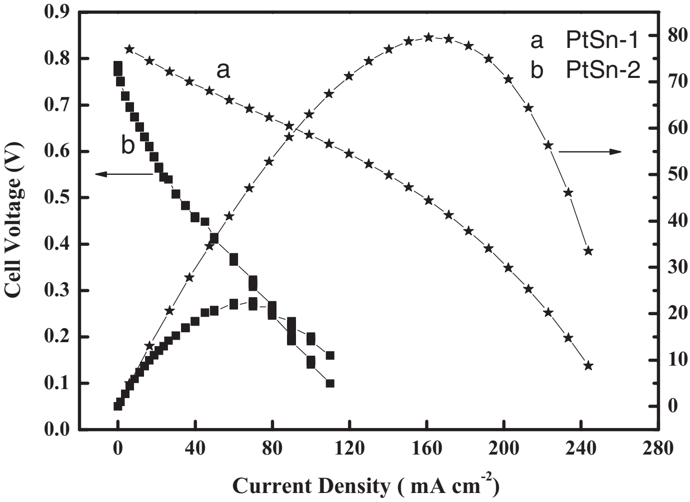

FIGURE 15.9. Performance comparison of PtSn anode based direct ethanol fuel cells at 90°C. Anode catalysts: Carbon supported PtSn with a Pt loading of 1.5 mg/cm^2, ethanol concentration: 1.0 mol/L, flow rate: 1.0 mL/min. Cathode: (20 Pt wt.%, Johnson Matthey Inc.) with a Pt loading of 1.0 mg/cm^2, $P_{O2} = 2$ bar. Electrolyte: Nafion®-115 membrane.

mass-transport controlled region (high current density region) than the PtSn-2 catalyst, i.e. the OCV (open circuit voltage) of the single cell with PtSn-1 is 0.819V, which is 34 mV higher than that of the PtSn-2 catalyst. At 0.7 V the current density for the cell with PtSn-1 as the anode catalyst is 63.4 mA/cm^2, while that of the cell with PtSn-2 is only 5.7 mA/cm^2. The difference of the output power density between the two PtSn catalysts increases with the current density. This is consistent with the above-discussed CV and CA results, which strongly support the relationship between improved single cell performance in single cell and enhancement of EOR on the PtSn-1 catalyst. The maximum power density of single cells with PtSn-1 catalyst reached nearly 80 mW/cm^2, while that of single cell with PtSn-2 catalyst was only 22.5 mW/cm^2.

From the above experimental results, it can be seen that the both PtSn catalysts have a similar particle size leading to the same physical surface area. However, the ESAs of these catalysts are significantly different, as indicated by the CV curves. The large difference between ESA values for the two catalysts could only be explained by differences in detailed nanostructure as a consequence of differences in the preparation of the respective catalyst. On the basis of the preparation process and the CV measurement results, a model has been developed for the structures of these PtSn catalysts as shown in Fig. 15.10. The PtSn-1 catalyst is believed to have a Sn core/Pt shell nanostructure while PtSn-2 is believed to have a Pt core/Sn shell structure. Both electrochemical results and fuel cell performance indicate that PtSn-1 catalyst significantly enhances ethanol electrooxidation. Our previous research found that an important difference between PtRu and PtSn catalysts is that the addition of Ru reduces the lattice parameter of Pt, while Sn dilates the lattice parameter. The reduced Pt lattice parameter resulting from Ru addition seems to be unfavorable for ethanol adsorption and degrades the DEFC performance. In this new work on PtSn catalysts with more

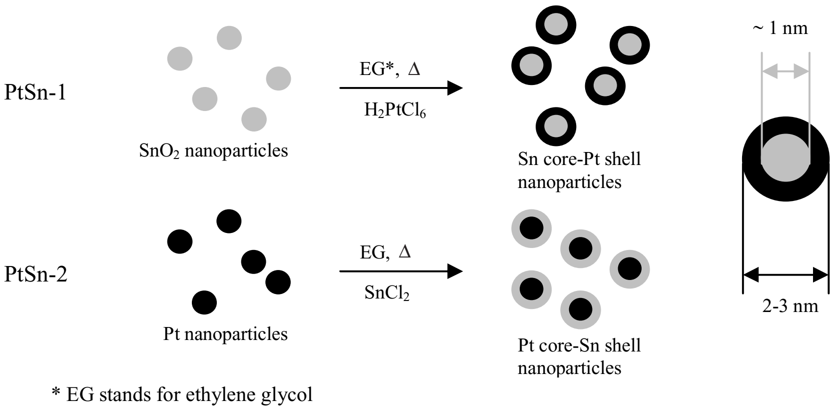

FIGURE 15.10. A model of the prepared PtSn/C electrocatalysts.

elaborate nanostructure, it is also apparent that dilation of the Pt lattice parameter is favorable for ethanol adsorption and electrooxidation. Although a catalyst with a tin oxide-rich surface layer might offer oxygen-containing species, they could also block the Pt active sites which are required to adsorb ethanol molecules. Moreover, the tin oxide-rich surface would increase the intrinsic resistance of the fuel cell, which is one of the main causes leading to inferior performance. Conversely, a catalyst with a Sn-core structure would not block the Pt-skin active sites, so this catalyst can still exhibit the electrochemical behavior of Pt, while still benefiting from the availability of oxygen-containing species to remove CO-like species. So the enhanced DEFC performance of PtSn catalysts has been attributed to the dilated Pt lattice parameter, the electronic effect of Pt/Sn and the oxygen-containing species offered by tin oxide in Pt-rich surface layer. More importantly, this structure, compared with Pt core-Sn shell, has less electric resistance and is very stable in acidic working conditions due to the high corrosive resistance of Pt surface layer.

15.4. CONCLUSIONS

Two carbon-supported PtSn catalysts for ethanol electrooxidation were prepared with stepwise preparation routes using a modified polyol method. XRD and TEM analyses show that the two PtSn catalysts have a similar particle size with a mean diameter of ∼2 to 3 nm. Moreover, XRD patterns indicated that tetragonal SnO_2 exists in both catalysts, separate from the Pt fcc crystalline structure. The distribution of Pt and Sn is uniform whether in particles or in bulk according to EDX analyses. The tested Pt/Sn ratio agrees well with the nominal one in both samples. In both catalysts, Pt occurs in zero valence and Sn exists in an oxidized state. Considering that the particle size of the catalysts is on the order of ∼2 to 3 nm, the XPS analyses have been attributed to the bulk rather than the surface. CV in acidic electrolyte indicated that the hydrogen desorption area on PtSn-2 was much less than that on PtSn-1, which implied that the tin oxide covers the Pt active sites in PtSn-2. CV and CA measurements indicate that PtSn-1 shows higher catalytic activity than PtSn-2. Furthermore, the performance of DEFCs

with PtSn-1 is much higher than that with PtSn-2 as the anode catalyst. The peak output power density of the former is 79.5 mW/cm^2, while the corresponding value of the latter is only 22.5 mW/cm^2. So Sn core-Pt shell is the favorable structure for ethanol electrooxidation. It is suggested that the slight dilation of Pt lattice parameter, together with the possible electric effect of Pt/Sn and the tin oxide species on the surface of Sn core-Pt shell nanoparticles enhanced the DEFC performance. More importantly, this structure, compared with Pt core-Sn shell, is very stable in acidic working condition due to the excellent corrosion resistance of Pt in the surface layer.

ACKNOWLEDGMENTS

This work was financially supported by Innovation Foundation of Chinese Academy of Science (K2003D2), National Natural Science Foundation of China (grant no. 20173060), Hi-Tech Research and Development Program of China (2003AA517040) and Knowledge Innovation Program of the Chinese Academy of Sciences (KGCX2-SW-310). Hundred Elites Program of Chinese Academy of Sciences (Dr. Bing Zhou) is also acknowledged.

REFERENCES

1. X. Ren, P. Zelenay, S. Thomas, J. Davey, and S. Gottesfeld, Recent advances in direct methanol fuel cells at Los Alamos National Laboratory, *J. Power Sources* **86,** 111–116 (2000).
2. C. Lamy, E. M. Belgsir, and J.-M. Léger, Electrocatalytic oxidation of aliphatic alcohols: Application to the direct alcohol fuel cell (DAFC), *J. Appl. Electrochem.* **31,** 799–809 (2001).
3. E. Peled, T. Duvdevani, A. Aharon, and A. Melman, New fuels as alternatives to methanol for direct oxidation fuel cells, *Electrochem. Solid-State Lett.* **4**(4), A38–A41 (2001).
4. J. Wang, S. Wasmus, and R.F. Savinell, Evaluation of ethanol, 1-propanol, and 5-propanol in a direct oxidation polymer-electrolyte fuel cell—A real-time mass spectrometry study, *J. Electrochem. Soc.* **142**(12), 4218–4224 (1995).
5. Z. G. Qi, M. Hollett, A. Attia, and A. Kaufman, Low temperature direct 2-propanol fuel cells, *Electrochem. Solid-State Lett.* **5**(6), A129–A130 (2002).
6. K. W. Park, J. H. Choi, B. K. Kwon, S. A. Lee, Y. E. Sung, H. Y. Ha, S. A. Hong, H. Kim, and A. Wieckowski, Chemical and electronic effects of Ni in Pt/Ni and Pt/Ru/Ni alloy nanoparticles in methanol electrooxidation, *J. Phys. Chem.* B **106**(8), 1869–1877 (2002).
7. T. Iwasita, and E. Pastor, A DEMS and FTIR spectroscopic investigation of adsorbed ethanol on polycrystalline platinum, *Electrochim. Acta* **39**(4), 531–537 (1994).
8. N. Fujiwara, K. A. Friedrich, and U. Stimming, Ethanol oxidation on PtRu electrode studied by differential electrochemical mass spectrometry, *J. Electroanal. Chem.* **472,** 120–125 (1999).
9. E. Pastor, and T. Iwasita, D/H exchange of ethanol at platinum electrodes, *Electrochim. Acta* **39**(4), 547–551 (1994).
10. J. Shin, W. J. Tornquist, C. Korzeniewski, and C. S. Hoaglund, Elementary steps in the oxidation and dissociative chemisorption of ethanol on smooth and stepped surface planes of platinum electrodes, *Surf. Sci.* **364,** 122–130 (1996).
11. C. Lamy, E. M. Belgsir, and J.-M. Leger, Electrocatalytic oxidation of aliphatic alcohols: Application to the direct alcohol fuel cell (DAFC), *J. Appl. Electrochem.* **31,** 799–809 (2001).
12. F. Delime, J.-M. Leger, and C. Lamy, Optimization of platinum dispersion in Pt-PEM electrodes: Application to the electrooxidation of ethanol, *J. Appl. Electrochem.* **28,** 27–35 (1998).
13. W. Zhou, Z. Zhou, S. Song, W. Li, G. Sun, P. Tsiakaras, and Q. Xin, Pt based anode catalysts for direct ethanol fuel cells, *Appl. Catal.* B **46,** 273–285 (2003).

14. W. Zhou, B. Zhou, W. Li, Z. Zhou, S. Song, G. Sun, Q. Xin, S. Douvartzides, M. Goula, and P. Tsiakaras, Bi- and tri-metallic Pt-based anode catalysts for direct ethanol fuel cells, *J. Power Sources.* **131**(1–2), 217–223 (2004).
15. C. Lamy, A. Lima, V. LeRhun, F. Deline, C. Coutancear, and J.-M. Leger, Recent advances in the development of direct alcohol fuel cells (DAFC), *J. Power Sources* **105,** 283–296 (2002).
16. A. S. Arico, P. Creti, P. L. Antonucci, and V. Antonucci, Comparison of ethanol and methanol oxidation in a liquid-feed solid polymer electrolyte fuel cell at high temperature, *Electrochem. Solid State Lett.* **1**(2), 66–68 (1998).
17. C. Lamy, S. Rousseau, E. M. Belgsir, C. Coutanceau, and J.-M. Léger, Recent progress in the direct ethanol fuel cell: Development of new platinum–tin electrocatalysts, *Electrochim. Acta* **49,** 3901–3908 (2004).
18. L. H. Jiang, Z. H. Zhou, W. Z. Li, W. J. Zhou, S. Q. Song, H. Q. Li, G. Q. Sun, and Q. Xin, Effects of treatment in different atmosphere on Pt_3Sn/C electrocatalysts for ethanol electro-oxidation, *Energy Fuels* **18,** 866–871 (2004).
19. L. H. Jiang, G. Q. Sun, Z. H. Zhou, W. J. Zhou, and Q. Xin, Preparation and characterization of PtSn/C anode electrocatalysts for direct ethanol fuel cell, *Catal. Today* **93-95C,** 665–670 (2004).
20. L. H. Jiang, G. Q. Sun, X. S. Zhao, Z. H. Zhou, S. Y. Yan, S. H. Tang, G. X. Wang, B. Zhou, and Q. Xin, Preparation of supported PtRu/C electrocatalyst for direct methanol fuel cells, *Electrochim. Acta* **50,** 2371–2376 (2005).
21. C. D. Wagner, W. M. Riggs, L. E. Davis, J. F. Moulder, and G. E. Muilenberg, In *Handbook of X-ray Photoelectron Spectroscopy*, (Perkin-Elmer Corp., 1979).
22. A. K. Shukla, A. S. Aric'o, K. M. E. Khatib, H. Kim, P. L. Antonucci, and V. Antonucci, An X-ray photoelectron spectroscopic study on the effect of Ru and Sn additions to platinised carbons, *Appl. Surf. Sci.* **137,** 20–29 (1999).

Index

$CuO–CeO_2–ZrO_2$, 205
α-Fe_2O_3, 44, 225, 257
δ-Al_2O_3, 271
γ-Al_2O_3, 45
γ-Fe_2O_3, 223
$NO_3{}^-$ ions, 258
^{119}Sn NMR spectroscopy, 271
(002) plane, 314
(211), 315
(311) crystalline plane, 315
(DENs), 94
(EG), 311
(EOR), 320
$(salen)^+$ complexes, 219
(X_2-Salen) complexes, 219
(XRD, TEM, EDX, XPS), 310
(SH), 86
SH–Ag clusters, 87
β–FeOOH, Co_3O_4, 257
colloidal catalysts, 281
coordinatively unsaturated metal atoms, 141
ensembles, 150
methanol cross-over, 289
platforming, 140
volcano shaped curves, 150
chemical anchoring, 143
volcano-shaped curves, 141
$CuO–CeO_2$–*ZrO_2*, 200
$Ni–CeO_2$–*ZrO_2*, 185
corrosive, 142
Ostwald ripening, 144
surface reconstruction, 142

nanometer diameter, 7

1,2-benzoquinone, 245
1,6-hexanediacid, 6
1-butene, 80

2,3-dimethylhydroquinone, 222
2-methylhydroquinone, 222
3-aminopropyl triethoxy silane, 196
3-dimensional silica network, 77
3-methylcatechol, 222

4-benzoquinone, 241

a surface sol–gel (SSG) method, 56
absorption peaks, 258
acetylacetonate, 280
acetylene/ethylene hydrogenation, 284
acetylides, 40
acid catalyzed polymerization, 140
acid strength, 77
acid–base strength, 260
acidic hydrosol, 273
acidic sites, 77
acidic working conditions, 322
acrolein, 147
acrylonitrile, 147
activated carbon, 42, 311
activation conditions, 103
activation energy, 236
activation of dioxygen, 45
activation-controlled region, 320
active phase, 257
active site, 5
active sites, 1, 2, 92, 183, 184, 208, 215, 234, 255, 262, 322
activity, 2, 39, 44, 49
adsorbates, 141
adsorbed molecules, 18
adsorption, 46
Ag, 81
Ag nanoparticles, 86
Ag^+, 278
Ag-(S)-$(CH_2)_3$-Si-$(OCH_3)_3$, 84
Ag/SiO_2 catalyst, 81
Ag/SiO_2 nanocomposites, 87
agglomerations, 314
aggregation, 262
aggregation of particles, 283
aggregation–desaggregation process, 264
AgL_2 type, 278
$AgNO_3$, 278
AgOH, 278
Al ions, 4
alcohol, 4
alkaline electrolytes, 290
alkaline fuel cells, 290
alkanethiolate monolayer shell, 292
alkoxide dimer, 4
alkyl anthraquinone, 50
alkylation, 80, 139
allotropic metastable forms, 56
alloy composition, 302
alloy nanoparticles, 290
alloy-type compound, 295
alumina supported Pt thin films, 16
aluminum oxide, 4
aluminum oxyhydroxide, 4
aluminum substrate, 7
ambient, 58
amine groups, 2
amino acids, 5
ammonia, 142
amorphous, 226
Amorphous Silica, 65
amorphous silicas, 58
an iron oxide, 223
anatase, 56, 59
anhydrous, 57
anode catalyst, 310
anode catalysts, 320
aqua regia, 42
aqueous hydrolysis, 63
aromatics, 184
as Colloids, 134
as-synthesized, 66

assembly on carbon support materials, 291
asymmetric, 64
asymmetry, 26
atom-molecule interactions, 1
atomic arrangements, 9
atomic compositions, 292
atomic layer, 7
atomic ratios, 316
Au, 9, 40, 42, 46, 49, 91, 93, 96, 99, 100, 101, 105, 107, 108, 109
Au catalyst, 50
Au catalysts, 40
Au nanoparticle catalysts, 301
Au nanoparticles, 47, 49
Au particles, 46
Au supported, 48, 49
Au^0, 43, 45, 46
Au^{3+}, 40, 42, 43, 45, 46
Au°, 42
Au^{n+}, 45
Au_{55} particles, 46
Au(OH), 46
$Au(OH)_3$, 46
Au–Pt, 196, 214, 215
Au-anatase catalyst, 60
Au-brookite catalysts, 60
Au/Al_2O_3, 50
Au/C catalyst, 299
Au/Fe_2O_3, 47
Au/Pd alloy, 50
Au/SiO_2, 87
Au/TiO_2, 46
Au/ZnO, 50
AuPt nanoparticles, 290, 301
autonomous, 35
autonomously, 31, 33
autothermal reforming, 185
average particle size, 315

back bonding, 14, 18
back-donation, 16, 18
band gap, 132
band structure, 128
band–band electron transition, 77
barium hexaaluminate, 4
basic hydrosols, 272
bcc, 141
benzene, 149, 194, 199, 237
BET surface area, 77, 222
bicyclic siloxane compounds, 6
bifunctional catalyst, 140
bifunctional catalysts, 144
bifunctional catalytic mechanism, 290
bifunctional electrocatalytic properties, 302
bifunctional mechanism, 302
bilayers, 6, 46
Bimetallic Au_mPt_{100-m} nanoparticles, 292
Bimetallic AuPt composition, 290
bimetallic AuPt metals, 303
bimetallic AuPt nanoparticles, 302
bimetallic catalyst, 283
bimetallic catalysts, 91, 92, 93, 105, 109, 110, 303
bimetallic catalytic properties, 291
bimetallic clusters, 3, 144
bimetallic composition, 290, 291, 302, 303
bimetallic interaction, 257
bimetallic miscibility gap, 303
bimetallic nanocrystalline core, 294
bimetallic nanoparticle catalysts, 303
bimetallic nanoparticles, 94, 154, 196, 215, 218
bimetallic palladium–tin catalyst, 281
bimetallic particles, 144
bimetallic surface composition, 303
bimetallic surface, 300
binding energies, 316
biosys calculation, 273
biotin, 8
Bond Thompson mechanistic proposal, 46
bridges, 6
bromide, 185
brookite, 56, 68
Brust method, 93
Brönsted acidic site, 77
Brønsted acid sites, 144
buta-1,3-diene hydrogenation, 283
butadiene, 241
butadiene hydrogenation, 281

cages, 2
calcination, 276, 294
calcination condition, 300
calcination temperature, 297, 303
calcination treatment, 294
calcined Au/Fe_2O_3, 47
capping shells, 294
carbenium ion intermediates, 139
carbon dioxide, 237
carbon monoxide, 47, 237
carbon monoxide oxidation, 43
carbon nanotubes, 7, 131
carbon-supported gold and gold–platinum catalysts, 291
carbon-supported gold nanoparticle catalyst, 300
carbon-supported PtSn catalysts, 312
carbonyl, 144
Cassiterite SnO_2 (rutile-type structure), 268
Casting microprobe analysis, 277
catalysis, 1, 46, 153, 234, 290
catalyst, 39, 40, 42, 44, 47, 48, 50, 51, 131, 222
catalyst activation, 91
catalyst formulations, 92
catalyst performance, 320
catalyst precursors, 93
catalyst preparation, 291
catalysts, 39, 42, 43, 44, 45, 46, 47, 48, 49, 50, 51
  thin-film, 13
catalytic, 23, 25, 27, 31, 33, 36, 45
catalytic activities, 55, 290, 319
catalytic activity, 46, 81, 281, 303
catalytic activity and selectivity, 183, 184, 200, 215
catalytic cycle, 42
catalytic mechanism, 302
catalytic oxidation, 140
catalytic properties, 302

catalytic property, 291
catalytic reaction, 302
catalytic reactions, 81, 290
catechol, 221
cationic, 42, 46
cationic gold, 42, 45
cationic gold species, 66
cationic surfactant, 273
cavity, 6
cell lifetimes, 47
centrifugation, 56
CeO_2, 185, 190, 191, 193, 202, 207, 208, 215
CeO_2, ZrO_2, 205
CeO_2/ZrO_2, 195
cethyl triammonium bromide (CTAB), 273
cetyltrimethylammonium, 185
channel, 6
channels, 2, 7, 64
chemical anchoring, 143, 144
chemical vapor deposition, 154
chemisorption, 142, 274
chemisorption energy, 15
chloride stannic ($SnCl_4$, $5H_2O$), 267
chronoamperometry, 312
cinnamic acid, 6
close-packed crystal faces, 140
clusters, 92, 93
CO, 47, 103, 105
CO adsorption, 291
Co atoms, 6
CO binding properties, 303
CO binding to transition metal surfaces, 16
CO chemisorption, 16
CO chemisorption energy, 18
CO conversion, 61
Co nanoparticle catalysts, 153
Co nanoparticles, 159
CO oxidation, 39, 45, 46, 47, 49, 51, 55, 58, 60, 65, 66, 91, 93, 100, 103, 104, 105, 107, 108, 109, 110, 290
CO oxidation catalyst, 45
CO oxidation reaction, 50
Co silicide nanoparticles, 155
CO stretching frequencies, 104, 105
Co-AlPO, 6
CO-like species, 290
co-planar, 234
cocomplexation, 3
Coiled nanowires, 157
colloid agglomeration, 74
colloid, 311
colloidal methods, 121
colloidal nanoparticles, 93
colloidal oxide synthesis, 257, 283
colloidal solution, 56
complete oxidation of ethanol, 310
Composite silver catalyst, 81
composition, 310
condensation, 77
condensation reaction, 81
consecutive mechanism, 283
controlled surface reactions, 255
Controlled surface reactions, 256
conventional methods, 3
coordination number, 183, 193, 215
coordination numbers, 184
coprecipitation, 185
coprecipitation synthesis, 186, 187
core-shell nanostructure, 310
core-shell structure, 77
corners, 281
cost reduction, 73
Cr_2O_3, 257
cracking, 81, 139, 222
crosslinking agent HSi $(OC_2H_5)_3$, 74
crosslinking agent TrEOS, 75
crystal faces, 140, 143
crystal phases, 84
crystal structure and growth direction, 124
crystalline, 59, 226
crystallinity, 226
crystallite morphology, 59
crystallite size, 188, 194, 202
crystallographic differences, 59
crystallographic structure, 120
Cu(5-X-salen) complexes, 220
Cu(salen) complexes, 220
cuboctahedral, 45
CuO–CeO, 201
$CuO–CeO_2–ZrO_2$, 202, 207, 208, 215
CuO/SiO_2, 87
custom design, 2
cyclic voltammetric (CV), 298
cyclic voltammetry, 312
cyclic voltammetry, chronoamperometry, 310
cyclic voltammograms, 318
cyclopentadienone, 237, 241
cyclopentane, 145

De-anchoring, 144
deactivation, 185, 190, 195, 196
Debye–Waller, 161
decomposition, 236
degree of alloying, 315
dehydro-condensation, 140
dehydrocyclyzation, 139
dendrimer, 2, 91, 94, 96, 97, 98, 99, 100, 101, 102, 103, 105, 108, 110
dendrimer encapsulated nanoparticles, 94
dendrimer-assisted method, 2, 3
ifp.fr, 255
DENs, 94
density functional theory, 14
density of states, 14
desulphurization, 185
detailed nanostructure, 321
diameter, 46
diethylene glycol, 75, 81
differential thermal analysis (DTA) curves, 84
digestion methods, 186
digestion synthesis, 186
dihydroxybenzene conversion, 225
dilated Pt lattice parameter, 322
dilation of the Pt lattice parameter, 322
dimeric copper acetate, 209, 210, 215
dimeric copper acetate complexes, 209
dimeric copper acetates, 215
dioxane, 75, 81
direct alcohol fuel cells (DAFCs), 309

direct bonding, 14
direct bonds, 18
Direct methanol fuel cells (DMFCs), 289
dispersing agents, 273
dispersion, 140, 184, 185, 188, 196, 201, 205, 208, 212, 215
distribution, 257
DOS, 18
drug delivery, 6
dual catalytic role, 177

E-α-phenylcinnamic acid, 6
edges, 281
EDX, 168
EDX analyses, 315
EELS, 223
eggshell, 277
eggshell repartition, 257
electrical conductivity, 8
electro-optical properties and quantum confinement, 126
electroactivities, 312
electrocatalysts, 310
electrocatalysts fuel cell reactions, 290
electrocatalytic activities, 291
electrocatalytic activity, 298, 301, 302
electrocatalytic reduction of oxygen, 298
electrochemical characterization, 298
electrochemical surface areas (ESA), 318
electron affinity, 40
electron transfer number, 300
electron withdrawing, 211, 214
electronegativity, 64
electronic effect, 318
electronic state, 46
electrooxidation, 322
electrophilic, 259
electrostatic adsorption, 274
electrostatic interaction, 256
enantioselectivity, 6
endothermic peaks, 84
energy diagram, 134
energy dispersive X-ray, 168
energy-dispersive X-ray (EDX) spectroscopy, 64
enzyme, 5
epoxidation, 197, 199, 215
ethanol adsorption, 321
ethanol electro-oxidation, 319
ethyne, 40
ethyne hydrochlorination, 40, 41, 42, 43
eutectic temperatures, 155
EXAFS, 161

face-centered cubic (fcc) structure, 315
faces (1 1 1) and (1 0 0), 260
factor analysis, 222
fcc crystals, 141
Fe_2O_3, 148
$Fe(OH)_3$ (bernalite), 225
Fe/MFI, 148
feed rate, 224
FeOOH (iron oxyhydroxide), 225
field emission microscope, 140
Fischer–Tropsch, 178
for back-bonding, 17
for direct bonding, 17
formic acid, 141
FTIR characterizations, 291
fuel cell, 47, 185, 290, 320
fuel cell catalyst, 290
fuel cell cathode reactions, 303
fuel cell reactions, 291
fuel cells, 47, 52, 177, 185, 200
fully ligated metal ions, 144
fumed silica, 56, 66
functional groups, 6
functionalization, 68

gasoline, 139
gelation, 77
glassy component, 226
global kinetic, 252
glycerate, 48
glyceric acid, 49
glycerol, 48
glycerol oxidation, 48, 49
glycerol/NaOH ratio, 49
gold, 25, 26, 28, 29, 30, 31, 39, 40, 42, 44, 45, 46, 47, 49, 51, 142, 150
gold catalysts, 43, 46, 47, 48, 55
gold cluster diameters, 46
gold hydroxyl precursor, 59
gold nanocatalysts, 56, 66, 68
gold nanocrystals, 43, 44, 45, 46, 52
gold nanoparticles, 42, 44, 45, 46, 60, 65, 66, 290
gold particles, 46, 61
gold precursor, 56
gold precursors, 62
gold–platinum (AuPt) nanoparticles, 290
gold-based alloy catalysts, 291
gold-based alloy nanoparticles, 291
gold-based bimetallic catalysts, 291
gold-based bimetallic nanoparticle catalysts, 303
gold-core, 290
grain growth, 226
grain size, 118
graphite, 48
grazing incidence, 160
green oil, 284
growth, 143

H$_2$O$_2$, 51
H/D exchange, 145, 146
half-cells., 319
Hammer and Nørskov, 14
heat of adsorption, 141, 142
heats of chemisorption, 142
heats of formation, 142
heterocatalyst, 133
heterogeneous, 1, 42
heterogeneous catalysis, 255
heterogeneous catalyst, 40
heterogeneous catalysts, 50
hexane, 6
$HgCl_2$/carbon, 40
high corrosive resistance, 322
high dispersion, 81
high efficiency, 81
high octane gasoline, 140

high stability, 81
highest occupied molecular orbital (HOMO), 14
histograms, 314
HN model, 14
HOMO, 16, 18
Horiuti–Polanyi mechanism, 280
Horvath–Kawazoe (HK) method, 75
$HSi(OC_2H_5)_3$, 77
hybrid orbitals, 17, 18
hydrated oxides, 117
hydrocarbon reforming, 149
hydrocarbon conversions, 139
hydrocarbons, 47
hydrochlorination, 40, 41
hydrodechlorination, 144
hydrogen, 47
hydrogen abstraction, 48
hydrogen bonding, 234
hydrogen desorption, 318
hydrogen peroxide, 9, 50, 51
hydrogen tetrachloroaurate(III) trihydrate, 56
hydrogenation, 50, 194, 278
hydrogenation activity, 281
hydrogenation catalyst, 40
hydrogenations, 149
hydrogenolysis of hydrocarbons, 8
hydrolytic adsorption, 256
hydrolyzation, 87
hydrophobic surface, 165
hydrophobic tail, 4
hydroquinone, 221
hydrosol, 271
hydrosols, 261
hydrothermal, 59
hydrothermal synthesis, 56, 185, 186, 188, 189, 190, 195, 215
hydroxyl, 56, 235
hydroxyl groups, 5, 63, 260
hydroxylation, 209, 210, 215
hydroxylations, 199

i-propyl, 81
immobilization, 65
impregnation, 42, 50
in situ, 163, 177
incipient wetness impregnation, 271
indanone, 237
indene, 237
infrared spectra, 105
infrared spectroscopy, 91, 100, 101
interaction, 66
interface, 62, 66
interfacial contact, 59
interfacial tension, 24, 28, 29, 30, 31, 35, 36
interfacial tensions, 28
intermolecular, 234
internal oxolation, 259
intramolecular, 235
intrinsic resistance, 322
Ionic exchange, 256
ionic strength, 264
iron, 142
iron oxide, 222
isobutane, 80
isoelectric point, 261
isoelectronic point (IEP), 55
isolated particles, 283
isomer shift δ, 274
isomerization, 81, 139

kinetic parameters, 236
kinetic point of view, 266
kinetic selectivity, 283

La-doped CeO_2, 46
laser vaporization, 154
lattice, 226
lattice parameters, 315
lepidocrocite, 223
Lewis acid sites, 4, 144
Lewis acidic sites, 77
ligand interactions, 163
lipid, 6
loading, 49
long utilizing lifetime, 81
lowest unoccupied molecular orbital (LUMO), 14
LUMO, 16, 18

maghemite, 223
magnetite, 223
maleic acid anhydride, 147
Mars and van Krevelen, 147
mass spectral, 235
mass-transport controlled region, 321
maximum power density, 321
MBMS, 222
MCM-41, 6
mean particle size, 312, 314
mechanical strength, 8
membrane electrode assemblies (MEAs), 312
mercuric chloride, 42
mesopore, 185, 189
mesoporous silica, 56, 62, 68
mesostructured, 62
metal agglomeration, 144
metal alkoxide, 4, 5
metal catalysts, 149
metal complexes, 183, 184, 209, 213, 214, 215, 216, 219, 220
metal nanoparticles, 13
metal oxide nanoparticle, 74
metal oxide nanoparticles, 4
metal oxide precursor, 58
metal oxides, 55
metal silicides, 157
metal–metal interaction, 318
metal-alkoxide, 63
metal-support interactions, 18
metallic bands, 18
metallic colloidal nanoparticles, 257
metallic precursors, 256
metastable phases, 59
methane combustion, 4
methanol, 47
methanol electrooxidation, 310
methanol oxidation reaction, 290, 298
methanol-to-gasoline, 139
methylbenzoquinone, 237, 245
methylcyclopentadienone, 237
MFI, 140
micro-mesoporous structure, 77
micrometer length, 7
microstructure, 310
mildly oxidative, 222
model, 14
modified polyol method, 322
modified two-phase method, 292
molecular adsorption, 14
Molecular Adsorption
Hückel molecular orbital theory, 16
molecular and atomic level, 9

molecular beam mass spectrometer, 222
molecular cluster, 92
molecular clusters, 105
molecular level, 257
molecular precursors, 92
molecular sieves, 139
monolayer, 66
monolayers, 46
monomeric alkoxide-amine, 4
monometallic, 257
monometallic PdO catalyst, 283
monomodal particle size distribution, 256
monomodal particle size distributions, 268
morphology, 257
motions, 9
multi-walled, 8
multicomponent oxide surfaces, 65
multimetallic, 257
multisite complexation model (MUSIC), 260, 274
multivariate, 222
Mössbauer spectroscopy, 42, 46

N$_2$ adsorption on Fe, 142
n-Decane, 195
n-heptane, 280
n-pentane, 81
Na_2PdCl_4, 266
NaCN leaching, 46
nano, 40
nano-sized, 3, 7
nano/micron, 25
nanocat, 222
nanocrystal core, 291
nanocrystalline, 46
nanocrystalline CeO_2-supported gold catalyst, 47
nanocrystalline gold, 51
nanocrystals, 77
nanomachinery, 9
nanomachines, 2, 9
nanomaterials, 2
nanometer scale, 255, 284
nanoparticle preparative techniques, 93
nanoparticle syntheses, 93
nanoparticles, 39, 48, 55, 59, 68, 104, 222, 274
nanoreactor, 6
nanoscale, 23, 25, 31, 32, 36
nanoscale gold, 290
nanoscale sizes, 290
nanoscaled control, 255
nanostructured Au and AuPt catalysts, 300
nanostructured catalysts, 298
nanostructured materials, 55
nanostructures, 2, 9
nanotubes, 116
NaOH, 48
narrow size distribution, 2
neo-pentane, 146
neutralization, 266
Ni–CeO_2–ZrO_2, 215
nickel, 187, 189, 190, 191, 192, 195, 215
NiO, 264
nitrogen adsorption–desorption isotherms, 74
nitrogen oxides, 148
nitrous oxide, 149
NO, 148
NO_2, 148
NO_x, 148, 149
noble metals, 257
nonpolar solvent, 4
nonsymmetric growth, 172
NOx, 110
nucleation, 143, 257, 266
nucleophilic, 259

O–H vibration, 86
o-benzoquinone, 237
octahedron, 59
OCV (open circuit voltage), 321
olation reactions, 259
olefin, 283
oligomers, 284
oligosilicates, 77
orbitals, 17
ordered mesopores, 64
ordered mesoporous materials, 65
organic monolayer encapsulation, 291
organometallic precursors, 257
Ostwald ripening, 267
output power density, 321
oxidation, 6, 39, 40, 47, 147
oxidation centers, 45
oxidation of alcohols, 48
oxidation of CO, 43, 45, 46, 47, 51
oxidation of methanol, 298
oxide carrier, 257
oxide channels, 7
oxide hydrosols synthesis, 258
oxide monolayers, 65
oxide precursor, 4
oxide supported gold and platinum catalysts, 291
oxide-supported gold, 291
oxide-supported metals, 13
oxidizing, 47
oxo-ions, 140, 148, 149, 150
oxygen, 223
oxygen defects, 127
oxygen reduction reaction, 290
oxygen reduction reaction (ORR), 289, 298
oxygen-containing species, 322
oxyhydroxymetal, 4

palladium hydroxide $Pd(OH)_2$, 259
palladium nitrate, 258
palladium oxide colloidal particles, 258
palladium proton adducts, 144
PAMAM dendrimers, 94
paramagnetic species, 191
partial charge model, 258
partial oxidation, 148
particle aggregation, 281
particle number density, 49
particle preparation methods, 92
particle size, 92, 183, 184, 195, 201, 214, 215, 216, 321, 322
particle size distribution, 280, 314
particle size distributions, 261
particle size, 215, 300
particles, 40
patterned channels, 7
Pd carbonyl, 144
Pd monometallic catalyst, 284

Pd_2Sn alloy, 277
$Pd(H_2O)_2ClOH$, 266
$Pd(H_2O)_4{}^{2+}$.[26], 258
$Pd(OH)_2(H_2O)_2$, 258
Pd, Sn, 257
Pd–Ag, 257
Pd–Sn, 257
Pd/ZnO, 50
PdAg catalyst, 284
$PdCl_3(H_2O)^-$, 266
PdO crystal, 261
PdO particles, 259
PdO-supported catalysts, 271
PdOSn catalyst, 283
PdSn catalyst, 283
peak output power density, 323
PEFCs, 47
pentenyne, 237
performance, 310
perpendicular fashion, 235
pH, 256, 259
phase diagram, 174
phase properties, 302
phase segregation, 301
phase separation, 74
phase-segregated, 302
phased-segregated metals, 297
phenol, 147, 149
phenolic compounds, 222
phenyl groups, 6
phenylacetylene hydrogenation reaction, 280
photocatalytic, 59
photoluminescence, 126, 156
photopolymerization, 7
physical surface area, 321
plasma assisted pyrolysis, 8
platinum, 25, 26, 27, 28, 30, 31, 33, 35, 140, 150
platinum–gold, 30
platinum/gold, 27, 28
poison, 47
poisonous species, 290
polar head group, 4
polar solvent, 4
polarization curves, 320
polyamidoamine dendrimers, 94
polymer electrolyte fuel cells (PEFC), 47
polyol preparation method, 310
polyols, 48
polyunsaturated compounds, 278
pore size distribution, 63, 75
pore sizes, 185, 189
pores, 2
porous membrane, 120
post treatments, 256
potentiometric titration method, 261
powder X-ray diffraction (XRD), 58
precious metals, 139
precursor, 277
preferential oxidation, 196, 200, 201, 202, 206, 208, 215, 218, 219
preferential oxidation of CO, 215
preparative routes, 92
primary products, 243
product distribution, 236
promoters, 283
propylene epoxidation, 59
proton exchange membrane fuel cells (PEMFCs), 289
PROX reactions, 201
pseudo-first-order, 236
Pt, 103, 105
Pt (111), (200), (220), 315
Pt anode, 47
Pt catalysts, 103
Pt core/Sn shell structure, 321
Pt fcc crystalline structure, 322
Pt nanoparticle, 105
Pt particles, 3
Pt,[26], 9
Pt–H adducts, 146
Pt–Re, 144
Pt-Au, 91, 96, 97, 99, 101, 107, 108, 109, 110
Pt/C catalyst, 312
Pt/mordenite, 140, 146
Pt/SiO_2, 87
PtRu catalyst, 310
PtSn catalysts, 310
pyridine adsorption, 75
pyridine adsorption/desorption infrared spectra, 77

quadrupole splitting Δ, 274
quasi-steady-state current density, 320
quasielastic light scattering (QELS) technique, 264
quinones, 245

R. Anderson principle, 259
Raman spectroscopy, 160
Re, 144
re-activated catalyst surface, 301
re-usability, 73
reactivity, 222
reference electrode, 312
reflux, 58
reformate, 47
regeneratability, 81
regeneration, 73
relationships between structure and reactivity, 255
removal of the poisonous species, 290
renewable energy source, 310
reverse micelles, 4
Rh complex, 6
Rh or Pd complex, 6
root growth, 155
rotating disk electrode (RDE), 299
rutile, 59

SAED, 223
salen complexe, 211
salen complexes, 211, 213, 214, 215
SAN, 159
saturated calomel electrode (SCE), 312
scanning electron microscopy (SEM), 59
scanning transmission electron microscope (STEM), 58
Schiff base, 211, 214
second order perturbation theory, 14
secondary products, 243, 245
selective, 40
selective hydrogenation, 256
selective oxidation, 50, 51, 52, 148, 197, 210, 215
selective oxidation reaction, 81
selectivity, 2, 6, 47, 278
self-aligned nanostructures, 159

shape-selectivity, 2
Si atoms, 6
silane, 176
silica network, 77
silica sol, 75
silicon oxide nanowires, 168
silicon-based nanowires, 154
siloxane units, 6
silsesquioxane, 5
silver, 142
silver nitrate, 278
silver oxide, 81
silver sol, 82
single atoms, 150
single-phase nanomaterials, 296
single-walled, 8
single-walled carbon nanotubes, 153
sintering, 62, 185
SiNW, 154
SiO_2, 74
size, 257
size distribution, 312
small cluster-size effects, 318
Sn core-Pt shell, 323
Sn core-Pt shell structure, 319
Sn core/Pt shell nanostructure, 321
Sn^{IV} complex, 274
$Sn(OH)^{3+}$, 268
$Sn(OH)_6{}^{2-}$, 268
SnO, 264
SnO_2, 264, 267
SnO_2 (101), 315
snow, 143
sol-gel, 91, 99, 100, 104, 105
sol-gel methods, 81
sol–gel process, 74
sol–gel technique, 87
solid–liquid–solid, 155
solubility, 267
solution–liquid–solid, 155
sonication, 59
specific activity, 281
stabilization, 65
stabilizing agent, 264, 273
stair-step mechanism, 133
standard electrode potential, 40
steam reforming, 184, 185, 186, 194, 195, 207, 217, 219
steam/autothermal reforming, 200
STEM imaging, 61
stepwise preparation routes, 322
steric hindrance, 5
STM, 45
stretching frequency, 104
structure sensitive, 2, 256
structure–activity relationships, 92, 285
styrene, 237
sublimation, 224
sulfated zirconia, 73
supercritical CO_2, 50
support, 45
support effects, 55, 91, 108, 109
support interaction, 183
support interactions, 184, 213, 214
support structures, 56
supported, 42, 44
supported gold catalysts, 48
supported gold nanoparticles, 48
supported heterogeneous catalysts, 255
supported metal oxides, 200, 214
supported metals, 184, 214, 216
supported particles, 255
supported Pd catalysts, 271
supported PdAg/α-Al_2O_3 bimetallic catalyst, 284
surface acidity, 77
surface adsorption properties, 291
surface area, 3, 188, 190, 195, 196, 202, 215
surface areas, 185
surface binding properties, 297
surface binding sites, 303
surface cations, 132
surface composition, 300
surface crystallographic planes, 2
surface defects, 3
surface density, 4
surface grafting, 255
surface modification, 66, 283
surface organometallic chemistry (SOMC), 256
surface photovoltage spectroscopy (SPS), 77
surface segregation, 154, 300
surface sol–gel, 62
surface-related transitions, 77
surfactant-assisted synthesis, 121
sursaturation values, 266
synergistic catalytic effect, 290
synergistic effect, 290
synthesis methodologies, 62
synthesized, 59
SZ/SiO_2, 74

TEM image, 64
temperature, 224
temperature effect, 162
temperature-programmed desorption of ammonia (TDP), 77
tertiary products, 245
tetrachloroaurate(III) trihydrate, 57
tetraethoxysilane, 74, 75
tetraethylorthosilicate, 57
tetragonal SnO_2, 322
tetraisopropyltitanate, 56
the chemical environment of particles, 310
The diffraction patterns, 294
the electronic effect, 322
the full width at half-maximum (FWHM), 315
thermal calcination, 291, 302
thermo-catalytic, 222
thermodynamic and kinetic properties, 118
thermogravimetric analysis (TGA), 84
thermohydrolysis, 266
thin film of SiNW, 173
thin films, 13
three-way catalysts, 185
Ti, 5
Ti alkoxide, 5
tin oxide-rich surface, 322
TiO_2, 45, 46

TiO_2 anatase, 68
TiO_2 brookite, 68
TiO_2 monolayer, 66
TiO_2 monolayers, 68
TiO_2 sublayer, 68
TiO_2-modified fumed silica, 66
TiO_2/SiO_2, 87
tip growth, 154
titania, 56, 59
titanium alkoxy group, 5
titanium oxide, 62, 133
titanium tetrachloride, 56
titanium(IV) butoxide, 57
titanosilicates, 197, 198, 200
titration curve, 259
toluene hydrogenation, 91, 103, 105
TPD-NH_3 curves, 75
transformation, 226
transition metal ions, 144
transition metal oxide, 115
transition metal oxides, 140
transmission electron microscopy, 58, 312
treatment conditions, 291
trimethylpentanes (TMPs), 80
trimethylsiloxane, 5
trivalent iron, 234
tubes, 7
tungsten, 142
turn over number, 280, 281
turnover frequencies, 209, 211
two-phase protocol, 291
two-phase synthesis, 291, 302
tyrosine, 209

uniform composition, 2, 3
uniform-sized, 3
unit cell parameter, 187
UV–visible spectroscopy, 258

vapor–liquid–solid, 155
vinyl acetylene, 237
Vulcan XC-72R, 311

water, 237
water gas shift reaction, 46

X-ray diffraction, 84, 259
x-ray diffraction (XRD), 294
X-ray extended absorption spectroscopy, 61
X-ray photoelectron spectroscopy, 46, 281, 312
XANES, 161
XAS, 160
XPS, 316
XRD patterns, 311

zeolite, 2
zeolite Beta, 80
zeolite cages, 144
zeolite Y, 81
zeolites, 2, 73, 139, 184, 209, 211, 213, 214, 216
zinc oxide, 132
zirconium butoxide, 74
$ZnCl_2$/carbon, 40
ZnO, 257
Zr $(OC_4H_9)_4$, 74
ZrO_2, 74, 187, 188, 190, 191, 193, 203, 207, 215, 257
ZrO_2 nanoparticles, 75
ZSM-5, 81